PROCEEDINGS OF SPIE

SPIE—The International Society for Optical Engineering

Laser Optics 2000

Control of Laser Beam Characteristics and Nonlinear Methods for Wavefront Control

Leonid N. Soms
Vladimir E. Sherstobitov
Editors

26–30 June 2000
St. Petersburg, Russia

20010927 028

Organized by
Institute for Laser Physics (Russia)
All-Russia Scientific Center, S.I. Vavilov State Optical Institute
General Physics Institute, Russian Academy of Sciences
P.N. Lebedev Physical Institute, Russian Academy of Sciences
A.F. Ioffe Physico-Technical Institute, Russian Academy of Sciences
Russian National Center of Laser Physics, St. Petersburg State University
St. Petersburg Institute of Fine Mechanics and Optics (Russia)
Scientific Council on Coherent and Nonlinear Optics, Russian Academy of Sciences
SPIE—The International Society for Optical Engineering
SPIE Russia Chapter
OSA—Optical Society of America
ROS—Rozhdestvensky Optical Society (Russia)
Government of St. Petersburg (Russia)
ISTC—International Scientific and Technological Center



Volume 4353

DISTRIBUTION STATEMENT A
Approved for Public Release
Distribution Unlimited

REPORT DOCUMENTATION PAGE

Form Approved OMB No. 0704-0188

Public reporting burden for this collection of information is estimated to average 1 hour per response, including the time for reviewing instructions, searching existing data sources, gathering and maintaining the data needed, and completing and reviewing the collection of information. Send comments regarding this burden estimate or any other aspect of this collection of information, including suggestions for reducing this burden to Washington Headquarters Services, Directorate for Information Operations and Reports, 1215 Jefferson Davis Highway, Suite 1204, Arlington, VA 22202-4302, and to the Office of Management and Budget, Paperwork Reduction Project (0704-0188), Washington, DC 20503.

1. AGENCY USE ONLY (Leave blank)	2. REPORT DATE	3. REPORT TYPE AND DATES COVERED
	14 September 2001	Conference Proceedings

4. TITLE AND SUBTITLE

Laser Optics 2000: Control of Laser Beam Characteristics and Nonlinear Methods for Wavefront Control (Volume 4353)

5. FUNDING NUMBERS

F61775-00-WF

6. AUTHOR(S)

Conference Committee

7. PERFORMING ORGANIZATION NAME(S) AND ADDRESS(ES)

Institute for Laser Physics
12 Birzhevaya line
St. Petersburg 199034
Russia

8. Performing Organization Report Number

N/A

9. SPONSORING/MONITORING AGENCY NAME(S) AND ADDRESS(ES

EOARD
PSC 802 Box 14
FPO 09499-0200

10. SPONSORING/MONITORING AGENCY REPORT NUMBER

CSP 00-5049

11. SUPPLEMENTARY NOTES

Conference Proceedings in five volumes. Proceedings of SPIE – The International Society for Optical Engineering, 26-30 June 2000, St. Petersburg, Russia. Volumes 4350 (Solid State Lasers), 4351 (High-Power Gas Lasers), 4352 (Ultrafast Optics and Superstrong Laser Fields), 4353 (Control of Laser Beam Characteristics and Nonlinear Methods for Wavefront Control), and 4354 (Semiconductor Lasers and Optical Communication), ISSN 0277-786X

12a. DISTRIBUTION/AVAILABILITY STATEMENT

Approved for public release; distribution is unlimited.

12b. DISTRIBUTION CODE

A

ABSTRACT (Maximum 200 words)

The Final Proceedings for the Tenth Conference on Laser Optics, 26-30 June 2000. This is an interdisciplinary conference. Topics include generation of ultrashort light pulses, application of nonlinear correction techniques in adaptive optics and lasers, advanced methods of beam control and pointing; diode-pumped solid state lasers; high average power gas and solid-state lasers; and lasers in medicine and medical applications.

14. SUBJECT TERMS

EOARD, Adaptive optics, Gas lasers, Solid state lasers, Aberration correction

15. NUMBER OF PAGES

Five bound volumes

16. PRICE CODE

17. SECURITY CLASSIFICATION OF REPORT	18. SECURITY CLASSIFICATION OF THIS PAGE	19. SECURITY CLASSIFICATION OF ABSTRACT	20. LIMITATION OF ABSTRACT
UNCLASSIFIED	UNCLASSIFIED	UNCLASSIFIED	UL

PROCEEDINGS OF SPIE
SPIE—The International Society for Optical Engineering

Laser Optics 2000

Control of Laser Beam Characteristics and Nonlinear Methods for Wavefront Control

Leonid N. Soms
Vladimir E. Sherstobitov
Editors

26–30 June 2000
St. Petersburg, Russia

Organized by
Institute for Laser Physics (Russia) • All-Russia Scientific Center, S.I. Vavilov State Optical Institute • General Physics Institute, RAS • P.N. Lebedev Physical Institute, RAS • A.F. Ioffe Physico-Technical Institute, RAS • Russian National Center of Laser Physics, St. Petersburg State University • St. Petersburg Institute of Fine Mechanics and Optics (Russia) • Scientific Council on Coherent and Nonlinear Optics, RAS • SPIE—The International Society for Optical Engineering • SPIE Russia Chapter • OSA—Optical Society of America • ROS—Rozhdestvensky Optical Society (Russia) • Government of St. Petersburg (Russia) • ISTC—International Scientific and Technological Center

Supported by
Ministry of Science and Technical Policy of the Russian Federation • Ministry for Economics of the Russian Federation • Ministry for Education of the Russian Federation • Federal Agency for Conventional Weapons (Russia) • Russian National Foundation for Basic Research • SPIE—The International Society for Optical Engineering • Lawrence Livermore National Laboratory (USA) • European Office of Aerospace Research and Development (USA) • OSA—Optical Society of America • ISTC—International Scientific and Technological Center • Amada Corporation (Japan) • Jenoptic GmbH (Germany) • Corning Inc. (USA) • IRE-Polus Group (Germany)



Published by
SPIE—The International Society for Optical Engineering

Volume 4353

SPIE is an international technical society dedicated to advancing engineering and scientific applications of optical, photonic, imaging, electronic, and optoelectronic technologies.

AQ F01-12-2761



The papers appearing in this book compose the proceedings of the technical conference cited on the cover and title page of this volume. They reflect the authors' opinions and are published as presented, in the interests of timely dissemination. Their inclusion in this publication does not necessarily constitute endorsement by the editors or by SPIE. Papers were selected by the conference program committee to be presented in oral or poster format, and were subject to review by volume editors or program committees.

Please use the following format to cite material from this book:

Author(s), "Title of paper," in *Laser Optics 2000: Control of Laser Beam Characteristics and Nonlinear Methods for Wavefront Control*, Leonid N. Soms, Vladimir E. Sherstobitov, Editors, Proceedings of SPIE Vol. 4353, page numbers (2001).

ISSN 0277-786X
ISBN 0-8194-4043-4

Published by
SPIE—The International Society for Optical Engineering
P.O. Box 10, Bellingham, Washington 98227-0010 USA
Telephone 1 360/676-3290 (Pacific Time) • Fax 1 360/647-1445
http://www.spie.org/

Copyright© 2001, The Society of Photo-Optical Instrumentation Engineers.

Copying of material in this book for internal or personal use, or for the internal or personal use of specific clients, beyond the fair use provisions granted by the U.S. Copyright Law is authorized by SPIE subject to payment of copying fees. The Transactional Reporting Service base fee for this volume is $15.00 per article (or portion thereof), which should be paid directly to the Copyright Clearance Center (CCC), 222 Rosewood Drive, Danvers, MA 01923 USA. Payment may also be made electronically through CCC Online at http://www.directory.net/copyright/. Other copying for republication, resale, advertising or promotion, or any form of systematic or multiple reproduction of any material in this book is prohibited except with permission in writing from the publisher. The CCC fee code is 0277-786X/01/$15.00.

Printed in the United States of America.

Contents

ix *Laser Optics 2000 Program Committee*

SECTION 1 ELEMENTS OF LASER SYSTEMS AND WAVEFRONT CONTROL

1 **Novel method of solid state laser thermal lens intracavity correction by a modal liquid crystal adaptive lens with optical control** [4353-01]
I. R. Guralnik, P.N. Lebedev Physical Institute (Russia) and Samara State Univ. (Russia); I. V. Sozinova, Samara State Univ. (Russia)

9 **Static and dynamic models of liquid crystal wavefront correctors** [4353-02]
M. Yu. Loktev, Delft Univ. of Technology (Netherlands) and P.N. Lebedev Physical Institute (Russia); A. F. Naumov, P.N. Lebedev Physical Institute (Russia) and Univ. of Durham (UK); I. R. Guralnik, P.N. Lebedev Physical Institute (Russia) and Samara State Univ. (Russia)

17 **Tunable acousto-optic filters and their applications in laser technology, optical communication, and processing of images** [4353-03]
V. B. Voloshinov, V. N. Parygin, M.V. Lomonosov Moscow State Univ. (Russia); V. Ya. Molchanov, Moscow Steel and Alloys Institute (Russia)

23 **Electro-optic glasses and glass ceramics for elements controlling laser radiation** [4353-04]
G. O. Karapetyan, A. A. Lipovskii, V. V. Loboda, L. V. Maksimov, D. V. Svistunov, D. K. Tagantsev, B. V. Tatarintsev, A. A. Vetrov, S.I. Vavilov State Optical Institute (Russia)

29 **Effect of crystal orientation on a high-power Faraday isolator** [4353-05]
E. A. Khazanov, N. F. Andreev, O. V. Palashov, A. K. Poteomkin, A. M. Sergeev, Institute of Applied Physics (Russia); D. H. Reitze, Univ. of Florida (USA); O. Mehl, Technische Univ. Berlin (Germany)

41 **Spectral selectivity of volume phase gratings with highly reflective boundaries** [4353-06]
Yu. P. Udoev, St. Petersburg State Technical Univ. (Russia)

46 **Optimization of the structure parameters of high-efficiency gratings with multilayer dielectric coating for laser pulse compression** [4353-07]
V. D. Vinokurova, Institute for Laser Physics (Russia); R. R. Gerke, S.I. Vavilov State Optical Institute (Russia); E. G. Sall, Institute for Laser Physics (Russia)

51 **Influence of phase distortion of soft-edge ouput mirror on the characteristics of laser modes of unstable and plane-parallel resonators** [4353-08]
V. B. Karasev, V. V. Nazarov, E. S. Putilin, P. N. Fimin, V. Yu. Khramov, St. Petersburg State Institute of Fine Mechanics and Optics (Russia)

59 **Coherent beam focusing by a two sequentially arranged aperture system** [4353-09]
R. R. Letfullin, O. A. Zayakin, P.N. Lebedev Physical Institute (Russia)

69 **Synthesis of unstable resonator output mirrors with phase front compensation** [4353-10]
E. N. Kotlikov, V. N. Prokashev, E. V. Khonineva, St. Petersburg State Univ. of Aerospace Instrumentation (Russia)

SECTION 2 NONLINEAR MEDIA FOR LASER BEAM CONTROL

75 **Photodynamics of nonlinear fullerene-containing media** [4353-11]
I. M. Belousova, V. P. Belousov, O. B. Danilov, V. A. Grigor'ev, A. G. Kalintsev, Institute for Laser Physics (Russia); V. N. Zgonnik, Institute of High-Molecular Compounds (Russia); N. V. Kamanina, S.I. Vavilov State Optical Institute (Russia); A. P. Zhevlakov, A. V. Kris'ko, N. G. Mironova, E. N. Sosnov, E. A. Gavronskaya, V. A. Smirnov, M. S. Yur'ev, Institute for Laser Physics (Russia); A. N. Ponomarev, Astrin Ltd. (Russia); V. E. Yashin, Institute for Laser Physics (Russia)

84 **Photorefractive effects in novel polymer nanocomposites** [4353-12]
A. S. Kuzhelev, I. V. Yurasova, O. L. Antipov, Institute of Applied Physics (Russia); W. E. Douglas, Univ. Montpellier II (France); L. G. Klapshina, V. V. Semenov, G. A. Domrachev, T. I. Lopatina, Institute of Metallo-organic Chemistry (Russia)

92 **Decoupling nonlinear optical elements for powerful iodine laser** [4353-13]
L. M. Vinogradsky, V. A. Kargin, V. A. Krotov, S. K. Sobolev, N. V. Jidkov, Russian Federal Nuclear Ctr.; V. M. Mizin, State Scientific Ctr. (Russia); M. V. Pyatakhin, Yu. V. Senatsky, I. G. Zubarev, P.N. Lebedev Physical Institute (Russia)

101 **Record of dynamic and static holograms in thin fullerene-doped organic films** [4353-14]
N. V. Kamanina, L. N. Kaporskii, V. N. Sizov, D. I. Stasel'ko, S.I. Vavilov State Optical Institute (Russia)

106 **Light-induced scattering in laser radiation nonlinear optical limiting based on fullerene-containing media** [4353-15]
I. M. Belousova, V. A. Grigor'ev, O. B. Danilov, A. G. Kalintsev, A. V. Kris'ko, N. G. Mironova, M. S. Yur'ev, Institute for Laser Physics (Russia)

115 **Fullerene-doped polyimide systems as effective optical-power-limiting materials in visible and IR ranges** [4353-16]
N. V. Kamanina, S.I. Vavilov State Optical Institute (Russia); I. M. Belousova, I. V. Bagrov, Institute for Laser Physics (Russia); L. N. Kaporskii, S.I. Vavilov State Optical Institute (Russia); S. A. Tul'skii, A. P. Zhevlakov, Institute for Laser Physics (Russia)

121 **Nonstationary mixing in $AgGaSe_2$ crystal** [4353-17]
V. V. Apollonov, Yu. A. Shakir, General Physics Institute (Russia)

125 **Photorefractive properties of doped cadmium telluride crystals** [4353-18]
I. N. Agishev, A. L. Tolstik, Belarusian State Univ.; V. N. Yakimovich, O. K. Khasanov, Institute of Solid State and Semiconductor Physics (Belarus)

130 **Splitting effects and power saturation in cw resonant four-wave mixing with two strong fields** [4353-19]
S. A. Babin, S. I. Kablukov, Institute of Automation and Electrometry (Russia); U. Hinze, E. Tiemann, B. Wellegehausen, Univ. Hannover (Germany)

SECTION 3 CONTROL IN LASER OSCILLATORS

138 **Intracavity self-adapted photorefractive Fabry-Perot** [4353-20]
N. Dubreuil, L. Meilhac, S. Victori, G. Pauliat, P. M. Georges, A. Brun, J.-M. Jonathan, G. Roosen, Institut d'Optique (France)

145 **One- and two-axis laser cavities for dual-frequency operation and microwave generation** [4353-21]
M. Alouini, F. Bretenaker, M. Brunel, D. Chauvat, O. Emile, A. Le Floch, G. Ropars, M. Vallet, Univ. de Rennes I (France)

151 **Phase locking of the arrays of linear and ring lasers** [4353-22]
A. F. Glova, E. A. Lebedev, A. Yu. Lysikov, E. I. Musyona, S. B. Shchetnikov, Troitsk Institute for Innovation and Fusion Research (Russia)

157 **Creation and annihilation of wavefront dislocations in the process of frequency doubling of Bessel light beams** [4353-23]
V. N. Belyi, N. S. Kazak, B.I. Stepanov Institute of Physics (Belarus); N. A. Khilo, Division for Optical Problems in Information Technologies/NAS Belarus; A. A. Ryzhevich, E. G. Katranji, B.I. Stepanov Institute of Physics (Belarus)

164 **Resonator with Bessel-Gauss modes** [4353-24]
N. A. Khilo, E. G. Katranji, A. A. Ryzhevich, B.I. Stepanov Institute of Physics (Belarus)

172 **New method of formation of high-order Bessel light beams using biaxial crystals** [4353-25]
N. S. Kazak, B.I. Stepanov Institute of Physics (Belarus); N. A. Khilo, Division for Optical Problems in Information Technologies/NAS Belarus; E. G. Katranji, A. A. Ryzhevich, B.I. Stepanov Institute of Physics (Belarus)

183 **Single-frequency stabilized dye jet laser pumped with a Cu-vapor laser through a fiber** [4353-26]
V. I. Baraulya, S. M. Kobtsev, S. V. Kukarin, A. A. Pustovskikh, V. B. Sorokin, Novosibirsk State Univ. (Russia)

189 **Efficient autoscanned single-frequency cw dye laser** [4353-27]
S. M. Kobtsev, A. V. Korablev, S. V. Kukarin, V. B. Sorokin, Novosibirsk State Univ. (Russia)

194 **Time-resolved autocorrelation measurements of transient ultrashort-pulse formation** [4353-28]
V. A. Zaporozhchenko, B.I. Stepanov Institute of Physics (Belarus)

198 **Characteristics and kinetics of Ti:sapphire oscillator pumped by SH of double-pulse Nd^{3+}:YAG laser** [4353-29]
Yu. V. Zaporozhchenko, Belarusian-Japanese Joint Venture Lotis TII (Belarus)

SECTION 4 PHASE CONJUGATION AND LASER BEAM CONTROL

202 **Superhigh fidelity of phase conjugation at SBS using new-generation kinoform optics** [4353-30]
F. A. Starikov, Yu. V. Dolgopolov, S. A. Kovaldov, G. G. Kochemasov, A. V. Kopalkin, S. M. Kulikov, V. K. Ladagin, S. A. Sukharev, N. N. Gerasimenko, Russian Federal Nuclear Ctr.

214 **Powerful neodymium lasers with self phase conjugation** [4353-31]
T. T. Basiev, General Physics Institute (Russia); A. V. Fedin, A. V. Gavrilov, A. V. Ruliov, S. N. Smetanin, S. A. Kyalbieva, Kovrov State Technological Academy (Russia)

221 **Role of resonant refractive-index grating in a nonreciprocal Nd:YAG self-pumped phase conjugator** [4353-32]
O. L. Antipov, D. V. Chausov, V. V. Yarovoy, Institute of Applied Physics (Russia)

230 **Simulations of wavefront correction of distorted laser beams** [4353-33]
H. H. Klingenberg, Th. Hall, G. Spindler, DLR (Germany)

237 **Spiral laser beams** [4353-34]
E. G. Abramochkin, V. G. Volostnikov, P.N. Lebedev Physical Institute (Russia)

242 **Real-time control of the rotation rate of a particle trapped in a focused laser beam** [4353-35]
M. A. Rakhmatulin, S. P. Kotova, V. G. Volostnikov, P.N. Lebedev Physical Institute (Russia)

SECTION 5 DYNAMIC HOLOGRAPHY AND WAVEFRONT CORRECTION IN IMAGING

247 **Photorefractive four-wave mixing for optical image restoration** [4353-36]
Y. Takayama, Communications Research Lab. (Japan); A. Okamoto, Hokkaido Univ. (Japan); K. Araki, Communications Research Lab. (Japan)

256 **Relation between the wave aberration function and the phase transfer function in an adaptive optical system for Earth observation** [4353-37]
A. J. Smirnov, Univ. da Beira Interior (Portugal); A. B. Utkin, Institute for Laser Physics (Russia)

266 **Brillouin nonlinearity as a mechanism of dynamic holography** [4353-38]
O. Kotiaev, S. Uchida, Osaka Univ. (Japan); H. Sawada, Kinki Univ. (Japan)

273 **Dual-conjugate adaptive optics** [4353-39]
T.-L. Kelly, Univ. of Durham (UK); D. F. Buscher, Univ. of Cambridge (UK); P. Clark, C. N. Dunlop, G. D. Love, R. M. Myers, R. M. Sharples, A. Zadrozny, Univ. of Durham (UK)

281 **Analysis of spectrally modulated interferograms by recurrence nonlinear filtering method** [4353-40]
I. P. Gurov, St. Petersburg State Institute of Fine Mechanics and Optics (Russia); P. Hlubina, Silesian Univ. at Opava (Czech Republic)

287 **Processing of noisy signals by four-wave mixing** [4353-41]
V. V. Kabanov, B.I. Stepanov Institute of Physics (Belarus)

292 **Noise-immune interference fringe analysis by modification of local intensity histogram and 2D Fourier transform method** [4353-42]
S. De Nicola, Istituto di Cibernetica (Italy); P. Ferraro, Istituto Nazionale di Ottica Applicata (Italy); I. P. Gurov, R. Koviazin, M. V. Volkov, St. Petersburg State Institute of Fine Mechanics and Optics (Russia)

298 **Analysis of the associative properties of thin holograms with superposed registration** [4353-43]
A. S. Rubanov, L. M. Serebryakova, B.I. Stepanov Institute of Physics (Belarus)

308 **Phase-sensitive parametric image amplification: application to noiseless image amplification** [4353-44]
F. Deveaux, E. Lantz, Univ. de Franche-Comté (France)

SECTION 6 NONLINEAR DYNAMICS OF LASERS

315 **Cnoidal wave propagation in a medium with delayed response** [4353-45]
V. A. Aleshkevich, M.V. Lomonosov Moscow State Univ. (Russia); V. A. Vysloukh, Univ. Autónomo del Estado de Morelos (Mexico); Y. V. Kartashov, M.V. Lomonosov Moscow State Univ. (Russia)

323 **Formation and propagation of localized surface waves at the interface between the linear dieletric and photorefractive medium** [4353-46]
V. A. Aleshkevich, M.V. Lomonosov Moscow State Univ. (Russia); V. A. Vysloukh, Univ. Autónomo del Estado de Morelos (Mexico); Y. V. Kartashov, M.V. Lomonosov Moscow State Univ. (Russia)

333 **Nonfeedback nonresonant control of laser systems** [4353-47]
A. N. Pisarchik, Ctr. de Investigaciones en Óptica (Mexico)

344 **Delayed-feedback control of the chaotic dynamics of the optoelectronic system with a laser diode** [4353-48]
V. V. Jakutkin, S. P. Kotova, P.N. Lebedev Physical Institute (Russia); H. D. Lamaghapov, Samara Railway Engineering Institute (Russia)

353 *Author Index*

Laser Optics 2000 Program Committee

Chair

Artur A. Mak, Institute for Laser Physics (Russia)

Vice-Chairs

Alexander A. Andreev, Institute for Laser Physics (Russia)
Vladimir Yu. Venediktov, Institute for Laser Physics (Russia)

Scientific Secretary

A. F. Vassil'yev, Institute for Laser Physics (Russia)

Members

Zhores I. Alferov, A.F. Ioffe Physico-Technical Institute (Russia)
Pavel A. Apanasevich, B.I. Stepanov Institute of Physics (Belarus)
Sergey N. Bagaev, Institute for Laser Physics (Russia)
Nikolai G. Basov, P.N. Lebedev Physical Institute (Russia)
Yuri D. Berezin, Institute for Laser Physics (Russia)
Viktor I. Bespalov, Institute of Applied Physics (Russia)
Ernest V. Boiko, Military Medical Academy (Russia)
F. V. Bunkin, General Physics Institute (Russia)
Oleg B. Danilov, Institute for Laser Physics (Russia)
Eugeni M. Dianov, General Physics Institute (Russia)
Sergei A. Dimakov, Institute for Laser Physics (Russia)
Alexander V. Dotsenko, Corning Scientific Center (Russia)
Valentin Gapontsev, IPG Laser GmbH (Germany)
Yu. D. Golyaev, Research and Development Institute Polyus (Russia)
Vyacheslav M. Gordienko, M.V. Lomonosov Moscow State University (Russia)
Serguei A. Gurevich, A.F. Ioffe Physico-Technical Institute (Russia)
Valerii P. Kandidov, M.V. Lomonosov Moscow State University (Russia)
Yakov I. Khanin, Institute of Applied Physics (Russia)
I. V. Kovsh, Laser Association (Russia)
O. N. Krohin, P.N. Lebedev Physical Institute (Russia)
Vladimir V. Lyubimov, Institute for Laser Physics (Russia)
Alexander A. Manenkov, General Physics Institute (Russia)
Yuri T. Mazurenko, S.I. Vavilov State Optical Institute (USA)
Anatoly P. Napartovich, Troitsk Institute of Innovation and Fusion Research (Russia)
Anatoly N. Oraevsky, P.N. Lebedev Physics Institute (Russia)
Vladislav Ya. Panchenko, Scientific Research Center for Technological Lasers (Russia)
Pavel P. Pashinin, General Physics Institute (Russia)
G. T. Petrovskiy, S.I. Vavilov State Optical Institute (Russia)
N. N. Rozanov, Institute for Laser Physics (Russia)
Alexander S. Rubanov, B.I. Stepanov Institute of Physics (Belarus)
Marat S. Soskin, Institute of Physics (Ukraine)

Victor A. Serebryakov, Institute for Laser Physics (Russia)
Ivan A. Shcherbakov, General Physics Institute (Russia)
Vladimir E. Sherstobitov, Institute for Laser Physics (Russia)
Leonid N. Soms, Institute for Laser Physics (Russia)
V. B. Smirnov, St. Petersburg State University (Russia)
Anatoli P. Sukhorukov, M.V. Lomonosov Moscow State University (Russia)
Vladimir I. Ustyugov, Institute for Laser Physics (Russia)
V. V. Valuev, GPO Almaz (Russia)
V. N. Vasilev, St. Petersburg State Institute of Fine Mechanics and Optics (Russia)
Evgeny A. Viktorov, Institute for Laser Physics (Russia)
Vadim P. Veiko, St. Petersburg State Institute of Fine Mechanics and Optics (Russia)
Vladimir E. Yashin, Institute for Laser Physics (Russia)
Georgii M. Zverev, Research and Development Institute Polyus (Russia)

A novel method of the solid-state laser thermal lens intra-cavity correction by a modal liquid-crystal adaptive lens with optical control.

I.R. Guralnik[a,b], I.V. Sozinova[b]

[a]Lebedev Physical Institute of Russian Academy of Sciences, Samara Branch, 443011, Novo-Sadovaya Street 221, Samara, Russia; guralnik@ssu.samara.ru
[b]Samara State University, 443011, Acad. Pavlov Street 1, Samara, Russia

ABSTRACT.

We suggest a new way to compensate for the thermal lensing effect in the mid-power solid-state lasers. This can be done by the use of a liquid-crystal adaptive lens with optically controlled focal length (optically addressed lens - OAL) which is a modification of the modal liquid crystal lens (MLCL) which has recently been suggested and successfully implemented. The phase shift introduced by OAL into the transmitted light wave is theoretically shown to correspond to a converging lens whose focal length depends on the light intensity distribution across the aperture. OAL implements an intra-cavity optical feedback, which can effectively compensate for the laser beam defocus resulted from the emerging thermal lensing. For various types of resonators the beam stability is improved by the use of OAL. Correction becomes more effective if the OAL is positioned close to the laser rod.

Keywords: liquid crystals, phase modulators, thermal lens

1. INTRODUCTION

Recently[1] we described a design and properties of a new liquid crystal (LC) device, viz. the optically addressed lens (OAL) that may prove to be useful for various laser beam control purposes. OAL is a spin-off of the modal LC wavefront correctors[2-4] but is different from the modal LC lens (MLCL) in that OAL's focal length is sensitive to the intensity of the transmitted light wave. In Ref. [1] we also outlined how OAL might be used for phase distortion correction in solid-state lasers. In the current paper we give a more detailed theoretical analysis of this problem for CW laser operation.

A cylindrical laser rod with uniform internal heat generation develops a quadratic radial temperature variation. This produces a quadratic radial profile of the refractive index, referred to as thermal lensing (TL). TL results in significant deterioration of the beam quality. The heat generation in the laser rod is the direct consequence of the optical pumping and therefore is unavoidable for flashlamp pumping. However, many researchers pointed out that TL is a critical issue for the diode-pumped lasers as well. To avoid the undesirable effects of TL, various methods were suggested. In early investigations[5], it was customary to shape the resonators parameters to minimize the influence of the TL on the beam width. Later, more efficient *adaptive* techniques were investigated which subdivided into two major variations. One was concerned with the use of deformable mirrors (see, e.g., extensive reports in Refs. [6-9] and references therein or a more recent Ref. [10]) and the other makes use of the phase conjugation techniques[11]. However, neither of the methods completely satisfies the requirements set for the best performance resonator since deformable mirrors require a fairly complex servo loop system and high control voltage while the PC control is limited by the diffraction efficiency of the non-linear medium. Therefore, new methods to compensate for TL are still welcome.

In this paper we theoretically investigate a laser system with a built-in optical feedback represented by OAL. In section 1 we describe the elements of the laser system separately. First the optical characteristics of OAL are obtained, and their dependence on the intensity of the transmitted light and its distribution over the aperture. Then we present correlation for the thermal lens optical power and the pump power. And finally, a resonator with TL and OAL is considered. In section 2 the results of the calculation are presented and the improvement of the beam width stability is demonstrated.

Laser Optics 2000: Control of Laser Beam Characteristics and Nonlinear Methods for Wavefront Control, Leonid N. Soms, Vladimir E. Sherstobitov, Editors, Proceedings of SPIE Vol. 4353 (2001)
© 2001 SPIE · 0277-786X/01/$15.00

2. BASIC EQUATIONS.

2.1. Optically addressed lens

Basically, OAL is a modification of a spherical MLCL[2] that is produced by replacing the high resistance coating of the control electrode (CE) with a photosensitive layer (PL). The design of OAL and its distinction from the design of traditional optically addressed spatial light modulators are shown in Fig. 1.

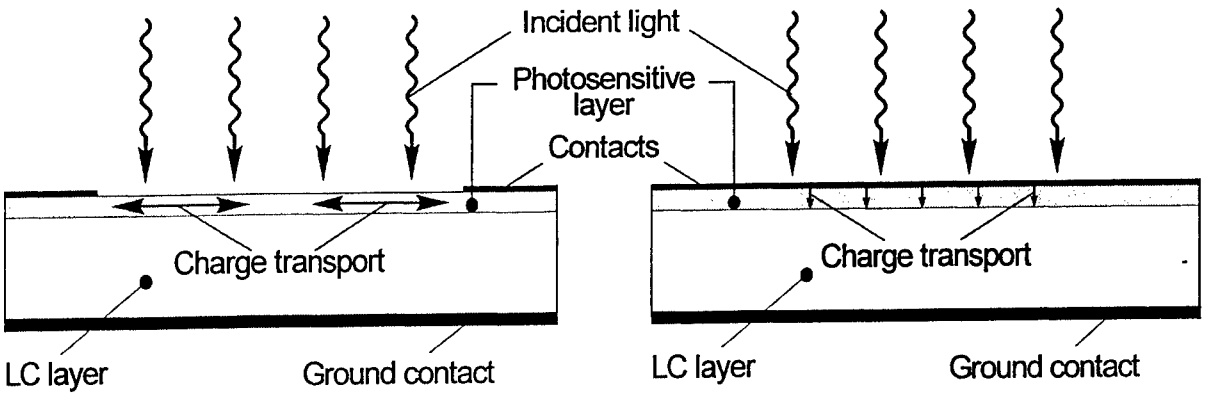


Fig. 1. In OAL (left) the photocurrent is perpendicular to the propagating light. In traditional optically addressed spatial light modulator (right) it is parallel to the light propagation.

Similar to MLCL, the photosensitive layer and the LC layer form a distributed *RC*-divider. If a sinusoidal voltage of the frequency ω is applied to the contacts, the changes in the voltage at the center of PL lag behind the changes in the voltage applied to the contacts. An increase in ω increases the delay and reduces the rms. value of the voltage at the center of the aperture. We found[1] that the voltage distribution across the aperture is described by the equation

$$\nabla_s(\sigma_s \nabla_s U) = (g - i\omega c)U\,, \tag{1}$$

where ∇_S means Hamilton operator with respect to the coordinates in the plane of the PL, $\sigma_S=\sigma h$ is the PL's sheet conductivity, σ and h are the conductivity and the thickness of PL, respectively, and c and g are specific (per unit LC area) capacitance and conductance of the LC layer, respectively.

The boundary conditions for Eq. (1) are:

$$U(l) = U_0 \quad \text{and} \quad \left.\frac{dU}{dr}\right|_{r=0} = 0\,, \tag{2}$$

where l is the aperture radius and U_0 is the rms. of the voltage applied to the upper contact in Fig. 1.

If the photosensitive material is a monopolar semiconductor, the spatial distribution of the specific conductance of PL is defined by the irradiation intensity distribution $I(r)$ by the formula

$$\sigma = e\mu\alpha\beta\tau I(r) + \sigma_d\,. \tag{3}$$

Here e, μ, and τ are the charge, the mobility, and the lifetime of the major carriers, respectively, α is the absorption coefficient of PL, β is the quantum efficiency of the photocurrent, and σ_d is the dark conductivity of PL. For a fundamental mode generation the intensity profile is Gaussian:

$$I(r) = \frac{J}{\pi w^2} e^{-r^2/w^2}\,, \tag{4}$$

where J is the integral power, w is the Gaussian beam width.

It follows from Eqs. (1)-(4) that the voltage distribution across the aperture is defined by a set of four parameters. One such set can be chosen as follows:

(a) the control voltage rms, U_0;

(b) the ratio of the beam width and the aperture, w/l;

(c) light-to-dark conductivity ratio, K;

(d) the numerical parameter, $\chi = \dfrac{\pi l^2 \omega c}{e\mu\tau\alpha\beta h J}$.

Due to the electrooptic S-effect in the LC, the voltage distribution causes the corresponding distribution of the phase delay that the LC layer introduces into the transmitted light wave according to the equation

$$\Delta\Phi = \frac{2\pi}{\lambda}\int_{-d/2}^{d/2}\left(\frac{n_{\|}n_{\perp}}{\sqrt{n_{\perp}^2\cos^2\theta + n_{\|}^2\sin^2\theta}} - n_{\perp}\right)dz, \qquad (5)$$

where λ is the wavelength, $n_{\perp}$, $n_{\|}$ are the refractive indices measured along and normal to the optical axis, $\theta(z)$ is the LC director deformation angle and integration is taken along the LC layer thickness. However in practice, to find the wavefront shape for a given voltage distribution, it is easier to use the experimental dependency (Fig. 2) or, for numerical simulations, an analytical approximation of such.

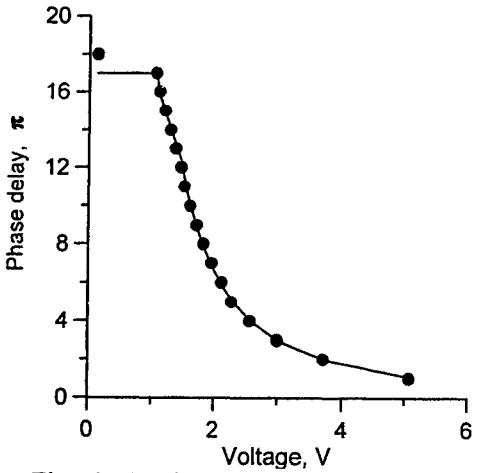


Fig. 2. Typical phase-voltage dependence for a nematic LC with zero pretilt (circles) and its analytical approximation.

2.2. Thermal lens.

The optical power of the TL is contributed by (a) temperature dependence of the refractive index, (b) "end effect", resulted from radially non-uniform thermal expansion of the rod, and (c) photoelastic effect. These effects are presented by the correspondent terms in the following relation[12]:

$$D = \frac{4d_0\Delta T}{r^2}\left[\frac{1}{2}\frac{dn}{dT} + \frac{\alpha_T r(n-1)}{d_0} + \alpha_T C_{r,\Phi} n^3\right], \qquad (6)$$

d_0 is the rod length, r is its radius, ΔT is the temperature difference between the rod center and its surface, n is the refractive index of the rod material, α_T is the thermal expansion coefficient, $C_{r,\Phi}$ are functions of the elasto-optical coefficients. The third term in Eq. (6) is often small and will be ignored in further treatment.

The temperature drop ΔT is found from the steady-state heat conduction equation and for a given rod is determined by the thermal power density q and the temperature of the rod side surface[13] T_S:

$$\Delta T = T_S\left(e^{(qr^2)/(4\gamma)} - 1\right), \qquad (7)$$

where γ is the coefficient in the temperature dependence of the thermal conductivity k

$$k(T)=\gamma/T\,. \tag{8}$$

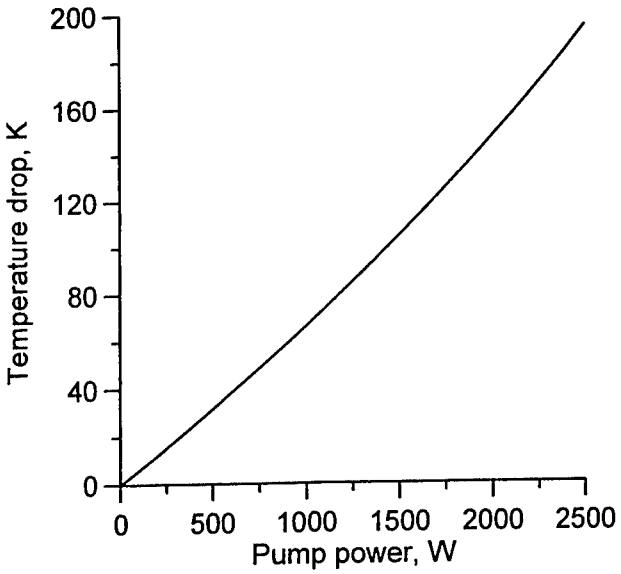


Fig. 3. Temperature difference at the center of the YAG:Nd rod and at its surface as a function of the pump power calculated by Eq. (7).

For Nd:YAG lasers in the temperature range $T\geq 200$ K $\gamma\approx 3980$ W/m. According to Eq. (7), the temperature drop is a quazi-linear function of the thermal density power. It is shown in Fig. for $q=0.01P$, P is the pump power.

2.3. Resonator.

The presence of lenses in the resonator modifies such parameters of the generated radiation as the wavefront curvature, beam width and divergence, beam waist position, etc. To calculate the new values of these parameters, we use a method of g-parameters[5]. According to this method, any resonator is characterized by a couple of numerical parameters g_1 and g_2 that facilitate the calculation of the beam width at any point within the cavity. By definition, for an empty resonator of the length L with the mirror curvatures R_1 и R_2

$$g_i=1-\frac{L}{R_i},\quad i=1,2. \tag{9}$$

The beam widths (spot sizes) at the mirrors in this case are equal to

$$w_{1,2}^2=\frac{\lambda L}{\pi}\cdot\left[\frac{g_{1,2}}{g_{2,1}(1-g_1g_2)}\right]^{1/2}. \tag{10}$$

With internal lenses the spot sizes at the mirrors are different. In this case, the resonator is equivalent to an empty resonator with modified parameters g_1^*, g_2^*, and L^*. For a single thin lens with the optical power D

$$\begin{aligned} g_1^* &= 1-\frac{L^*}{R_1}-bD,\\ g_2^* &= 1-\frac{L^*}{R_2}-aD,\\ L^* &= a+b-abD, \end{aligned} \tag{11}$$

where a and b are the lens distances from the mirrors 1 and 2, respectively. However, if the resonator length is comparable to that of the internal lens, the latter can no longer be considered as thin but should be ascribed the length of the laser rod d_0. Then[5]

$$\begin{aligned} g_1^* &= \left(1-\frac{d_0D}{n}\right)^{1/2}-\frac{L}{R_1}-bD,\\ g_2^* &= \left(1-\frac{d_0D}{n}\right)-\frac{L}{R_2}-aD,\\ L^* &= \left(1-\frac{d_0D}{n}\right)(a+b)+\frac{d_0}{n}-abD, \end{aligned} \tag{12}$$

where n is the refractive index of the rod.

Now let there is both OAL and TL in the resonator. We have found that the compensation of TL is most effective if the source of distortions (TL) and the correcting element (OAL) are set next to each other. Therefore, we consider only such geometry. In addition, we shall treat the OAL as a thin lens, since its thickness is about several millimeters. Denoting optical powers of OAL and TL as D_{OAL} and D_{TL}, respectively, we assume

$$D=D_{OAL}+D_{TL}. \tag{13}$$

Substituting this equation into Eq. (12), one can find g^*-parameters for a resonator with two internal lenses. Then the corresponding spot sizes at the mirrors can be found from Eq. (10). Besides the spot sizes, the beam width at the OAL, w, is of interest too, since it defines the intensity distribution according to Eq. (4). With OAL and the rod put together as shown in Fig. 4 the corresponding formula has a form[5]:

$$w^2 = w_1^2\left[\left(1-\frac{a}{R_1}\right)^2+\left(a\frac{\lambda}{\pi w_1^2}\right)^2\right]. \tag{14}$$

Solving together Eqs. (6), (7), (10), (12), and (14), one can compute the beam width at the mirrors and the OAL as functions of the thermal power density q. The density q is proportional to the pump power P which is an actual reason for the onset of TL. If, additionally, we take the laser system efficiency η to be independent of the pump power (for solid-state lasers $\eta\approx0.01$), then $J=\eta P$. Hence, we can use a single parameter P for both lenses. Since P can be chosen arbitrarily, it is convenient to choose P (or J) as an overall independent variable.

Thus, a resonator with a spherical OAL and TL under the steady state pumping conditions is described by the following self-consistent set of equations:

$$U''+\left(\frac{1}{r}-\frac{2}{w^2}r\right)U'-\chi e^{\left(r^2/w^2\right)}U=0, \tag{15}$$

$$D_{OAL}(U)=\frac{\lambda}{l^2}\cdot\begin{cases}17 & \text{for} \quad U<1V,\\ (-10U+27) & \text{for} \quad 1B<U<1.5\,\text{V},\\ 25.6U^{-1.95} & \text{for} \quad U>1.5\,\text{V},\end{cases} \tag{16}$$

$$D_{TL}=\frac{4d_0T_c}{r^2}\left[\frac{1}{2}\frac{dn}{dT}+\frac{\alpha r(n-1)}{d_0}\right]\left(e^{P/4\pi\gamma d_0}-1\right), \tag{17}$$

$$\begin{aligned}
g_1^* &= \left[1-\frac{d_0(D_{TL}+D_{OAL})}{n}\right]^{1/2}-\frac{L^*}{R_1}-b(D_{TL}+D_{OAL}),\\
g_2^* &= \left[1-\frac{d_0(D_{TL}+D_{OAL})}{n}\right]^{1/2}-\frac{L^*}{R_2}-a(D_{TL}+D_{OAL}),\\
L^* &= \left[1-\frac{d_0(D_{TL}+D_{OAL})}{n}\right]^{1/2}(a+b)+\frac{d_0}{n}-ab(D_{TL}+D_{OAL}),\\
w_{1,2}^2 &= \frac{\lambda L^*}{\pi}\cdot\left[\frac{g_{1,2}^*}{g_{2,1}^*(1-g_1^*g_2^*)}\right]^{1/2},\quad w^2=w_1^2\left[\left(1-\frac{a}{R_1}\right)^2+\left(a\frac{\lambda}{\pi w_1^2}\right)^2\right].
\end{aligned} \tag{18}$$

Eq. (15) is the result of Eqs. (1), (3), and (4) and Eq. (16) is an analytical representation of the phase-voltage dependence shown in Fig. 2. Both equations refer to the OAL operation. As it is clear from the previous analysis, eqs. (17) and (18) describe the TL and the resonator, respectively.

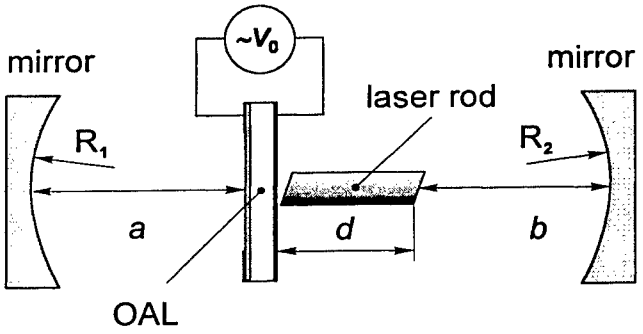


Fig. 4. Schematic representation of a simple laser cavity with TL (laser rod) and the optical feedback (OAL).

3. RESULTS AND DISCUSSION.

3.1. Optically addressed lens characterization.

The phase delay spatial distribution over OAL's aperture is almost parabolic (Fig. 5). Therefore, for a given light wavelength λ and the aperture radius l the OAL's optical power D_{OAL} depends on the phase sag $\delta\Phi$ only:

$$D_{OAL} = \frac{\lambda\delta\Phi}{\pi l^2}. \tag{19}$$

If the control voltage rms. U_0 and its frequency ω are kept constant, the sag $\delta\Phi$ is a unique function of the intensity distribution. We presented this function as a 3D surface in Fig. 6. In this figure, the dots (in Fig. 6 they merge to appear like bold lines) were obtained by solving Eq. (15) and subsequent use of the approximation (16). Then we reconstructed the 3D function by interpolation with these dots as reference points.

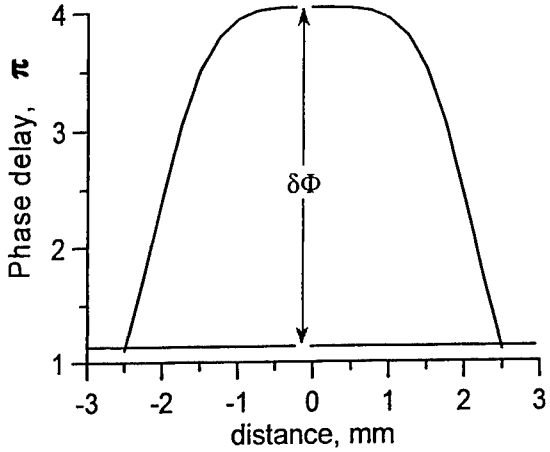


Fig. 5. A phase delay distribution at the OAL for χ=5, l=w=2.5 mm, and U_0=3 V and definition of the phase sag $\delta\Phi$.

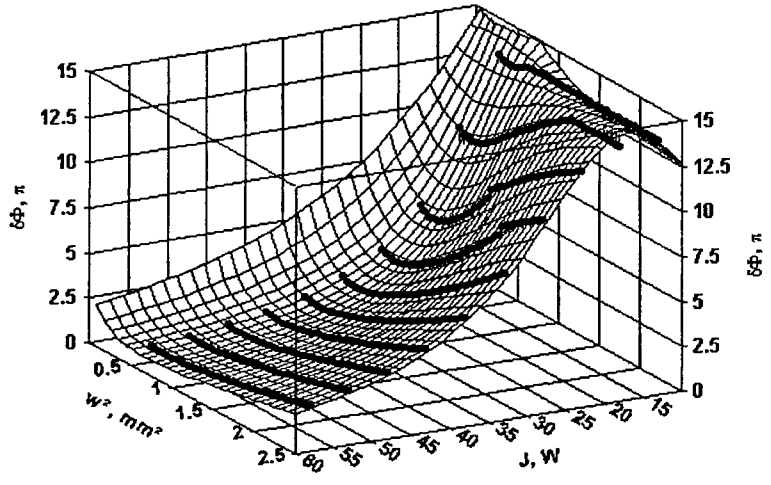


Fig. 6. Phase sag $\delta\Phi$ at OAL as a function of the beam width square at OAL and the cavity radiation power J.

We should note that the OAL will not operate when the beam width is much smaller than the aperture radius, $w<<l$. This is because for narrow beams the periphery of the aperture stays very dark and its resistance is very high. The voltage drops almost entirely in the narrow region beside the ring-shaped contact while on the major par of the aperture it remains constant. Therefore, the phase delay contributed by OAL will be essentially uniform.

3.2. Resonator performance stabilization.

TL degrades the output parameters of the laser radiation, i.e., beam width and divergence, in that they become radiation power dependent. If this dependence could be eliminated or limited, the overall system performance is improved. Therefore, we have chosen the beam width at the output mirror as the objective function, searching to smooth out its power dependence.

Parameter	Value
Curvature of the 1st mirror R_1, m	-0.325
Curvature of the 1st mirror R_2, m	-0.325
Mirror separation L, m	0.25
Distance between the 1st mirror and the OUL a, m	0.075
The rod length d_0, mm	100
The rod radius r_0, mm	2,5
Temperature at the rod surface T_c, K	300
Thermal expansion coefficient α_T, 10^{-6}/K	6,96
Refractive index n	1,81633
dn/dt, 10^{-6}/K	9,86
Average power of heat generation P_0, W	500

Table 1. Resonator parameters that were used in calculations.

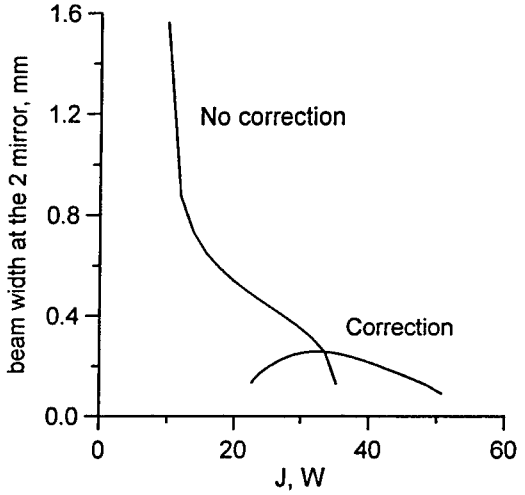


Fig. 7. Stabilization of the output beam width by OAL with the LC thickness d=5 μm.

The calculations were carried out for a resonator with $Y_3Al_5O_{12}$:Nd rod for the set of parameters listed in the table 1. The OAL's parameters were chosen to facilitate the most effective correction. The results of the calculation are presented in Fig. 7.

One can see that the OAL results in two features of the resonator performance. First, the working power range is shifted to higher powers, and, second, over the working range the beam width varies between 0.35 mm and 0.51 mm while without correction it varies between 0.13 and 1.56.

In summary, we demonstrated theoretically that the phase distortions that arise due to the thermal lensing in a YAG:Nd laser system can be significantly corrected by OAL, a modal liquid-crystal lens whose wavefront shape is controlled by the intensity and spatial distribution of the transmitted light.

REFERENCES

1. I. R. Guralnik, "Modal adaptive liquid crystal lens with optical control", *Avtometria, N 1*, pp. 107-114, 2000.
2. A. F. Naumov , M. Yu. Loktev, I. R. Guralnik, and G. V. Vdovin, "Liquid crystal adaptive lenses with modal control," *Opt. Lett.* **23**, pp. 992-994, 1998.
3. A. F. Naumov, M. Yu. Loktev, I. R. Guralnik, and G. V. Vdovin, "Liquid crystal wavefront correctors of new type", *Proc. SPIE* **3688**, pp. 479-486, 1998.
4. G. V. Vdovin, I. R. Guralnik, S. P. Kotova, M. Yu. Loktev, and A. F. Naumov, "LC lenses with variable focal lengths. I. Theory", *Quantum Electronics* **26**, pp. 256-260, 1999; "LC lenses with variable focal lengths. II, Experiment and computer simulations", *Quantum Electronics* **26**, pp. 261-264, 1999.
5. J. Steffen, J. P. Lortscher, G. Herziger, "Fundamental mode radiation with solid-state lasers", *IEEE J. Quantum Electron.* **QE-8**, pp. 239-245, 1972.
6. J. M. Spinhirne, D. Anafi, R. H. Freeman, and H. R. Garcia, "Intracavity adaptive optics. 1: Astigmatism correction performance", *Appl. Opt.* **20**, pp. 976-984, 1981.
7. D. Anafi, J. M. Spinhirne, R. H. Freeman, and K. E. Oughstun, "Intracavity adaptive optics. 2: Tilt correction performance", *Appl. Opt.* **20**, pp. 1926-1932, 1981.
8. J. M. Spinhirne, D. Anafi, and R. H. Freeman, "Intracavity adaptive optics. 3: Hsuria performance", *Appl. Opt.* **21**, pp. 3969-3982, 1982.
9. Kurt E. Oughstun, J. M. Spinhirne, and D. Anafi, "Intracavity adaptive optics. 4: Comparison of theory and experiment", *Appl. Opt.* **23**, pp. 1529-1541, 1983.
10. I. Moshe, S. Jackal, and R. Lallouz, "Dynamic correction of thermal focusing in Nd:YAG confocal unstable resonators by use of a variable radius mirror", *Appl. Opt.* **37**, pp. 7044-7048, 1998.
11. E. Rosas, V. Aboites, "Self-adaptive resonators", *SPIE* **3684**, pp. 64-69, 1998.
12. R. Weber, B. Neuenschwander, and H. P. Weber, "Thermal effects in solid-state laser materials", *Optical Materials* **11**, pp. 245-254, 1999.
13. A. G. Rozanov, "Non-linear model of thermal effects in YAG:Nd laser crystals", *Quantum Electronics* **18**, pp. 1185-1188, 1991.

Static and dynamic models of liquid crystal wavefront correctors

M.Yu.Loktev[a,b], A.F.Naumov[b,c], I.R.Guralnik[b,d]

[a]Electronic Instrumentation Laboratory,
Delft University of Technology, The Netherlands.

[b]P.N. Lebedev Physical Institute of the Russian
Academy of Science, Samara Branch, Russia.

[c]Department of Physics, University of Durham, United Kingdom.

[d]Department of Physics, Samara State University, Russia.

ABSTRACT

Static and dynamic numerical models of electro-optical characteristics of nematics are presented. A numerical model is used for the optimisation of phase delay distribution in modal LC lenses The dynamic control mode for modal LC lenses is simulated. The results are in a good agreement with experiment.

Keywords: liquid crystals, adaptive optics, numerical simulation.

Using of liquid crystals in adaptive optics seems to be promising because they have a lot of advantages: low half-wave voltages (fractions of volts should be applied to change phase delay on half wave), large stroke range (tens wavelengths), small consumed capacities (0.1 mW/cm^2), small volume of a flat design, no-moved parts, wide interval of working temperatures (-20...100°C), significant service life (more than 10^4 h), and low cost of initial materials. Essential progress in application of LC wavefront correctors in adaptive optics is observed in recent years; its implementation for correction of atmospheric aberrations[1] and retinal imaging[2] is reported recently. The use of LC correctors is still limited by their narrow temporal bandwidth. However, synthesis of liquid crystals with special properties and implementation of dual-frequency control technique[3] can alleviate this problem in some applications.

Although most of the applications now involve pixelated devices where the voltage is controlled for each pixel individually[1,4], modal LC adaptive lenses[5] and multi-channel wavefront correctors[6] were recently proposed. The most attractive feature of these correctors is the ability to produce a smooth non-pixelated phase distribution with rather small number of control channels. The voltage distribution producing the required phase profile is formed mainly due to the capacitative and resistive properties of LC material. Thus, for investigation of performance and optimisation of the modal LC correctors one needs to consider electro-optical characteristics of the LC materials.

To achieve maximum speed and maximum dynamic range of wavefront control for zonal LC correctors and to optimise phase delay distributions for modal LC correctors it is necessary to take into account different LC parameters characterising their mechanical, optical and electrical properties. Nematic liquid crystal is a uniaxial electro-optical medium whose molecules are reoriented by application of electric and magnetic fields. As a rule, the analysis of the distribution of LC director is based on minimisation of the functional of the nematic free energy[7]. The basic equation for LC director deformation angle proposed by Ericksen and Leslie

$$\frac{\partial}{\partial z}\left[\left(K_{11}\cos^2\Theta + K_{33}\sin^2\Theta\right)\frac{\partial\Theta}{\partial z}\right] - \left(K_{33}-K_{11}\right)\sin\Theta\cos\Theta\left(\frac{\partial\Theta}{\partial z}\right)^2 + \\ + \left(\alpha_2\sin^2\Theta - \alpha_3\cos^2\Theta\right)\frac{\partial v}{\partial z} + \Delta\varepsilon\varepsilon_0 E^2\sin\Theta\cos\Theta = \gamma_1\frac{\partial\Theta}{\partial t} + I\frac{\partial^2\Theta}{\partial t^2}. \quad (1)$$

is rather complicated and cannot be solved analytically[8].

Laser Optics 2000: Control of Laser Beam Characteristics and Nonlinear Methods for Wavefront Control,
Leonid N. Soms, Vladimir E. Sherstobitov, Editors, Proceedings of SPIE Vol. 4353 (2001)
© 2001 SPIE · 0277-786X/01/$15.00

Here Θ is the deformation angle of the director, K_{11} and K_{33} are splay and bend Frank elastic constants, respectively, $\Delta\varepsilon = \varepsilon_{\parallel} - \varepsilon_{\perp}$ is dielectric anisotropy, υ is the flow velocity, α_2 and α_3 are viscosity coefficients in Leslie's notation, $\gamma_1=\alpha_3-\alpha_2$ is the rotational viscosity, I represents the inertia, and E is the electric field in the LC medium. Due to LC director deformation, E is non-uniformly distributed across the LC layer. It can be expressed in terms of the deformation angle Θ and the voltage V applied to the LC:

$$E = \frac{V}{\left(\varepsilon_{\perp}\cos^2\Theta + \varepsilon_{\parallel}\sin^2\Theta\right)\int_0^d \frac{dz}{\varepsilon_{\perp}\cos^2\Theta + \varepsilon_{\parallel}\sin^2\Theta}} \tag{2}$$

Here d is the thickness of LC layer.

The most common approximation consisting in neglecting of angular momentum is justified by the fact that the change of orientation is strongly damped by rotational viscosity. Another approximation that greatly simplifies the problem is in neglecting of the backflow. As it is shown in Ref. [9], this effect can be partly taken into account by using effective viscosity instead of γ_1:

$$\gamma_S^* = \gamma_1 - 2\alpha_3^2/(\alpha_3+\alpha_4+\alpha_6) \text{ for splay deformation (S-effect),}$$
$$\gamma_B^* = \gamma_1 - 2\alpha_2^2/(\alpha_4+\alpha_5-\alpha_2) \text{ for bend deformation (B-effect).} \tag{3}$$

In the series of works[8,10,11] the useful results for S- and B-effects were obtained in the small-signal approximation corresponding to the case of small (< 50°) deformation angles. For large voltages corresponding to maximum deformations the most straightforward way is in numerical solution of Eq. (1) (except for the terms concerned with inertia and backflow) in combination with experimental investigation of their electro-optical static and dynamic characteristics.

In this work we present the numerical model and the software for calculation of phase delay in LC layer, and also its specific capacitance and conductance. We performed also numerical simulation of usual nematics on the example of E49 (Merck) with initial planar alignment and small pretilt of molecules on the surface. This situation corresponds to electro-optical S-effect.

First we consider a static case. Even without the backflow effect, Ericksen-Leslie's equation is essentially nonlinear, especially if we take electric field as non-homogeneous. However, static distribution of the LC director can be calculated using an iterative technique based on the dynamic Eq. (1). In our method the temporal variable t is used only as an auxiliary variable. We replace Ericksen-Leslie equation by equivalent presentation introducing finite differences instead of derivatives

$$\Theta_{i,j+1} = \Theta_{ij} + \frac{\Delta t}{\gamma_1}\left[\left(K_{11}\cos^2\Theta_{ij} + K_{33}\sin^2\Theta_{ij}\right)\frac{\Theta_{i-1,j} - 2\Theta_{ij} + \Theta_{i+1,j}}{(\Delta z)^2} + \right.$$
$$\left. + (K_{33}-K_{11})\sin\Theta_{ij}\cos\Theta_{ij}\left(\frac{\Theta_{i+1,j}-\Theta_{i-1,j}}{2\Delta z}\right)^2 + \varepsilon_0\Delta\varepsilon E_{ij}^2\sin\Theta_{ij}\cos\Theta_{ij}\right]. \tag{4}$$

Here i and j are coordinate and time indices correspondingly, Δz is the coordinate step, and Δt is the time step. γ_1 has an arbitrary value, it can be set to 1, and the value of Δt is limited by the condition of stability of finite-differential scheme

$$\Delta t = \frac{\gamma_1(\Delta x)^2}{8K_{11}}. \tag{5}$$

This condition is found by the method described in Ref. [12]. Boundary conditions are set according to initial alignment with pretilt angle Θ_0

$$\begin{cases}\Theta_{0,j} = \Theta_0 \\ \Theta_{N,j} = \Theta_0\end{cases}, \tag{6}$$

where N+1 is the number of points by coordinate. We start from the uniform distribution of the deformation angle Θ and uniform distribution of electric field $E=V/d$, and then iterate by calculation of the next j+1-th level until the required accuracy is reached. The electric field on each step by j is corrected by the formula

$$E_{i,j+1} = \frac{V}{\left(\varepsilon_\perp \cos^2\Theta_{ij} + \varepsilon_\parallel \sin^2\Theta_{ij}\right)\int_0^d \frac{dz}{\varepsilon_\perp \cos^2\Theta_{ij} + \varepsilon_\parallel \sin^2\Theta_{ij}}}. \quad (7)$$

From obtained distributions of the LC deformation angle we calculate electro-optical characteristic: dependencies of phase delay $\Delta\Phi$ in the LC layer, its specific capacitance c and conductance g by formulas given in our previous paper [13]:

$$\Delta\Phi = \frac{2\pi}{\lambda}\int_0^d \left[\frac{n_\parallel n_\perp}{\sqrt{n_\perp^2 \cos^2\theta + n_\parallel^2 \sin^2\theta}} - n_\perp\right] dz, \quad (8)$$

$$c = \varepsilon_0 \frac{\alpha}{\alpha^2+\beta^2}, g = \varepsilon_0 \omega \frac{\beta}{\alpha^2+\beta^2}, \quad (9)$$

where we denoted

$$\alpha = \int_0^d \frac{\varepsilon' dz}{\varepsilon'^2 + \varepsilon''^2}, \beta = \int_0^d \frac{\varepsilon'' dz}{\varepsilon'^2 + \varepsilon''^2}, \quad (10)$$

ε' and ε'' are real and imaginary parts of the dielectric constant, correspondingly.

This numerical model was already used for optimisation of phase delay distribution in modal spherical [14] and cylindrical [15] LC lenses. As it is seen from Figure 1, the fitting of the theoretical curves to experimental ones gives a very good approximation The mechanism of fitting is described in [16]. The experimental results were obtained for the cell filled by 25 mic layer of Merck's LC E49 with initial pretilt of the molecules. The best correspondence was observed at $K_{11} = K_{33} = 1.68\ 10^{-11}$ N, $\varepsilon_\parallel = 16.3$, $\varepsilon_\perp = 5.1$, $n_\parallel = 1.775$, $n_\perp = 1.53$, and the pretilt angle is equal to $\Theta_0 = 44°$. Last value is in a good agreement with those measured by other methods.

In some cases the approximation of uniform electric field can essentially simplify

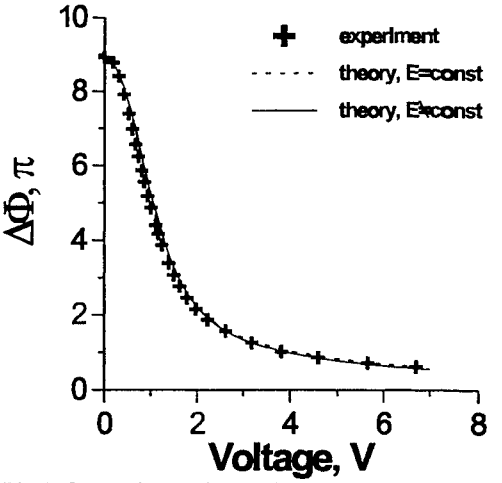


Fig.1. Comparison of experimental and calculated dependencies of phase delay in LC layer from *rms* value of control voltage. The results for the cases of uniform and non-uniform electric field are given

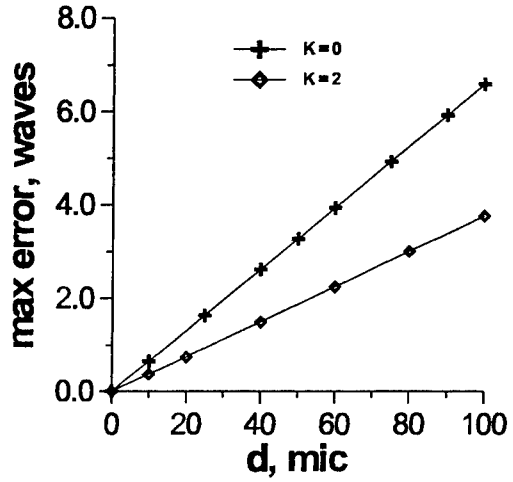


Fig.2. Dependence of maximum absolute error caused by approximation of uniform electric field on the thickness of the LC layer

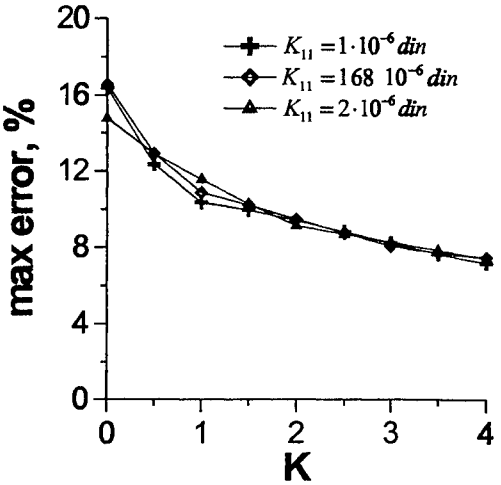


Fig.3. Dependence of maximum relative error caused by approximation of uniform electric field on parameter $K = (K_{33}-K_{11})/K_{11}$.

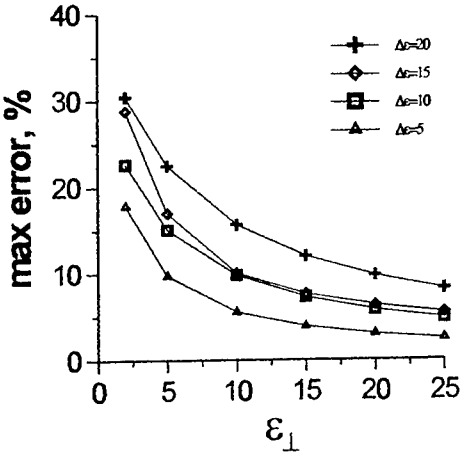


Fig.4. Maximum relative error caused by approximation of uniform electric field vs dielectric constant $\varepsilon_{\perp}$.

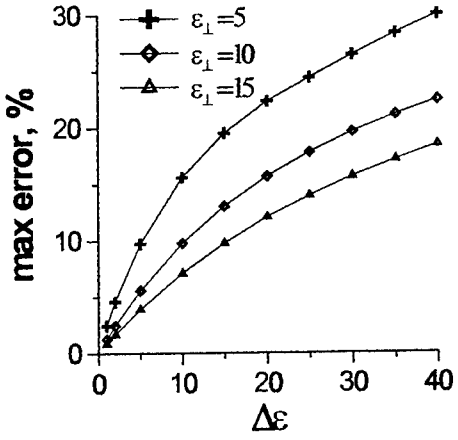


Fig.5. Maximum relative error caused by approximation of uniform electric field vs dielectric anisotropy $\Delta\varepsilon = \varepsilon_{\parallel} - \varepsilon_{\perp}$.

the task without significant losses of accuracy[10,11,17] as it is seen from Fig. 1. The value of electric field is supposed to be constant across the LC layer and equal to $E=V/d$. We analysed the errors caused by this approximation. We compared phase distributions calculated in approximations of uniform and non-uniform field. For the simulation we used parameters of cell filled with planarly aligned LC E49 of 25 mic thickness.

Results are shown in Figs.2-6. As it is seen from Fig.2, the absolute error increases proportionally to LC thickness. For zero value of parameter $K = (K_{33}-K_{11})/K_{11}$ the relative error (maximum error divided by total phase delay variation) was equal to 16.6%, and for K=2 it was 9.5%. It decreased with parameters K and $\varepsilon_{\perp}$, increased with dielectric anisotropy $\Delta\varepsilon = \varepsilon_{\parallel} - \varepsilon_{\perp}$, and did not vary with K_{11}.

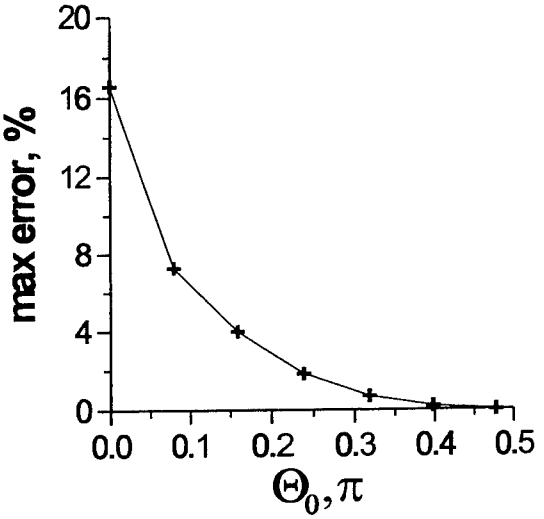


Fig.6. Maximum relative error caused by approximation of uniform electric field vs initial pretilt angle Θ_0.

Maximum deviation was observed at voltages near the threshold value V_{th} and was very small at voltages much higher than V_{th}. It decreased fast with pretilt angle Θ_0.

To consider dynamic behaviour of the liquid crystal we used the finite-differential presentation given by equations (4)-(6) and the approximation of the uniform electric field. In our

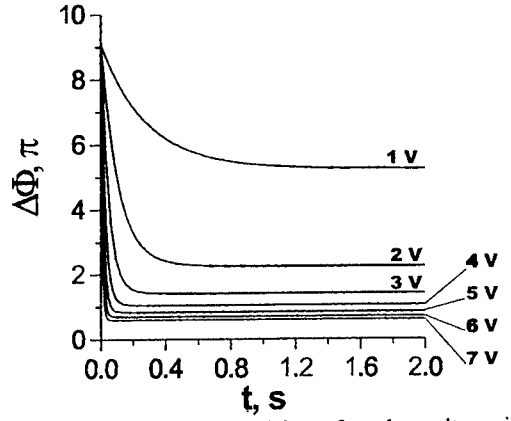


Fig.7. Dynamics of phase delay after the voltage is

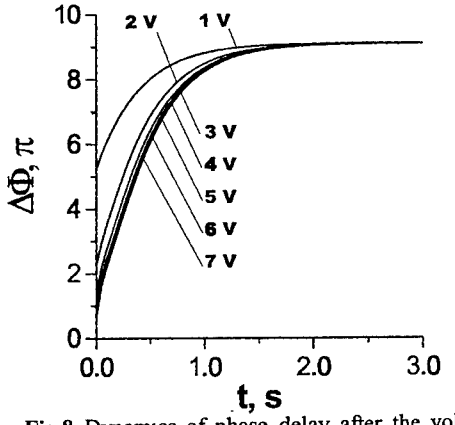


Fig.8. Dynamics of phase delay after the voltage is

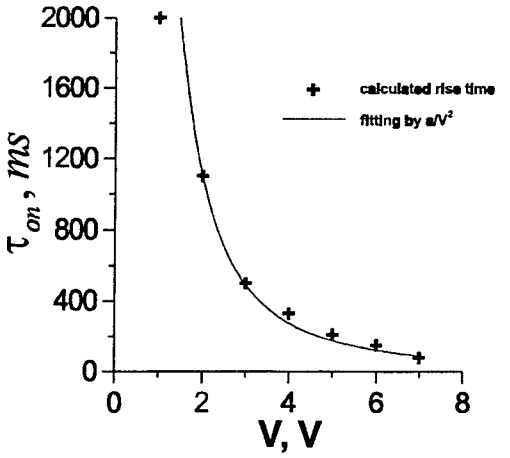


Fig.9. Rise time vs control voltage. Fitting of calculated data by function of a type $\tilde{\tau} = a/V^2$ is also shown.

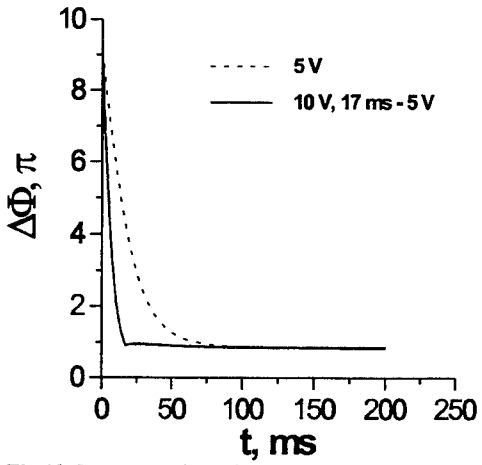


Fig.10. Demonstration of decreasing of LC rise time by short-time application of high voltage. Signal of 10 V amplitude was applied for 17 s before switching on 5 V signal (solid curve).

calculations we set the rotational viscosity γ_1 to 1 Poise which is a typical value for liquid crystal materials. In the first series of calculations we evaluated the characteristic rise and decay times for different feeding voltages. We determined the characteristic time as a time of variation of phase delay up to the value that differs from its final state by less than 1%. Dynamics of rise and decay is shown in Figs.7 and 8, and the dependence of rise time τ_{on} from *rms* feeding voltage is given in Fig.9. We also fitted our results by function $\tilde{\tau} = a/V^2$ and showed that for voltages ≥2 V the rise time is inversely proportional to square of the voltage. Decay time is almost independent of the control voltage and is equal to 2.4 s. These calculations are in a good agreement with evaluations obtained in a small-signal approximation[7].

The dynamic control of the LCs is of a special interest for solution of the problem of LC switching speed. As LC molecules reorients much faster at higher voltages, one of the possibilities to decrease the rise time is to apply for a short time the voltage much higher than it is necessary to get the required phase delay. After the phase delay achieves the required level, the voltage must be decreased to stop the process of molecules reorientation. This is demonstrated by Fig.10 where preliminary application of 10 V voltage during 17 ms allows to set the required phase delay three times faster than by only switching it to 5 V.

Furthermore, we used our model for investigation of dynamics of spherical modal LC lens (MLCL). The design of MLCL is shown in Fig.11. A layer of nematic LC is sandwiched between two glass substrates with transparent electrodes. Dielectric spacers placed between the substrates define the thickness of LC layer. One of the electrodes (ground) has a low sheet resistance of 50 to 200 Ω/sq. and another one (control) has a high sheet resistance of 3 to 8 MΩ/sq. Annular contact is deposited at the control electrode periphery, and an AC voltage is applied between this contact and the ground electrode. Electrically, the MLCL is equivalent to the circuit with distributed parameters. Due to the circular symmetry of the device the voltage is distributed symmetrically across the aperture, as described by equation[5]

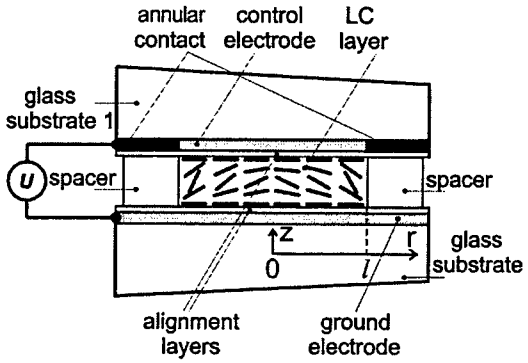


Fig.11. Construction of the spherical modal LC lens.

$$\frac{\partial^2 V}{\partial r^2} + \frac{1}{r}\frac{\partial V}{\partial r} = \rho_S c \frac{\partial V}{\partial t} + \rho_S g V. \qquad (11)$$

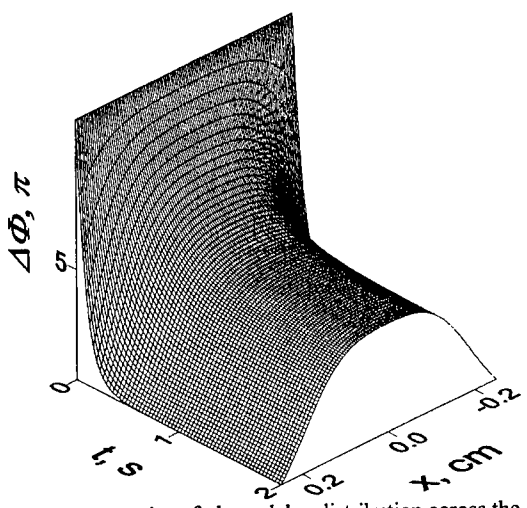


Fig.12. Dynamics of phase delay distribution across the LC lens aperture. Lens is switched on; focal length is 3 m. Parameters of control voltage: amplitude is 3.15 V, frequency is 9.6 kHz.

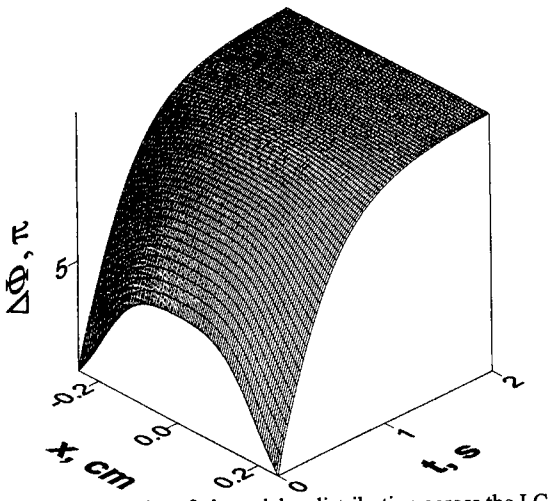


Fig.13. Dynamics of phase delay distribution across the LC lens aperture. Lens is switched off; focal length is 3 m.

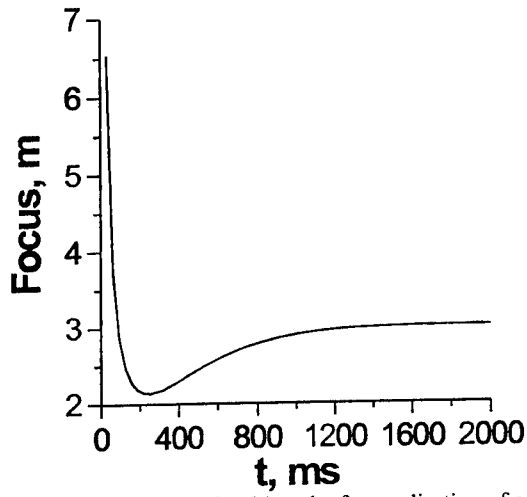


Fig.14. Dynamics of focal length after application of a voltage corresponding to 3 m focus.

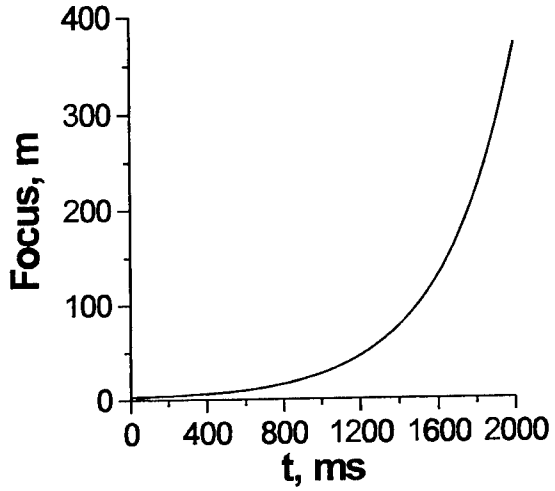


Fig.15. Dynamics of focal length after switching off voltage corresponding to 3 m focus.

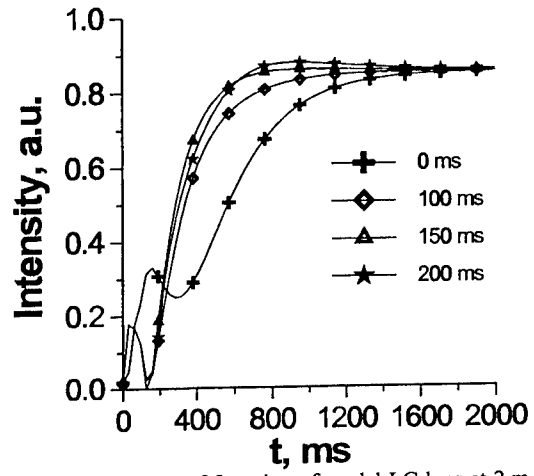


Fig.16. Dynamics of focusing of modal LC lens at 2 m focal distance. First the voltage two times more than an optimal one for this focus was applied, and then we applied an optimal voltage (3.05 V, 13.8 kHz).

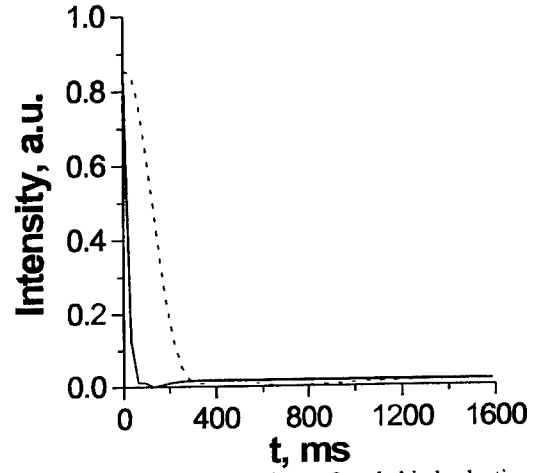


Fig.17. Variation of intensity at 2 m behind adaptive lens demonstrates two ways of transition from 2 m focus to infinity: switching off the control voltage (dashed curve) and application of a low-frequency signal (solid curve).

The distributed voltage induces reorientation of LC molecules, and thus, produces axially symmetrical phase deformation. The static problem of the calculation of phase distribution in MLCL was studied in our previous paper[16]. In this work we use these results and our dynamic model of LCs for investigation of dynamics of MLCL.

The speed of LC adaptive lens is determined by two factors: voltage stabilization in modal LC lens and realignment of LC molecules. First process is concerned with MLCL's reactive nature brought about by the presence of the distributed conductance of CE and distributed capacitance of the LC layer. Its speed is characterised by time constant *RC*. The measured value of this constant was about 40 μs[16], whereas characteristic times of LC reorientation is about hundreds of milliseconds. Thus, in our calculation we can suppose that voltage distribution changes instantly, and phase transient process in the LC lens is concerned only with reorientation of LCs. In general, the speed of LC lenses is determined by the lowest value of voltage at the aperture.

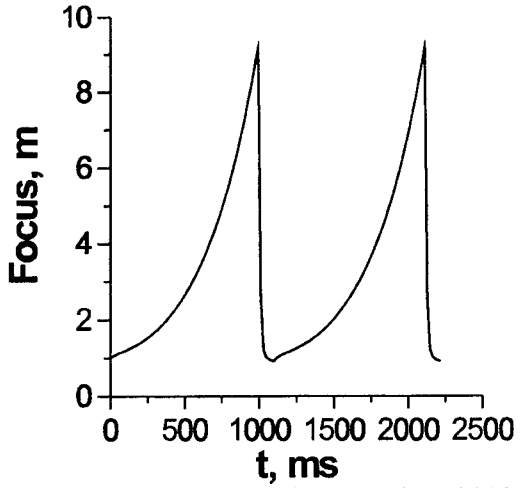


Fig.18. Periodical variation of focal length in modal LC lens. Control is performed by periodical sequence consisting of 10 V voltage with frequency 60 kHz of 0.1 s duration and zero signal of 1 s duration.

First we calculated static voltage distributions for each control signal using our static model of LC lens. Then we considered the process of relaxation of the LC in each point of the aperture. We investigated temporal variation of phase distribution and parameters of a light passed through the lens: wavefront curvature characterized by focus, and intensity of light at a given focal distance. Intensity was normalized, i.e., it reached its maximal value equal to 1 only for ideal parabolic phase distribution corresponding to a given focal length.

The dynamics of phase delay and focal length at lens switching is shown in Figs.12-15. As local value of voltage at the edge of LC lens aperture is higher than at its centre, LC reorientation goes faster at the edge, and the focal length changes from infinity to 3 m passing through the minimum (Fig.14). Otherwise, the process of focus variation at switching off voltage is monotonous, as it is seen from Fig.15.

We also tested the method described above for increasing the speed of LC focal length transition from infinity to 2 m. First the voltage two times higher than the optimal one for this focus was applied, and then we applied the optimal voltage (3.05 V, 13.8 kHz). As it is shown in Fig.16, application of a higher voltage during 150 ms approximately doubles the speed.

Characteristic time of lens switching off can also be decreased. As it is demonstrated by our calculations, the time of LC relaxation is practically independent of the value of initial voltage (Fig.8). However, in modal LC lens we can reach an infinity focus not only by switching off voltage but also by applying a low-frequency signal. At frequencies much lower than the working frequencies of a lens the reactivity of LC lens does not work, and the voltage have the same value in each point of an aperture. If we does not change the amplitude and change the frequency to its lowest possible value (few hundreds of Hz) the local voltage in the centre of the aperture grows, and the LC is realigned much faster. In our example (Fig.17) the characteristic time of switching off reaches 100 ms.

We also found that there is a dynamic operating condition when the focal distance is changed fast and periodically from infinity to 1 m and back, but the pause between these variations is quite long so that the LC molecules relax to their initial alignment (Fig. 18). The dynamic operating condition is achieved by applying a voltage with amplitude and frequency higher than it is necessary for the shortest focal distance.

Further implementation of the numerical model presented in this paper will include investigation of dynamic aspects of two-frequency control[1,3], numerical simulation and optimisation of control parameters of multi-element modal LC correctors[6]. This approach allows us to set the requirements for parameters of the LC materials developed specially for the use in adaptive optics.

This work was partially supported by INTAS foundation (project 99ESA-00523).

REFERENCES

1. S. Restaino, D. Dayton, S. Browne, J. Gonglewski, J. Baker, S. Rogers, S. McDermott, J. Gallegos and M. Shilko, "On the use of dual frequency nematic material for adaptive optics systems: first results of a closed-loop experiment", *Optics Express 6*, pp.2-6, 2000.
2. F. Vargas-Martin, P. M. Prieto, and P. Artal, "Correction of the aberrations in the human eye with a liquid-crystal spatial light modulator: limits to performance", *JOSA A 15*, pp.2552-2562, 1998.
3. A. F. Naumov, and V. N. Belopukhov, "Dynamical properties of LC wavefront correctors and adaptive system for optimal control selecting", *Proceedings of SPIE 3688*, pp.476-484, 1999.
4. D. J. Cho, S. T. Thurman, J. T. Donner, and G. M. Morris, "Characteristics of a 128x128 liquid-crystal spatial light modulator for wave-front generation", *Optics Letters 23*, pp.969-971, 1998.
5. A. F. Naumov, M. Yu. Loktev, I. R. Guralnik, and G. V. Vdovin, "Liquid crystal adaptive lenses with modal control", *Optics Letters 23*, pp.992-994, 1998.
6. A. F. Naumov, and G. V. Vdovin, "Multichannel liquid-crystal-based wave-front corrector with modal influence functions", *Optics Letters 23*, pp.1550-1552, 1998.
7. V. G. Chigrinov, "Liquid crystal devices: physics and applications", *Artech House, Boston*, 359 p, 1999.
8. S.-T. Wu, and C.-S. Wu, "Small angle relaxation of highly deformed nematic liquid crystals", *Applied Physics Letters 53*, pp.1794-1796, 1988.
9. V. G. Chigrinov, and V. V. Belyaev, "Temporal characteristics of oriented electro-optic effects in nematic liquid crystals", *Crystallography 22*, pp.603-607, 1977, in Russian.
10. G. Labrunie, J. Robert, "Transient behavior of the electrically controlled birefringence in a nematic liquid crystal", *Journal of Applied Physics 44*, pp.4869-4874, 1973.
11. A. F. Naumov, "Liquid crystal modulators in wave front control problems", *Candidate (PhD) thesis. Moscow State University, Moscow*, 134 p, 1988.
12. K. S. Kunz, "Numerical analysis", *McGraw Hill Book Company, New York*, 381 p, 1957.
13. I. R. Guralnik, V. N. Belopukhov, G. D. Love, and A. F. Naumov, "Interdependence of the electrical and optical properties of liquid crystals for phase modulation applications", *Journal of Applied Physics 87*, pp.4069-4074, 2000.
14. A. F. Naumov, G. D. Love, M. Yu. Loktev, and F. L. Vladimirov, "Control optimization of spherical modal liquid crystal lenses", *Optics Express 4*, p. 344, 1999. http://epubs.osa.org/opticsexpress/framestocv4n9.htm
15. O. A. Zayakin, M. Yu. Loktev, G. D. Love, A. F. Naumov, "Cylindrical adaptive lenses", *Proceedings of SPIE 3983*, p.112-117, 1999.
16. I.R.Guralnik, M.Yu.Loktev, and A.F.Naumov, "Electrophysics of adaptive LC lens with modal control", *Proceedings of SPIE 4071*, p.209-218, 2000.
17. P. D. Berezin, I. N. Kompanets, V. V. Nikitin, and S. A. Pickin, "The orienting effect of an electric field on nematic liquid crystals", *Journal of Experimental and Theoretical Physics 64*, pp.599-607, 1973.

Tunable acousto-optic filters and their applications in laser technology, optical communication and processing of images

Vitaly Voloshinov*, Vladimir Parygin* and Vladimir Molchanov**

* Physics Faculty, M.V.Lomonosov Moscow State University, 119899 Moscow, Russia
Tel: 7-095-939-4404; Fax: 7-095-292-6511; E-mail: volosh@osc162.phys.msu.su

** Moscow Steel and Alloys Institute, 117936 Moscow, Russia
Tel: 7-095-973-2723; Fax: 7-095-128-5152; E-mail: welsy@orc.ru

ABSTRACT

The paper presents results on research of tunable acousto-optic filters operating in ultraviolet, visible and infrared regions of spectrum. High spectral and spatial resolution, perfect diffraction efficiency and low driving power provide application of the filters in optics and spectroscopy as well as in optical information processing and laser technology. Precise and efficient electronic control of laser light intensity and fast electronic tuning of lasing wavelength was executed by means of collinear acousto-optic devices. Application of the collinear filters as selectors of arbitrary polarized optical signals in modern WDM waveguide communication lines has also demonstrated high capabilities of the acousto-optic instruments. Experiments with the acousto-optic devices on base of the wide-angular geometry of interaction confirmed the unique possibility to regulate spatial structure of convergent laser beams and optical rays forming images.

Keywords: acousto-optics, tunable acousto-optic filters, Bragg phase matching, spectral resolution, convergent optical beams, optical images, Ti:sapphire laser, optical communication, WDM waveguide systems

1. INTRODUCTION

Acousto-optical methods of modulation of optical beams find wide applications in optics, spectroscopy and laser technology[1-3]. The principle of operation of acousto-optical devices is based on the phenomenon of light diffraction by ultrasonic waves in crystals. As known, acousto-optic instruments provide control of both coherent and non-coherent optical beams[4]. In particular, optical intensity and spectral composition of a non-coherent optical beam may be easily regulated by means of acousto-optics. In case of radiation with a broad band of optical wavelengths λ, acousto-optical filters execute spectral filtration of light in narrow bandwidths of optical wavelengths $\Delta\lambda$ corresponding to high resolution values $R=\lambda/\Delta\lambda$[4-10].

The filters on base of light diffraction by ultrasound may be installed inside a cavity of a laser characterized by high gain in a wide range of optical wavelengths λ. Application of a filter in a laser cavity makes the lasing line narrower. In addition, the filter may provide quick and precise tuning of the quantum generator all over the wavelengths of gain.

Operation of the filters in case of multiwavelength radiation proved the advantages of the acousto-optic devices as selectors of optical signals[7]. For example, if a number of optical signals with different optical wavelengths λ_i simultaneously propagate along an optical fiber (WDM communication line) then application of the acousto-optic instrument provides selection of the signals with the required wavelengths. Additionally to the filtration, intensities of the transmitted signals at the filter output may be regulated by the acousto-optic devices.

The acousto-optic filters possess other advantages, e.g. they can filtrate both collimated and convergent optical beams. Consequently, there appears a principal possibility to perform acousto-optically processing of images[8-10]. Owing to acousto-optics, it becomes possible to tune electronically colour of an image and to obtain fruitful information about spectral and

Laser Optics 2000: Control of Laser Beam Characteristics and Nonlinear Methods for Wavefront Control,
Leonid N. Soms, Vladimir E. Sherstobitov, Editors, Proceedings of SPIE Vol. 4353 (2001)
© 2001 SPIE · 0277-786X/01/$15.00

polarization composition of radiation in a picture[8-10] . On the other hand, if an optical image is formed by coherent monochromatic rays then the devices demonstrate the capability to control optical waves propagating along chosen directions in space[11].

2. OPERATION PRINCIPLES OF ACOUSTO-OPTIC FILTERS

A typical acousto-optic cell consists of a birefringent crystal and a piezoelectric transducer generating travelling acoustic waves in the specimen. If driving RF electrical signal is applied to the transducer terminals then the acoustic wave modulates refraction index n of the crystal[1-3] . Therefore, it may be concluded that a diffraction grating is ultrasonically induced in the cell. Spatial period of the grating is equal to the acoustic wavelength $\Lambda = V / f$, where V and f are correspondingly phase velocity and frequency of ultrasound. As a result of the acousto-optic interaction, a diffracted beam occurs at the output of the cell. This beam is shifted in space relatively to the transmitted light. The transmitted radiation may be considered as the zero diffractional order while the diffracted radiation represents the filtrated/diffracted maximums with the numbers +1 or -1 . It is evident that variations of the driving electrical RF power applied to the transducer result in the control of light intensity[1-3] .

Strong acousto-optical interaction takes place in the cell only if Bragg laws of diffraction are satisfied[1-3]. Bragg matching condition couples the optical wavelength λ with the acoustic frequency f and the angle θ of light incidence on ultrasound . If a collimated optical beam is incident on the acoustic wave front at fixed angle θ then only a small number of optical wavelengths $\Delta\lambda$ may take part in the process of diffraction. Selection of the opical wavelengths is executed in the cell due to the laws of Bragg interaction. Therefore, the ultrasonically induced diffraction grating executes the desired selection of optical wavelengths while the optical wavelength of maximum transmission λ during the filtration is determined by the acoustic frequency. This wavelength may be easily tuned by variations of the acoustic frequency f. Consequently, both spectral composition and intensity of the filtrated signal are controlled by frequency and power of the driving electrical RF signal[1-3] .

Two different basic types of the filters are known in acousto-optics: the collinear and non-collinear acousto-optic devices[1-4]. The collinear devices usually possess the highest spectral resolution among other modifications of the filters. However, linear and angular apertures of the collinear filters are limited in comparison with the non-collinear instruments[5]. Moreover, relatively high levels of driving RF power in the case of the collinear filters restricted wide applications of the collinear devices in science and technology. On the other hand, wide-angular non-collinear filters possess much better optical throughput because of wide linear and angular optical apertures as well as low RF driving power levels. Spectral resolution of the non-collinear filters occurs not so perfect as in the collinear instruments[6-10] . Nevertheless, the devices on base of the wide-angular diffraction are promising for processing of optical images.

3. ACOUSTO-OPTIC TUNING OF SOLID STATE LASERS

Many types of optical quantum generators are characterized by a relatively wide spectral range of gain $G(\lambda)$. The well-known solid state Ti:sapphire lasers may be mentioned in this context. Figure 1 illustrates the dependency of output power P of a typical Ti:sapphire laser on optical wavelength λ . As seen in the picture, optical gain provides a principle possibility of tuning of the laser form visible light at optical wavelength $\lambda = 700$ nm up to the near infrared region of spectrum at the wavelengths about $\lambda = 1000\ nm$.

Tuning of the lasers over the wide range of optical wavelengths λ is usually performed by application in a laser cavity of dispersive elements such prisms or diffraction gratings. The major disadvantage of the traditional method of tuning consists in the fact that the transition from one wavelength λ_1 to another, e.g. to λ_2 is obtained by mechanical methods, i.e. by a rotation of the prism or the grating. It is evident that in the majority of cases, quick-action, reliability and precision of the mechanical tuning not aplways satisfy the requirements of practice.

As known, application of an optical diffraction grating in the cavity of the Ti:sapphire laser makes it possible to generate light in the lasing bandwidth $\Delta\lambda$ of about a few angstroms. This peculiarity is illustrated by Fig. 2 where profile of a lasing line of a typical Ti:sapphire laser is presented.

In order to avoid the disadvantages of mechanical tuning, a specially designed acousto-optic filter was installed in the laser cavity instead of the grating. The so-called *close to collinear regime* of light diffraction in paratellurite single crystal was chosen during the filter design[5].

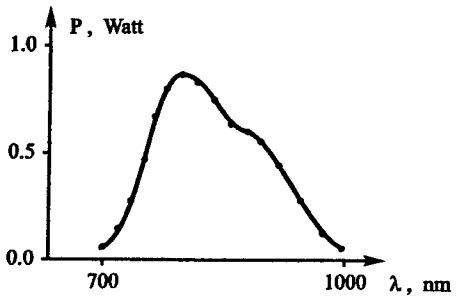


Figure 1. Optical output power of a typical Ti:sapphire laser

The choice of tellurium dioxide as the medium of light and sound interaction was made due to the high acousto-optic figure of merit of the material[4]. Perfect acousto-optic efficiency of the crystal provided low levels of driving RF power in the instrument compared to other known so far collinear acousto-optic devices. Moreover, the quasi-collinear geometry of interaction in paratellurite makes it possible to develop filters with the spectral resolution $R = \lambda / \Delta\lambda > 1000$ that is much better than in filters on base of TeO_2 of other types[5].

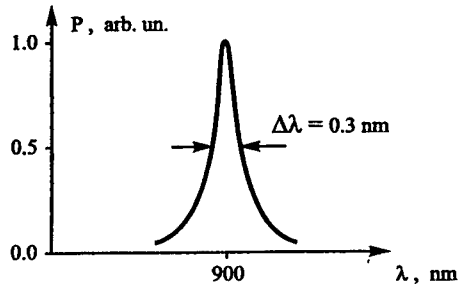


Figure 2. Line shape of a Ti:sapphire laser tuned by optical grating

The designed acousto-optic filter was fabricated in form of a prism, as shown in Fig. 3 . Slow shear acoustic waves were launched in the specimen by the transducer made of $LiNbO_3$ single crystal. Acoustic absorber was used in order to avoid reflections of sound in the crystal. Optical radiation was incident on the filter orthogonally to the input facet of the cell. Optical facets were antireflection coated so that total optical insertion losses of the cell were as low as 1% .

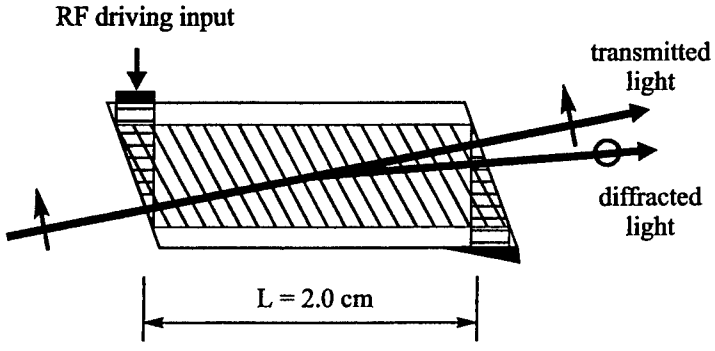


Figure 3. Tunable acousto-optic filter on base of tellurium dioxide

Frequency characteristics of the piezotransducer $P_a(f)$ is presented in Fig. 4 where frequency dependence of normalized acoustic power P_a in the cell is shown. Acoustic and electronic matching of the transducer correspondingly with the paratellurite crystal and with the driving RF generator was made by intermediate acoustic layers and by application of electrical matching networks. As a result, the transducer launched shear acoustic waves in the crystal in the frequency interval $f = 70 - 180\ MHz$, as illustrated in Fig. 4.

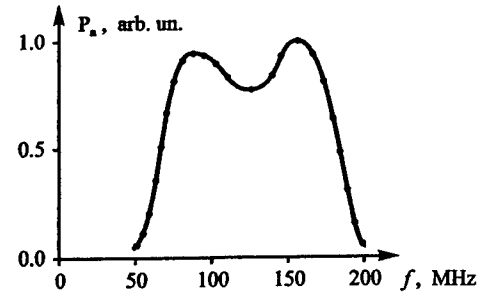


Figure 4. Frequency characteristics of piezotransducer

The proper matching of the transducer provided tuning of the filter over visible light and in the near infrared region of spectrum, as proved by the tuning curve $\lambda(f)$ of the filter in Fig. 5 . The tuning curve of the instrument was verified experimentally during calibration of the filter with the help of laser radiation. Comparison of data in Fig. 5 and Fig. 4 confirm that the filter was capable of electronic tuning in the range of optical wavelengths $\lambda = 580 - 1350\ nm$. This spectral range occurred much wider than

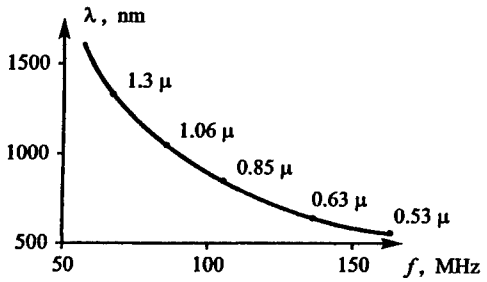


Figure 5. Tuning curve of the filter

the bandwidth of the laser gain in Fig. 1 . Consequently, it was reasonable to apply the filter in the laser cavity so as to expect tuning of the quantum generator all over the spectral interval of gain.

As proved experimentally, spectral passband of the filter occurred to be about $\Delta\lambda = 0.15 - 0.30\ nm$ depending on the wavelength value λ. Figure 6 presents results of measurements of the filter transmission characteristics $T(\lambda)$. It is evident that spectral passband of the filter was dependent on the length of light and sound interaction $L = 2.0\ cm$, as shown in Fig. 3.

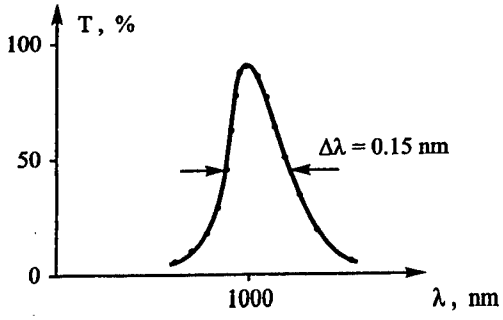


Figure 6. Spectral transmission of the filter

The experiment demonstrated that installation of the filter in the laser cavity results in narrowing of the lasing bandwidth compared to the case withthe traditional optical grating in Fig. 3 . It is evident that the improvement of the line shape originated from multiple passes of laser radiation through the filter in the cavity.

4. APPLICATION OF FILTERS IN WDM WAVEGUIDE COMMUNICATION LINES

Recently there has been an increasing interest in application of the acousto-optic filters on bulk acoustic and optic waves for fast and reliable selection of optical signals propagating at different optical wavelengths in fibers[7]. Application of the quasi-collinear geometry of light and sound interaction resulted in a design of an instrument possessing a number of advantages in comparison with other known so far collinear acousto-optic filters. These advantages are relatively high spectral resolution, low driving RF power levels of the instrument, sufficient suppression of side lobes and the possibility to operate with arbitrary polarized light[5,7] .

The filter was designed in such a manner that optic and acoustic beams were propagating in paratellurite with approximately collinear group velocities of the waves. The length of acousto-optic interaction $L = 4.0\ cm$ was determined by the size of the crystal used in the filter. As evident, the interaction length determined spectral passband of the device $\Delta\lambda < 9\ nm$ at optical wavelengths near $\lambda = 1.55\ mkm$. Piezoelectric transducer fabricated of $LiNbO_3$ generated acoustic waves at frequencies of ultrasound about $f = 45\ MHz$ satisfying the condition of Bragg matching at optical wavelength $\lambda = 1.55\ mkm$. Cross-section of the acoustic column in the cell was about $0.35 \times 0.3\ cm^2$.

The filter consisted of a couple of antireflection coated input and output fiber connectors intended for termination of the device to a single-mode WDM communication line. The device had additional output terminal for selection of the filtrated light. Incident on the filter arbitrary polarized optical radiation consisted of a number of signals possessing different optical wavelengths λ_i . These signals belonged to the traditional for WDM communication lines interval of wavelengths $\lambda = 1530 - 1565\ nm$. Spectral spacing between the optical signals was chosen about $2.0 - 4.0\ nm$ during the experiments.

Optical beam expander was used at the filter input in order to form a collimated optical beam with the diameter $2w = 0.12$ cm. A couple of similar beam expanders were installed at the filter outputs with the goal to direct the transmitted and the filtrated radiation to the outputfibers. As much as 3 polarization splitters made of $CaCO_3$ and three SiO_2 phase plates were applied in the instrument in order to provide operation of the filter with arbitrary polarized light.

In the absence of the driving RF signal, the filter transmitted the incident multiwavelength radiation along the fiber line. Total insertion losses of the instrument including the connectors, the splitters, the phase plates, the crystal and the pigtails were less than $2.0\ dB$. Application of RF driving signal to the filter terminal resulted in filtration of one of the incident optical signals. Optical wavelength of the filtrated signal depended on the value of the acoustic frequency f . As much as 90% of the incident radiation was filtrated by the device with the driving electric power as low as $P = 50\ mW$. If the driving RF signal consisted of a number of electric frequencies then the filter was capable of operation in the multiwavelength regime. Moreover, the instrument executed filtration of optical wavelength and simultaneously regulation of light intensity in each of the chosen channels.

Optical crosstalk at the device output was less than $-20\ dB$ if the signal spacing was more than $3.2\ nm$. On the other hand, the spacing of the signals about $0.8\ nm$ resulted in the crosstalk about $-10\ dB$. It was observed that further decrease of the crosstalk may be achieved in a number of ways, e.g. by application of a couple of identical filters in tandem. Experimental testing of the instrument proved that sensitivity of the filter to optical polarization was less than $-0.35\ dB$ confirming the general statement that the filter was not sensitive to optical polarization.

5. ACOUSTO-OPTIC PROCESSING OF IMAGES

Tunable acousto-optic filters have been successfully used in systems of optical information processing operating with images[6-10]. As found, perfect quality of a filtrated image may be obtained only with a filter possessing wide linear and angular apertures. Growth of the apertures in the acousto-optic filters may be achieved by means of the wide-angular geometry of interaction. This geometry of diffraction has been successfully used in systems of information processing

operating with non-coherent radiation. However, recently it was proposed that processing of images formed in coherent light may also be carried out with the help of the wide-angular acousto-optic filters[11].

The report reviews developed systems of image processing intended for the application with non-coherent radiation in the ultraviolet, visible light, near and middle infrared regions of spectrum. High quality of the filtrated images, wide tuning range of the filters and relatively low levels of driving power were obtained in the imaging filters due to optimization of the interaction geometry in TeO_2 single crystals and owing to accurate fabrication of transducers of the acousto-optic cells.

Tuning range of the developed filters exceeded an octave while transmission coefficients in the UV, visible light and near IR regions of spectrum were close to 90%. Driving RF power levels in the mentioned spectral intervals were less than $P = 1.0 - 3.0$ *Watt* . Linear apertures of the imaging systems were as large as $1.5 \times 1.5\ cm^2$. The filters were also designed with angular apertures up to 8° providing the filtration of arbitrary polarized images with spatial resolution better or compatible with the TV standard.

Application of the imaging devices for processing of images formed in coherent light resulted in development of new models of acousto-optic filters for regulation of spatial structure of coherent beams[11]. Electronic two-dimensional selection of spatial frequencies of convergent laser beams has been executed by means of the designed acousto-optic paratellurite devices. The developed filters of spatial frequencies could perform edge enhancement of the images. The advantage of the method consists in the fact that the procedure of edge enhancement was carried out in real time.

6. CONCLUSIONS

It may be concluded that successful application of the acousto-optic filters in laser technology, optical communication and processing of information became possible due to the high operation parameters of the designed filters. If the acousto-optic filter is installed inside a cavity of a Ti:sapphire laser then it provides the possibility to tune electronically the instrument all over the wavelengths of laser gain. In addition, due to multiple transitions of light through the filter in the laser cavity, the lasing line becomes narrow. High resolution filters may be also recommended for applications in WDM waveguide communication lines. Though spectral passband of the designed filters is wider than required by the existing standards, the advantages of the instruments in optical WDM communication lines are evident. As for the acousto-optic imaging filters, the perfromed analysis has proved that processing of coherent and non-coherent images has already become a new branch of acousto-optic technology.

7. REFERENCES

1. V.Balakshy, V.Parygin and L.Chirkov, *Physical Principles of Acousto-Optics,* Radio and Communication, Moscow, Russia, 1985.
2. J.Xu and R.Stroud, *Acousto-Optic Devices,* Wiley, New York, 1992.
3. A.Goutzoulis and D.Pape, *Design and Fabrication of Acousto-Optic Devices*, Marcell Dekker Inc., N.Y., USA, 1994.
4. I.C.Chang, "Tunable Acousto-optic filters:an overview", *Proc.SPIE* , **90,** pp.12-22, 1976.
5. V.B.Voloshinov, "Close to collinear acousto-optical interaction in paratellurite", *Opt. Eng.*, **31**, N.10, pp.2089-2094, 1992.
6. V.B.Voloshinov and V.Ya.Molchanov, "Acousto-optical modulation of radiation with arbitrary polarization direction", *Optics and Laser Technology*, **27**, N5, pp.307-313, 1995.
7. J.Sapriel, V.B.Voloshinov, V.Ya. Molchanov and M.Choumanne, "Tunable filter for telecommunication using bulk collinear acousto-optic interaction", *EOS Topical Digest*, **27**, pp.63-64, 2000.
8. V.B.Voloshinov, V.Ya.Molchanov and J.C.Mosquera, "Spectral and polarization analysis of optical images by means of acousto-optics", *Optics and Laser Technology*, **28**, N2, pp.119-127, 1996.
9. V.B.Voloshinov, "Imaging experiments based on application of non-collinear tunable acousto-optic filters", *Proc. SPIE*, **3584**, pp.116-127, 1998.
10. V.B.Voloshinov and N.Gupta, "Acousto-optic imaging in the middle infrared region of spectrum", *Proc SPIE*, **3900**, pp.68-73, 1999.
11. V.B.Voloshinov and T.M.Babkina, "New method of image processing and edge enhancement", *EOS Topical Digest*, **27**, pp.28-29, 2000.

Electrooptic glasses and glass-ceramics for elements controlling laser radiation

G. O. Karapetyan, A. A. Lipovskii, V. V. Loboda, L. V. Maksimov, D. V. Svistunov, D. K. Tagantsev, B. V. Tatarintsev, A. A. Vetrov

All-Russian Scientific Center "Vavilov State Optical Institute"
36-1 Babushkina, St Petersburg, 193171, Russia

ABSTRACT

The results of studying the electrooptical sensitivity of industrial glasses are presented, and it is shown that Kerr constant, B, of them does not exceed 10^{-15} m/V^2 An approach to the choice of compositions of the glasses of high Kerr sensitivity is developed, and experimental sodium-niobium-silicate glasses with $B>10^{-14}$ m/V^2 have been designed and formed. The approach is based on the hypothesis of "crystalline motifs" (structural inhomogeneities responsible for electrooptical sensitivity of the glasses), which are the ordered regions (several coordination spheres) with the crystal-like structure. When heat-treated the designed glasses crystallize, with the phase precipitated being $NaNbO_3$ microcrystals. Temporal-thermal conditions of the glass crystallization to form a transparent glass-ceramics with $B\approx10^{-12}$ m/V^2 have been found. It has been also shown that such glass-ceramics can be produced by high-temperature alkaline ion exchange. A low-temperature silver ion exchange in the designed glasses and glass-ceramics has been studied and optical waveguides supporting from 1 to 50 modes have been formed. In these waveguides the index variation equal to 0.15 is achieved.

Keywords: glass, glass-ceramics, electrooptical phenomenon, integrated optics, ion exchange

1. INTRODUCTION

The research was aimed at designing glasses and glass-ceramics demonstrating enhanced Kerr electrooptical sensitivity and suitable for the formation of active optical elements for controlling laser radiation by applied electric field. Glassy materials could be prospective if they demonstrated proper light modulation under the fields of reasonable amplitude. Since the manufacturing of glasses and glass-ceramics is less expensive than the manufacturing of electrooptical crystals, low cost of novel electrooptical elements for controlling laser radiation, including bulk and integrated optical ones, was expected.

The activities of the research were: i) the elaboration of the approach to predict electrooptical properties of glasses; ii) the design of compositions, the synthesis and characterization of glasses of enhanced electrooptical sensitivity; iii) the formation of electrooptic glass-ceramics and optical waveguides based on those ceramics; iv) the formation of GRIN optical waveguides based on electrooptical glasses. The usage of the materials to be designed lies in the fields of integrated, fiber, GRIN and non-linear optics, particularly, for manufacturing electrooptical light modulators.

2. STUDIES OF KERR SENSITIVITY OF GLASSES AND APPROACH TO THE PROBLEM OF DESIGNING ELECTROOPTICAL GLASSES

Different types of the Russian commercial optical glasses were tested by Kerr constant measurement and it was established that glasses of the flint type demonstrated highest Kerr constants, B. For the best flint glasses, that constant turned out to be about 5×10^{-16} m/V^2. Besides, series of experimental silicate, germanium, and phosphate glasses containing heavy metals (like Bi, Ta, Ti, Te, Nb, Pb, and others) and the glasses containing barium or alkaline metals additionally were produced and Kerr measurements were performed as well. A short list of the several experimental glass-forming systems studied and demonstrating a measurable value of Kerr constant is i) Silicate systems: $BaO–SiO_2–Al_2O_3–TiO_2$ (BT-series), $K_2O–PbO–TiO_2–SiO_2$ (PT-series), $Na_2O–K_2O–Nb_2O_5–SiO_2$ (S-series). $SiO_2–B_2O_3–PbO–TeO_2–Ga_2O_3$ (VF-series), $(Li+Na)_2O–(Ta+Nb)_2O_5–(Ti+Zr)O_2–SiO_2–GeO_2$ (NGS-series); ii) Germanium systems: $PbO–GeO_2$; $PbO–Nb_2O_5–GeO_2$; iii) Phosphate systems: $Li_2O–La_2O_3–P_2O_5–Nb_2O_5$, $PbO–BaO–P_2O_5$; $PbO–TeO_2–P_2O_5$; iv) Heavy metal systems: $PbO–Bi_2O_3–Ga_2O_3$ (H-

Laser Optics 2000: Control of Laser Beam Characteristics and Nonlinear Methods for Wavefront Control, Leonid N. Soms, Vladimir E. Sherstobitov, Editors, Proceedings of SPIE Vol. 4353 (2001)
© 2001 SPIE · 0277-786X/01/$15.00

Li_2O–La_2O_3–P_2O_5–Nb_2O_5, PbO–BaO–P_2O_5; PbO–TeO_2–P_2O_5; iv) Heavy metal systems: PbO–Bi_2O_3–Ga_2O_3 (H-series). Figure 1 summarizes the results of Kerr constant measurements.

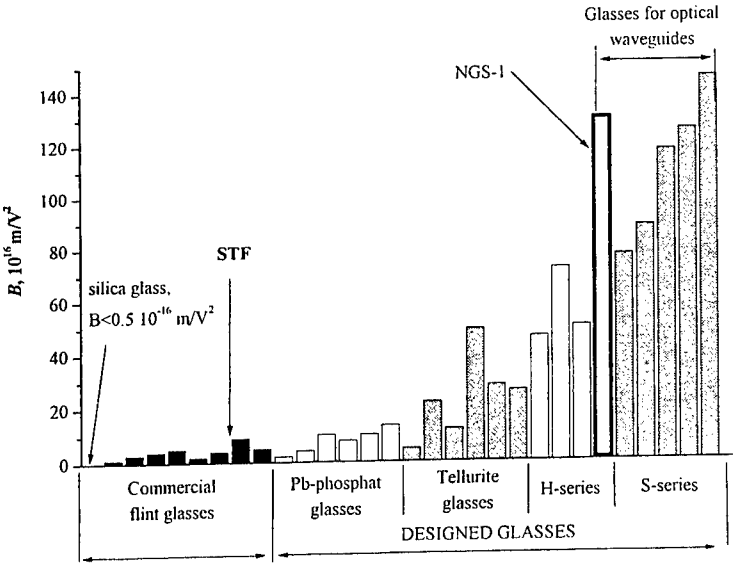


Fig.1. Kerr constant, ***B***, of the commercial flint glasses and the glasses designed in the present work.

Of all the studied glasses, silica-niobate ones (S-series) demonstrate highest Kerr constant (up to $1.5 \cdot 10^{-14}$ m/V^2 in glass S5) that is higher by 1.5 order of magnitude as compared with best commercial flint glasses (10^{-15} m/V^2). The bar diagram in Fig.1 does not include the results on all the glasses studied because they do not demonstrate Kerr sensitivity higher than one for the commercial flint glasses. Although it could be expected that, for example, glasses of BT-series should demonstrate a high magnitude of B, for these glasses contain up to 40 mol.% of TiO_2 and the same amount of BaO (both metals are of high polarizability). It was found that some telluride glasses, which contained more than 70 mol. % of TeO_2 and 15 mol.% of PbO, demonstrated Kerr constants 3 times lower than it was in the glasses of S-series, which contained only up to 37 mol.% of Nb_2O_5 (S5 glass). Besides, it should be noted that NGS-1 glass (see Fig.1), which is a lithium-silicate glass containing only 20 mol.% of Nb_2O_5, demonstrates rather high B=1.3×10^{-14} m/V^2. Thus, a high percentage of heavy metals or other highly polarizable elements is not the only condition for the glasses to demonstrate high Kerr sensitivity. This was mentioned earlier by N. F. Borrelli *et al.*[1] by whom a dependence of the concentration of the network forming components on B was suggested. A dependence of the electrooptical sensitivity of glasses on the network composition is also well-illustrated by our measurements. For example, Kerr constants of niobium-phosphate glasses and of S-series glasses, which are the glasses with the same niobium contents but different network forming components, differ by about two orders of magnitude. Today, it is not clear yet what the reason of Kerr sensitivity of glasses is.

Electrooptical (EO) phenomenon is the change of refractive index of medium due to the rearrangement of the internal electric charges under external electric field. Glasses demonstrate features of both the liquid state and the solid one and this dualism enables one to assume two reasons of their EO sensitivity. In isotropic liquids, the rearrangement and, therefore, EO phenomenon is caused by the reorientation of molecules and the deformation of electronic shells. In glasses, only the latter is possible, for any electric-field-induced reorientation (or rotation) of polar glass structure fragments at room temperature is strongly obstructed by kinetic restrictions. Thus, if one regards glasses as a liquid, then the glasses containing multielectron ions with high polarizability, such as Pb, Ba, Bi, Te, and others, appear to be perspective ones to demonstrate enhanced EO sensitivity. In crystals, EO phenomenon is caused by the rearrangement of ionic charges resulting from changing the local symmetry of the crystal lattice under external field, a maximal EO response being observed at temperatures close to the temperature of ferroelectric phase transition, if any. Therefore, the highest EO sensitivity is expected in glasses as a solid, the local structure of which has some similarity with the structure of EO crystals. This similarity (structural motifs) should exist within several coordination spheres and most enhanced Kerr constants are supposed to be in case the corresponding EO crystal exists in ferroelectric phase at temperatures near and below the glass transition temperature region. This crystalline structure can be 'frozen' in glass cooling because below the glass transition temperature any structural relaxation does not take place. Seeing that EO sensitivity of ferroelectric crystals is much higher than one of the best EO liquids, the presence of crystalline structural motifs in glasses appears to be a most likely reason for glasses demonstrating high Kerr constants as compared with the presence of highly polarizable multielectron ions only.

The data on light[2] and small-angle X-ray[3] scattering, on disturbance of Newton character of the glass viscosity at extra low loading[4] as well as the analysis of thermodynamic functions of glasses at absolute temperature zero[5], and others[6, 7, 8, 9] show that, in glasses, there actually are fluctuation inhomogeneities of about 10 Å in sizes with like-crystal structure[2,3], which do not have phase boundaries[5]. We will call those regions the crystalline motifs (CMs). Our approach to the problem of de-

signing glasses with high Kerr constants is reduced to the following. A glass can demonstrate high Kerr constants, if CMs are similar to the structure of the crystals of high EO sensitivity. Thus, one of the necessary (but not sufficient) conditions to form EO glasses consists in the glasses to contain all the components entering some of known EO crystals.

In the present report we do not discuss all the conditions to ensure the formation of appropriate CMs, but only try to corroborate the validity of the approach. In accordance with the approach, the improvement of EO sensitivity of glassy material should be expected if the material were to contain nano- or microcrystals of high EO sensitivity. It appears that such microcrystals can precipitate in annealing of the glasses with corresponding EO CMs, for these motifs, being almost crystalline, can be easily transformed to the corresponding nano- or microcrystals. Since those motifs are also responsible for high EO sensitivity of homogeneous glasses, it seems to be correct to assume that the EO microcrystals would precipitate in the glasses demonstrating high Kerr constants

Glass crystallization in two glass-forming systems (S-series and BT-series) with appropriate for EO glasses compositions has been studied, and Kerr measurements in the glasses and glass-ceramics formed have been performed to find evidence of the validity of the approach.

3. ELECTROOPTICAL GLASSES AND GLASS-CERAMICS

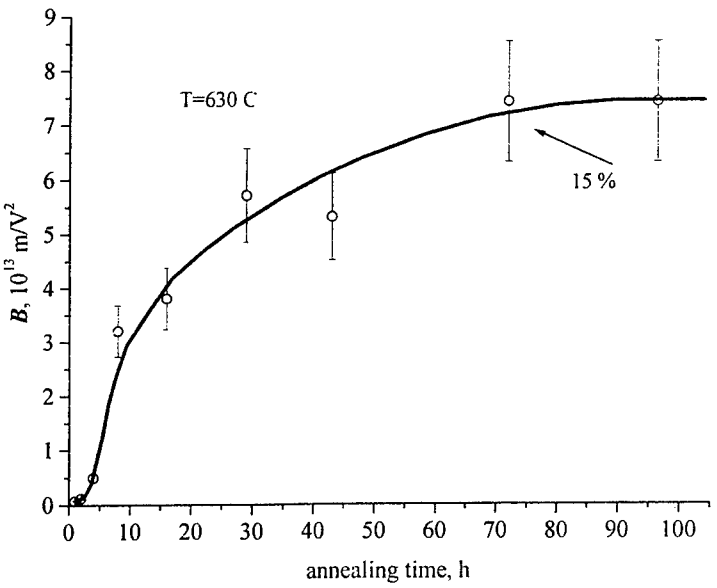


Fig.2. The increase of the Kerr constant of S2 glass with a rise in annealing time.

The compositions of the designed and studied silica-niobate (S-series) glasses can be formularized as $19Na_2O$-$11K_2O$-xNb_2O_5-$(66-x)SiO_2$-4(others), with x varying from 0 to 37. (The first brief study of this system with $29<x<37$ has been performed in 1986 year[10].) It was expected that CMs of EO crystals $NaNbO_3$ or $KNbO_3$ or $(K,Na)NbO_3$ would appear in the glasses in their formation. In these glasses Kerr constant increased from about 0 to 1.5×10^{-14} m/V^2 with a rise in Nb_2O_5 concentration. All the glasses of S-series were studied by differential thermal analysis (DTA) In glasses (S1-S5), for which Nb_2O_5 content exceeds 30 mol %, only two peaks (near 680°C and 930°C) related to the glass crystallization have been observed. The first one belongs to the $NaNbO_3$ crystal precipitation, which is confirmed by X-ray diffraction (XRD) analysis of the glass samples after heating at temperatures higher than 680°C but lower than 720°C

Systematic heat treatments of S2 and S4 glasses at 610°C, 630°C, and 650°C for times varying form 1 h to 150 h showed increasing the volume fraction of $NaNbO_3$ crystalline phase with a rise in annealing time. The volume fractions were estimated by the height of XRD peaks. During the initial time intervals of heat treatments (up to 16 h) the glasses became non-transparent, however after 30-h treatment they became transparent again. The Kerr constant of the material (Fig. 2) increased from $\sim10^{-14}$ m/V^2, which was typical for the initial glasses, up to $\sim10^{-12}$ m/V^2 with a rise in processing time. After 80-h treatment, Kerr constant of the ceramics formed ceased rising, and that corresponded to the saturation.

The increase in Kerr constant was accompanied with changes in Raman spectra of the material Fig 3 depicts these spectra. In the initial glass, Nb-atoms can occupy 3 different positions[11]: in separate octahedron (the band at about 900 cm^{-1}), in chains of octahedrons (the band at about 830 cm^{-1}), and in the crystalline net of octahedrons (the band at about 650 cm^{-1}). After annealing, most of Nb-atoms are in the net that corresponds to crystal lattice The formation of crystalline lattice was also checked in XRD measurements. The results of the measurements are presented in Fig.4 Comparison of this figure with Fis 3 shows that the CMs are the origin of microcrystals arising

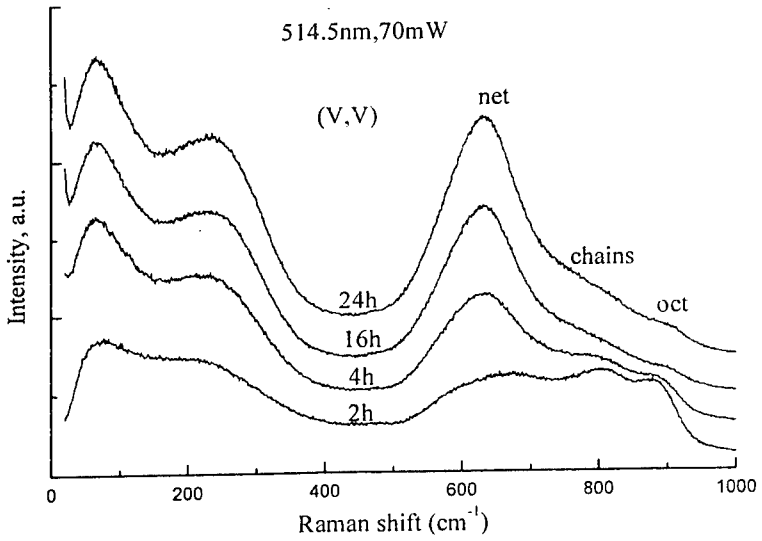


Fig.3. Changes in Raman spectra of S2 glass in annealing at 630 C for different time.

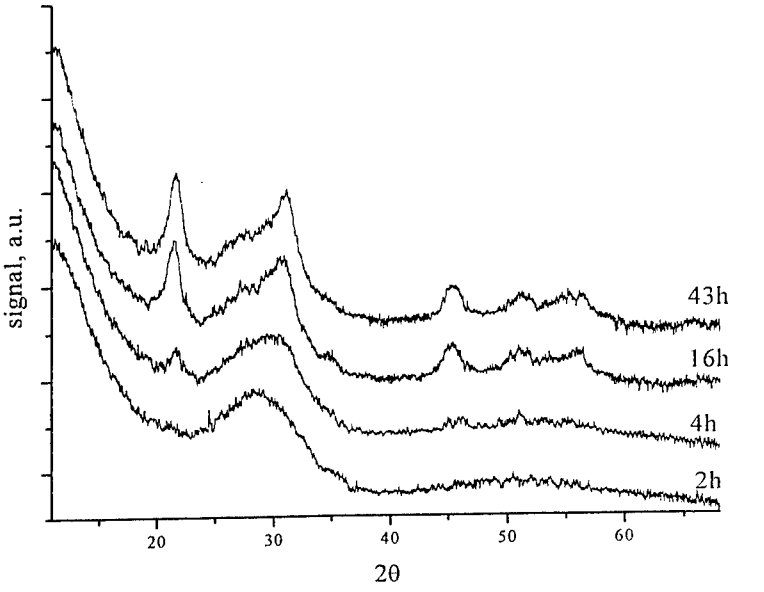


Fig.4. Changes in XRD pattern of S2 glass in annealing at 630 C for different time. All the peaks belong to $NaNO_3$.

Kerr measurements in the glasses of BT-series were also performed. The compositions of the glasses of BT-series can be formularized as x[BaO-TiO_2]-(100-x)[Al_2O_3-2SiO_2-BaO], with x varying from 20 to 80. It was expected that CMs of the EO crystal $BaTiO_3$ would appear in the glasses in their formation. In spite of the fact that these glasses contained large amounts of the components necessary to form $BaTiO_3$ crystals, which are known as one of the high sensitive EO crystals, Kerr constants in these glasses proved to be equal about the same as for commercial flint glasses ($\sim 10^{-16}$ m/V^2). Several glasses of BT-series were studied by polythermal heat treatment in a furnace with temperature gradient for 2 h. Glass crystallization has been found to occur at temperatures higher than 980°C. The crystallized glasses were non-transparent and Kerr measurements of those crystallized glass were impossible. EO measurements in the samples of transparent glasses, which were heat treated at temperatures below the crystallization temperature (800-950°C), showed that Kerr constants of the samples did not change compared to the initial (untreated) glasses. The crystallized glasses of BT-series were studied by XRD technique. The expected crystals of $BaTiO_3$ were not determined, and the precipitated crystalline phases could not be identified.

Comparison of the results on Kerr measurements and on crystallization of these two glass-forming systems allows, in our opinion, to conclude that the developed approach is valid and can be used in designing new EO glasses and glass-ceramics. The first condition, necessary but not sufficient, in designing EO glasses and glass-ceramics consists in the following; the glass composition must include the oxides of all the elements entering some known EO crystal. The high Kerr constant of the glass points to the presence of CMs of that EO crystal, and it is a sufficient condition for the corresponding EO crystals to precipitate in forming EO glass-ceramic materials.

4. ION EXCHANGE IN NEW ELECTROOPTICAL MATERIALS

The study of a high-temperature (above glass transition) alkali-alkali ion exchange in new EO glasses was undertaken to form surface EO glass-ceramic films. Those films were supposed to be suitable for low-temperature alkali-silver ion exchange, which could lead to the formation of active waveguide structures for controlling laser radiation. The NGS glass (with Kerr constant equal to 1.3×10^{-14} m/V^2) was used in those experiments. The NGS glass is a lithium-niobate-silicate glass (26 mol.% of Li_2O, 32 mol.% of SiO_2, 20 mol.% of Nb_2O_5, and others), which under heat treatment above its glass transition temperature yields a non-transparent glass-ceramics with $LiNbO_3$ crystals as precipitates. Since all the attempts to synthesize the same glass containing sodium instead of lithium were failures because of the glass crystallization, it appeared that the Li-Na ion exchange in NGS glass could allow the controllable formation of sodium-niobate glass-ceramic films.

The Li-Na ion exchange has been performed in a salt melt of $NaNO_3$ at two temperatures (620°C and 650°C) and for times varying from 1 to 16 hours. Microscopic observations showed that after the ion exchange at 650°C non-transparent under-surface layer formed, with the layer thickness depending on the processing time. The bulks of the processed samples remained homogeneous and transparent. The samples after ion exchange were powdered and analyzed by the XRD technique. The only phase has been found to be $NaNbO_3$ crystals (see Fig.5). At 620°C, the ion exchange led to the formation of layers, which became non-transparent or translucent only after additional 3-h heat treatment at 650°C. The XRD analysis showed that it was due to the growth of $NaNbO_3$ microcrystals as well. These experiments have illustrated a new possibility to form EO glass-ceramics in controllable manner.

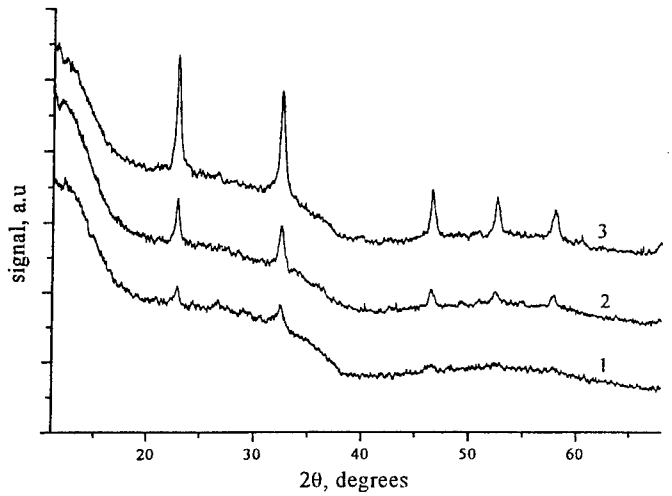


Fig.5. XRD patterns of the NGS glass samples exposed to a $NaNO_3$ salt melt at 650°C for 4h (1), 8h (2), and 16h (3). All the peaks belong to $NaNO_3$

A study of the low-temperature silver ion exchange in the NGS glass has been performed as well. The study aimed at trying to form waveguiding structures in one of the designed EO glasses. At the temperatures used (260°C, 300°C, and 340°C), there were not any phase transformations in the glass. The glass samples were exposed to a salt melt of dilute $AgNO_3$ (5 mol.% of $AgNO_3$ + 95 mol.% of $NaNO_3$) during 1, 3, and 6 hours. Those ion exchange treatments resulted in waveguides supporting from 10 to 50 modes. Mode spectra were measured by the prism coupling technique. The characterization of the diffusion and ion exchange parameters of the glass has been performed by the recently developed technique[12], for which a large number of modes is a factor defining high precision of the technique. As a result, the concentration-dependent diffusion coefficient and the possible index variation (up to about 0.16) in the ion exchange processing used have been determined and then checked in simulating and forming graded-index structures.

An attempt to form optical waveguides in the designed transparent EO glass-ceramics with high Kerr constant (7×10^{-13} m/V^2) has been undertaken. The glass-ceramics used was produced from S2 glass in two step annealing at 610°C (4.5 h) and 650°C (1 h). A sample of this glass-ceramics was exposed to a salt melt of $NaNO_3$ at 360°C for 1 h. This resulted in a single-mode waveguide, but light scattering in that structure was rather high. Here it should be noted that the processing of the initial S2 glass at the same ion exchange conditions gave rise to a 12-mode waveguide. It was not an unexpected result, for the majority of alkaline ions (in case of S2 glass, they are Na ions) was incorporated by the $NaNbO_3$ microcrystals during the glass-ceramics formation, and in the vitreous part of the glass-ceramics there were not enough alkali ions capable of taking part in the ion exchange. It resulted in a decrease in the index variation and therefore in quantity of modes. The latter should be taken into account in designing EO glass-ceramics, which is supposed to be used in the formation of active glass-ceramics waveguiding structures.

5. CONCLUSIONS

Studying the Kerr sensitivity of most types of Russian industrial glasses shows that glasses of the flint type demonstrate highest Kerr constants, B, which do not exceed 10^{-15} m/V^2. The experimental silicate, germanium, and phosphate glasses containing ions of heavy and other highly polarizable elements have been formed, and the measurements of their Kerr constants have shown that the presence of those ions is not sufficient for glasses to demonstrate high Kerr sensitivity. An approach based on the hypothesis of "crystalline motifs" responsible for Kerr sensitivity of the glasses has been suggested and verified by comparing electrooptical and crystallization properties of the glasses designed. The highest magnitudes of Kerr constant are achieved in sodium-niobium-silicate glasses ($B>10^{-14}$ m/V^2) and glass-ceramics formed from those glasses ($B>10^{-12}$ m/V^2) by annealing. In annealing, $NaNbO_3$ microcrystals precipitated. It has been also shown that sodium-niobate glass-ceramics can be produced by high-temperature Na ion exchange in a glass containing other alkali ions. In this case glass-ceramics formation can be performed in controllable manner. In the electrooptical glasses and glass-ceramics designed optical waveguides supporting from 1 to 50 modes have been formed by low-temperature silver ion exchange, the maximal index variation being equal to 0.15. Thus, the suggested approach, the designed glassy materials and techniques of their

production, as well as the developed ion exchange technique of waveguide formation are the first step to design active electrooptical glassy structures for controlling laser radiation.

6. ACKNOWLEDGEMENTS

This work was supported by the International Science and Technology Center under Project #979.

7. REFERENCES

1. N. F. Borrelli, B. G. Aitken, M. A. Newhouse, D. W. Hall, "Electric-field-induced birefringence properties of high-refractive-index glasses exhibiting large Kerr nonlinearities, *J. Appl. Phys.*, **70**, pp.2774-2779, 1991.
2. G. O. Karapetyan, L. V. Maksimov, O. V. Yanush, "The manifestation of disorder and inhomogeneity of vitreous substances in scattering light spectra", *Glass Phys. and Chem.*, **18**, pp.412-422, 1992.
3. V. V. Golubkov, E. A. Parai-Koshits, Peculiarities of temperature dependence of the structure of single-component glasses at glass formation temperature range, *Glass Phys. and Chem.*, 7, pp.278-282, 1981.
4. G. M. Berteniev, A. S. Eremeeva, "Rheological properties of glasses above glass transition temperature and their structure", *High-molecular compounds*, **3**, pp.740-747, 1961.
5. S. V. Nemilov, Thermodynamic functions of non-equilibrium disordered systems at absolute temperature zero and nature of vitreous sate, *Glass Phys. and Chem.*, **8**, pp.11-24, 1982.
6. V. G. Zhdanov, B. T. Kolomiets, V. M. Lyubin, V. K. Malinovsky, "Photoinduced optical anisotropy in chalcogenide vitreous semiconducting films", *Phys.Stat.Sol.(a)*, **59**, pp.621-626, 1979.
7. V. G. Zhdanov, V. K. Malinovsky, "Photoinduced birefringence and dichroism of As_2S_3 films", *Pis'ma v ZhTF (Rus)*, **3**, pp.943-946, 1977.
8. D. K. Tagantsev, "Nature of the photoviscous effect in terms of the valence-configuration theory of viscous flow of glasses", *Glass Phys. and Chem.*, **13**, pp.839-846, 1987.
9. V. N. Sigaev, E. N. Smelyanskaya, V. G. Potnichenko, V. V. Koltashev, A. A. Volkov, P. Pernice, "Low-frequency band at 50 cm^{-1} in the Raman spectrum of cristobalite: identification of similar structural motifs in glasses and crystals of similar composition", *J. Non-Crys. Sol.*, **248**, pp.141-146, 1999.
10. G. O. Karapetyan, Yu. G. Korolyov, L. V. Maksimov, S. V. Nemilov, "Physico-chemical peculiarities of niobate glasses with electrooptic properties", *Glass Phys. and Chem.*, **22**, pp.598-601,1986.
11. T. Cardinal, E. Fargin, G. Le Flem, S. Leboiteux, "Correlation between structural properties of Nb_2O_5-$NaPO_3$-$Na_2B_4O_7$ glasses and non-linear optical activities", *J. Non-Crys. Sol.*, **222**, pp.228-234, 1997.
12. J. Liñares, A. A. Lipovskii, D. K. Tagantsev, J. Turunen, Characterization of diffusion process in glasses with a simple mode-index measurements, *Optical materials*, **14**, pp.115-120, 2000.

Effect of crystal orientation on a high power Faraday isolator.

Efim A. Khazanov[a], Nikolay F. Andreev[a], Oleg V. Palashov[a], Anatoly K. Poteomkin[a], Alexandr M. Sergeev[a], David H. Reitze[b], Oliver Mehl[c]

[a]Institute of Applied Physics, 46 Uljanov St., Nizhny Novgorod, 603600, Russia
[b]Department of Physics, University of Florida, Gainesville, Florida, 32611
[b]TU Berlin, Optisches Institut, Sekr. P1-1, Strasse des 17. Juni 135 10623 Berlin, Germany

ABSTRACT

The operation of various designs of a Faraday isolator at high average power with an arbitrary orientation of a cubic magneto-optical crystal is studied theoretically. It is shown that in different Faraday isolator designs, different crystal orientations may be optimal from the standpoint of isolation. Thermo-optic and photoelastic constants for terbium gallium garnet crystals grown by different producers were measured. Measurements of self-induced depolarization were made for various orientations of crystallographic axes. The measurements are in good agreement with theoretical predictions. Based on the obtained results it is possible to choose such crystal orientation for Faraday isolators which is optimal from the standpoint of isolation at high average powers.

Keywords: photoelastic effect, TGG, Faraday isolator, thermo-optic constants, compensation of self-induced depolarization

INTRODUCTION

Since the average power of continuous wave and repetitively pulsed lasers has significantly increased over the past years, investigations of thermal effects caused by absorption of laser radiation in Faraday isolators (FI) are becoming more important[1-6]. Many applications require a combination of high average power, great isolation ratios and small aberrations introduced by FI. An illustrative example is a laser interferometer for gravitational wave observatory[7]. When choosing materials for magneto-optics, specific features of different thermal effects should be considered. In a number of papers, figures of merit were introduced, which allows comparing different magneto-optical materials. From the standpoint of energy losses, such figure of merit is the ratio V/α_0 [8,9], where V is the Verdet constant and α_0 is the absorption coefficient per a length unit. From the standpoint of thermal self-focusing the figure of merit is VW_{cr} [10] (where W_{cr} is the critical energy of thermal self-focusing [11]) for pulsed lasers, and κVW_{cr} [10,12] (where κ is the coefficient of thermal conductivity) for high average power lasers. However, these effects have almost no influence upon the main parameter of a Faraday isolator - its isolation ratio, because they affect only the amplitude and phase of laser radiation but do not alter the state of polarization. The thermal effects that lead to depolarization of laser radiation and, consequently, to isolation deterioration, namely the temperature dependence of the Verdet constant and the photoelastic effect, were studied for the first time in Refs. [13-16]. Ref.[14] predicted theoretically that it is the photoelastic effect that limits the isolation ratio at high average powers, and the effect of the temperature dependence of the Verdet constant may be neglected. In Refs.[15,17] this theoretical prediction was confirmed in experiment. In Ref.[14] for crystals with the [001] orientation (and also for glass magneto-optical elements) a figure of merit μ, which characterizes a magneto-optical medium from this standpoint (the higher μ, the greater the isolation ratio and, consequently, the better the medium), was defined as

$$\mu = \frac{V\kappa}{\alpha Q}$$

where Q is a thermo-optic constant characterizing the thermo-photoelastic effect for the components of rod configuration.

$$Q = \left(\frac{1}{L}\frac{dL}{dT}\right)\frac{n_0^3}{4}\frac{1+\nu}{1-\nu}(p_{11} - p_{12}) \qquad (1)$$

Here L, ν, p_{ij} and n_0 are the length, the Poison's ratio, and the refraction index, respectively, T is the temperature, and p_{ij} (i,j=1,2..6) are elements of the photoelasticity tensor in two-index Nye's convection[18]. Recently, new designs of a Faraday isolator that allow for compensation of the self-induced depolarization in the magneto-optic medium were reported and studied in detail[12,15-17]. In these designs, the nonisolation (depolarization ratio) even for the [001] orientation depends not only on μ but also on the parameter ξ defined as

Laser Optics 2000: Control of Laser Beam Characteristics and Nonlinear Methods for Wavefront Control,
Leonid N. Soms, Vladimir E. Sherstobitov, Editors, Proceedings of SPIE Vol. 4353 (2001)
© 2001 SPIE · 0277-786X/01/$15.00

$$\xi = \frac{2p_{44}}{p_{11} - p_{12}}$$

Therefore, it is essential to measure ξ and the values included into μ for a terbium gallium garnet (TGG) crystal, a crystal most commonly used in high power lasers, and to study the operation of different FI designs with an arbitrary orientation of the crystal.

The Verdet constant V and the thermal conductivity κ are important characteristics, which determine the advantages of TGG over magneto-optical glasses. Their values are well known (V=0.135min/cmOe at a wavelength of 1064 nm, κ=7.4 W/m). The absorption coefficient may strongly depend on a sample, as found in practice. For magnetically active media, values of Q were measured, to the best of our knowledge, only for glasses[19,20], whereas ξ - only for a YIG crystal (ξ=1.7) [21]. In Ref.[14] an attempt was made to measure ξ and the product $Q\alpha_0$ for a TGG crystal. However, the measurement accuracy was insignificant, because a laser of not very high power was used and only one sample was studied. The uncertainty in values of ξ, Q and α_0 makes it impossible to determine the isolation ratio of FIs even with the [001] orientation. In the present paper (in Section 2), we measure the values of ξ and the product $Q\alpha$ for ten TGG crystal samples with different orientation and from various producers.

The characteristics of the traditional and novel designs of the Faraday isolator at an arbitrary crystal orientation have been neither studied nor even discussed by the researchers so far. Even in the absence of the magnetic field the thermally induced birefringence in a cubic crystal was investigated analytically[22-24] only for [001] and [111] orientations and numerically[25] for an arbitrary orientation of a YAG crystal. In all these papers only uniform heat release was considered, which for self-induced birefringence is valid only for a flat-shaped beam. In Section 1 of this paper we present analytical expressions of the isolation ratio obtained for different FI designs at high average powers of an axially symmetric beam of an arbitrary shape with an arbitrary orientation of a cubic crystal. In Section 3 these dependences are investigated in experiment for a Gaussian beam and TGG crystals with different orientations. The data obtained in sections 1-3 are discussed in Section 4 to determine optimal orientations of a TGG crystal for the different FI designs. The results are generalized for the case of depolarization without any magnetic field.

2. DEPENDENCE OF DEPOLARIZATION RATIO ON CRYSTAL ORIENTATION

The depolarization ratio (depolarization) γ is defined as the ratio of power of a depolarized component of laser radiation to the total power. The isolation ratio is γ^{-1}. Let us find the depolarization in FI at a high average power with an arbitrary orientation of crystal axis relative to the wave vector of an optical wave. Investigations have shown[12,15-17] that the best FI design at a high average power is that comprising two 22.5° Faraday rotators and a 67.5° reciprocal quartz rotator (QR) placed between them. Below we shall call this design "design with QR". At the same time, most widely used now is the traditional FR design that consists of a single 45° Faraday rotator. In this paper, we shall consider only these two FI designs. The computation procedure is as follows. We shall use expressions for γ obtained in Refs.[15,16] as a function of phase difference δ_l and of the direction of eigenaxes ψ of linear birefringence caused by the photoelastic effect. The values of δ_l and ψ are determined by the tensor of dielectric impermeability B. To calculate elements of this tensor for an arbitrary orientation, we shall apply the procedure used in Ref.[25]. However, unlike this paper, where only numerical calculations were made for a uniform distribution of heat release in a YAG crystal, we shall yield analytical expressions for B and γ at any axially symmetric distribution of laser intensity for any cubic crystal of arbitrary orientation. Based on the obtained expressions we shall define an optimal orientation from the standpoint of isolation.

Let us assume that the wave vector is parallel to the z axis, and the crystal has a cylindrical shape with the axis of symmetry parallel to the z axis (Fig. 1). In Refs.[15,16] the following expressions for γ were obtained

$$\gamma_0 = \frac{2}{\pi^2 P_0}\int_0^{2\pi} d\varphi \int_0^{R_0} \delta_l^2 \cdot \sin^2(2\Psi - 2\theta - \pi/4)\cdot I(r) r dr \qquad \gamma_R = \frac{(\pi/2-\sqrt{2})^2}{\pi^4 P_0}\int_0^{2\pi} d\varphi \int_0^{R_0} \delta_l^4 \cdot I(r) r dr \tag{2}$$

$$I(r) = I_0 f\left(\frac{r^2}{r_0^2}\right) \qquad P_0 = 2\pi I_0 \int_0^{R_0} f\left(\frac{r^2}{r_0^2}\right) r dr = \pi r_0^2 I_0 \int_0^{R} f(y)dy \qquad R = \frac{R_0^2}{r_0^2}$$

where $\delta_l=\delta_l(r,\varphi)$ and $\Psi=\Psi(r,\varphi)$ are the phase difference and the direction of eigenaxes of linear birefringence; $I(r)$, P_0 are the intensity distribution and power of laser radiation; R_0, r_0 are the crystal radius and effective beam radius; θ is the

inclination angle of incident polarization relative to the x axis; and r, φ are polar coordinates (Fig. 1). The subscripts 0 and R used here and later refer to, respectively, the traditional design and the design with QR. These expressions are valid at an optimal rotation angle of QR (67.5°) and at small thermally induced birefrigence δ_l <<1. In this paper we won't go beyond these conditions.

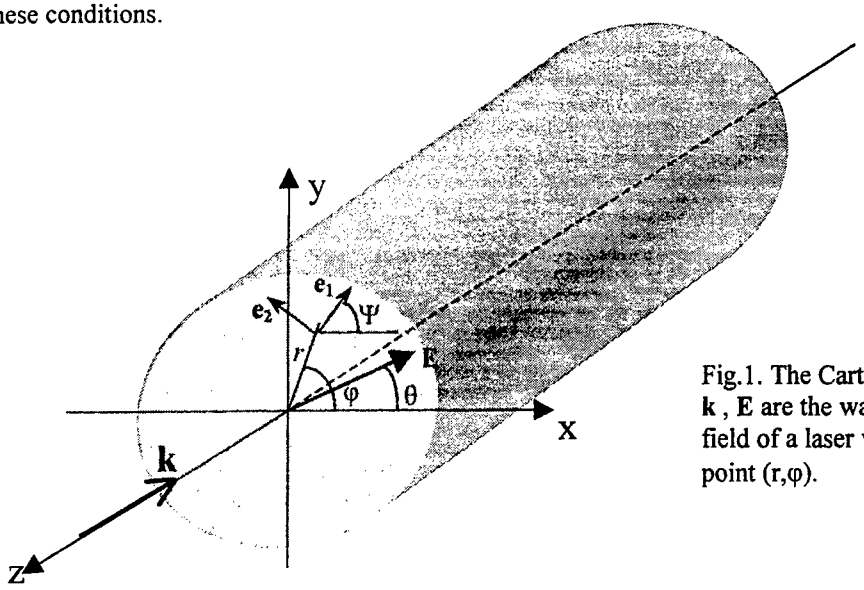


Fig.1. The Cartesian xyz and cylindrical rφz coordinates. **k** , **E** are the wave vector and the direction of the electric field of a laser wave, $\mathbf{e}_1$ and $\mathbf{e}_2$ are eigenpolarizations at a point (r,φ).

The values of δ_l and ψ can be found knowing the tensor of dielectric impermeability B, written in the Cartesian coordinates xyz (see, for example[25])

$$\delta_l = kL\frac{n_0^3}{2}\sqrt{(B_{11}-B_{22})^2+4B_{12}^2} \qquad \tan(2\Psi)=\frac{2B_{12}}{B_{11}-B_{22}} \tag{3}$$

Elements of the tensor B depend on temperature distribution and crystal orientation, i.e., on the mutual position of the crystallographic axes (no matter which one, since the crystal is cubic) and the wave vector. In the simplest case the crystallographic axes *abc* coincide with the directions *xyz*, which corresponds to the [001] orientation. An arbitrary orientation can be given by use of two sequential rotations of the coordinate frame *xyz* relative to the crystallographic pattern at angles α and β [25], as shown in Fig. 2. First the coordinate frame *xyz* rotates at an angle α around the axis *z* that coincides with the crystallographic axis *c* (Fig. 2a), and then at an angle β around the *y* axis (Fig. 2b). By varying the values of α and β we can obtain any orientation of the crystal. Ref.[25] describes a procedure for calculating the tensor B through elements of the strain tensor ε written in the cylindrical coordinates rφz where it has a diagonal form. In this paper no analytical expressions were obtained. The authors limited oneselves to numerical calculation for the YAG crystal. Not repeating all the formulas of this paper, we shall describe only the calculation procedure in general. The strain tensor is transformed from the cylindrical to Cartensian coordinate frame rotated relative to the *xyz* frame at angles α and β so that its axes coincide with the crystallographic axes of the crystal *abc*. In these coordinates the change of tensor B due to photoelastic effect can be found by simply multiplying the tensor of photoelastic coefficients by the strain tensor. Thereafter, the tensor B is transformed into the Cartensian coordinates *xyz*. As a result, the following analytical expressions can be obtained in a general form

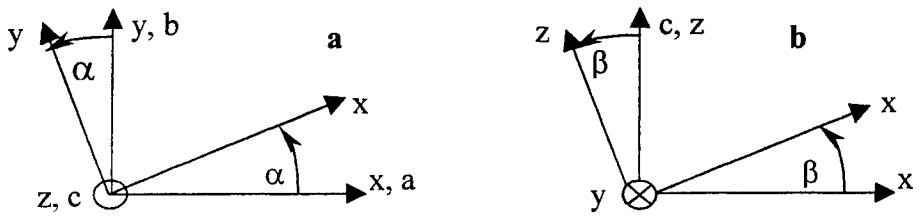


Fig.2. The xyz coordinates rotated relative to the crystal pattern abc.

$$B_{11} - B_{22} = (p_{11} - p_{12})\{\Sigma a_1(1-\xi) + \Delta\cos(2\varphi)(a_2(1-\xi)+\xi) + \Delta\sin(2\varphi)a_3(1-\xi)\}$$
$$2B_{21} = (p_{11} - p_{12})\{\Sigma b_1(1-\xi) + \Delta\cos(2\varphi)b_2(1-\xi) + \Delta\sin(2\varphi)(b_3(1-\xi)+\xi)\} \quad (4)$$

where

$$a_1 = -\sin^2\beta\cdot\{\cos^2\beta - \cos^2\alpha\cdot\sin^2\alpha\cdot(\cos^2\beta+1)\} \qquad b_1 = \frac{\sin 4\alpha\cdot\cos\beta\cdot\sin^2\beta}{4}$$
$$a_2 = 1 - \sin^2\beta\cdot\cos^2\beta - \cos^2\alpha\cdot\sin^2\alpha\cdot(\cos^2\beta+1)^2 \qquad b_2 = a_3 \quad (5)$$
$$a_3 = -\frac{\sin 4\alpha\cdot\cos\beta\cdot(\cos^2\beta+1)}{4} \qquad b_3 = \sin^2 2\alpha\cdot\cos^2\beta$$

$$\Delta = \varepsilon_{rr} - \varepsilon_{\varphi\varphi} \qquad \Sigma = \varepsilon_{rr} + \varepsilon_{\varphi\varphi} - 2\varepsilon_{zz} \quad (6)$$

$\varepsilon_{rr,\varphi\varphi,zz}$ are diagonal elements of the strain tensor in the cylindrical coordinates (non-diagonal elements are equal to zero). Note that coefficients a_i and b_i depend only on angles α and β, i.e., are fully determined by crystal orientation. Substituting expressions for $\varepsilon_{rr,\varphi\varphi,zz}$ known from the elasticity theory for a cylindrical sample with radius R_0 (see, for example[26,27]) into expression (6) yields

$$\Delta = \frac{1+\nu}{1-\nu}\left(\frac{1}{L}\frac{dL}{dT}\right)\frac{1}{r^2}\int_0^r \frac{dT}{dr}r^2 dr \qquad \Sigma = \frac{1+\nu}{1-\nu}\left(\frac{1}{L}\frac{dL}{dT}\right)\left[\frac{1}{R_0^2}\int_0^{R_0}\frac{dT}{dr}r^2 dr - \int_r^{R_0}\frac{dT}{dr}dr\right] \quad (7)$$

By substituting in these expressions the solution of the equation for thermal conductivity for a infinite-long cylindrical sample (see, for example[12,16])

$$\frac{dT}{dr} = -\frac{\alpha_0 I_0}{\kappa}\frac{r_0^2}{2r}\cdot\int_0^{r^2/r_0^2} f(y)dy \ , \quad (8)$$

and the result of this substitution into expression (4), we obtain

$$B_{11} - B_{22} = \frac{-Q\alpha_0 I_0 \pi r_0^2}{\pi\kappa n_0^3}\{g a_1(1-\xi) + h\cos(2\varphi)(a_2(1-\xi)+\xi) + h\sin(2\varphi)a_3(1-\xi)\}$$
$$2B_{21} = \frac{-Q\alpha_0 I_0 \pi r_0^2}{\pi\kappa n_0^3}\{g b_1(1-\xi) + h\cos(2\varphi)b_2(1-\xi) + h\sin(2\varphi)(b_3(1-\xi)+\xi)\} \quad (9)$$

where

$$g\left(\frac{r^2}{r_0^2}, R\right) = \frac{1}{R}\int_0^R dz\int_0^z f(y)dy - \int_{r^2/r_0^2}^R \frac{dz}{z}\int_0^z f(y)dy \qquad h\left(\frac{r^2}{r_0^2}\right) = \frac{r_0^2}{r^2}\cdot\int_0^{r^2/r_0^2} dz\int_0^z f(y)dy$$

Substitution of expression (9) into expression (3), and then substitution of the result into (2), followed by integration, yields expressions for depolarization

$$\gamma_0 = \frac{p^2}{\pi^2}\left(Fd_1 + Hd_2 + \sin 4\theta[Fd_7 + Hd_3] - \cos 4\theta[Fd_8 + Hd_6]\right) \quad (10)$$

$$\gamma_R = \frac{(\pi/2-\sqrt{2})^2 p^4}{2\pi^4}\left(2Nd_1^2 + M[4d_1d_2 + d_4^2 + d_5^2] + K[2d_2^2 + d_3^2 + d_6^2]\right) \ , \quad (11)$$

where

$$p = \frac{L}{\lambda}\frac{\alpha_0 Q}{\kappa}P_0 \quad (12)$$

$$
\begin{aligned}
d_1 &= (a_1^2 + b_1^2)(1-\xi)^2 \\
d_2 &= \frac{1}{2}(a_2^2 + 2a_3^2 + b_3^2)(1-\xi)^2 + (a_2 + b_3)(1-\xi)\xi + \xi^2 \\
d_3 &= \frac{1}{2}(a_2^2 - b_3^2)(1-\xi)^2 + (a_2 - b_3)(1-\xi)\xi \\
d_4 &= 2(a_1 a_2 + b_1 b_2)(1-\xi)^2 + 2a_1(1-\xi)\xi \\
d_5 &= 2(a_1 a_3 + b_1 b_3)(1-\xi)^2 + 2b_1(1-\xi)\xi \\
d_6 &= a_3(a_2 + b_3)(1-\xi)^2 + 2a_3(1-\xi)\xi \\
d_7 &= (a_1^2 - b_1^2)(1-\xi)^2 \\
d_8 &= 2a_1 b_1(1-\xi)^2
\end{aligned}
\qquad (13)
$$

$$
F = \frac{\int_0^R f g^2(y,R)dy}{\left(\int_0^R f dy\right)^3} \qquad H = \frac{\int_0^R f h^2 dy}{\left(\int_0^R f dy\right)^3} \qquad K = \frac{\int_0^R f h^4 dy}{\left(\int_0^R f dy\right)^5} \qquad M = \frac{\int_0^R f h^2 g^2(y,R)dy}{\left(\int_0^R f dy\right)^5} \qquad N = \frac{\int_0^R f g^4(y,R)dy}{\left(\int_0^R f dy\right)^5} \qquad (14)
$$

Note that the coefficients d_i depend only on α, β and ξ. The values of *F, H, K, M, N* are determined only by the beam shape and the size of the crystal and depend only on *R*. Integrals (14) can be readily calculated for any beam. From a practical point of view, of most interest are Gaussian and flat-shaped beams, for which

$$
f(y) = \exp(-y) \qquad f(y) = \begin{cases} 1 & npu \quad y < 1 \\ 0 & npu \quad y > 1 \end{cases}
$$

respectively. For a flat-shaped beam under the obvious condition $R \geq 1$, the values of *F, H, K, M, N* do not depend on *R*. They are given in Tabl. 1. In view of these values, the formulas (10,11) are simplified correspondingly. Table 1 presents also formulas (14) for a Gaussian beam and values of *F, H, K, M, N* at certain *R*, calculated using these formulas.

	flat-shaped beam	**Gaussian beam** $q(R,y) = \int_0^R (1-\exp(-z))\frac{R-z}{Rz}dz - \int_0^y \frac{1-\exp(-z)}{z}dz$			
		formulae	***R*=5**	***R*=10**	***R*=15**
F	$\frac{1}{12}$	$\frac{1}{(1-\exp(-R))^3}\int_0^R \exp(-y)q^2(R,y)dy$	0.76	1.9	3.02
H	$\frac{1}{12}$	$\frac{1}{(1-\exp(-R))^3}\int_0^R \exp(-y)(1+[\exp(-y)-1]/y)^2 dy$	0.135	0.137	0.137
K	$\frac{1}{80}$	$\frac{1}{(1-\exp(-R))^5}\int_0^R \exp(-y)(1+[\exp(-y)-1]/y)^4 dy$	0.041	0.042	0.042
M	$\frac{1}{120}$	$\frac{1}{(1-\exp(-R))^5}\int_0^R \frac{q^2(R,y)(1+[\exp(-y)-1]/y)^2}{\exp(y)}dy$	0.032	0.104	0.197
N	$\frac{1}{80}$	$\frac{1}{(1-\exp(-R))^5}\int_0^R \exp(-y)q^4(R,y)dy$	0.94	5.05	11.5

Table 1. The values of constants *F, H, K, M, N* for flat-shaped and Gaussian beams at different *R*.

In Refs[15,16] it was shown that at the [001] orientation an important advantage of the design with QR is that depolarization is independent of polarization of the incident field (γ_R is independent of θ). From (11) it is seen that this advantageous feature is preserved at any orientation. In the traditional design, the depolarization depends on θ, and, as follows from expression (10), this dependence is periodic with a period 90° at any orientation. It is possible to minimize γ_0 by varying θ. By differentiating (10) with respect to θ and putting the derivative to zero, we find the optimal angle θ_{opt} and minimum depolarization γ_{0min}

$$\tan(4\theta_{opt}) = -\frac{Fd_7 + Hd_3}{Fd_8 + Hd_6} \tag{15}$$

$$\gamma_{0\min} = \gamma_0(\theta_{opt}) = \frac{p^2}{\pi^2}\left(Fd_1 + Hd_2 - \sqrt{(Fd_7 + Hd_3)^2 + (Fd_8 + Hd_6)^2}\right) \tag{16}$$

Expressions (16) and (11) permit to find depolarization and, consequently, the isolation ratio of FR (as a quantity reverse to depolarization) for the traditional design and the design with QR, respectively. For the both designs the depolarization is determined by crystal orientation (angles α and β), beam shape (constants F, H, K, M, N) and also by the normalized power of radiation p and the parameter ξ which characterizes the properties of the crystallographic lattice.

In conclusion, we shall describe some particular cases. First, we shall consider the [001] orientation in case when all three crystallographic axes coincide with axes of the xyz coordinates. For a cubic crystal, corresponding values of angles α and β are $\pi n/2$ (n is an integral number). In this case from expressions (10,11) we yield expressions

$$\gamma_0([001]) = \frac{p^2}{\pi^2} H \cdot \left(\sin^2\left(2\theta + \frac{\pi}{4}\right) + \xi^2 \cos^2\left(2\theta + \frac{\pi}{4}\right)\right) \tag{17}$$

$$\gamma_R([001]) = \frac{3(\pi/2 - \sqrt{2})^2 p^4}{8\pi^4} K \cdot \left(\xi^4 + \frac{2}{3}\xi^2 + 1\right), \tag{18}$$

which coincide with expressions given in Ref.[14-16]. A second practically important particular case is the [111] orientation for which α=45° and β=54.8° ($\tan\beta = \sqrt{2}$). In this case the depolarization does not depend on θ, and from (10,11) we obtain

$$\gamma_0([111]) = \frac{p^2}{9\pi^2} H \cdot (1 + 2\xi)^2 \tag{19}$$

$$\gamma_R([111]) = \frac{(\pi/2 - \sqrt{2})^2 p^4}{81\pi^4} K \cdot (1 + 2\xi)^4 \tag{20}$$

These expressions also can be obtained using the procedure described in Ref.[16] if we use the expression for δ_1 at the [111] orientation from Refs.[22,23]. Note that for magnetically active glass (ξ=1) from expression (13) we yield d_i=0 (i≠2), d_2=1, and depolarization $\gamma_{0,R}$ does not depend on angles θ, α and β, while expression (10,11) come to expressions obtained for this case in Refs.[14-16].

In Ref.[14] it was shown that in the absence of magnetic field the self-induced thermal depolarization $\gamma_{H=0}$, after replacement of $\theta+\pi/8$ by θ, is different from the depolarization in the traditional design γ_0 only by a multiple of $\pi^2/8$

$$\gamma_{H=0}(\theta) = \frac{\pi^2}{8}\gamma_0(\theta + \pi/8) \tag{21}$$

Thus all expressions obtained for γ_0 to an accuracy of (21) shall be valid also for self-induced depolarization without any magnetic field. We shall use this fact later in measurements of Q and ξ (see section 2). Additionally, this can be used to calculate depolarization in active elements of laser amplifiers. In the latter case it is necessary to substitute into expression (8) the volume density of heat release power instead of $\alpha_0 I_0 f(y)$.

3. MEASUREMENTS OF PARAMETERS Q AND ξ FOR DIFFERENT TGG CRYSTALS

In our measurements of Q and ξ we used the depolarization effect of powerful laser radiation during its propagation in an absorbing medium without any magnetic field. A crystal was placed between a pair of cross-aligned polarizers, as shown in Fig. 3a. In experiment we measured the nonisolation ratio $\gamma_{H=0}$ as a function of power of laser radiation P_0. This measurement technique was used in Ref.[14] and also in measurements of the parameter Q for magneto-optical glasses in Refs.[19,20]. For optical glasses this measurement technique gave values of Q that differed only by 10-20 % from those known from the literature, indicating that the measurement accuracy provided by this technique is rather high.

In our experiments a quasi-CW Nd:YALO laser[3] with power up to 100 W (λ=1080 nm) and a commercial CW Nd:YLF laser (Photonics Industries) with power up to 60 W (λ=1053 nm) were used as the radiation source. An optical beam had a

Gaussian profile with a diameter of approximately 2.5 mm (Nd:YLF) and 8 mm (Nd:YALO). Ten crystals were studied. The results are summarized in Table 2 (Nos. 1-10).

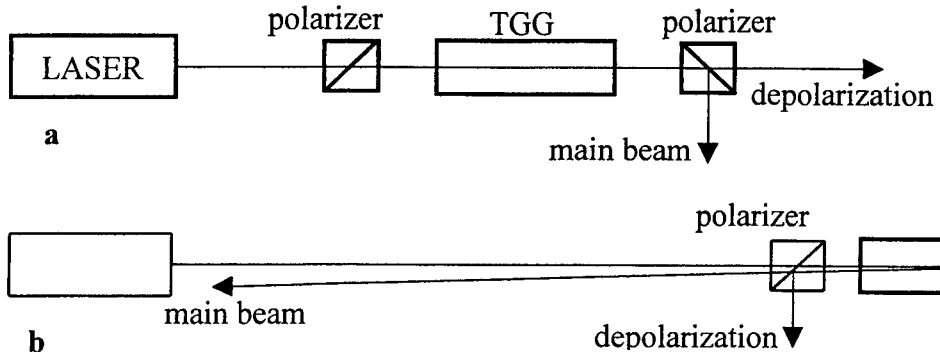


Fig.3. A single-pass (a) and a two-pass (b) schemes of the experiment.

The dependences $\gamma_{H=0}(P_0)$, measured for different crystal samples, were compared with theoretical predictions. The measurements were carried out first for crystals with the [001] orientation at $\theta=\pi/4$. In this case the radiation polarization is parallel to the prevailing (preferred) direction of the eigenaxes which go along the bisector between the crystallographic axes (in this direction the crystal's resistance to deformation is the worst). It follows from expressions (17,21) that at this value of θ the depolarization is minimum and does not depend on the parameter ξ. The product $Q\alpha_0$ was used as a fitting parameter. Then the measurements were repeated for $\theta=0$. In this case the radiation polarization is inclined at 45° to the prevailing direction of the eigenaxes. At this value of θ the depolarization is maximum and exceeds the depolarization at $\theta=\pi/4$ by a factor of ξ^2. For crystals with the [111] orientation the dependences $\gamma_{H=0}(P_0)$ were compared with (19,21). This measurement technique does not allow us to measure ξ and $Q\alpha_0$ independently for this orientation. Therefore, the value of ξ was considered known from previous measurements, and $Q\alpha_0$ was used again as a fitting parameter.

It should be noted that errors in measurements of P_0, as well as an insignificant ellipticity of a beam and an imperfect symmetry of cooling lead to errors in measurements of $Q\alpha_0$ and ξ. Another serious source of errors is the presence of residual («cold») depolarization and light scattering in the crystal. All these parasitic effects are not considered by the theory. The latter two effects are linear in power and hence the depolarization induced by them is power-independent. At the same time, the thermal effects lead to a quadratic dependence of the depolarization on power. It is evident that starting from some high power these effects may be neglected. It is possible to define whether this power is achieved or not in experiment by analyzing the character of the dependence $\gamma_{H=0}(P_0)$. On the double logarithmic scale, the quadratic dependence corresponds to an inclined line, whereas no-dependence is a horizontal line. The $\gamma_{H=0}(P_0)$ plot, measured in a wide range of power values, must change from a horizontal line to an inclined line, corresponding (on the logarithmic scale) to the quadratic dependence at high powers.

In measurements of fairly long crystals by a 100-W laser we managed to cover this power range. (see Fig. 4 and Table 2, Nos. 1-4,7). It is seen from this figure that at a high power the experimental data were in good agreement with theoretical predictions. However, the 60 W power of laser radiation was too low for the thermal effects to dominate in short and weakly absorbing crystals. Therefore, it was impossible to determine reliably the parameters $Q\alpha_0$ and ξ using a single-pass scheme (Fig. 3a). To overcome this obstacle, we used a two-pass scheme of measurements, as shown in Fig. 3b. After a first pass through the sample, a mirror directs a laser beam in the backward direction at a small angle. This angle was chosen small so that the distance between the axes of the forward and backward beams in the sample was negligibly small in comparison with the beam radius, and hence the beam shift may be neglected. Then it is obvious that the power released in the optical element as heat is twice increased in comparison with the single-pass scheme (Fig. 3a), still preserving the Gaussian transverse distribution. The length of the optical pass is also twice increased, whereas the other parameters are kept the same. Therefore, after the replacement of P_0 by $2P_0$ and L by 2L in expression (12) the parameter p increases by 4 times, and the depolarization, according to (17,19), by 16 times. This increase allowed us to measure the parameters for all crystals.

Other aspects of the measurement procedure were the same as in the single-pass measurements (Fig. 2) Using the two-pass scheme and a Nd:YLF laser with a laser power of 60 W, parameters of seven crystals were measured, see Table 2 Nos. 4-10. Figure 5 presents the dependence $\gamma_{H=0}(P_0)$ for samples Nos. 4,8.

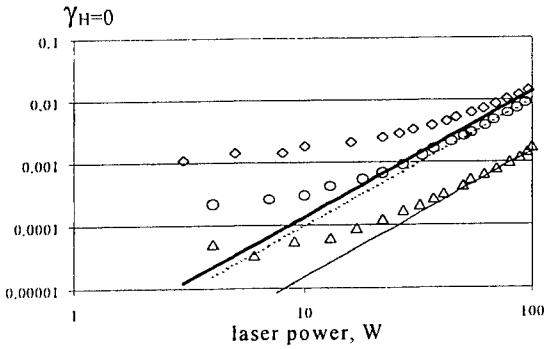


Fig.4. Experimental (in a single-pass scheme) and theoretical dependences of depolarization on power for crystal No 1 (rhombuses $Q\alpha_0=11x10^{-7}$/Km), No 2 (triangles $Q\alpha_0=3.7x10^{-7}$/Km) and No 3 (circles $Q\alpha_0=9.3x10^{-7}$/Km).

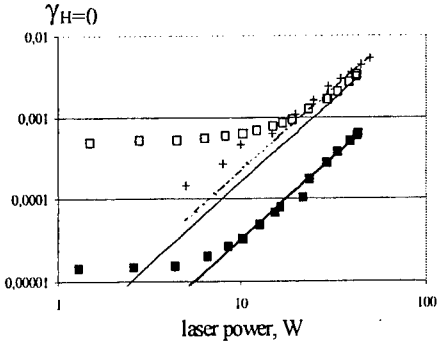


Fig.5. Experimental (in a two-pass scheme) and theoretical dependences of depolarization on power for crystal No 8 at $Q\alpha_0=7.7x10^{-7}$/Km, $\xi=2.2$ ($\theta=0°$ - open squares, thin line; $\theta=45°$ - filled squares, solid line) and for crystal No 4 at $Q\alpha_0=6x10^{-7}$/Km, $\xi=2.2$ (crosses, dotted line).

No	diameter (length), mm	orientation	vendor	λ, nm	$Q\alpha_0$, 10^{-7}/Км	ξ	$1/\gamma_{0min}$ @300Вт, dB	$1/\gamma_R$ @300Вт, dB
1	15 (36)	[111]	Litton (USA)	1080	11	-	11	34
2	15 (36)	[111]	Litton (USA)	1080	3.7	-	20	53
3	15 (36)	[111]	Litton (USA)	1080	9.3	-	12	37
4	10 (20)	[111]	Litton (USA)	1053	6.0	-	16	45
				1080	6.2	-	16	44
5	5 (54)	[111]	OFR (USA)	1053	2.5	-	24	60
6	5.5 (29)	[111]	Deltronix (USA)	1053	5.2	-	17	48
7	13 (20)	[001]	EOT (USA)	1053	5.4	2.3	22	47
				1080	6.5	2.2	21	44
8	11 (11)	[001]	Lynx (Russia)	1053	7.7	2.2	19	41
9	11 (11)	[001]	Lynx (Russia)	1053	7.0	2.3	20	42
10	11 (11)	[001]	Lynx (Russia)	1053	7.8	2.1	19	41

Table 2. Parameters of TGG crystals and isolation ratios achievable with these crystals in the traditional design ($1/\gamma_{0min}$) and the design with QR ($1/\gamma_R$) at laser power of 300 W ($L/\lambda=30000$).

4. MEASUREMENT OF DEPOLARIZATION AT AN ARBITRARY ORIENTATION OF THE CRYSTAL

As seen from Figs. 4,5, for [001] and [111] orientations the theoretical results are in excellent agreement with experiments. To check the theoretical predictions for other orientations one needs to have many expensive crystal samples cut at different angles with respect to the crystallographic axis. Instead, we used a relatively short and wide-aperture crystal No 8. Laser light was transmitted through this crystal at an angle to the face surface (Fig. 6). Maximum angle between the crystal axis (which coincides with cylinder's symmetry axis) and a wave vector was 25.6°. This allowed us to measure the depolarization at $0<\beta<25.6°$ and at any values of α.

In such geometry of the experiment and when an angle θ is different from 0 or 90°, polarization effects may occur, which are associated with a difference in the transmission coefficients of s- and p-polarizations through the air-crystal and crystal-air boundaries. To exclude these parasitic effects, we conducted experiments only with s-polarization ($\theta=90°$).

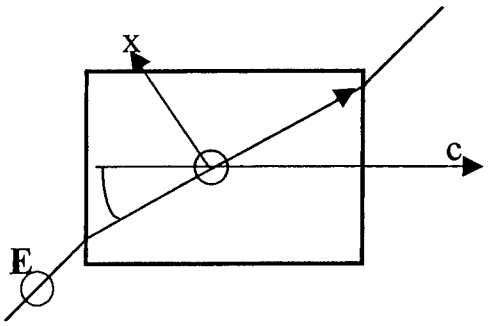


Fig.6. Geometry of experiment at an arbitrary orientation.

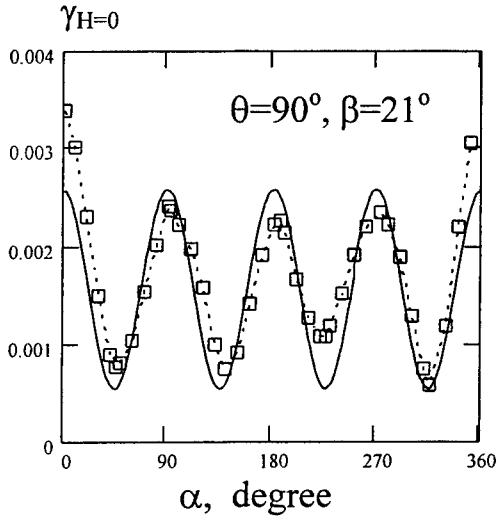


Fig.7. Depolarization in crystal No 8 vs angle α at θ=90°, β=21°.

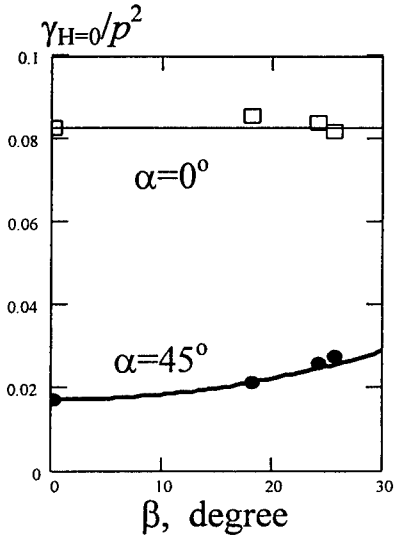


Fig.8. Theoretical (lines) and experimental (points) dependences of depolarization normalized to p^2 in crystal No 8 on angle β at θ=90°, α=0° and α=45°.

We used a Nd:YLF laser radiation and a two-pass scheme (Fig. 3b). At β=21° and P=36 W the dependence of the depolarization on α was measured. The results are shown in Fig. 7. This figure also presents a theoretical dependence plotted by formulas (10,21). When plotting this dependence we considered an increase in the pass length of the light beam in crystal L due to the non-zero inclination angle. Values of $Q\alpha_0$ and ξ were taken from Tabl. 2.

Analysis of expressions (10,21) shows that when θ=90° the depolarization has its maximum at α=0° and minimum at α=45° for any values of β and P_0. Figure 8 displays theoretical and experimental dependences of γ(β) for these experimental values of the angle α at P=38 W. It is seen from Figs. 7,8 that the extremum data are in good agreement with theory also for an arbitrary orientation of the crystal.

5. DISCUSSION AND CONCLUSIONS

We shall first discuss the results of measurements of $Q\alpha_0$ and ξ. The parameter ξ was measured to have close values for all four crystals with the [001] orientation, see Tabl. 2. Since in the measurement procedure we used, an error in measurements of ξ depends neither the absorption coefficient nor on Q, it is possible to say that the value ξ=2.2±0.2 was measured quite reliably. Note that this value is less than that given in Ref.[14]. It is likely that the inaccuracy in measurements made in Ref.[14] is connected with the "cold" depolarization whose influence appears significant at a low laser power (9 W) and for a single-pass measurement scheme.

The comparison of values of $Q\alpha_0$ obtained for different samples shows a wide spread in this parameter from sample to sample. Even the three crystals with the same orientation, the same size and from the same producer (Nos. 1-3 in Tabl. 2)

are no exception here. All the quantities included in expression (1) cannot, apparently, vary from sample to sample. Hence, it is the absorption coefficient that has such a wide spread in value. Most likely the absorption is connected with the presence of an insignificant amount of highly absorbing mixtures. The higher their concentration in the sample, the higher the absorption. Of the ten samples we studied the weakest absorption was in sample No 5. Perhaps it is free of absorbing mixtures and has the absorption of a proper TGG crystal. It is also possible that this sample still contains some amount of the mixtures but the absorption of the proper crystal is even lower.

A small difference in the wavelength (1053 nm for Nd:YLF and 1080 nm for Nd:YALO) is not very significant for measurements of Q, since all quantities included in expression (1) are very slow functions of the wavelength. For example, for glasses, Q changes only by 10-20 % during conversion from the first into the second harmonic of the Nd laser[20]. A proper TGG crystal does not have absorption resonances near these wavelengths. Though it is possible that the highly absorbing mixtures have. Maybe that is the reason for a small spread in values of $Q\alpha$ for crystal No 7 measured at different wavelengths. At the same time, this spread is insignificant and is comparable with the experimental error 10-20%.

Let us now discuss the dependence of the depolarization on crystal orientation. First of all, it should be underlined that all results we obtained are valid not only for a CW but also for a pulse repetitive laser, provided a change in the temperature gradient during one pulse is small in comparison with its average value. Although we did not study in experiment the whole range of angles α, β and θ, the good agreement between theory and experiment (Fig. 7,8) proves that the predictions of the theory used are quite correct. Analysis of expressions (16), taking into account data of Tabl. 1, shows that in case of a uniform intensity distribution the depolarization is independent of R. At a Gaussian distribution there is such dependence, though it is not very strong and does not lead to any qualitative changes. When R is varied from 5 to 15 (corresponding to intensities at the boundary of the optical element $I(R_0)/I(0)$ from 7×10^{-3} to 3×10^{-7}) $\gamma_{0,R}$ changes by no more than 40%, and for the [001] and [111] orientations the depolarization does not depend on F,M,N at all. Therefore, taking into account the data presented in Tabl.1, the dependence on R can be neglected.

As it follows from expressions (11,16), to compare different orientations with regard to minimum depolarization at high average powers in the traditional design and the design with QR, it is enough to know only the parameter ξ, which we consider to be equal to 2.2. The dependences of minimum depolarization on angles α, β for this value of ξ in the traditional FI design are shown in Fig. 9a. The plots are built for a Gaussian beam by formula (16) at p=1 and R=5. Since γ is proportional to p^2 at any orientation, the value of p is chosen arbitrarily. The figure shows that the [001] orientation (β=0) is the best, and the [111] orientation (α=45°, β=54.8°) is the worst. The difference in depolarization in these two cases is $(1+2\xi)^2/9=3.2$

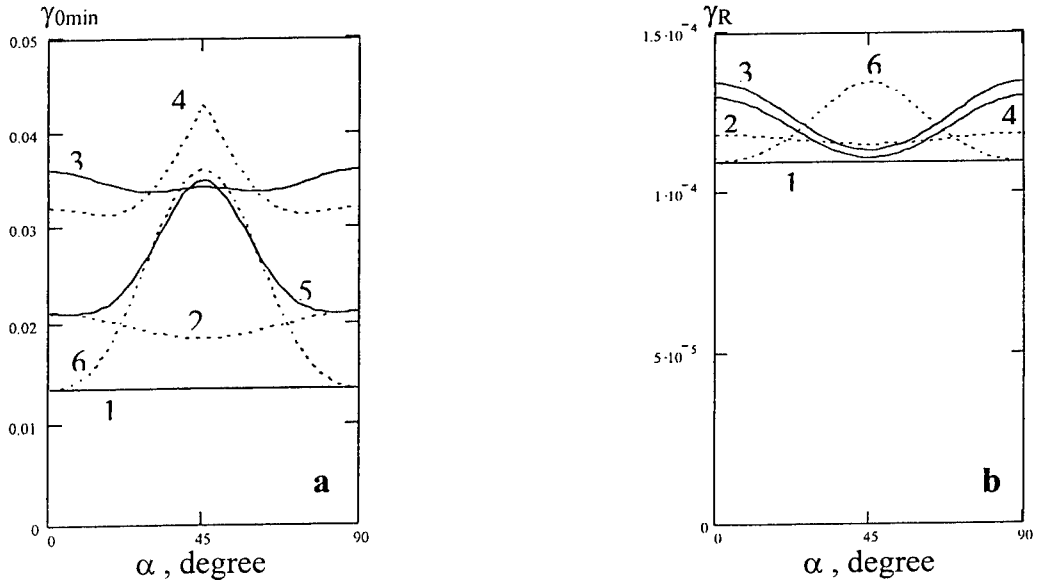


Fig.9. Dependence of depolarization at R=5, ξ=2.2, p=1 in the traditional design (a) and the design with QR (b) at β=0° (1), β=22.5° (2), β=45° (3), β=54.8° (4), β=67.5° (5), β=90° (6).

The situation is different in principle for the FI design with QR. Figure 9b shows the dependences of depolarization on angles α, β plotted by formula (11) for a Gaussian beam at p=1, R=5, ξ=2.2. It is seen from this figure that, first, the design is weakly sensitive to crystal orientation – the difference in depolarization ratios with the optimal [001] orientation and with the worst orientation is less than 30%. The values of depolarization ratios at orientations [001] (β=0) and [111] (α=45°, β=54.8°) almost coincide, differing by only 1%. At the [001] orientation, minimization of depolarization requires a fine mutual alignment of magneto-optical elements with respect to a horizontal angle (crystallographic axes of two elements must be parallel to each other [15,16]). The [111] orientation is free of this disadvantage. Thus for the design with QR most preferable from a practical point of view is the [111] orientation.

It is seen from expressions (11,16) that γ_R is proportional to p^4, whereas γ_{0min} is proportional p^2 at any α, β, *F, H, K, M, N.* This speaks for effective compensation of depolarization in the design with QR at any crystal orientation and at any beam shape, if p<<1. Moreover, even if p is on the order of unity, γ_R is also much less than γ_{0min}, as seen from Figs. 9a and 9b.

Based on the theoretical and experimental results presented herein we evaluate the isolation ratio in the both FI designs at a high average power. Let us assume $L/\lambda=3\times10^4$ and ξ=2.2. Table 2 presents values of isolation ratio for each crystal we studied at a power of 300 W in the both FI designs. If we take for $Q\alpha_0$ the minimal value of the ten crystals $2.5\times10^{-7}K^{-1}m^{-1}$, and consider that the TGG crystal has the [001] orientation, then at power 1 kW we obtain from expression (16) the isolation ratio $(\gamma_{0min})^{-1}$ = 18 dB for the traditional FI design and from expression (11) $(\gamma_R)^{-1}$ = 39 dB for the design with QR. Note that when the power or the value of $Q\alpha_0$ are increased by 3 times, these formulas give values 9 dB and 20 dB, respectively. At such large values of depolarization the condition of small birefringence δ_l <<1 is already violated, leading to even greater difference between the traditional design and the design with QR [16].

In conclusion, we summarize the main results obtained in our study.

1. For an arbitrary orientation of a cubic crystal we obtained analytical expressions for self-induced depolarization in the traditional FI design and the design with QR [15,16], and also for self-induced depolarization without any magnetic field. For all three cases it is shown that at a given beam shape the depolarization is determined only by the parameters ξ and p at any orientation. For comparison of different orientations it is enough to know only the parameter ξ.

2. It is shown that for the traditional FI design, and for the case when the magnetic field is absent, the [001] orientation is the best and the [111] orientation is the worst. Depolarization at the [111] orientation is higher by a factor of $(1+2\xi)^2/9$.

3. It is shown that in the FI design with QR based on TGG crystals the depolarization is minimal at orientations [001] and [111]. The [111] orientation is more preferable in this case, because it does not require alignment of crystals with respect to a horizontal angle.

4. For a TGG crystal the value of ξ=2.2±0.2 was measured experimentally. For 10 TGG crystal samples the values of $Q\alpha_0$ were measured (the results are summarized in Tabl. 2).

5. The FI design with QR based on commercially available TGG crystals allows the creation of FI with isolation ratio more than 35 dB at power 1kW.

6. ACKNOWLEDGEMENTS

The work was supported by the NSF grant PHY-9900786.

7.REFERENCES

1. N.Andreev, O.Palashov, E.Khazanov, G.Pasmanik. "Four-channel pulse-periodic Nd:YAG laser with diffraction-limited output radiation" *Quantum Electronics* **27**, pp.565-569, 1997 [*Kvantovaya electronika*, **24**, pp.581-585, 1997].
2. N.Andreev, E.Khazanov, O.Kulagin, B.Movshevich, O.Palashov, G.Pasmanik, V.Rodchenkov, A.Scott, P.Soan "Two-Channel Repetitively-Pulsed YAG:Nd Laser with Diffraction-Limited Output Radiation" IEEE J. Quant. Electr. **35**, pp.110-114, 1999.
3. H.J.Eichler; O.Mehl, J.Eichler "Multi-amplifier arrangements with phase conjugation for power scaling of solid state lasers with high beam qualtiy" *Proc. SPIE* **3613**, pp.166-176, 1999.
4. K.S.Lai; R.Wu and P.B.Phua "Multiwatt $KTiOPO_4$ Optical Parametric Oscillators Pumped within Randomly and Linearly Polarized Nd:YAG Laser Cavities" Proc. SPIE, **3928** paper 3928-06, 2000.

5. Y.Hirano, S.Yamamoto, T.TajimeH, H.Taniguchi, M.Nakamura. "High Average Power, Room Temperature Operation of PPMgLN OPO" Proc. CLEO'2000, paper CPD7, 2000.
6. T.Kanabe, T.Kawashima, H.Matsui, Y.Okada, Y.Kawada, T.Eguchi, R.Kandasamy, Y.Kato, M.Terada, M.Yamanaka, M.Nakatsuka, Y.Izawa, S.Nakai, T.Kanzaki, H.Miyajima,, M.Miyamoto, H.Kan. "Laser Diode Pumped 10Jx10Hz Nd:glass Slab Laser" Proc.SPIE, **3889**, pp.190-197, 2000.
7. A. Abramovici, W. E. Althouse, R. W. P. Drever, Y. Gursel, S. Kawamura, F. J. Raab, D. Shoemaker, L. Sievers, R. E. Spero, K. S. Thorne, R. E. Vogt, R. Weiss, S. E. Whitcomb, and M. E. Zucker, "LIGO - The Laser-Interferometer-Gravitational-Wave-Observatory" Science **256**, pp.325-333, 1992.
8. C.C.Robinson, The Faraday rotation of diamagnetic glasses from 0.334 μm to 1.9 μm" Appl. Opt., **3**, pp.1163-1166, 1964.
9. T.V.Zarubina, G.T.Petrovsky. "Magnetooptical glasses made in Russia" *Opticheskii zhurnal*, **59**, #11, pp.48-52, 1992.
10. T.V.Zarubina, A.N.Mal'shakov, G.A.Pasmanik, A.K.Poteomkin. "Comparative characteristics of magnetooptical glasses" *Opticheskii zhurnal (Journal of optical technology)*, **64**, #11, pp.67-71, 1997.
11. Averbakh V.S., Betin A.A., Gaponov V.A. "Effects of stimulated self-action and scattering in gases and their influence on propagation of optical radiation (review)" *Izv. VUZov Radiofizika* **21**, pp.1077-1106, 1978..
12. E.A. Khazanov, "Characteristic Features of the Operation of Different Designs of the Faraday Isolator for High Average Laser-Radiation Power", *Quantum Electronics* **30**, pp.147-151, 2000. [*Kvantovaya electronika*, **30**, pp.147-151, 2000].
13. Khazanov E.A., Kulagin O.V., Yoshida S., Reitze D. In Proc. "Investigation of Self-Induced Distortions of Laser Radiation in Lithium Niobate and Terbium Gallium Garnet" In Proc. CLEO'98, paper CWF34, 1998.
14. Khazanov E.A., Kulagin O.V., Yoshida S., Tanner D., Reitze D. "Investigation of Self-Induced Depolarization of Laser Radiation in Terbium Gallium Garnet" *IEEE J. of Quantum Electronics* **35**, pp.1116-1122, 1999.
15. Khazanov E.A *Proc.*" Suppression of Self-Induced Depolarization of Laser Radiation in Faraday Isolators" *SPIE* **3609**, pp.181-192, 1999.
16. E.A. Khazanov, "Compensation of Thermally Induced Polarization Distortions in Faraday isolators", *Quantum Electronics* **29**, pp.59-64, 1999. [*Kvantovaya electronika*, **26**, pp.59-64, 1999].
17. Khazanov E., Andreev N., Babin A., Kiselev A., Palashov O., Reitze D. "Suppression of Self-Induced Depolarization of High-Power Laser Radiation in Glass-Based Faraday Isolators" *JOSA B* **17**, pp.99-102, 2000.
18. J.F.Nye, Physical Properties of Crystals. London: Oxford University Press, 1964.
19. Khazanov E, Andreev N., Babin A., Kiselev A., Palashov O., "Measurements of thermooptic characteristics of magnetoactive glasses" In Proc. CLEO'99, paper CThW6, 1999.
20. Andreev N., Babin A., Kiselev A., Palashov O., Khazanov E, Zarubina T., Shaveleov O. "Thermooptical constant of magneto-active glasses" *Opticheskii zhurnal (Journal of optical technology)*, **67**, #6, pp.66-69, 2000.
21. R.W.Dixon. Photoelastic Propertoes of Selected Materials and Their Relevance for Applications to Acoustic Light Modulators and Scanners. J.Appl.Phys. 38, pp.5149-5153, 1967.
22. W.Koechner, D.K.Rice. Effect of Birefringence on the Perfomance of Linearky Polarized YAG:Nd Lasers. IEEE J. Quant Electr. **QE-6**, pp.557-566, 1970.
23. L.N.Soms, A.A.Tarasov Thermal Deformation in Color-Center Laser Active Elements. 1.Theoty. *Kvantovaya electronika*, **6**, pp.2546-2551, 1979.
24. Soms L.M., Tarasov A.A., Shashkin V.V. "On the problem of depolarization of linearly polarized light by a YAG:Nd^{3+} laser rod under conditions of thermally induced birefringence" *Kvantovaya electronika* 7, pp.619-621, 1980.
25. W.Koechner, D.K.Rice. Birefringence of YAG:Nd Laser Rods as a Function of Growth Direction. JOSA **61**, pp.758-766, 1971.
26. F.W.Quelle, Jr. Themal Distortion of Diffraction-Limited Optical Elements Appl. Optics, **5**, pp.633-637, 1966.
27. B.A.Boley, J,H,Weiner, Theory of Thermal Stresses. John Willey & Sons, Inc., New York, 1960.

Spectral Selectivity of Volume Phase Gratings with High--Reflective Boundaries

Yuri P. Udoev

St.Petersburg State Technical University
29 Polytechnicheskaya str., St.Petersburg, 195251, Russia

ABSTRACT

Theoretical analysis of spectral properties of volume phase gratings with high-reflective boundaries has been carried out for both transmission and reflection gratings. High Fresnel reflection at grating boundaries was shown can result in radical changing diffraction properties and significant increasing spectral selectivity in comparison to well-known Bragg selectivity. Structures considered can be of interest in developing demultiplexers for WDM optical networks, selective absorbers of laser power and other photonics devices.

Keywords: volume phase gratings, spectral selectivity.

1. INTRODUCTION

Spectral properties of volume phase gratings (VPG) are well known for the case when Fresnel reflection at grating boundaries is negligibly low[1]. In this case, physical mechanism of spectral selectivity (SS) is determined by detuning kinematics Bragg condition . Detuning Bragg resonance results in phase mismatch of waves reflected from different "planes" of a grating. As a result of destructive interference, diffraction efficiency (DE) becomes equal to zero at some value of light frequency ω_{min} near resonant frequency ω_0 , at which Bragg condition is strictly fulfilled. The results of theory[1] of coupled waves make it possible to show that for gratings of rather high Bragg DE $|\omega_0 - \omega_{min}| / \omega_0 \cong 1/N$, where N is the number of grating periods crossed by a ray of primary wave at Bragg incidence.

The present work deals with results of theoretical analysis of other limit case when Fresnel reflection at one or both of grating boundaries is high, including total reflection. As it will be shown, diffraction properties of VPG can be radically changed in this case. Specifically, the additional mechanism of SS springs up due to multiwave interference of waves repeatedly reflected from the boundaries of transmission grating. The spectral width of resonant peak of DE becomes depending on Fresnel coefficients and transverse optical path of light wave. With proper conditions, it results in significant increasing SS of transmission gratings in comparison to Bragg selectivity. Reflection grating attains also qualitatively new spectral properties when Fresnel reflection is high at back boundary of a grating. Some of recently published results[2] for reflection gratings have been shortly considered here for illustration of deep influence of boundary effects on spectral properties of VPG.

2. STATING THE PROBLEM AND THE PROCEDURE OF SOLVING

The schemes of diffraction are shown in fig.1, where I – incident plane monochromatic wave of TE-polarization, R_m and T_m – diffracted waves of m-th order in reflected and transmitted light respectively, θ_{01} and θ_{02} - Bragg angles for frequency ω_0 in media 1,2 with refraction indices n_1, n_2 (the latter is average value). Modulation of refraction index n_2 was supposed to be sinusoidal with modulation amplitude $\Delta n << n_2$, grating "planes" being non-slanting in respect of planes of grating boundaries. The modified method of coupled waves, taking into account slight absorption inside a grating , was used in analysis of reflection gratings. Details of the theory have been recently reported[2]. In the case of transmission gratings, the known method of characteristic modes[3] was used. In both cases, theoretical analysis was carried out in two-wave approximation supposing known limitations[4] on parameters of gratings.

Laser Optics 2000: Control of Laser Beam Characteristics and Nonlinear Methods for Wavefront Control,
Leonid N. Soms, Vladimir E. Sherstobitov, Editors, Proceedings of SPIE Vol. 4353 (2001)
© 2001 SPIE · 0277-786X/01/$15.00

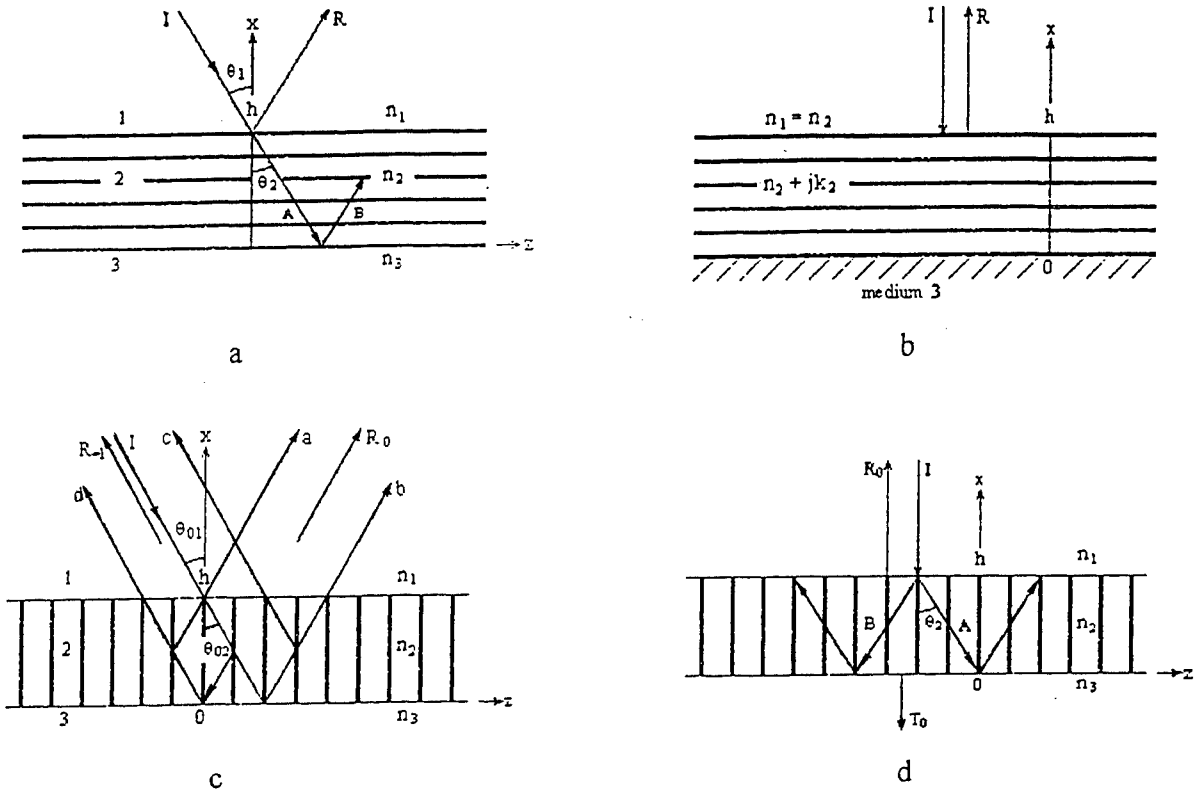


Fig.1. The schemes of diffraction.
a) non-absorptive reflection grating with TIR at back boundary ($n_3 < n_1 = n_2$) b) normal incidence on slight – absorptive reflection grating ($n_1 = n_2$) with high-reflective medium 3 c) Bragg incidence on modulated TIR-resonator ($n_1 > n_2 > n_3$) d) normal incidence on modulated waveguide ($n_2 > n_1, n_3$).

Strength of electric field inside a transmission grating was presented as following:

$$E_2(x,z) = \sum_n [P_n B_n(z) \exp(-j\xi_n x) + Q_n B_n(z) \exp(j\xi_n x)] \quad (1)$$

where $B_n(z) = \exp(j\beta z)\Phi_n(z)$ – Bloch function for n-th root ξ_n of dispersion equation, $\Phi_n(z)$ – periodic with grating period Λ function, $\beta = k n_1 \sin\theta_{01}$, $k = \omega/c$, c - light velocity, λ - operating wavelength, P_n and Q_n amplitudes to be found. Strength of electric fields in media 1,3 was described in a standard way:

$$E_1(x,z) = E_{0i} \exp(-j\rho x) \exp(j\beta z) + \sum_{m=0,-1} [R_m \exp(j k N_m^{(1)} x) \exp(j k N_m z)] \quad (2)$$

$$E_3(x,z) = \sum_{m=0,-1} [T_m \exp(-j k N_m^{(3)} x) \exp(j k N_m z)] \quad (3)$$

where E_{0i} –the amplitude of incident wave, $\rho = k n_1 \cos\theta_{01}$, $N_m = n_1 \sin\theta_{01} + m\lambda/\Lambda$, $N_m^{(p)} = [n_p^2 - (N_m)^2]^{1/2}$, p=1,3 – the number of medium, m = 0,-1 – the order of diffraction, R_m and T_m – amplitudes to be found and time dependence exp(-jωt) is omitted. Amplitudes sought were found by analytic solving the system of equations following the rigorous boundary conditions of electrodynamics. It should be noted that the expression (1) is applicable for oblique incidence geometry shown in fig.1c. In this case the roots of dispersion equation are equal to

$$(\xi_{1,2})^2 = k^2 n_2^2 - (K/2)^2 \{1 + \chi^2 \pm [4\chi^2 + \delta^2]^{1/2}\} \quad (4)$$

where $\chi = (\omega - \omega_0)/\omega_0$ - relative frequency offset, $\delta = k^2 \Delta\varepsilon / [2 (K/2)^2]$, $\Delta\varepsilon \cong 2 n_2 \Delta n$, $K = 2\pi/\Lambda$.

When primary wave I is incident along the normal to grating boundary (fig1.d), it is necessary to use three-wave approximation because diffracted waves propagate on the left of the normal as well as on the right. Indeed, calculations have shown that dispersion equation has in this case three roots. One of them, ξ_1, was close to $k n_2$. Another root, ξ_2, was close to $\xi_f = [k^2 n_2^2 - K^2]^{1/2}$ and the third root ξ_3 was equal to ξ_f. The root ξ_3 corresponds formally to x-projection of the wave vector of a wave, diffracted by non-homogeneous boundary but propagated in homogeneous medium 2. It is not the case under consideration. Formal making use of the root ξ_3 resulted in zero amplitudes P_3, Q_3. Because of this, only ξ_1, ξ_2 were used in the present work. Due to symmetry of diffraction, the root ξ_2 was used in describing fields of both the right wave A and the left wave B (fig.1d).

3. RESULTS

a) Reflection gratings

Two cases are of the most interest when a grating is reflective. One of them is inclined Bragg incidence on a grating, internal Bragg angle of which is more than critical angle θ_{23} of total internal reflection (TIR) at back boundary, contacting to transparent medium 3 (fig1.a). Another is normal incidence on a grating, back boundary of which contacts to high-reflective medium 3 (f.i.,metal) (fig.1b). It was supposed in both cases that $n_1 = n_2$, i.e. $\theta_{01} = \theta_{02}$. It follows energy conservation law that non-absorptive grating loses totally its spectral selectivity (curve 1 in fig.2) in the limit case $\rho_b=1$ ($r_b \equiv \rho_b \exp(j \varphi_b)$ – amplitude coefficient of reflection at back boundary). However, it has been found earlier[5,6] that strong resonant effect takes place in these conditions. This effect manifests itself in resonant amplification of light field inside the grating. The structure as a whole acts as hybrid Fabry-Perot resonator in which functions of mirrors are fulfilled by the grating (distributed mirror) and back boundary (lumped mirror). Due to this effect the structure becomes very sensitive to absorption and deep (up to zero) minimum can arise (curve 2 in fig.2) inside usual Bragg peak (curve 3 in fig.2). The spectral width of the minimum, depending on absorption index k_2 and intrinsic DE of the grating, can be many times less than that of central Bragg peak of non-absorptive reflection grating with non-reflective boundaries.

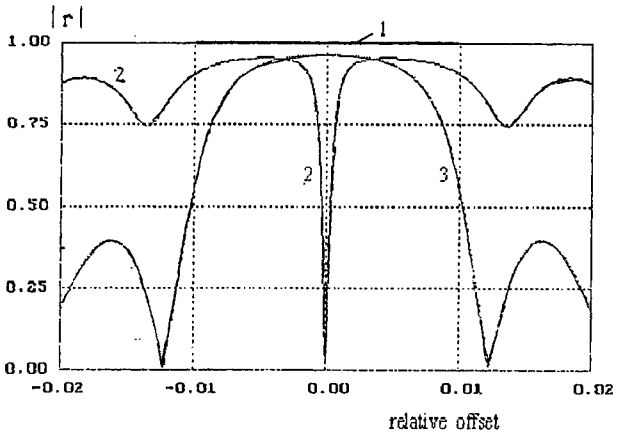


Fig.2. Spectral dependence of amplitude coefficient of reflection from the structure shown in fig.1b.
1-$\rho_b = 1$, $k_2 = 0$; *2*- $\rho_b = 1$, $k_2 = 0.0004$; *3*- $\rho_b = 0$, $k_2 = 0$
1-3: $n_2 = 1.52$, $\Delta n = 0.02$, $h = 20$ μm, $\lambda_0 = 0.63$ μm.

b) Non-absorptive transmission gratings: inclined incidence

When the back boundary of a grating has high Fresnel reflection, diffracted waves in reflected light are of interest. If Fresnel reflection at front boundary is negligibly low, diffraction properties in reflected light are similar to that of a grating of doubled depth[7,8]. However, new properties have been revealed in the present work in the case of high reflection at both of grating boundaries. This case takes place at structures shown in fig.1c where $n_1 > n_2 > n_3$, $\theta_{13} < \theta_{01} < \theta_{12}$ (θ_{13}, θ_{12} - critical angles of TIR for medium1/medium3, medium1/medium2 interfaces). Being non-modulated, this structure acts as resonant cavity of Fabry-Perot type (TIR – resonator [9]). Reflection coefficient of such a structure is equal to 1 independently of both wavelength and incidence angle θ_1 if the latter is within the range $\theta_{13} \div \theta_{12}$. It was found that situation changes radically in the case of modulated structure. Diffraction efficiency of 0th order at Bragg incidence becomes strongly dependent on the value of Bragg angle. It is due to leaking light power into -1st diffraction order. Diffraction efficiency of -1st order depends resonantly on the value of Bragg angle and can achieve 100% even if the grating depth is small (~ 2 μm). Peak values of DE were shown to arise when

$$2 \xi_i h - 2 \varphi_{23}^{(i)} \cong (2m + 1) \pi, \qquad (5)$$

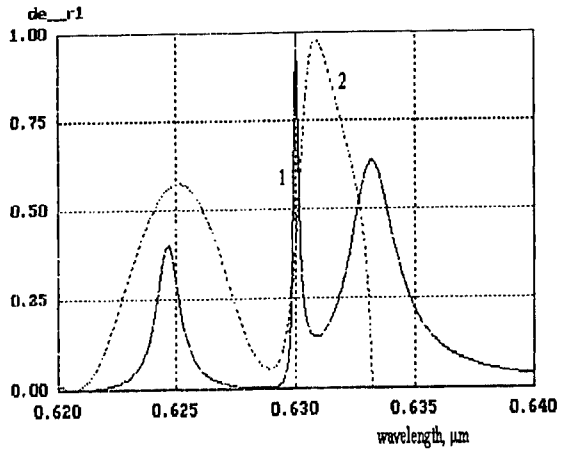


Fig.3. Spectral dependence of DE of -1st order in reflected light for the structure shown in fig. 1c. n_2=1.51, n_3=1.0, Δn=0.02, h=2.5 μm, θ_{02}=81.94 deg.
1- n_1 = 2.0 *2*- n_1 = 1.51

where i =1, 2., ξ_i – a root of dispersion equation, $2\varphi_{23}^{(i)}$ – phase shift in reflection of i-th partial Bloch wave from medium2/medium3 interface. It follows results[9] that the expression (5) can be considered as the condition of exiting modes of TIR-resonator by partial Bloch waves. Due to this effect, the spectral dependence of DE at Bragg incidence acquires more resonant character in comparison to usual spectral dependence (fig.3) . Spectral selectivity was found to depend on the number of exited mode and to be the most strong for the lowest modes. It is due to increasing Q-factor because of increasing reflectance at front boundary of a grating. Fig.3 shows that full spectral half-width of DE peaks can achieve ~ 0.2 nm at operating wavelengths ~ 630 nm, grating depth 2.5 μm.

c) Non-absorptive transmission gratings: normal incidence

It was supposed in this case that refraction indices of media 1..3 (fig.1d) satisfy to inequalities $n_2 > n_1, n_3$, i.e. the structure, being non – modulated, is a usual planar waveguide. Grating periods were chosen in such a way so that diffracted waves of $\pm 1^{st}$ orders were evanescent in media 1,3 but diffracted waves could exist in the medium 2. If $n_3 > n_1$, such a situation is realized when $k n_3 < K < k n_2$. From physical point of view, there are two sources of diffracted waves inside the grating: boundary diffraction due to periodicity of Fresnel coefficients of transmission at front boundary[10] and scattering by volume non-homogeneity of medium 2. Both of this effects result in arising partial Bloch waves A,B (fig.1d) with x-projection ξ_2 of quasi-wave vectors (see sec.2). Because of TIR of these waves at both of grating boundaries , a mode of modulated waveguide can be exited when

$$2\xi_2 h \approx 2\varphi_{21}^{(2)} + 2\varphi_{23}^{(2)} + 2m\pi , \qquad (6)$$

where $2\varphi_{21}^{(2)}$, $2\varphi_{23}^{(2)}$ - phase shifts in reflection of partial wave. It should be noted that reflection of partial wave at grating boundaries is not TIR in the strict sense. It is frustrated by reversed boundary diffraction that results in leaking a mode into media 1,3. Reversed diffracted waves propagate along the normal to grating boundary, so amplitudes of waves R_0 , T_0 can be greatly different from ones expected in the case of non-modulated layer. Indeed, the dependence of energetic coefficients R_0 , T_0 on grating period was found to have resonant character with R_0 =1, T_0 =0 at some values Λ_m depending on modulation amplitude Δn. Formal angle of boundary diffraction of primary wave I into media 2 for periods Λ_m was near to the angle of incidence of zigzag wave for a guided mode of non-modulated waveguide. Resonant character of diffraction process described resulted in very high spectral selectivity when grating period was chosen equal to Λ_m (fig.4). Full half-width of spectral peaks was dependent on modulation amplitude Δn and could

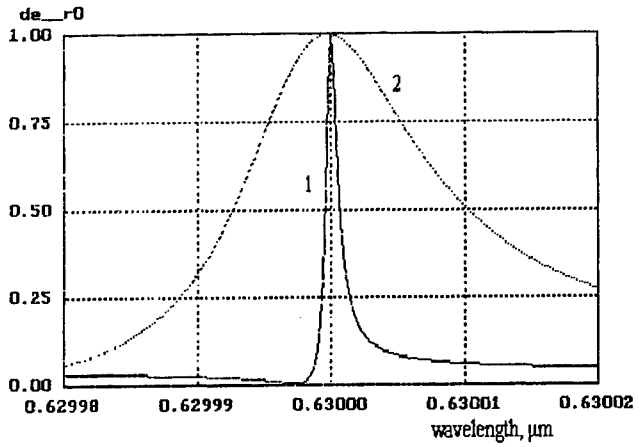


Fig.4. Spectral dependence of DE of 0-th order in reflected light for the modulated waveguide shown in fig.1d.
n_1= 1.0, n_2=1.51, n_3=1.45, h=1.0 μm
1 - Δn = 0.02, Λ=0.422427 μm; *2* - Δn = 0.04, Λ=0.422641 μm

achieve ~ 0.001 nm for operating wavelengths ~ 630 nm in spite of very small grating depths (~ 1 μm). Results obtained are very close to that obtained earlier on the basis of rigorous theory of coupled waves [11]. It should be also noted that effect of resonant increasing R_0 up to 1 is similar to that revealed for planar waveguides with sinusoidal corrugated boundary [12].

4. CONCLUSION

Results considered show that high Fresnel reflection at grating boundaries influences to a great extent diffraction properties of both transmission and reflection gratings. Due to different physical mechanisms, boundary effects result in significant increasing spectral selectivity in comparison to usual Bragg selectivity. The highest spectral selectivity is achieved for waveguide transmission gratings. Structures considered can be of interest for developing a number of components for optoelectronics (broad-aperture laser mirrors, selective absorbers of laser power, demultiplexers of WDM optical networks etc.).

5. REFERENCES

1. H. Kogelnik, "Coupled wave theory for thick hologram gratings", Bell Syst. Tech. J., **48**,pp.2909-2947,1969.
2.Yu. P. Udoev, "Spectral properties of volume phase gratings of reflection type with a reflecting boundary", Optika i Spektroskopiya, **87**,pp.139-144,1999.
3 R. S. Chu, T. Tamir, " Guided wave theory of light diffraction by acoustics microwaves", IEEE Trans. Microwave Theory Tech., **MTT-18,** pp.486-504, 1970.
4. M. G. Moharam, L. Young, " Criterion for Bragg and Raman-Nath diffraction regimes", Appl. Opt. **17**, pp.1757-1759,1978.
5. D. V. Bernikov, Yu. P. Udoev, "Resonant cavity effect in light diffraction by volume reflection grating", Optika i Spectroskopiya, **81**, pp.1028-1032,1996.
6.Yu.P.Udoev, "Boundary effects in light diffraction by volume gratings.1.Phase reflection gratings", Optika i Spectroskopiya, **84**, pp. 635-641, 1998.
7. H. Kogelnik, C. V. Shank, T. P. Sosnowski, A. Dienes, "Hologram wavelength selector for dye lasers", Appl.Phys.Lett., **16**,pp.499-501,1970.
8. M. S. Soskin, V. B. Taranenko, " Holographic selector of total internal reflection for lasers with tuned frequency of generation", Kvantovaya elektronika, **4**, pp.536- 544, 1977.
9. S. F. Kintero, A. D. Gutenko, Yu. P. Udoev, " Some peculiarities of TIR-interference of light in thin films", Optika i Spectroskopiya, pp.795-799, 1992.
10. J. T. Sheridan, L. Solimar, "Boundary diffraction coefficients for calculating spurious beams produced by volume gratings", Electron. Lett., **26**, pp.1840-1841,1990.
11. S. S. Wang, R. Magnusson, J. S. Bagby, M. G. Moharam, " Guided mode resonances in planar dielectric-layer diffraction gratings", JOSA, **7A**, pp.1470-1474,1990.
12.G. A. Golubenko, A. S. Svakhin, V. A. Sychugov, A. T. Titshenko, " Total reflection of light reflected from corrugated surface of dielectric waveguide", Kvantovaya Electronika, **12**, pp.1334-1336, 1985.

Optimization of the structure parameters of the high-efficiency gratings with multilayer dielectric coating for laser pulse compression.

V.D.Vinokurova [a], R.R.Gerke [b], E.G.Sall [a]

Inst. For Laser Phys. [a], Vavilov State Optical Institut [b], Russia

ABSTRACT

Optimization of the grating structure parameters at the working wavelength 1.06 μ is made on the basis of the calculation method for the diffraction gratings with nonequidistant coatings. The comparison of the experimental and calculation data has revealed the considerable smoothing of an initial grating relief by evaporation of multi-layered coating. On the basis of theoretical estimations the untraditional area of optimum layer thickness is suggested. The theoretical diffraction efficiency for this area at real relief smoothing is 96%.

Keywords: diffraction gratings, multilayer dielectric coatings

1. INTRODUCTION

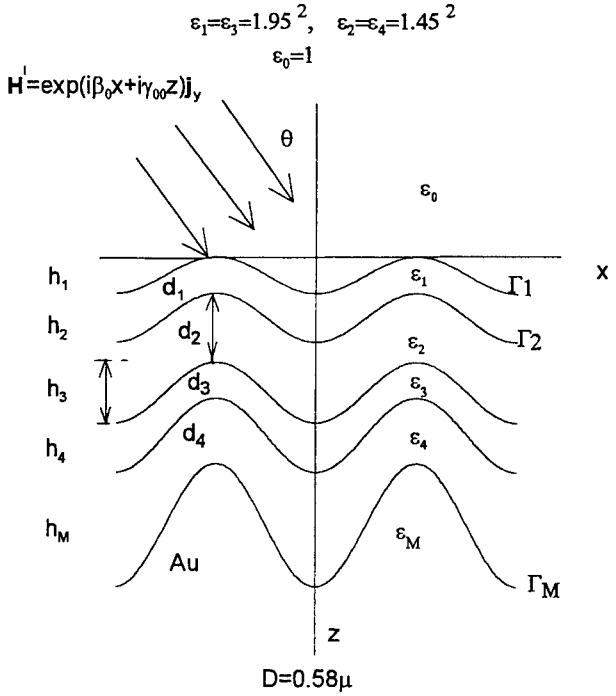
The work is devoted to research and optimization of the diffraction properties of holographic gratings with multiplayer dielectric coating. It is known, that diffraction efficiency and the radiation tolerance of diffraction gratings with multiplayer dielectric coating strongly depends on quantity, thickness and profile shape of coatings. The increase of attention recently to such elements [1-4] is explained to that they, as follows from accounts, at the certain parameters of structure of a coating have high diffraction efficiency DE in the autocollimation regime (DE~1). This work is about real possibilities of making of such diffraction elements with high DE.

2. FORMULATION OF THE PROBLEM

Hopeful theoretical results are received for gratings with the equidistant coatings, that is when the structures of borders between dielectric layers turn out by parallel carry of a grating profile lengthways the normal to its plane. However is real by evaporation of coating probably smoothing of a relief of a boundaries (fig. 1). On the fig.1 D - period of a grating, ε_i - permittivity, Γ_i – boundaries profile between regions with different i , h_M - depth of a metal grating, h_i - depth of a profile Γ_i, d_i - distance between Γ_i and Γ_{i+1} in a maximum of a profile. Such smoothing at rather small number of layers in a covering can make worse diffraction property of such elements. The necessary tool of research of such situation is our method [5], allowing to calculate a diffraction field of a grating with nonequidistant coatings, in which the boundaries profiles have various depth.

Laser Optics 2000: Control of Laser Beam Characteristics and Nonlinear Methods for Wavefront Control, Leonid N. Soms, Vladimir E. Sherstobitov, Editors, Proceedings of SPIE Vol. 4353 (2001)
© 2001 SPIE · 0277-786X/01/$15.00

Fig.1. Model of the diffraction grating with the multilayer coating



We consider the two-dimensional problem of diffraction of a plane H-polarized electromagnetic wave of the unit amplitude in the XZ-plane incident at an angle of θ on a metal diffraction grating with a multilayer dielectric coating (fig.1). The magnetic field strength vector of the incident wave has the form

$$\boldsymbol{H}^{i} = \exp\left(i\beta_0 x + i\gamma_{00} z\right)\boldsymbol{j}_y \qquad (1)$$

were $\beta_0 = \sin\theta D/\lambda$, $\gamma_{00} = \sqrt{\varepsilon_0 (D/\lambda)^2 - \beta_0^{\,2}}$, $\varepsilon_0 = 1$, λ is the wavelength and $\boldsymbol{j}_y$ is the unit vector along the OY-axis. A scalar factor of the required field H_j should satisfy the Helmholtz equation in all regions of the system

$$\left(\Delta + k_j^{\,2}\right) H_j = 0\ , \qquad (2)$$

where $k_j^{\,2} = \varepsilon_j (D/\lambda)^2$, j being the region number. At the boundaries Γ_j between regions with different j, the continuity conditions should be satisfied for the magnetic field and tangential components of the electric field.

3. RESULTS AND DISCUSSIONS

Fig. 2-3 show the results of calculation of a 1700 g/mm diffraction grating with two pairs of dielectric layers in a coating for two value of depth of a sinusoidal metal (golden) grating : $h_M/D=0.38$ and $h_M/D=0.3$. The refractive indexes of dielectric layers are $n_1=n_3=1.95$ and $n_2=n_4=1.45$.

Fig.2. Diffraction efficiency at different smoothing

for $h_M/D=0.3$, $d_1=d_3=125$ nm , $d_2=d_4=210$ nm

1. $h_i=h_M$
2. $h_1=0.3h_M$, $h_2=0.4h_M$, $h_3=0.5h_M$, $h_4=0.6h_M$

\+ experiment

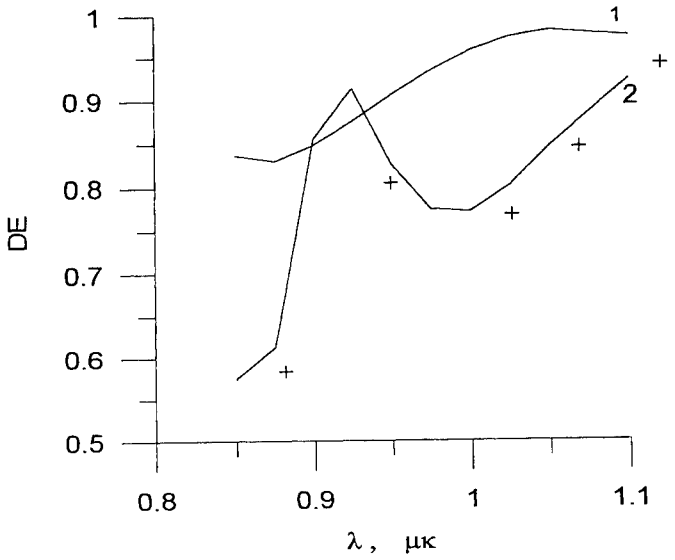
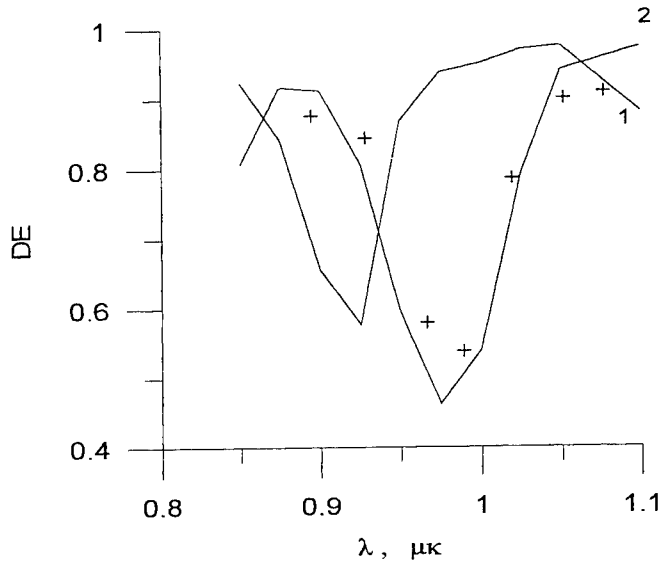


Fig. 3. Diffraction efficiency at different smoothing

for $h_M/D=0.38$, $d_1=d_3=155$ nm , $d_2=d_4=255$ nm

1. $h_i=h_M$
2. $h_1=0.3h_M$, $h_2=0.4h_M$, $h_3=0.5h_M$, $h_4=0.6h_M$

\+ experiment



Curve 1 in a fig. 2,3 represent theoretical results for the equidistant coatings, and curves 2 for nonequidistant coatings. Thus was considered, that nonequidistant structure of dielectric borders is determined by uniformity of growth in time of thickness of a dielectric layer during evaporation along the normal to boundary of the previous layer (fig. 1). The points in a fig. 2,3 designate the data of experiment. The comparison theoretical and experimental data has revealed a presence smoothing of a relief of dielectric layers borders.

In view of it the numerical study of dependence DE of a grating on working wavelength $\lambda=1.06\mu$ from thickness of layers was made. As a result of these researches the area of value d_i appreciablly distinguished from traditional $\sim\lambda/4$ is revealed with high value DE~0.96. At change of thickness of coatings d_i within the limits of 10 % and change of depth h_i over a wide range, DE (fig. 4,5) essentially does not vary.

Fig 4.Diffraction efficiency dependence on the layers thickness variation for the new area at the real smoothing

(h_M /D = 0.3)

$h_1=0.3h_M$, $h_2=0.4h_M$, $h_3=0.5h_M$, $h_4=0.6h_M$

1. $d_1=d_3=230$ nm, $d_2=d_4=285$ nm
2. $d_1=d_2=220$ nm, $d_2=d_4=275$ nm

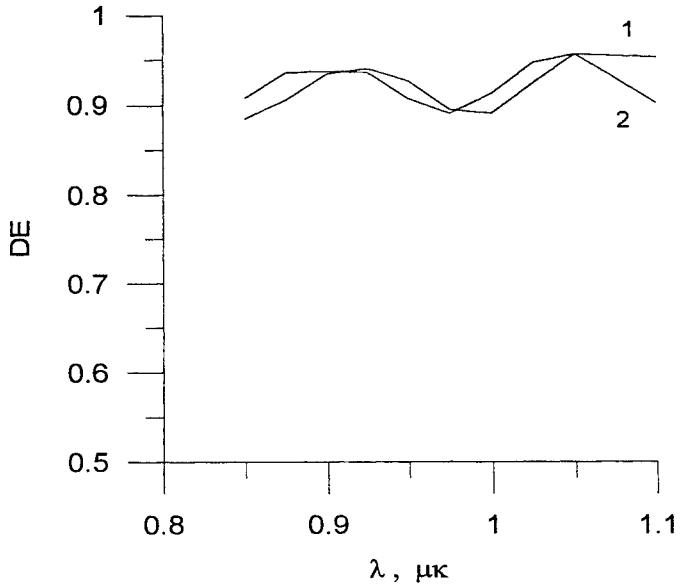
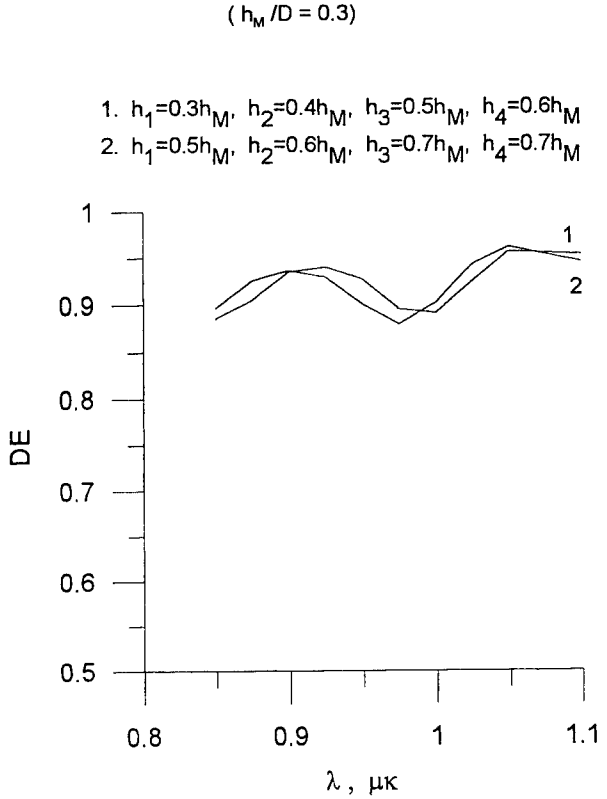


Fig.5. Diffraction efficiency for the new thickness area $d_1=d_2=230$ nm, $d_3=d_4=285$ nm, for different smoothing



Due to stability DE on thickness and size of smoothing of a coatings relief the new area of thickness of dielectric layers makes to real manufacturing of diffraction elements with high DE.

4. REFERENS

1. L.Li, "Multilayer modal method for diffraction gratings of arbitrary profile, depth and permittivity", *J. Opt. Soc. Amer.* **A10**, p.2581, 1993.
2. L.Li, J.Chandezon et al, "Rigorous and efficient grating-analysis method made easy for optical engineers", *Appl. Opt.* **38**, p.304, 1999.
3. J.Chandezon, M.T.Dupuis, G.Cornet, D.Maystre, "Multicoated gratings: a differential formalism applicable in the entire optical region" *J. Opt. Soc. Amer.* 72, p.p.839-846, 1982.
4. A.A.Andreev, V.D.Vinokurova, and A.N.Shatsev, "Optimization of radiation tolerance of diffraction gratings using numerical modeling", *Opt. and Spectr.* **85**, p.p.281-286, 1998.
5. V.D.Vinokurova, R.R.Gerke, "Numerical simulation of coated holographic diffraction gratings for compression of high-power laser pulses", *Opt, and Spectr.* **83**, p.p.916-920.

Influence of phase distortion of soft-edge output mirror on the characteristics of laser modes of unstable and plane-parallel resonators

Vyacheslav B. Karasev, Vyacheslav V. Nazarov, Eduard S. Putilin,
Pavel N. Fimin, and Valery Yu. Khramov*

St.-Petersburg State Institute for Fine Mechanics and Optics (Technical University)
197101, Sablinskaya st., 14, St.-Petersburg, Russia

ABSTRACT

This work analyzes the influence of phase distortions caused by variable-reflectivity multilayer dielectric mirrors on the spatial and energetic characteristics of the output radiation of lasers with unstable and plane-parallel resonators. The phase distortion of such mirrors has been considered in dependence on design parameters of optical coating. Some application peculiarities of soft-edge mirrors for the Cassegrain and Fabry - Perot resonators of lasers are discussed. The work represents some recommendations for the mirror design that ensures the optimal output laser beam characteristics.

Keywords: variable-reflectivity multilayer dielectric mirror, soft-edge mirror, unstable laser resonator, plane-parallel laser resonator

1. INTRODUCTION

At present time, an application of variable reflectivity mirrors (VRM)[1] as the intracavity elements is regarded as one of the most effective methods of the control over laser spatial and energetic characteristics. The soft-edge mirrors installed as output reflectors in unstable optical resonators (see, for example, review[2] and references therein) prevent from the appearance of undesirable diffraction effects at the output aperture edge and eliminate a loss degeneracy of fundamental and high-order transverse modes. Although the replacement of the standard hard-edge output mirror with the variable-reflectivity mirror in the stable resonators[3] and the resonators close to the stability region[4] results in the decrease of the power output, but it allows, due to the significant transverse mode selection, to reduce essentially the angular divergence of the output radiation and to increase the beam brightness in the far-field. The positive results of VRM application in laser systems became possible due to the development of manufacturing technique using the vacuum deposition of graded-thickness multilayer dielectric coatings. However such mirror inevitably adds the distortions to the wavefront of the reflected and transmitted radiation due to the thickness gradient of the dielectric coating, shaping its variable-surface reflectivity[5]. In a number of cases of the VRM application (in particular, for unstable resonators with a small magnification factor and for resonators on the boundary of stability) the given circumstance could become decisive and result not in the expected improvement, but in the deterioration of the spatial-energetic characteristics of the output radiation[6,7]. Meanwhile, the problem of the effect of the intracavity VRM phase response (in particular, for the resonators on the boundary of stability) on the integral characteristics of the output laser radiation have been discussed insufficiently.

This work represents the numerical analysis for the formation conditions of the transverse modes in the unstable and plane-parallel laser resonators containing VRM as the output reflector. Basing on the obtained results, the recommendations for the application of soft-edge mirrors in the resonators of the given types have been worked out.

2. VRM DESIGN AND PHASE SHIFT OF REFLECTED AND TRANSMITTED LIGHT WAVE

In general the complex reflectivity coefficient of a multilayer dielectric mirror is determined by the shape of the substrate surface and by the thickness distribution of the layers composing the reflecting coating. The total reflectivity depends also on the refraction indices of the layers, on their order sequence and on the ratio between the refraction indices of the coating layers and the substrate as well. Generally, the increase of the number of graded-thickness layers in a dielectric

* Correspondence: Email: khramov@itcs.spb.ru; Telephone: (812)-312-23-23; Fax: (812)-315-71-33

Laser Optics 2000: Control of Laser Beam Characteristics and Nonlinear Methods for Wavefront Control,
Leonid N. Soms, Vladimir E. Sherstobitov, Editors, Proceedings of SPIE Vol. 4353 (2001)
© 2001 SPIE · 0277-786X/01/$15.00

coating results in the increase of VRM phase distortions, which may significantly complicate the procedure of search for the optimal mirror design[8].

The present work deals with the variable reflectivity mirrors of the three-component design (substrate - antireflective coating - reflecting coating) (Fig. 1). In the previous studies[4,9] we have tested such mirrors in high-energy pulsed YAG:Nd laser systems. The layers with a high refraction index relative to the K8 glass substrate ($n_S = 1.51$) were made of the Zirconium dioxide ($n_H = 1.92$), while those with a low refraction index were made of the Silicon dioxide ($n_L = 1.45$). The uniform two-layer coating 1.5H 0.78L was used as antireflection coating of the substrate. Generally for numerical experiments the mirrors with the axially symmetric trapezoidal and exponential thickness profile of the layers of the reflecting coating were selected. Quasi-trapezoidal and quasi-exponential thickness distributions can be obtained, for example, by the vacuum evaporation of medium from a small surface source on the rotating substrate through the round diaphragms or screens disposed between the evaporator and the substrate[10].

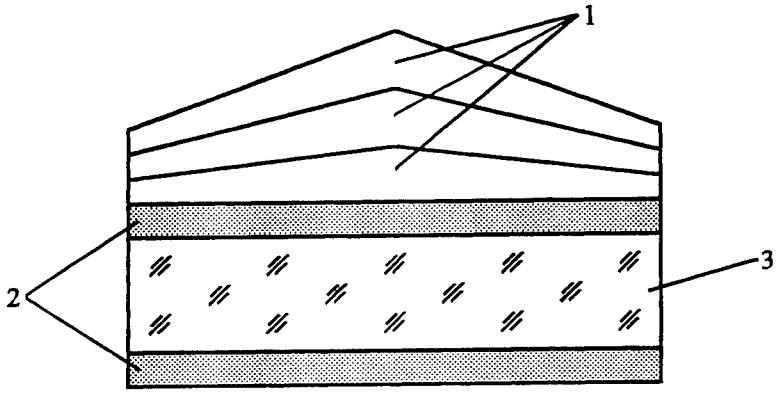


Fig. 1. Design of variable reflectivity mirror. 1 - graded-thickness layers, 2 - antireflective coating, 3 - substrate.

This work considers the application peculiarities of the output mirrors, the reflectivity distribution of which is shaped by the simultaneous thickness variation of all layers forming the reflecting coating. In this case an optical thickness of each layer $n_j t_j(r)$ does not depend on its order number j and is determined by the radial coordinate of the substrate surface r:

$$\frac{n_j t_j(r)}{n_{j+1} t_{j+1}(r)} = \text{const}, \qquad n_j t_j(r) = d(r). \tag{1}$$

Here n_j is the refraction index of the j layer and $t_j(r)$ is the function of the thickness distribution across the substrate surface.

The multilayer coatings of the given design allow varying the amplitude - phase characteristics of laser mirror within wide boundaries, and their deposition does not require a complicated technological equipment[11].

The phase shift of the reflected wave $\Delta\Phi_\rho(r)$ at the reflection of the VRM can be expressed in the following form:

$$\Delta\Phi_\rho(r) = \Delta\varphi_\rho(r) - \frac{4\pi}{\lambda}[\Delta h(r) + \Delta\varepsilon(r)]. \tag{2}$$

Here $\Delta\varphi_\rho(r) = \varphi_\rho(r) - \varphi_\rho(0)$ is the phase shift between the reflected and incident wave along the substrate radius, $\Delta h(r) = h(r) - h(0)$ - is the air interspace change due to the thickness gradient of layers, composing the dielectric coating, $\Delta\varepsilon(r)$ - is the variance of the shape of the substrate from the plain, passing through the mirror center normally to the rotation axis, and λ is the beam wavelength.

Similarly the phase shift of the wave transmitted through the VRM, $\Delta\Phi_\tau(r)$,is given by

$$\Delta\Phi_\tau(r) = \Delta\varphi_\tau(r) - \frac{2\pi}{\lambda}[\Delta h(r) + (n_s - 1)\Delta\varepsilon(r)], \tag{3}$$

where $\Delta\varphi_\tau(r) = \varphi_\tau(r) - \varphi_\tau(0)$ is the phase shift between the transmitted and incident waves along the substrate radial coordinate, while n_s is the substrate refractive index.

3. INFLUENCE OF PHASE RESPONSE OF VARIABLE MIRROR ON SPATIAL CHARACTERISTICS OF OUTPUT BEAM FOR LASER WITH UNSTABLE RESONATOR

The unstable resonators are traditionally used for generation of single-mode beams in powerful lasers with a high amplifier coefficient of the active medium (e.g. in eximer and CO_2 lasers) and in those with large cross-section of the active medium (e.g. Nd:glass lasers[12]). This section deals with the Cassegrain resonators made of totally reflecting concave rear mirror and an output convex mirror having radially variable reflectivity. Fox and Li[13] iterative procedure has been taken as a mathematical model, describing the formation of transverse modes in laser resonators. The mathematical model provided for the analysis of arbitrary resonator configurations in a paraxial approximation, as well as for the assessment of influence of amplitude-phase aberrations of intracavity components on the steady-state transverse distribution of the complex field amplitude in the plane of the output resonator aperture. The eigenfunctions and eigenvalues of the integral equation describing the laser mode formation in resonators with large Fresnel number values $N = a^2/\lambda L$ (a – aperture range of the rod, L – resonator base, λ - beam wavelength) were calculated in terms of the fast Hankel-Gardner transform[14].

At the first stage of the numerical experiments, multilayer dielectric mirrors were studied with the radial variation of the optical thickness of the gradient layers obeying linear $n \cdot t(r) = (\lambda/4)(1 - r/w)$ and exponential $n \cdot t(r) = (\lambda/4)\exp[-(r/w)^p]$ laws. (The parameter w is character size of coating area.) The degree of the exponent p varied from 1.5 to 3.5 with the step 0.5. Figure 2 demonstrates the phase characteristics of the model mirrors.

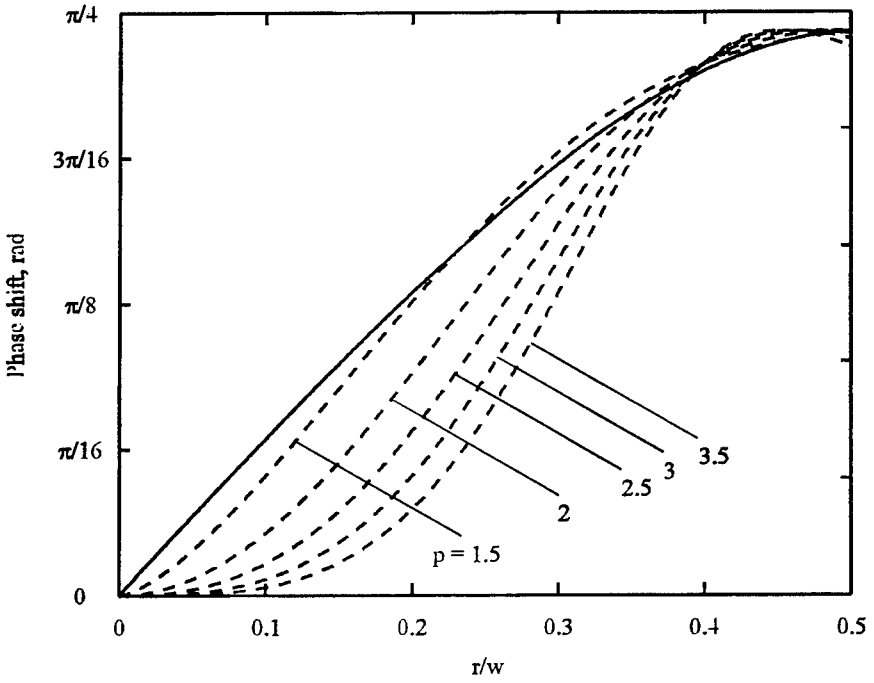


Fig. 2. Phase distortion of reflected wave caused by variable-thickness dielectric coating of output mirror. The curves were calculated for optical coating having linear dependence of optical thickness of a profiled layer (solid line) and exponential dependence of profiled layer thickness (dashed lines) on the parameter p from 1.5 to 3.5 through 0.5.

Figure 3 represents the results of the calculation of the radial steady-state intensity distribution for the Cassegrain resonator based on the VRM. The beam enters the resonator output mirror (solid lines) that is composed by the layers with the radial variation of thickness obeying linear law and passes through it. The numerical calculations are carried out for the Cassegrain resonators with Fresnel number N = 300 and the magnification varying from 1.2 to 2. The radius of the optical coating area varied depending on the value M. The output mirror design and the dielectric layer parameters were chosen to obtain the optimal value of the on-axis mirror reflectivity[15]. It is shown that the negative influence of the phase response of VRM significantly decreases at the increase of M. It can be seen that the presence of VRM phase distortion much deteriorates not only the output, but also the intracavity intensity distribution. The increase of the dip depth in the central zone of radial intensity distribution at the reduction of M we explicate with the effect of the phase response at reflection from the VRM, which near the resonator axis behaves as an intracavity axicon (see solid curve in Fig. 2).

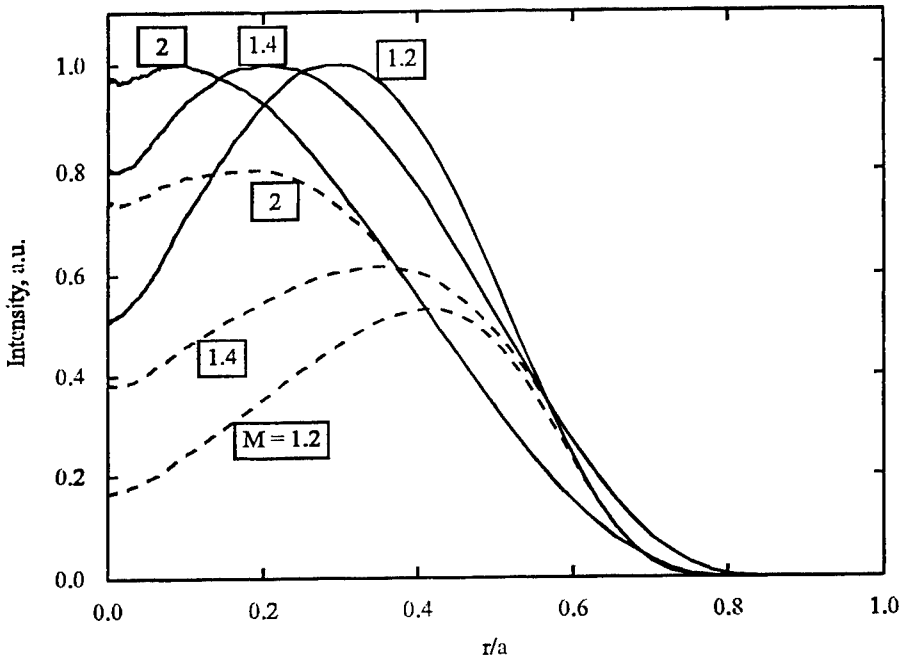


Fig. 3. Intracavity (solid lines) and output (dashed lines) radial steady-state intensity distribution for the Cassegrain resonator with magnification factors M = 1.2, 1.4, and 2 based on the VRM with linear radial distribution of optical thickness of profiled layers.

In Fig. 4 the radial intensity distribution for various values of magnification factor M and parameter p = 2.5 is indicated. At the value p = 2.5 the output laser intensity distribution is closest to that for an "ideal" phase-aberration-free Gaussian mirror. Figure 2 shows, that at $2 \le p \le 2.5$ the reflectivity phase distortion is the closest to a parabolic shape corresponding to spherical part of wavefront.

The next stage of the numerical experiments dealt with the influence of the phase response of the 21-layer dielectric output soft-edge mirror on the spatial characteristics of the laser beam of an unstable resonator. The reflectance distribution variation across the mirror surface is formed by nineteen variable layers of the trapezoidal profile covering the antireflective substrate. A high number of local extrema of the radial reflectance distribution (Fig. 5a) as well the large phase distortions by the reflection and transmission (Fig. 5b) are caused by the change of the optical thickness in all nineteen layers of the reflecting coating from 0.25λ to zero (λ being the beam wavelength). As a variable parameters were chosen the magnification of the resonator M and the relative value of the edge smoothing zone $\Delta w/w$ (w is the radius of mirror zone, where the layer thickness of reflecting coating was uniform, and Δw is the size of the annular zone, where the layer thickness decreases from its maximal value 0.25λ to zero). The curves in Fig. 5 correspond to a linear variation of optical thickness of dielectric layers within the range $w \le r \le w + \Delta w$.

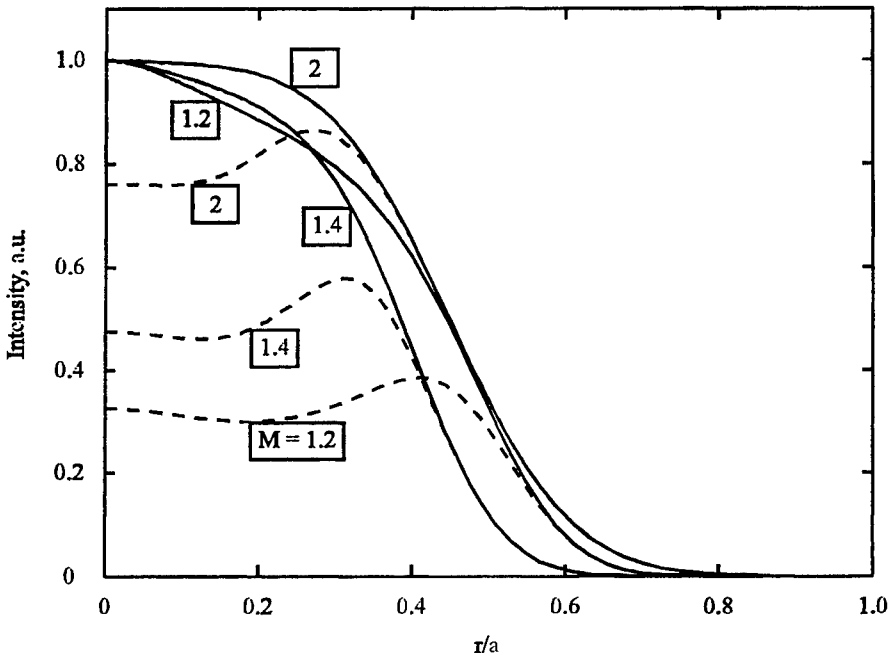


Fig. 4. Intracavity (solid lines) and output (dashed lines) steady-state radial intensity distribution for the Cassegrain resonator with magnification factors M = 1.2, 1.4, and 2 based on the VRM with exponential (p = 2.5) radial distribution of optical thickness of profiled layers.

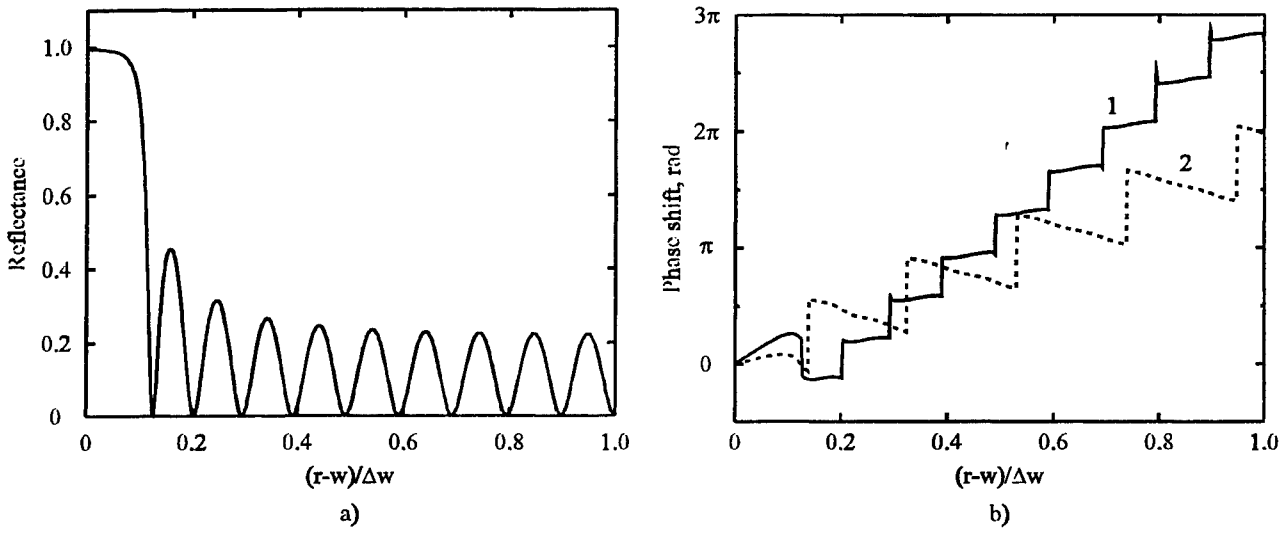


Fig. 5. Reflectance (a) and phase shift (b) of smoothing-edge model mirror. 1 - phase distortion of reflected wave, 2 - phase distortion of transmitted wave.

Figure 6 represents the dependence of the divergence of the output beam at 0.83-energy-level $\theta_{0.83}$ on the relative size of mirror edge smoothing zone $\Delta w/w$. As a base level of the angular divergence we use the divergence $\theta_{d\,0.83}$ of the "ideal" aberration-free unstable resonator with the same magnification M. The growth of angular divergence starts as the parameter $\Delta w/w$ approaches to 0.05. One can see also, that the divergence of the output beam noticeably increases with the increase of the mirror smoothing zone size and with the reduction of the resonator magnification.

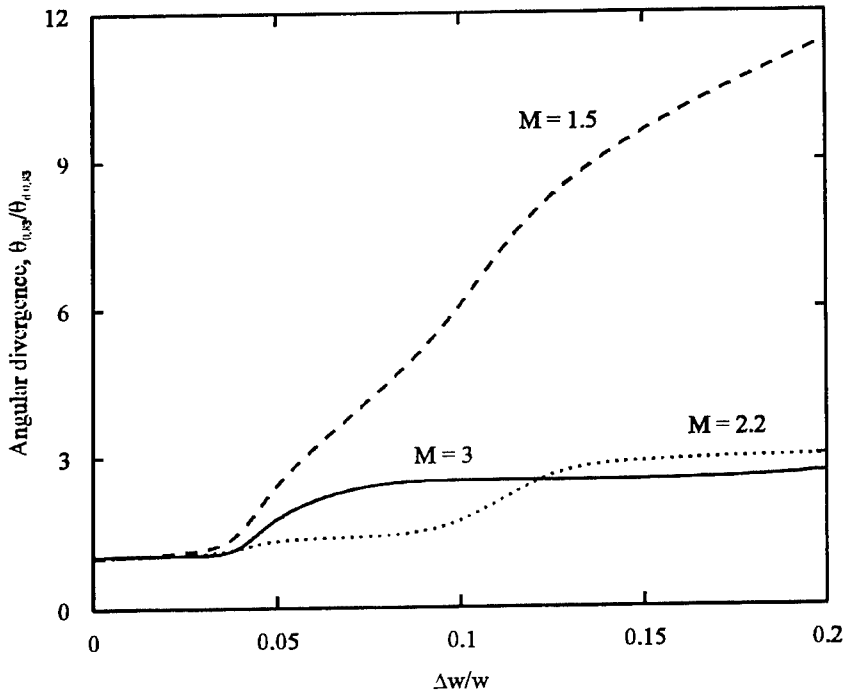


Fig. 6. Dependencies of normalized angular divergence of output radiation on the relative size of the edge smoothing zone Δw/w for magnification factors of resonator M = 1.5 (dashed line), 2.2 (dotted line), and 3 (solid line).

4. EFFECT OF AMPLITUDE - PHASE RESPONSE OF OUTPUT MIRROR ON CHARACTERISTICS OF LASER MODES OF PLANE-PARALLEL RESONATOR

In this section the base objects for the numerical studies were Fabry - Perot resonators, the output mirrors of which consisted of three components: substrate – antireflecting coating – reflecting coating. The uniform two-layer coating 1.5H 0.78L was used as antireflection coating of the substrate. The reflecting coating is created by three layers with radially-variable thickness. For numerical experiments in the general case the mirrors were selected with axially symmetric trapezoidal thickness profile of layers of the reflecting coating. The ratio of diameter of area, in which the thickness of the variable reflectivity layers was uniform, to the mirror aperture diameter was used as a varied parameter η. In the central zone of the mirror the optical thickness of each layer equals to 0.25λ (λ is the beam wavelength), and the corresponding reflectivity of the mirror is close to 0.53. As the optical thickness of all variable layers decreases from 0.25 up to 0.145 (in the rim of mirror), the reflectivity of the edge zone smoothly reduces from the peak value down to zero. As for the phase characteristics of such a mirror, according to our previous computations[7], the plane wave after the reflection from VRM becomes diverging. As it has been shown in the paper[7], this phase response of the output mirror imparts some unstable features to the usual plane-parallel resonator. These features reveal themselves, in particular, in the growth of resonator aperture filling by laser modes. Therefore one can expect the increase of the extraction efficiency of stored energy by the fundamental laser mode.

The numerical analysis of two-mirror plane-parallel resonators with an infinite rear mirror and the output soft-edge mirror, the structure and the amplitude - phase characteristics of which were described in the previous paragraph. The analysis was made basing on the iterative Fox and Li procedure[13]. The resonator Fresnel number $N = a^2/2\lambda L$ (where a is the aperture radius of the output mirror, L is the cavity length and λ is the beam wavelength) was changed in the range from 0.5 up to 10. The profile parameter η of the reflecting coating varied from 0 up to 1 with the step 0.1 due to the variation of diameter of area where the gradient layer thickness was uniform. The effective laser mode volume was evaluated by the filling coefficient of the resonator output aperture with its radiation. Such an evaluation corresponds to the model where the laser rod is assumed to be located close to the resonator output mirror, its diameter - to coincide with the output aperture diameter, and its length - to be negligible in comparison with the spacing between mirrors.

Figure 7 shows the two-dimensional dependence of the filling factor of the output aperture with the fundamental laser mode vs. the resonator Fresnel number N and the profile parameter of the reflecting coating of the output mirror η. It can be seen that the replacement of the standard output mirror with the uniform reflectivity ($\eta = 1$) by the tapered-edge mirror with the profile parameter $\eta = 0$ makes it possible to enhance the extraction efficiency of the energy stored in the active medium up to 15 - 70%. It should be noted that in the mentioned range of N the effective volume of the fundamental mode of the resonator with such a mirror remains practically invariable. However in the range $1 \le N \le 10$ the replacement of the standard output mirror with the variable-reflectivity mirror with $\eta = 0$ is not optimal from the viewpoint of the stored energy extraction by the fundamental laser mode. The dependence of the maximal filling value on the Fresnel number N and the profile parameter η for the plane-parallel resonator has a nontrivial character: within the range $1 \le N \le 6$ the largest value of the filling factor occurs at $\eta = 0.3$, within the range $6 \le N \le 9$ - at $\eta = 0.4$, while in case of $9 \le N \le 10$ - at $\eta = 0.2$. At the increase of η from 0.4 up to 0.6 - 0.7 in the range $1 \le N \le 10$ the fast reduction of value of filling factor of resonator aperture by the fundamental laser mode can be observed, but at further growth of η it becomes practically not depending on the profile of the output mirror reflecting coating.

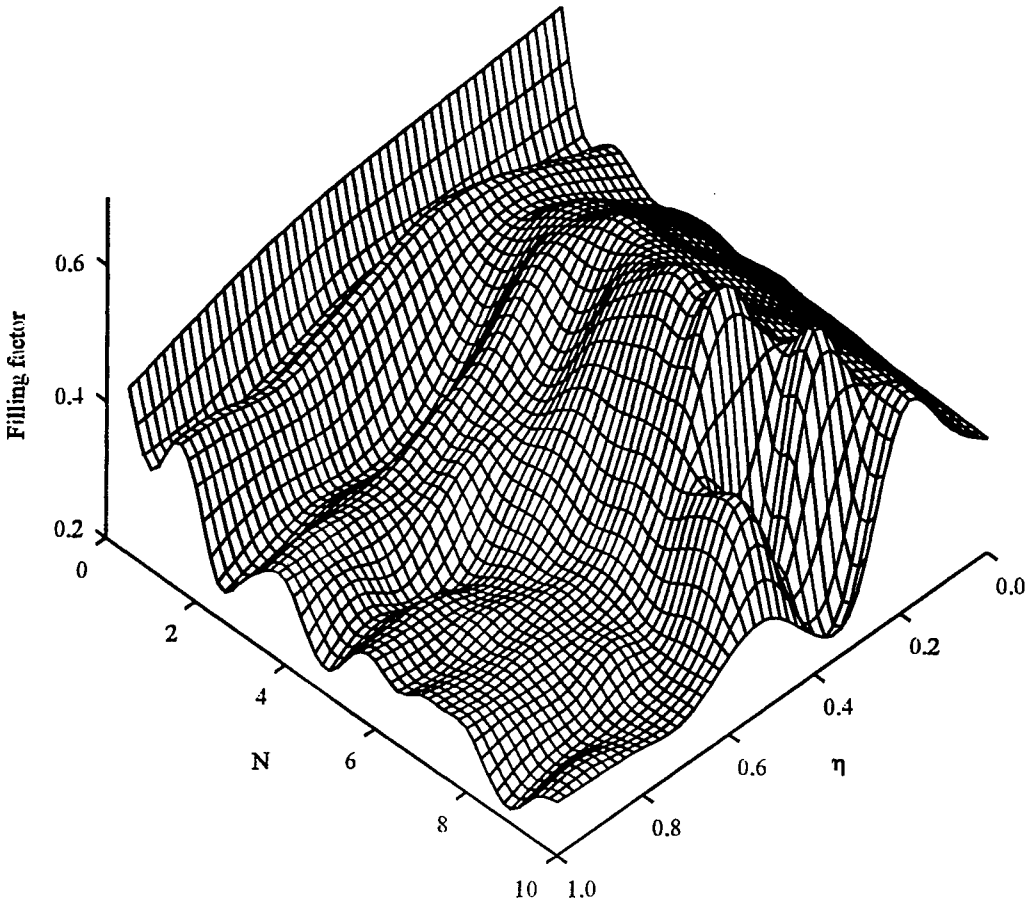


Fig. 7. Dependence of the filling factor of the output aperture with the fundamental laser mode versus the resonator Fresnel number N and the profile parameter of the reflecting coating of the output mirror η.

The existence of an optimal value of the profile parameter ensuring the maximal extraction of energy stored into an active medium by the fundamental laser mode has a simple meaning. At the expansion of the mirror-smoothing zone, the area size, in which its phase response undergoes noticeable modifications, also increases. The optimum is achieved at the appropriate relation of the amplitude - phase characteristics of the output mirror. In our case the application of profile-optimized output mirror could yield the enhancement of the extraction efficiency of stored energy by the fundamental mode of the plane-parallel laser resonator at least twice.

5. SUMMARY

The formation of the fundamental laser mode in unstable resonators as well as in Fabry – Perot resonators with an output soft-edge mirror was studied. The output mirrors were regarded having a complex reflectivity formed by the simultaneous change of thickness of the dielectric coating. It was shown that the phase response could have significant influence on the characteristics of laser modes being formed into the cavity. The most important result of this work was in determining the appropriate thickness profiles of dielectric layers of output mirrors. This, firstly, ensured the minimal amplitude - phase distortions of output beam in an unstable resonator and, secondly, provided the enhancement of the extraction efficiency of the energy stored into the laser medium by the fundamental mode of the plane-parallel resonator.

REFERENCES

1. G. Duplain, P. G. Verly, J. A. Dobrowolski et al., "Grade-reflectance mirrors for beam quality control in laser resonators," *Appl. Opt.* **32**, pp. 1145-1153, 1993
2. M. Morin, "Graded reflectivity mirror unstable resonators," *Opt. Quantum Electron.* **29**, pp. 819-866, 1997.
3. S. G. Lukishova, S. A. Chetkin, N. V. Mettus, E. A. Magularya, "Techniques for fabrication of multilayer dielectric graded-reflectivity mirrors and their use for enhancement of the brightness of radiation from a multimode YAG:Nd^{3+} laser with a stable cavity," *Quantum Electron.* **26**, pp. 1014-1017, 1996.
4. A. V. Aladov, V. V. Bezzubik, N. R. Belashenkov et. al., "The application of mirrors with variable reflectivity in compact solid-state laser systems," *Izvestya vuzov. Priborostroyeniye.* **41** (3), pp. 53-57, 1998. *In Russian.*
5. P. Lavigne, N. McCarthy, J.-G. Demers, "Design and characterization of complementary Gaussian reflectivity mirrors," *Appl. Opt.* **24**, pp. 2581-2586, 1985.
6. H. Bartels, N. A. Generalov, U. Habich et al., "VRM resonator performance in high-power cw CO_2 lasers," *Proc. SPIE.* **3686**, pp. 121-129, 1999.
7. N. R. Belashenkov, V. B. Karasev, V. V. Nazarov et al. "Effect of the phase response of a graded-reflectivity output mirror on the characteristics of laser modes in a plane-parallel resonator," *J. Opt. Technol.* **67**, pp. 20-22, 2000.
8. A. Piegari, G. Emiliani, "Laser mirrors with variable reflected intensity and uniform phase shift: design process," *Appl. Opt.* **32**, pp. 5454-5461, 1993.
9. A. V. Aladov, V. V. Bezzubik, N. R. Belashenkov et. al., "Using mirrors with quasi-trapezoidal reflectance distribution profiles in the cavities of high-radiance solid-state lasers," *J. Opt. Technol.* **62**, pp. 505-508, 1995.
10. E. S. Putilin, L. A. Gubanova, "Interference filters that form the phase and amplitude characteristics of reflected and transmitted radiation," *J. Opt. Technol.* **62**, pp. 557-562, 1995.
11. L. A. Gubanova, V. A. Dmitrenko, E. S. Putilin, "Multilayer dielectric mirrors with a variable reflectance profile for laser systems," *J. Opt. Technol.* **67**, pp. 284-289, 2000.
12. G. B. Al'tshuler, V. V. Kramnik, V. F. Petrov et al., "Neodymium-glass laser with a high output energy and a beam divergence close to the diffraction limit," *J. Opt. Technol.* **67**, pp. 375-378, 2000.
13. A. G. Fox, T. Li, "Resonant modes in a maser interferometer," *Bell System Tech. J.* **40**, pp. 453-488, 1961.
14. A. E. Siegman, "Quasi fast Hankel transform," *Opt. Lett.* **1**, pp. 13-15, 1977.
15. S. De Silvestri, P. Laporta, V. Magni, "Laser output coupler based on a radially variable interferometer," *J. Opt. Soc. Amer. A.* **4**, pp. 1413-1418, 1987.

Coherent beam focussing by a two sequently arranged apertures system

Renat R. Letfullin[1], Oleg A. Zayakin[2]

P. N. Lebedev Physics Institute, Russian Academy of Sciences (Samara Branch)
Novo-Sadovaya str. 221, 443011 Samara, Russia
Phone: 007/8462/340536, Fax: 007/8462/355600

The new optical effect of a diffractive multifocal focussing of radiation, predicted by the theory, on a bicomponent diffraction system with small Fresnel numbers, consisting of two plane screens with circular apertures on a given optical axes, is confirmed experimentally. Is shown, that the diffraction picture in the focal planes of such system represents the circular nonlocal bands of the Fresnel zones with a bright narrow peak at the center, whose intensity in the experiment can exceed by six to ten times the value of the incident plane wave intensity. Experimentally is established, that the diffractive multifocal focussing of a radiation on a real screens with axial circular apertures, whose diameters exceed a radiation wavelength, is insensitive to the "rough" external conditions: to a thickness of screens, to the irregularities of edges and non-ideal form of apertures, to a heterogeneity of initial distribution of an incident wave intensity, to changes in the medium of the wave propagation.

Keywords: wave diffraction, diffractive focussing of a radiation, bicomponent diffracting system.

1. INTRODUCTION

The researches of the diffraction phenomena concern to the most complicated in the optics and they are seldom carried out up to the exact solution because of large mathematical difficulties. Now, the exact solution is known only for the several diffraction problems, that testifies to an incompleteness of the investigations in this field and keeps a huge field of activity for the modern physicist.

For the last years, the development of the computer techniques and numerical methods of a solution of the diffraction problems has led to the discovery of the new optical effects and phenomena, which are observed when a plane or spherical wave is diffracted even by the simple two-dimensional screens [1-6]. So, for example, when a monochromatic converging spherical wave is diffracted by a circular aperture the point of maximum intensity in the diffracted field is not at the geometric focus but displaced toward the aperture, resulting in the so-called focal-shift effect [1-3]. In [4] has been recognized the existence of a certain kind of a rotational symmetric diffracting screen where the expected focal-shift effect can be accompanied by another focal switch effect: an increase in the height on ~ 25% of the lateral lobe of the axial-intensity distribution over that of the central lobe.

More recently another new optical effect on a rather simple diffracting system with the small Fresnel numbers has been detected theoretically [5,6]. Here, has been shown, that if in a diffracted field, formed by the first open Fresnel zone from a screen with a hole, the next parallel plane screen is located with an axial aperture of a smaller diameter (see Fig. 1), then in a near zone of the second screen the effect of a diffractive multifocal focussing of a radiation (DMFR) is observed. In this case, the diffraction picture from the second screen in the focal planes represents the circular nonlocal bands of the Fresnel zones with a bright narrow peak at the centre, whose intensity can exceed by six to ten times the value of the incident wave intensity. The detected optical effect is observed over a wide range of wavelengths and ratios of the aperture diameters, and it is also insensitive to changes in the medium of the wave propagation. For large diameters of the input holes, $d_1 = 2d_2 > 100\lambda$, or for wavelengths in the radiofrequency region of the spectrum, such bicomponent diffracting

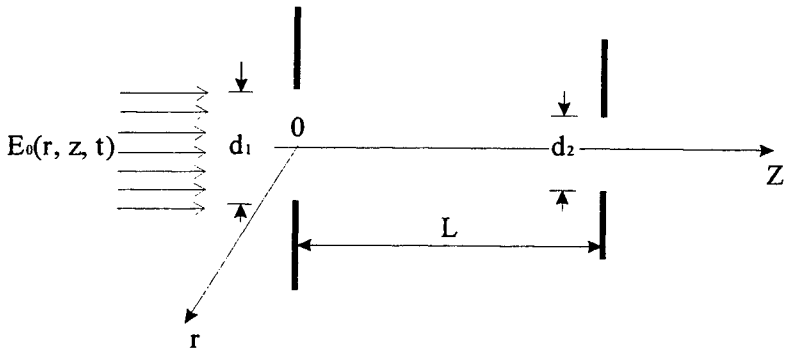


Fig.1. Geometry of the plane wave diffraction problem on a bicomponent diffraction system, consisting from the two definitive plane screens with axial circular apertures of diameters d_1 and d_2. L is a distance between the screens.

[1] E-mail: renat@fian.samara.ru
[2] E-mail: olegz@fian.samara.ru

Laser Optics 2000: Control of Laser Beam Characteristics and Nonlinear Methods for Wavefront Control,
Leonid N. Soms, Vladimir E. Sherstobitov, Editors, Proceedings of SPIE Vol. 4353 (2001)
© 2001 SPIE · 0277-786X/01/$15.00

system acts like a long-focus lens with a high-intensity Gassian distribution of radiation, at times exceeding the initial intensity, persisting at large distances (z = 1 to 100 cm) from the diffraction system.

The goal of this research is the experimental check the theoretical conclusion about a possibility of DMFR on a bicomponent diffracting system. The DMFR effect can have fundamental significance both for optics in general and for quantum mechanics for the focussing of atomic and molecular beams, which, as is known, have the wave properties. The diffracting system based on two definitive plane screens with axial holes allows focusing the beams without using classical refraction elements such as lenses and prisms. Also, such system has a number of advantages above elements of diffraction quasi-optics: all possible zonal plates, film-forms, refractors, elements of computer optics, etc. First of all, the system is applicable to both low-intensive and high-power radiation where the traditional elements of diffraction quasi-optics are not applicable. Secondly, it is simple to fabricate and does not require the development of special phototechnologies or computer syntheses of diffracting elements.

The above advantages open a wide range of possible applications of the DMFR effect and two-aperture diffracting system for situations where it is required effectively to introduce or to extract radiation. Such a diffracting system can be perspective for solving the next laser technology problems: efficiency transmission the wide-aperture semiconductor laser beams by optical fiber; increasing the quality of the saving and reading of information on the optical discs in the computer optics; perfection of the opto-electronic household devices such as laser printers, record-players, plotters, cash registers etc.; improvement of the therapeutic radiators and laser surgical scalpels in the laser medicine; and so on. The bicomponent diffracting system can be important, also, for the creation of quasi-point light sources with high intensity for the purpose of high-resolution microscopy, since it enables one effectively to introduce radiation in a small area of space with minimal power losses. Thus, the experimental observation of the DMFR effect will be important for both, fundamental and applied investigations.

2. THEORY

The problem of diffraction of a plane electromagnetic wave on two parallel opaque screens with the axial apertures of different diameters $d_1 > d_2 \gg \lambda$ (see Fig. 1) has been solved in [5,6] within the quasi-optical approximation for indefinitely thin ($\delta \ll \lambda$, where δ is the screen thickness) and ideal opaque ($\sigma_{scr} \to \infty$ and $m_{scr} \to \infty$, where σ_{scr} and m_{scr} are the conductivity and refraction index of the screen) screens. Note that the diffraction at the second aperture is not of the Fresnel type, since the condition $r \gg \lambda$ requires that at each point of a wavefront set, incident on the second hole, the curvature radius should be large compared to the wavelength λ. In our case, the wavefront set, incident on the second aperture, represents a diffraction picture with a narrow peak at the center created by the first aperture in the first open Fresnel zone at the distance $z = L$. At this curvature, the radii of a wavefront set at the second hole will be significantly less than the radius of the first Fresnel zone, i.e., $r < r_1 \approx \sqrt{L\lambda}$. Here, the Babinet principle of the distribution of light to diffraction on additional screens is not applies, also, because in our case the holes are axial. The solution of the problem of diffraction of a wave on two plane screens with axial apertures is possible on the basis of the wave equations:

$$2ik_0 m \frac{\partial E}{\partial z} + \frac{1}{r}\frac{\partial}{\partial r}\left(r\frac{\partial E}{\partial r}\right) = 0; \tag{1}$$

$$E(r,z)\big|_{z=0} = E_0 R_1(r); \qquad E(r,z)\big|_{z=L} = E(r,L)R_2(r);$$
$$E(r,z)\big|_{|z|\to\infty} = E(r,z)\big|_{|r|\to\infty} = 0; \qquad E(r,z)\big|_{|z|\to\infty} = E(r,z)\big|_{|r|\to\infty} = 0. \tag{2}$$

Here, $R_{1,2}(r)$ are the passage factors for the screens with an aperture. Based on the continuity of boundary conditions for a wave equation, the factors $R_{1,2}(r)$ can be approximated by an exponential function [5,6]. On a problem condition the distance between screens L is equal exactly to a distance, on which the first Fresnel zone for a specific diameter of an input aperture d_1 is opened: $L = d_1^2/4\lambda$. Thus, from the wave equation (1) the boundary conditions (2) we can determine the wave intensity distribution in a diffraction picture, created by the plane screens with a circular apertures, as

$$I(r,z) = \frac{cm}{4\pi} E^*(r,z)E(r,z) \tag{3}$$

where the asterisk means complex conjugation.

The solving of the problem posed by Eqs. (1)-(3) about diffraction of an electromagnetic wave on two screens – an ideally thin ($\delta \ll \lambda$) and an ideally opaque ($m_{scr} \to \infty$) screens with axial circular apertures with diameters $d_1 > d_2$, has been led to the detection in [5,6] of a new optical effect DMFR. Has appeared, that the the diffraction picture, formed by a such

diffracting system, in the focal planes represents the circular nonlocal bands of the Fresnel zones with a bright narrow peak at the centre, whose intensity can exceed by six to ten times the value of the incident wave intensity.

From the executed accounts [5,6] follows also, that the DMFR effect is observed over a wide range of wavelengths, $\lambda = 0.4$ to 10^3 μm, and ratios of the aperture diameters $d_1 \geq 2d_2 = 25$ to 1000 λ. For large diameters of the input holes, $d_1 = 2d_2 > 100\lambda$, or for wavelengths in the radiofrequency region of the spectrum, the bicomponent diffraction system acts like a long-focus lens with a high-intensity Gaussian distribution of radiation, at times exceeding the initial intensity, persisting at large distances ($z = 1$ *to* 100 *cm)* from the diffraction system.

In the numerical accounts [5,6] have been established also, that the detected effect is insensitive to changes in the medium of the wave propagation. For the model mediums were considered not absorbing (m = 1) and the homogeneously absorbing and scattering gas-dispersed medium. The statement of a problem of wave diffraction on a bicomponent diffractive system in an aerosol medium is similar to that of a homogeneous medium (1)-(3), but with a complex wavevector $\hat{k}(\tilde{m})$ in the wave equation

$$\hat{k}(\tilde{m}) = k\tilde{m} = i\sqrt[3]{\frac{2\pi NS(0)}{\tilde{m}-1}}, \qquad (4)$$

where $S(0) = \frac{1}{2}\sum_{l=1}^{\infty}(2l+1)(a_l + b_l)$ is the amplitude function describing the scattering of an electromagnetic wave by a particle with a scattering angle of zero; a_l and b_l are the Mie coefficients containing the characteristics of the gas-disperse medium: the radius r_0 and concentration N of particles; $\tilde{m}$ is the relative refractive index of the medium. In particular has been shown [5,6], that the qualitative picture of the diffracted field distribution in a homogeneously absorbing and scattering medium, consisting from aluminum aerosol with the radius of $r_0 = 0.2$ μm and concentration of $N = 1.3 \times 10^7$ cm^{-3}, did not vary.

3. EXPERIMENTAL SET-UP

A following experiment was carried out to confirm the existence of DMFR effect of a plane electromagnetic wave on a bicomponent diffraction system. A set-up of this experiment is shown in Fig.2 (a). The radiation of a *HeNe* laser 1 has passed through the beam expander 2 with a space filter 3, and then it has fallen on a testing system of diafragms 4. A micro-objective 5 has created an optical image of diffraction pattern on a computer-aided CCD-line photodetector 6. A photodiode gauge 8 has read the output laser beam power level.

The focussing of the system 5 - 6 on a required object plane in the diffraction zone of a testing system 4 was conducted by a displacement of a bicomponent system along a main optical axes of an expanded and collimated light beam.

Let's adduce some paremeters, characterising the components of measurement system, those are important, in our opinion, in the interpretation of the experimental results.

The *HeNe* laser has radiated a continious beam of light with wavelength of 0.630 μm. This light beam has represented the one fundamental Gaussian mode. After the expanding the beam of light had a diameter about 3 *cm* (on the level of $1/e^2$ from the maximum of intensity) and it has hitted on a bicomponent diffraction system. The image of a part of collimated beam, enlarged by the microscope objective 5, is shown in Fig. 2 (c). Inhomogeneity and roughness of measured collimated beam intensity profile may be explaned as an effect of an incident beam interference with a waves reflected from a CCD-line photosensitive cells surface and from its protective glass.

The testing diffraction system has been consisted of two pinholes, executed from aluminium foil with a thickness δ_1=20±4 μm for the first screen and δ_2=10±4 μm for the second screen, that many times over exceeds a wavelength of a radiation. In the second pinhole an aluminium foil has been placed between two thin glass plane-parallel plates. The diameters of pinholes in the experiment have made: d_1=365±10λ, d_2=80±10λ. Photos of these pinholes are presented in Fig.2 (d)-(e), on those may be seen the unroundness of these pinholes and roughness of its edges.

A micro-objective 5 had a focal length of 16 *mm*. A linear photosensitive charge couple device of type *K 1200 CL1* [7] was used in a photodetector device 6. This chip has been consisted of 1024 photosensitive cells arranged into line, each of them had a length of 15 μm. According to a reference data [7], sensitivity of a chip is 2.5 *mV/lux* and dynamic range on voltage is 60 *dB*. On those to dates, the various photosensitive cells of a chip differ from each other on sensitivity up to 8 % and on the noise level up to 4%. In a Fig. 2(b) the dependence of a CCD-photodetector output voltage on the light exposure is shown. The curve appropriates to one of photosensitive cells of the CCD-line. This dependence was obtained in [8] at the illumination by *HeNe* laser beam with a wavelength of 0.630 μm. It is most typical dependence for the CCD device, used in

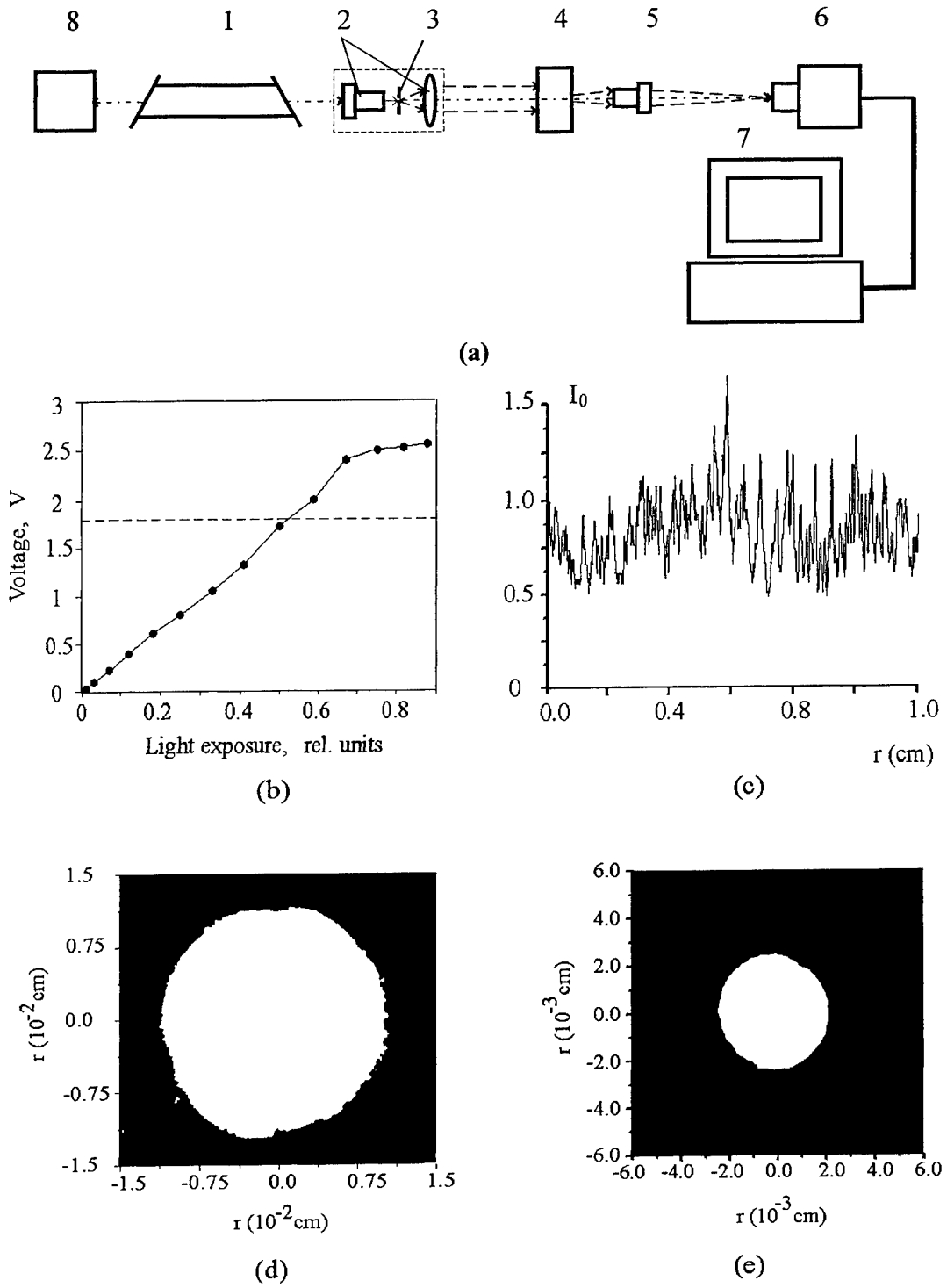


Fig.2. Principle of (a) experimental set-up for the detection of an optical DMFR effect ((1) *HeNe* laser, (2) beam expander, (3) space filter, (4) investigated system of diaphragmes, (5) microscope objective, (6) CCD-line photodetector, (7) computer, (8) photodiode gauge); the dependence of (b) a CCD-photodetector output voltage on light exposure; the images of (c) collimated beam enlarged by microscope; the photos of (d)-(e) investigated pinholes.

this work. As follows from the graphic the non-linearity of the CCD photodetector transfer performance has made of the order 10%. In our experiments the measurements have been conducted within a linear part of this dependence up to 2 V, limited to a dashed line on the Fig 2(b).

The indications of signals, obtained in each point of scanning from both of the photodetector devices, have been treated on a computer, and then have been represented as a two-dimensional diffraction wave intensity distribution. The values of intensity presented here on graphics had been divided on the average intensity of incident wave. The registration of diffracted fields was carried out in two different media: for non- - absorbing (m = 1) gas medium and for homogeneous absorbing gas-dispersed medium. The cigarette smoke has been used as a dispersed medium, containing the carbon particles by the radius $r_0 \approx 0.1\ \mu m$ and concentration $N \approx 10^9\ cm^{-3}$.

4. RESULTS AND DISCUSSION

The experiments were conducted in the three stages. At the first stage the debugging of experimental set-up and determination of the measurement errors were carried out on the basis of registration of a well known diffraction picture formed by the circular aperture in a Fresnel zone. At the second stage for a diffracted field from the first pinhole in the open one Fresnel zone we were locating the second pinhole of smaller diameter. At the third stage the testing diffraction system has been placed in an aerosol. The results of experimental researches and theoretical accounts are represented in a fig.3,4,5.

Fig. 3 illustrates the diffraction of the collimated plane wave on the first pinhole with aperture diameter, $d_1 = 365 \pm 10\ \lambda$, and the thickness of walls $\delta_1 = 20 \pm 4\ \mu m \gg \lambda$. The presence "of horns" at the edges of transversal distribution of a wave intensity, passed through such pinhole (Fig. 3a), is explained by an inevitable diffraction of a wave on internal walls of the aperture. The solid line shows theoretical account of average value of an input wave intensity, relatively which the comparisons of all consequent distributions of diffraction fields intensities, obtained as from the first, and from the second screens, were conducted. As follows from the Fig. 3b,c,d,e,f the distribution of intensity in a diffraction picture in the near zone $z \leq d_1^2/4\lambda$ is determined by the number (NF) of open Fresnel zones. Moving from a screen along an axis $\overline{OZ}$ results in a decrease in the number of open Fresnel zones and in a gradual growth of the radiation intensity along the axis. The first Fresnel zone (NF = 1) is open at the distance $z = L = d_1^2/4\lambda$, where the maximum value of the intensity is $I_{max} = 4I_0$ at the center of the diffraction picture (Fig. 3(f)).

The theoretical account [5,6], executed within the quasi-optical approximation for indefinitely thin and ideal opaque screen (the solid line on Figures), qualitatively and quantitatively agrees with results of experiments, in which the real screen had a finite thickness: $\delta_1 \approx 30\lambda$. The greatest concurrence of the theory to experiment is observed in the maximum points of intensity of a diffraction picture. The inhomogeneity of an initial distribution of the incident wave intensity (see Fig. 2(c) and 3(a)), a thickness of screens, the interference of reflected waves with an incident beam, the irregularities of edges and non-ideal form of aperture (see Fig. 2(d)-(e)) have not made some essential influence on a Fresnel diffractional picture. All this testifies that the Fresnel diffraction on the real objects, whose linear size exceeds a radiation wavelength, is insensitive to the "rough" external conditions. The requirements of ideality for the screen ($\delta \ll \lambda$, $\sigma_{sh} \to \infty$ and $m_{sh} \to \infty$) are necessary for a mathematical solution of a wave equation and have not played the essence significance in the experiment.

The small divergences of the theoretical curves from the experimental dates are explained by an error of measurements. The experimental distributions of relative intensities are obtained as the ratio of the diffraction field intensity to average initial intensity of an input wave. Here, both, the type of optical elements and their mutual disposition were saved constant, when the optical set-up had been regulated in the various series of measurements. Besides, the statistical selection of obtained experimental dates was conducted. By virtue of it, the influence of the most significant factors of measurement errors of the relative intensities practically was compensated. In a result, the measurement error was determined by a precision of the laser power monitoring, which in experiment made about 3% (see paragraph 5 of the present paper). This value was accepted as a relative error of the measurements of the diffraction system focussing capacity at a stage of experiments with one pinhole.

Located at the point $z = L$, another plane screen with a circular aperture of diameter $d_2 = 80 \pm 10\lambda$ results in a cutting the central peak in the diffraction picture generated by the first hole at the first open Fresnel zone (see Fig. 4(a)). Thus, the initial plane wave, spreading through the first component of a bicomponent diffraction system, has a space distribution closed to Gaussian profile and intensity of radiation at the second pinhole exceeding by four times the value of the initial wave intensity (see Fig. 3(a)). The diffraction of this wave on the second pinhole is shown on a photo (see Fig. 4(b)), which has confirmed a conclusion of the theory that the qualitative picture of a plane wave diffraction on a two-aperture system is similar to a Fresnel diffraction picture. Here, five open Fresnel zones with a bright narrow peak at the center are observed. Further propagation of the wave is accompanied by a fall in its intensity along the optical axis down to a certain minimum

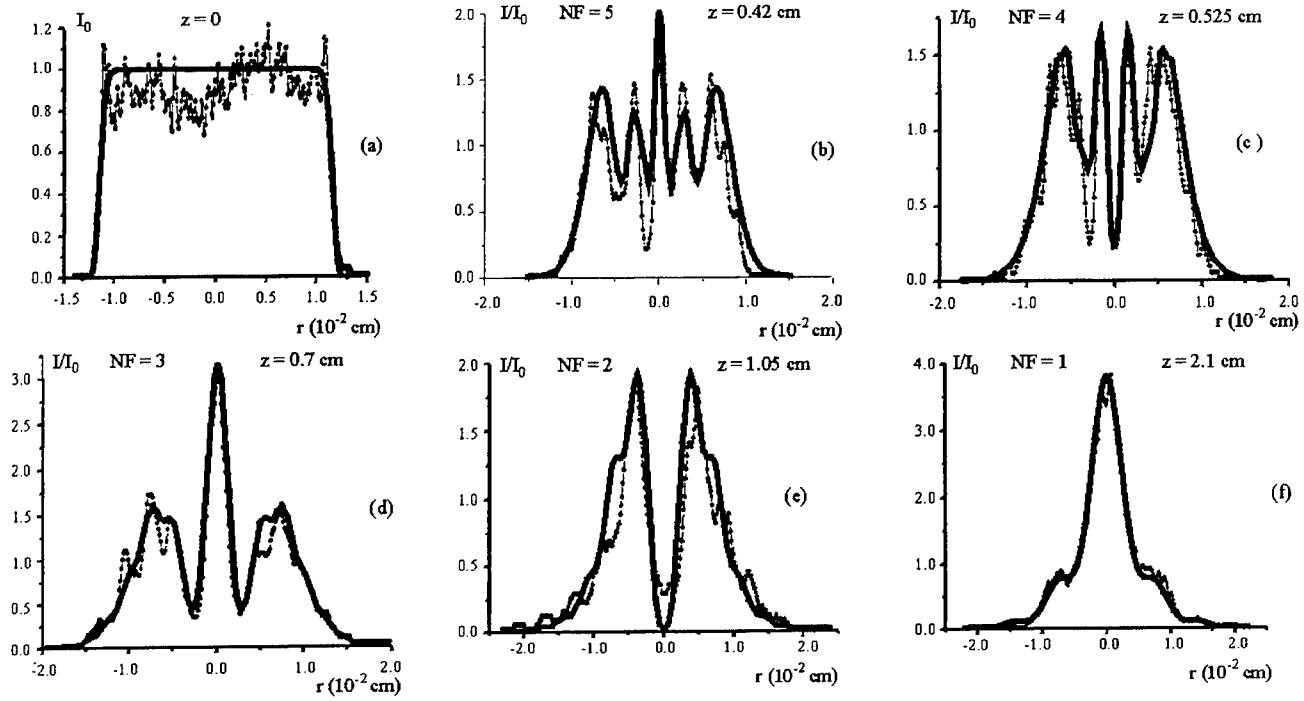


Fig.3. Fresnel diffraction of a plane wave (a) by a circular aperture of diameter $d_1 = 365 \pm 10\ \lambda$, presented for various distances z along the optical axis (b)-(f). A solid line is the theoretical account, dashed line with points is the experiment.

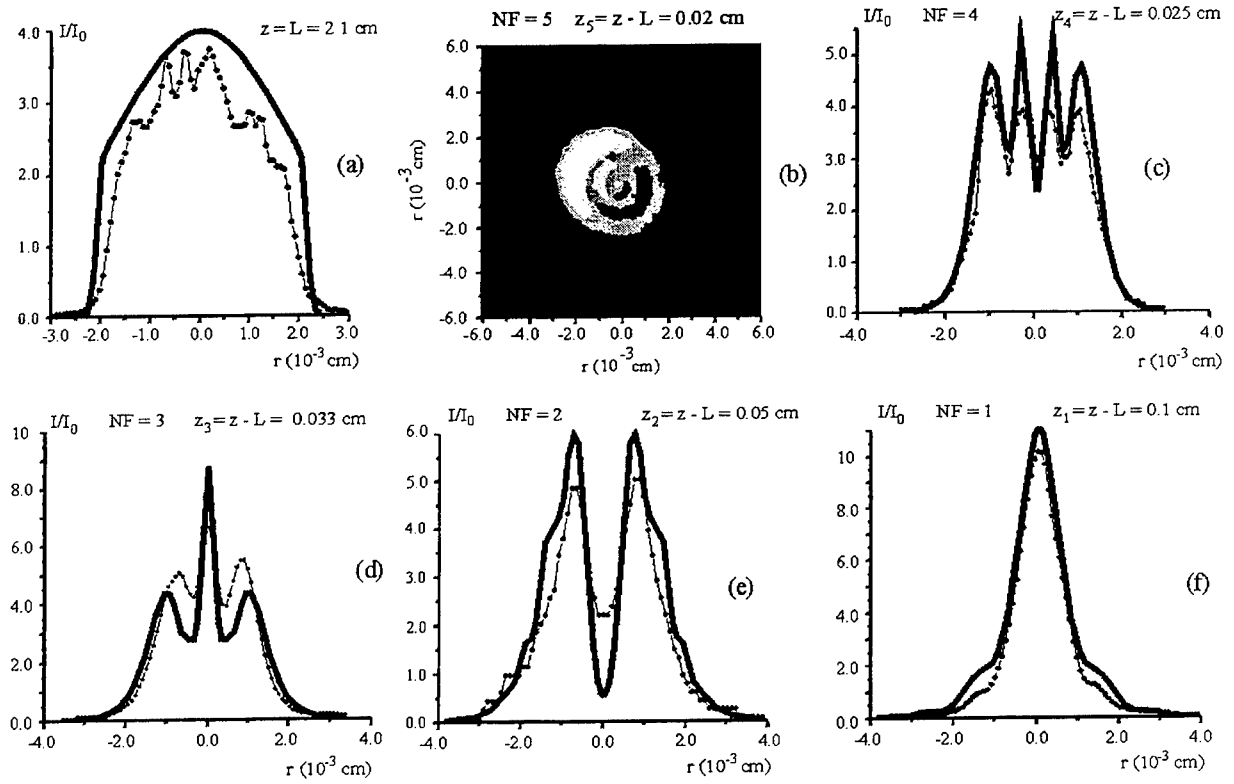


Fig.4. Diffractive focusing of a conical wave (a) by a second circular aperture of diameter $d_2 = 80 \pm 10\ \lambda$, presented for various distances z from the aperture along the optical axis (c)-(f) and a photo of (b) a diffraction picture. A solid line is the theoretical account, dashed line with points is the experiment.

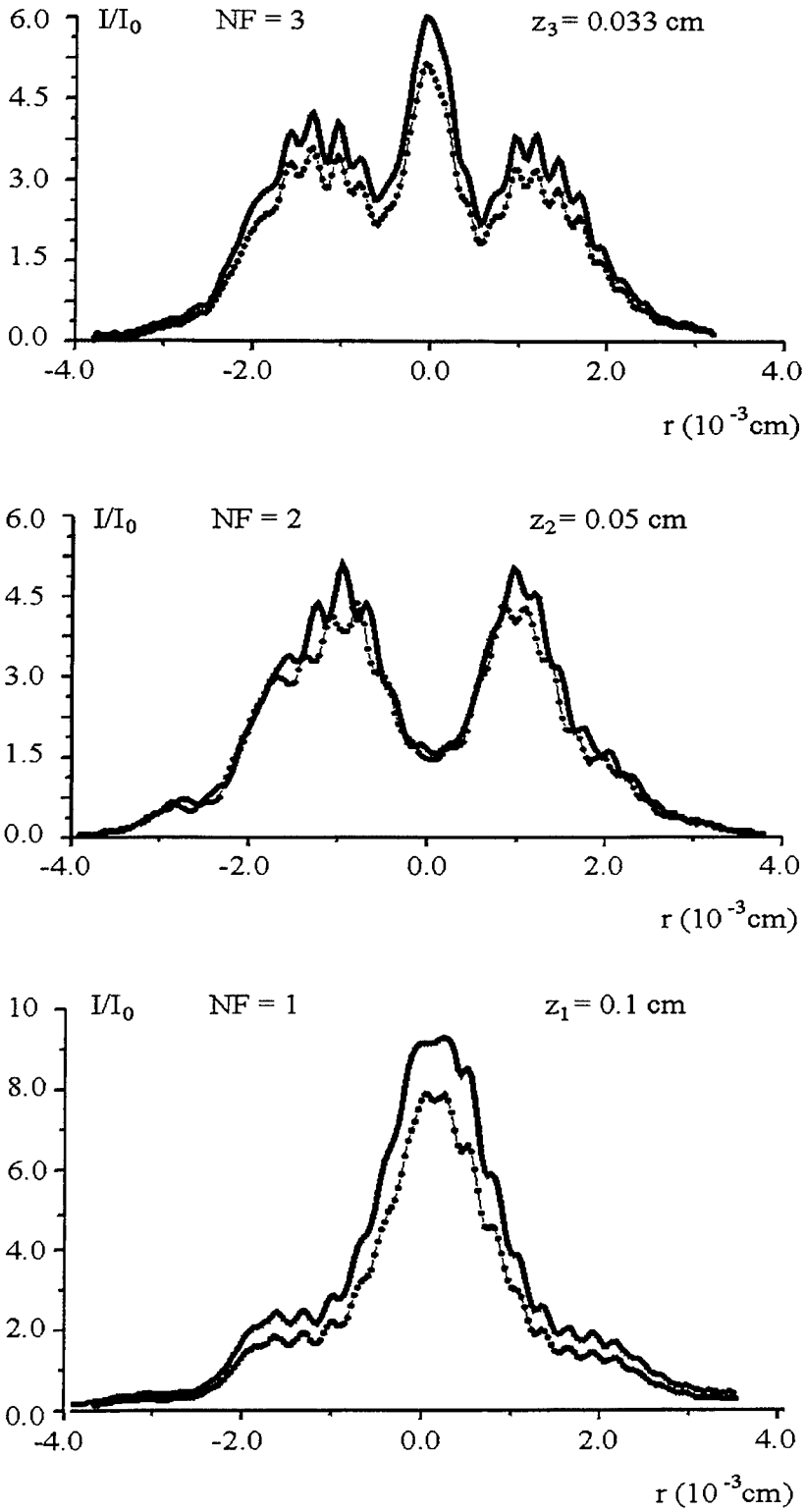


Fig.5. Experimental distributions of (a)-(c) the relative intensities of diffracted fields, observed in the homogeneous not absorbing (solid line) and aerosol (a dashed line with points) mediums on the different distances z from an investigated diffraction system along the optical axes. The aerosol consists of carbon particles by the radius $r_0 \approx 0.1$ μm and the concentration $N \approx 10^9$ cm^{-3}.

value (dark center of the diffraction picture) that corresponds to the diffraction picture for an even number of open Fresnel zones: NF = 4 (see Fig. 4(c)). Then, at a distance $z_2 = 0.33$ *mm* from the second diaphragm, a phase shift of the wave develops such that the beam focusses again with the maximum ratio in the experiment $I/I_0 = 6.5$ (and in the theory $I/I_0 = 8.5$) at the center of the diffraction picture (see Fig. 4(d)) created by three open Fresnel zones. Finally, at the point $z_3 = z - L = 1.0$ *mm,* the first Fresnel zone is open, where a maximum diffractive focusing of the radiation is observed, and the intensity at the focal point is ten times in the experiment (and is eleven times in the theory) higher than the initial wave intensity I_0 entering the bicomponent diffraction system (Fig. 4(f)).

Thus, the qualitative picture of a Fresnel diffraction is observed behind the second pinhole, which has been accompanied by a multifocal focussing of radiation and magnification of initial wave intensity at the open odd Fresnel zones. This phenomenon is effect DMFR, which is observed on a bicomponent diffraction system with small Fresnel numbers.

The maximum divergence of the theoretical accounts [5,6] from the experimental results at the second stage of experiments with two screens reaches already ~ 20%. It in many respects is explained to an additional component of error, introduced by a second pinhole due to the reflection of the radiation on glass plane-parallel plates, between which the second screen with a hole has been located. The losses of the beam intensity on a wavelength $\lambda = 0{,}630$ *μm* during a reflection on each from four edges of glass plates make till 4% (the refraction index of a glass $n = 1.5$). Thus, the measurement results can be improved on 16% if to use a pinhole without glass plates.

The replacement of homogeneous gas medium of the wave propagation on an aerosol, consisting of carbon particles by the radius $r_0 \approx 0.1$ *μm* and the concentration $N \approx 10^9$ cm^{-3}, as well as predicted the theory [5,6], had not influenced on a qualitative character of the wave diffraction on a investigated bicomponent diffraction system (see Fig.5). The presence of an aerosol has reduced the intensity of diffraction fields, but has saved the focusing ability of a system. Thus, experimentally is established, that the diffractive multifocal focussing of a radiation on a real screens with axial circular apertures, whose diameters exceed a radiation wavelength, is insensitive to the "rough" external conditions: to a thickness of screens, to the irregularities of edges and non-ideal form of apertures, to a heterogeneity of initial distribution of an incident wave intensity, to changes in the medium of the wave propagation.

5. ESTIMATION OF MEASUREMENT ERRORS

The two methods of the estimation of measurement errors are used in the present work. One of them took into account the influence of major factors, defining exactitude of measurements, and other was based to the statistical processing of the experimental dates. The values of standard errors (mean square errors) have been used in the numerical calculations of the measurement accuracy. The reference dates, characterizing the errors of the measurement devices used in the work, have been transformed to the view like mean square error.

The total error of measurements is estimated as a quadratic sum of a systematic δ_c and a random δ_s errors [10]: $\delta = \sqrt{\delta_c^2 + \delta_s^2}$.

In our experiment it is possible to select the following main components of a systematic error δ_c: δ_c^{MO} is the error because of limitation in resolution of the micro-objective; δ_c^{CCD} is the error because of non-linearity of CCD-photodetector unit scale characteristic. The resulting systematic error is determined here as a result of a mean-quadratic sum [10]:

$$\delta_c = \sqrt{\frac{1}{3}\left[\left(\delta_c^{MO}\right)^2 + \left(\delta_c^{CCD}\right)^2\right]}.$$

Let's present a basic components of the random error δ_s: $\delta_s^{(1)CCD}$ includes the errors because of an interference on the protective glass of a CCD-line chip, and because of the non-efficiency of charge transfer process in a CCD-line chip; $\delta_s^{(2)CCD}$ is the error because of inhomogeneous sensitivity of CCD line cells; $\delta_s^{(3)CCD}$ is the error because of an electronic noise in the CCD-line chip; δ_s^{FD} is the error of laser radiation power measurement by the photo-diode device. A total random error is estimated as a quadratic sum:

$$\delta_s = \sqrt{\left(\delta_s^{(1)CCD}\right)^2 + \left(\delta_s^{(2)CCD}\right)^2 + \left(\delta_s^{(3)CCD}\right)^2 + \left(\delta_s^{FD}\right)^2}.$$

All other factors of an experimental error, those were not named here, have been neglected by virtue of a smallness of their values. For simplification of accounts all components of errors were considered as a multiplicate.

During the estimating the values of δ_c^{MO} and $\delta_s^{(1)CCD}$, their dependencies on a spectrum of a signal frequencies have been taken into account. For this purpose a space frequencies spectrum of measured intensity distribution dependencies was used.

This spectrum was obtained with the help of the discrete Fourier converter according to a technique [11]. The value of error component $\delta_s^{(1)CCD}$ was determined by using the experimental frequency – contrast performance, obtained in [8]. The evaluation of error component δ_c^{MO} was performed from the measurement of resolution for concrete the micro-objective, used in our scheme. This resolution of micro-objective has made 200 *lines/mm* in our experiment. The total error of these components δ_c^{MO} and $\delta_s^{(1)CCD}$ on whole spectrum was determined as a quadratic sum of its components corresponding to each harmonic of the spectrum.

The evaluation of a maximum relative error $\delta_s^{(2)CCD}$ has been performed on the basis of experimental scale performances for the CCD-photodetector unit. It has got up to 4%. This obtained value has appeared twice less, than dates in the reference [7]. It can be explained by, at first, in our experiment the image has filled only about 20% of total aperture of the CCD-line chip. Secondly, a sample of the CCD-line chip, used by us, had a little bit large homogeneity of sensitivity.

According to [9], the non-linearity of the photo-diode unit 8 scale performance is about 3%. Then, taking into consideration an error in the measurement of an output signal level from the unit 8, we receive $\delta_S^{FD} = 3\%$.

In Table 1 the calculated dates of the absolute values of the systematic, random components and total error are presented, and also the evaluation of a statistical error is indicated. During the statistical estimation of errors, the mean square error was estimated for each point of the experimental profiles of light intensity. The error values for each diffraction picture are integrally averaged within an effective aperture of the CCD-photodetector, and they are derived by the mean value of the intensity within this aperture.

Table 1. The integrally averaged within an aperture absolute values of the systematic, random components and total error (from left to right in the column), and also the evaluation of a statistical error.

Configuration of an optical system	**Kind of errors**	**Number of Fresnel zones**				**Image of the pinhole**
		1	**2**	**3**	**4**	
One pinhole	systematic/random/total, %	0.5/5/5	1/10/10	1.5/10/10	3/8/10	1.5/10/10
	statistical, %	5	5	8	10	10
Two pinholes	systematic/random/total, %	5/5/7	5/10/10	5/8/10	7/15/15	5/8/10
	statistical, %	5	5	8	10	10

The calculations have shown that δ_c^{MO} and $\delta_s^{(1)CCD}$ make the greatest contribution to a total error. A contribution of other components named above does not exceed 1/5 of a total error value.

As follows from the table, the absolute value of the total error has reached 10% for diffraction patterns with the Fresnel number of NF ≤ 2. This value has got up to 15% for diffraction patterns with higher Fresnel numbers, that is explained by the fall of pattern contrast at high space frequencies. The same total error values have been observed and for the series of experiments on a wave diffraction in an aerosol medium, consisting of carbon particles by the radius $r_0 \approx 0.1$ μm and the concentration $N \approx 10^9$ cm^{-3}.

6. CONCLUSIONS

Thus, predicted by the theory the new optical DMFR effect, observed on a bicomponent diffraction system with small Fresnel numbers, is confirmed experimentally. Is shown, that the diffraction picture in the focal planes of such system represents the circular nonlocal bands of the Fresnel zones with a bright narrow peak at the center, whose intensity in the experiment can exceed by six to ten times the value of the incident plane wave intensity.

The theoretical account, executed within the quasi-optical approximation for indefinitely thin and ideal opaque screen, qualitatively and quantitatively agrees with results of experiments, in which the real screen had a finite thickness: $\delta_1 \gg \lambda$. The greatest concurrence of the theory to experiment is observed in the maximum points of intensity of a diffraction picture. The experiments have confirmed a conclusion of the theory, that the qualitative picture of a plane wave diffraction on a two-aperture system is similar a Fresnel diffraction picture. Experimentally is established, that the diffractive multifocal focussing of a radiation on a real screens with axial circular apertures, whose diameters exceed a radiation wavelength, is insensitive to the "rough" external conditions: to a thickness of screens, to the irregularities of edges and non-ideal form of apertures, to a heterogeneity of initial distribution of an incident wave intensity, to changes in the medium of the wave

propagation. The requirements of ideality for the screens ($\delta \ll \lambda$, $\sigma_{sh} \to \infty$ и $m_{sh} \to \infty$) are necessary for a mathematical solution of a wave equation and have not played the essence significance in the experiment. The replacement of homogeneous gas medium of the wave propagation on an aerosol, consisting of carbon particles by the radius $r_0 \approx 0.1$ μm and the concentration $N \approx 10^9$ cm^{-3}, had not influenced on a qualitative character of the wave diffraction on a investigated bicomponent diffraction system.

7. ACKNOWLEDGEMENTS

The computer-aided CCD-line photodetector device used in this work was developed earlier by Valentin N. Belopukhov and Sergey I. Bestalanny, when they were with Samara branch of P. N. Lebedev Physics Institute. We want to greatly thank them to their inestimable aim in supplying us with this apparatus.

8. REFERENCES

1. Y. Li and E. Wolf, "Focal shifts in diffracted converging spherical waves", *Opt. Commun.* **39**, 211-215 (1981).
2. V. N. Mahajan, "Axial irradiance and optimal focusing of laser beams", *Appl. Opt.* **22**, 3042-3053 (1983).
3. J. Ojeda-Castaneda, M. Martinez-Corral, P. Andres, and A. Pons, "Strehl ratio versus defocus for noncentrally obscured pupils", *Appl. Opt.*, 33, 7611 (1994).
4. M. Martinez-Corral and V. Climent, "Focal switch: a new effect in low-Fresnel-number systems", *Appl. Opt.* **35**, 24-27 (1996).
5. R. R. Letfullin, "Bicomponent diffraction system for focussing of radiation. 1. Theory", *Preprint of Lebedev Physical Institute of RAS*, Moscow, **4** (2000).
6. R. R. Letfullin and T. F. George, "Optical effect of diffractive multifocal focusing of radiation on a bicomponent diffraction system", *Appl. Opt.*, 39, № 16 (2000).
7. A. A. Aksenenko, M. L. Baranotsnikov, "Detectors of an optical radiation: Reference book" (Radio i Svyaz', Moscow, 1987).
8. A. A. Abrosimov, S. P. Kotova, E. A. Mnatsakanyan, etc., "Development of a special-aided measurement system on the base of Linear Photosensitive Charge Couple Device". *Laser technology and automation* (Nauka, Moscow, 1989).
9. S. P. Kalashnikov, A. A. Matcveiko, "Photo-diode gauge for a power of a laser radiation", *Pribory i tekhika experimenta*, **2**, 189 (1981).
10. M. F. Yudin, M. N. Selivanov, O. F. Tishenko, A. I. Skorokhodov, "Basic terms in metrology: Dictionary and reference book" (Izdatel'stvo standartov, Moscow, 1989).
11. D. Kahaner, C. Moler, S. Nash, "Numerical Methods and Software" (Prentice-Hall, NY, 1989).
12. H. C. van de Hulst, "Light Scattering by Small Particles" (Wiley, NY, 1957).

Synthesis of unstable resonator's output mirrors with phase front compensation.

E. N. Kotlikov, V. N. Prokashev, E. V. Khonineva
St. Petersburg State University of Airspace Instruments Making,
67, Bolshaya Morskaya, St. Petersburg, 190000, Russia

ABSTRACT

The phase distortion's influence on the radial luminosity of the laser radiation in distant zone occurred in mirrors with radial reflection coefficient has been investigated. It was shown that the radial luminosity diminished 1.5-2 times in comparison with mirrors characterized by constant or having spherical front radial phase's distribution along a mirror coating. New methods of radial phase distortion compensation are suggested for increasing of the radial luminosity of the phase front: 1) a deposition of additional layers with required radial thickness function, 2) a special choice of reflective coating's structure.

Examples of the synthesis and practical making of output mirrors of CO_2-laser's unstable resonators are demonstrated. Due to the mirrors with phase distortion compensation of laser radiation the radial luminosity increased 3 times in comparison with the usual mirrors.

INTRODUCTION

For the effective technological application of high power CO_2-lasers one needs to receive a going out laser mode with a quasi-Gaussian profile and a little diffraction divergence. The radiation from resonators having such properties is the most convenient to be transmitted and focused. However, a widely used (for media such as CO_2 with a large amplification) telescopic unstable resonator with going out radiation around an output opaque mirror cannot satisfy needs (Fig.1).

In published papers [1, 2] the conditions of the shaping of laser radiation's transverse mode in that scheme have been studied very well. These investigations have carried out based on numeral analytic methods and experimental researches. Authors [1, 3] have proved that the edge diffraction scattering on mirror's borders (taken place in the resonator shown in Fig. 1) has led to the degeneracy of resonator's transverse modes and, in another words, to the mode multiplicity of going out radiation. In 3D-resonator with spherical mirrors the degeneracy stayed even in case of considerable amplification coefficients[3]. In real resonators with active amplifying medium the distortions of intercavity profile of radiation's transverse mode were still more essential. For example, in pulse-periodic lasers with a large amplification coefficient the presence of scattered light led to the modulation of medium's amplification coefficient during a pulse and, as result, to the changing of the shape of radiation's transverse distribution. Lastly the serious defect of this resonator's scheme was the fact that the output radiation's profile had the annular form. Therefore the radiation's diffraction divergence increased and the central maximum's intensity diminished after the focusing of the radiation.

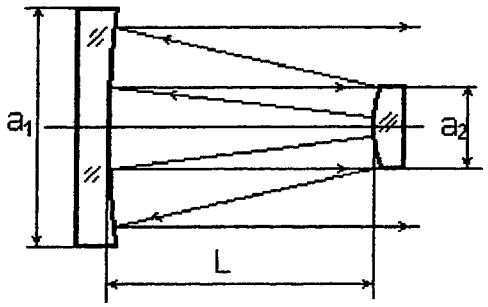


Fig. 1. Unstable telescopic resonator.

Laser Optics 2000: Control of Laser Beam Characteristics and Nonlinear Methods for Wavefront Control,
Leonid N. Soms, Vladimir E. Sherstobitov, Editors, Proceedings of SPIE Vol. 4353 (2001)
© 2001 SPIE · 0277-786X/01/$15.00

It is clear that the use of optical elements with variable radial reflection coefficient instead ordinary output opaque mirrors allows to improve parameters of the going out radiation considerably. These are two types of such output elements. The first type has "step-form" reflectivity profile. It is simpler for producing (Fig. 2). The second type has smooth reflectivity profile nearing to Gaussian one. Output optical elements of last type correspond to requirements of the shaping of the radiation's smooth transverse field best of all. Unfortunately, these elements are more complicated for producing (Fig. 3). At last time a set of papers was published reports about the elaboration and the successful employment of elements of two types mentioned above (with "step-form" reflectivity radial distribution[4, 5, 6] and with smooth one[7, 8, 9]).

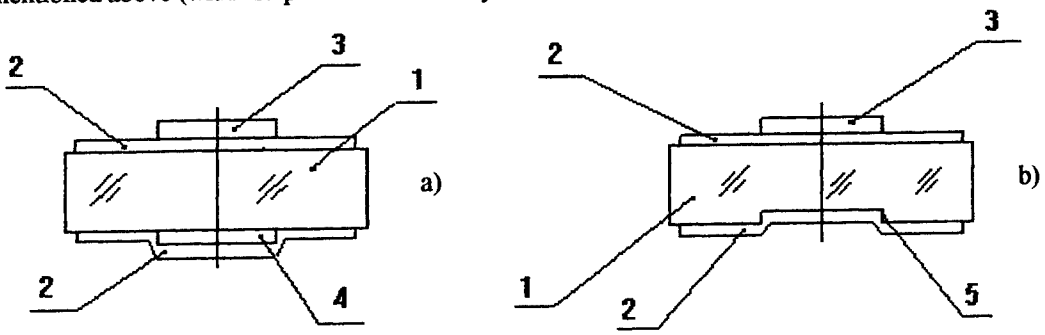


Fig. 2. Constructions of elements with "step-form" reflectivity profile realizing different (a, b) ways of phase compensation.
1 – a substrate, 2 – an antireflection coating, 3 – a reflective coating, 4 – a phase compensative layer, 5 – a section without a part taken out of the opposite side of a substrate by the method of ion polishing.

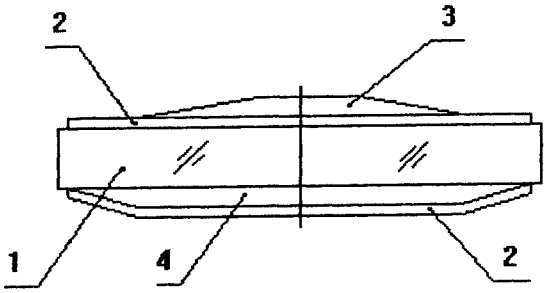


Fig. 3. Construction of an output element with a smooth reflectivity profile.
1 – a substrate, 2 – an antireflection coating, 3 – a reflective coating, 4 – a compensative layer.

Numeral and analytic calculations[2, 3, 5] gave following results. Elements of first type in resonators with about small Fresnel number $N_F = a^2 / \lambda L$ (in case of great amplifications especially) did not cause yet the essential distortion of intercavity main fundamental mode. The effect of so-called "soft edge" near central reflective part of the element (that was about a narrow zone of the smooth falling of a reflection coefficient with a width $\Delta = a / 2N_{equiv}$) decreased the diffraction scattering from mirror's border to a marked degree. It could be achieved by simple technological ways during element's making. In real resonators the use of output elements of the first type with "step-form" reflectivity profile is possible in case of repeated propagation of a laser beam in an active medium. When a considerable spatial irregularity of a active medium's amplification coefficient takes place, particularly, in case of a high power pulse laser with a transverse pumping of a gas medium, it should be put into practice output elements with a smooth reflectivity profile.

During processes of the shaping of smooth profile of intercavity mode and of propagation and a focusing of a going out radiation two magnitudes have the great significance. The other one is the amplitude reflection coefficient of an output element. And the another one is phase distortions of wave front of reflected and transmitted radiation. In many reports concerning discussed problem it was founded that the profile of a real resonator's transverse mode might be differ from calculated profile of the resonator with the same configuration but empty. This fact was conditioned by phase aberrations. It must bear in mind that similar phase distortions arise inevitably in process of making of output elements with

a radial reflectivity profile. Hence, the phase compensation to admissible limits of such distortions for reflected and transmitted radiation may permit to improve parameters of output beam's divergence.

In order to estimate the admissible value of phase distortions of a radiation's wave front transmitting through the element we researched the laser beam's propagation in distant zone in the presence of different values of wave front's phase aberrations. The calculation of radiation's field intensity in a distant zone was made on a base of a well-known fluent Reley – Zommerfeld's relation. Moreover it was used the method of fast Fourier's transformations.

For example we consider the propagation of a radiation having one of two kinds of an initial distribution of radiation's field. The first is described by the function

$U(r) = circ(r/a)exp[i\varphi(r)]$

and has a form of a small disk of a plane wave. The second is described by the function

$U(r) = exp[r^2/w^2]exp[i\varphi(r)]$

and has a Gaussian form. Here a – an output aperture of a beam, w – a certain number which is smaller than a : $w < a$, $\varphi(r)$ – a function describing phase distortions of initially plane front of a radiation.

It is supposed the phase distortions are described by a function

$\varphi(r) = csin(2\pi fr/a)$,

where c and f – variable parameters. Similar phase distortions of a transmitting radiation are typical for output elements having dielectric profiled coatings. Results of calculations are following magnitudes: the beam's intensity distribution in a distant zone $I(r)$ and the power part $W(\delta)/W_0$ in an angle δ from an optical axis of radiation's propagation. W_0 is the total power of a radiation.

The changing of power part $W(\delta)/W_0$ when the amplitude of phase distortions c increases and has values $c = 0$, 0.2π, 0.4π is shown in Fig. 4. Here $f = 1$. An initial function has a form of a small disk of a plane wave, r is a radius of the disk. If the amplitude of phase distortions c increases curves of a power part $W(\delta)/W_0$ and of intensity distribution $I(r)$ get broader. When c is equal $c = 0.4\pi$ the power part $W(\delta_D)/W_0$ in a diffraction angle δ_D decreases 1.5÷2 times approximately. Phase distortions being smaller than 0.1π increase the value of radiation's divergence slightly. Therefore the value $c = 0.1\pi$ should be considered as the top value for transmitting radiation's phase distortions caused by resonator's output element.

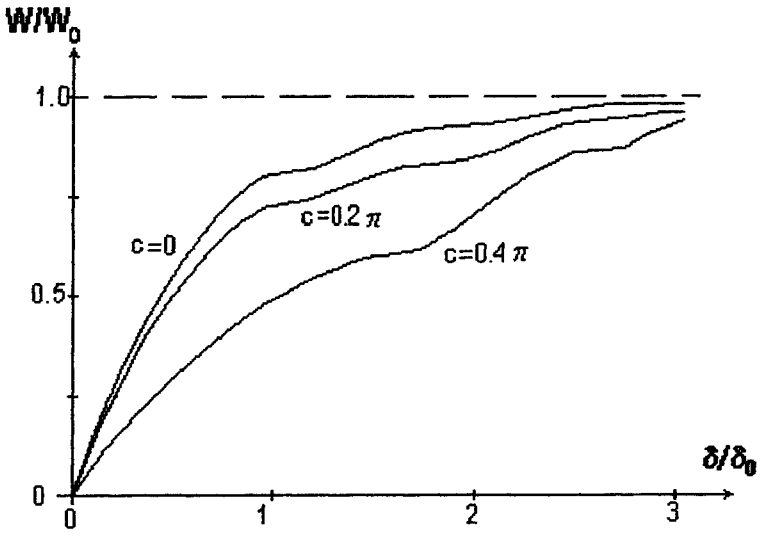


Fig. 4. Power part W/W_0 of the laser beam at distant zone in cases of different values of phase distortion amplitude.

The calculation of the degree of the phase distortion's influence on the structure of transverse mode in real resonators with an active medium is very difficult because of numerous factors influencing on the mode's forming. Still results of different independent investigators (for example in the paper[2]) have shown that phase variations from spherical wave front of intercavity mode of empty telescopic resonator, as a rule, were not 0.1π.

So the value of 0.1π is reasonably to choose as an admissible one for phase distortions caused by optical reflecting element.

ELEMENTS WITH 'STEP-FORM" PROFILE OF A REFLECTION COEFFICIENT.

These elements consist of a substrate and an applied coating. In the center of the element the reflective partially dielectric mirror is situated which surrounded by an antireflection region (Fig 2). For such elements the phase compensation of a reflected radiation is not necessary as the reflection of peripheral part is equal zero. Authors of reports[4, 6] have said about the elaboration and successful using of output elements of this type for unstable resonators of CO_2-lasers. The compensation of phase difference of beams transmitting through the reflective and antireflection regions has been achieved by the taking out the part of the opposite side of a substrate. The operation has been produced by the method of ion polishing.

We have synthesized and have put into the practice [5] resonator's output mirrors of this type for the using in the industrial laser "Hebre". For the compensation of phase distortions the certain technological ways were less complicated than mentioned above. We used two ways: 1) the deposition of the phase compensative layer to the opposite side of the mirror or 2) the choice of defined structure of the interference reflective coating.

In the first way a compensative layer has such optical thickness to supply a phase difference of beams transmitting through reflective and antireflection regions to the divisible 2π value. So an optical thickness of a compensative layer t_C in units of $\lambda/4$ is defined by the relation

$$t_C = [4m - t_L(1-1/n_L) - t_H(1-1/n_H)] / (1-1/n_C).$$

Here m is a minimum natural number when t_C is positive yet, n_L and n_H are refractive indexes having smaller (low) or larger (high) values, t_L and t_H are values of optical thickness of corresponding layers.

In order to receive a reflection coefficient of central zone having the order of $R \approx 80\%$ in our case it was used 6-layer dielectric mirror with high refractive layers made of zink selenium (n_H = 2.35÷2.38) and with low refractive layers made of plumbum fluoride (n_L = 1.65). The refractive index of a compensative layer made of zink selenium (n_C = 2.35÷2.38) corresponded really to a refractive index of a substrate. Finally the thickness of a compensative layer in units of $\lambda/4$ was equal t_C = 1.93 in a case of m = 1 and λ= 10.6 μm.

Another way of the phase compensation is connected with the opportunity of the creating of reflective systems in which the additional phase compensation of a transmitting radiation is not required. The good example of such systems is the 8-layer mirror made of applied films with high H and low L refractive indexes. It has the structure

$$L; H; L; H; xL; (2-x)H; (2-x)L; xH.$$

Here x and $(2-x)$ are coefficients defined optical thickness of layers in units of $\lambda/4$. Using PbF_2 (n_L = 1.65) and $ZnSe$ (or As_2S_3, n_H = 2.35) as film-forming materials in multilayer mirror it is easy to calculate that a geometrical thickness of the mirror with this structure be equal 2π and an optical thickness be equal 4π. As a result a phase difference is equal 2π at any values of the parameter x. Varying the parameter x from 0.4 to 1 it may to receive reflective coefficients R from 0.7 to 0.9. These values of R are better than values belonging to the interval of admissible reflective coefficients of central zone for considered reflective systems.

Based on two described above methods of phase compensation we manufactured output mirrors with phase compensation. For the configuration of the laser "Hebre" resonator's parameters are equal L = 4.5 m, a l = 25 mm, M = 1.36, a Fresnel number is not large $N = a^2/\lambda L$, $N_{equiv} = N(M-1)/2 \approx 2.5$. To decrease more the negative influence of diffraction scattering from mirror's borders the effect of a "soft edge" was used. As it was mentioned before a zone of a smooth falling of reflection on the border had to be equal $\Delta \approx 2.5$ mm in a case of definite diameter of central reflective part of an output element $2a_2$ = 28 mm. The value of this zone might be achieved in following combined conditions : 1) of definite situation of cells with evaporating film-forming materials inside the vacuum evaporation installation and 2) of placing of the special screen at the distance about 1.3 mm from a substrate in time of applying of a central mirror.

OUTPUT ELEMENTS WITH A SMOOTH REFLECTIVITY PROFILE.

Constructions and techniques of similar elements without phase compensation have were described in papers[7, 8]. For example [7] researchers have given data concerning a construction and characteristics of the element consisting of 1) the substrate of $NaCl$, 2) the applied antireflection dielectric coating in the first place and 3) single-layer mirror of Ge (n = 4.0) applied on the coating (2) after. The mirror (3) have had Gaussian reflectivity profile. The reflection coefficient in the center of the element has been equal 80% approximately. In a case of these data the maximum phase difference for radiation's transmitted wave front along mirror's surface achieves the value of 0.4π and one for reflected wave front – 0.6π. So considerable phase distortions influence on the forming of the main resonator's mode and on conditions of radiation's focusing.

We synthesized produced and explored[9] the phase compensated output element for the telescopic resonator of a pulse laser having following parameters : L = 4 m, M = 1.23 and exit aperture 6 cm. The profile of radial reflective coefficient distribution was approaching to the function

$R = R_0 \exp\{-[x^2+y^2)/1.5^2]^2\}$,

where $R_0 = 0.6$ – reflective coefficient in the center of the element, x and y – in units of cm.

The construction of this element is represented in Fig.3 and its characteristics are shown in Fig.5. The mirror was applied on the substrate of KCl with diameter 60 cm. Conditionally it consists of three radial zones. The first is a form of the small disk and has maximum reflection of order 57%. It consists of layers with constant thickness along a radius. The second is ring zone and has size from 5 to 20mm along a radius. Also it is a zone of a smooth falling of reflective coefficient from 57% to 0 because of uniform reduction of thickness of reflective coating. The third zone is an antireflection coating. Radial profile of reflection is shown by a curve 1 in Fig.5. For this construction of the element examining variations of a phase of reflected radiation (a curve 2 in Fig.5) are not more than 0.1π. Maximum value of phase variation is concentrated in a narrow ring on a border of second zone where the reflection coefficient is minimum.

The curve 3 in Fig.5 shows the calculated phase variations of transmitted radiation. The difference of phases of beams between the element's center and the border of second zone x_0 = 2 cm along a radius has opposite symbol and is equal about 1 rad or $\pi/3$.

The compensation of phase distortion of transmitted radiation was done by applying of a compensative layer on mirror's opposite side under the antireflection coating. Changing of a thickness of a compensative layer is equal to the same value. The value takes a place when total phase dependence of transmitted radiation along the whole radius of output element corresponds to spherical wave front with certain and large radius of curvature (a curve 4 in Fig. 5).

The thickness of the compensative layer had a constant value in first and second zones and was decreasing to zero in third zone according to the definite law. So the multiply layer structure of output mirror in transmitted light may be represented as a convex lens with a large focal distance (about 70 m). If it will be need the brought sphere may be compensated easily by the changing of parameters of external optical system. The changing of the thickness of compensative layer in third zone influences in limits of 0.2% on antireflection characteristics slightly.

As film-forming materials for the applying of multiply coatings it was used As_2Se_3 (n = 2.65) and As_2S_3 (n = 2.25) forming smooth films with a small absorption and high radiation resistance and without scattering. Plumbum fluoride PbF_2 (n = 1.55) was used for low refractive and compensative layers.

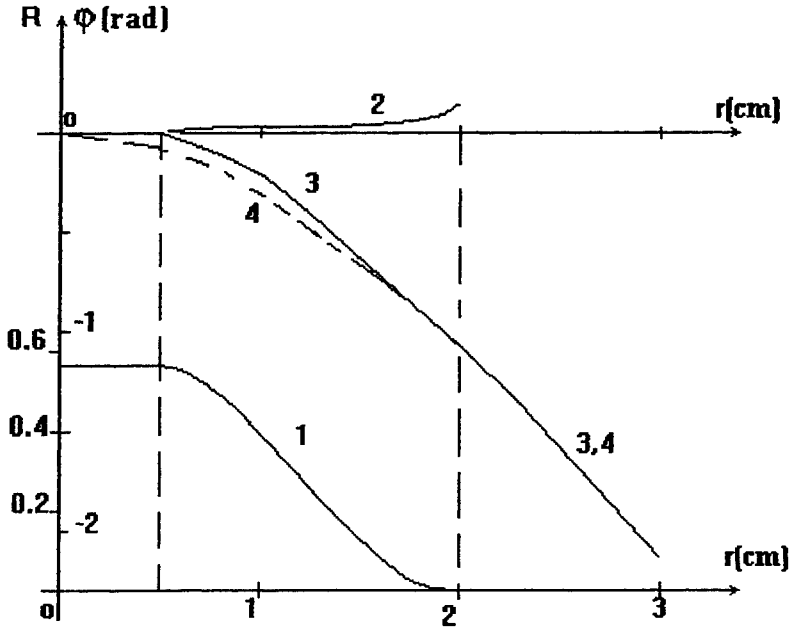


Fig. 5. Characteristics of the output element with smooth reflectivity profile. The mirror was applied on the substrate of *KCl*.

1 – radial profile of reflection, 2 – phase variations of reflected radiation, 3 – calculated phase variations of transmitted radiation, 4 – total phase dependence of transmitted radiation.

PARAMETERS OF GOING OUT RADIATION IN A CASE OF USING OF OUTPUT ELEMENTS WITH DIFFERENT TYPES OF REFLECTION PROFILE.

Output elements **with "step-form" mirror's profile** were placed and investigated in the industrial laser as "Hebre". They were transforming the laser's working regime in single-mode. The output power was equal about 80÷90% of the power in multimode regime of laser with standard output mirror (having a reflection coefficient R = 30÷35%). Laser's radiation divergence did not exceed a value of $1.5\ \delta_D$. Therefore a power density in lens focus multiplied 5÷6 times. As a result this laser with output power about 800 Wt cut aluminium sheets having surface roughness and thickness 1.5 mm.

Experimental investigations of made element **with a smooth reflection profile** carried out on the installation. It based on 1) an electro-injector CO_2-laser cell of atmospheric pressure with a volume 2.5 liter, 2) a pulse time of pumping about 18 μs, 3) and specific energy to 200 J to liter. Two different resonators with an exit aperture 6 cm were used. First resonator had a length $L = 4$ m , a multiplier coefficient M = 1.23 and smooth output mirror of second type. Second one had L = 6 m, M = 1.5 and copper mirror with a diameter 3.2 cm.

Energy distribution of a near field was checking by imprints on thermo-paper and on a liquid crystal. The one of a distant field was checking by imprints on lighted out and developed thermo-paper. Energy distributions in near (1) and distant (2) zones for both resonators are shown in Fig. 6.

If to compare results for two resonators it is seen that the use of a output element with a smooth reflectivity profile allows to improve the quality of going out radiation to a marked degree since in this case a radial luminosity increases in 3 times. Besides of this fact our experimental researches carried out befire[9] have shown that angular divergence has been constant during a laser pulse. Consequently effects accompanied the process of generation don't the influence upon the field structure inside a resonator.

Hence the use of output elements with a phase front compensation permits to increase the efficiency of power CO_2-laser applications.

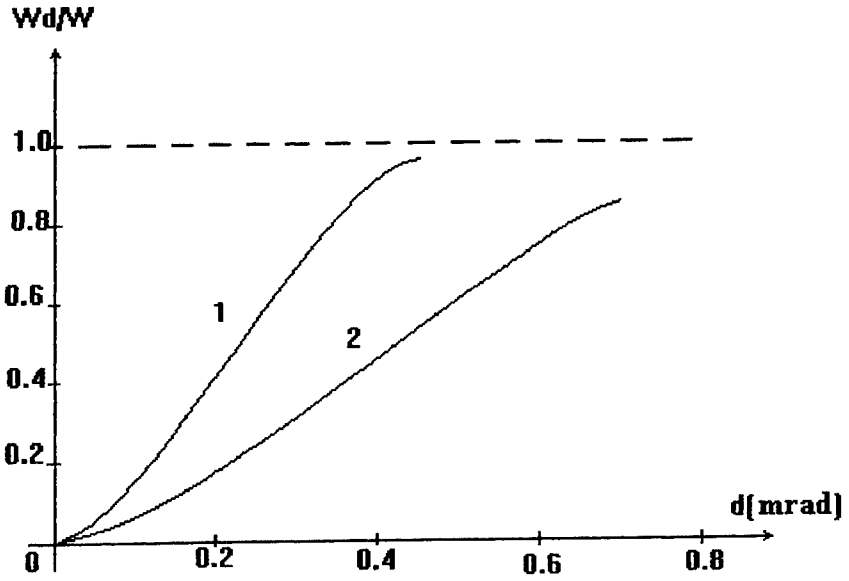


Fig. 6. Energy distributions in near (1) and distant (2) zones for the resonator.

REFERENCES

1. Ананьев Ю.А. Оптические резонаторы и лазерные пучки. М: Наука, 1990
2. Rensch D., Chester A. // Appl. Optics. - 1973 - V.12 - №5 - P.997.
3. Шерстобитов В.Е., Винокуров Г.Н. // Квантовая электроника. - 1972 - №3 - С.36.
4. K. Yasui, M. Tanaka, S. Yagi // J. Appl. Phys. - 1989 - V.65(1)- P.17.
5. Аникичев С.Г., Котликов Е.Н., Прокашев В.Н. // Тезисы докладов конф. "Оптика лазеров-93".- 1993 -Т.2 - С.258.
6. Y. Takenaka, Y. Motoki // IEEE J. of Quant. Elect. -1996- V.32 - №8, P.1299.
7. P.Lavigni, N.McCarthy, and J.-G.Demers // J. Appl. Opt.- 1985.- V.24. -№4 - P.2581.
8. Генералов Н.А., Зимаков В.П. и др. // Тезисы докладов конф. "Оптика лазеров-93". - 1993 - Т.1 - С. 277.
9. Борисов М.Ф., Котликов Е.Н., Прокашев В.Н., Родионов А.Ю. // Оптический журнал - 1999 - Т.66 - №11. - С.90.

Photodynamics of nonlinear fullerene-containing media

I. M. Belousova*, V. P. Belousov*, O. B. Danilov*, V. A. Grigor'ev*,
A. G. Kalintsev*, V. N. Zgonnik***, N. V. Kamanina**, A. P. Zhevlakov*,
A. V. Kris'ko*, N. G. Mironova*, E. N. Sosnov*, E. A. Gavronskaya*,
V. A. Smirnov*, M. S. Yur'ev*, A. N. Ponomarev****, V. E. Yashin*

* Research Institute for Laser Physics, ** Vavilov State Optical Institute,
*** Institute of High-Molecular Compounds, **** "Astrin Ltd."
* 12 Birjevaya line, 199034, St.-Petersburg, Russia

Abstract

The results of theoretical and experimental studies on photodynamics and mechanism of nonlinear optical processes, responsible for optical limiting of power radiation in the wavelength range from 0.3 to 1.3 microns, are presented. Peculiarities in the mechanisms of optical limiting for different fullerene-containing matrices, including solutions, solid-state and polymer systems, are shown.

1. Introduction

Discovering of fullerenes in 1985 by Kroto, Heath, O'Brien, Kerl, and Smoly, and later creation of nanotubes on their base initiated activities on their studies and search for application of them in physics, chemistry, nonlinear optics, electronics, and technology of constructive materials.

At present thousands of publications are devoted to studying properties of fullerenes and materials on their base as well as to prospects of their application.

We hardly make a mistake if say that fullerenes and fullerene-containing media are the technologies of the new century (Figure 1).

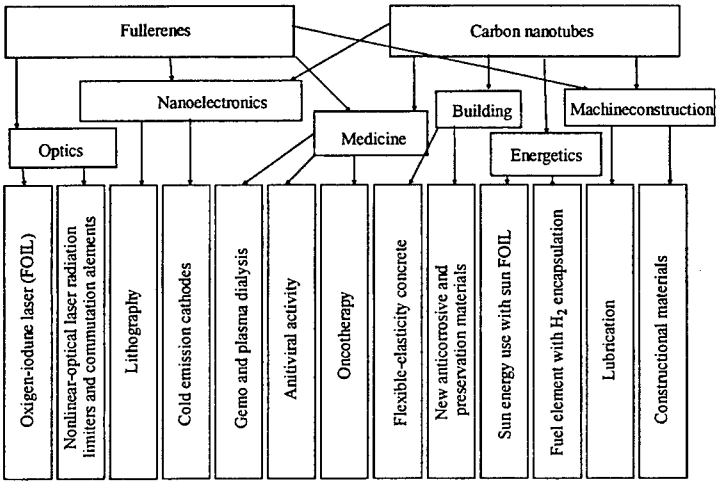


Figure 1.

The fullerenes are of interest for us because of their strong nonlinear properties due to the structures of the molecules, having a shell of non-localized π-electrons.

The fullerene molecules are promising for creation of the following nonlinear-optical systems:

Laser Optics 2000: Control of Laser Beam Characteristics and Nonlinear Methods for Wavefront Control,
Leonid N. Soms, Vladimir E. Sherstobitov, Editors, Proceedings of SPIE Vol. 4353 (2001)
© 2001 SPIE · 0277-786X/01/$15.00

- wideband fast-response limiters of power, including laser, radiation;
- photorefractive media for writing-in of dynamic holograms and phase conjugation;
- controlling duration and spatial structure of laser radiation;
- optical fast-response (down to femtoseconds) shutters for optical computers and so on.

The most efforts were applied to study and design of the optical limiters of power, including laser, radiation.

2. Computer simulation of the photodynamics of the absorption mechanisms in the optical limiting

Optical limiting mechanism in fullerene-containing media is based on the reversible photoinduced processes, which are absorption processes and the processes connected with change in a path of laser beam (self-defocusing, induced scattering and reflection) [1]. The basis of the absorption mechanism in the optical limiting is the absorption with inverse saturation from excited vibronic states of the fullerene molecule. This phenomenon is called as the "reverse saturable absorption (RSA)". When the incident radiation energy (or power) density is high, the RSA process is accompanied by the other photoinduced processes, a role of which varies in different fullerene-containing media.

First of all, we consider the photodynamics of the absorption mechanisms in the optical limiting.

Figure 2 presents the simplified schematic for the energetic states of the fullerene molecule, responsible for the limiting in the visible and near IR range [2]. It also shows the main processes: absorption of light from the ground singlet state S_0 (transition S_0-S_x), interconversion between the singlet and triplet states of the molecule (S_1-T_1), light absorption from the excited states S_1-S_n and T_1-T_n, and inverse non-radiative transitions. If the cross-section of excitation from the excited states exceeds the cross-section of the transition from the ground singlet state, i.e., if $\sigma_{ex}^S \approx \sigma_{ex}^T > \sigma_0^S$, the rate of light absorption increases with rise of light intensity and population of the excited states. In this case, the RSA process takes place and limits the transmitted radiation. If the pulse duration τ_L exceeds the time of interconversion τ_1 (for C_{60} molecule equal to 1.2 ns), the reverse saturable absorption goes through the triplet transitions (T_1-T_n). Otherwise, if $\tau_L<\tau_1$, the absorption goes through the singlet transitions (S_1-S_n).

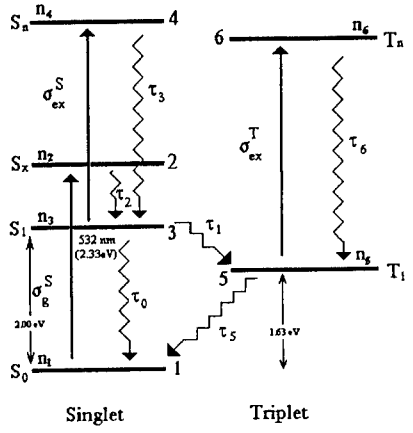


Figure 2. Schematic for the energetic states of the fullerene molecule

Spectra of absorption due to electronic transitions extend from 200 to 650 nm for C_{60}, up to 700 nm, for C_{70}, and even to 1100-1200 nm, for higher fullerenes $C_{76\text{-}84}$ [3]. So, application of different fullerenes makes it possible to obtain the optical limiting in

the wide spectral range at the required ratio of cross-sections from the excited and ground states.

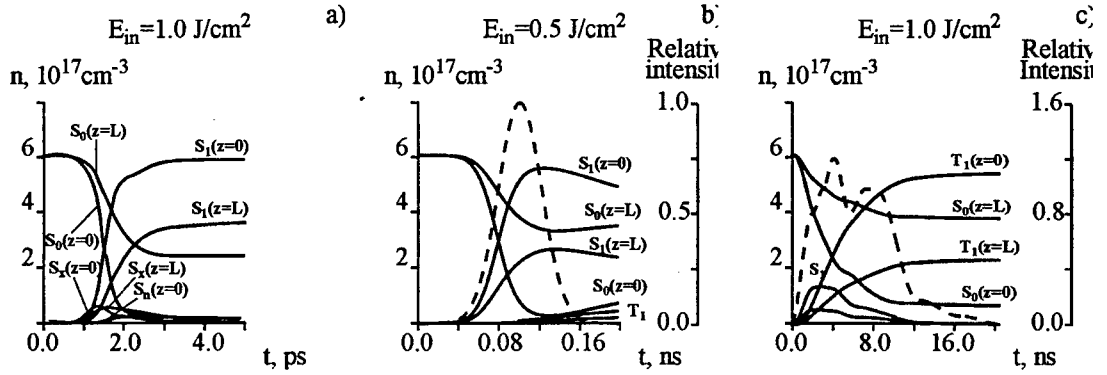


Figure 3. Calculated evolution for state population: C_{60} in toluene, C=1mM, λ=532nm.
a) 1 ps, b) 50 ps, c) 10ns.

We illustrate this with the calculated evolution for state population of fullerene C_{60} molecule presented in Fig. 3 for pulses with duration of 1 ps, 50 ps, and 10 ns. As it is seen, at pulse duration less than the time of interconversion, population of the singlet states significantly exceeds population of the triplet states during the pulse. Otherwise, population of the triplet states dominates already about 1 ns after the pulse beginning.

Figure 4 presents the calculated transmission of the fullerene-containing specimen

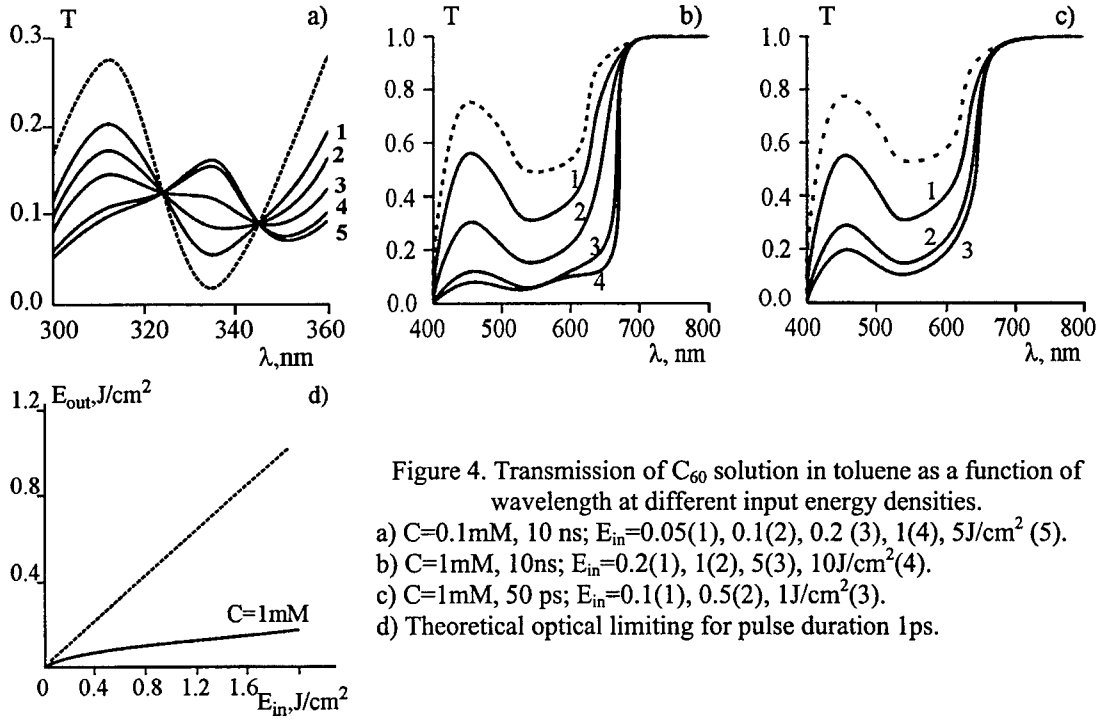


Figure 4. Transmission of C_{60} solution in toluene as a function of wavelength at different input energy densities.
a) C=0.1mM, 10 ns; E_{in}=0.05(1), 0.1(2), 0.2 (3), 1(4), 5J/cm^2 (5).
b) C=1mM, 10ns; E_{in}=0.2(1), 1(2), 5(3), 10J/cm^2(4).
c) C=1mM, 50 ps; E_{in}=0.1(1), 0.5(2), 1J/cm^2(3).
d) Theoretical optical limiting for pulse duration 1ps.

(C_{60} in toluene) as a function of the incident radiation wavelength from 300 to 650 nm at different input energy densities and pulse duration of 10 ns. As it is seen from the figure, at increase of the input energy density from 50 mJ/cm^2 to 5-10 J/cm^2 in the specified spectral range except the area from 330 to 340 nm, we observe decrease of transmission with saturation and limiting of the passing radiation energy. Analogous dependencies take place also for pulse duration of 50 ps, although the optical limiting in

this case is performed through the channel of singlet transitions. The same dependencies are presented also for pulse duration of 1 ps; the signal attenuation is obviously observed.

The presented results show that the fullerene-containing media such as solution of C_{60} is the wideband fast-response limiter of laser radiation in the range from 300 to 650 nm. However, it is necessary to consider the potentialities of protection from power laser radiation at wavelengths of 1.06 and 1.315 μm. For this purpose, we pay attention to higher fullerenes C_{70} and $C_{76\text{-}84}$. Calculation of state populations in C_{76} shows that due to low quantum yield at interconversion (ϑ=0.05) during a nanosecond pulse, the RSA at wavelength of 1.06 μm may be performed via the singlet states (Fig. 5).

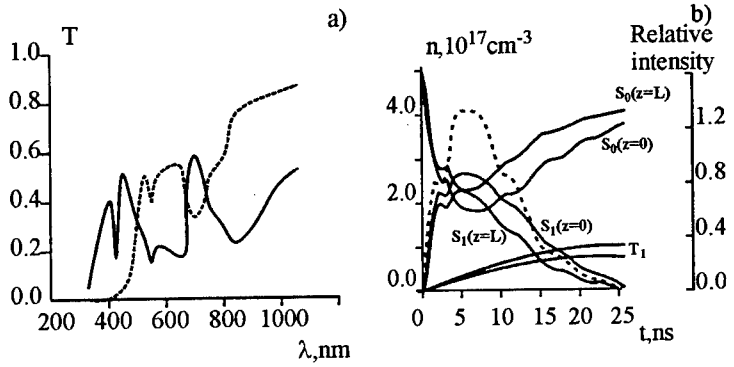


Figure 5. a) Transmission of C_{76} solution in toluene (C=0.8mM) as a function of wavelength. Input energy density is 10J/cm^2, pulse duration is 10 ns. Dashed curve shows a transmission at low input energy density.

b) Calculated population of levels S_0, S_1, and T_1 during a laser pulse at two edges of cell with solution C_{76} in toluene (C=0.8mM): E_{in}=5J/cm^2, λ=1062nm, 10ns. Dashed curve shows an experimental profile of a Nd:YAG laser pulse.

3. Experimental results

The experimental studies of the optical limiting by the fullerene-containing media were performed with a Nd:YAG laser at wavelengths of 1.064 μm, 532, and 354 nm and pulse duration of 8-10 ns, a Nd:glass laser with pulse duration of 1.5 ps, an excimer laser at wavelength of 308 nm and pulse duration of 20 ns, and a photodissociative iodine laser with wavelength of 1.315 μm and pulse duration of 10 ns. We studied different fullerene-containing media: C_{60} and C_{70} in different solvents: toluene, CCl_4, o-xylene and so on. For the optical limiting in the near IR range, we used higher fullerenes $C_{76\text{-}84}$ in solutions.

Figure 6 presents typical nonlinear dependencies of the output energy densities upon the input ones with saturation for wavelengths of 308 nm, 582 nm (C_{60} in toluene), and 1.064 μm ($C_{76\text{-}84}$ in toluene). At wavelength of 308 nm, the 40-fold attenuation of radiation was reached, at 532 nm, 60-fold and 100-fold, for concentrations of 0.6 and 1.5 mM, respectively. At wavelength of 1.064 μm, the optical limiting is less (4-5-fold attenuation) because of low absorption from the ground state in this spectral range even for higher fullerenes.

We succeeded to widen the spectral range above 1 μm and obtain the optical limiting at 1.315 μm by application of complex composition C_{70}-photosensitized polyimide 6B in 1,1,2,2-tetrachloroethane. Its use results in occurrence of new

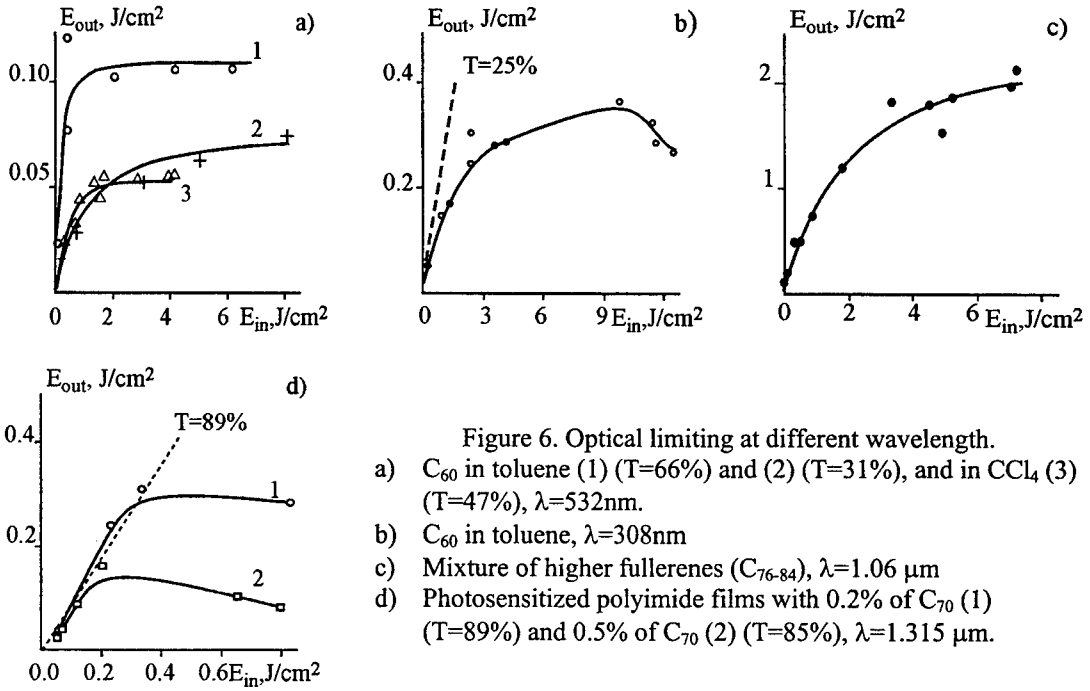


Figure 6. Optical limiting at different wavelength.

a) C_{60} in toluene (1) (T=66%) and (2) (T=31%), and in CCl_4 (3) (T=47%), λ=532nm.
b) C_{60} in toluene, λ=308nm
c) Mixture of higher fullerenes (C_{76-84}), λ=1.06 μm
d) Photosensitized polyimide films with 0.2% of C_{70} (1) (T=89%) and 0.5% of C_{70} (2) (T=85%), λ=1.315 μm.

maximum in the absorption spectrum near 1.3 μm due to intermolecular interactions. Figure 6d presents the optical limiting at 1.315 μm.

So, we can see that application of different fullerenes allows us to obtain the optical limiting for all important ranges of laser radiation.

Now we pay attention to the threshold and level of the optical limiting in the presented data. From Fig. 6 it is seen that the level of the saturated limiting for C_{60} in toluene at 532 nm is about 0.1 J/cm^2 (for concentration of 0.6 mM and initial transmission of 66%) and 0.05 J/cm^2 (for concentration of 1.5 mM and initial transmission of 31%). Here we present the results for C_{60} in tetrachlorine carbon, also. The limiting threshold and level of the saturated limiting are significantly lower, practically for the same concentrations of C_{60}. This result is due to influence of solvent on the fullerene properties.

So, here we have illustrated the certain potentialities in controlling the limiting threshold and spectral range by selection of the fullerene-containing media.

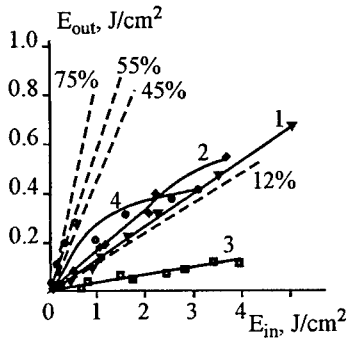


Figure 7.
1 – 2 nm microporous glass with C_{60}, T=45%;
2 - 7 nm microporous glass with C_{60}, T=46%;
3 - 17 nm microporous glass with C_{60}, T=12%;
4 – sol-gel medium with C_{60}, T=75%.

For application of optical limiters of power radiation, the possibility to create the protective devices on base of fullerenes in solid-state matrices and polymer films is very important.

As solid-state matrices, we developed sol-gel and microporous SiO_2 matrices doped with fullerenes C_{60} and C_{70}. The best results were obtained at specimens with fullerenes introduced into the microporous glasses with pore sizes of 2, 7, and 17 nm performed by a special technology. Fig. 7 presents output energy density as a function of input

density for solid-state specimens of C_{60} in sol-gel matrix and microporous SiO_2 matrices with different pore sizes.

Here it is important to note that damage threshold of C_{60} specimens in microporous SiO_2 matrix was 8-10 J/cm^2 at 532 nm for pulse duration of 8-10 ns and more than 10 J/cm^2, for 1.5 ps. With these specimens, we obtained 10-fold optical limiting at initial 45% transmission. Close results were obtained for the polymer films doped with fullerenes.

4. Comparison the theoretical and experimental results. Function of photo-induced scattering

Now we compare the experimental data on the optical limiting at 532 and 308 nm by the fullerene-containing media such as C_{60} in solutions, in solid-state, and polymer matrices, with calculations, taking into account only absorption mechanism (Fig. 8). The comparison shows that the experimentally obtained attenuation of transmission significantly exceeds the calculated one for fullerene solutions in toluene, tetrachlorine carbon, and so on and practically the same for solid-state and polymer matrices. To explain these phenomena, we have supposed that essential contribution to attenuation of the passed radiation is made by photoinduced processes connected with change in refractive index of the medium under action of power radiation. These processes are: change in molecular polarizability due to populating of excited molecule states and thermal nonlinearity of the refractive index due to extraction of the absorbed energy at non-radiative transitions. The estimates show that change in the refractive index because of molecular polarizability variation is essentially (above 10-fold) less than the change caused by the temperature factor.

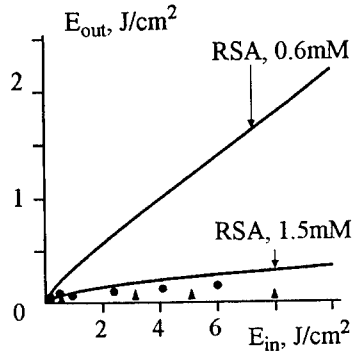


Figure 8. Comparison of the experimental and calculated (accounting the RSA) data for different concentration of C_{60} in toluene. Points are an experimental data.

These factors may cause defocusing of the transmitted radiation at common over cross section variation of the refractive index or photoinduced scattering of radiation on its small-scale inhomogeneities. They occur because of non-uniform, as a rule, laser radiation intensity distribution and fluctuations of fullerenes in solution.

To define value of fluctuations in the refractive index of the fullerene-containing medium during pass of laser pulse through it, we used an interferometer technique. Contribution of the photoinduced scattering was determined by indicatrix of the transmitted radiation, its pulse shape, and field structure of the scattered radiation.

Figure 9 presents the example of measuring the output radiation scattering indicatrix at density of 2.8 J/cm^2 and angular distribution of energy for C_{60} in toluene and in SiO_2 matrix. As it is seen from figures, we observe maximum of the scattered radiation at 1-2° and sufficiently uniform field of the scattered radiation extended up to angles of about 30-40°. Energetic measurements have shown that practically whole transmitted through the specimen energy is within the angle of about 40° and energetic transmission in this angle is 0.3.

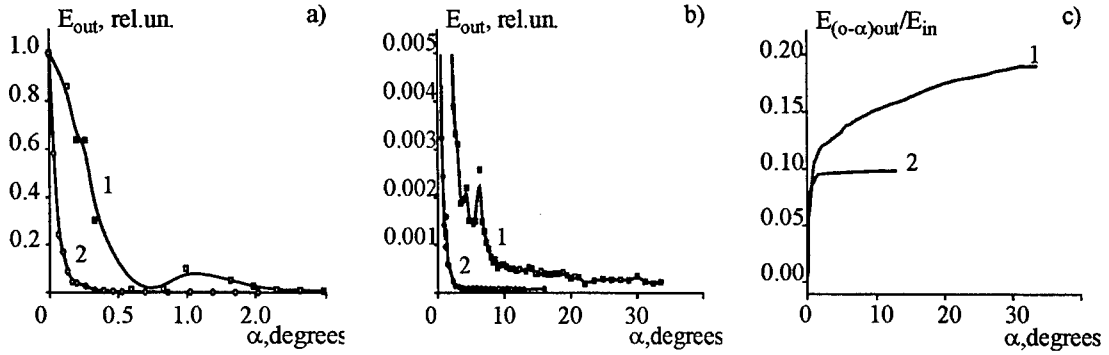


Figure 9.

a,b) – Scattering of laser radiation for C_{60} in toluene (1) and SiO_2-matrix doped by fulleren (2).

c) – Limiting level as a function vision field angle: (1) – C_{60} in toluene, (2) – microporous glass with C_{60}

It is necessary to note that at low-intensity irradiation of C_{60} in toluene, we did not observe the scattering. It appears at occurrence of nonlinear absorption and increases with rise of the input energy. The photo of the photoinduced-scattered radiation field shows that it is coherent, since the obtained image has a speckled form. The scattering is observed during the laser radiation pulse passing through the medium.

It is clear that the degree of the optical limiting strongly depends on the vision field angle of the receiver. At the angle of 1-2° as it is in our experiments and that corresponds to the parameters of most optical devices, the scattered radiation is cut off, and we observe 60-100-fold limiting for C_{60} in solutions.

For C_{60} in solid-state SiO_2 matrix, the photoinduced scattering is practically absent, as it is seen in the plot. Sharp peak of the energetic distribution corresponds to angular divergence ($1.8 \cdot 10^{-3}$ rad.) of the laser and low-intensity (approximately 3%) wing of the scattered radiation covers about 1°. Due to this, the optical limiting by solid-state fullerene-containing media is satisfactorily described with the RSA mechanism only.

The theoretical analysis is performed in the framework of self-congruent solutions of the equations for laser radiation propagation in the medium and acoustic equation for relative perturbation of density due to spatial inhomogeneities of the incident beam radiation and, hence, temperature non-uniformity. The task was solved for "thick" medium, where diffraction length L_d is less than the cell length L ($L_d = \frac{\lambda_T^2}{\lambda} << L$, where λ_T is the typical size of inhomogeneities and λ is the radiation wavelength). In these conditions, scattering on the inhomogeneities leads to change in spatial structure of radiation. Considering the conditions of thermal evolution of the inhomogeneities and wave interaction, we can estimate scales of the inhomogeneities, evolving in the medium:

$$2\ \mu m < \lambda_T < 40\ \mu m.$$

This range corresponds to the scattering angles

$$0.5° < \alpha < 10°$$

Scattering into larger angles, observed in the experiment seems to be connected with scattering to higher orders of diffraction (Fig. 10). For evolution of small-scale inhomogeneities of density and, hence, of refractive index, medium viscosity is the important parameter. The higher viscosity, the narrower range of small-scale

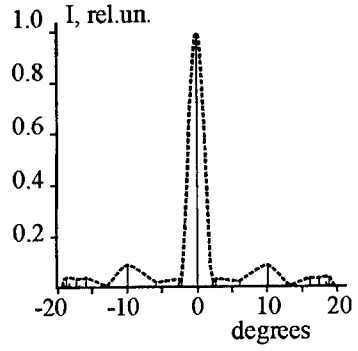


Figure 10. Scattering indicatrice of Gauss pulse, containing a number of FS initial inhomogeneities in the range 3-13 μm. Modulation depth =5-30%. Input energy density = 1.5 J/cm^2.

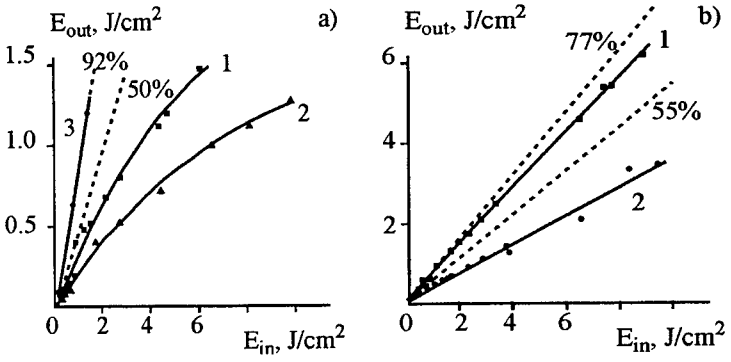


Figure 11. Optical limiting laser pilse during 1.5 ps in fullerene-containing solutions and solid-state matrices.
a) C_{60}+CCl_4, T=50% (1); C_{60}+toluene, T=48% (2), pure CCl_4, T=92% (3).
b) 2 nm microporous glass with C_{60}, T=77% (1), 7 nm microporous glass with C_{60}, T=55% (2).

inhomogeneities, which can evolve in the medium. It seems to us that sound decay due to viscosity results in absence of nonlinear scattering in the fullerene-containing glass matrices contrary to the solutions. Here it is necessary to note that the nonlinear scattering was not observed in our experiments on the optical limiting in fullerene-containing media (C_{60} in toluene and tetrachlorine carbon) at 532 nm, when the pulse duration was 1.5 ps. It is clear that during this time, the small-scale inhomogeneities do not succeed to evolve, and only the RSA mechanism operates.

Figure 11 presents the results of experiments and calculations (with account of the RSA, only) for the optical limiting in the fullerene-containing solutions and solid-state SiO_2 matrix at pulse duration of 1.5 ps, confirming these suppositions. Amplification of the photoinduced scattering role may significantly increase the dynamic range of the optical limiting in the fullerene-containing media.

5. Multistep optical limiter

For the optical limiting, the dynamic range is a significant factor. Its upper limit is defined by the damage threshold of the fullerene-containing matrix (or cell walls) and lower limit, by the nonlinear limiting threshold. This is why the possible approach to design of the optical limiter is a multistep system with location of limiting units in the converging beam.

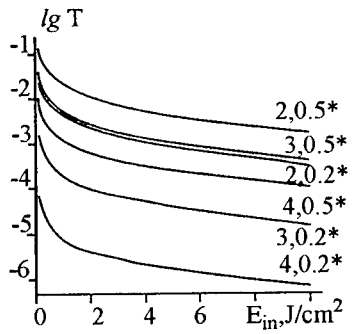


Figure 12. Results of model calculations for multistep limiting (one section thickness is 3 mm).

The experimental test of two-step scheme with focusing at second pass through the cell allowed us to obtain radiation attenuation equal to $5 \cdot 10^3$ at maximum input energy density of 8 J/cm^2. Figure 12 presents our model calculations of radiation attenuation by multistep limiters on C60 in toluene with concentration of 1 mM and initial one-step transmission of 50%. These results take into account the RSA and

nonlinear scattering by introduction of effective empiric coefficient of absorption. It is seen that the four-step limiter makes it possible to realize dynamic range of more than 10^6 (from 10 J/cm^2 of input energy density defined by the damage threshold of the cell to several mJ/cm^2 of the output energy). The system optimization (on number of steps, fullerene concentration, and location of elements) may increase the dynamic range approximately to 10^7 [4].

6. Conclusions

Study of photodynamic processes in the fullerene-containing media shows the various role of photoinduced processes (absorption and photoinduced scattering) in solutions and solid-state matrixes.

For fullerene-containing media it is possible to obtain essentially wide dynamic range of optical limiters.

7. References

1. V. P. Belousov, I. M. Belousova, V. P. Budtov, O. B. Danilov, V. V. Danilov, et al. Fullerenes: structural, physical, chemical and nonlinear-optical properties. *Opticheskii Journal*, 1997, **64**, n 12, p.3 (in Russian).
2. F. Henari, V. Callghan, et al. Intensity-dependent absorption and resonant optical nonlinearity of C_{60} solutions. *Chem. Phys. Lett.*, 1994, **199**, p.144.
3. L. W. Tutt, A. Kost. Optical limiting performance of C_{60} and C_{70} solution. *Nature*, 1992, **356**, p.225.
4. I. M. Belousova, V. P. Belousov, E. A. Gavronskaya, V. A. Grigir'ev, et al. *Optika and Spectroscopia*, 1999, **87**, n 5, p.845 (in Russian).

Photorefractive effects in novel polymer nanocomposites

A.S. Kuzhelev*, I.V. Yurasova*, O.L. Antipov*
W.E Douglas**,
L.G. Klapshina***, V.V. Semenov***, G.A. Domrachev***, T.I. Lopatina***
*Institute of Applied Physics of the Russian Academy of Science, 46 Uljanov St., Nizhny Novgorod, 603600 Russia,
**Laboratoire de Chimie Moléculaire et Organisation du Solide, CNRS UMR 5637, Université Montpellier II, 34095 Montpellier cedex 5, France,
***Institute of Metallo-organic Chemistry, Russian Academy of Sciences, Tropinin Street 49, GSP-445, Nizhny Novgorod, 603600 Russia;

ABSTRACT

We present the results of chemical development and optical investigation of the extraordinarily large photorefractive effect in the new polymer nanocomposites. The composites are composed of poly(ethynylene)arylenesilanes as optical chromophores, poly(9-vinylcarbazole) as photoconductor, N-ethylcarbazole and phenyltrimethoxysilane as plasticizer, and C_{70} and C_{60} fullerenes as charge generators. The magnitude of the change in photorefractive index and its origin, and temporal behavior were studied at 633 nm by a variety of nonlinear optical techniques, including nonlinear lens method, four-wave mixing and two-beam coupling. The relaxation time of the photorefractive index changed in a range from a few seconds to tens of minutes at changing beam intensity.

Keywords: Photorefraction in polymers; four-wave mixing, two-beam coupling, optical chromophores.

1. INTRODUCTION

The photorefractive (PR) polymeric materials have been extensively investigated since early 1990s due to a variety of potentially important applications, including high-density optical data storage, many image processing techniques, phase conjugation, simulations of neural networks and associative memories, and programmable optical interconnection. Some kinds of polymeric materials are investigated as components for PR compositions.[1-3] We report on the investigation of new PR polymer nanocomposites. The composites are composed of several components and include new nonlinear optical materials, Si-containing conjugated polymers – poly(ethynylene)arylenesilanes (PEASs) as optical chromophores.

The PR effect can be observed in certain materials which both photoconduct and show a dependence of the refractive index on the electric field. The components necessary to produce PR-material are therefore a photoionizable charge generator, a transporting medium, trapping sites, and a dependence of index of refraction upon space-charge field. The microscopic processes required to produce a hologram by the PR mechanism, are shown in Fig. 1 (a drawing from the considerable body of prior work).[1,2] The pattern of light intensity, interference field of two plane waves with spatial period Λ_g for instance, produces charge generation. In our composites the fullerenes C_{60} and C_{70} play a role of charge generator. The fullerenes are known to be used as charge generator components in a number of previous works.[1-5] The generated in the illuminated area holes with positive charge move to a dark area due to diffusion caused by density gradients or drift in externally applied electric field. In essentially all of the cases described in the literature, drift is the dominant mechanism for charge transport which stimulates charge to hop from one transport molecule to another.[3] To realize this step we used a well known charge transport agent poly(9-vinylcarbazole) (PVK) in our composites.[1-6] The next element for the PR effect is the trapping sites which hold the mobile charge. In polymeric materials, the exact identity of the trapping sites is hardly known in detail. In general, a trapping site is a local region of the material where the mobile charge is prevented from movement for some period of time. When charge carriers are separated, the space charge distribution produces a space

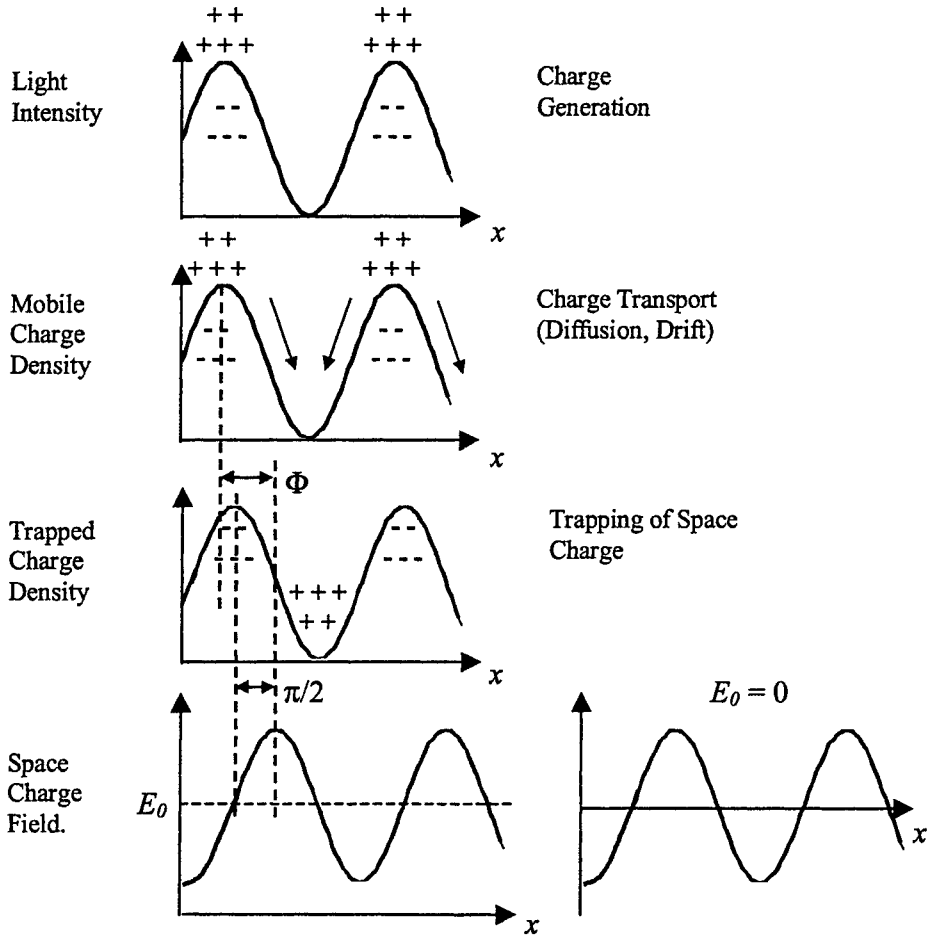
A.S. Kuzhelev et.al.: Tel.:+7(8312)384547; Fax:+7(8312)363792; e-mail: kuzhelev@appl.sci-nnov.ru

Laser Optics 2000: Control of Laser Beam Characteristics and Nonlinear Methods for Wavefront Control, Leonid N. Soms, Vladimir E. Sherstobitov, Editors, Proceedings of SPIE Vol. 4353 (2001)
© 2001 SPIE · 0277-786X/01/$15.00

charge electric field. Since Poisson electrostatic equation relates the spatial gradient of the electric field to the charge distribution, the resulting internal electric field is shifted in space by $\pi/2$ relative to the trapped charge. Finally, if the material has a linear electrooptic effect, the magnitude of the index modulation Δn is related to the magnitude of the space-charge field E_{sc} by the relation

$$\Delta n = -(1/2)n^3 r_e E_{sc} \tag{1}$$

where r_e is the effective electrooptic coefficient for the geometry under consideration. To provide the dependence of



Electro-optic and orientational Index Modulation

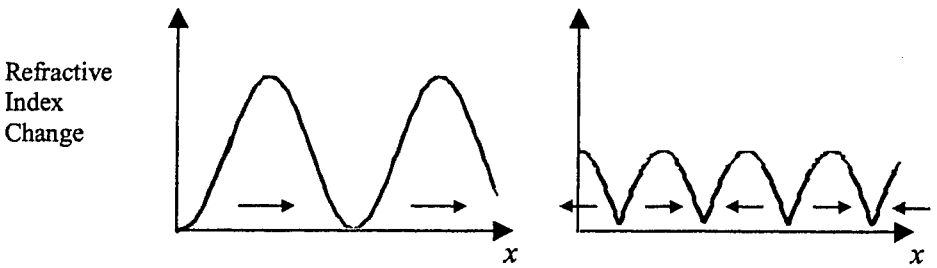


Fig. 1. The mechanism of photorefractive grating formation in polymer composition

the refractive index on the electric field the Si-based conjugated polymers poly(ethynylene)arylenesilanes (PEASs) with extraordinary large hyperpolarizability were used as optical chromophores. The second-order nonlinearity must be induced in the polymer by applying the electric field to align the chromophores and remove the center of symmetry which would be present in a random distribution. Since the chromophores have orientational mobility, a spatially periodic orientational pattern is produced as the electric field orients the molecules by virtue of their ground-state dipole moment. As Fig. 1 illustrates (right side), if no dc electric bias field is present, the resulting modulation of index of refraction is at half the spatial period Λ_g of the intensity pattern. When the bias field is present (left side of Fig. 1), the modulation appears at Λ_g as well and can contribute to the first-order Bragg-diffracted beam.

Thus, we used the following structure of the polymer composites:

1. Charge generator – fullerene C_{70} or C_{60}
2. Charge transport agent – poly(9-vinylcarbazole) (PVK)
3. Optical chromophore – poly(ethynylene)arylenesilanes (PEASs)
4. Plasticizer – N-ethylcarbazole (EK) and phenyltrimethoxysilane (PTMS)

The chemical structure of three modifications of PAES is shown in Fig. 2. These polymers contain donor and acceptor groups, which are necessary for these materials to be used as optical chromophores. The large values of hyperpolarizability of these polymers were tested recently by four-wave mixing.[7] Samples were prepared by sandwiching a layer of composite material 50-250 μm in thickness between glass slides coated with transparent indium tin oxide electrodes.

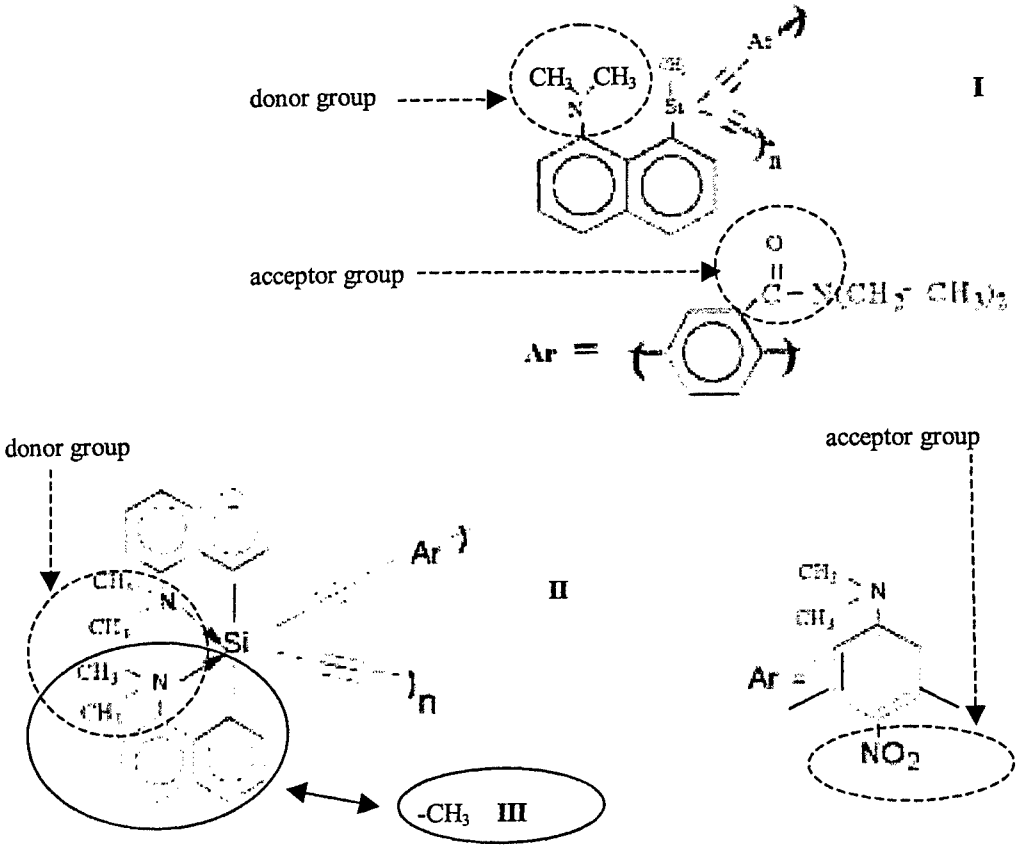


Fig. 2 Chemical structure of three modifications of PAES.

2. NONLINEAR LENS FORMATION IN POLYMER PR COMPOSITES

The simplest test for optical nonlinearity is nonlinear lens formation. The setup used for this test is shown in Fig. 3. A beam from a cw He-Ne laser at a wavelength of 633 nm was focused by a lens with a focal distance of 12 cm. The polymer film was placed in the plane of maximum sensitivity after the focal plane. The formation of diffraction rings was observed. The number of rings and the relaxation time depended on the beam intensity (Fig. 4). A change of intensity by one order of magnitude (from 120 to 5 Wcm^{-2}) led to an increase in relaxation time also by one order of magnitude (from 30 s to 7 min), which is common for PR nonlinearity. The maximum number of rings achieved 10, which corresponds to refractive index changes up to 0.02.

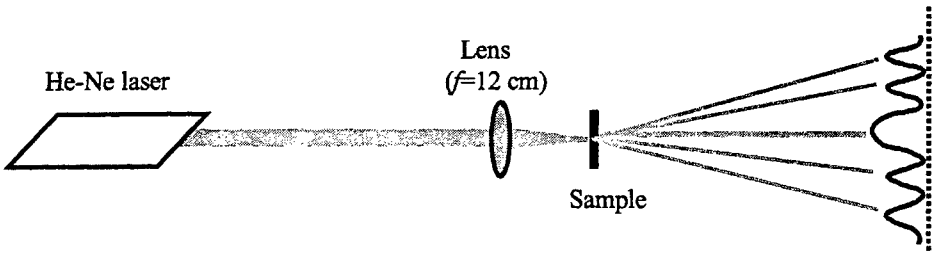


Fig. 3. The setup for observation of nonlinear lens formation.

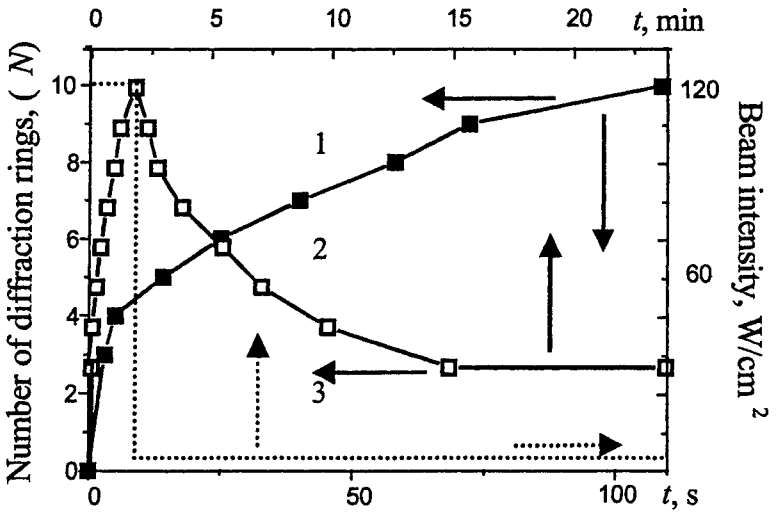


Fig. 4. Number of rings (1,2) and intensity (3) as a function of time for polymer film with length l=250 μm and ingredients: PVK-35%, PAES(I)-5%, C_{70}-1%, Plasticizer-59%. Relaxation time depends on the beam intensity. 1 – number of rings at beam intensity I = 120 Wcm^{-2}, 2 – number of rings at beam intensity oscillogram of which is shown by curve 3.

Fig. 5 illustrates the formation of a nonlinear lens in PR composition. The focused beam produces charge generation in the center of the beam. The mobile charges move to the dark area and are trapped there. So the axial space-charge field is produced. The space-charge field leads to orientation of the chromophores and refractive index change.

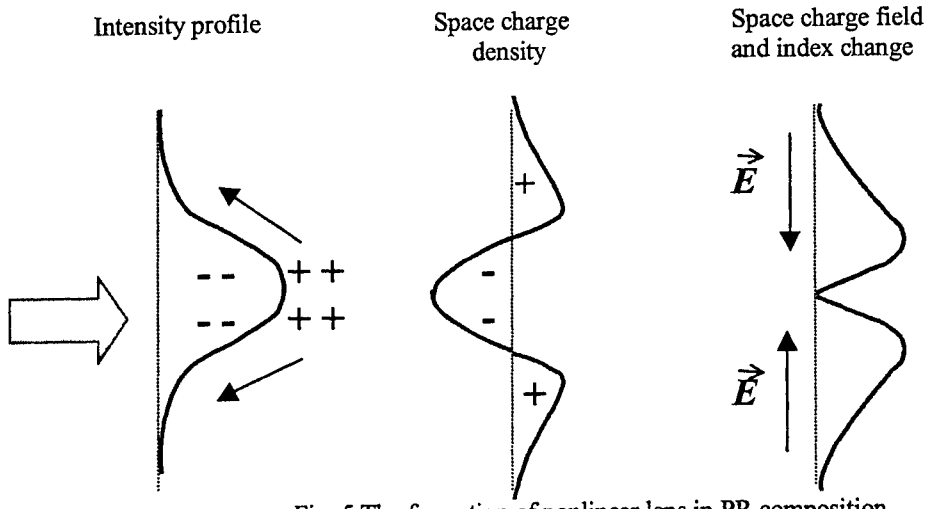


Fig. 5 The formation of nonlinear lens in PR composition.

3. FOUR-WAVE MIXING GRATING MEASUREMENTS

The refractive index grating formation was investigated in PR composites using four-wave mixing (FWM) technique. The FWM setup is shown in Fig. 6. The original beam of a He-Ne laser at 633 nm was split into two beams with equal intensities ($I_{w1}=I_{w2}$ =0.5Wcm^{-2}). These beams write the grating. The third wave with intensity $I_r \approx 0.5 \cdot I_{w1}$, obtained by reflecting the first writing wave backward from the mirror, read the grating. The wave diffracted on the grating I_d was registered. The diffraction efficiency of the grating, determined as $D = I_d / I_r$ was studied (Fig. 7). It took about 7 min for the grating to be written. The lifetime of the grating after recording depended on the illumination.

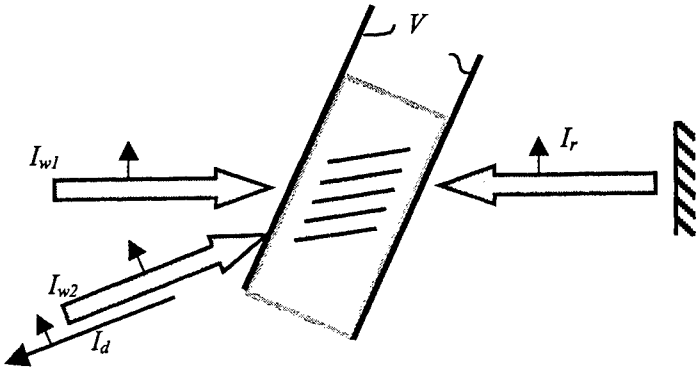


Fig. 6. The setup of FWM measurements.

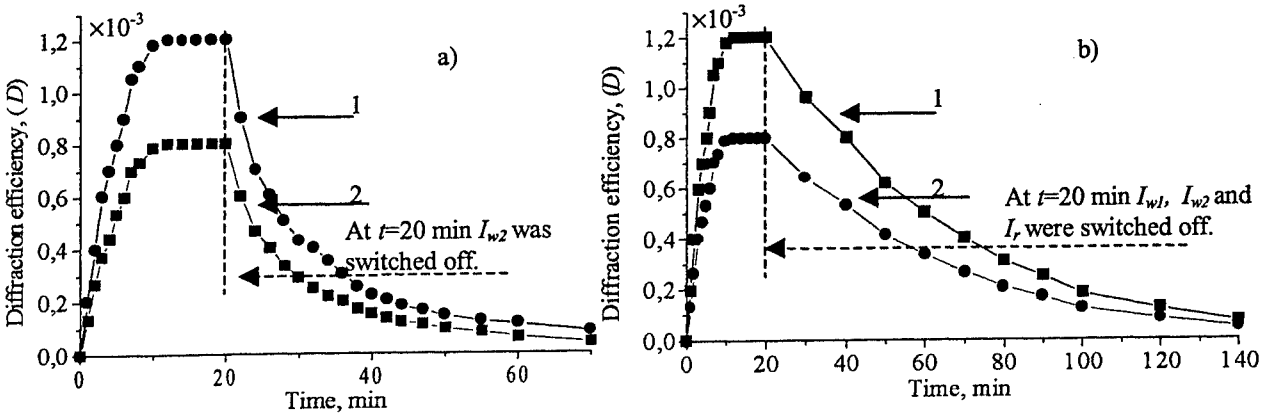


Fig. 7. Diffraction efficiency of the grating ($D = I_d / I_r$) as a function of time on different time-scales and under different erasure conditions: a) after recording, I_{w2} was switched off, the erasure of the grating was caused by waves I_{w2} and I_r, b)

after recording, I_{w1}, I_{w2} and I_r were switched off, the erasure of the grating was caused by dark conductivity and pulsed illumination with period of 2 min made for measurement of D. 1 – l=50 μm, PEAS(II)-5%, PVK-45%, C_{70}-1%, EK-25%, PTMS-24%, 2 – l=50 μm, PEAS(I)-5%, PVK-45%, C_{70}-1%, EK-25%, PTMS-24%

Two cases were compared: 1) only one of the writing waves I_{w2} is switched off after the grating has been written, and 2) all beams are switched off after the grating has been written, the diffraction efficiency was measured by pulses of I_{w1} and I_r with period of 2 min. It was found that the grating's lifetime increased from 10 min under illumination to 40 min under dark conditions. The maximum value of D achieved 1.2×10^{-3}.

4. TWO-BEAM COUPLING EXPERIMENT

The PR nonlocal origin of the optical nonlinearity of the samples was verified using a standard two-beam coupling (TBC) setup (Fig. 8). The pump and probe beams intersected in the sample at an angle of about 0.03 rad. The pump-to-probe ratio was $\beta=I_{pump}/I_{probe}=625$. It was observed that the probe beam increases in the presence of a pump beam (Fig. 9). The two-beam coupling gain coefficient was determined: $\Gamma=[\ln(\gamma\beta)-\ln(\beta+1-\gamma)]/l_{eff}$, where $\gamma=I_{probe,with\ pump}/I_{probe,without\ pump}$, l_{eff} is the effective length. TBC gain Γ was 67 cm^{-1}, with no net gain due to relatively high absorption coefficient α=87 cm^{-1}.

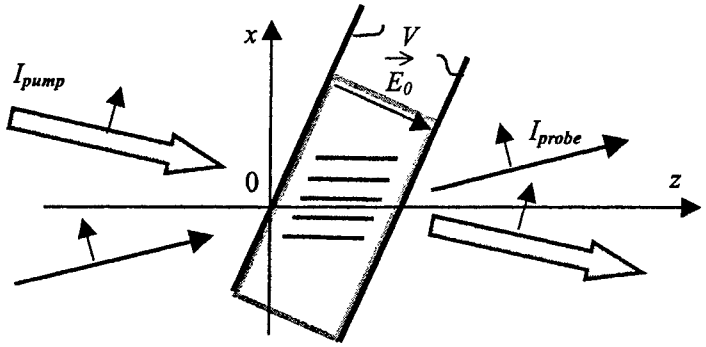


Fig. 8 TBC setup l=50 μm, I_{pump}=0.2 Wcm^{-2}, $\beta=I_{pump}/I_{probe}=625$.

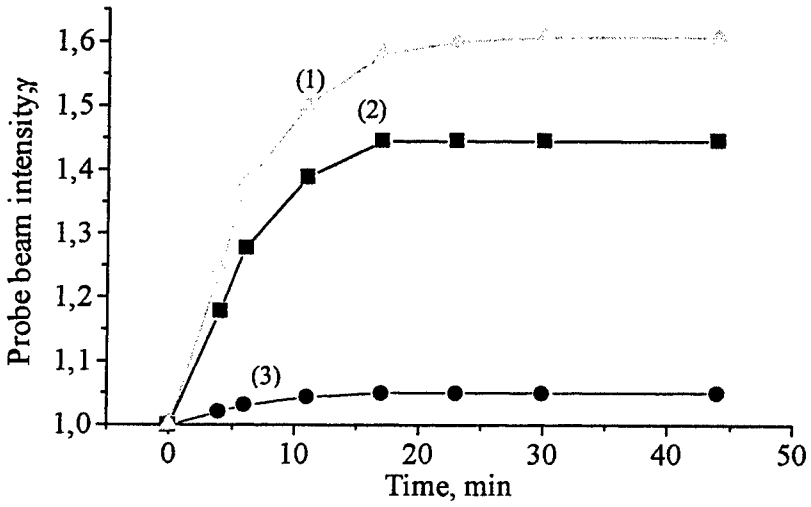


Fig. 9. Oscillograms of the probe beam. The moment t = 0 corresponds to switching-on the pump beam. (1) PEAS(I)-5%, PVK-45%, C_{60}-1%, EK-25%, PTMS-24%; $\Gamma_{(1)}$=67 cm^{-1}, absorption coefficient $\alpha_{(2)}$=87 cm^{-1}, E_0=16 V/μm; (2) PEAS(III)-5%, PVK-45%, C_{70}-1%, EK-25%, PTMS-24%; $\Gamma_{(2)}$=52 cm^{-1}, absorption coefficient $\alpha_{(1)}$=194 cm^{-1}, E_0=16

V/μm; (3) PEAS(I)-5%, PVK-45%, C_{60}-1%, EK-25%, PTMS-24%; $\Gamma_{(3)}$=7 cm^{-1}, absorption coefficient $\alpha_{(2)}$=87 cm^{-1}, E_0=0

It should be noted that small TBC gain Γ = 7 cm^{-1} was observed even at zero bias field. This fact can be explained by asymmetry of orientations of chromophores. Such asymmetry can take place similarly as in sol-gel composites based on a similar host polymer.[8]

Direct measurements of the phase shift of the refractive index grating Φ from the light intensity pattern were carried out. When the grating was written, the sample was moved along the x-axis. The dependence of the probe beam power on the x-shift was studied (Fig. 10). A maximum of the TBC gain was observed at x = 0. This fact shows a $\pi/2$-phase shift between the grating and the interference field. The theoretical prediction of this dependence can be written as:

$$\gamma \sim \exp\{\sin[2\pi x/\Lambda+\Phi]\}, \quad (2)$$

where Λ=22 μm is the grating period. The theoretical curve $\gamma(x)$ (2), assuming $\Phi = \pi/2$, is shown in Fig. 10. Good agreement between theory and experiment can be seen.

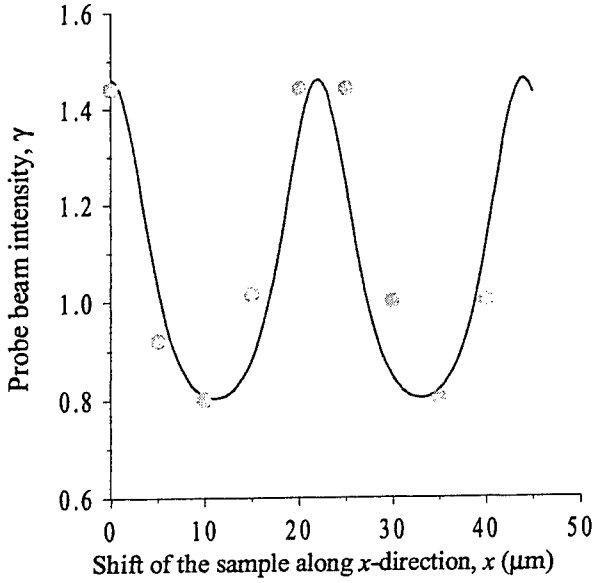


Fig. 10. The dependence of the probe beam power on the x-shift of the sample PEAS(III)-5%, PVK-45%, C_{70}-1%, EK-25%, PTMS-24%. Circles – experimental data and theoretical curve.

5. CONCLUSION

The photorefractive properties of compositions based on fullerene as a charge generator, PVK as an electroconductor, novel optical chromophores PEAS's and plasticizers EK and PTMS are investigated.

1. The experiments on nonlinear lens formation and four-wave mixing showed the formation of refractive index pattern with relaxation time dependent on beam intensity.
2. Two-beam coupling gain and a $\pi/2$-phase shift of the grating from the interference field were demonstrated. These facts indicate the nonlocal photorefractive origin of the refractive index changes.

ACKNOWLEDGEMENT

This research was supported in part by the Russian Foundation for Basic Research (Grant № 00-02-81206 Bel2000_a) and by INTAS (through the grant 97-1785).

REFERENCES

1. W.E. Moerner and S.M. Silence, "Polymeric photorefractive materials," *Chem. Rev.*, **94**, pp. 127-155 (1994).
2. S.R. Marder, B. Kippelen, A.K.-Y. Jen and N. Peyghambarian, "Design and synthesis of chromophores and polymars for electro-optic and photorefractive applications," *Nature*, **388**, pp. 845-851 (1997).
3. Y. Zhang, T. Wada and H. Sasabe, "Carbazole photorefractive materials," *J. Mater. Chem.*, **8**(4), pp. 809-828 (1998).
4. D. Wright, M.A. Diaz-Garcia, J.D. Casperson, M. DeClue, W.E. Moerner and R.J. Twieg, "High-speed photorefractive polymer composites," *Appl. Phys. Lett.*, **73**, pp. 1490-1493 (1998).
5. K.B. Ferrio, J.A. Herlocker, E. Hendrickx, J.F. Wang, Y. Zhang, A.P. Persoons, N. Peyghambarian, B. Kippelen, "Stabilized response-time in a photorefractive polymer composite doped with a styrene chromophore and C_{60}," *Technical digest of CLEO'2000*, paper CMB5, p. 9 (2000).
6. K. Meerholz, B.L. Volodin, V. Standalphon, B. Kippelen, and N.A. Peyghambarian, " Photorefractive polymer with high optical gain and diffraction efficiency near 100%," Nature, 383, pp. 58-60 (1996).
7. Antipov O.L., Afanas'ev A.V., Domrachev G.A., Douglas W.E., Guy D.M.H., Klapshina L.G., Kuzhelev A.S. "Degenerate four-wave mixing measurements of the non-linear response of conjugated silicon-ethynylene polymers," *Proceedings of SPIE (Laser Material Crystal Growth and Nonlinear Materials and Devices, K I Schaffers and L E Myers, Editors)* **3610**, pp. 95-102 (1999).
8. B. Boury, R.J.P. Corriu, V. Lestrat, R. Delord, M. Nobili, "Nanostructured silica-based organic-inorganic self-organization of a xorogel prepared by sol-gel polymerization," *Angew. Chem. Int. Ed.*, **38**, pp. 3172-3175 (1999).

Decoupling nonlinear optical elements for powerful iodine laser

L.M.Vinogradsky*+, V.A.Kargin*, V.A.Krotov*, S.K.Sobolev*, N.V. Jidkov*, V.M. Mizin**, M.V. Pyatakhin***, Yu.V. Senatsky***, I.G. Zubarev***

* Russian Federal Nuclear Center - VNIIEF, 607190 Sarov, Nizhegorodskaya obl., Russia; e-mail: vinogr@iskra5.vniief.ru

** The State Scientific Center RF-NIOPiK, Moscow, Russia

*** P.N.Lebedev Physical Institute, RAS, Moscow, Russia

ABSTRACT

High contrast fast switch of transmission in optical channels of iodine laser facilities is supplied with liquid bleachable dye cells. New dye cell designs which combine the functions of an optical shutter and a soft diaphragm are considered. 70-100 mm in diameter cell-apodizers of two types (with profiled absorbing liquid layer and profiled transmission of optical components) are developed. Cells with profiled absorbing layer contain meniscus-lens spacer, which cancels the optical power of the device. Cells with plane parallel liquid layer contain windows with profiled transmission. The laser shot-blasted technology for the surface and volume processing of the cell windows was used. For ≈ 1% initial transmission at the laser beam axis the cells' bleaching reaches 70%, and the contrast ratio of the cells' transmision profile from the beam axis to the periphery may reach K≈1000. The application of high-aperture cell apodizers in the iodine laser optical channel will make it possible to eliminate the influence on the beam profile of the disturbances in a gaseous active medium at the periphery of amplifier modules caused by the open discharge used for pumping, and to form a smoothed spatial profile of the laser beam.

Key words: decoupling dye cells, apodizers.

One of the important requirements to the laser-matter interaction experiments lies in the availability of high contrast fast optical shutters in optical channels of the laser facility, which decouple the amplifier's modules and break the laser-target feedback. Liquid bleachable dye cells are reliably used as such optical shutters in powerful iodine laser facilities of different optical schemes. The cells with the apertures from ∅ 100 to ∅ 400 mm and filled with the N 1067 dye solution have been successfully utilized in the optical channels of "Iskra-5" laser facility [1], Fig.1, for many years. For ≅1% initial transmission of the dye solution at 1.315 μm working wavelength of the iodine laser the cells' bleaching reaches 70%. Such characteristics of the cell-passive shutters are reproduced with practically no degradation during hundreds of shots. When the pulse with the energy of ≅ 0.4 J comes from the master oscillator-preamplifier system to the input of the channel, the output radiation energy,

+ Correspondence: e-mail: vinogr@iskra5.vniief.ru fax: (83130)45613

Laser Optics 2000: Control of Laser Beam Characteristics and Nonlinear Methods for Wavefront Control, Leonid N. Soms, Vladimir E. Sherstobitov, Editors, Proceedings of SPIE Vol. 4353 (2001)
© 2001 SPIE · 0277-786X/01/$15.00

after 5 amplifying cascades, reaches ≅2600 J, the pulse duration being 0.25 ns and the divergence, 0.1 mrad [1]. The radiation contrast at the output exceeds the registration threshold of $\cong 10^8$. So, the availability of a set of cell-shutters in the "Iskra-5" laser facility allows one both making the experiments on plasma heating by the laser pulses with the brightness of $\cong 4 \cdot 10^{21}$ W/sterad, and blocking (at the target) of the amplified spontaneous emission radiation of the laser with the contrast ratio of $K \cong 10^8$.

High-aperture dye cell was used also in the optical scheme of a two-pass iodine laser amplifier with the output energy of 10^3 J. The optical scheme of such an amplifier is analogous [2], and is shown in Fig. 2. The scheme involves the following elements: the amplifier module; the turning mirrors; the cell with liquid nonlinear absorber; the spatial filter with diaphragms. A two-pass amplifier provides a necessary amplification of ≅ 1J input pulse energy. With the help of a spatial filter the radiation is introduced into the amplifier (A), the beams are spatially separated at the 1st (B) and 2nd (C) passes, where the pulse is extracted from the amplifier. The nonlinear liquid absorber cell with the light diameter ∅ 400 mm provides the necessary stability of the amplifier to self-excitation.

So, the cell-shutters with bleachable liquid present an important functional element of the optical channel of a powerful iodine laser. Here we report about the development of passive cell-shutters with soft apertures. Such cells combine the functions of an optical shutter and a laser beam apodizer. The apodization (smoothing of the periphery parts) of the laser beams in the iodine lasers pumped by an open discharge may be used to eliminate the influence on the beam profile of the disturbances in a gaseous medium at the periphery of the amplifier modules caused by the open discharge. Moreover, it is known that the apodized laser beams turn to be more stable to self-focusing [3].

Figure 3 illustrates the schemes of the developed cell-apodizers of two types. The cell presented in Fig.3a consists of two windows in the form of plane-parallel plates at the optical contact with the cell spacer (O-ring plate). The soft diaphragm is formed in one of the cell windows by means of the laser treatment of the plate volume [4]. In the cell shown in Fig. 3b the soft diaphragm is formed by means of the profiling of a bleaching liquid layer. The dye solution fills the gap of a variable thickness between one of the cell windows and a glass meniscus spacer, the other (buffer) gap is filled with a transparent liquid [4].

In the calculations of the characteristics of the bleaching dye cell-apodizers we have used the data on the N 1067 dye from the experiments made at "Iskra-5" facility and at the high-aperture two-pass amplifier facility. The experimental data on the N 1067 dye bleaching for nanosecond pulses were approximated by a semi-empirical dependence between the transmission coefficient of the absorbing layer T and the incident intensity [4]. Figure 4 presents the calculated data for the cell-apodizer of Fig.3a-type, but with the light diameter of 96 mm. Figure 4a illustrates computer simulation for the small-scale inhomogeneities distribution in the cell window aperture, which provides the super-Gaussian transmission function with the index N=12:

$$T(r) = \exp(-\ln(K \cdot (r/r_0)^{12})) \qquad (1)$$

Here r is the radius; $2r_0$ = 96 mm, the plate light diameter; K =T(0)/T(48)=100, the transmission contrast. The cell with the window-apodizer ensures different transmission functions for two possible orientations of the cell to the incident laser beam. If the window-apodizer is placed at the cell output, then the intensity profile of the passed laser beam will correspond to the apodizer transmission function. When the window-apodizer is placed at the cell input, then the contrast of the laser beam profile at the cell output may be increased due to the nonlinear properties of the dye. The curves in

Fig.4b illustrate the transformation of the profile of the incident laser beam with a homogeneous intensity distribution I(r)=I(0)=0.4 J/cm^2 which passes successively the window-apodizer and the plane-parallel layer of the dye in the cell with the initial transmission T ≅ 1%. The upper curve illustrates the super-Gaussian transmission profile (1) with K=100 of the window-apodizer. After passing the dye layer this profile is transformed into the profile with K ≅ 1000. So, there is a possibility to choose the transmission function of the cell-apodizer with a bleaching dye. Figure 5c presents a comparison of the calculated intensity profiles of the laser beams in the Fresnel diffraction zone (200 m from the aperture) which have passed through the ∅96 mm cell-apodizer with the super-Gaussian transmission function (1) and ∅96 mm "hard" aperture (upper curve).

The profile of the front surface of the glass meniscus spacer for the cell of Fig.3b type (the light aperture, $2r_0$ = 70 mm) has been calculated in such a way that the cell transmission profile for the 0.4 ns laser pulse (the energy density 0.4 J/cm^2) would correspond to a super-Gaussian function with an index N=6. The initial data are as follows: T_0=1%, h_0=0.5 mm, $2r_0$=70 mm; indices of refraction for liquid n_1 = 1.6945, and for glass n_2 = 1.5031; dye absorption coefficient k =92 cm^{-1}. The expected transmission coefficient at the cell axis under the dye bleaching is 65 %; the transmission coefficient over the aperture in the bleached state is 30%; the contrast K=1000. Figure 5 presents the intensity distribution in the beams from the "soft"(left) and "hard" (right) diaphragms ∅ 70 mm in the Fresnel diffraction zone, the distances from the point of observation to the diaphragms, z =20 m (a), z = 200 m (b). The comparison of beam profiles in Figs.4 and 5 shows that for the developed cell-apodizers with a super-Gaussian functions of transmission one can expect a sufficiently high level of smoothing of the intensity distribution in the passing laser beam.

Presently, within the framework of ISTC Project 651-B we have manufactured and prepared for the experiments several samples of cell-apodizers for the iodine laser.

The cell-apodizers developed within this ISTC Project combine the functions of a passive shutter and a soft diaphragm, and can be of interest for the application in different lasers. The existing set of bleaching liquids makes possible the application of cell-apodizers in solid-state (Nd, Yb, Ti-sapphire) and gas (iodine, excimer) lasers. Such cells may find application not only in the optical channels of powerful laser facilities, but also for Q-switching and selection of transversal modes in master oscillators.

ACKNOWLEDGEMENTS

The authors are grateful to Prof. K. Ueda, the collaborator of the ISTC Project N 651-B, for fruitful discussions and support of the work. The authors also thank the colleagues from the Scientific-Research Institute for Comprehensive Testing of Optoelectronic Devices and Systems, S.I.Vavilov State Optical Center for their help in the performance of the experiments.

REFERENCES

1. V.I. Annenkov, V.A.Bagretsov, L.M.Vinogradsky et al. "A 120 TW pulsed laser "Iskra-5", Kvantovaya Elektronika, 18, 536 (1991).
2. H.Baumhacker, G.Brederlow, E.Fill et al. "Layout and performance of the Asterix-4 iodine laser at MPQ, Garching", Appl.Phys. B61, 325-332 (1995).
3. N.B.Baranova, B.Ya.Zel'dovich, N.E.Bykovsky, Yu.V.Senatsky, "The radiation diffraction and self-focusing in the high-power beam amplifier", Kvantovaya Elektronika, 1, 11, 2435-2458 (1974).
4. L.M.Vinogradsky, V.A.Kargin, S.K.Sobolev et al. "Soft diaphragms for apodization of powerful laser beams". In Advanced High-Power Lasers, M.Osinski, H.Powell, K.Toyoda, Editors, Proc. of SPIE, 3889, pp.849-860 (2000).

Figure Captions

Fig.1. Optical scheme of a laser channel of "Iskra-5" facility: (MO-PA) - master oscillator-preamplifier system; (BS) – beam splitting system; A1-A4 – main amplification cascades; SF1-3 - spatial filters; C1-C4 - dye cells.

Fig.2. Optical scheme of a two-pass iodine laser with a high-aperture decoupling cell: 1,8 – turning mirrors; 2 – a cell with a nonlinear liquid absorber; 3 – amplifying module; 4,7,9 – spatial filter lenses; 5 – spatial filter cell; 6 – diaphragm; A – input beam; B – a beam at the 1st passage through the amplifier; C – output beam.

Fig.3. Schemes of the cell-apodizers with the light diameters 70 mm: (a) a cell with plane-parallel windows (1) and a nonlinear absorber layer (3); «soft» diaphragm (2) is formed in the volume of a glass plate window, b) cell-apodizer with a glass meniscus spacer (2); (1) – windows; (3) – nonlinear absorber layer; (4) transparent liquid.

Fig.4. Parameters of the cell-apodizer (Fig3a type) with a volume distribution of small-size scatterers over the window aperture: a) illustration of laser caverns distribution over the plate aperture (computer simulation), one scale division – 10 mm; b) calculated profiles of the cell-apodizer transmission: only the window-apodizer profile (upper curve); the profile of the dye-cell with the window apodizer (lower curve); c) calculated distributions of intensity in the laser beams, which passed the cell-apodizer Ø 96 mm with a super-Gaussian transmission function, N=12 (lower curve) and a «hard» diaphragm Ø 96 mm (upper curve) in the Fresnel diffraction zone.

Fig.5. Calculated intensity distributions in the Fresnel diffraction zone of the laser beams which passed the cell-apodizer Ø 70 mm with a super-Gaussian transmission function, N=6 (left curves) and a «hard» diaphragm with Ø 70 mm .

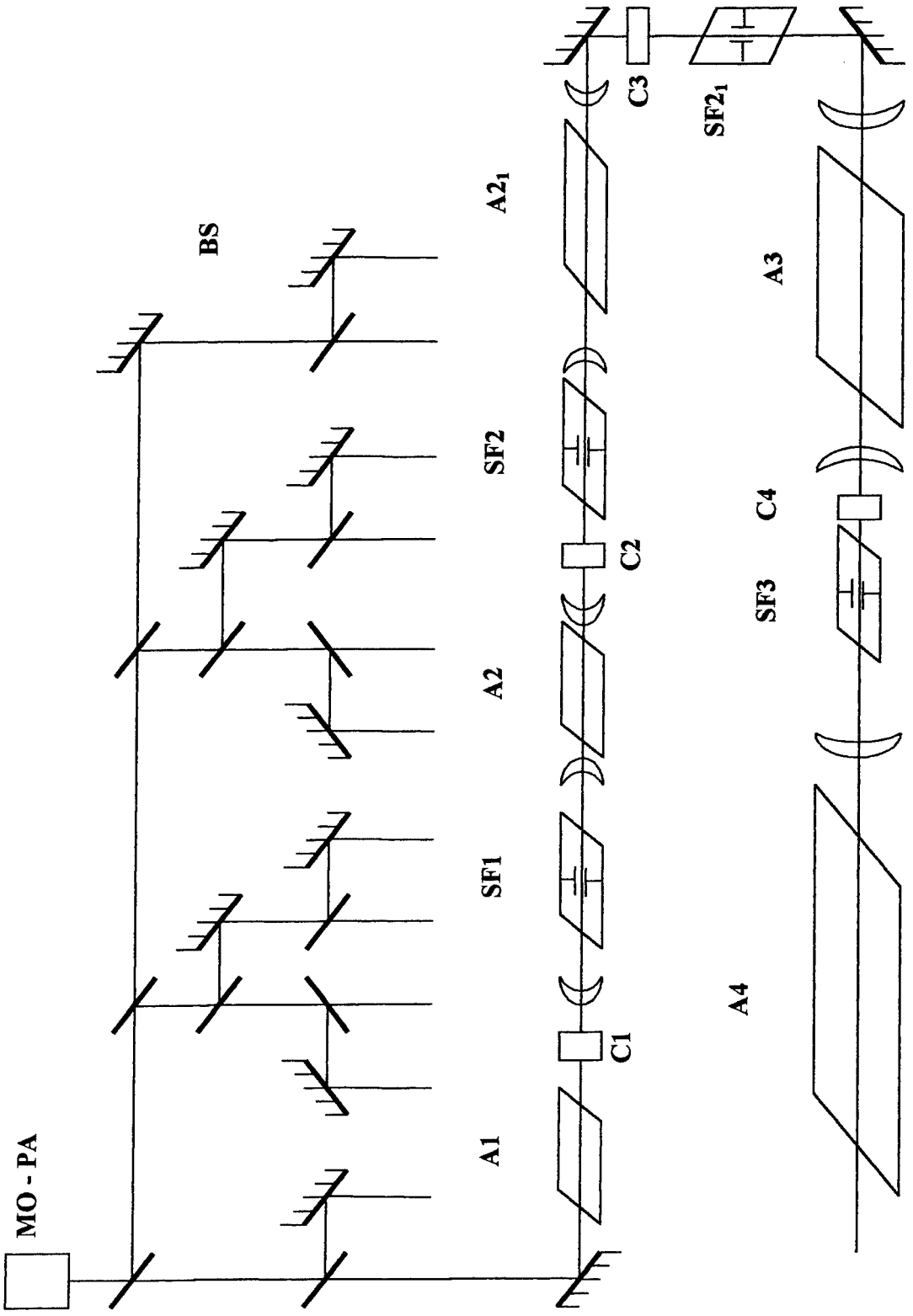


Fig. 1

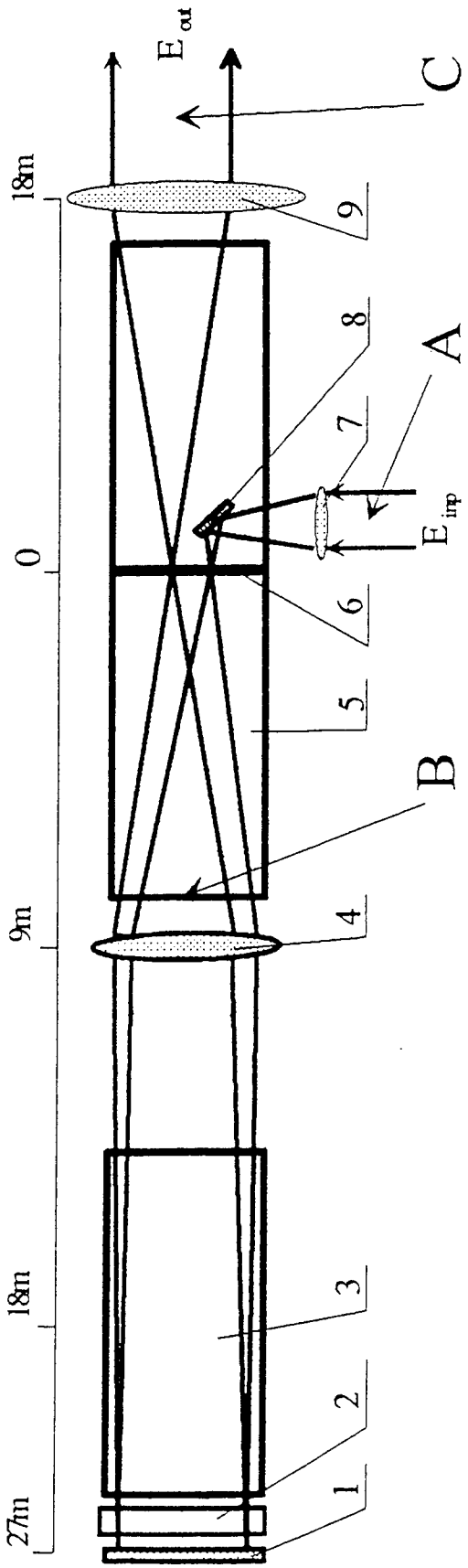


Fig.2

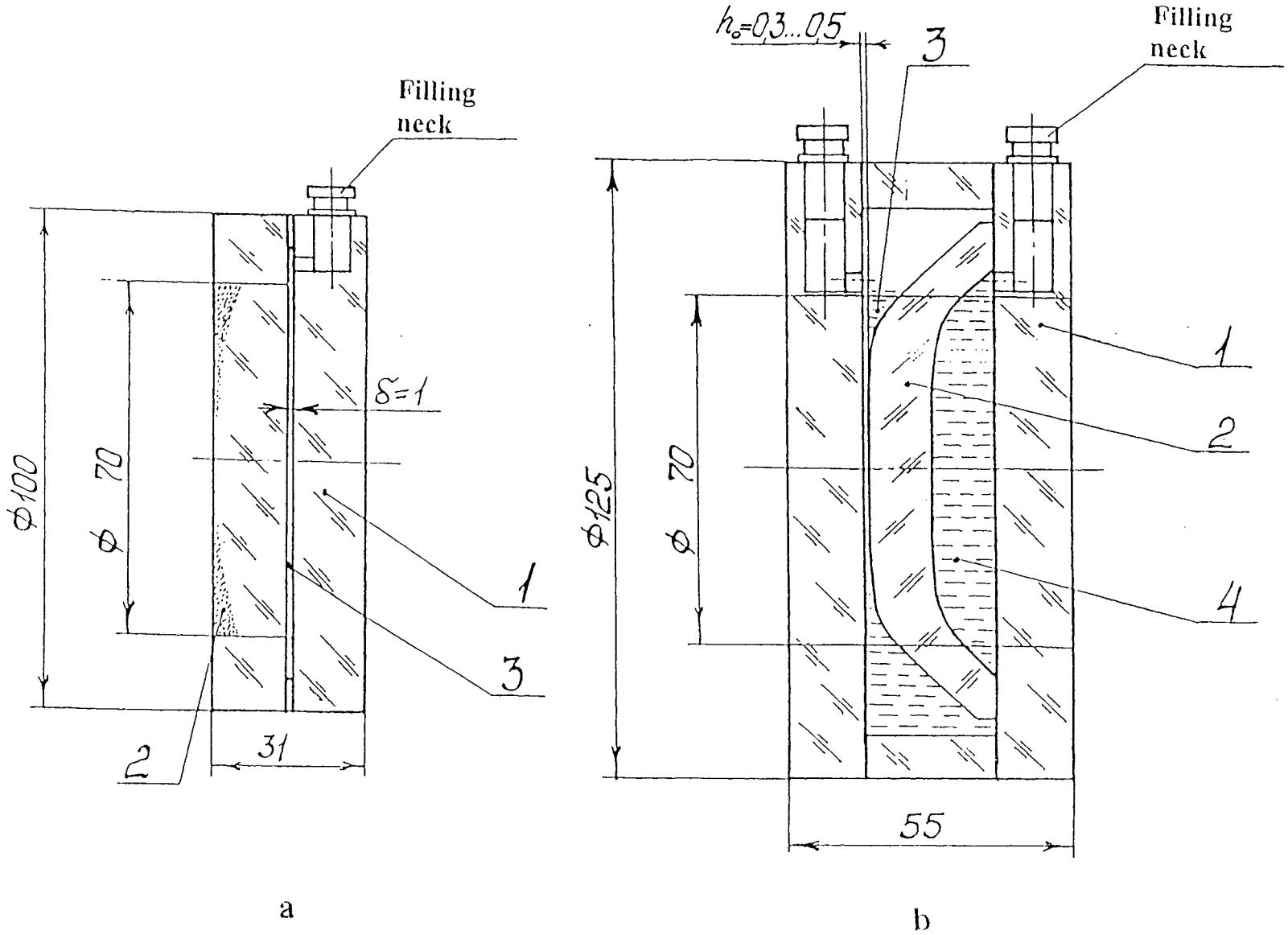
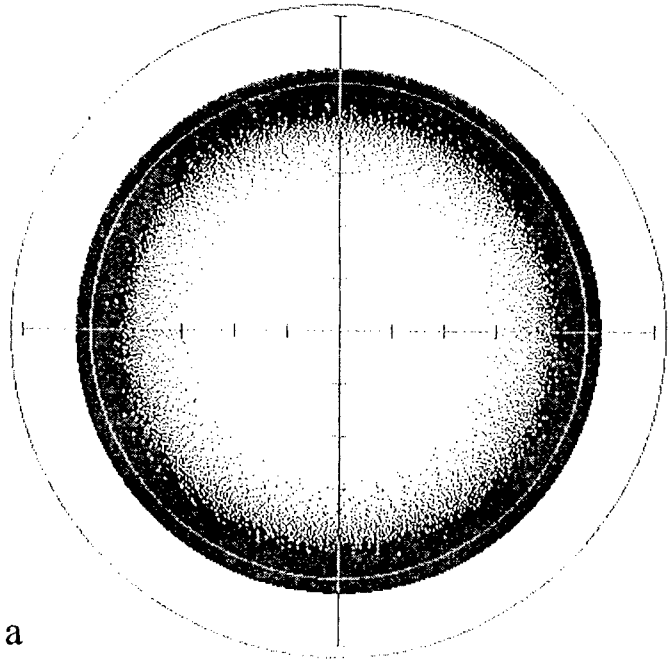
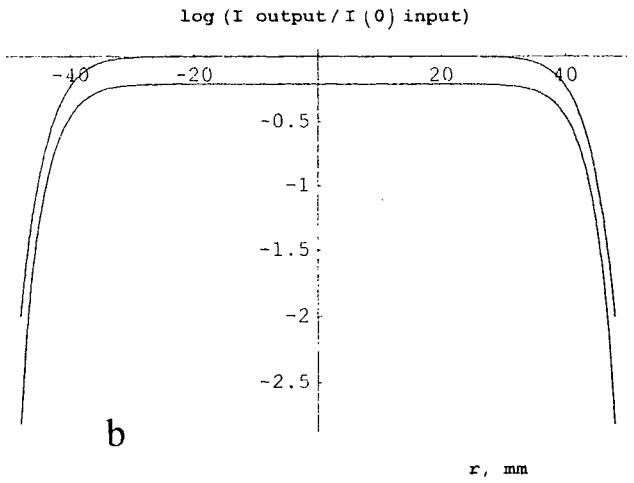

Filling neck
δ=1
Φ100
Φ 70
1
3
2
31
a
h=0,3...0,5
3
Filling neck
1
2
Φ125
Φ 70
4
55
b

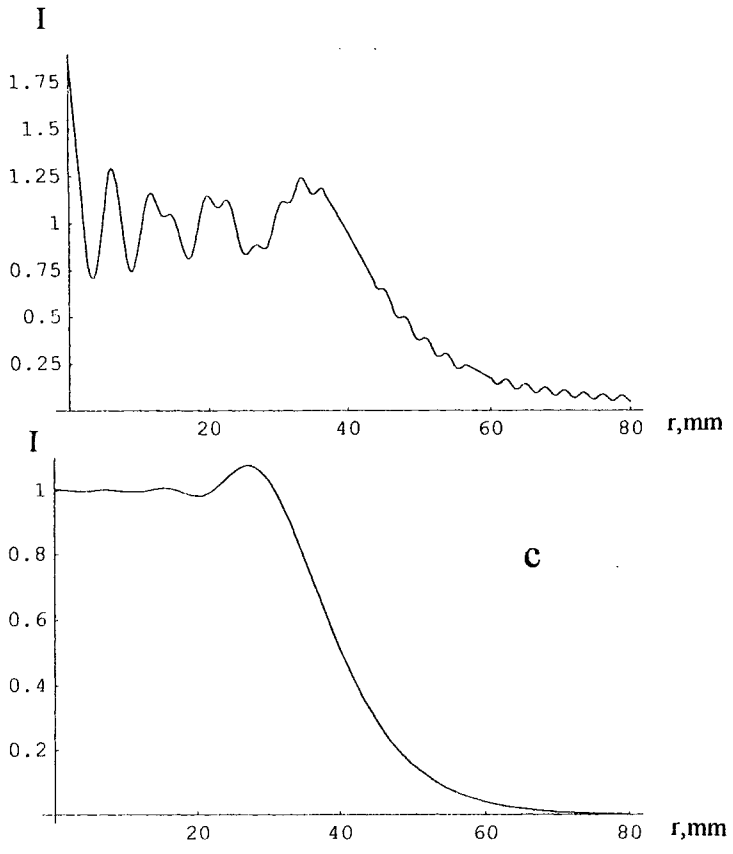
Fig.3



a


log (I output / I (0) input)
-40
-20
20
40
-0.5
-1
-1.5
-2
-2.5
r, mm

b


I
1.75
1.5
1.25
1
0.75
0.5
0.25
20
40
60
80
r,mm

I
1
0.8
0.6
0.4
0.2
20
40
60
80
r,mm

c

Fig.4

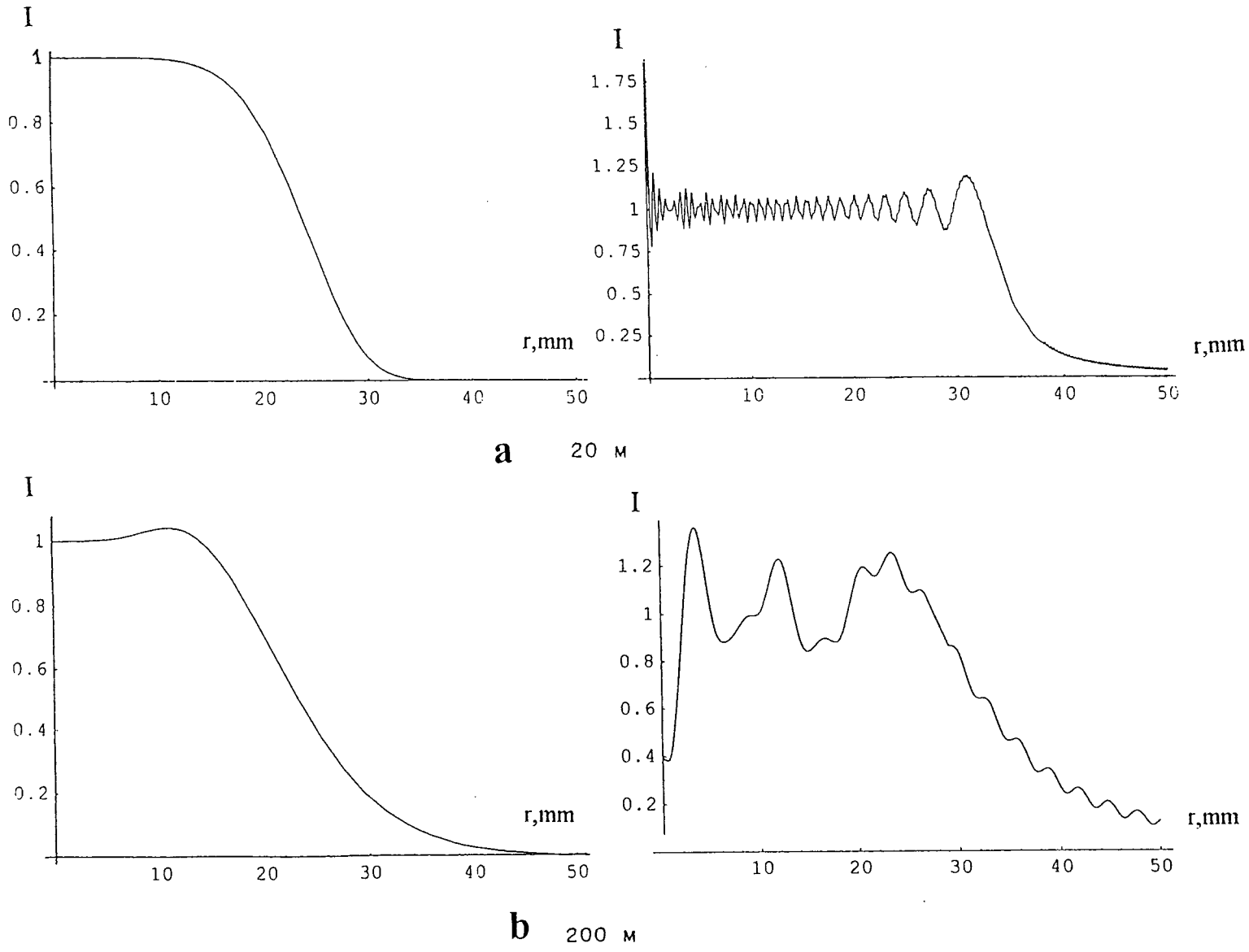

I
1
0.8
0.6
0.4
0.2
r,mm
10
20
30
40
50
I
1.75
1.5
1.25
1
0.75
0.5
0.25
r,mm
10
20
30
40
50
a 20 м
I
1
0.8
0.6
0.4
0.2
r,mm
10
20
30
40
50
I
1.2
1
0.8
0.6
0.4
0.2
r,mm
10
20
30
40
50
b 200 м

Fig. 5.

Record of dynamic and static holograms in thin fullerene-doped organic films

N.V.Kamanina*, L.N. Kaporskii, V.N.Sizov, D.I. Stasel'ko

Vavilov State Optical Institute, 12 Birzhevaya Line, St. Petersburg 199034, Russia

ABSTRACT

Under the Raman-Nath diffraction conditions the thin holographic gratings have been recorded in a promising class of π-conjugate organic materials based on polyimide and 2-cyclooctylamino-5-nitropyridine. The drastic change of refractive index has been observed in the systems doped with fullerene C_{70}. The results have been explained both by laser-induced conformational transformations of organic materials and by their spectral and thermal properties.

Keywords: organic compound, fullerene, holographic grating, laser

1. INTRODUCTION

At present time a fullerene introduction in organic materials is widely used due to high electron affinity of fullerene that allows the intramolecular donor-acceptor interaction to be essentially reinforced and the organic compound properties to be modified with ease. These effects were investigated in C_{60}-poly [(disilanylene) oligophenylenes] structures,[1] C_{60}-2,6-bis(2,2-bicyanovinyl)pyridine thin films,[2] C_{60}-polymethacrylate,[3,4] and polyimide-fullerene systems.[5,6] Electro-optic modulation and the angular dependence of holographic diffraction in C_{60}-doped diethylaminonitrostyrene and poly(N-vinylcarbazole) were observed in the paper.[7] A significant increase in storage time by thermal fixing of photorefractive gratings in a fullerene-doped polymeric composite of poly-9-vinycarbazole and 4-N,N-diethylamino-β-nitrostyrene was demonstrated in the publication.[8] It was established that the investigation of the reversible media, where the writing was realized, in particular, with variations of refractive index, offered few advantages over study of irreversible media, where a thermal write mechanism was revealed. Recent investigations of fullerene-doped organic systems have shown that they hold the great promise in this direction.[9,10]

In the present paper the record of thin phase holograms have been investigated in new nonlinear optical materials based on fullerene-doped photosensitive polyimide (PI) and 2-cyclooctylamino-5-nitropyridine (COANP).

2. EXPERIMENT

Photosensitive polyimide 6B with chemical formula, which was described in paper,[11] and COANP compound, which peculiarities were investigated in papers,[12-14] have been studied on doping with fullerene C_{70}. The films were prepared as follows. A 3% solution of PI6B in 1,1,2,2-tetrachloroetane (TClE) and a 5% solution of COANP in TClE were made. A 2.5% solution of non-photosensitive polyimide 81A[15] in TClE was used as a film-forming base for COANP compound. The relation between COANP and the film-forming base was 2:1. 1-1.5 μm thick films were spun on glass substrates coated with transparent indium-tin-oxide contact and then were dried in order to remove the solvent. The C_{70} concentration in PI6B and COANP materials was varied from 0.2 wt.% to 5 wt.%.

Holographic grating was recorded with a pulsed Nd–laser at a wavelength of 532 nm and a pulsewidth of 20 ns. The experimental scheme was similar to that presented in paper.[16] Two laser beams, which were used to record a sinusoidal grating, formed a spot of diameter 5 mm on the film surface. Power density was varied from 0.1 to 3 J cm^{-2} in the plane of the film. The investigations were carried out at spatial frequency (Λ) of 100 mm^{-1}. The grating was read out in self-diffraction mode. Because the condition $\Lambda^{-1} >> d$, where d was a thickness of the films, was met, the diffraction was obtained in the Raman–Nath regime.

* E-mail: kamanin@ffm.ioffe.rssi.ru

Laser Optics 2000: Control of Laser Beam Characteristics and Nonlinear Methods for Wavefront Control, Leonid N. Soms, Vladimir E. Sherstobitov, Editors, Proceedings of SPIE Vol. 4353 (2001)
© 2001 SPIE · 0277-786X/01/$15.00

3. RESULTS AND DISCUSSION

The dependence of a first diffraction order response (η^*) on an input laser power density (W_{in}) is shown in Fig. 1. Curves 1, 2 and 3, 4 correspond to PI6B and COANP films, respectively. Curves 1 and 3 indicate the fullerene-free samples and curves 2 and 4 present the fullerene-doped systems. The C_{70} concentration is 0.2 wt.% and 5 wt.% in PI6B and COANP films, respectively. We have obtained high homogenous films, the electronic photographs one of them, namely, PI6B with 0.2 wt.% C_{70}, was shown in paper.[17] It should be noticed that the samples remained undecomposed at the laser radiation power density more than 2 J·cm^{-2}. It can be explained by a very high melting temperature[18] of 1000°-1100°C for the film forming base, that a little bit more than its destruction temperature.

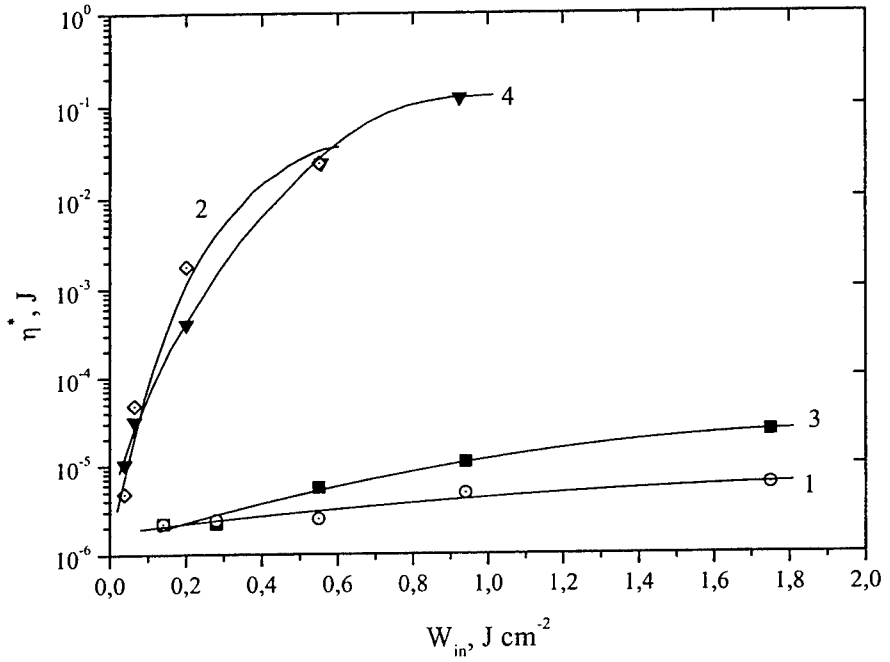


Fig. 1. The dependence of the first diffraction order response (η^*) on the input laser power density (W_{in}) for fullerene-free (1,3) and C_{70}-doped (2,4) films. The curves of 1-2 and 3-4 correspond to PI6B and COANP, respectively.

Let us to discuss the data presented in Fig. 1. The C_{70} fullerene is shown to sensitize a photosensitive polymer. Thus, when fullerene is introduced in the polymer matrix, the diffraction efficiency increases drastically. The sensitization is likely to result from a larger increase in the optical absorption at the laser wavelength of 532 nm for the fullerene-doped PI6B and COANP structures. The absorption edge for fullerene-free polyimide is located close to 380–400 nm. We observed before that the absorption spectrum of PI6B doped with the fullerene mixture[5] of C_{60} and C_{70} was red-shifted to compare with fullerene-free systems. The absorption spectrum of the C_{70}-PI6B system was red-shifted by 25-30 nm from the absorption spectrum of polyimide sensitized by the C_{60}-C_{70} mixture. As the result, the absorption spectrum of C_{70}-PI6B was more overlapped with the fluorescence spectrum of the polyimide matrix at the wavelength of 532 nm and thus the excitation was transmitted more efficiently.

COANP absorption spectra showed that the fullerene-doped samples had significantly different spectral features than fullerene-free COANP films, namely, there were two additional absorption peaks[19] at 490 nm and 810-820 nm. It should be noticed that the absorption edge of pure COANP compound was 430 nm.[20] Therefore in the current experiment the wavelength of laser radiation coincides with the absorption band of fullerene-doped films more than that of fullerene-free structures.

It should be noticed that fullerenes reinforce the intramolecular donor-acceptor interaction because they have larger electron affinity than acceptor fragments of both PI and COANP molecules. Moreover, the carriers become free after the charge transfer to the fullerene molecule, where the surface charge is delocalized.[1] Therefore the reinforcement of donor-acceptor interaction in the films investigated because of the free-carrier absorption influence the drastic change of the diffraction efficiency in fullerene-doped structures. As an additional evidence of the free-carrier existence, dark conductivity and photoconductivity of the fullerene-doped systems are at least one order of magnitude more than those of fullerene-free sample. The conductivity has been measured under bias voltage of 20-60 V.

Using the data from dependence presented in Fig.1, the threshold of the transition from phase grating to amplitude one has been determined. Its value is 0.5-0.6 J·cm^{-2} and 0.9-1.0 J·cm^{-2} for fullerene-doped PI6B and fullerene-doped COANP films. In this case the transition from the dynamic hologram to the static one has been observed. The corresponding photograph for the C_{70}-doped COANP film is presented in the Fig. 2.

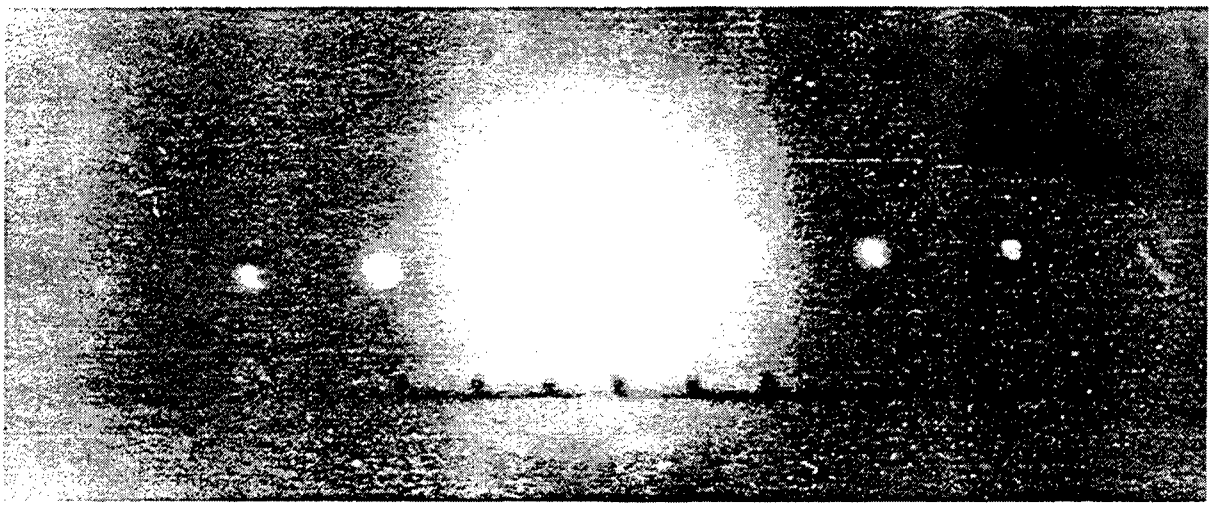


Fig. 2. The photograph of diffraction order maximums for C_{70}-doped COANP thin film.

It should be noticed that the change in the laser-induced refractive index has been found at the threshold of the transition. We have estimated the change in refractive index using the relationship given in the paper:[21]

$$\eta = I_1 / I_0 = (\pi \Delta n_i d / 2\lambda)^2 \qquad (1)$$

where η is diffraction efficiency, I_1 and I_0 are laser intensity in first and zero diffraction orders, respectively, d is a film thickness, λ is a laser wavelength, and Δn_i is a laser-induced change of refractive index. Therefore a hundred-fold increase in the laser-induced change of refractive index has been observed in C_{70}-doped PI6B (at W_{in} = 0.6 J·cm^{-2}) and C_{70}-doped COANP (at W_{in} = 1.0 J·cm^{-2}) in comparison with the fullerene-free films. In spite of the fact that, in the nanosecond and longer time scales, the principal mechanisms for grating recorded nonlinearities are thermal and density fluctuations, the values of input energy density, at which the effect was observed, do not contradict to the high value of conformational rotation energy in the polyimide matrix.

Really, it should be noticed that the values of the write energy density, which are applied in this work, make possible conformational modifications of the polymer chain. For example, for fullerene-doped polyimide PI6B, the write energy density of 0.5–0.6 J·cm^{-2} corresponds to 350-400 kcal·mol^{-1} at molecular mass of a monomeric unit of 750 as well as at the sample thickness and the spot diameter mentioned above. The rotation threshold is 10-700 kcal·mol^{-1} for cyclic groups relative to ordinary bonds in polyimide.[18,22] Therefore, the write energy density values applied suffice to the rotation of hinge-joint bonds in polyimide, making the conformational modifications of polymer chains easier. This effect is likely to

result in a better arrangement of macromolecule donor fragment and fullerene planes, and hence in efficient transfer of excitation between them.

The results obtained suggest that, in addition to laser heating of the medium, conformational transformations of organic molecules influence the laser-induced change of refractive index. It should be noticed that thermal stability of the organic films was significantly augmented by the fullerene introduction.

Thus, the structures based on both fullerene-doped polyimide and COANP can be applied as effective diffractive laser elements with good laser strength. They may be used in real time systems of information processing with both reversible and irreversible mechanisms of laser recording.

4. CONCLUSION

The thin holographic gratings have been recorded in the organic materials based on polyimide and 2-cyclooctylamino-5-nitropyridine doped by fullerene C_{70}. The drastic change of refractive index has been observed in the system studied. The threshold of the transition from phase grating to amplitude one has been determined. In this case from 3 to 7 diffraction orders have been observed. The results obtained have been explained by both the laser-induced thermal and density fluctuations as well as both by the conformational transformations of organic materials and by their spectral properties. It has been noticed that reinforcement of donor-acceptor interaction in the fullerene-doped structures influence the efficiency of excitation transmitted and thus drastic change of diffraction efficiency. It has been shown that the fullerene-doped system could be applied as dynamic and static diffractive optical elements. The films studied can be used as photosensitive layers in the optically addressed spatial light modulators and other optical processing devices operated in real time scale.

5. ACKNOWLEDGEMENTS

The authors would like to thank Prof. B.V.Kotov, Dr. V.I.Berendyaev, Dr. N.A.Vasilenko (Karpov Research Physical-Chemical Institute, Moscow, Russia) and Dr. A.Leyderman, Dr. A. Barrientos (University of Puerto-Rico, Mayagüez, PR, USA) for their help in this study. This work was supported by Russian National Program "Optoelectronic and Laser Technologies".

6. REFERENCE

1. K. Hosoda, K. Tada, M. Ishikawa, and K. Yoshino, "Effect of C_{60} doping on electrical and optical properties of poly [(disilanylene) oligophenylenes]," *Jpn. J. Appl. Phys., Part 2* **36**, pp. L372-L375, 1997.
2. M. Ouyang, K.Z. Wang, H.X. Zhang, Z.Q. Xue, C.H. Huang, D. Qiang, "Study of a novel C_{60}-2,6-bis(2,2-bicyanovinyl)pyridine complex thin film", *Appl. Phys. Lett.* **68**, pp. 2441-2443, 1996.
3. A. Kost, L. Tutt, M.B. Klein, T.K. Dougherty, and W.E. Elias, "Optical limiting with C_{60} in polymethyl methacrylate," *Opt. Lett.* **18**, pp. 334-336, 1993.
4. V.P. Belousov, I.M. Belousova, V.G. Bespalov, V.P. Budtov, V.M. Volynkin, V.A. Grigor'ev, O.B. Danilov, A.P. Zhevlakov, A.G. Kalintsev, A.N. Ponomarev, S.A. Tul'skii and E.Yu. Yutanova, "Nonlinear optical properties of fullerene-containing media," *J. Opt. Technol.*, **64**, pp. 870-871, 1997.
5. N.V. Kamanina, L.N. Kaporskii, and B.V. Kotov, "Absorption spectra and optical limiting of the fullerene-polyimide system," *Opt. Commun.* **152**, pp. 280-282, 1998.
6. N.V.Kamanina, "Reverse saturable absorption in fullerene-containing polyimides. Applicability of the Förster model," *Opt. Commun.* **162**, pp. 228-232, 1999.
7. M.E. Orczyk, J. Zieba, P.N. Prasad. Proceed,"Photorefractivity in polymeric composite materials," *Proceed. of SPIE* **2025**, pp.298-309, 1993.
8. N. Cheng, B. Swedek, P.N. Prasad, "Thermal fixing of refractive index gratings in a photorefractive polymer", *Appl. Phys. Lett.*, **71**, pp.1828-1830, 1997.
9. E.S. Maniloff, D. Vacar, D. McBranch, Hsinglin Wang, B. Mattes, A.J. Heeger, "Femtosecond electron-transfer holography in C_{60}/polymer blends," *Synth. Met.*, **84**, pp.547-548, 1997.
10. Y. Cui, B. Swedek, N. Cheng, J. Zieba, P.N. Prasad, "Dynamics of photorefractive grating erasure in polymeric composirtes," *J. Appl. Phys.*, **85**, pp.38-43, 1999.
11. B. M. Rumyantsev, V. I. Berendyaev, N. A. Vasilenko, S. V. Malenko, and B. V. Kotov, "Photogeneration of charge carriers in layers of soluble photoconducting polyimides sensitized by dyes," *Polym. Sci. A* **39**, pp. 506–512, 1997.

12. J.Zyss, J.F. Nicoud, M.Coquillay. "Chirality and hydrogen bonding in molecular crystals for phase-macthed second-harmonic generation: N-(4-nitrophenyl)-(L)-prolinol (NPP)," *J. Chem. Phys.*, **81**, pp.4160-4167, 1984.
13. G.Lahajnar, I.Zupan i , R.Blinc, A.Zidanšek, R.Kind, M.Ehrensperger, "NMR self-diffusion study of organic glasses: COANP, MBANP, PNP, NPP," *Z. Phys B*, **95**, pp.243-247, 1994
14. Y.Cui, J.Wu, N.Kamanina, A.Pasaje, A.Leyderman, A.Barrientos, M.Vlasse and B.G.Penn, "Dielectric study of dynamics of organic glasses," *J. Phys. D: Appl. Phys.*, **32**, p.3215-3221, 1999.
15. N.V.Kamanina, and V.I.Berendyaev, "Influence of solid – liquid crystal interface on characteristics of liquid crystal cells," *Proceed. of SPIE* **3292**, pp. 154–158, 1998.
16. V. V. Danilov and N. V. Kamanina, "Self-diffraction and relaxation in a resonant liquid crystal medium", *J. Opt. A: Pure Appl. Opt.* **1**, p.37–40, 1999.
17. N.V.Kamanina, N.A.Vasilenko, S.O. Kognovitsky, and N.M.Kozhevnikov, "LC SLM with fullerene-dye-polyimide photosensitive layer," *Proceed. of SPIE*, **3951**, pp. 174–178, 2000.
18. M. I. Bessonov, N. P. Kuznetsov, and M. M. Koton "Transition temperatures of aromatic polyimides and the physical principles of their chemical classification," *Vysokomol. Soedin., Ser. A*, **20**, pp.347-354, 1978 [in Russian].
19. N. V. Kamanina, L. N. Kaporskiĭ, Alex Leyderman, and Alfonso Barrientos, "The effect of optical attenuation of laser radiation in a fullerene-containing COANP–polyimide system," *Tech. Phys. Lett.* **26**, pp. 279–281, 2000.
20. K. Sutter, J. Hulliger, and P. Günter, "Photorefractive effects observed in the organic crystal 2-cyclooctylamino-5-nitropyridine doped with 7,7,8,8,-tetracyanoquinodimethane," *Solid State Commun.* **74**, pp. 867-870, 1990.
21. R.J.Collier, C.B.Burckhardt, and L.H.Lin. Optical Holography, Academic Press, New York and London, 1971.
22. V.A. Bershtein, V.M. Egorov. Differential Scanning Calorimetry in Physical Chemistry of Polymers, Chemistry, Leningrad, 1990.

Light induced scattering in laser radiation nonlinear optical limiting on the base of fullerene-containing media

I. M. Belousova, V. A. Grigor'ev, O. B. Danilov, A. G. Kalintsev, A. V. Kris'ko, N. G. Mironova, and M. S. Yur'ev.

Institute for Laser Physics, Birzhevaya line 12,
199034 St. Petersburg, Russia

ABSTRACT

The contribution of light induced scattering to nonlinear optical limiting is theoretically and experimentally investigated. It is shown that light induced scattering is caused by fine-scale (1÷10 μm) inhomogeneities formation, very low (comparable to spontaneous noise) laser beam inhomogeneities can evolve into light induced scattering. The numerical modeling of scattered radiation angular distribution and laser radiation attenuation in optical limiters was performed. The modeling results were compared with the experimental ones.
Keywords: fullerenes, optical limiting, light induced scattering, computer simulation

1. INTRODUCTION

It is well known that fullerenes and fullerene-containing media have strong nonlinear-optical properties, which makes it possible to use them as nonlinear optical limiters. Of these properties, reverse saturable absorption from the metastable level (RSA)[1] has received the most study. In fullerene solutions RSA is followed by strong scattering[2,3]. It has been supposed that this scattering is caused by light-induced refractive index fine-scale inhomogeneities which develop when high intensity laser radiation passes through a cell. The light induced heating is proved to be the main channel of refractive index change[4].

The quantitative evaluations of light-induced heating are performed and typical scales of inhomogeneities as well as scattering angles are presented. The boundaries of domain of unstable perturbations, caused by laser beam thermal self-action are defined. The increments of instability are calculated. The numerical modeling of nonlinear scattering is performed. The experimental conditions[4] were used in calculations. The experimental conditions are: M=0.6 mM C_{60}-toluene solution, incident radiation wavelength λ=532 nm, incident radiation intensity $I\approx10^8$ W/cm^2, pulse duration τ_p=10 ns, beam aperture a=2 mm, cell length L=3 mm. Calculation results are compared with the experimental ones.

2. EXPERIMENTAL RESULTS

The contribution of processes, responsible for radiation attenuation to nonlinear optical limiting is experimentally investigated. Schemes of setups for investigation of optical limiting are presented at Fig. 1(a,b,c). The parameters of radiation at the output of the facility are:

- wavelength 1.06 μm, 0.532 μm, 0.353 μm (Nd:YAG laser),
- radiation energy in pulse 0.6 J (1.06 μm), 0.35 J (0.532 μm), 0.3 J (0.353 μm),
- radiation pulse duration 10 ns,
- radiation angular divergence $\leq 2\times10^{-3}$ rad,
- beam diameter 2 ÷ 8 mm (according to telescoping).

Laser Optics 2000: Control of Laser Beam Characteristics and Nonlinear Methods for Wavefront Control,
Leonid N. Soms, Vladimir E. Sherstobitov, Editors, Proceedings of SPIE Vol. 4353 (2001)
© 2001 SPIE · 0277-786X/01/$15.00

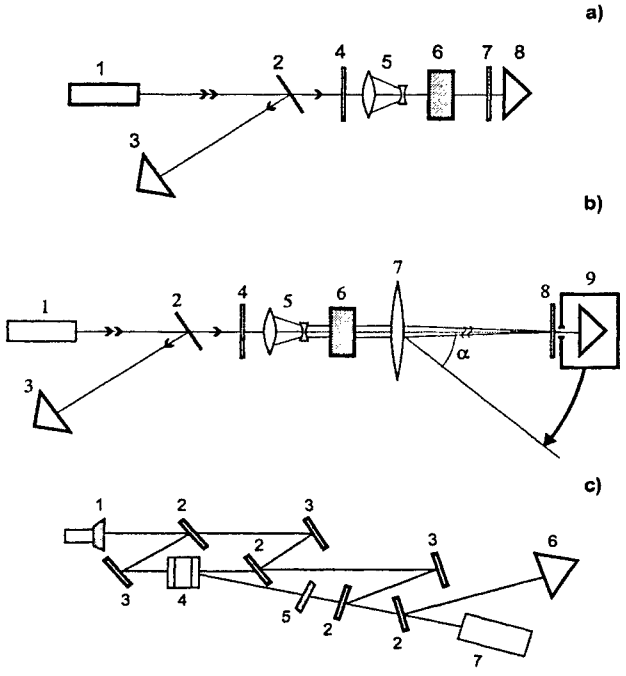


Fig.1 Experimental setup for investigation of optical limiting

a) calorimetric experimental setup 1 – 0.53 μm Nd:YAG laser, 2 – beam splitter, 3- input energy meter, 4 – input changeable filter, 5 – telescope, 6 – fullerene-containing cell, 7 – output changeable filter, 8 – output energy meter
b) setup for measurement of the indicatrix of light induced scattering setup 1 – 0.53 μm Nd:YAG laser, 2 – beam splitter, 3- input energy meter, 4 – input changeable filter, 5 – telescope, 6 – fullerene-containing cell, 7 – long-focused lens output changeable filter, 8 – output filter, 9 – movable energy meter with 3 mm aperture
c) setup for measurements of the change of refractive index during a laser pulse 1- camera with removable filters, 2 – beam splitter, 3 – mirrors, 4 –fullerene-containing cell, 5 – removable filters, 6 – input energy meter, 7 -0.53 μm Nd:YAG laser

The length of cell with C_{60}-toluene solution was 3 mm and the length of solid-state samples was 1-2 mm. The study of optical limiting was performed with the calorimetric technique in collimated beams (Fig.1a). Input energy density was varied from 0 to 10 J/cm^2; energy densities before and after sample were measured . The pulse shape of incident and passed radiation was also recorded. To study the contribution of self-defocusing and light induced scattering we used schemes b and c (Fig. 1b,c). The change of refractive index was measured with the aid of laser interferometer. The determination of the transmitted radiation energy in the far zone with a small aperture of the field of vision ($\theta=1.8\times10^{-3}$ rad) and measurements of scattering indicatrix in angles from 0 to 30° from the beam axis were performed. The optical limiting results (C_{60}-toluene, $\lambda=0.532$ μm) are presented at Fig.2a . One can see strong nonlinear $E_{out}(E_{in})$ dependence with saturation. 60 and 100-fold energy attenuation was obtained in collimated beam system for C_{60}-toluene solution. The same dependencies for solid-state sample presented at Fig. 2b. Here one can see only 1-10-fold energy attenuation.

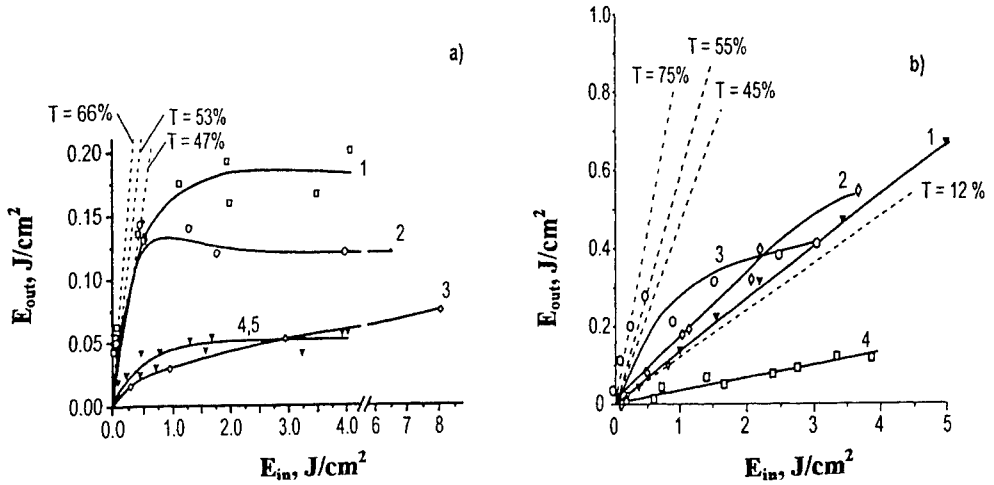


Fig.2 a) optical limiting in fullerene-containing solutions λ=0.53μm, τ=10 ns:
1 – C_{60}-polyacrylnitrile in DMF, T = 48%; 2 – C_{60}-toluene solution (C=0.6 mM), T= 66 %; 3 – C_{60}-toluene solution (C=1.5 mM), T=33 %; 4- C_{60} – fat CCL_4 solution , T=47 %; 5 – polyvinylpyrrolidine C_{60} in water, T=17%

b)optical limiting in fullerene-containing solid-state matrices λ=0.53μm, τ=10 ns: 1 –2 nm microporous glass with C_{60}, T=45 %; 2 -7 nm microporous glass with C_{60}, T=46 %; 3 -17 nm microporous glass with C_{70}, T=12 %; 4 – sol-gel medium with C_{60}, T= 75 %.

Calculations show that RSA can give 10-fold attenuation.We studied the contribution of some other process to nonlinear optical limiting. Our investigations have shown the strong influence of light induced scattering ,caused by fine scale refractive index perturbations in fullerene-containing solutions, whereas the one is practically absent in solid state samples. Optical limiting in solid-state samples is defined exclusively by RSA process. (Fig. 3a,b,c).

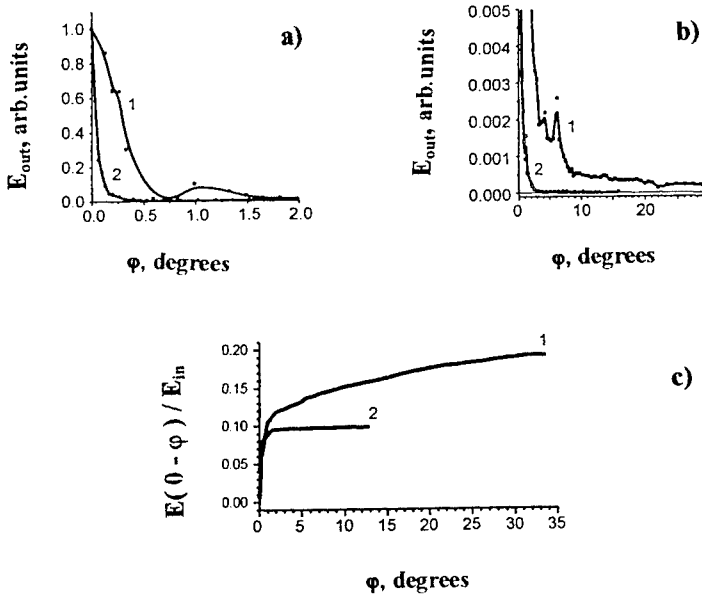


Fig. 3 Results of the measurement of radiation scattering

a), b) scaterring indicatrixes near axis and in large angles correspondingly

c) dependence of limitation level on the angle in which radiation is collected

1 - C_{60}-toluene solution

2 – microporous glass (2 nm microporous glass) with C_{60}

3. THEORETICAL INVESTIGATION OF LIGHT-INDUCED SCATTERING

3.1. *Light-induced heating of fullerene-containing media.*

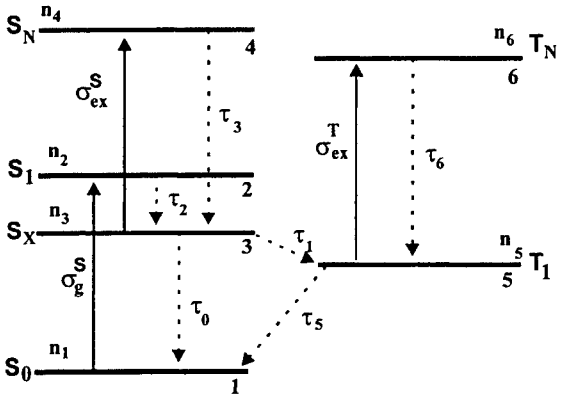


Fig. 4. Energy level diagram. The absorption cross sections are given by σ_g^S, σ_{ex}^S, σ_{ex}^T, where g denotes ground state, ex denotes excited state and S,T denote singlet and triplet state respectively. The life-times are given by τ_0, τ_2, τ_3, τ_5, τ_6 and intersystem crossing by τ_1.; n_i – are the population densities of their respective states. Solid arrowed lines denote radiative transitions; the dotted one denote nonradiative transitions

Fig. 4 shows a simplified diagram of the main six energy levels of fullerenes which take part in RSA mechamism as well in light-induced scattering. Simultaneous solution of rate equations, describing six-level scheme and heating rate equation enables to calculate light-induced heating. The formulas for light-induced heating could be approximated by simple expression:

$$Q(I,\tau) = (T - T_0)/T_0 = \kappa I t / I_s t_p, \qquad (1)$$

where T_0 is initial temperature, I is the incident intensity, I_s is the saturation intensity, t_p is pulse duration. One can see, that medium heating is linear both in intensity and in time. κ is expressed by Eq. (2).

$$\kappa = \delta_F \Delta E_{56} (\sigma_{ex}^T / \sigma_0) / c_p T_0. \qquad (2)$$

where δ_F is a portion of fullerene molecules c_p is one molecule specific heat, σ_0 and σ_{ex}^T are the absorption cross sections from ground state and exited triplet state, ΔE_{56} – energy gap between levels T_1 и T_N. Most of molecules during the pulse are in triplet state, and the main channel of light induced heating is non-radiative decay of the upper triplet level T_N, which lifetime is about 1 fs. All these causes the simplicity of equations 1 and 2. Numerical value κ=0.072 and when $I=10^8$ W/cm^2 the temperature increase to the end of pulse (t_p= *10 ns*) is about 15°.

Therefore, the medium heating is proportional both with intensity and time, the constant of proportionality can be expressed in medium parameters and the main channel of light induced heating is non-radiative decay of the upper triplet level.

3.2 Fine-scale density and refractive index inhomogeneities.

Incident laser beam inhomogeneities are transformed into the heating inhomogeneities, which result in the density and refractive index inhomogeneities. Density change induced by propagation of a nanosecond laser pulse can be described by acoustic-wave equation (3)

$$\partial^2 u/\partial t^2 - G_0 \partial^3 u/\partial t \partial x^2 - c_s^2 \partial^2 u/\partial x^2 = c_s^2 \partial^2 Q(I)/\partial x^2 \qquad (3)$$

$$I(x) = I_0 + I_1(x) = I_0(1 + \varepsilon_L \cos k_T x) \quad (4)$$

Where ε_L is incident beam modulation depth ($\varepsilon_L << 1$), λ_T –is the transverse size of inhomogeneities. Using simplified equation (1) one can obtain the solution of acoustic equation (3):

$$u = I_0 \varepsilon_L \kappa \exp(-G_T \tau / 2)[\tau - \sin(a_\tau \tau)/a_T]\cos(k_T x). \quad (5)$$

Where $a_T = c_s k_T t_p$, $G_T = G_0 k_T^2 t_p$. Two limiting cases have been considered: 1) $a_T >> 1$ and 2) $a_T << 1$. In the first case the sound runs to distance much greater than λ_T in a time of pulse duration. We shall call such perturbations the fine-scale (FS) perturbations. In the second case sound has a time to travel a distance considerable smaller than inhomogeneity size λ_T. We shall call such perturbations large-scale (LS) perturbations.

From (5) one can obtain that FS perturbation growth rate is much higher than the LS one. Therefore FS perturbations make a main contribution to light-induced scattering. Under experimental conditions [4] the condition $a_T >> 1$ is satisfied for $\lambda_T << 80$ μm. The excitation of FS perturbation is limited from the side of high spatial frequencies by the sound damping. Sound damping is proportional to medium viscosity. The higher is viscosity, the smaller is the domain of unstable perturbations. The inclusion of sound damping in toluene leads to the conclusion that $\lambda_T > 0.5$ μm. We think that it is sound damping that is responsible for the absence of light induced scattering in fullerene-containing glass matrices (the glass viscosity is several orders higher than toluene one).

The acoustic equation solution makes it possible to calculate nonlinear phase variation, caused by FS perturbations.

$$\Phi = k \int_0^L \delta n dz \quad (6)$$

where Φ – phase variation, $k = 2\pi/\lambda$, λ is incident radiation wave length, δn refraction index perturbation. One can obtain an average on time and on aperture phase shift:

$$\langle \Phi \rangle = 0.25 k k_{GD} \varepsilon_L \kappa I_{0,0} (1 - \exp(-\alpha L))/\alpha, \quad (7)$$

where k_{GD} - Gladston-Deil constant, for toluene (n_0 =1.49) k_{GD} = 0.6.With a knowledge of $<\Phi>$ we can calculate Strel parameter[5], which defines the decrease of on-axis far-field intensity .

$$St = J_0^2(\langle \Phi \rangle),$$

where J_0 is the Bessel function. The numerical values of St parameter for different values of incident beam modulation depth ε_L are presented in table 1.

Table 1. Nonlinear phase variation and St parameter for different values of ε_L. $M=0.6$ mM, absorption coefficient $\alpha = 3.1$ cm^{-1}, $I=I_{sat}$ (saturation intensity).

ε_L	$5 \cdot 10^{-2}$	10^{-2}	$5 \cdot 10^{-3}$	10^{-3}
St	0.085	0.291	0.762	0.99

By this means, the analysis of FS perturbations development, based on acoustic equation solution with source of heating (1) shows that under experimental conditions[4] the perturbation with transverse scale 0.5 $\mu m < \lambda_T < 80$ μm are developing. Such inhomogeneities cause sufficient decrease of on-axis far-field intensity even when initial modulation depth of incident beam is sufficiently small.

3.3 Laser beam instability, caused by thermal self-action

The approach discussed above can be applied only for sufficient thin medium layer. Otherwise we must take into account that scattering by inhomogeneities leads to change of radiation spatial structure and we must consider density perturbation development and laser pulse propagation simultaneously. Let us estimate diffraction length L_d for FS perturbation. If $L_d = \lambda_T^2/\lambda << L$, the phase distortions created by density perturbations are converted into amplitude distortions by light diffraction many times on the medium length. This medium cannot be considered as thin. For thick medium correct description we must use simultaneous solution of acoustic equation and equation for the complex amplitude of electromagnetic field. In experimental conditions the condition $L_d << L$ is satisfied for $\lambda_T << 40$ μm.

On the other hand for effective interaction of basic and scattered wave the last one should not leave the aperture of the basic beam. Such limitation is defined by the inequality $\lambda_T > 2$ μm. Therefore the range of unstable λ_T values, over which perturbation growth rates are large, is decreased. By this means four inequalities define the conditions of effective FS perturbation development:

$$a_T >> 1, \quad N_F << 1,$$
$$\Gamma_T < 1, \quad N_a < 1.$$

Where $N_F = L_d/L$ – Fresnel number, $N_a = 2\lambda L/a\lambda_T$. In experimental conditions (L = 3 mm, a= 2 mm) these four unequalities are satisfied for 2 μm < λ_T < 40 μm. This transverse scales range is consistent with scattering angle range 0.5°<φ<10°. This result qualitatively correlates with the experimental result[4]. In experimental conditions scattering was observed up to 30°, which probably corresponds to scattering in higher diffraction orders .

Taking into account interaction between density perturbation and intensity spatial distribution the acoustic equation and quasioptic equation for the complex amplitude of electromagnetic field must be solved simultaneously:

$$\begin{aligned} &\partial E/\partial z + (i/2k)\partial^2 E/\partial x^2 + ikk_{GD}uE = 0, \\ &\partial^2 u/\partial t^2 - G_0\partial^3 u/\partial t\partial x^2 - c_s^2\partial^2 u/\partial x^2 = c_s^2\partial^2 Q(I)/\partial x^2, \end{aligned} \tag{8}$$

where z is the longitudial coordinate, E is the complex amplitude of electromagnetic field, $I = |EE^*|$. We linearize the set of equation (8), considering that perturbations of the light field and density are small. The solution of linearized system for amplitude modulation is:

$$w = w_0 \exp[(B_T z k_T \tau)^{0.5} - G_T\tau - \alpha z/2], \tag{9}$$

where w_0 is incident beam modulation depth, $B_T = kLk_{GD}\kappa I/I_s$. Exponential growth of initial inhomogeneity w_0 is indicative of laser beam instability , increment type is typical for convective instability. On the other hand, this instability may be considered as non-stationary stimulated absorption scattering.

4. NUMERICAL SIMULATION

Numerical simulation of thermal self-action of the laser radiation was performed. Maxwell's wave equation in the parabolic or Freshnel approximation is solved. The medium length is divided in N_z amplitude-phase screens. The algorithm for field propagation over a distance $\Delta z = L/N_z$ consists of three parts:

1) Radiation propagation over a distance Δz (diffraction equation solution).
2) Phase incrementing in accordance with nonlinear medium changes (acoustic equation solution)
3) Intensity attenuation in accordance with RSA calculation.

The next system of equations was solved:

$$\begin{aligned} &dn_1/dt = -A_1(n_1 - n_2) + n_3/t_0 + n_5/t_5, \\ &dn_2/dt = A_1(n_1 - n_2) - n_2/t_2, \\ &dn_3/dt = -A_3(n_3 - n_4) + n_2/t_2 - n_3/t_0 - n_3/t_1 + n_4/t_3, \\ &dn_4/dt = A_3(n_3 - n_4) - n_4/t_3, \\ &dn_5/dt = A_5(n_5 - n_6) + n_3/t_1 - n_5/t_5 + n_6/t_6, \\ &dn_6/dt = A_5(n_5 - n_6) - n_6/t_6. \\ &cdT/dt = \delta_F(E_{13}n_3/t_0 + E_{23}n_2/t_{20} + E_{35}n_3/t_1 + E_{34}n_4/t_3 + E_{56}n_6/t_6), \\ &dI/dz = -[A_1n_1 + A_2n_3 + A_3n_5], \\ &\partial^2 u/\partial x^2 - \Gamma_0\partial^3 u/\partial x^2\partial t - c_s^2\partial^2 u/\partial x^2 = c_s^2\partial^2[(T - T_0)/T_0]/\partial x^2, \\ &\partial E/\partial z + (i/2k)\partial^2 E/\partial x^2 = 0. \end{aligned} \tag{10}$$

Here $n_i = N_i/N$ are levels population (see Fig.4), N – fullerene concentration. The system (10) was supplemented by the initial and boundary conditions:

$$
\begin{aligned}
&n_1(t=0)=1, n_3(t=0)=n_5(t=0)=0.\\
&T(t=0)=T_0.\\
&I(z=0)=I_0.\\
&u(t=0)=u'(t=0)=0.\\
&u(x=a/2)=u(x=-a/2)=0.\\
&E(z=0)=A_0+i\Phi_0.\\
&I=|EE^*|,
\end{aligned}
\qquad (11)
$$

where A_0 – initial radiation amplitude, Φ_0 – initial radiation phase. The splitting method yields accurate results if step size Δz is chosen to be small enough (the nonlinear phase variation must be less than π). Minimal size of transverse modulation (scale), considered in calculations, is $\lambda_{T,min} = 2\ \mu m$. The number of screens N_z must be ≥ 200 under the test conditions L = 3mm, $I = 10^8$ - $2.\times10^8$ W/cm^2. The number of transverse coordinate steps N_x is defined by the minimal size of transverse modulation scale. In addition, fast Fourier transform procedure, used in calculations, requires $N_x=2^i$, where i=1,2,3,..m. For $\lambda_{T,min}$ = 2 μm and beam aperture $a \approx 2$ mm we must use N_x=8192.

Two types of incident laser beam were examined:

1) Smooth Gauss intensity profile
2) Beam inntensity profile, modulated by FS inhomogeneities with given modulation scale and depth.

The next calculation results were obtained.

1) Smooth Gauss intensity profile.

Calculations show that very low laser beam inhomogeneities can evolve into light induced scattering if input energy density is sufficiently high (≈ 1.2-1.5 J/cm^2). Dependence of far field axial intensity attenuation, caused by light induced scattering, on incident radiation energy density, is presented at Fig. 5.

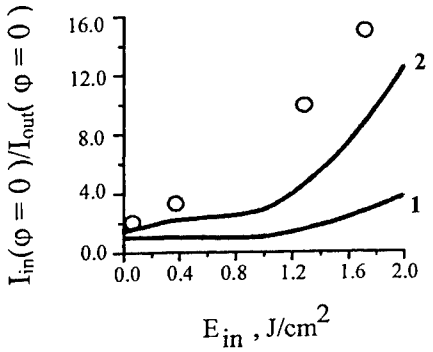


Fig. 5 Dependence of far-field axial intensity attenuation $I_{in}(\varphi = 0)/ I_{out}(\varphi = 0)$ on input energy density (input pulse has gauss shape)
1 - only light induced scattering was taken into account
2 - light induced scattering , RSA and linear absorption were taken into account
o - experimental values (see fig. 2 a) – curve 2)

It is seen that the calculated curve, which takes into account linear absorption, RSA and light induced scattering, lies somewhat lower than the experimental one. It could be accounted by the fact that in calculations pulse had a Gauss shape, whereas a real pulse always contains some inhomogeneities. Fig. 6 demonstrates the dependence of transverse modulation scales, for which instability exhibits maximal spatial – temporal growth, on incident energy density. One can see that the successively higher spatial frequencies (which are beyond the aperture limitation) evolve into light induced scattering as the incident energy density increases. The region of the main and scattered beam interaction, needed for effective energy transferring from the main beam to the scattered one, may be less than cell length if incident energy density is sufficiently high.

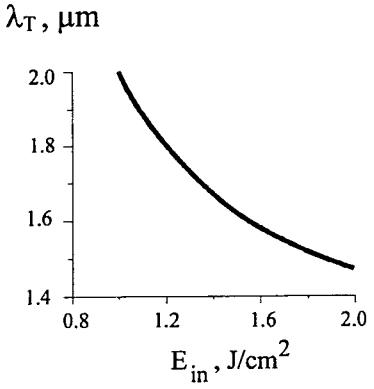


Fig. 6 . The dependence of transverse modulation periods λ_T, for which instability exhibits maximal spatial-temporal growth on incident energy density. (incident pulse has Gauss shape)

2) Gauss intensity profile, modulated by FS inhomogeneities

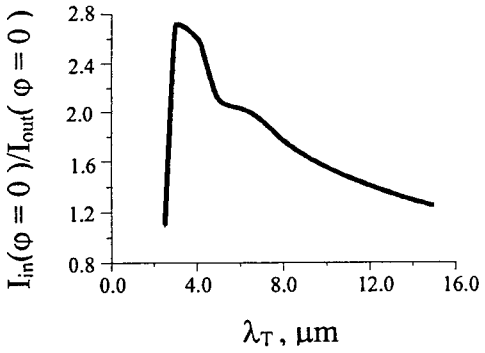


Fig.7 The dependence of far field axial intensity attenuation on transverse modulation period. Calculations were performed for input energy density = 0.5 J/cm^2, i.e. in region where smooth Gauss pulse intensity attenuation is absent. Modulation depth was 30 %. This figure presents attenuation only due to light induced scattering. Taking into account the linear absorption and RSA will make the attenuation 2.3 times more.

Fig. 7 demonstrates the dependence of far field axial intensity attenuation on transverse modulation period. Calculations were performed for input energy density = 0.5 J/cm^2, i.e. in region where smooth Gauss pulse intensity attenuaton is absent. Modulation depth was 30 %. Far field axial intensity attenuation increases with transverse modulation scale decreasing, reaches a maximum when $\lambda_T \approx 3$ μm and then rapidly decreases in accordance with aperture limitation. This correlates well with the evaluations, given in 3.3.

The scattering indicatrix of beam, which contains a number of FS initial inhomogeneities im the range of 3 ÷ 13 μm) is presented at Fig. 8. Modulation depth is 10 %. Incident energy density is 1.5 J/cm^2. In this case axial intensity attenuation on account of scattering is about 5 times. Taking into account the linear dispersion and RSA will make the attenuation 3 times more. Therefore the resulting attenuation will be about 15 times, whereas the experimental one is almost twice as lower (see Fig. 5). It means that in experiment the input pulse modulation depth was less than 10 %.

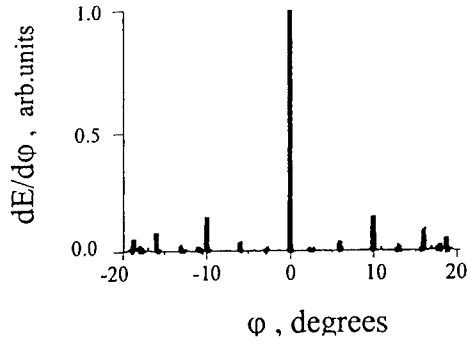


Fig. 8 The scattering indicatrix of beam, which contains a number of FS inhomogeneities in the range of 3-13 μm. Modulation depth is 10 %. Incident energy density is 1.5 J/cm^2.

5. CONCLUSIONS

The propagation of 532 nm 10 ns pulse through C_{60}-toluene solution causes notable light induced heating. Incident laser beam inhomogeneities are transformed into the heating inhomogeneities, which result in the density and refractive index inhomogeneities. It is shown that during 10 ns pulse only fine scale inhomogeneities (2 - 40 μm) have a good chance of progressing.

The excitation of fine-scale perturbations is limited from the side of high spatial frequencies by the sound damping and mainly by diffraction losses due to the finite aperture of the basic beam. The scattering phenomenon caused by light induced fine-scale inhomogeneities leads to notable far-field axial intensity attenuation in addition to RSA effect. Simultaneous consideration of processes of laser beam propagation and perturbations development shows the laser beam instability, caused by thermal self-action.

Numerical simulation of nonlinear scattering is performed. The scattering indicatrixes is presented. Dependencies of far-field axial intensity attenuation on experimental parameters are presented.

6. ACKNOWLEDGMENTS

This work was supported in part by ISTC under Grant № 1454.

7. REFERENCES.

1. V.P.Belousov, I.M. Belousova et al."Fullerenes: structural, physicochemical and nonlinear optical properties." *Journal of Optical Technology* **64**,pp 1081-1109, 1997
2. S. R. Mishra et al. "Investigation of optical limiting in C_{60} solution *"Appl. Phys. Lett.* 1993. **V. 62**, pp.1763-1765;. S.R.Mishra et al ."The role of non-linear scattering in optical limiting in C_{60} solutions." J.Phys.B. At.Mol.Opt.Phys. 27, pp 157-163, 1994
3. I.M.Belousova, V.P.Belousov et al. "Fullerene-based nonlinear optical devices for fast control of spatial, power and temporal characteristics of laser radiation"*Proc.SPIE*, **vol. 3682**, pp.201-209, 1998
4. V.P.Belousov, I.M.Belousova, E.A.Gavronskaya, V.A.Grigor'ev, O.B.Danilov, A.G.Kalintsev, V.E.Krasnopolskii, V.A.Smirnov and E.N.Sosnov,"On the mechanism of optical limitation of laser radiation by fullerene-containing media". *Optics and Spectroscopy*, **87**, pp.772-778, 1999
5. M. Born, E. Wolf *"Principles of Optics"*. Fifth Edition, Pergamon Press. Oxford, 1975.

Fullerene-doped polyimide systems as effective optical power limiting materials in visible and IR ranges

N.V.Kamanina[a*], I.M.Belousova[b], I.V.Bagrov[b], L.N Kaporskii[a], S.A.Tul'skii[b], A.P.Zhevlakov[b]

[a] Vavilov State Optical Institute, 12 Birzhevaya Line, St. Petersburg 199034, Russia

[b] Institute for Laser Physics, 14 Birzhevaya Line, St. Petersburg 199034, Russia

ABSTRACT

The optical limiting of the laser radiation over visible and IR ranges in organic material based on polyimide has been studied. The role of the donor-acceptor interaction mechanism in manifestation of organic molecules nonlinear-optical properties has been established. The fullerene-doped photosensitive polyimide structures have been determined to be effective optical limiting materials for attenuating a power density of more than 2-4 J·cm^{-2}.

Keywords: organic media, nonlinear effects, optical limiting, laser

1. INTRODUCTION

Recently thin fullerene-doped films have been demonstrated to be desirable for the eye and sensor protection from laser radiation.[1,2] Therefore, a proper choice of the polymer matrix, which allows nonlinear optical properties to be revealed over a wide spectral range, is important. For this purpose, A. Kost et al.[3] studied mechanisms of the optical limiting effect in polymethacrylate doped with C_{60}. M.Ouyang et al.[4] synthesized the new complex based on thin films of bicyanovinylpyridine–C_{60} and observed a bistability effect in this system. K. Hosoda et al.[5] found new properties in polysilanes doped with C_{60}. Peculiarities of the optical limiting effect in C_{60}-SiO_2-sol-gel matrix was shown in the paper by V. Belousov et al.[6] V. Danilov et al.[7] investigated the liquid crystal compound doped with C_{70} and found the extreme low value of the threshold energy density for optical limiting. N. Kamanina et al.[8,9] applied the C_{60} and C_{70} mixture as a sensitizer for photosensitive polyimides, which had been before used for spatial light modulator with very high resolution of more than 760 mm^{-1} at a 0.1 level of diffraction efficiency.[10]

In the present paper the optical limiting (OL) of the laser radiation over visible and IR ranges along with spectral properties have been studied in a promising class of the organic materials based on polyimides doped by fullerene C_{70}.

2. EXPERIMENT

3 % and 6.5 % solutions of both non-photosensitive polyimide 81A and photosensitive polyimide 6B in 1,1,2,2–tetrachloroethane were investigated. The general formula of the aromatic polyimide 6B was described in other papers.[11,12] Non-photosensitive polyimide 81A was previously used as a high quality alignment layer for liquid crystal cells[13] and as a film-forming base for solid π-conjugated organic materials.[14] The polyimide solution was doped with fullerene C_{70}. The fullerene concentration was varied from 0.2 wt.% to 0.5 wt.%. It should be mentioned that fullerenes are of relatively high solubility in tetrachloroethane.[15] The 1–3 μm thick polyimide films were spun on the glass substrates coated with transparent indium-tin-oxide contacts.

The experimental setup for the optical limiting investigations in the visible spectral range is analogous to presented in the paper.[9] A pulsed Nd–YAG laser with a pulsewidth of 15 ns was applied as a radiation source. The passive modulation was performed with a LiF crystal. A KDP or CDA crystal was used as a second-harmonic converter. A wavelength of the incident beam was 532 nm. The laser spot was 3-3.5 mm. Energies of the beam incident on the sample and of the beam transmitted through it were measured. A set of light filters was used to vary the incident beam energy. Spectroscopic measurements were carried out with a Perkin–Elmer Lambda 9 instrument in the wavelength range 200-3000 nm.

* E-mail: kamanin@ffm.ioffe.rssi.ru

Laser Optics 2000: Control of Laser Beam Characteristics and Nonlinear Methods for Wavefront Control, Leonid N. Soms, Vladimir E. Sherstobitov, Editors, Proceedings of SPIE Vol. 4353 (2001)
© 2001 SPIE · 0277-786X/01/$15.00

A transmission dependence on an input energy for IR spectral range was measured with a use of a photodissociation iodine laser at a wavelength of 1315 nm. The laser was pumped by a nonmagnetic coaxial Xe lamp in which an interior quartz tube was filled by components of a laser mixture: n-C_3F_7I (RI) and SF_6. Partial pressure of n-C_3F_7I (RI) and SF_6 was 35 and 500 mm of Hg, respectively. The diameter and length of the active zone were 0.8 cm and 50 cm, respectively. The pumping and laser pulsewidth was 8 μs and 50 ns, respectively. A spot on the sample surface was 2 mm. The input energy was measured with a calorimeter. The energy transmitted through a set of filters and the sample was measured with a pyroelectric photometer. The low-power transmission for photosensitive polyimide 6B was about 0.7 and 0.85 at wavelength of 532 nm and 1315 nm, respectively, while the one for non-photosensitive polyimide 81A was about 0.83 and 0.75 at wavelength of 532 nm and 1315 nm, respectively.

3. RESULTS AND DISCUSSION

Since the absorption spectrum of the fullerene-polyimide system is overlapped with the fluorescence spectrum of polyimide matrix at the excitation radiation wavelength of 532 nm, resonance conditions are fulfilled in the polyimide–fullerene structure. This fact allows the OL effect peculiarities in the visible spectral range to be explained in the framework of the Förster model.[9,16] When the electron shell of the polyimide donor fragment overlaps with the one of the fullerene molecule the free electron exchange between donor and acceptor creates the favourable conditions for the formation of charge transfer complexes. An absorption spectrum of the fullerene–polyimide film and a fluorescence spectrum of polyimide matrix is shown in the Fig.1.

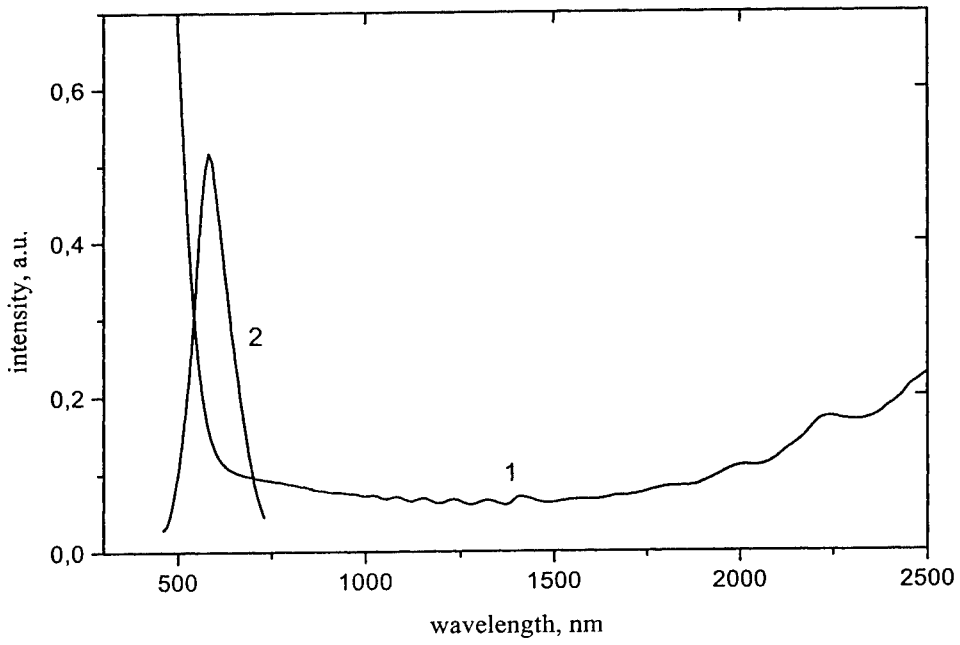


Fig. 1. An absorption spectrum of 0.2 wt% C_{70}–polyimide 6B film (1) and a fluorescence spectrum of pure polyimide matrix (2).

The OL effect is observed in the C_{70}-doped polyimide 6B films, in this case a level of the effect depends on the dopant concentration. The dependence of the output energy density (W_{out}) on the input energy density (W_{in}) is shown in Fig.2. The effect is associated with a formation of excited states in the C_{70} molecule. This effect is determined by a population increase of fullerene excited states. Because the laser pulsewidth (τp) of 15 ns is longer than a time of singlet–triplet interaction (1.2 ns),[17] the triplet state accumulates the excited states. As contrasted to C_{60}, there are some peculiarities of C_{70}. Fullerene C_{70} is of 3-10 times higher absorbance in the 400-700 nm region than C_{60}.[18] Moreover, the absorption spectrum of the C_{70}-polyimide 6B system is red-shifted by 25-30 nm from the absorption spectrum of polyimide sensitized by the C_{60}-C_{70}

mixture. As the result, the absorption spectrum of the C_{70}-polyimide system is more overlapped with the fluorescence spectrum of the polyimide matrix at the wavelength of 532 nm and thus the excitation is transmitted more efficiently.

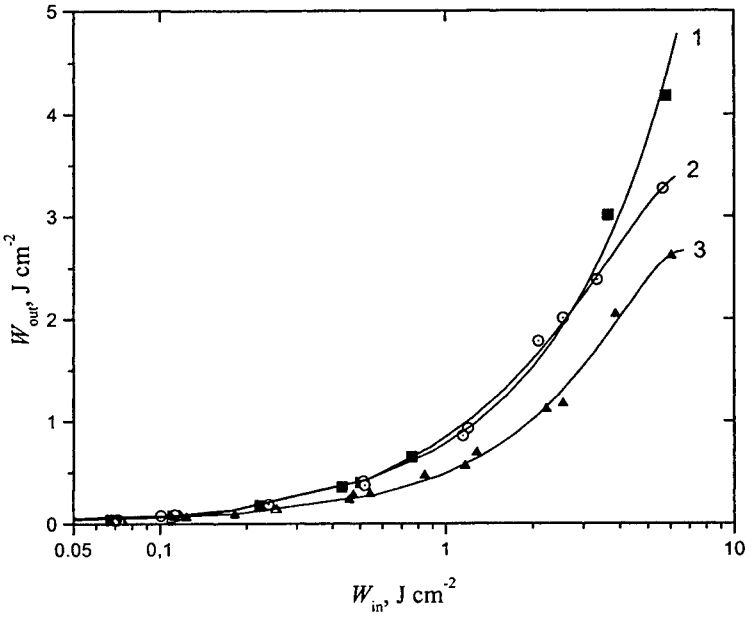


Fig. 2. A dependence of the output energy density (W_{out}) on the input energy density (W_{in}) at λ=532 nm in films: (1) Pure polyimide 6B; (2) polyimide 6B with the 0.2 wt.% fullerene C_{70}; (3) polyimide 6B with 0.5 wt.% fullerene C_{70}.

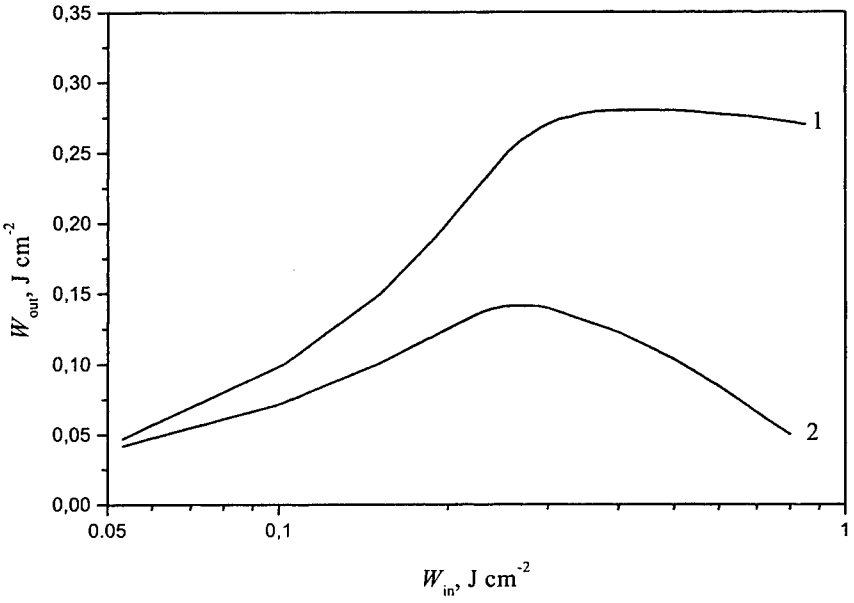


Fig. 3. A dependence of the output energy density (W_{out}) on the input energy density (W_{in}) at λ=1315 nm in films: (1) Polyimide 6B with the 0.2 wt.% fullerene C_{70} and (2) polyimide 6B with 0.5 wt.% fullerene C_{70}.

In this case (see Fig. 2) the nonlinear dependence of transmission begins from the input energy of 350-400 mJ for the C_{70}-polyimide 6B system, while the nonlinearity appears at 150 mJ in the C_{60}-C_{70}-polyimide 6B system (see papers[8,9]), for the same fullerene concentration of 0.5 wt.%. Since the OL level in the C_{70}-polyimide 6B film is about 4 J·cm^{-2}. Therefore, fullerene C_{70}-doped polyimides can be applied in nonlinear optical limiters operating at sufficiently high power densities of the input beam.

The OL effect is first observed in the C_{70}-doped polyimide 6B films in the IR spectral range at wavelength of 1315 nm. The results are presented in the Fig.3. The IR spectral changes are caused by a donor-acceptor complex formation between an polyimide 6B donor fragment and fullerene, because of more electron affinity of fullerene. An intramolecular polyimide 6B acceptor fragment is a diimide group with electron affinity of 1.12–1.46 eV that is smaller than the one of fullerene (2.65 eV).[19] Both the spectral peculiarities (see Fig.1, curve 1) and OL observed in the IR range (see Fig.3, curves 1 and 2) have provoked creation of reverse saturable absorption materials based on polyimide with the high absorption cross section. The absorption cross section of donor-acceptor complex of fullerene with donor polyimide 6B fragment (triphenylamine) was recently estimated by Yu.A. Cherkasov in the paper.[20] It is really about 300 times more than the one of intramolecular polyimide complexes. Therefore the fullerenes are more effective acceptors for the system studied. Moreover, the carriers become free after the charge transfer to the fullerene molecule, where the surface charge is delocalized.[5] Thus the reinforcement of donor-acceptor interaction in the films investigated because of the free-carrier absorption influence the OL effect in the IR spectral range for fullerene-doped structures.

The dependence of W_{out} on W_{in} for fullerene-doped non-photosensitive polyimide 81A at λ=532 nm is shown in Fig.4. As seen from this figure, there are no OL peculiarities for the fullerene-doped structure, while the dopant concentration is twice as more as that in fullerene-doped polyimide 6B (Fig.2, curve 3). Therefore, the processes observed in the fullerene-doped non-photosensitive polyimide films are not associated with reinforcement of the intramolecular donor-acceptor interaction, which is caused by the fullerene introduction in the photosensitive polyimide 6B. Thus, to reveal nonlinear properties in organic materials, the carrier transfer mechanism is to manifest itself in the molecules sensitized by fullerenes. In this case the effective multi-step interaction is possible in the multi-component system. The interaction causes, among other processes, the intramolecular complex formation both in polyimide and between fullerene and polyimide donor fragment, as it was above shown for polyimide 6B structure.

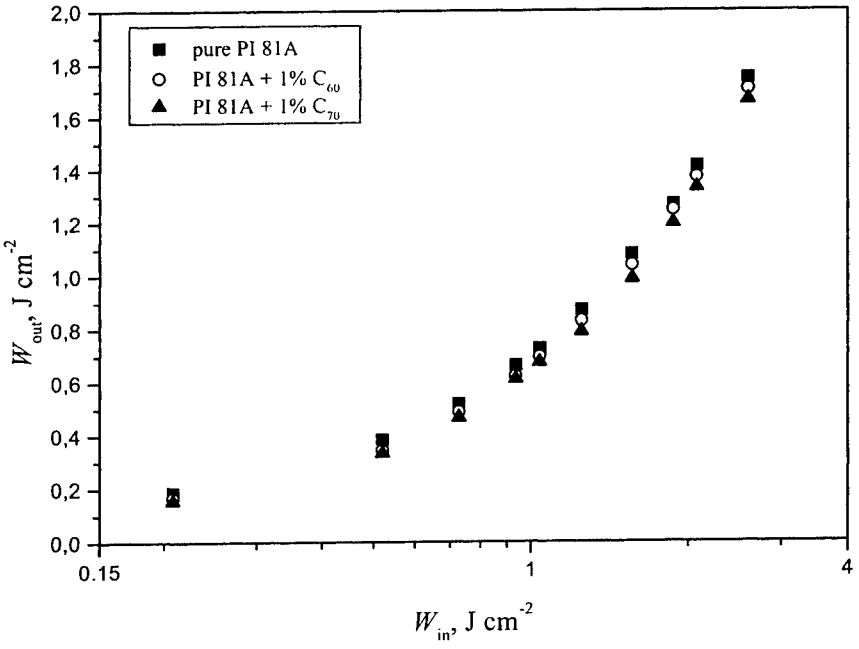


Fig. 4. A dependence of the output energy density (W_{out}) on the input energy density (W_{in}) at λ=532 nm in films: () Pure po lyimide 81A; ( ) polyimide 81A with the 1 wt.% fullerene C_{60}; ( ) polyimide 81A with 1 wt.% fullerene C_{70}.

The OL effect has not been found for non-photosensitive polyimide 81A in the IR spectral range, because the complex formation is absent there. However, OL is likely to be observed at more intense laser beams, when IR-active vibrational modes of fullerene are activated.[21]

4. CONCLUSION

In conclusion, the optical limiting has been detected in C_{70}-doped polyimide 6B structures over visible and IR spectral range. The peculiarities observed could be confirmed by both the essential overlapping of the fullerene-polyimide absorption spectrum with the fluorescence spectrum of polyimide matrix and the complex formation mechanism in the systems investigated. The results obtained have testified the fullerene-doped polyimide 6B structures could be applied as effective optical limiting materials for attenuating a power density of more than 2-4 $J \cdot cm^{-2}$.

No optical limiting effect has been found in the fullerene-doped non-photosensitive polyimide 81A structures in the visible and IR spectral range for laser beam power densities, which were used in the experiments. These results do not contradict with the idea about importance of donor-acceptor interaction mechanism for nonlinear-optical properties existence.

5. ACKNOWLEDGEMENTS

The authors would like to thank Prof. B.V.Kotov and Dr. N.A.Vasilenko (Karpov Research Physical-Chemical Institute, Moscow, Russia) for their help in the work. This work was supported by Russian National Program "Optoelectronic and Laser Technologies" and International Grant ISTC Project 145 "Optical barrier".

6. REFERENCES

1. L.W. Tutt and A. Kost, "Optical limiting performance of C_{60} and C_{70} solutions," *Nature* **356**, pp. 225-226, 1992.
2. S. Couris, E. Koudoumas, A.A. Ruth, and S. Leach, "Concentration and wavelength dependence of the effective third-order susceptibility and optical limiting of C_{60} in toluene solution," *J. Phys. B: At. Mol. Opt. Phys.* **28**, pp. 4537-4554, 1995.
3. A. Kost, L. Tutt, M.B. Klein, T.K. Dougherty, and W.E. Elias, "Optical limiting with C_{60} in polymethyl methacrylate," *Opt. Lett.* **18**, pp. 334-336, 1993.
4. M. Ouyang, K.Z. Wang, H.X. Zhang, Z.Q. Xue, C.H. Huang, D. Qiang, "Study of a novel C_{60}-2,6-bis(2,2-bicyanovinyl)pyridine complex thin film", *Appl. Phys. Lett.* **68**, pp. 2441-2443, 1996.
5. K. Hosoda, K. Tada, M. Ishikawa, and K. Yoshino, "Effect of C_{60} doping on electrical and optical properties of poly [(disilanylene) oligophenylenes]," *Jpn. J. Appl. Phys., Part 2* **36**, pp. L372-L375, 1997.
6. V.P. Belousov, I.M. Belousova, V.G. Bespalov, V.P. Budtov, V.M. Volynkin, V.A. Grigor'ev, O.B. Danilov, A.P. Zhevlakov, A.G. Kalintsev, A.N. Ponomarev, S.A. Tul'skii and E.Yu. Yutanova, "Nonlinear optical properties of fullerene-containing media," *J. Opt. Technol.*, **64**, pp. 870-871, 1997.
7. V.V. Danilov, A.G. Kalintsev, N.V. Kamanina, and S.A. Tul'skii, "Optical limitation effect in a cholesteric liquid crystal - fullerene system," *Tech. Phys. Lett.* **24**, pp. 359-360, 1998.
8. N.V. Kamanina, L.N. Kaporskii, and B.V. Kotov, "Absorption spectra and optical limiting of the fullerene-polyimide system," *Opt. Commun.* **152**, pp. 280-282, 1998.
9. N.V.Kamanina, "Reverse saturable absorption in fullerene-containing polyimides. Applicability of the Förster model," *Opt. Commun.* **162**, pp. 228-232, 1999.
10. N.V. Kamanina and N.A. Vasilenko, "Influence of operating conditions and of interface properties on dynamic characteristics of liquid-crystal spatial light modulators," *Opt. Quantum Electron.* **29**, pp. 1–9, 1997.
11. P. I. Dubenskov, T. S. Zhuravleva, A. V. Vannikov, N. A. Vasilenko, E. V. Lamskaya, V. I. Berendyaev, "Photoconductive properties of some soluble aromatic polyimides," *Vysokomol. Soedin. A*, **30**, pp. 1211–1217, 1988 [in Russian].
12. B. M. Rumyantsev, V. I. Berendyaev, N. A. Vasilenko, S. V. Malenko, and B. V. Kotov, "Photogeneration of charge carriers in layers of soluble photoconducting polyimides sensitized by dyes," *Polym. Sci. A* **39**, pp. 506–512, 1997.
13. N.V.Kamanina, and V.I.Berendyaev, "Influence of solid – liquid crystal interface on characteristics of liquid crystal cells," *Proceed. of SPIE* **3292**, pp. 154–158, 1998.
14. N.V. Kamanina, L.N. Kaporskii, A. Barrientos, A. Leyderman, "Reverse saturable absorption effect in the 2-cyclooctylamino-5-nitropyridine -fullerene doped system," *Proceed. of SPIE*, **3737**, 2000 (to be published).

15. R. S. Ruoff, D. S. Tse, R. Malhotra, and D. S. Lorets, "Solubility of C_{60} in a variety of solvents," *J. Phys. Chem.* **97**, pp. 3379–3383, 1993.
16. T. Förster, "Transfer mechanisms of electronnic excitation," *Disc. Farad. Soc.*, **27**, pp.7-17, 1959.
17. V. P. Belousov, I. M. Belousova, V. P. Budtov, V. V. Danilov, O. B. Danilov, A. G. Kalintsev, and A. A. Mak, "Fullerenes: Structural, physical-chemical, and nonlinear optical properties," *J. Opt. Technol.* **64**, pp. 1081–1109, 1997
18. R.V. Bensasson, T. Hill, C. Lambert, E.J. Land, S. Leach, and T.G. Truscott, "Triplet state absorption studies of C_{70} in benzene solution," *Chem. Phys. Lett.* **206**, pp. 197-202, 1993.
19. A.V. Eletskii and B.M. Smirnov, "Fullerenes and structures of carbon," *Usp. Fiz. Nauk* **165**, pp. 977-1009, 1995 [in Russian].
20. Y. A. Cherkasov, N. V. Kamanina, E. L. Alexandrova, V. I. Berendyaev, N. A. Vasilenko, and B. V. Kotov, "Polyimides: New properties of xerographic, thermoplastic, and liquid-crystal structures," *Proceed. of SPIE* **3471**, pp. 254–260, 1998.
21. K.Lee, R.A.J.Janssen, N.S.Sariciftci, and A.J.Heeger, "Direct evidence of photoinduced electron transfer in conducting-polymer–C_{60} composites by infrared photoexcitation spectroscopy," *Phys. Rev. B*, **49**, pp. 5781-5784, 1994.

Nonstationary mixing in $AgGaSe_2$ crystal

V.V.Apollonov, Yu.A.Shakir*

General Physics Institute RAS, 38 Vavilov str., Moscow, 117333 Russia

ABSTRACT

For the first time three-wave interaction of picosecond pulses was investigated as difference frequency generation with $AgGaSe_2$ crystal. Group velocities and radiation absorption were taken into account during spectral analysis realization. Calculations were executed for CO_2 laser parameters: $100 \div 5$ ps, $15 \div 150$ GW/cm^2. Spectral characteristics and pulse power versus crystal length are represented for difference wavelength 800.5 μm.

Keywords: pulsed CO_2 laser, nonstationary mixing, nonlinear crystal.

1. INTRODUCTION

We proposed to generate powerful half-cycle pulse by difference frequency generation (**DFG**) using CO_2 laser pulses with duration ≥ 100 ps, nonlinear crystal $ZnGeP_2$ and both laser semiconductor reflection and absorption switching to shorten the submillimeter pulse down to half cycle.[1] Later it was found that both $AgGaSe_2$ and $AgGa_{1-x}In_xSe_2$ crystal properties better correspond to this problem solving.[2] Calculation results promised to obtain pulse with more than 10 MW power at duration ~ 200 ps. Refraction data of these crystals [2] allow to present phase-matching characteristic for **DFG** with $AgGaSe_2$ when different combinations of CO_2 lines from both 9-μm and 10-μm branches interact by type 'oe → e' (Fig. 1).

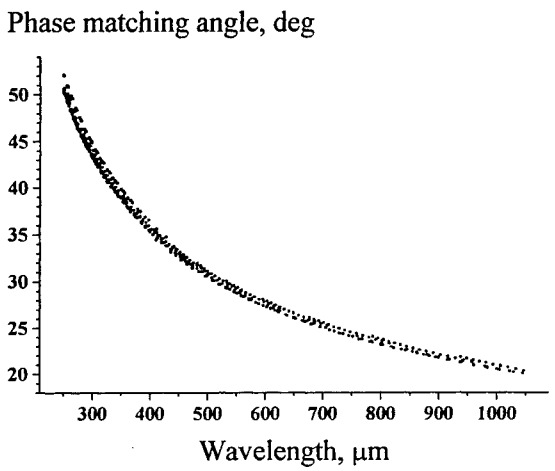


Figure 1. Phase matching angle of DFG with $AgGaSe_2$ by both branches of CO_2 lines.

Also we represent investigation results on three-wave interaction in the $AgGaSe_2$ when laser pulse duration ≤ 100 ps. **DFG** spectral analysis was executed with account of group velocities and radiation absorption. Formulas, figures and table present calculation results.

2. NONSTATIONARY OPTICAL MIXING

We considered plane-wave mixing in approximation of laser fields fixed with frequencies ω_2, ω_3. It is necessary to notice that CO_2 laser frequency absorption is much less than one of difference frequency at submillimeter region.[2] We suppose that phase-matching conditions were fulfiled: $k_1 = k_3 - k_2$. For ultrashort laser pulses process of **DFG** is described by equation:

* Correspondence: Email: shakir@kapella.gpi.ru; Fax: (095) 135-3005.

Laser Optics 2000: Control of Laser Beam Characteristics and Nonlinear Methods for Wavefront Control, Leonid N. Soms, Vladimir E. Sherstobitov, Editors, Proceedings of SPIE Vol. 4353 (2001)
© 2001 SPIE · 0277-786X/01/$15.00

$$\partial A_1/\partial z + 1/u_1 * \partial A_1/\partial t + \delta_1 A_1 = - i\gamma_1 A_3(t-z/u_3)\, A^*_2(t-z/u_2), \quad (1)$$

where $\omega_1=\omega_3-\omega_2$, $A_j(t,z)$ is complex field amplitude, u_j - group velocity, δ_1 - absorption coefficient, nonlinear coupling coefficient is $\gamma_1 = 4\pi\omega_1 d_{eff}/cn_1$, c is light velocity, n_1 - refractive index of crystal at frequency ω_1, d_{eff} - effective nonlinearity.

For spectral analysis an equation (1) solution was represented by Fourier spectrum of amplitudes $A_j(t, z)$. In result

$$(\partial A_1(\Omega_1, z)/\partial z + \delta_1 A_1(\Omega_1, z)) \exp(i\Omega_1 z/u_1) = - i\gamma_1/2\pi \int A_3(\Omega_3, z)\, A^*_2(\Omega_3-\Omega_1, z) \exp(iz(\Omega_2/u_2 - \Omega_3/u_3))\, d\Omega_3,$$

there $A_j(t, z) = 1/2\pi \int A_j(\Omega, z) \exp(i\Omega (t-z/u_j))\, d\Omega$.

If to consider laser Fourier spectrum with Lorentz form i.e.

$$A_{2,3}(\Omega) = (S_{2,3}(0))^{0.5}\, \Delta\omega_{2,3}/(\Delta\omega_{2,3} + i\Omega),$$

where $\Delta\omega_j$ is halfwidth of spectrum then spectral density of difference frequency $S_1(\Omega, z) = |A_1(\Omega, z)|^2$ would be presented by

$$S_1(\Omega, z) = (2\gamma_1/\nu_{13})^2 \exp(-\delta_1 z - z/L_{32})\, F(\Omega, z)\, S_2(0)\, S_3(0)\, S^q_1(\Omega), \quad (2)$$

there length of pulses mismatch is $L_{jk} = 1/(\nu_{jk}\Delta\omega_k)$, inverse group-velocity mismatch is $\nu_{jk} = 1/u_j - 1/u_{jk}$,

$F(\Omega, z) = (\Delta\omega_2\Delta\omega_3/\Delta\omega)^2[\sin^2(\Omega\nu_{13}z/2) + \mathrm{sh}^2(Kz/2)]/(M\Delta\omega_2^2 + \Omega^2)$,

$K=\delta_1 - 1/L_{32}$,

$S^q_1(\Omega)=\Delta\omega^2/(\Delta\omega^2 + \Omega^2)$,

$\Delta\omega = \Delta\omega_2 + \Delta\omega_3$,

$M=[(1-\delta_1 L_{32})/\mu]^2$,

$\mu = \nu_{13}/\nu_{32}$,

Standardized spectral density of difference frequency is defined from (2) by expression

$$S_{1N}(\Omega, z) = M\Delta\omega_2^2/(M\Delta\omega_2^2 + \Omega^2) * [\sin^2(\Omega\nu_{13}z/2) + \mathrm{sh}^2(Kz/2)] / \mathrm{sh}^2(Kz/2) * S^q_1(\Omega). \quad (3)$$

Group-velocity values were calculated using $AgGaSe_2$ refractive index approximation in both submillimeter [2] and infrared [3] ranges. According to these calculations and experiment data[2] we present both used radiation parameters and the crystal characteristics: λ_1=800.5 μm, λ_2=9.24 μm, λ_3=9.13 μm, δ_1= 0.7 cm^{-1}, $\delta_2 \approx \delta_3$= 0.046 cm^{-1}, $\nu_{13} = 1.61*10^{-11}$ c/cm, $\nu_{32} = 1.06*10^{-12}$ c/cm, laser beam square 1 cm^2, crystal length $z \le 1$ cm. The wavelength λ_1 was selected because of convenient cycle value (~2.6 ps).

When $z << L_{32}/(\delta_1 L_{32} - 1)$ and $z << L_{13}$ conditions simultaneously are fulfiled we have quasi-static regime of frequencies mixing and obtain from (3) that $S_{1N}(\Omega, z) = S^q_1(\Omega)$. And therefore halfwidth of **DFG** spectrum $\Delta\omega^{qs}_1 = \Delta\omega = \Delta\omega_2 + \Delta\omega_3$.

In the $AgGaSe_2$ sample case we can realize $z < L_{32}/(\delta_1 L_{32} - 1)$ condition when laser pulses are not separated but second condition ($z << L_{13}$) is fulfiled only for pulse duration ≥ 50 ps (see Table 1). Thus for pulse duration less than 50 ps nonstationary regime has to take place and **DFG** spectrum is described by (3) then halfwidth is $\Delta\omega^{ns}_1 = G(\Delta\omega_2) * \Delta\omega^{qs}_1$.

Table 1. Calculation results.

Laser pulses duration, ps	Mismatch length L_{32}, cm	Mismatch length L_{13}, cm	Quasi-static sum halfwidth, cm^{-1}	Nonstationary halfwidth, cm^{-1}	Submm pulse duration, ps
100	94.2	6.2	0.11	0.1	33.8
50	47.1	3.1	0.21	0.2	20.3
25	23.5	1.56	0.42	0.37	13.8
10	9.4	0.62	1.06	0.66	10.1
5	4.7	0.31	2.12	0.82	9.1
2.5	2.35	0.16	4.24	0.89	8.6

From **DFG** spectrum relative to 12.5 cm^{-1} carrier presented at Figure 2 we determined halfwidth values $\Delta\omega^{ns}_1/(2\pi c)$ for selected laser duration values (Table 1). Comparison of quasi-static and nonstationary halfwidth values shows that coefficient $G(\Delta\omega_2) < 1$. Inverse Fouirier-transformation of spectral density (3) allowed to define submillimeter pulse duration values. At Table 1 it is possible to observe that nonstationary mixing is accompanied by submillimeter pulse narrowing in

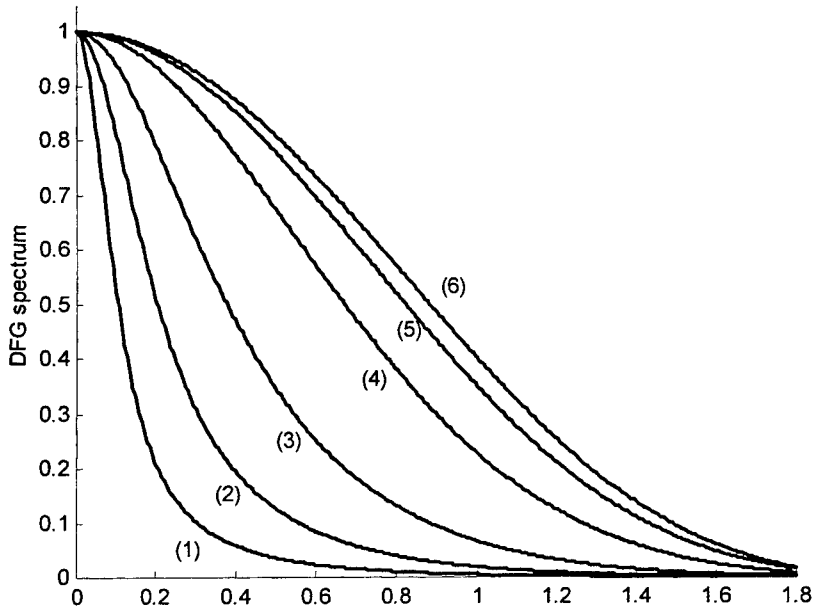


Figure 2. Standardized spectral density of DFG radiation with crystal $AgGaSe_2$ for next values of CO_2 laser pulses duration: (1) 100 ps, (2) 50 ps, (3) 25 ps, (4) 10 ps, (5) 5 ps, (6) 2.5 ps. Crystal length 1 cm.

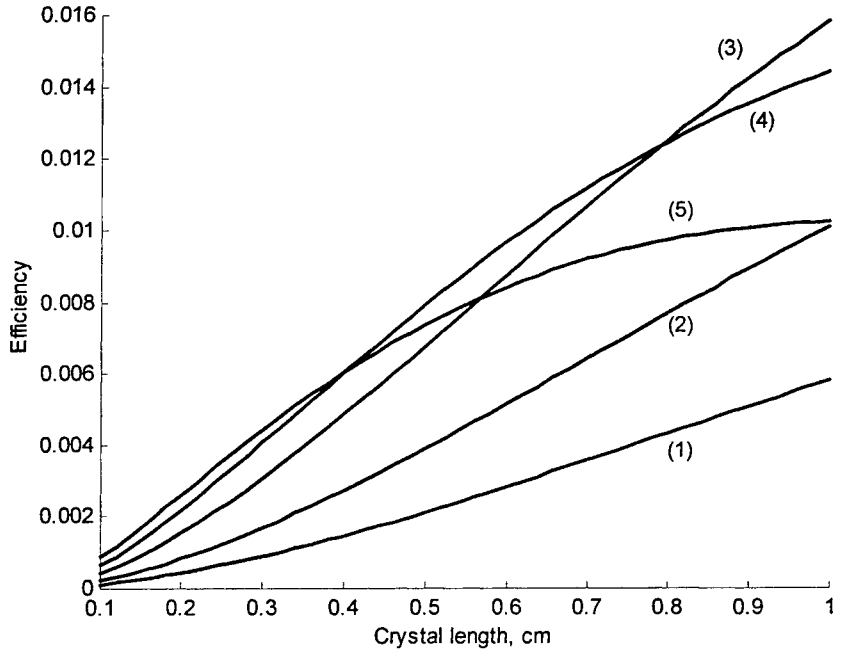


Figure 3. DFG efficiency versus crystal length for next duration and total intensity of laser pulses: (1) 100 ps, 15 GW/cm^2; (2) 50 ps, 30 GW/cm^2; (3) 25 ps, 60 GW/cm^2; (4) 10 ps, 100 GW/cm^2; (5) 5 ps, 150 GW/cm^2.

comparison with laser pulses down to 25 ps. But conversion of the shorter laser pulses drives to submillimeter pulse extention and production of these duration pulses would be complicated. Evidently it will be hard to get the half-cycle pulse by means of $AgGaSe_2$ without additional shortening of submillimeter pulse.

It will be a good plan to shorten laser pulses if it is possible to increase radiation intensity at crystal face.[4] For pulse energy the correlation is known:

$W = cn\rho^2/8 \int\int | A(\Omega, z) |^2 d\Omega,$

where "ρ" is radiation ray radius.

Therefore after (2) integration by frequency we get expression for **DFG** efficiency:

$$\eta = 16\pi\gamma^2 L_{32}^2/(cN\rho^2 q K_1 K_3) * G(z) * P_2 P_3/(P_2 + P_3), \quad (4)$$

where $K_1 = (| q\mu | +1+ \delta_1 L_{32})$,

$K_2 = (| q\mu | -1- \delta_1 L_{32})$,

$K_3 = 1+\delta_1 L_{32}$,

$q = \Delta\omega/\Delta\omega_2$,

$N = n_2 n_3 / n_1$,

$G(z)=\exp(-2\delta_1 z) + \exp(-2z/ L_{32}) -2 * [| q\mu |\exp(-2\delta_1 z -2z/L_{32}) - K_3\exp(-\delta_1 z-(| q\mu | +1)z/L_{32})]/K_2$,

pulse power is $P_j = W_j*\Delta\omega_j$.

DFG efficiency was calculated for above-mentioned parameters and for total laser intensity $P_2 + P_3$ from 15 up to 150 GW/cm^2 (suppose that q = 2). Calculation results are presented on Figure 3. Maximum efficiency values are located between the limits 0.006 and 0.016. These results allow to plan **DFG** radiation realization with pulse power from 90 MW up to 1.5 GW depending on both laser pulse duration and power. It is evidently laser total intensity more than 60 GW/cm^2 using has meaning if you want to obtain high **DFG** power by smaller crystal length. If after radiation mixing ending we'll shorten the producted pulse down to half-cycle duration by refered method[1] then evidently pulse peak power would be close to primordial value.

3. CONCLUSION

Nonstationary mixing of picosecond pulses was investigated for difference frequency generation with $AgGaSe_2$ crystal. Calculations were executed for next parameters of CO_2 laser pump: 100, 50, 25, 10, 5 ps and correspondingly 15, 30, 60, 100, 150 GW/cm^2. Spectral characteristics and pulse power versus crystal length are represented for difference wavelength 800.5 μm. **DFG** efficiency limitation is achieved by calculation results. It was revealed that submillimeter pulse shortening is inescapable for half-cycle duration attainment. Calculation results are comparable with values obtained[2] for 200-ps pulse and allow to plan higher power generation (up to 1.5 GW) with both shorter and half-cycle duration.

REFERENCES

1. V.V.Apollonov, Yu.A.Shakir. "Generation of a Submillimeter Half-Cycle Radiation Pulse". Laser Physics, **9**, pp. 741-743, 1999.
2. V.V.Apollonov, S.P.Lebedev, G.A.Komandin, Yu.A.Shakir, V.V.Badikov, Yu.M.Andreev, A.I.Gribenyukov. "High Power CO_2-Laser Radiation Conversion with $AgGaSe_2$ and $AgGa_{1-x}In_xSe_2$ Crystals". Laser Physics, **9**, pp. 1236-1239, 1999.
3. Eiko Tanaka, Kiyoshi Kato. "Thermo-Optic Dispersion Formula of $AgGaSe_2$ and Its Practical Applications". Appl. Opt., **37**, pp. 561-564, 1998.
4. Acharekar M.A., Morton L.H., van Stryland E.W. "2-μm laser damage and 3–6 μm optical parametric oscillation in $AgGaSe_2$". Proc. SPIE , **2114**, pp. 69-81, 1994.

PHOTOREFRACTIVE PROPERTIES OF DOPED CADMIUM TELLURIDE CRYSTALS

I.N.Agishev[a], A.L.Tolstik[a], V.N.Yakimovich[b], O.K.Khasanov[b]

[a]Department of Laser Physics and Spectroscopy, Belarusian State University,
4, F.Skaryna av., 220050 Minsk, Belarus,
[b]Institute of Solid State and Semiconductor Physics,
Belarus National Academy of Sciences, 220072 Minsk, Belarus

ABSTRACT

In the work consideration was given to investigation into the spectroscopic and nonlinear optical properties of photorefractive semiconductor cadmium telluride crystals doped with vanadium, ferrum and titanium. Introduction of dopants was required to produce an impurity absorption band in the near IR region and enhance the photorefractive properties. Two methods have been used for the production of doped crystals: diffused post-growth doping and growth of doped crystals from melt. Nonlinear optical properties of samples were studied at the wavelength of 1.06 μm in a four-wave mixing scheme. Maximum diffraction efficiency was revealed for the convergence angle of light beams approximating 8°, with the grating period of 7 μm and was equal to 2%. The dynamic grating lifetime was about 0.2 μs.
Keywords: photorefractive nonlinearity, dynamic holograms, cadmium telluride crystals.

1. INTRODUCTION

As is known, photorefractive crystals are used extensively. It suffices to mention the following applications: optical data processing, holographic storage, quantum electronics including dynamic grating lasers and telecommunication systems. The most important requirements for photorefractive materials are the speed of response and sensitivity as well as spectral range of photorefractivity. Among the advantages of photorefractive semiconductor materials, we should note faster response times and batter sensitivity in both the visible and near-infrared regions compared to the conventional oxide-based materials. A notable advance has been made in this field when the photorefractive effect had been revealed in cubic semiconductors without inversion center and belonging to the point $\bar{4}3m$ symmetry group. Their speed of response is due to high mobility of electrons making the afore-mentioned crystals superior to the traditional photorefractive media, such as ferroelectrics and sillenites. Photorefractive effect was observed upon pulse and continuous excitation of a number of crystals from these groups: *InP:Fe*, *CdTe:V*, *CdTe:Mn,V*, *CdTe:Fe*, *CdTe:Ge* [1-6]. As compared to *GaAs* and *InP*, the electro-optical constant of *CdTe* is nearly three times as large. Among other advantages of *CdTe* crystals, one should name their speed and spectral range from 1.0 to 1.5μm. Besides, applications of photorefractive properties may be modified by the appropriate changes in the elemental composition of impurities. Thus, doping of *CdTe* crystal with germanium results in the photorefractive properties of the crystals revealed in a shorter wavelength region with $\lambda \leq 1.0 \mu m$. When passing from single crystals of *CdTe* to solid solutions of *CdMnTe* or *CdHgTe* , modification of the band gap becomes possible. However, it has been previously stated that photorefractive properties are greatly varying from sample to sample [6]. Even an insignificant difference in the concentrations of donor and acceptor centers, or the presence of inevitable residual impurities in nondoped as-grown crystals of *CdTe* may exert a profound effect on the photorefractivity and photorefractive properties [7]. All the foregoing makes the *CdTe*-family crystals very promising candidates for use in fiber-optic communication lines, telecommunication systems, quantum and optoelectronics.

This work presents an experimental investigation of the spectroscopic and nonlinear optical properties for both pure and doped cadmium telluride crystals. *CdTe* crystals were doped with *V*, *Ti* and *Fe* using two methods: diffused post-growth doping and growth of doped crystals from melt.

[a] e-mail:tolstik@phys.bsu.unibel.by

Laser Optics 2000: Control of Laser Beam Characteristics and Nonlinear Methods for Wavefront Control,
Leonid N. Soms, Vladimir E. Sherstobitov, Editors, Proceedings of SPIE Vol. 4353 (2001)
© 2001 SPIE · 0277-786X/01/$15.00

2. GROWTH AND DOPING OF *CdTe* CRYSTALS

The crystals were grown by the modified Bridgman method under the controlled partial pressure of cadmium vapors in quartz ampoules. The growth rate was 10 mm/day at the temperature gradient of 28K/day. The temperature of the melt-containing ampoule was 1390K. The pressure of cadmium vapors was set by the temperature of an empty end of the quartz ampoule that never exceeded 1040 K. The growth conditions lead to the formation of cadmium vacancies in the *CdTe* lattice facilitating subsequent diffusion of the dopant in the crystal and its localization in the cadmium sublattice.

First for the introduction of impurity atoms (vannadium, ferrum or titanium) in cadmium telluride we have used the post-growth diffusion doping of single crystals. This method allows for minimization of structural defects and for optimization of the doping process at various technological stages. Such an approach is easier and more efficient than the multiparametric optimization. The grown single-crystals of *CdTe* were cut into the optical elements with the dimensions 7 x 7 x 5mm, the entrance face of which was coincident with the $(1\bar{1}0)$. This plane also contained the crystallographic orientations [001] and [111] which are essential for the crystal alignment aimed at writing of the photorefractive grating. The process of diffusion was carried out in sealed vacuum-pumped quartz ampoules at a temperature from 1100 to 1200K over a period of 3 –10 days. After annealing the elements were grinded and polished with diamond micropowder having the grain size of $0{,}5\mu m$.

In the process of work we have revealed a strong dependence of the optical properties exhibited by the doped single crystals on the growth conditions and deviation from the stoichiometric composition, and found it necessary to perform a comparative study of the two above-mentioned doping methods.

When the doped crystals were grown from melt, the dopants (vanadium, titanium, ferrum) have been introduced into the initial polycrystalline *CdTe* in amounts of 10^{19} cm^{-3}. Optimum growth conditions for the single crystals were reached when a temperature gradient at the interface was 20-25 K/cm. It has been found that the crystal perfection was dependent on the rate of their post-growth cooling. Reproducibility of the characteristics necessitates that the cooling rate up to temperature of 1170 K should never be greater than 3 K/hour. The developed methods make it possible to produce the samples vanadium-, ferrum- or titanium-doped single crystals of *CdTe* with a mass up to 50 g.

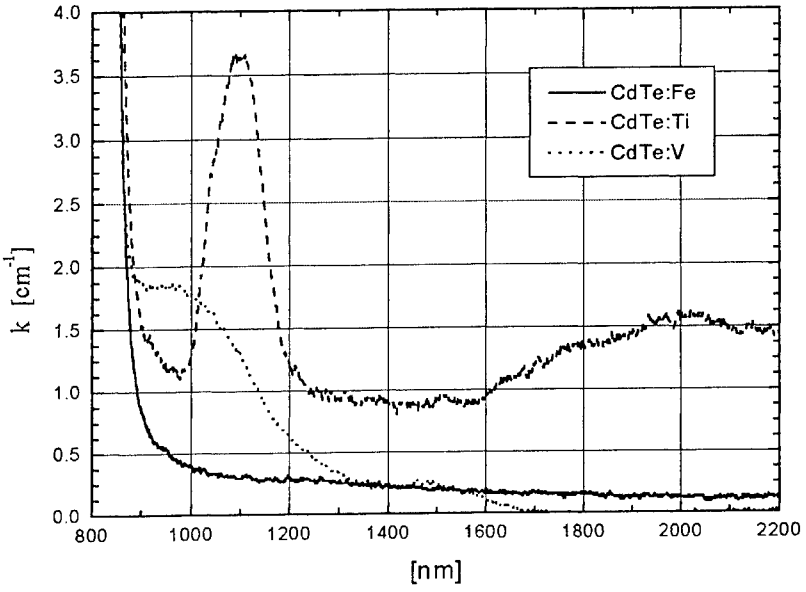


Fig.1. Absorption spectra of doped single crystals of cadmium telluride.

As shown in Fig.1, the absorption spectra of the produced photorefractive optical elements in the region 800 to 2200 nm reveal characteristic bands associated with the dopant presence in the crystal lattice of *CdTe* and display high quality of the investigated samples. As compared to pure *CdTe* sample, the absorption edge of doped crystals is shifted to the region of

longer wavelengths. It has been demonstrated that the absorption spectra of *CdTe:V* single crystals revealed three absorption bands of the impurity , whereas in case of doping with titanium two marked maxima were observed. This is indicative of the difference in energy states for the ions V^{2+} and Ti^{2+} in the crystalline lattice of *CdTe*. As opposed to the spectra of *CdTe:Fe* samples produced in the process of diffusion, absorption spectra of *CdTe:Fe* doped from melt represent broad absorption bands over the whole wavelength range studied. Probably, this is conditioned by the occurrence of associated defects when cadmium telluride is doped from melt by ferrum. Spectral positions of absorption bands characteristic for impurities of vanadium, ferrum or titanium in doped cadmium telluride single crystals point to feasibility of their photorefractivity in the near IR region.

3. FORMATION OF PHOTOREFRACTIVE GRATINGS IN DOPED *CdTe* CRYSTALS

The diffraction efficiency of dynamic holograms in doped *CdTe* crystals has been investigated using the four-wave mixing pattern (Fig.2.). A pulsed yttrium aluminate garnet laser (radiation wavelength λ =1.06μm, generation energy - 10 mJ, pulse duration τ=20ns) was used as a radiation source (1). A dynamic hologram in *CdTe* crystals (8) was formed by signal $E_S = A_S \exp\left[i\left(\vec{k}_S\vec{r} - \omega t + \varphi_S\right)\right]$ and reference $E_1 = A_1 \exp\left[i\left(\vec{k}_1\vec{r} - \omega t + \varphi_1\right)\right]$ waves formed by the mirrors (3,4,7,9). The mirror (5) directed the reconstructing wave $E_2 = A_2 \exp\left[i\left(\vec{k}_2\vec{r} - \omega t + \varphi_2\right)\right]$ opposite to the reference one.

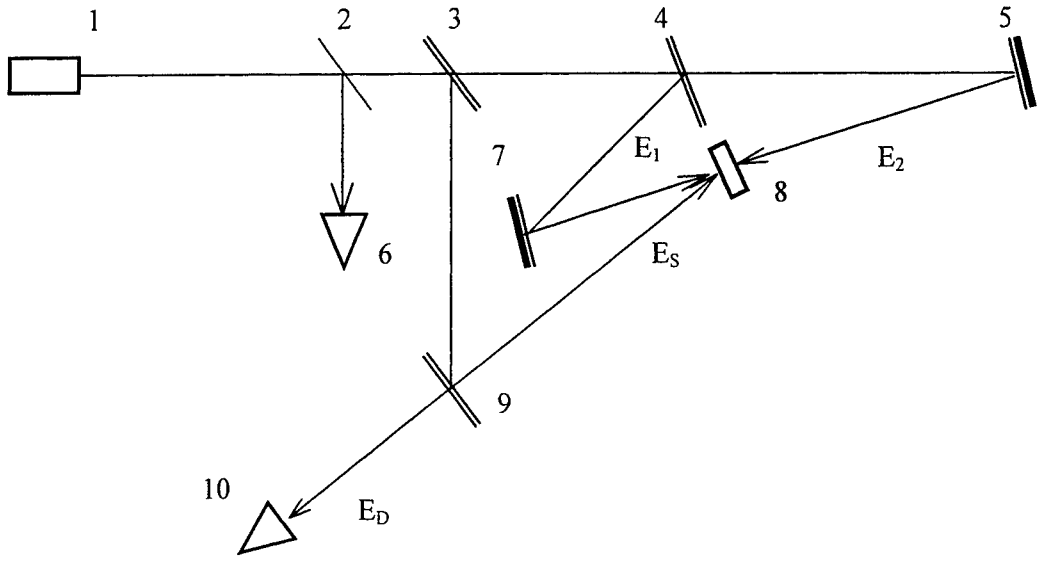


Fig.2. Experimental setup: (1) laser; (2-5,7,9) mirrors; (6) meter measuring the laser energy; (8) *CdTe* crystals; (10) recording system.

In conditions of the hologram reconstruction with opposite propagation directions of the plane reference and reconstructing waves ($\vec{k}_1 + \vec{k}_2 = 0$), the induced wave E_D propagates counter to the signal one E_S ($\vec{k}_D = -\vec{k}_S$). And we have the effect of phase conjugation. The mirror (9) was movable enabling the angle between the directions of the co-propagating pump wave and signal beam to be variable. In this way the spatial period of the recorded dynamic grating was adjustable. The reference wave intensity was monitored with a laser energy meter (6). The energy efficiency of the radiation conversion (i.e. the intensity ratio of the diffracted and reconstructing beams) was determined by a recording system (10) based on photodiode and pulse digital voltmeter.

The diffraction efficiencies have been analyzed depending on the crystal orientation, grating period and intensity of light beams. The intensity ratio of the signal wave and pumping beams was 1:40 providing for the condition of recording linearity. Fig. 3 shows the diffraction efficiency of conversion as a function of the dynamic grating period ***L*** for a single crystal of pure cadmium telluride. The greatest energy exchange has been realized at the cone angle of light beams ~ 8° associated with the grating period of $L = 7\mu m$.

Fig. 4 gives the diffraction efficiency $\xi = I_D / I_2$ as a function of the crystal orientation for the most perfect grown samples. The rotation angle of the crystal β with respect to the normal to the entrance surface was measured between the grating vector $\vec{K} = \vec{k}_1 + \vec{k}_S$ and the crystallographic axis direction [001]. As seen, doping of the crystals has resulted in the appreciable improvement of the diffraction efficiency of dynamic gratings as compared to pure cadmium telluride.

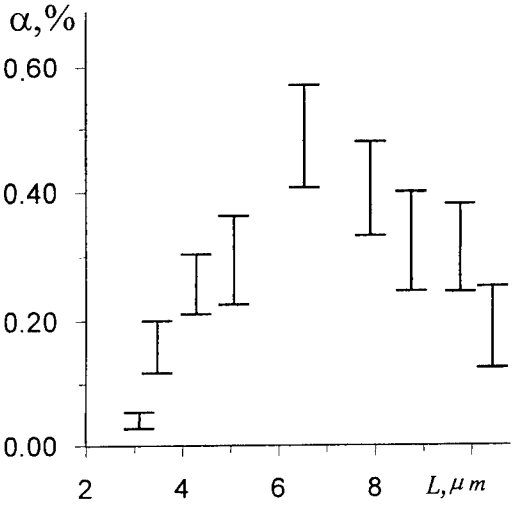


Fig. 3 Diffraction efficiency α as a function of the grating period of the dynamic hologram L for energy of the reference wave 5 mJ.

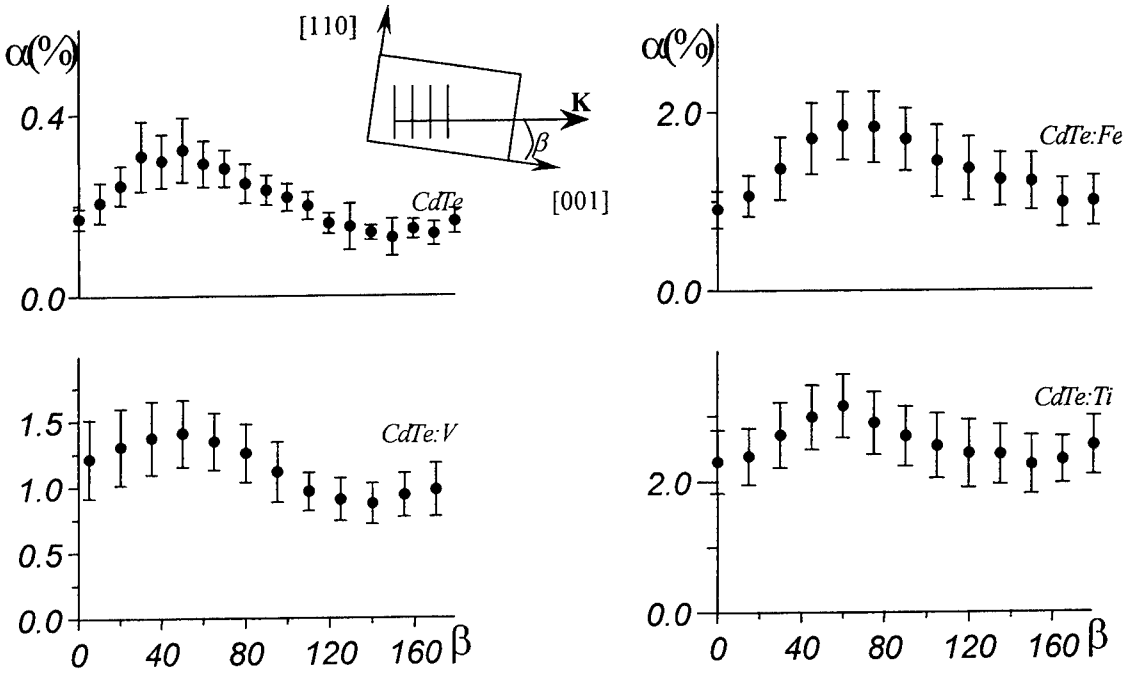


Fig. 4 Diffraction efficiency α as a function of the angle of crystal orientation β for energy of the reference wave 5 mJ, dynamic grating period L=7μm.

Recording of dynamic gratings in all doped crystals was realized with a diffraction efficiency of about 2 % without the use of an external electric field. The best results for *CdTe:V and CdTe:Fe* crystals have been obtained when using the method of growth from melt. In case of doping with titanium the diffusion method was preferable.

Dynamics of the nonlinear response formation in the process of recording photorefractive gratings in a single crystal of cadmium telluride has been studied using the same scheme as in Fig. 2, except of the second YAG laser for the generation of reconstructing wave. The diffraction efficiency as a function of the delay time was measured varying the generation time of the second laser. Fig. 5 presents the experimental results obtained for different doped single crystals of cadmium telluride. As seen, the grating lifetime is ~ 200 ns, and it is practically independent of the dopant. It should be remarked that this value correlates well with the data of Ref.2.

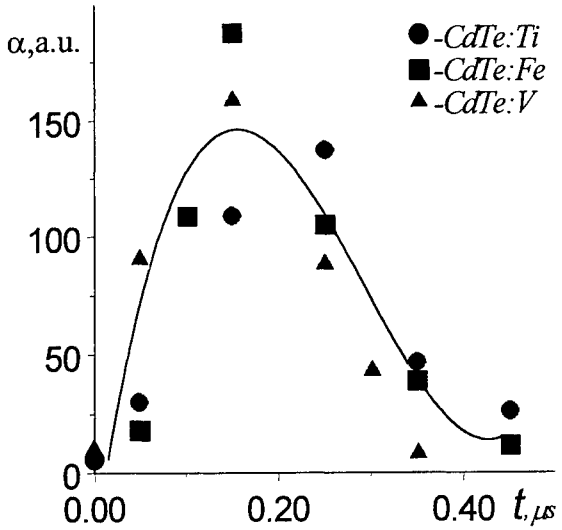


Fig.5 Diffraction efficiency as a function of the delay time of probing impulse

At the same time, the value measured is consistent with the relaxation time of thermal dynamic gratings. Thus, for the thermal diffusivity of cadmium telluride $a \approx 0{,}05$ cm^2/s the time of thermal relaxation of the grating with a period of $L = 7\mu m$ is amounting to $\tau = L^2/4\pi^2 a \approx 250$ ns. Introduction of dopants leads to an increase in the absorption factor (Fig. 1) and results in the optical density value that is approximating the optimum one for thermal nonlinearity ($kd \approx 1.1$) [8].

4. CONCLUSION

In such a manner the experiments performed has demonstrated that doped *CdTe* crystals hold much promise as photorefractive media in the near IR region. Doping of the crystal with vanadium, ferrum and titanium has made it possible to increase diffraction efficiency by a factor of three and more. The diffraction efficiency was about 2% when using a scheme of four-wave mixing without an external electrical field. In the process one should keep in mind that single crystals of cadmium telluride may reveal different mechanisms of nonlinearity necessitating further investigation.

5. REFERENCES

1. J.Strout, A.M.Glass, "Time-resolved photorefractive four-wave mixing in semiconductor materiales", *J. Opt. Soc. Am. B*, **3**, pp.342-344, 1986.
2. R.B.Bylsma, P.M.Bridenbaugh, D.H.Olson, A.M.Glass, "Photorefractive properties of doped cadmium telluride", *Appl. Phys. Letts*, **51**, pp.889-891, 1987.
3. A.Partovi, J.Millerd, E.M.Garmire, M.Ziari, W.H.Steier, S.B.Trivedi, M.B.Klein, "Photorefractivity at 1.5μm in CdTe:V", *Appl. Phys. Lett.*, **57**, pp.846-848, 1990.
4. A.A.Borshch, M.S.Brodin, V.I.Volkov, V.I.Rudenko, "Photorefractive gratings formed in a CdTe cristal by nanosecond laser pulses", *Sov. J. Quantum Electron*, **25**. pp.69-72, 1998.
5. R.N.Schwartz, C.Wang, S.Trivedi, G.V.Jagannathan, F.M.Davidson, P.R.Boyd, U.Lee. "Spectroscopic and photorefractive characterization of cadmium telluride crystals codoped with vanadium and manganese", *Phys. Rev B*, **55**, pp.15378-15381, 1997.
6. K.Shcherbin, F.Ramaz, B.Farid, B.Briat, H.Bardeleben, "Photoinduced charge transfer processes in photorefractive CdTe:Ge", OSA TOPS "Advances in Photorefractive Materials, Effects, and Devices", **27**. pp.54-58. 1999.
7. W.Jantsch, G.Bruntaler. "Persident electron redistribution among deep levels in CdTe", *Appl. Phys. Lett*, **46**. pp.666-668, 1985.
8. H.J.Hoffman, "Thermally induced phase conjugation by transient real-time holography: a review", *J. Opt. Soc. Am. B*, **3**, pp.253-273, 1986.

Splitting effects and power saturation in CW resonant four-wave mixing with two strong fields

S.A. Babin*, S.I. Kablukov*,
U. Hinze, E. Tiemann, B. Wellegehausen,

* Institute of Automation and Electrometry,
Novosibirsk 630090, Russia

Institut für Quantenoptik, Universität Hannover,
Welfengarten 1, D-30167 Hannover, Germany

ABSTRACT

Investigations of resonant spectral structures of four wave mixing (FWM) in molecular sodium are presented. For a double-Λ configuration with strong-weak-strong-weak fields, split components in FWM spectra induced by the strong pump fields are observed. It is shown, that the split components merge into a single peak for a certain ratio of the strong field intensities. A strong correlation between the level splitting effects and saturation behaviour of the FWM-signal is experimentally demonstrated.

1. INTRODUCTION

Nondegenerate four-wave mixing (FWM) is a well established technique for generation of short-wavelength radiation in pulsed and even in continuous-wave (CW) mode.[1–3] For efficient CW FWM resonant interaction with multilevel systems is necessary. By resonant sum-frequency mixing Lyman-α radiation at 121.56 nm of nW power level has been generated recently.[4] Whereas sum-frequency mixing provides shorter output wavelengths, difference frequency mixing delivers higher output powers due to better phase-matching capabilities and compensation of Doppler shifts in gaseous media. In resonantly driven double-Λ configurations of molecular sodium mW power levels have been obtained with powers of the pump fields in the order of ten to hundred mW.[5–7] The demonstrated conversion efficiencies in these experiments appear to be comparable with that achieved in FWM schemes in atomic Pb with pulses of MW pump power,[8] where resonant enhancement is combined with electromagnetically induced transparency (EIT) that eliminates resonant absorption.

The double-Λ configuration has also been explored for parametric generation and self-oscillation in.[9,10] Using counterpropagating pump waves with powers of about 10 μW resonant to transitions in atomic Rb, mirrorless self-oscillation of Stokes- and anti-Stokes output waves was induced. New features of well-known phenomena appear in double-Λ schemes, e.g. phase dependent EIT, which has been demonstrated in atomic Na.[11] Analogous schemes have also been used in experiments on phase conjugation[12,13] and nondegenerate FWM enhanced by the use of coherent population trapping.[14]

In resonant FWM schemes, Stark splitting of levels may be significant, when one or several pump fields are strong. In particular, the EIT effect is closely related to the splitting effect as it occurs because of destructive interference of the split Autler-Townes components.[15] From the above it follows, that the splitting may lead to the elimination of absorption, but on the other hand it may be also one of the limiting factors for the nonlinear susceptibility and as a consequence for the conversion efficiency.[16] Indeed, FWM often exhibits saturation of the output power with an increase of the pump power.[5–7,14,17]

In[17] level splitting in degenerated FWM (DFWM) has been studied in Rb. In that experiment only one pump wave was strong enough to induce a significant splitting, all other waves just served as probe fields in the two-level system. Three peaks observed in DFWM-spectra are closely related to the well-known Mollow triplet[18] in resonance fluorescence.

In the present paper we report on investigations of level splitting effects in nondegenerate four-wave difference frequency mixing, and their relation to saturation of the output signal. A double-Λ configuration in molecular sodium (Fig. 1) with a strong-weak-strong-weak field topology is studied with all the involved levels being split

Laser Optics 2000: Control of Laser Beam Characteristics and Nonlinear Methods for Wavefront Control,
Leonid N. Soms, Vladimir E. Sherstobitov, Editors, Proceedings of SPIE Vol. 4353 (2001)
© 2001 SPIE · 0277-786X/01/$15.00

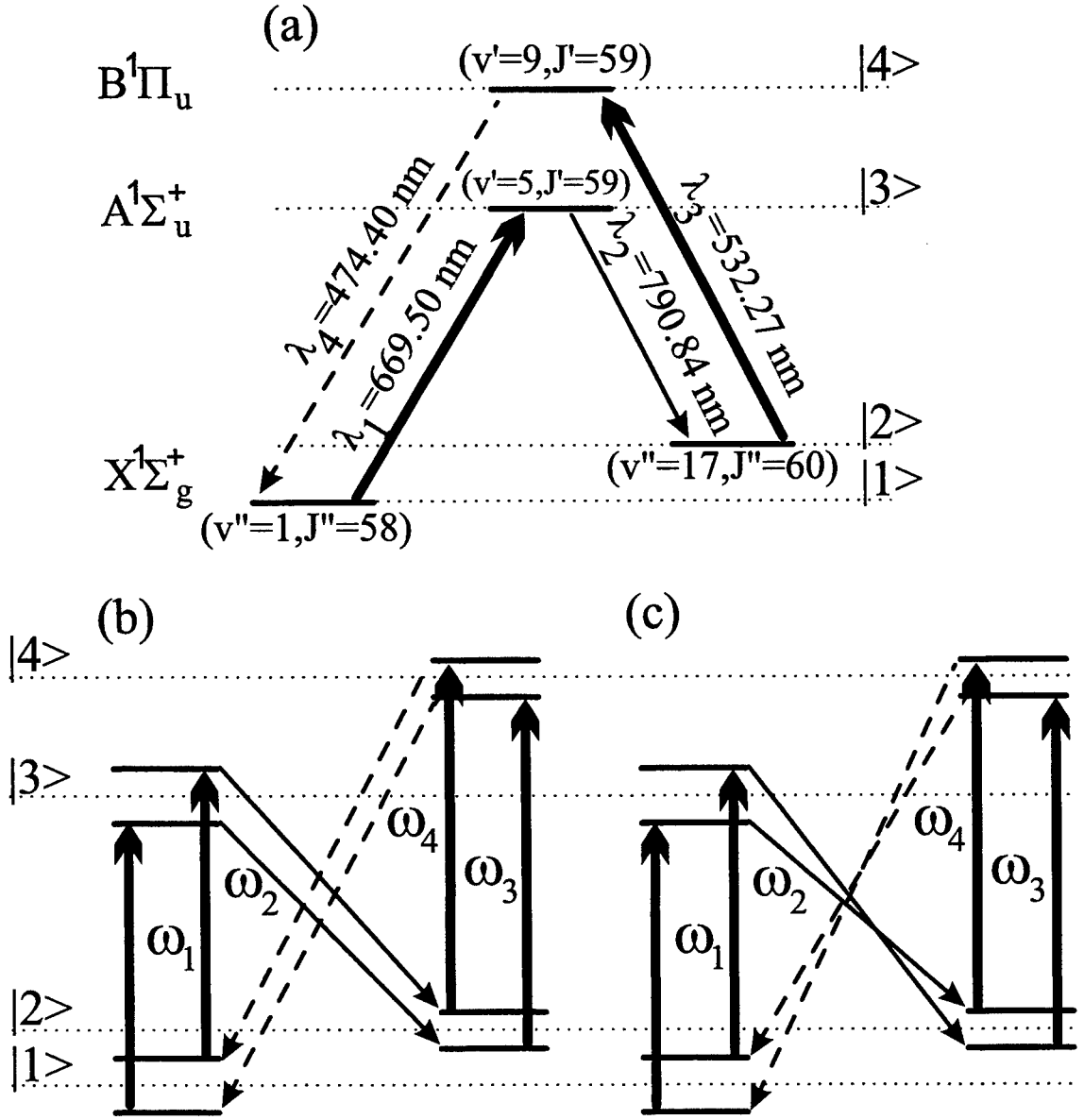


Figure 1. (a) Double Λ-scheme realized in Na_2: $(v,\ J)$ are vibrational and rotational quantum numbers of electronic X, A and B states. Parts (b) and (c) illustrate 4 resonance cycles: levels $|1\rangle$, $|3\rangle$ and $|2\rangle$, $|4\rangle$ are splitted by strong fields with frequencies ω_1 and ω_3, respectively. Thick and thin arrows correspond to strong and weak fields. Dashed arrows represent waves generated in the FWM-process.

and with significant Doppler broadening. It is demonstrated that the presence of a second strong field may change the output spectrum dramatically. Split components can be merged into a single peak for a certain ratio of the intensities of the strong fields. This appearance strongly affects the saturation behavior of the FWM.

2. EXPERIMENTAL

In the configuration under study (Fig. 1), strong fields with frequencies ω_1 and ω_3 are resonant to transitions 1–3 and 2–4 accordingly. A weak probe field ω_2 couples these strongly driven 2-level systems. As a result, a fourth field with frequency $\omega_4 = \omega_1 - \omega_2 + \omega_3$ is generated closing the cycle. A sketch of the experimental setup is shown in Fig. 2. As a pump laser for the strong field at frequency ω_1 we use a DCM dye laser (linewidth $\approx$ 8 MHz) stabilized

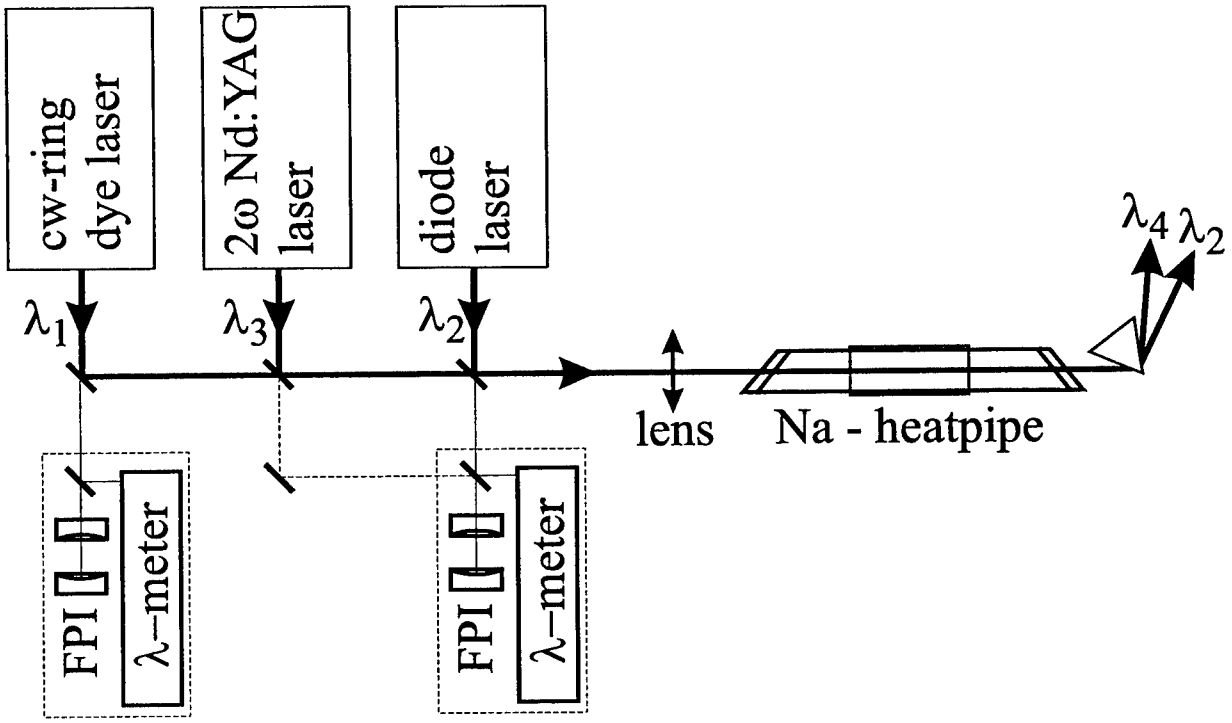


Figure 2. Schematic experimental setup.

by means of a reference cavity. The strong pump field at frequency ω_3 originates from a frequency-doubled Nd:YAG laser (linewidth $\approx$ 10 kHz,[19]) having a tuning range of more than 60 GHz. In our previous experiments[5–7] the 2nd field (ω_2) was generated by operating a Raman laser, pumped by the 1st wave ω_1. However, this did not allow an independent tuning of this field. Therefore, in the present experiments, a diode laser is used as a source of the weak probe field ω_2. This laser has a linewidth of $\approx$100 kHz and can be tuned from 788 to 804 nm with 1 GHz continuous scans. Fabry-Perot interferometers and λ-meters are used for frequency control of all fields.

All three beams are linearly polarized in the same plane and are focused in collinear geometry into a sodium heatpipe (medium length $\approx$ 9 cm). Waist radii of 80 and 90 μm, and intensities 300 and 400 W/cm^2 are estimated for strong 1 and 3 waves, respectively. At the operation temperature (680K) the partial pressure of Na is 0.54 mbar and of Na_2 is 0.15 mbar, giving at thermal equilibrium populations of the involved levels $N_{3,4} \ll N_2 \approx 3 \cdot 10^9 \ll N_1 \approx 4 \cdot 10^{11}$ cm^{-3}.

For investigations of spectral splitting effects caused by the strong pump fields 1 and 3, the weak field 2 serves as a probe field. Tuning the frequency ω_2, the structure of the levels 2 and 3 is tested. The generated fourth field does not tune independently, but follows the frequencies of all involved fields according to $\omega_4 = \omega_1 - \omega_2 + \omega_3$. Detuning the second field, while ω_1 and ω_3 are resonant and kept fixed, leads to a corresponding detuning of the generated fourth field $\Delta_4 = -\Delta_2$. Here $\Delta_4 = \omega_4 - \omega_{41}, \Delta_2 = \omega_2 - \omega_{32}$, and ω_{ij} is the Bohr frequency of $i - j$ transition. The synchronous tuning allows to check the structure of the levels 2,3 and 4,1 simultaneously. Experimentally, this is done by measuring the amplification $g_2(\Delta_2)$ (Raman gain) of a probe field and the generated four-wave mixing power $P_4(\Delta_2)$ at the same time. For that purpose, the 1st pump beam is modulated by a chopper and corresponding signals are detected using lock-in technique.

In the split level picture (Fig. 1b, c) one can immediately construct the expected spectral structure for motionless atoms. The strong fields ω_1 and ω_3 induce a splitting of the levels 1,3 and 2,4, respectively. In general, these splittings are different, according to different Rabi frequencies of the fields. The weak fields ω_2 and ω_4 can connect these levels to closed cycles on four different paths as depicted in Fig. 1b,c. Therefore, the spectrum $P_4(\Delta_2)$ will consist of up to 4 peaks. In case that the Rabi frequencies of the strong fields are equal ($\Omega_1 = \Omega_3$), the splittings of the levels 1,2 and 3,4 become equal. Consequently, the two cycles shown in Fig. 1b degenerate and the spectrum

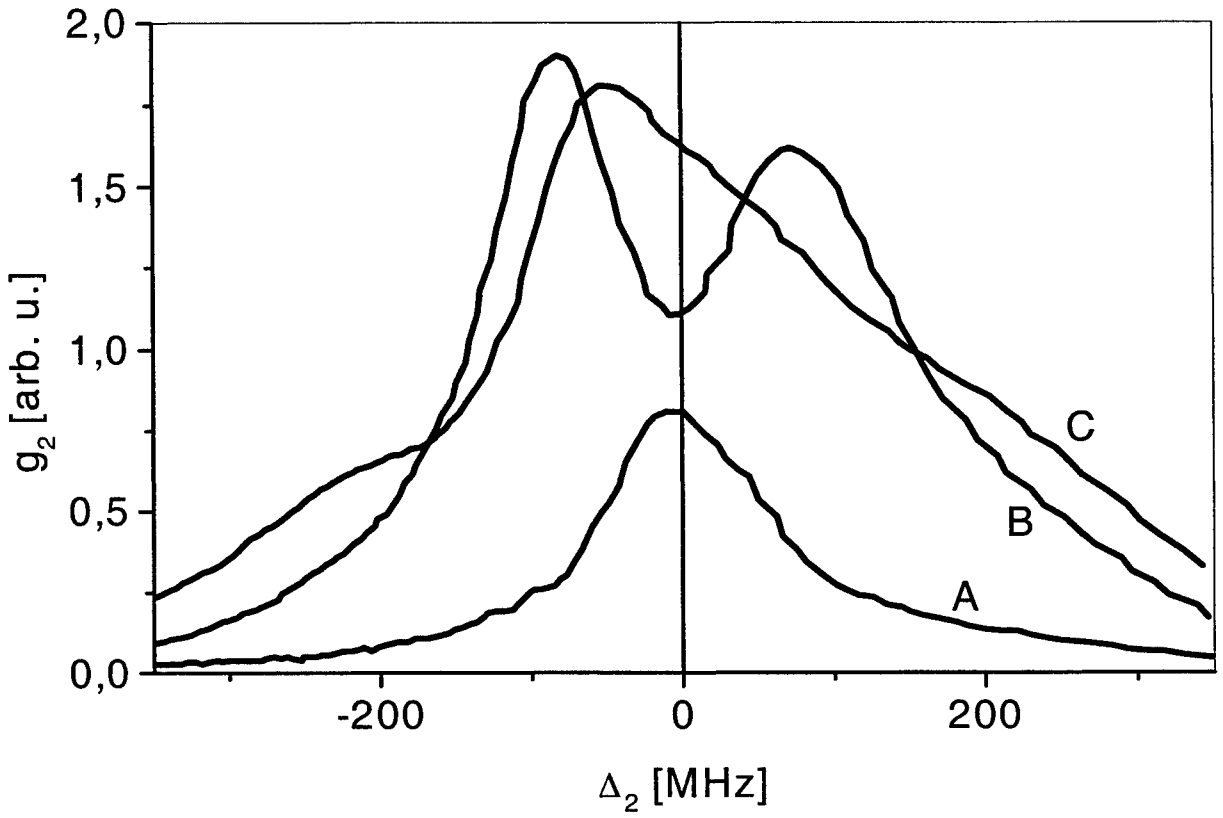


Figure 3. Raman amplification g_2 of the probe field versus its detuning from resonance Δ_2 at the following pump power: curve A: $P_1 = 2$ mW, $P_3 = 0$; curve B: $P_1 = 55$ mW, $P_3 = 0$; curve C: $P_1 = 55$ mW, $P_3 = 100$ mW.

$P_4(\Delta_2)$ reduces to three peaks, where the two paths from Fig. 1c are shifted by $\pm|\Omega_1 + \Omega_3|$ from the degenerate system of Fig. 1b.

A more general theoretical treatment of the spectral behaviour in a Doppler-broadened medium is given in ref.,[16] where analytical expressions have been obtained for the special case $\omega_4 \approx \omega_2$. It was demonstrated that the spectrum may show additional peaks, which arise from interference between different velocity groups, and it was shown that even in a Doppler-broadened medium degeneracy can be achieved for $\Omega_1 \simeq \Omega_3$.

3. RESULTS AND DISCUSSIONS

Typical probe-field spectra $g_2(\Delta_2)$ are shown in Fig. 3. At low pump power P_1 (see Fig. 3, curve A) we observe a single peak of about 130 MHz width (FWHM), which corresponds to Raman amplification in this system. An increase of the pump intensity up to $P_1 \approx 50$ mW results in a splitting of the levels 1,3 and as a consequence in a splitting of the spectrum (Fig. 3, curve B); these two peaks are well-known as the Autler-Townes doublet. The slight asymmetry of the doublet shown here is caused by a small detuning from the exact resonance $\Delta_1 = 0$. In our experiments we use this high sensitivity of the spectrum to set the pump laser frequency ω_1 to the line center (accuracy $\lesssim 100$ MHz). The curves shown here, are measured with a detuning $\Delta_1 \approx -200$ MHz from exact resonance; the position of $\Delta_2 = 0$ in the graphs is conventionally set to the center of the curves.

When a weak third field ω_3 is added, the influence of the splitted levels 1 and 3 is also seen in detuning curve of the generated FWM radiation $P_4(\Delta_2)$ (Fig. 4a, curve A). With increasing P_3 (Fig. 4a, curves A-D) an increasing splitting for the levels 2 and 4 arises. By this, degeneration is approached and finally the two peaks in Fig. 4a almost merge into a single peak (curve D). Exact compensation of the splittings is reached when P_1 is reduced to $P_1 = 30$ mW, while P_3 is kept at the maximum laser output power $P_3 = 100$ mW (curve E). A similar behavior is observed in the spectral dependence of the probe-field $g_2(\Delta_2)$ (Fig. 3, curve C), but here weak side components of

a triplet become noticeable. The power dependence $P_4(P_3)$ (inset of Fig. 4a) is extracted from Fig. 4a at $\Delta_2 \approx 0$ and exhibits a linear growth.

Let us investigate the opposite situation: the power of the first field is set to a relatively low value $P_1 \approx 4$ mW (and by this the splitting of the levels 1 and 3 is reduced). With increasing power P_3 the FWM spectrum $P_4(\Delta_2)$ gets broader (see Fig. 4b, curves A-C). For $P_3 \gg P_1$ ($\Omega_3 \gg \Omega_1$) (curve C), the distorted spectrum resembles splitting, but the peaks are not as clearly separated as in the opposite case $P_1 \gg P_3$ ($\Omega_1 \gg \Omega_3$) (Fig. 4a). The power dependence $P_4(P_3)$ in this case (see inset of Fig. 4b) demonstrates saturation and even a decrease of the output signal at $P_3 > 30$ mW.

Absolute values of the powers are $P_4 \approx 6$ μW for $P_1 = 35$ mW, $P_2 = 0.16$ mW, $P_3 = 65$ mW. The conversion efficiency P_4/P_2 estimated from this is about 4% and the FWM coefficient $c = P_4/(P_1P_2P_3) \approx 16$ W^{-2}. Note, that these are directly measured values. Taking into account losses in the medium and at the cell windows, not complete overlapping of beams etc. (the same reasons as in[5–8]) the primary values will be significantly higher.

Let us compare the characteristic frequency scales in more detail. The Rabi frequencies of the strong fields 1 and 3 at the beam waist are estimated to be $\Omega_{1,3} \approx 0.3$ GHz whereas Ω_2 and Ω_4 are by 2 and 3 orders of magnitude smaller. The relaxation rates of the levels are about $\gamma_1 \approx \gamma_2 \approx 3$ MHz, $\gamma_3 \approx \gamma_4 \approx 30$ MHz including collisional relaxation,[20,16] and Doppler widths are $kv_T^i \approx 0.74, 0.62, 0.93, 1.04$ GHz for the transitions in resonance with the fields $i = 1, 2, 3, 4$ correspondingly. Thus, the condition $\Omega_{2,4} \leq \gamma_i, \gamma_{ij} \ll \Omega_{1,3} < kv_T$ is valid: the Rabi frequencies of the pump fields are larger than the relaxation constants, but smaller than the Doppler width. In this situation the weak field intensities (fields 2,4) do not disturb the system, but the thermal motion may influence the resulting spectra.

Note, that the measured weak-field spectra $g_2(\Delta_2)$ (Fig. 3, curve A) and $P_4(\Delta_2)$ (Fig. 4b, curve A) have a width of about 100 MHz, which is significantly larger than the decay rates. Such broad spectra have been already observed for Na_2 Raman lines (see[20] and references therein), and the broadening effects have been discussed in detail. On the contrary, the observed splitting is smaller than the estimated one (taking the Doppler broadening into account, the separation is $\kappa\Omega_1$, $\kappa = 4\sqrt{(1 - k_2/k_1)k_2/k_1} \simeq 1.4$ in our system). This discrepancy might be caused by transverse and longitudinal intensity variations, which reduce the average intensity by a factor of about 2 in our case. For a quantitative comparison accurate spontaneous decay rates A_{ij} and a consideration of the magnetic sublevels are necessary.

It is remarkable, that for $\Omega_3 \ll \Omega_1$ we see similar pictures in $g_2(\Delta_2)$ and $P_4(\Delta_2)$ (Fig. 3, curve B and Fig. 4a, curves A, B). This means that the 2nd field plays the main role in testing the split structure, while the 3rd field just closes the FWM cycle. In the opposite case, $\Omega_1 \ll \Omega_3$, the 3rd field induces splitting itself, but we observe only broadening without clear splitting in the FWM spectrum (Fig. 4b, curve C). This is because the upper levels in the V-type scheme formed by the fields ω_2, ω_3 (levels 3-2-4) are empty. Consequently two-photon processes are suppressed. In the Λ-type scheme, which is formed by the fields ω_3, ω_4 (levels 2,4,1), with $\omega_4 > \omega_3$ the splitting should be washed out under Doppler broadening.

At $\Omega_3 \approx \Omega_1$, the split components converge in both spectra (Fig. 4a, curves D, E and Fig. 3, curve C). This situation corresponds to Fig. 1b, when the cycles degenerate. The side components in $g_2(\Delta_2)$ correspond to the crossed cycles shown in Fig. 1c and have lower amplitude. Therefore these side peaks are not seen in the FWM spectrum $P_4(\Delta_2)$ (Fig. 4a) and the spectrum is dominated by the degenerated cycles corresponding to Fig. 1b.

Our analysis of the saturation behavior (insets in Fig. 4a,b) leads to the conclusion that the dependence $P_4(P_3)$ starts to saturate at an intensity ratio $P_3/P_1 \approx A_{31}/A_{42}$, corresponding to equal Rabi frequencies $\Omega_3 \approx \Omega_1$. This means, that the saturation parameter for this dependence is not set by the medium but by the intensity of the pump fields 1,3, mutually: increasing P_1 moves the saturation level for P_3 to higher intensities and vice versa. This is not normal saturation, but similar to resonance behavior, i.e. above the resonance value $\Omega_3 > \Omega_1$ the output signal should decrease, which is confirmed by the experiment (see inset in Fig. 4b).

This saturation mechanism has been proposed in[16] and is proved by direct measurements in this work. The picture is consistent with experimental data obtained earlier.[5–7] In case of strong fields resonant to adjacent transitions[14] such a clear picture of Rabi frequency resonance is no more valid, since the fields influence each other and split each level into three components. Velocity averaging complicates the picture further.[21,22] Nevertheless, one expects that in this case, too, the ratio between strong field intensities should influence the number of peaks, their separation and power saturation behavior.

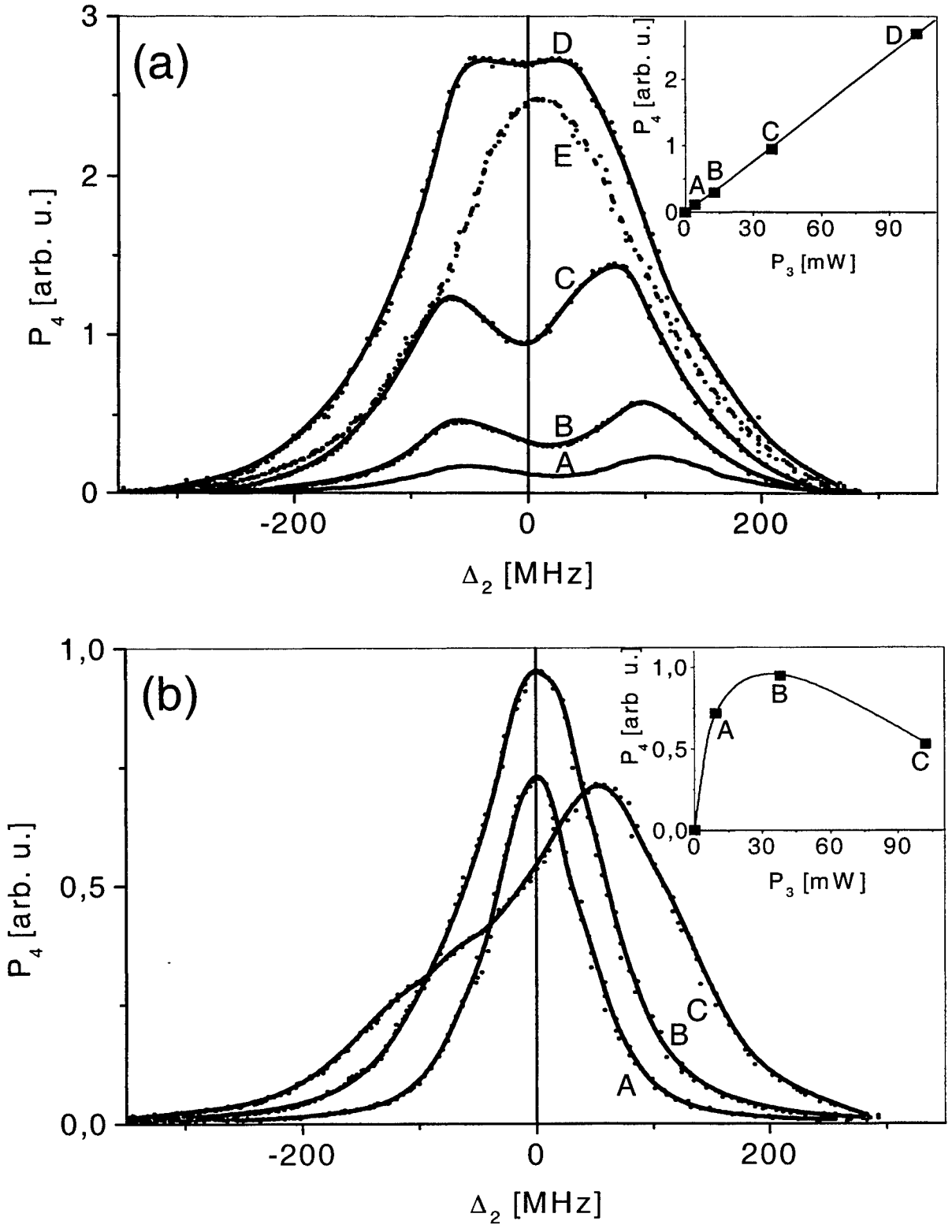


Figure 4. FWM output P_4 at frequency ω_4 versus probe-field detuning Δ_2 at the following pump powers: (a) $P_1 = 65$ mW; $P_3 = 4$ mW (curve A), 13 mW (B), 40 mW (C), 100 mW (D); curve E (dotted) for $P_1 = 30$ mW; $P_3 = 100$ mW; (b) $P_1 = 4$ mW; $P_3 = 10$ mW (curve A), 40 mW (B), 100 mW (C). Insets show the corresponding dependencies $P_4(P_3)$ at $\Delta_2 \approx 0$.

4. CONCLUSION

Summarizing, we demonstrate in the present paper, that splittings in FWM spectra, induced by strong pump fields, can be merged by choosing nearly equal Rabi frequencies of the pump fields. This can be understood as a mutual compensation of the splittings induced by different fields. As a result the FWM signal shows the maximum value at the line center and grows without saturation up to Rabi frequencies comparable with the Doppler width. This is important for the efficient generation of radiation by nonlinear processes, which are currently under investigation.

The authors gratefully acknowledge stimulating discussions with Yu.I.Belousov, E.V. Podivilov and D.A. Shapiro. This work was supported by the Deutsche Forschungsgemeinschaft and RFBR (grant 96-02-0069G/97-02-0016G).

REFERENCES

1. R. R. Freeman, G. C. Bjorklund, N. P. Economou, P. F. Liao, and J. E. Bjorkholm, "Generation of CW VUV coherent radiation by four-wave sum frequency mixing in Sr vapour," *Appl. Phys. Lett.* **33**(8), p. 739, 1978.
2. A. Timmerman and R. Wallenstein, "Generation of tunable single-frequency continuous-wave coherent vacuum-ultraviolet radiation," *Opt. Lett.* **8**(10), p. 517, 1983.
3. L. P. Bolotskikh, A. L. Vysotin, I. Thek-de, O. P. Podavalova, and A. K. Popov, "Continuous-wave frequency mixing and UV generation in sodium vapor," *Appl. Phys. B* **35**(4), pp. 249–252, 1984.
4. K. S. E. Eikema, J. Waltz, and T. W. Hänsch, "Continuous wave coherent lyman-α radiation," *Phys. Rev. Lett.* **83**(19), pp. 3828–3831, 1999.
5. S. Babin, U. Hinze, E. Tiemann, and B. Wellegehausen, "Continuous resonant four-wave mixing in double-Λ level configuration of Na_2," *Opt. Lett.* **21**(15), pp. 1186–1188, 1996.
6. A. Apolonsky, S. Baluschev, U. Hinze, E. Tiemann, and B. Wellegehausen, "Continuous frequency up-conversion in double-Λ scheme in Na_2," *Appl. Phys. B* **64**(4), pp. 435–442, 1997.
7. U. Hinze, L. Meyer, E. Chichkov, B. Tiemann, and B. Wellegehausen, "Continuous parametric amplification in a resonantly driven double-Λ system," *Opt. Comm* **166**(1-6), pp. 127–132, 1999.
8. M. Jain, H. Xia, G. Y. Yin, A. J. Merriam, and S. E. Harris, "Efficient nonlinear frequency conversion with maximal atomic coherence," *Phys. Rev. Lett.* **77**(21), pp. 4326–4329, 1996.
9. M. D. Lukin, P. R. Hemmer, M. Löffer, and M. O. Scully, "Resonant enhancement of parametric processes via radiative interference and induced coherence," *Phys. Rev. Lett.* **81**(13), pp. 2675–2678, 1998.
10. A. S. Zibrov, M. D. Lukin, and M. O. Scully, "Nondegenerate parametric self-oscillation via multiwave mixing ih coherent atomic media," *Phys. Rev. Lett.* **83**(20), p. 4049, 1999.
11. E. A. Korsunsky, N. Leinfellner, A. Huss, S. Balushev, and L. Windholz, "Phase-dependent electomagnetically induced transparency," *Phys. Rev. A* **59**(3), p. 2302, 1999.
12. P. R. Hemmer, D. P. Katz, J. Donohue, M. Cronin-Golomb, M. S. Shahriar, and P. Kumar, "Efficient low-intensity phase conjugation based on coherent population trapping in sodium," *Opt. Lett.* **20**(9), pp. 982–984, 1995.
13. T. T. Grove, E. Rousseau, X.-W. Xia, D. S. Hsiung, and M. S. Shahriar, "Efficient and fast optical phase conjugation by use of two-photon-induced gratings in the orientation of angular momentum," *Opt. Lett.* **22**(22), p. 1677, 1997.
14. B. Lü, W. H. Burkett, and M. Xiao, "Nondegenerate four-wave mixing in a double-Λ system under the influence of coherent population trapping," *Opt. Lett.* **23**(10), p. 804, 19.
15. S. E. Harris, J. E. Field, and A. Imamoğlu, "Nonlinear optical processes using electomagnetically induced transparency," *Phys. Rev. Lett.* **64**(10), pp. 1107–1110, 1990.
16. S. A. Babin, E. V. Podivilov, D. A. Shapiro, U. Hinze, E. Tiemann, and B. Wellegehausen, "Effects of strong driving fields in resonant four-wave mixing schemes with down-conversion," *Phys. Rev. A* **59**(2), pp. 1355–1366, 1999.
17. J. Lin, A. Rubiera, and Y. Zhu, "Nearly resonant four-wave mixing with bichromatic laser fields in a Rb atomic systems," *Phys. Rev. A* **52**(6), pp. 4882–4885, 1995.
18. B. R. Mollow, "Stimulated emission and absorption near resonance for driven systems," *Phys. Rev. A* **5**(5), pp. 2217–2222, 1972.

19. M. Bode, I. Freitag, A. Tünnermann, and H. Welling, "Frequency-tunable 500-mW continous-wave all-solid-state single-frequency source in the blue spectral region," *Opt. Lett.* **22**(16), pp. 1220–1222, 1997.
20. B. Wellegehausen, "Optically pumped CW dimer lasers," *IEEE J. Quant. Electr.* **15**(10), pp. 1108–1130, 1979.
21. A. K. Popov and S. A. Myslivets, "Resonant four-wave frequency mixing in Doppler broadened transitions," *Kvant. Elektr.* **24**(11), pp. 1033–1038, 1997.
22. Y. I. Belousov, E. V. Podivilov, M. G. Stepanov, and D. A. Shapiro, "Nonlinear resonances free of intensity and Doppler broadening," *JETP* **118**(8), 2000.

Intracavity self-adapted photorefractive Fabry-Perot

Nicolas Dubreuil, Laurent Meilhac, Stéphane Victori, Gilles Pauliat, Patrick Georges, Alain Brun, Jean-Michel Jonathan, and Gérald Roosen

Laboratoire Charles Fabry de l'Institut d'Optique, Unité Mixte de Recherche 8501 du Centre National de la Recherche Scientifique, Bât. 503, Centre Scientifique, B.P. 147, 91403 Orsay Cedex, France

ABSTRACT

Dramatic reduction of the number of oscillating modes in CW and pulsed lasers has been observed using a photorefractive crystal placed inside the cavity. Reflective Bragg gratings recorded by the standing waves inside the crystal act with the output coupler as a self-adapted Fabry-Perot filter. Its spectral characteristics enhance mode competitions which can lead to a single mode operation.

Keywords: lasers, photorefractive, mode selection, Fabry-Perot

1. INTRODUCTION

Many lasers oscillate over several simultaneous modes. The reduction of their number may be achieved by intracavity filtering. The insertion of differential losses between the modes can force the laser to operate over a single-mode. Intracavity filters are divided in two classes. The first covers "static" filters using etalons, Lyot filters, interferometer, multiple-mirror cavities, etc.[1] They impose additional return-phase conditions to the oscillating modes, are inserted inside the laser cavity in a fixed geometry and may require precise alignment and adjustments. "Dynamic" filters form a second class, with the particularity to be self-adapted to laser modes. Among them, a wide variety is based on the principle of the intracavity dynamic holography. These holograms that selectively introduce losses on laser modes, are recorded inside various kinds of media by the modes themselves using several physical mechanics, e.g., saturable amplifiers[2], saturable absorbers[3], optically induced thermal gratings[4].

This article focuses on the use of holograms recorded inside photorefractive crystals, where index gratings are generated by an optical interference pattern.[5] Up to now, the main application of photorefractive effect in lasers was phase-conjugate mirrors for self-adaptive correction of mode distorsions.[6] This novel application has been proposed for axial laser mode selection inside the cavity.[7,8] A hologram, recorded in a two wave mixing configuration by the mode structure of the laser itself introduces a strong selectivity between axial modes. We show that the photorefractive filter, which has been used, is similar to a Fabry-Perot filter. The dynamic properties of the photorefractive effect is such that this filter continuously adapts itself to the laser modes. Its spectral behavior is described, as well as the competition process that takes place between oscillating modes. Demonstrations of axial mode selection in CW dye laser, pulsed Ti:Sapphire laser and CW Nd:YVO_4 laser are presented. Finally, we analyze laser mode competition in CW lasers, taking into account laser gain properties and wavelength dependence of the cavity losses induced by the self-adapted Fabry-Perot.

Laser Optics 2000: Control of Laser Beam Characteristics and Nonlinear Methods for Wavefront Control, Leonid N. Soms, Vladimir E. Sherstobitov, Editors, Proceedings of SPIE Vol. 4353 (2001)
© 2001 SPIE · 0277-786X/01/$15.00

3. DEMONSTRATIONS OF AXIAL MODE SELECTION IN CW AND PULSED LASERS

The first experiment with an intracavity photorefractive element (a $BaTiO_3$ crystal) was performed in a continuous-wave dye laser.[7,10]. A drastic reduction of the number of oscillating modes was achieved and single-mode operation reported for a specific position of the $BaTiO_3$ crystal inside the linear cavity. However, this situation could only be observed close to the threshold pump level.

Recently, we applied this technique with success and observed a dramatic reduction of the number of oscillating modes in a pulsed Ti:Sapphire laser,[8] pumped by a Q-switched frequency doubled Nd:YAG laser operating at 10 Hz repetition rate (figure 3). The Ti:Sapphire cavity is closed by a concave mirror and an output plane mirror with a reflectivity of 60 %. Two intracavity prisms allow, by tilting the concave mirror, some spectral tunability and a reduction of the laser spectrum. In these conditions, 40 ns pulses around 760 nm are produced with a maximum energy of 21 mJ. The output light has been analyzed with a 50 GHz free spectral range planar Fabry-Perot interferometer. The measured spectrum is reproduced in figure 4.(a) and shows a spectral line width of 300 GHz.

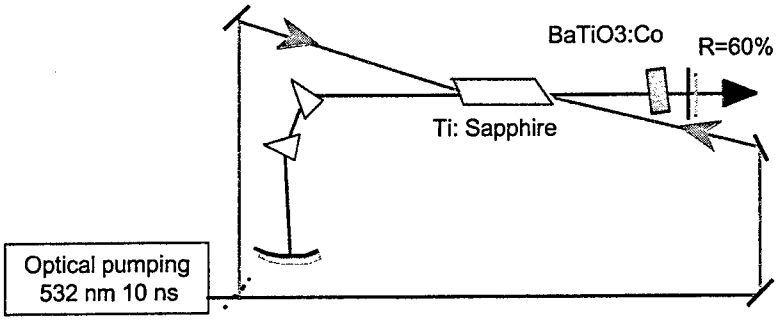
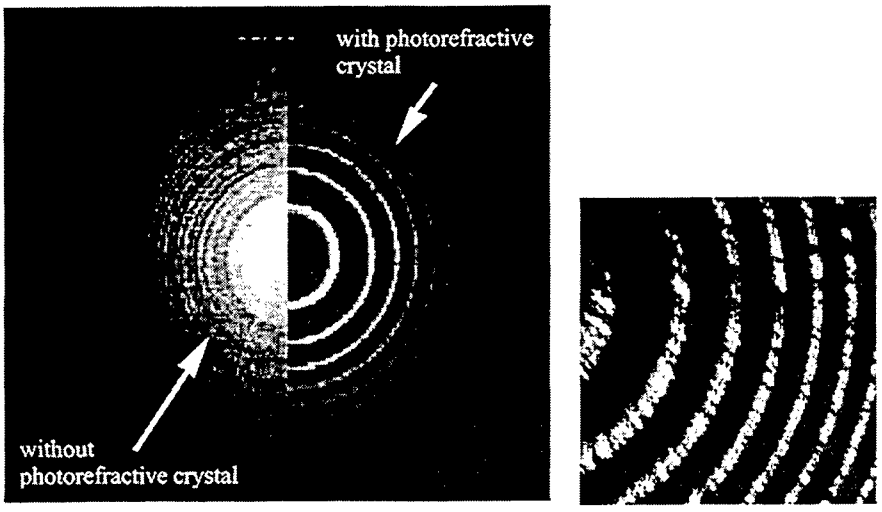


Figure 3. Ti:Sapphire laser cavity with a $BaTiO_3$:Co photorefractive crystal is inserted close to the output coupler.



(a) (b) (c)

Figure 4. Spectrum of the Ti:sapphire laser obtained without (a) and with (b,c) the photorefractive $BaTiO_3$:Co crystal inside the cavity. The initial spectrum is reduced by a ratio of 300. Spectra have been measured with Fabry-Perot interferometers of free spectral range of 50 GHz (a) and 2.2 GHz (b-c).

A 45° cut $BaTiO_3$:Co photorefractive crystal is then inserted inside the cavity, close to the output coupler. Its thickness is 2 mm and its photorefractive gain around 760 nm is approximately equal to 6 cm^{-1}. The laser spectrum measured few seconds later is much narrower (figure 4.(b)). Decreasing the free spectral range of the Fabry-Perot interferometer to 2.2 GHz shows the final doublet structure for the laser (figure 4.(c)). Its line width, estimated to 1 GHz, has therefore been reduced by a ratio 300 from the initial laser spectrum. This doublet structure possibly originates from the inhomogeneous broadening caused by spatial hole burning effect in the amplifier medium.

We performed a second experiment in the continuous-wave regime with a diode-pumped Nd:YVO_4 laser emitting at 1.06 μm.[8] Its cavity arrangement is described in figure 5. The high-reflectivity mirror is directly coated on the input face of the laser crystal and the output mirror reflectivity is taken equal to 50 %. The cavity length is 75 cm. The output spectrum is monitored using a confocal Fabry-Perot scanning interferometer with a 1.5 GHz free spectral range. Figure 6-a (doted curve) represents the initial spectrum which characterizes a multiple mode behavior of the laser.

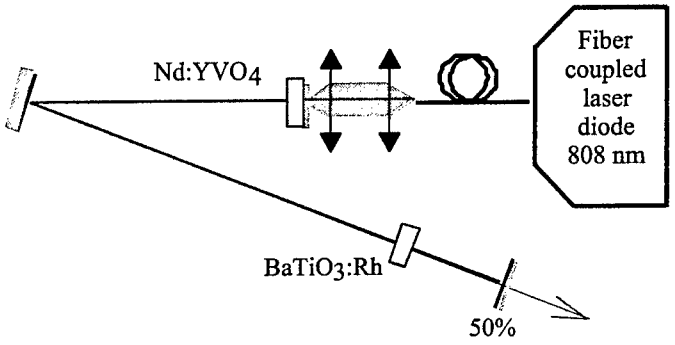


Figure 5. Nd:YVO_4 laser cavity scheme. A $BaTiO_3$:Rh photorefractive crystal is inserted close to the 50 % output coupler.

A 3.5 mm thick, antireflection coated, 45° cut $BaTiO_3$:Rh photorefractive crystal is inserted close to the output coupler. The doping of $BaTiO_3$ crystal with Rhodium extends its sensitivity to longer wavelength and gives comparable photorefractive gain to the previous case. The spectrum of the output light analyzed a few seconds after the insertion of the crystal is shown by curve (b) in figure 6. Its narrow line proves the single-mode operation of the laser. This behavior has been obtained whatever the position of the $BaTiO_3$:Rh crystal with respect to the output coupler.

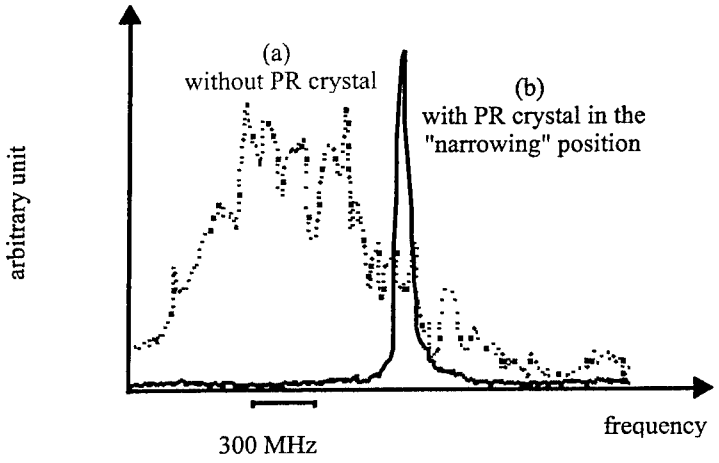


Figure 6. Measured spectra of the Nd:YVO_4 laser without (a) and with (b) an inserted $BaTiO_3$:Rh photorefractive crystal.

2. INTRACAVITY SELF-ADAPTED PHOTOREFRACTIVE FABRY-PEROT

We consider a linear laser cavity inside which a photorefractive crystal is placed close to the output coupler, as shown in figure 1. The standing waves patterns corresponding to each axial mode record competing index gratings inside the photorefractive crystal. This competition is caused by the fact that, in the photorefractive effect, the modulation rate of these gratings is proportional to the mode intensity and inversely proportional to the total intracavity laser intensity. Let's now consider, for simplicity, that a single axial mode (referred to as mode "0") oscillates in the cavity. The contra-propagating waves E+ and E- (figure 1), associated to mode "0" are diffracted by the grating they have just recorded. In the case of the photorefractive crystals used here, the induced index grating is phase shifted by +/- $\pi/2$ with respect to the interference pattern. The crystal orientation may be chosen for constructive interference (see figure1) between wave 2, (diffracted from E+ by the grating), and wave 1 (E- transmitted through the crystal). Consequently, the component made of the Bragg grating and the output coupler mirror is similar to a Fabry-Perot, filter self-adapted to laser modes.

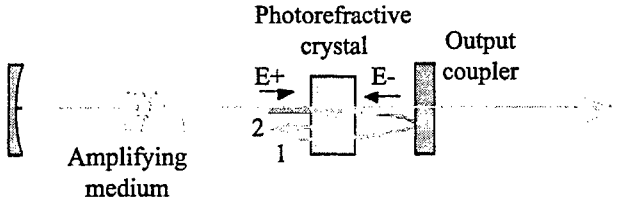


Figure1. Linear laser cavity with a self-adapted Fabry-Perot made by a photorefractive crystal and the output mirror.

The spectral reflectivity of this self-adapted Fabry-Perot is plotted in figure 2 in a single mode case. We supposed that other modes have been suppressed by their respective loss. This is the reflectivity experienced by a reading wave whose wavelength is shifted by $\Delta\lambda$ relatively to the wavelength of the writing wave. In this example, the photorefractive gain of the crystal has been taken equal to 6 cm^{-1}, its thickness is 2 mm; the output coupler reflectivity is 50 % and is placed at 2 cm from the photorefractive crystal. This reflectivity was obtained by solving numerically the classical two waves coupling equations, taking into account the phase relation imposed by the output mirror.[9] The envelope of the curve reflects the Bragg selectivity of the thick grating written in the crystal. The periodic structure describes the multiple interference phenomena taking place between the grating and the output mirror. The frequency spacing between two peaks is the free spectral range of this Fabry-Perot and is inversely proportional to the distance from the crystal to the mirror.

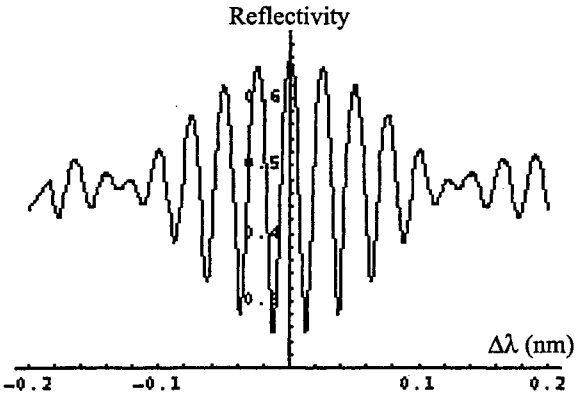


Figure 2. Reflectivity behavior of the self-adapted phototrefractive Fabry-Perot.

4. MODELING OF CW LASERS

The previous experimental results show the efficiency of an intracavity self-adapted photrefractive Fabry-Perot for reducing the number of oscillating laser modes. Although, some difficulties remain, as reported in the case of the dye laser experiment. For a better understanding we analyzed CW laser mode competition with a model taking into account the laser gain properties and the slective losses of the photorefractive Fabry-Perot.[11]

A CW standing wave laser cavity with a 4-level, homogeneously broadened gain medium is considered. We take into account the residual inhomogeneity, induced by spatial hole burning effect, which shapes the population inversion. An other laser axial mode can take advantage of this non-uniform gain distribution to oscillate. A diffusion process is also considered, which smoothes the spatial hole burning effect.[12] In a first step, one mode is considered to oscillate. From the rate equations and the cavity geometry we calculate the longitudinal gain distribution along the laser crystal. This laser mode records a grating inside the photorefractive crystal. The calculated gain experienced by the other laser modes is then compared to their losses imposed by the spectral behavior of the photorefractive Fabry-Perot.

We first applied our model to the dye laser experiment reported by Whitten and Ramsey.[7,10] Energy diffusion is negligible in such a laser. We assume that mode "0" is the only one to oscillate. The calculated gain and losses experienced by 20 modes close to mode "0" are plotted in figure 7. The gain (doted curve) has been calculated for pump intensities equal to 1.5 and 3 times the dye laser threshold intensity. The losses are imposed by the self-adapted Fabry-Perot transmission and have been plotted (solid and dashed lines) for two positions of the photorefractive crystal inside the cavity. The solid line curve is obtained when the distance between the front mirror and the active medium (d_2 of figure 7) is equal to the Fabry-Perot thickness (d_1 of figure 7). The dashed line curve represents loss evolution when $d_1 < d_2$. This simulation agrees with the observation of Whitten and Ramsey. Particularly, the loss level is higher than the gain level for any mode, except mode "0", near to threshold and in the situation where $d_1 = d_2$. A single-mode operation can be achieved in this situation because the loss and gain curve periodicities are equal. But this is limited to a moderate pump level, as reported in reference 7. In addition, a change in the Fabry-Perot thickness induces a variation of the loss periodicity and a single-mode operation can never be achieved. This is illustrated in figure 7, where the dashed line curve need to be compared to the gain curves. A couple of modes have a gain higher than their loss and reach the threshold condition. The number of oscillating modes is reduced but the laser can not oscillate over one single-mode.

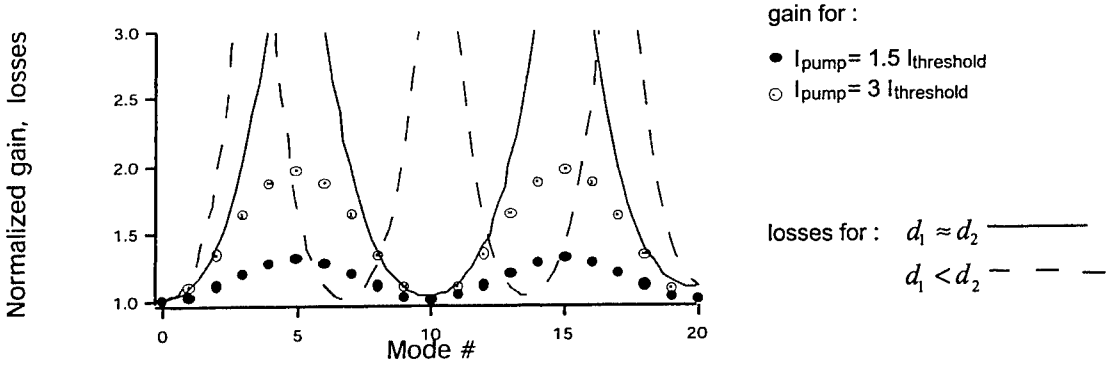


Figure 7. Calculated gain (dots) and loss levels (lines) for 20 modes close to the oscillating mode "0' in the case of the dye laser. The pump intensity is 1.5 and 3 times the threshold pump intensity. The selective loss level (Fabry-Perot transmission) is plotted when the distance d_2 between the front mirror and the active medium is equal (solid line) or longer (dashed line) than the Fabry-Perot thickness d_1 .

The same comparisons have been performed for the Nd:YVO_4 laser experiment reported in part 3. As the diffusion coefficient is unknown is this medium, we set it to 0 $m^2.s^{-1}$, which favors multimode operation. Considering the cavity geometry described previously, the calculated gain and losses experienced for 20 modes near to lasing mode "0" are plotted in figure 8. One can see that for a pump intensity as high as 10 times above threshold pump intensity a single-mode oscillates. It is mainly because the amplifier medium is placed at one end of the laser cavity. It is worth noticing that such a laser is not sensitive to the Fabry-Perot thickness, as it was experimentaly reported.

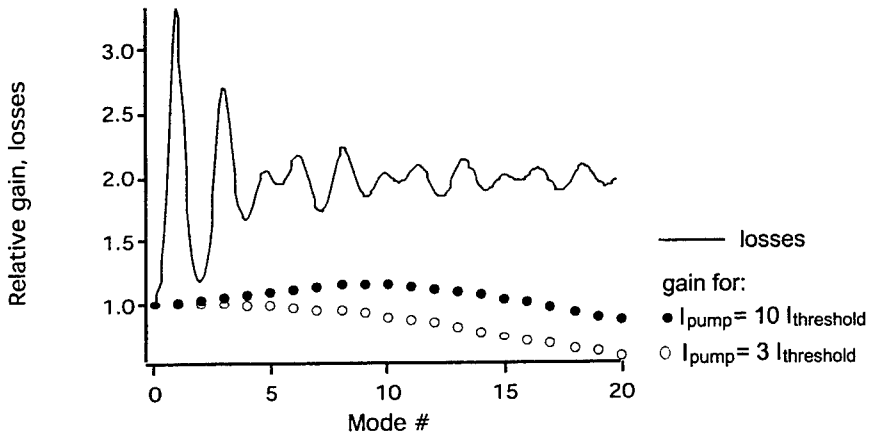


Figure 8. Calculated gain (dots) and loss levels (line curve) for 20 modes close to the only oscillating mode "0' in the case of Nd:YVO_4 laser experiment reported in part 3. The gain is plotted for pump intensities equal to 3 and 10 times the threshold pump intensity.

5. CONCLUSIONS

We have reviewed experimental results on the use of a self-adapted photorefractive Fabry-Perot inside laser cavity. This technique has been used with success in both CW and pulsed laser. By self-adaptation to the laser modes, it does not require, as fixed Fabry-Perot étalons or Lyot filters do, precise adjustment to the wavelength of oscillating modes. In addition, the insertion of the crystal does not significantly change the geometry of the laser. The wide variety of existing photorefractive crystals makes the principle applicable to many lasers. The numerical model that we elaborated, is able to predict the maximum pump intensity under which single-mode operation is maintained. Specific tailoring of the Fabry-Perot characteristics (photorefractive gain, crystal thickness and position) may be achieved to favor single-mode operation. We are studying new geometries, in two and four waves mixing configuration. Other perspectives are the use of this intracavity dynamic holography principle for spatial mode shapping.

6. ACKNOWLEDGEMENTS

We wish to thank Nicolas Huot who participated to the realization of the Ti:Sapphire and Nd:YVO_4 laser experiments. We are also grateful to Daniel Rytz from Forschungsinstitut für Minerallische Werkstoffe Edelsteine/Edelmetalle GmbH, Struthstr. 2, 55743 Idar-Oberstein, Germany (FEE) for his continuing support, for many fruitful discussions, and for providing the $BaTiO_3$ samples.

7. REFERENCES

1. A. E. Siegman, *Lasers*, pp. 524-531, University Science Books, Sausalito, California, 1986.
2. P. Sillard, A. Brignon, and J.-P. Huignard, "Loop resonators with self-pumped phase-conjugate mirrors in solid-state saturable amplifiers," *J. Opt. Soc. Am.* **B 14**, pp. 2049-2058, 1997.
3. M. Horowitz, R. Daisy, and B. Fisher, "Filtering behavior of a self-induced three mirror cavity formed by intracavity wave mixing in saturable absorber," *Opt. Lett.* 21, pp. 2[illegible]-501, 1996
4. S. Camacho-Lopez, and M. J. Damzen, "Self-starting Nd:YAG holographic laser oscillator with a thermal grating," *Opt. Lett.* 24, pp. 753-755, 1999.
5. A. Yariv, *Quantum Electronics*, Ch. 19, pp. 516-527, Third edition, Wiley, New York, 1989.
6. J. Feinberg and K. R. MacDonald in *Photorefractive materials and their applications II*, chapter 5, Topics in Applied Physics, Vol. 62, SpringerVerlag, Berlin, 1989.
7. W. B. Whitten and J. M. Ramsey, "Mode selection in a continuous-wave dye laser with an intracavity photorefractive element," *Opt. Lett.* **12**, pp. 117-119, 1987.
8. N. Huot, J. M. Jonathan, G. Pauliat, P. Georges, A. Brun, and G. Roosen, "Laser mode manipulation by intracavity dynamic holography: Application to mode selection," *Appl. Phys.* **B 69**, pp. 155-157, 1999.
9. L. Meilhac, N. Dubreuil, J.-M. Jonathan, G. Pauliat, G. Roosen, "Selectivity and stability of an intracavity dynamic holographic mode selector," PR'99, *Seventh Topical Meeting on Photorefractive Materials Effects and Devices*, June 1999, Elsinore, Denmark, paper WA23PD.
10. J. M. Ramsey, W. B. Whitten, "Controlled scanning of a continuous-wave dye laser with an intracavity photorefractive element," *Opt. Lett.* **12**, pp. 915-917, 1987.
11. L. Meilhac, N. Dubreuil, G. Pauliat, G. Roosen, "Modeling of laser mode self-adapted filtering by photorefractive Fabry-Perot interferometers," *EMRS Conference*, paper J-III.2, Strasbourg, France, 2000.
12. H. G. Danielmeyer, "Effect of drift diffusion of excited states on spatial hole burning and laser oscillation," *J. Appl. Phys.* **42**, pp. 3125-3132, 1971.

One- and two-axis laser cavities for dual-frequency operation and microwave generation

M. Alouini, F. Bretenaker, M. Brunel, D. Chauvat, O. Emile, A. Le Floch, G. Ropars, and M. Vallet
Laboratoire d'Electronique Quantique–Physique des Lasers, Unité Mixte de Recherche du Centre National de la Recherche Scientifique 6627, Université de Rennes I, Campus de Beaulieu, F–35042 Rennes Cedex, France

Two-frequency solid-state lasers are shown to provide beat notes at frequencies from dc to the THz range with continuous tunability, high spectral purity and 100% modulation depth. Depending on the desired range, one- and two-axis cavities are built. Applications of such lasers as a local oscillator in radio-over-fibre communication systems or as a quasi-absolute tunable frequency source for highly-dense wavelength division multiplexed networks are emphasized.

I. INTRODUCTION

Optical generation of microwaves is desired in the 1-10 GHz range for radars and mobile phones [1,2], in the 55-60 GHz range for short-range radio [3], and in the THz range (sub-millimeter wavelengths) for imaging and spectroscopy [4]. An ideal source would generate an optical beat note from a single laser cavity, with a continuous tunability, high spectral purity, and high output power. We aim to show that a diode-pumped solid-state laser containing an adjustable birefringence provides a solution to fulfill these requirements. We first describe a single axis laser cavity in the GHz range (Section II). Then, we emphasize the use of a two-axis cavity to obtain a dual-absolute frequency source at 1.55 μm with a frequency difference up to the THz range (Section III). Conclusions are drawn in Section IV.

II. HIGHLY STABLE OPTICAL MICROWAVE GENERATION

We first consider the laser cavity depicted in Fig. 1. It is closed by mirrors M_1 and M_2, and contains an isotropic solid-state active medium axially pumped by a diode laser. It also contains a phase anisotropy (linear birefringence), which creates an optical path length difference between x- and y-polarized waves inside the cavity. The resonance condition is obtained from the relation $M\vec{E} = \lambda\vec{E}$, where M is the round-trip Jones matrix of the cavity, $\vec{E}$ the electromagnetic field and λ the eigenvalue which yields the eigen-frequencies of the laser. In this case, the eigenvectors are a x-polarized eigenstate with eigenfrequency ν_x and a y-polarized eigenstate with eigenfrequency ν_y. The eigenfrequency difference is linked to the birefringence $\Delta\varphi$ through the relation:

$$\Delta\nu = \nu_x - \nu_y = \frac{\Delta\varphi}{\pi}\frac{c}{2L}, \qquad (1)$$

where c is the velocity of light and L the length of the cavity. Hence, continuous tuning of the birefringence permits to adjust the beat note

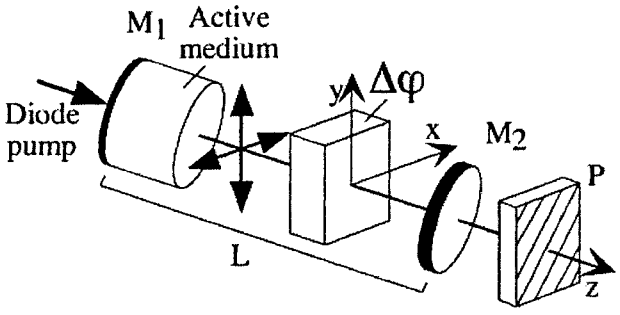


Fig. 1: Two-frequency solid-state laser. M_1, M_2: mirrors. P: polarizer.

frequency continuously within $0 \le \Delta\nu \le c/4L$. The experiment is realized with a Nd:YAG laser operating at 1.064 μm, pumped by a diode laser emitting at 808 nm. The phase anisotropy is

Laser Optics 2000: Control of Laser Beam Characteristics and Nonlinear Methods for Wavefront Control, Leonid N. Soms, Vladimir E. Sherstobitov, Editors, Proceedings of SPIE Vol. 4353 (2001)
© 2001 SPIE · 0277-786X/01/$15.00

realized using two orientable quarter-wave plates [5]. In a first step, a L=52 mm-long cavity is built. This gives a beat note frequency range of 1.5 GHz. The laser output is sent to a photodiode placed behind a polarizer which mixes the two eigenpolarizations. Fig. 2 depicts the 700 MHz

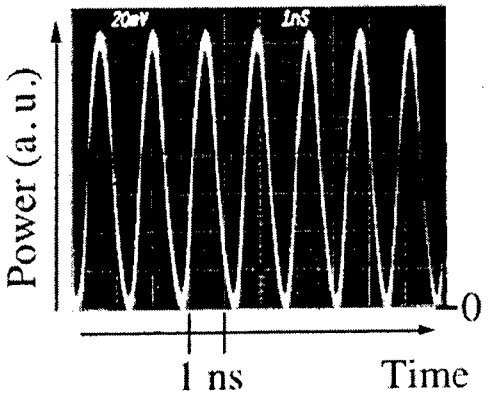


Fig. 2: Experimental observation of the 700 MHz beat note from the two-frequency Nd:YAG laser.

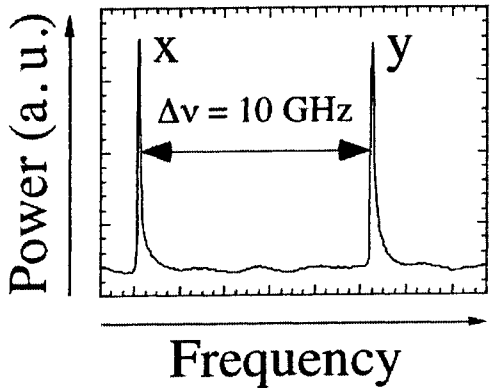


Fig. 3: Experimental observation of the optical spectrum of the 8 mm long cavity.

beat note obtained with an optical power of 10 mW. Note the 100 % modulation depth. We also verify that this frequency is continuously tunable between dc and 1.5 GHz by rotating one of the quarter-wave plates. Moreover, one can see from Eq. 1 that the beat frequency range is increased by shortening the cavity. The optical spectrum obtained when the cavity length is reduced to L=8 mm is shown in Fig. 3, where an expected 10 GHz frequency difference is evidenced.

To turn such a two-frequency laser source into a local oscillator for radio-over-fibre applications, we move to the 1.55 μm wavelength range. It is reached using an Er:Yb:Glass active medium, as shown in Fig. 4. The active medium is now pumped by a laser diode emitting at 975 nm. When a 50 μm-thick étalon is inserted inside the 5 cm-long cavity, we obtain longitudinally monomode

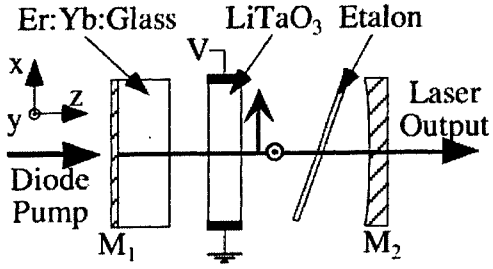


Fig. 4: Two-tunable frequency laser at 1.55 μm.

oscillation. (see Fig. 5). Then, introducing a $LiTaO_3$ birefringent crystal permits to split this longitudinal mode into two x and y eigenpolarization modes (x and y are defined by the neutral axes of the crystal). The dual-frequency operation is witnessed in the insert of Fig. 5. Furthermore, thanks to the electro-optic properties of $LiTaO_3$, one can voltage-control the frequency difference. The frequency difference is now written $\Delta\nu = \Delta\nu_0 + \Gamma V$, where $\Delta\nu_0$ is the frequency difference as defined by Eq. 1 without any voltage applied to the crystal, Γ is a scale

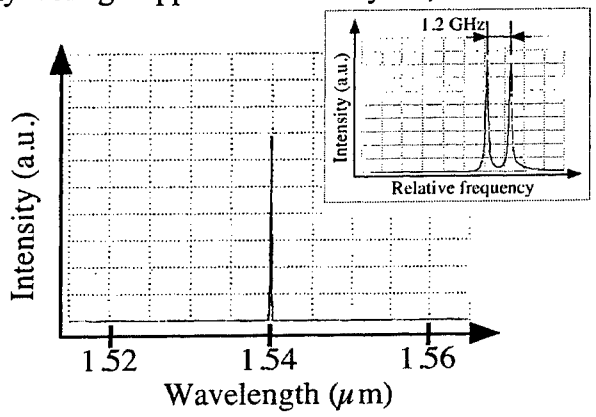


Fig. 5: Experimental optical spectrum of the laser of Fig. 4.

factor which is 1.2 MHz/V in our case and V is the voltage applied to the electrodes placed along the x_3 axis of the crystal. Thus, this permits to turn the laser into a voltage controlled oscillator at around 1 GHz and, as such, to implement it into an optical phase locked loop to yield the desired highly stable beat note [6]. The loop scheme is given in Fig. 6. Part of the laser output is sent to a photodiode D_1 whose signal is mixed to a reference oscillator at 1 GHz. The resulting error signal is amplified and fed back to the electrodes of the $LiTaO_3$ crystal. We then obtain the spectrum depicted in Fig. 7(a). To remove the spurious relaxation oscillation-induced sidebands at 65 kHz, we close a second feedback loop (see Fig. 6): the output of the photodiode D_2 is fed back through a loop filter to the laser diode driver [7]. Thanks to this loop, a reduction by 20 dB of the relative intensity noise (RIN) is obtained [see Fig. 7(a)]. With these two stabilization loops closed, we now zoom on the beat note spectrum. Fig. 7(b) reveals that the –3 dB width of this signal is less than 10 Hz, limited here by the spectrum analyzer resolution bandwidth. We also measure a phase noise of –100 dBc/Hz at 10 kHz and –120 dBc/Hz at 100 kHz, corresponding to local oscillator requirements for phase-shift keying modulation schemes at a few Mb/s rate.

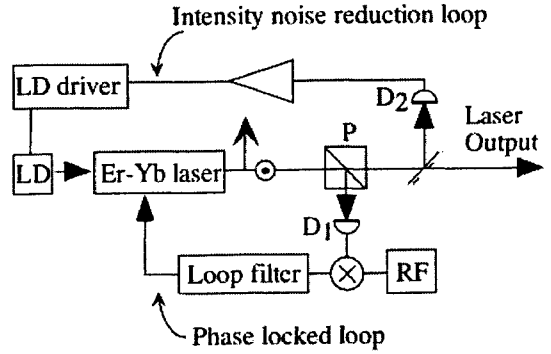


Fig. 6: Phase locked and intensity noise reduction loops. LD: laser diode; D_1, D_2: photodiodes; P: Glan polarizer; RF: microwave reference oscillator.

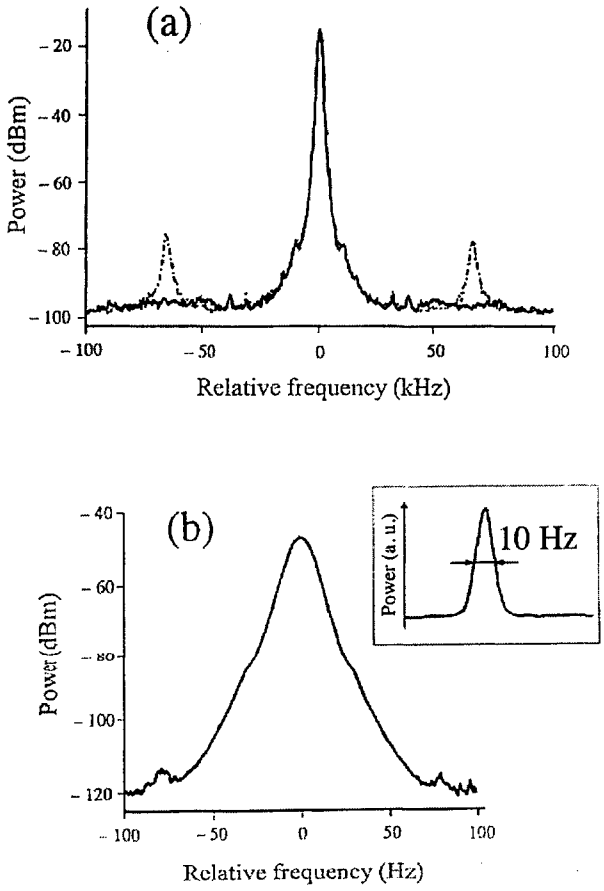


Fig. 7: (a) Beat note spectrum (span 200 kHz, resolution bandwidth 1 kHz); dashed line, no RIN reduction loop; full line, closed RIN reduction loop. (b) Same as (a) with span 200 Hz, resolution bandwidth 10 Hz and closed RIN reduction loop.

With short-range radio applications in view, such a local oscillator should oscillate in the 55-60 GHz range. To this aim, the cavity length has to be reduced to less than 1 mm. This means that introducing an étalon becomes impossible due to the space needed for a sufficiently long active medium and the electro-optic crystal. One may hence wonder how the laser can still be longitudinally monomode, as its gain bandwidth is several THz wide. Surprisingly, 200 μm-long microchip lasers have been shown to oscillate with a single frequency, despite a relatively small free-spectral range (500 GHz) compared to the phosphate glass bandwidth (more than 3 THz) [8]. This questions the role of nonlinear couplings between modes in such lasers. Hence, we have built two different set-ups to measure a Lamb-type coupling constant C in Er:Yb:Glass microchip lasers and proved that (i) a Lamb's

approach [9] can be used to describe the couplings in such systems in spite of the use of solid-state lasers for which Lamb's approximations are usually not valid, (ii) the coupling constant is measured to be C=0.80 between adjacent longitudinal modes, and (iii) C=0.95 between linearly polarized eigenstates [10]. The relatively high values of these constants explain that monomode oscillation is easily obtained in microchip lasers. It also confirms that two-frequency operation is feasible at 55-60 GHz, when gain and losses are kept equal for both eigenpolarizations. Practical realization of such a device is currently under progress. This frequency range is however the highest reachable, since shortening further the cavity would not allow enough gain length any more. As a consequence, obtaining higher beat note frequencies relies on the use of another kind of laser cavity, as is now described.

III TUNABLE DUAL ABSOLUTE FREQUENCY LASER AT 1.55 µm

Consider the two-axis laser cavity depicted in Fig. 8. A calcite crystal C_2 is inserted inside the cavity closed by mirrors M_1 and M_2, and containing the Er:Yb:Glass active medium. C_2 is cut at 45° to its optical axis, and thus provides a macroscopic walk-off (1 mm in this case) between x and y polarized fields. With this

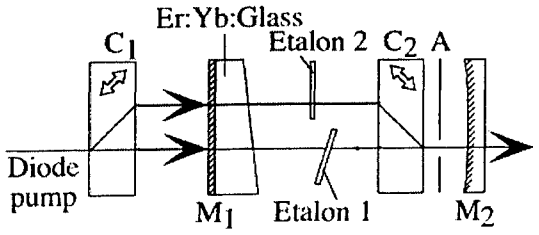


Fig. 8: Two-axis 1.55 µm laser scheme.

element, the laser eigenstates, calculated using $\vec{ME} = \lambda\vec{E}$ with spatially generalized Jones matrices [11], are then a y-polarized ordinary eigenstate and an x-polarized extraordinary eigenstate. They are superimposed in one part of the cavity (at the output coupler), but spatially separated in the other part of the cavity (where the active medium is located). Owing to the spatial separation of the eigenstates, one can then introduce two étalons, allowing (i) monomode oscillation to occur on each arm of the laser, and (ii) independent tuning of the eigenfrequencies. Note that the coupling constant between the two eigenstates is null in this case. A symmetric crystal C_1 is used to separate the pump light into two parts (see Fig. 8). In addition, an aperture A is introduced to ensure TEM_{00} operation on both arms. When the laser output is sent to an optical spectrum analyzer, this ability to tune one frequency over the whole gain spectrum without changing the other frequency is monitored [12]. Fig. 9 shows the spectra obtained when the étalon in the extraordinary arm is rotated, while the étalon in the ordinary arm remains fixed. The maximum eigenfrequency we have obtained with this laser is $\Delta\nu$= 2.7 THz. Note that continuous tuning may be obtained at the expense of an electro-optic crystal, like in the previous scheme. One may hence wonder whether such a source would serve as a probe for highly-dense

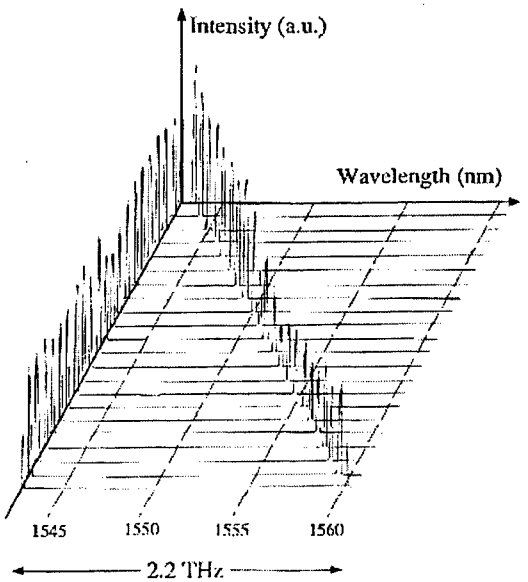


Fig. 9: Output spectrum of the two-axis laser. The ordinary wavelength is fixed at 1542.6 nm, while the extraordinary wavelength is increased with a 0.8 mm step. Here, the output power is 7 mW.

wavelength division multiplexed (HDWDM) networks. In particular, by using standard stabilization schemes for one of the laser frequencies, we aim to show now that the second (tunable) frequency itself may be stabilized.

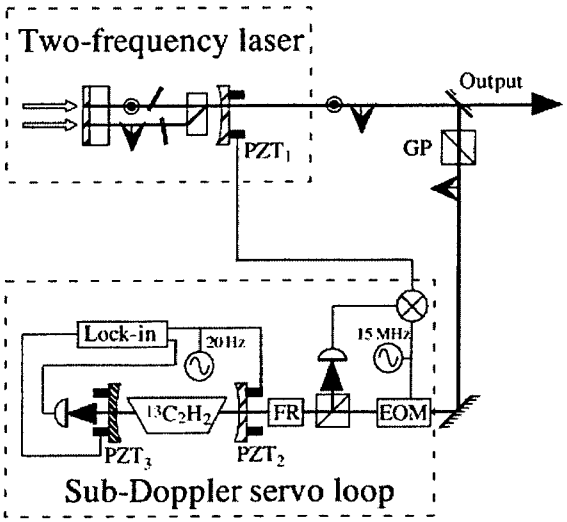


Fig. 10: Stabilization loop on saturated-absorption peaks of the $^{13}C_2H_2$ lines. PZTs: piezo-electric transducers; GP: Glan prism; EOM: electro-optic phase modulator; FR: Faraday rotator.

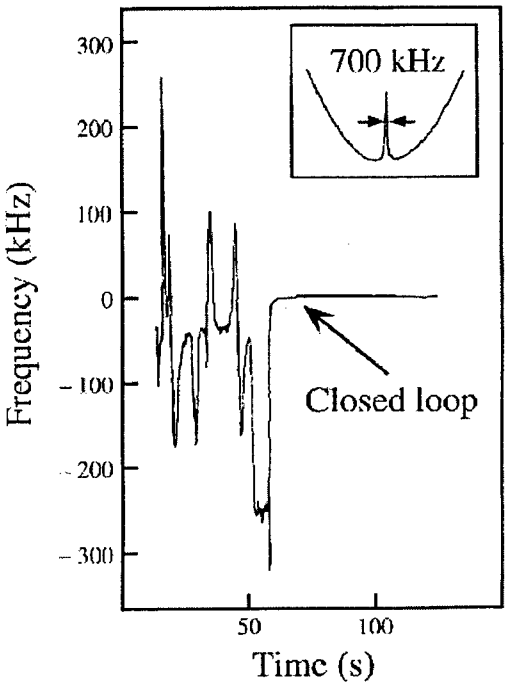


Fig. 11: Evolution of the error signal while closing the Doppler-free loop. Inset: observed saturation-dip of the P(6) line.

One of the laser output polarization is sent to a stabilization loop, as shown in Fig. 10. The extraordinary beam is sent, via an electro-optic modulator, to an optical cavity containing a $^{13}C_2H_2$ cell. Carbon-thirteen acetylene has numerous absorption lines around 1.5 μm [13]. First, the laser extraordinary eigenfrequency is maintained resonant with the Fabry-Perot (and hence with the $^{13}C_2H_2$ absolute reference) by means of standard side-band locking technique [14]. The error signal of this loop is used to control the two-frequency laser cavity length (see Fig. 10). Second, using a simple modulation-demodulation technique, the Fabry-Perot cavity is locked to resonance with the saturated absorption peak, corresponding to the chosen line. When the loop is

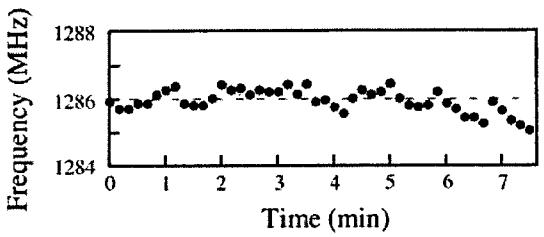


Fig. 12: Evolution of the beat note frequency. The laser is locked to the P(6) line.

closed, one then obtains the error signal depicted in Fig. 11, showing a frequency accuracy of 10 kHz for a loop response time of 10. s. The saturated absorption peak observed at the output of the passive Fabry-Perot cavity confirms that stabilization to an absolute reference to better than 10 kHz is obtained for the extraordinary frequency. Remarkably, the free-running beat note obtained when only the extraordinary eigenfrequency is locked is stable to better than 1 MHz over a few minutes, as shown in Fig. 12 [15]. This proves that, owing to the dual-frequency oscillation in a single cavity, the correction signal intended to lock one frequency also tracks the other frequency to better than

1 MHz. Such a laser hence provides a dual quasi-absolute frequency source which can be used with one frequency locked to the molecular reference, and the other tunable continuously over the C-band of telecommunications.

IV Conclusion

We have built one- and two-frequency laser cavities to obtain either highly stable microwave signals in the GHz range or tunable absolute-frequency operation with frequency differences up to the THz range. The introduction of an electro-optic crystal inside a dual-frequency solid-state laser permits to create a voltage-controlled beat note generator. Moreover, the shortcomings in terms of bandwidth in the one-axis case are resolved using a two-axis laser scheme. The only limitation is then the gain bandwidth of the active medium. The obtained beat notes are continuously tunable, of high spectral purity, and with 100% modulation depths. Applications of such sources include radio-over-fiber systems (local oscillator at 60 GHz for instance), spectroscopy, DWDM probe, radar/lidar systems. In addition, it has been shown elsewhere that a pulsed regime is also obtainable when a passive Q switch is properly chosen in such a laser [16]. Future developments are expected in the generation of highly coherent THz waves, the realization of pulsed two-frequency sources emitting at 1.55 μm, and in the complete understanding of the nonlinear coupling mechanisms in Er-doped glasses.

Acknowledgements

The authors wish to acknowledge contributions from B. Benazet, P. Di Bin, P. Thony, J. Marty, S. Jiang, and M. Myers.

[1] K. J. Williams and R. D. Esman, IEEE Photon. Technol. Lett. **8**, 148-150 (1996).

[2] D. C. Ni, H. R. Fetterman, and W. Chew, IEEE Trans. Microwave Theory Tech. **38**, 608-614 (1990).

[3] K. Kitayama, Fiber and Integrated Optics **19**, 167-186 (2000).

[4] See, e. g., *Terahertz spectroscopy and applications II*, Proceedings of SPIE **3828** (1999).

[5] M. Brunel, O. Emile, F. Bretenaker, A. Le Floch, B. Ferrand, and E. Molva, Opt. Rev. **4**, 550-552 (1997).

[6] M. Alouini, B. Benazet, M. Vallet, M. Brunel, P. Di Bin, F. Bretenaker, A. Le Floch, and P. Thony, "Offset phase locking of Er:Yb:Glass laser eigenstates for radio-frequency photonics applications," submitted.

[7] S. Taccheo, P. Laporta, O. Svelto, and G. de Geronimo, Opt. Lett. **21**, 1747-1749 (1996).

[8] S. Taccheo, P. Laporta, S. Longhi, and O. Svelto, Opt. Lett. **20**, 889-891 (1995).

[9] M. Sargent III, M. O. Scully, and W. E. Lamb, Jr., *Laser Physics*, Addison-Wesley, Reading, Mass., 1974, Chap. 9.

[10] M. Alouini, F. Bretenaker, M. Brunel, A. Le Floch, M. Vallet, P. Thony, Opt. Lett. **25**, 896-898 (2000).

[11] F. Bretenaker and A. Le Floch, J. Opt. Soc. Am. B **8**, 230-238 (1991).

[12] M. Alouini, M. Brunel, F. Bretenaker, M. Vallet, and A. Le Floch, IEEE Photon. Technol. Lett. **10**, 1554-1556 (1998).

[13] C. Latrasse, M. Breton, M. Têtu, N. Cyr, R. Robergé, and B. Villeneuve, Opt. Lett. **19**, 1885-1887 (1994).

[14] R. W. P. Drewer, J. L. Hall, F. V. Kowalski, J. Hough, G. M. Ford, A. J. Munley, and H. Ward, Appl. Phys. B **31**, 97-105 (1983).

[15] M. Alouini, M. Vallet, M. Brunel, F. Bretenaker, and A. Le Floch, "Tunable absolute-frequency laser at 1.5 μm," submitted.

[16] M. Brunel et al., Phys. Rev. A **60**, 4052-4058 (1999).

Phase locking of the arrays of linear and ring lasers

A.F. Glova, E.A. Lebedev, A.Yu. Lysikov, E.I. Musyona and S.B. Shchetnikov

Troitsk Institute for Innovation and Fusion Research,
Russia 142092, Troitsk, Moscow reg., TRINITI

ABSTRACT

Experimental investigations of radiation parameters of 2*D* arrays of waveguide CO_2 lasers synchronized by in-cavity spatial filter method are carried out. Phase locked regime in a system of two ring waveguide CO_2 lasers with a common cavity and unidirectional lazing was achieved and investigated.

Keywords: phase locking, waveguide lasers, 2*D* array, ring cavity, locking band

1. 2D ARRAYS OF LINEAR WAVEGUIDE CO_2 LASERS

2*D* arrays of waveguide CO_2 lasers are the base for construction of multi-beam technological lasers for material treatment [1-3]. The investigations of radiation phase locking of such type arrays at introducing of optical coupling between single lasers were carried out in Refs. [4-10]. Specifically, external flat mirror leading to optical coupling between adjacent lasers was applied [4], Talbot effect [5,6] and the methods of focal [7,8] and afocal [9,10] spatial filters providing close to global optical coupling were used. The objective of this part of the work is investigation of influence of the array and of the filter parameters on phase locking efficiency and axial brightness of array radiation.

1.1. Schematic of the setup

The experimental setup is shown in Fig.1. 2*D* laser array *1* with hexagonal packing of the discharge tubes with the length equal to 1.5 m, inner diameter $a = 5.5$ mm and the period $d = 8.5$ mm is placed into common flat-parallel cavity with output mirror *2* and equivalent blank mirror formed by conjugated telescope. This telescope contains the focusing lens *3* with the focus length $F = 430$ mm and the concave spherical mirror *4*. Replacement in-cavity diaphragms *5* extract the fixed number N of single lasers in an array equal to 7, 19 or 37. External diaphragm *6* extracts if necessary the required number $N_1 < N$ of the laser beams at the array exit. The power of radiation is being measured by receiver *7* with the diaphragm *8* mounting before it for determination of the power fraction in near-axial regions of the far-field intensity distributions. The receiver *9* with the scanning slit *10* serves for control of the shape of the spatial intensity distributions.

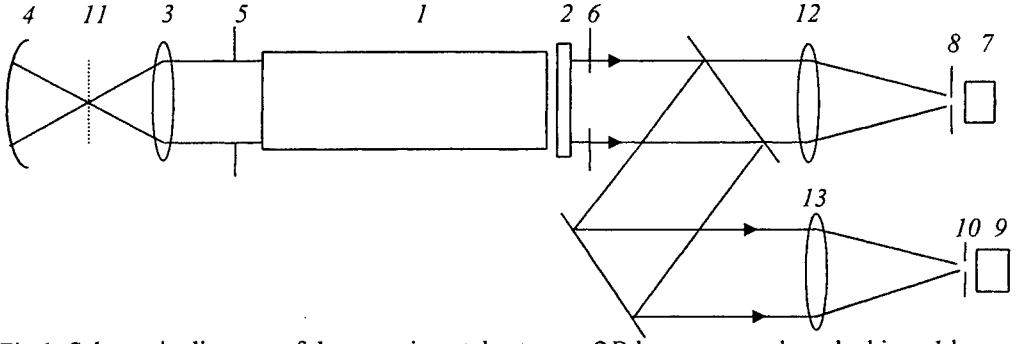


Fig.1. Schematic diagram of the experimental setup on 2*D* laser arrays phase locking: *1* laser array; *2* output cavity mirror; *3,12,13* focusing lenses; *4* metallic mirror; *5,6,8* aperture diaphragms; *7,9* radiation receivers; *10* scanning slit; *11* spatial filter.

For laser array phase locking the spatial filter *11* installed in lens *3* focus was used. The spatial filter represents a set of identical holes in the copper plate and its spatial position corresponds to selection of the in-phase array super-mode. For this super-mode the size d_0 of the far-field intensity maximums at the base level for the plane wave-front and the distance d_1 between maximums axes may be found, respectively, from the following expressions: $d_0 = 2\varphi_0 F$ and $d_1 = \varphi_1 F$, where $\varphi_0 = 1.22\lambda/D$, $\varphi_1 = (2/\sqrt{3})\lambda/d$, $D = D(N)$ is the diameter of the array, $\lambda = 10.6$ μm is the radiation wavelength. It is clear that for given $F = 430$ mm the distance $d_1 = 0.58$ mm is the same for any array used. On the other hand the size d_0 depends on the number N of single lasers in an array: $d_0 = 0.47$ mm for $N = 7$, $d_0 = 0.27$ mm for $N = 19$ and $d_0 = 0.19$ mm for $N = 37$. Two replacement filters with the holes conjugated to the intensity distributions were used in the experiments. The size of the

Laser Optics 2000: Control of Laser Beam Characteristics and Nonlinear Methods for Wavefront Control,
Leonid N. Soms, Vladimir E. Sherstobitov, Editors, Proceedings of SPIE Vol. 4353 (2001)
© 2001 SPIE · 0277-786X/01/$15.00

holes for the first filter is d_{01} = 0.3 mm and for the second filter is d_{02} = 0.4 mm. It is seen that the transparence of the first filter is smaller in comparison with the second one and the size of the holes for both filters may be larger or smaller than d_0 depending on the number of single lasers in an array.

1.2. Radiation parameters of the arrays

The dependencies of phase locking efficiency η at the same discharge current in a tubes as a function of number N of single lasers in Fig.2 are shown. Phase locking efficiency is defined as the ratio $\eta = P_s/P$ where P_s and P is the generation power of laser array with installed filter and without of filter respectively. We shall now compare phase locking efficiencies as a function of filter parameters. It is seen that for fixed N-values phase locking efficiency decreases if the transparence of the filter also decreases. This effect is associated with the increase of in-cavity losses for filter with smaller transparence and corresponds to phase locking efficiency alteration in the case of $1D$ laser arrays [11,12]. It is necessary to point out that the losses mentioned above so much high for the first filter at N = 7 that lead to suppression of coherent oscillation of the array.

Phase locking efficiency for both filters in dependence on N has non-monotonic character. Its increase if number N of single lasers increases from N = 7 to N = 19 may be explained by decrease of in-cavity losses because in this case the size d_0 of the pattern maximums in the filter plane also decreases. This reason, as it seems, must lead to further phase locking efficiency increase if the number N of single lasers increases up to N = 37. But for both filters the experiment shows the inverse dependence. It appears, this effect is connected with the dominance of destructive influence on phase locking efficiency of the spread in initial lazing frequencies [12] if N increases in comparison with constructive influence due to decrease of the generation threshold. To confirm this supposal we have measured the values of normalized parameter α depending on N which are presented in Fig.3. This parameter is defined as the ratio $\alpha = P_0/P_s$ (here P_0 is the radiation power contained in a calculated angle size $2\varphi_0$ of the central lobe of far-field intensity distribution in the lens *12* focus) and proportional to axial brightness of array radiation. The band of the spread in initial lazing frequencies fatally increases if the number N of single lasers also increases. Therefore α-parameter decrease depending on N for given filter may be associated with this phenomenon and explains the effect of decrease of phase locking efficiency for N = 37. We shall note that on analogy with the α-parameter, the monotonic decrease of axial brightness of array radiation depending on initial detunings in lazing frequencies was received in calculations [13,14] for $1D$- and $2D$ arrays of a large number of optically coupled lasers with different type of optical coupling. Such type decrease may be associated with the decrease of the degree of coherence in an array radiation. We shall note also that the optical coupling between lasers becomes more forceful if the filter transparence decreases. It explains the growth of the α-parameter for the first filter in comparison with the second one for the 37-lasers array.

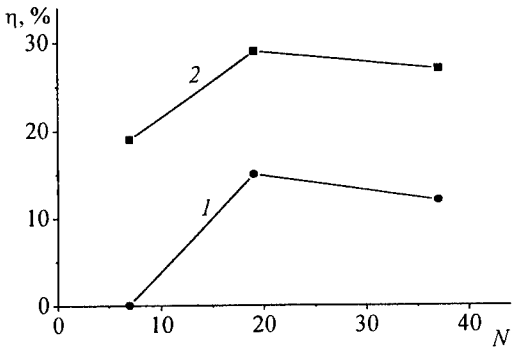


Fig.2. Dependencies of η on N for d_{01} = 0.3 mm (*1*) and for d_{02} = 0.4 mm (*2*).

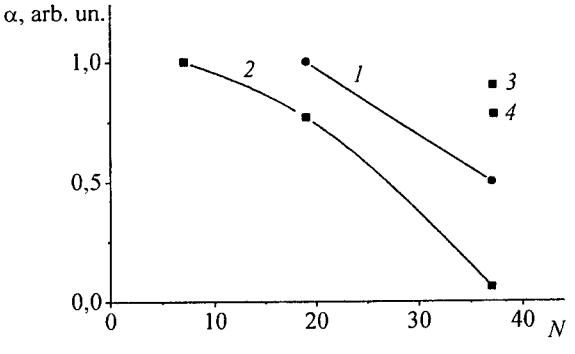


Fig.3. Dependencies of α on N for d_{01} = 0.3 mm (*1*) and for d_{02} = 0.4 mm (*2-4*); N_1 = 7 for central (*3*) and periphery (*4*) lasers.

We shall now compare the α-values in Fig.3 for seven central and seven periphery lasers extracted from the 37-lasers array with the help of diaphragm *6*. It is seen that the degree of coherence for periphery group of lasers is less than for central group. The reason of this dissimilarity is decrease of optical coupling strength on the array periphery that leads to decrease of phase locking band and as consequence to partial coherence in radiation of the array. It is known [13] that partial coherence in the arrays with large number of phase locked lasers may emerge due to formation of domain-like structure in an arrays emission. Experimental determination of domain number and their boundaries is very complex task. We can conclude

only that mentioned above dissimilarity may serve as the qualitative experimental confirmation of the possibility of existence of domain-like structure.

2. TWO RING UNIDIRECTIONAL WAVEGUIDE CO_2 LASERS

Phase locked regime in a system of two ring TEA CO_2 lasers with individual cavities was received in Ref. [15]. For direct waves it occurred under condition of in-cavity injection of the power part of a reverse wave from one laser to another. The visibility parameter of the radiation intensity distributions in the experiments [15] was varied from pulse to pulse in the range 0.3 – 0.9 and its average value was 0.6. In a number of other studies [16-25] involving external injection of radiation, individual ring lasers [16-19], linear lasers [20-22], and arrays of linear lasers [23-25] were synchronized with a master oscillator. In this part of the work we have investigated phase locked lazing of two unidirectional ring waveguide CO_2 lasers with a common cavity at injection of part of the power from one laser to the other.

2.1. Experimental setup

The scheme of experimental setup is shown in Fig.4. Each laser with a ring perimeter equal to 4 m is connected to a common power supply end each contains two discharge tubes, *1* (first laser) and *2* (second laser). The length of the tubes is $l/2$ = 1.5 m and its inner diameter is equal to 5.5 mm. The distance d between the axes of tubes *1* and *2* is equal to 8.5 mm. The end-faces of the tubes are closed on either side by Brewster-windows; their orientation selects the direction of polarization of the radiation perpendicular to the plane of Fig.4. The common cavity of the lasers consists of rotary mirrors *3-5* with the reflection coefficients of 0.96, 0.98 and 0.85, respectively, and an output mirror *6* in the form of a plane-parallel sylvite plate. The thickness h of the plate is selected on the basis of the condition $h = d(n^2 - \sin^2\gamma)^{1/2}/\sin 2\gamma$, where $\gamma = \pi/4$ is the angle of incidence of the radiation and n is the refractive index of sylvite. Under this condition an effective direct exchange of radiation between lasers is provided. A mirror *7* with the reflection coefficient close to unity is used to suppress the reverse waves in each laser [26] and leads to unidirectional lazing with injection of part of the output power of the direct wave (travelling clockwise) of the first laser into the second laser.

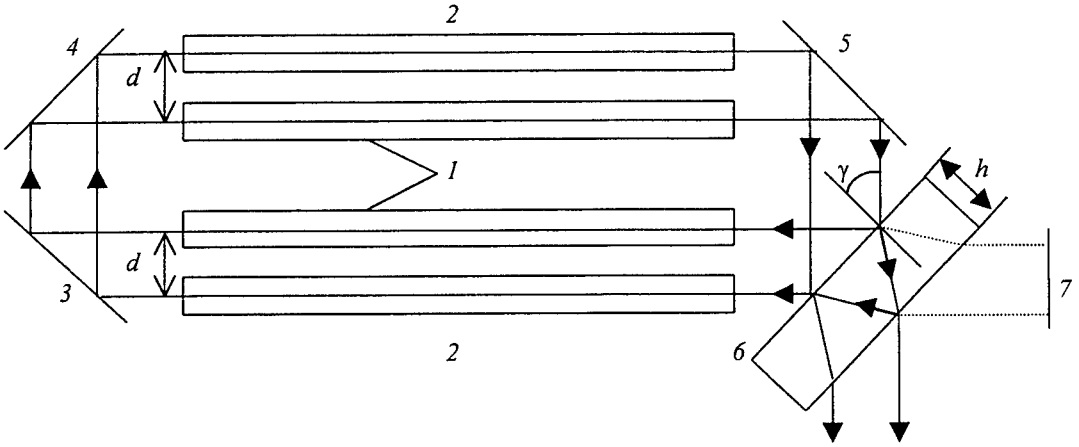


Fig.4. Schematic diagram of a system of two ring unidirectional lasers: *1,2* discharge tubes; *3-5* rotary mirrors; *6* output mirror; *7* external mirror.

This setup may be considered as a system of two optically coupled lasers with one-sided optical coupling [27] or as a master oscillator (first laser) – regenerative amplifier (second laser) system. In contrast to standard amplifying systems of this type (see, for example, Ref.[28]), the detuning of the common cavity in this system may lead to an unequal frequency change and hence to different changes in the output powers of the lasers in self-oscillatory regime and in consequence of this the locking band becomes depended on the frequency detuning in the regime with injection frequency locking. This dependence at scanning of the lazing frequency of master oscillator within limits exceeding the free spectral range of the amplifier was demonstrated in Ref.[16].

The output radiation power P of the lasers and the visibility parameter V of the far-field intensity distributions as well as their dependencies on the angle β of rotation of the mirror *6* around an axis perpendicular to the plane of Fig.4 were measured in the experiments. A CO_2:N_2:He = 1:3:12 gas mixture at a pressure of 20 Torr was used as the active medium. The discharge current in the tubes was 15 mA. The change in the lengths of the laser cavities owing to vibrations of the unit and during rotation of the mirror *6* was not monitored.

2.2. Experimental and numerical results

For a fixed value of β, the power P varied with the time in the range 10 - 20 W, whereas the parameter V for the distributions with a central maximum assumed values in the range 0.2 – 0.9. For $P < 10$ W, the distributions with a central maximum could be transformed into distributions with a minimum at the centre, which corresponded to negative $V = -(0.3 - 0.4)$. The variations of P and V were of the same type also as the function of $\beta = \pm 2\times10^{-4}$ rad. It is necessary to point out that the distributions with $V = 0$ were virtually not observed, i.e. in the given system with the mentioned above parameters of the pump, of the active medium and of the mirror *6* the phase locked regime was attained much more easy than the non-phase-locked regime.

We shall now calculate the locking frequency band, the total output power and the parameter V within the limits of the locking band as a function of the initial detunings of the laser frequencies taking into account the radiation losses. We shall confine our analysis by consideration of amplification of plane waves taking into account the losses in the mirrors *3-5* and the losses owing to phase conjugation for the main waveguide mode [29]. These losses will be regarded as distributed and identical for both lasers.

For the radiation power P_{1a} of the first laser in the self-oscillatory regime may be received the following expression:

$$P_{1a} = \frac{(1 - R)^2(1 - \xi)P_s(1 - \alpha_1)\alpha_1^{-1}[(RG_{01}^{1-\alpha_1})^{\alpha_1} - 1]}{[(RG_{01}^{1-\alpha_1})^{\alpha_1} - R]}, \quad (1)$$

where $G_{01} = \exp(g_{00}L_1 l)$; $L_1 = [1 + (\delta\nu_1/0.5\delta\nu_0)^2]^{-1}$; $\alpha_1 = a/g_{00}L_1$; a is the loss factor; g_{00} is the small-signal gain at the line centre; $\delta\nu_1$ is the detuning of the laser frequency from the line centre; $\delta\nu_0$ is the FWHM of the gain line; P_s is the saturation power; R is the reflection coefficient of each surface of the mirror *6*, ξ is the losses in absorption in the mirror *6*. Calculations by formula (1) for the experimental conditions ($g_{00} \approx 1.2$ m^{-1}, $a \approx 0.16$ m^{-1}, $P_s \approx 10$ W, $R = 0.08$ and $\xi \approx 10^{-2}$) and $\delta\nu_1 = 0$ gives $P_{1a} = 4.5$ W, which with a precision adequate for further treatment agrees with the average power measurements (3–4 W).

The locking band $\delta\nu_s$ for the second laser is found from the solution of the transcendental equation

$$\delta\nu_s = (\delta\nu_m/\pi)\arcsin[0.5(1 - R)(1 - \xi)(P_{11a}/P_{2a})^{1/2}], \quad (2)$$

where $\delta\nu_m$ is the free spectral range; P_{11a} and P_{2a} are the powers for the self-oscillations of the first and second lasers expressed by formula (1) with the appropriate replacement of G_{01}, L_1 and α_1 by $G_{011} = \exp(g_{00}L_{11}l)$, $L_{11} = \{1 + [(\delta\nu_2 \pm \delta\nu_S)/0.5\delta\nu_0]^2\}^{-1}$, $\alpha_{11} = a/g_{00}L_{11}$ and by $G_{02} = \exp(g_{00}L_2 l)$, $L_2 = [1 + (\delta\nu_2/0.5\delta\nu_0)^2]^{-1}$, $\alpha_2 = a/g_{00}L_2$; $\delta\nu_2$ is the detuning of the second laser frequency from the line centre. The total locking band calculated for the mentioned above experimental conditions and $\delta\nu_2 > 0$ is confined by curves *1* and *2* in Fig.5. The asymmetry of the band relative to the $\delta\nu_s = 0$ straight line (shown dashed in Fig.5) is associated with the change in the ratio P_{11a}/P_{2a} in equation (2) with decrease or increase in the operating frequency of the first laser relative to the frequency of the second laser. On increase in $\delta\nu_2$, the band asymmetry increases while its maximum value approaches to the maximum possible detuning of the operating frequency of the lasers above the generation threshold $2\delta\nu_{max} \approx 44.6$ MHz $\approx 0.6\delta\nu_m$. The possibility of locking the radiation of the lasers regardless of the appreciable detuning of the operating frequencies, occurring either spontaneously as a consequence of vibrations or during the adjustment of the output mirror *6*, can be explained by the existence of a broad locking band. On increase in R, a narrowing of the band is observed and the radiation-locking conditions become more stringent.

The radiation power P_{2i} of the second laser in the injection-locked regime was calculated from the formula

$$P_{2i} = \frac{(1 - R)^2(1 - \xi)^3P_s(1 - \alpha_1)\alpha_1^{-1}[(RG_{01}^{1-\alpha_1})^{\alpha_1} - 1]\{[(G_2R)^{1/2} - R]^2 + 4R(G_2R)^{1/2}\sin^2(\pi\delta\nu/\delta\nu_m)\}}{[(RG_{01}^{1-\alpha_1})^{\alpha_1} - R]\{[1 - (G_2R)^{1/2}]^2 + 4(G_2R)^{1/2}\sin^2(\pi\delta\nu/\delta\nu_m)\}} \quad (3)$$

after substituting in formula (3) the product G_2R found from the expression

$$\frac{(1-R)^2(1-\xi)^2 P_s(1-\alpha_1)\alpha_1^{-1}[(RG_{01}{}^{1-\alpha_1})^{\alpha_1}-1]}{[(RG_{01}{}^{1-\alpha_1})^{\alpha_1}-R]\{[1-(G_2R)^{1/2})^2+4(G_2R)^{1/2}\sin^2(\pi\delta\nu/\delta\nu_m)\}} = \frac{(1-\alpha_{22})\alpha_{22}^{-1}[(RG_{022}{}^{1-\alpha_{22}})^{\alpha_{22}}-(G_2R)^{\alpha_{22}}]}{G_2R(RG_{022}{}^{1-\alpha_{22}})^{\alpha_{22}}-R(G_2R)^{\alpha_{22}}}, \quad (4)$$

where $G_{022} = \exp(g_{00}L_{22}l)$; $L_{22} = \{1 + [(\delta\nu_1 \pm \delta\nu)/0.5\delta\nu_0]^2\}^{-1}$; $\alpha_{22} = a/g_{00}L_{22}$; $\delta\nu$ is the detuning of the second-laser frequency from the "centre" ($\delta\nu_s = 0$) of the locking band; G_2 is the per-pass gain of the radiation in the second laser. The calculated dependence of $P = P_{1a} + P_{2i}$ on $\delta\nu_1$ for $\delta\nu = 0$ is given in Fig.6 (curve *1*). This dependence is compared with dependence of P on $\delta\nu_1$ at the left-hand (curve *2*) and right-hand (curve *3*) internal boundaries of the locking band of the second laser. It is seen from Fig.6 that under the conditions of uncontrolled variation of the lengths of the cavities the measured power of the locked operation of the lasers (10 – 20 W) is closed to the calculated value.

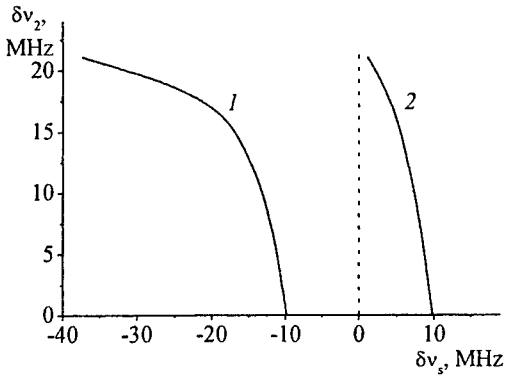


Fig.5. Dependencies of the lockinf band $\delta\nu_s$ on $\delta\nu_2$ for $\delta\nu_1 = \delta\nu_2 - \delta\nu_s$ (*1*) and $\delta\nu_1 = \delta\nu_2 + \delta\nu_s$ (*2*).

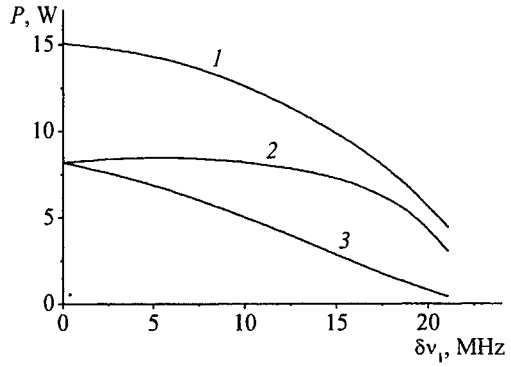


Fig.6. Dependencies of the total radiation power P on $\delta\nu_1$ for $\delta\nu_2 = \delta\nu_1$ (*1*), $\delta\nu_2 = \delta\nu_1 - \delta\nu_s$ (*2*) and $\delta\nu_2 = \delta\nu_1 + \delta\nu_s$ (*3*).

The change in the phase difference $\delta\varphi$ of the interfering laser beams is linked to the angle β by the following relationship: $\delta\varphi = 4\pi\beta d/\lambda$, where λ is the radiation wavelength. Since within the limits of the locking band the difference between the laser frequencies $\delta\nu_{12} = \delta\nu_1 - \delta\nu_2$ depends as $\delta\nu_{12} = 2d\beta_s\delta\nu_m/\lambda$ on the angle β_s corresponding to this band, the visibility parameter is evidently influenced both by the change in the powers P_{1a} and P_{2i} as the frequencies are varied and by the additional phase shift. The calculated dependencies of V on $\delta\nu_1$ at the "centre" of the locking band and at its boundaries are presented in Fig.7. It is seen that distributions with an intensity minimum at the centre are entirely possible for a total lazing power of about 5 – 10 W and a large detuning $\delta\nu_1$.

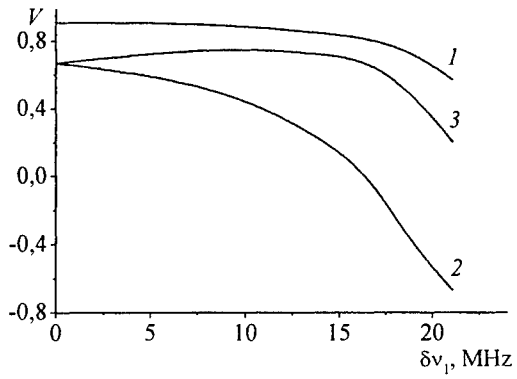


Fig.7. Dependencies of the visibility parameter V on $\delta\nu_1$ for $\delta\nu_2 = \delta\nu_1$ (*1*), $\delta\nu_2 = \delta\nu_1 - \delta\nu_s$ (*2*) and $\delta\nu_2 = \delta\nu_1 + \delta\nu_s$ (*3*).

3. SUMMARY

Phase locking efficiency close to 30% for 2*D* arrays of waveguide CO_2 lasers synchronized by in-cavity spatial filter method was achieved without of the additional facilities allowing to align the optical lengths of the cavities of individual lasers. It was shown experimentally that the axial brightness of radiation for different groups of lasers containing the same number of lasers within a common aperture of the array is differed from each other.

In a system of two ring waveguide CO_2 lasers with unidirectional lazing under condition of slight exceeding of the generation threshold it was shown the possibility of receiving of single- and double-lobe angular intensity distributions. Experimental results agreed qualitatively with calculations for the amplification of plane waves.

4. REFERENCES

1. G.I. Kozlov and V.A. Kuznetsov, *Kvantovaya Elektron. (Moscow) 16*, pp. 1360-1363, 1989.
2. G.A. Abil'siitov, A.I. Bondarenko, V.V. Vasil'tsov et. al., *Kvantovaya Elektron. (Moscow) 17*, pp. 672-677, 1990.
3. I.V. Bukhanova, V.M. Zhuravel and V.V. Divinsky, *Proc. SPIE 2109*, pp. 48-53.
4. A.F. Glova, Yu.A. Dreizin, O.R. Kachurin et. al., *Pis'ma Zh. Tekh. Fiz. 11*, pp. 249-252, 1985.
5. V.V. Antyukhov, A.F. Glova, O.R. Kachurin et. al., *Pis'ma Zh. Eksp. Teor. Fiz. 44*, pp. 63-65, 1986.
6. V.V. Vasil'tsov, Ye.V. Zelenov, Ye.A. Kurushin and D.Yu. Filimonov, *Proc. SPIE 2109*, pp. 107-114.
7. A.G. Aleksandrov, A.A. Angeluts, V.V. Vasil'tsov et. al., *Kvantovaya Elektron. (Moscow) 17*, pp. 1462-1463, 1990.
8. I.V. Babanov, A.F. Glova and E.A. Lebedev, *Quantum Electronics 23*, pp. 184-185, 1993.
9. A.A. Golubentsev, O.R. Kachurin, F.V. Lebedev and A.P. Napartovich, *Kvantovaya Elektron. (Moscow) 17*, p. 1018 1989.
10. V.V. Vasil'tsov, V.S. Golubev, Ye. V. Zelenov, Ye.A. Kurushin and D.Yu. Filimonov, *Proc. SPIE 2109*, pp. 122-128.
11. A.F. Glova, S.Yu. Kurchatov, V.V. Likhanskii, A.Yu. Lysikov and A.P. Napartovich, *Quantum Electronics 26*, pp. 500-502, 1996.
12. A.F. Glova, S.Yu. Kurchatov, V.V. Likhanskii et. al., *Quantum Electronics 27*, pp. 309-311, 1997.
13. A.A. Golubentsev and V.V. Likhanskii, *Kvantovaya Elektron. (Moscow) 17*, pp. 592-593, 1990.
14. S.Yu. Kurchatov, V.V. Likhanskii and A.P. Napartovich, *Zh. Eksp. Teor. Fiz. 107*, pp. 1491-1502, 1995.
15. S. Hofswade, R. Riviere, K. Calahan, C. Clayton and C.A. Huguley, *Appl. Optics 26*, p. 2290, 1987.
16. G.L Bourdet., R.A. Muller, G.M. Mullot and J.V. Vinet, *Appl. Phys. B43*, p. 273, 1987.
17. V.V. Burmistrov, A.F. Glova, V.V. Dylev and F.V. Lebedev, *Sov. J. Quantum Electron. 21*, p. 19, 1991.
18. V.M. Gordienko and Yu.Ya. Putivskii, *Sov. J. Quantum Electron. 21*, p. 284, 1991.
19. N. Lesage, G. Mullot, Y.B. Andre and G.L. Bourdet, *Opt. Commun. 115*, p. 291, 1995.
20. P. Cassard and J.-M. Lourtioz, *Opt. Commun. 51*, p. 325, 1984.
21. C. Angelie, R. Capitini and P. Girard, *Appl. Opt. 26*, p. 1074, 1987.
22. V.V. Apollonov, K.Kh. Kazakov and Yu.A. Shakir, *Sov. J. Tech. Phys. 34*, p.1226, 1989.
23. E.A. Chanchard, Y.S. Wey, S.N. Lee and G. Burdge, *IEEE Trans. Photon. Tech. Lett. 3*, p. 1069, 1991.
24. D.A. Rockwell and C.R. Giuliano, *Opt. Lett. 11*, p. 147, 1986.
25. L.R. Brewer, *Appl. Opt. 30*, p. 317, 1991.
26. Yu. M. Golubev, V.E. Privalov and S.A. Fridrikhov, *Opt. Spectrosc. (USSR) 27*, p. 278, 1969.
27. V.V. Likhanskii and A.P. Napartovich, *Sov. Phys. Usp. 33*, p.228, 1990.
28. K. Smith and R.M. Thomson, *Computer Modeling of Gas Lasers*, New York: Plenum Press, 1978.
29. J.J. Degnan and D.R. Hall, *IEEE J. Quantum Electron. QE-9*, p. 901, 1973.

Creation and annihilation of wavefront dislocations in the process of frequency-doubling of Bessel light beams

V.N.Belyi[a], N.S.Kazak[a], N.A.Khilo[b], A.A.Ryzhevich[a], E.G.Katranji[a]

[a] Institute of Physics, NAS of Belarus, 70 F.Skaryna ave., 220072, Minsk, Belarus*
[b] Division for optical problems in information technologies, NAS of Belarus, 1-2 Kuprevich str., 220141, Minsk, Belarus

ABSTRACT

We have studied, both theoretically and experimentally, the doubling of topological charge of dislocations of Bessel light beams, transfer of a dislocation to a second harmonic radiation without change of its topological charge, and annihilation of screw dislocations of the opposite sign.

1. INTRODUCTION

An optical wavefront dislocation is a singularity in the transverse phase of an optical field [1]. Screw dislocations, or vortices, is a point defect in which the phase of the field is undefined, and amplitude vanishes. Vortices possess a topological charge m, where m is the number of 2π phase shifts in one cycle around the singularity. Screw dislocations have attracted considerable attention in linear and nonlinear optics, and in laser physics [2-8].

Bessel light beams are the new example of optical beams with screw wavefront dislocations. These nondiverging optical beams are of interest for alignment and guiding of atoms. For this purpose, both zero-order and higher-order BLBs can be used [9-11]. Besides, higher-order Bessel and Laguerre-Gaussian beams are of interest for studying the processes of creation and annihilation of wavefront dislocations [3,6,7].

A most important question concerning nonlinear properties of higher order BLB is the efficiency of frequency conversion. It is important particularly for applications of processes of creation and annihilation of dislocations in optical information processing. In this report the primary attention is focused to this problem. We submit a theoretical and experimental results on doubling of topological charge of dislocations, transfer of a dislocation to a second harmonic radiation without change of its topological charge and annihilation of screw dislocations of the opposite sign.

The main properties of SHG by Bessel beams can be interpreted in most cases by assuming the second harmonic radiation to be a single-mode Bessel beam. More exact form of second harmonic field is a superposition of Bessel beams with closely spaced conicity parameters. This approximation is justified also by experiment. The mentioned above superposition can be either continuous or discrete. In the latter case we can choose the second harmonic field as a superposition of modes of cylindrical domain with radius equal to the radius of the fundamental Bessel beam. The total number of modes, which are to be taken into account, is usually not very large. It is also important that the discrete representation of second harmonics field allows to develop the analytically solvable model of three-wave interaction.

Thus, the electric field amplitude of Bessel beams of fundamental and second harmonic frequencies propagating along the z axis of a system of cylindrical coordinates (ρ, φ, z) is given by

$$\begin{aligned} E_{1o}(\rho,z) &= A_{1o}(z) j_m(q_1\rho)\exp(ik_{oz}z - i\omega t + im\varphi), \\ E_{1e}(\rho,z) &= A_{1e}(z) j_n(q_1\rho)\exp(ik_{ez}z - i\omega t + in\varphi), \\ E_2(\rho,z) &= \sum_p A_{2p}(z) j_{m+n}(q_{2p}\rho)\exp[ik_{2z}z - 2i\omega t + i(m+n)\varphi], \end{aligned} \tag{1}$$

where $q_1 \approx k_0\gamma$, $k_{1oz,ez} \approx k_{1o,e} - q_1^2/2k_{1o,e}$. In Eqs. (1) we introduced a normalized Bessel functions $j_m(q_1\rho)$:

* Send correspondence to Anatol Ryzhevich
E-mail: tol@dragon.bas-net.by; phone in Minsk 284-16-16

Laser Optics 2000: Control of Laser Beam Characteristics and Nonlinear Methods for Wavefront Control, Leonid N. Soms, Vladimir E. Sherstobitov, Editors, Proceedings of SPIE Vol. 4353 (2001)
© 2001 SPIE · 0277-786X/01/$15.00

$$j_m(q\rho) = \frac{J_m(q\rho)}{\sqrt{W_m(q, R_B)}} \quad \text{if } \rho < R_B, \tag{2}$$

$$j_m(q\rho) = 0 \quad \text{if } \rho \geq R_B,$$

where J_m(x) is m-th order Bessel function, R_B is the radius of fundamental Bessel beam, $W_m(q, R_B) = 2\pi \int_0^{R_B} J_m^2(q\rho)\rho d\rho$.

Therefore, the normalization condition is $2\pi \int_0^{R_B} j_0^2(q_1\rho)\rho d\rho = 1$.

The spatial structure of second harmonic field is determined by an overlap integral

$$g(q_2) = 2\pi \int_0^{R_B} j_m(q_1\rho) j_n(q_1\rho) j_{m+n}(q_2\rho)\rho d\rho. \tag{3}$$

This integral describes a general case of three beam interaction if two fundamental Bessel beams have different orders. As follows from the law of conservation of angular momentum of optical field, the generated second harmonic Bessel beam can only be of $m+n$ order. If both numbers m and n have the same sign, a process of summation of topological charges takes place. Otherwise the subtraction of topological charges is realized.

Further we investigate these overlap integrals as a function of conicity parameter q_2. According to the second harmonic field representation used above, the parameter q_2 can be either continuous or discrete.

We investigate the processes of summation and subtraction of dislocations separately.

2. SECOND HARMONIC GENERATION WITH TWO BESSEL BEAMS WITH EQUAL SIGN OF TOPOLOGICAL CHARGE

The typical property of an overlap function (3) is the well-defined maximum for $q_2 \approx 2q_1$. This maximum corresponds to collinear interactions of plane wave components of beams.

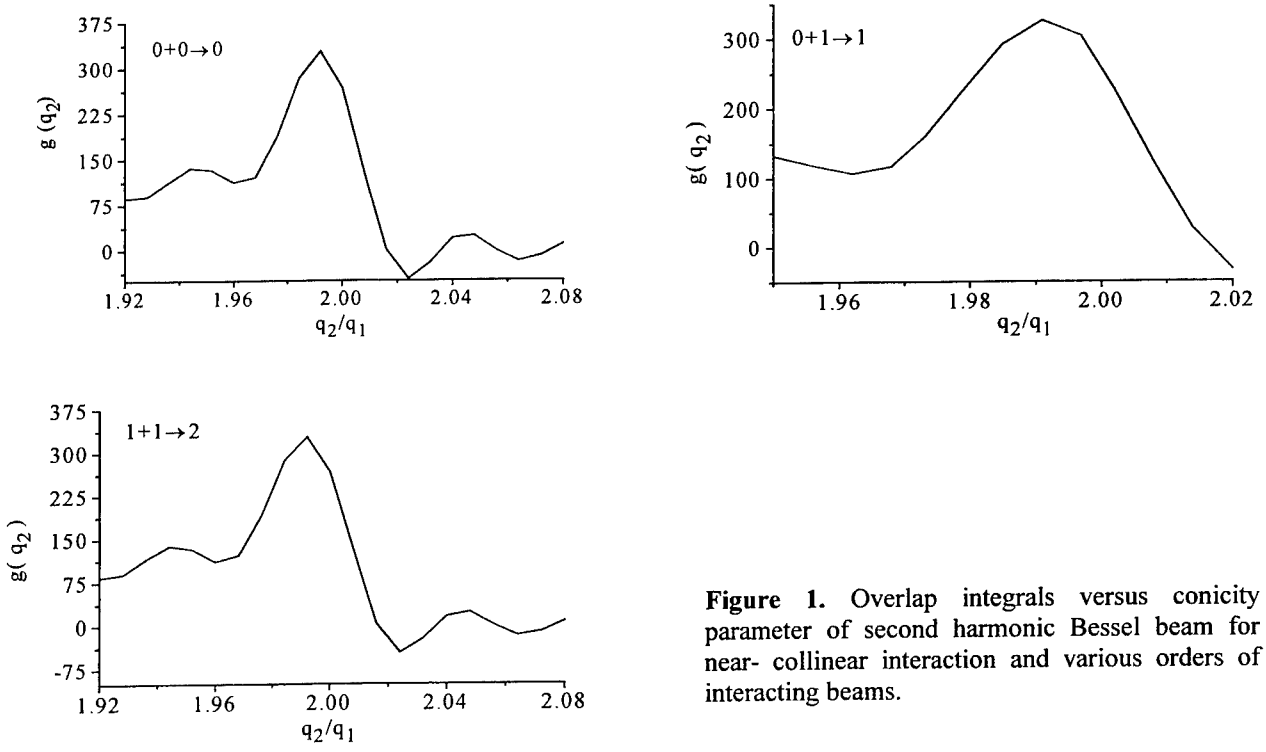


Figure 1. Overlap integrals versus conicity parameter of second harmonic Bessel beam for near- collinear interaction and various orders of interacting beams.

The dependence $g(q_2)$ in the vicinity of the given maximum for processes $0+1 \rightarrow 1$ and $1+1 \rightarrow 2$ is shown in Fig. 1. For numerical estimations we supposed that conicity angle is $\gamma = 1$ deg. and Bessel beam radius is $R_B = 1.5$ mm.

As it follows from Fig. 1, the profile of function $g(q_2)$ for three different processes is practically the same. The peak values of these overlap integrals are also close. Similar is the behavior of overlap integrals for the other investigated processes, in particular $1+2 \rightarrow 3$, $3+3 \rightarrow 6$ etc.

Thus nonlinear interaction of higher order Bessel beams does not decrease the maximum value of the overlap integral in comparison with the basic process $0+0 \rightarrow 0$. Hence the collinear interactions will be carried out with no decrease in efficiency.

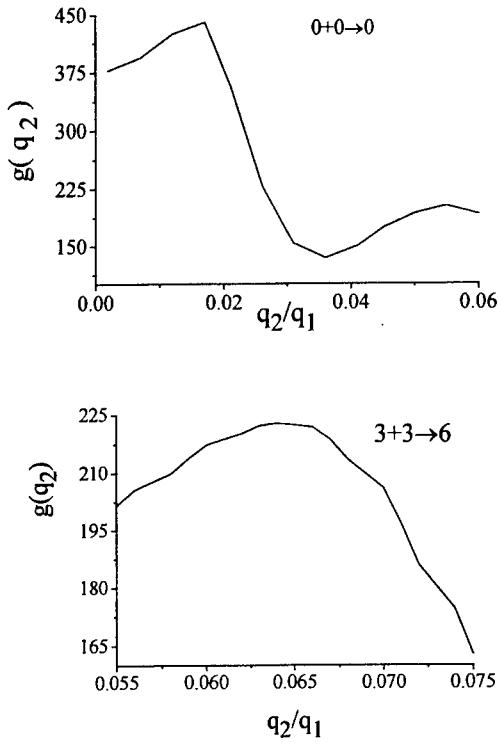


Figure 2. Overlap integrals versus conicity parameter of second harmonic Bessel beam for near π-vectorial interaction and various orders of interacting beams.

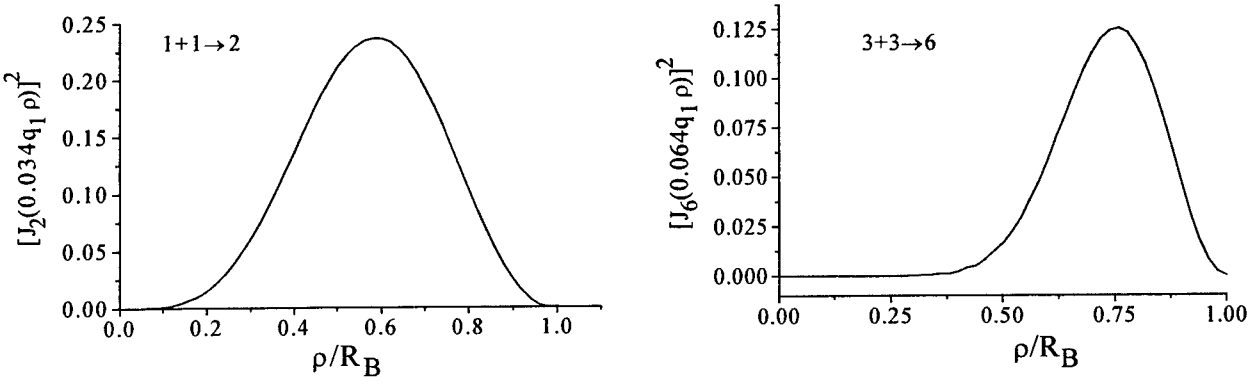


Figure 3. Fundamental modes of second harmonic generated as a result of π-vectorial interaction.

In the process under consideration, a summation of dislocations of axial second harmonics beam is possible as well. A typical structure of the corresponding overlap integrals is shown in Fig.2. It is important that the overlap integral decreases when Bessel function order increases. Let us also note that the peak value of an overlap integral is always realized for a second harmonic beam, which is a fundamental mode of a cylindrical domain with radius R_B. For illustration of this rule Fig.3 shows the intensity distribution of fields generated in conditions of the peak value of an overlap integral.

The novelty of the general case of second harmonic generation accompanied by summation of dislocations is that, unlike the basic process, there exists a possibility of vanishing of the axial second harmonic beam. It takes place when orders of interacting Bessel are not equal each other.

For production of higher order Bessel beams we use the optical scheme shown in Fig.4. Utilized here is the effect of transformation of the order of the Bessel beam in biaxial crystals [12].

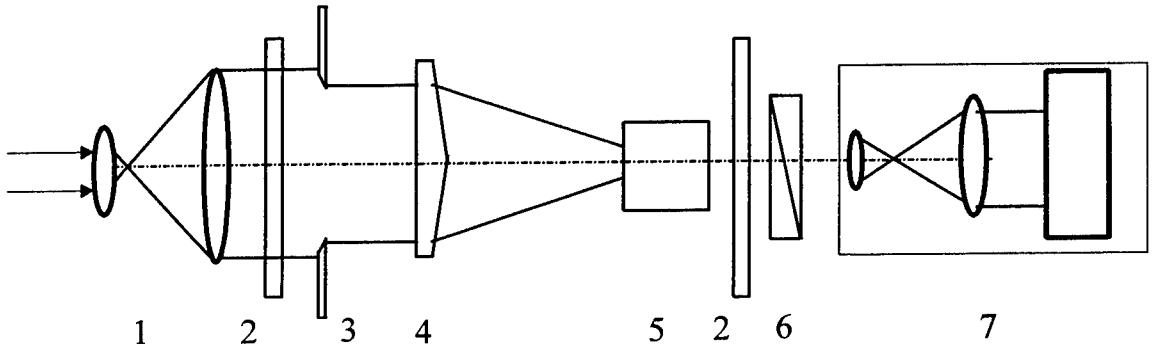


Figure 4. Experimental set-up: 1 - 16× telescope; 2 - λ/4 plate, 3 - diaphragm, 4 - axicon; 5 - KTP crystal; 6 - polarization analyzer; 7 - viewing and recording system.

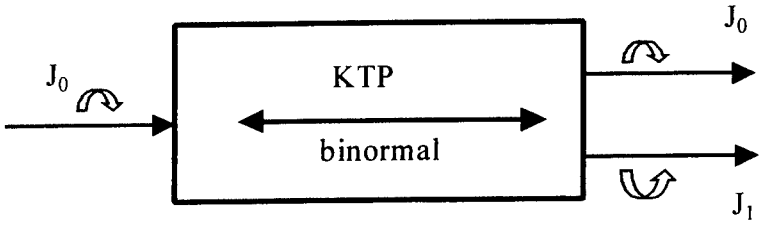


Figure 5. Basic optical element for transformation of Bessel beam order

The transformation of the order of a Bessel function is not limited to the process $J_0(x) \rightarrow J_1(x)\exp(i\varphi)$ and may be continued until second and higher-order Bessel beams are obtained (Fig. 6). In this scheme one can obtain $J_1(x)\exp(i\varphi)$ field as well as $J_2(x)\exp(2i\varphi)$ field.

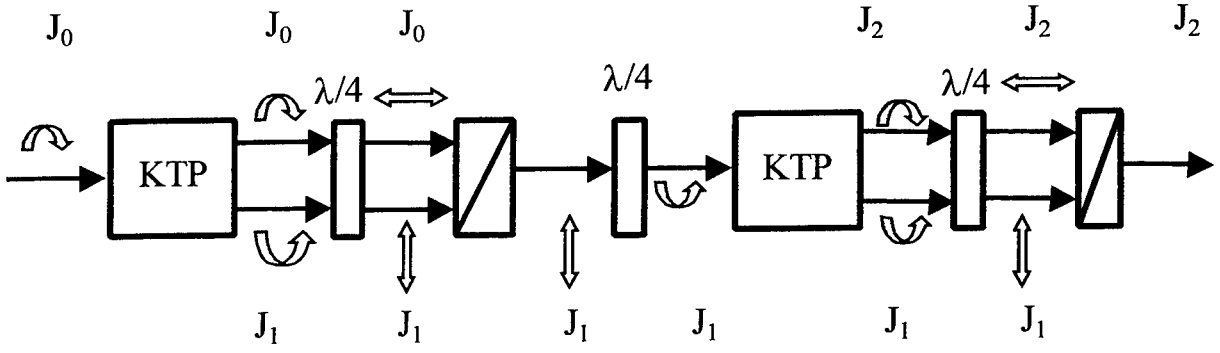


Figure 6. Principal scheme for production of Bessel beams of first and second orders.

For second harmonic generation we used a KTP crystal with a large width of angular synchronism. It allowed us to observe simultaneously the transformation of dislocations in both axial and ring beams of second harmonics.

Fig. 7a shows a typical second harmonic field for $1+1\rightarrow 2$ interaction. Both the annular field and axial beam have a second-order dislocation, which is confirmed by decay of second-order dislocation in axial field into two first-order dislocations.

The annular second harmonic field obtained in the $0+1\rightarrow 1$ process is shown in Fig. 7b.

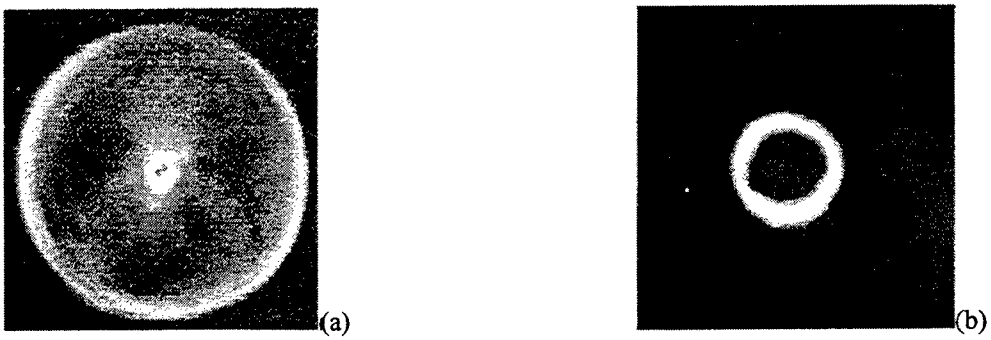


Figure 7. Far field of second harmonic for processes (a) $1+1\rightarrow 2$ and (b) $0+1\rightarrow 1$.

3. SECOND HARMONIC GENERATION BY TWO BESSEL BEAMS WITH OPPOSITE SIGNS OF TOPOLOGICAL CHARGE

In order to obtain Bessel light beams with opposite dislocation signs we used a modification of the above scheme (Fig. 8). The input beam in this case was linearly polarized. The output field was a superposition of two first-order Bessel beams $J_1(x)\exp(i\varphi)+ \tau J_{-1}(x)\exp(-i\varphi)$, where $\tau \leq 1$ (Fig. 9).

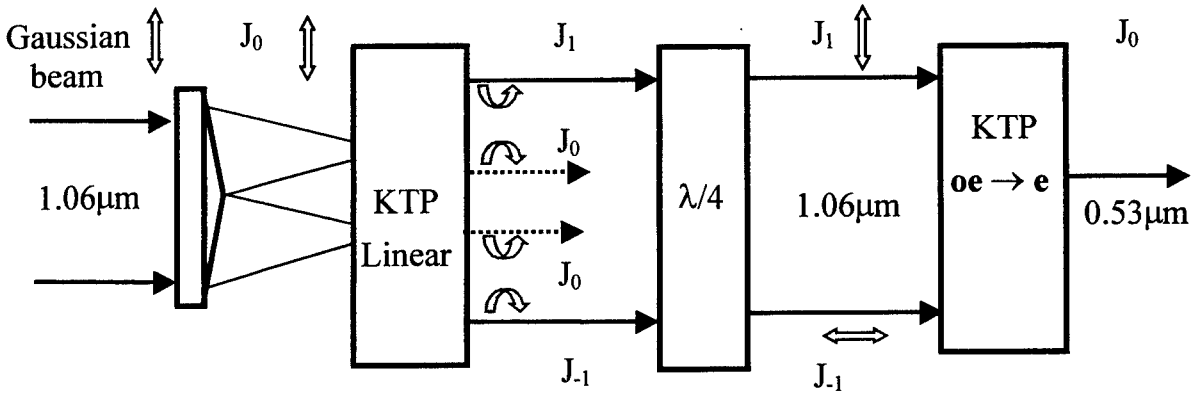


Figure 8. Principal scheme for production of superposition of Bessel beams of +1 and -1 orders.

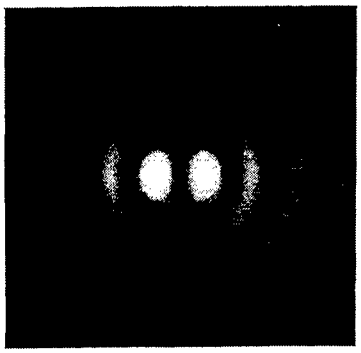
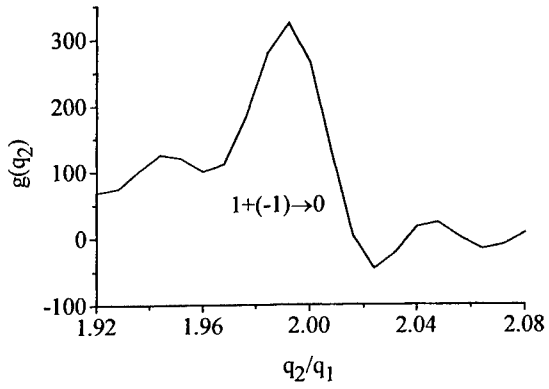


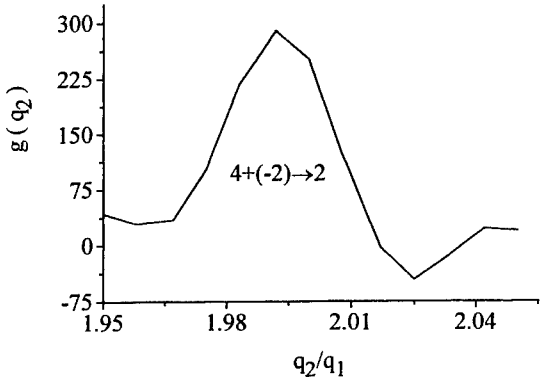
Figure 9. Intensity distribution of superposition of Bessel beams of +1 and -1 orders.



Figure 10. Zero-order Bessel beam of second harmonic generated in process $1-1\rightarrow 0$.

Experimentally registered zero-order Bessel beam of second harmonic generated in process $1-1\rightarrow 0$ is shown in Fig. 10.





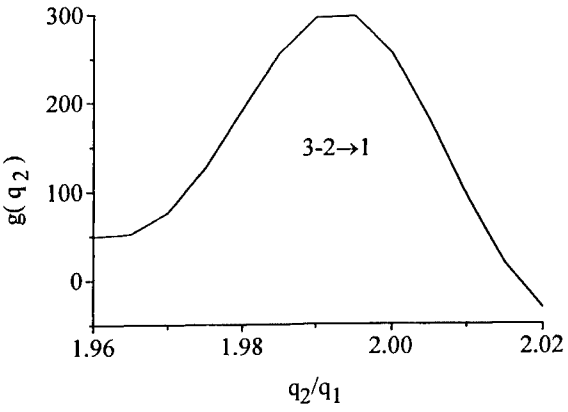


Figure 11. Overlap integrals versus conicity parameter of second harmonic Bessel beam for near collinear interaction of two Bessel beams with opposite signs of dislocation order.

The examination of overlap integral shows that in this case a collinear interactions are also effectively realized. This conclusion is correct for both cases, namely, for two Bessel beams of fundamental frequency having equal and different orders (see. Fig. 11).

A generation of an axial field is also possible for interaction under consideration. Several examples of overlap integrals for this case are shown in Fig. 12. One can see that, in contrast to the previous case, the peak value of overlap integral remains almost unchanged when the order of Bessel function increases.

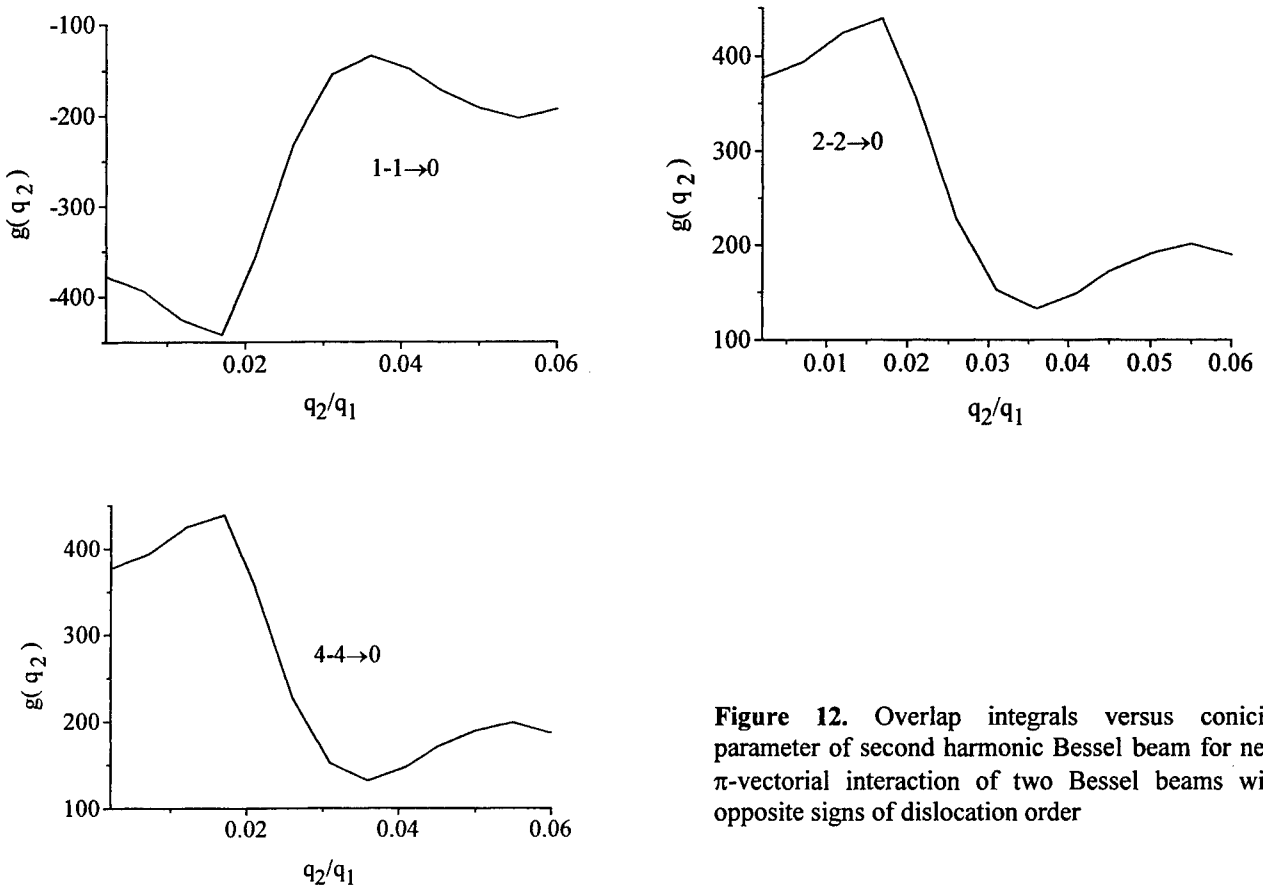


Figure 12. Overlap integrals versus conicity parameter of second harmonic Bessel beam for near π-vectorial interaction of two Bessel beams with opposite signs of dislocation order

Besides, an inversion of sign of the overlap integral takes place for Bessel beams of odd orders. Finally, the axial field of second harmonic is absent for interaction of Bessel beams of not coinciding orders.

CONCLUSION

Thus, we have shown both theoretically and experimentally that Bessel beams of higher orders can efficiently interact in the processes of second harmonic generation, accompanied by summation and substraction of wave front dislocations.

REFERENCES

1. J.F. Nye and M.V. Berry, *Proc. R. Soc. Lond. A* **336**, p. 165, 1974.
2. I.V.Basistiy, V.Yu.Bazhenov, M.S.Soskin, M.V.Vasnetsov, *Optics Comm.* **103**, p. 422, 1993.
3. I.V.Basistiy, I. G. Marienko, M.S.Soskin, M.V.Vasnetsov, *Proc. SPIE* **2792**, p. 172, 1998.
4. G.P. Karman, M.W. Beijersbergen, A. Van Duijl, and J.P. Woerdman, *Opt. Lett.* **22**, p. 1503, 1997.
5. M.V. Berry, *J. Modern Optics*, **45**, p. 1845, 1998.
6. K. Dholakia, N.B. Simpson, M.J. Padgett, L. Allen, *Phys. Rev. A* **54**, p. R3742, 1996.
7. A. Berzanskis, A. Matijosius, A., Piskarskas A., V. Smilgevicius, A. Stabinis, *Optics Comm.*, **140**, p. 273, 1997; **150**, p. 372, 1998.
8. C.O. Weiss, M. Vaupel, K. Staliunas, G. Slekus, V.B. Taranenko, *Appl. Phys. B*, **68**, p. 151, 1999.
9. M. Florjanczyk, R. Tremblay, *Optics Comm.* **73**, p. 448, 1989.
10. C. Paterson, R. Smith, *Optics Comm.* **124**, p. 121, 1996.
11. I. Manek, Yu. B. Ovchinnikov, R. Grimm, *Optics Comm.* **147**, p. 67, 1998.
12. N.S. Kazak, N.A. Khilo, A.A. Ryzhevitch, *Quantum Electronics*, **29**, p. 1020, 1999.

Resonator with Bessel-Gauss modes

A.N. Khilo, E.G. Katranji, A.A. Ryzhevich

Institute of Physics, National Academy of Sciences of Belarus,
70 F.Skaryna ave., 220072, Minsk, Belarus. e-mail: khilo@dragon.bas-net.by

ABSTRACT

We present a new scheme of optical resonator for production of Bessel and Bessel-Gauss beams. This resonator, employing only spherical mirrors and axicons, does not contain any complicated optical elements. Analytical expressions relating parameters of resonator and characteristics of its modes are obtained and analyzed. Diffraction energy losses are calculated with Fox-Li algorithm, and modal discrimination is studied.

1. INTRODUCTION

Bessel light beams are being investigated intensively since their introduction by Durnin *at. al.* [1-2]. Initial interest to these beams was arisen by their useful property of suppressed diffraction divergence and ability to reconstruct their intensity profile during propagation in uniform media if their initial profile was partially distorted. Now investigations are in progress on usage of Bessel beams in processes of second [3-5] and third [6-8] harmonic generation, parametric frequency conversion [9-11], etc. Bessel light beams of higher orders [12-13] are promising for atom trapping because they have zero axial intensity, large gradients of intensity, and small central spot size.

Infinite Bessel light beams, which are exactly propagation-invariant, cannot be realized in practice because they possess infinite energy. Bessel-Gauss light beams [14], being the generalization of Bessel beams, have finite of energy and are approximately diffractionless over certain propagation distance.

An important feature of Bessel light beams is that they can be easily obtained by illuminating an axicon with a conventional Gaussian beam . The field in an extended region behind an axicon is approximately a zero-order Bessel light beam. Illuminating the axicon with Laguerre-Gaussian beams we can obtain higher-order Bessel beams [15]. This axicon-based method is now probably most widely used method of Bessel beams production. Among other methods of Bessel beam production are holographic method [16], and a method where a lens Fourier-transforms a ring field into a Bessel light beam.

Passive schemes of Bessel beam production have some disadvantages. First of all, the beams produced by these schemes are not exactly the Bessel light beams. While their quality may be sufficient for some applications, active methods of Bessel beam generation allow to produce Bessel beams with higher quality. Furthermore, the volume of Bessel modes is higher than the volume of Gaussian modes, which allows to increase the energy of generation. Also important is a development of inracavity schemes of nonlinear frequency conversion of Bessel beams.

Several optical resonators with Bessel modes have been proposed by now. Uehara and Kikuchi [17] suggested and studied experimentally a resonator scheme based on a transformation of a ring field into a Bessel light beam with an intracavity Fourier-transforming lens. One of the resonator's mirrors was plane, and the other was also plane but with annular aperture. In theoretical work [18] Jabzyński proposed to generate Bessel light beams in a confocal resonator with an annular-aperture cylindrical active medium. Pertti Pääkkönen and Jari Turunen [19] suggested and studied resonators with aspheric mirrors, which conjugate the phase of the incident field of Bessel-Gauss modes. Using resonator with such mirrors, it is possible to obtain Bessel-Gauss light beams of zero and higher order, and it is also possible to attain high discrimination of transverse modes to ensure single-mode operation of the resonator.

This article introduces a new scheme of optical resonator for Bessel and Bessel-Gauss light beams production. Our method does not require any intracavity optics or special shape of active medium. Although it is based on the same idea of phase-conjugating mirrors which was used in [19], it employs only conventional spherical (or plane) mirrors and axicons, and does not use any complex-shape mirrors.

In the first section we briefly describe Bessel and Bessel-Gauss light beams. Then we apply the phase-conjugating-mirrors concept to construct a scheme of a resonator with Bessel and Bessel-Gauss modes in section 2. Then we obtain analytical relationships between parameters of resonator and parameters of its modes and analyze them in section 3. Fourth section discusses diffraction losses and modal discrimination of finite-mirror resonators.

Laser Optics 2000: Control of Laser Beam Characteristics and Nonlinear Methods for Wavefront Control,
Leonid N. Soms, Vladimir E. Sherstobitov, Editors, Proceedings of SPIE Vol. 4353 (2001)
© 2001 SPIE · 0277-786X/01/$15.00

1. BESSEL AND BESSEL-GAUSS LIGHT BEAMS

Let us briefly describe Bessel and Bessel-Gauss light beams in order to establish notation and to provide a reference point for necessary formulas.

Bessel light beams are the beams with components of electric or magnetic field vectors described by Bessel functions. In general case, different field components are described by Bessel functions of different orders, and also by their linear combinations. Most simple is a Bessel light beam with a transverse field component

$$U_m(\rho,\phi,z) = cJ_m(k\gamma\rho)\exp\big(i(k_z z + m\phi)\big), \tag{1}$$

where ρ, ϕ, and z are the radial, azimuthal, and axial coordinates, J_m is an m-order Bessel function, $k = 2\pi/\lambda$, γ is the conicity angle of Bessel beam, $k_z = k\cos\gamma$, and c is a constant.

The field at the waist of the m-order Bessel-Gauss beam is

$$U_m(\rho,\phi) = cJ_m(k\gamma\rho)\exp\Big(-\rho^2/w_0^2\Big)\exp(im\phi), \tag{2}$$

where w_0 is radius at the waist of corresponding Gaussian beam

$$U \sim \exp(-\rho^2/w_0^2). \tag{3}$$

When $w_0 \to \infty$, Eq. (2) describes a usual Bessel beam. Field of Bessel-Gauss light beam at a distance z from the waist in paraxial approximation is

$$A_m(\rho,\phi,z) = c\frac{w_0}{w(z)}e^{i\Phi(z)}J_m\left(\frac{k\gamma\rho}{1+iz/z_R}\right)\cdot\exp\left(-\left[\frac{1}{w^2(z)}-\frac{ik}{2R_g(z)}\right]\cdot\left(\rho^2+\gamma^2z^2\right)\right)e^{im\phi}, \tag{4}$$

where $w(z) = w_0\sqrt{1+(z/z_R)^2}$ describes the longitudinal evolution of the radius of Gaussian beam (3) ($z=0$ at its waist), $R_g(z) = z + z_R^2/z$ is the wavefront curvature of Gaussian beam (3), $z_R = kw_0^2/2$ is its Rayleigh range. The function $\Phi(z) = k(1-\gamma^2/2)z - arctg\,(z/z_R)$ describes the axial phase of Bessel-Gauss beam.

While Bessel-Gauss light beams approximately maintain its intensity profiles when propagating over rather extended region, its intensity distributions at larger distances from the waist ($z>>z_R$) are ring-shaped. This fact is illustrated in Fig. 1a and 1b, which show sample radial distributions of amplitude at two distances from the waist. Plotted in Figs. 1c and 1d are radial phase distributions for these two cases. It can be seen that radial phase has some oscillations while almost linearly increasing with ρ for small z (Fig. 1c). These oscillations are very small in the area of energy localization of the beam for large z (Fig. 2d, 2b).

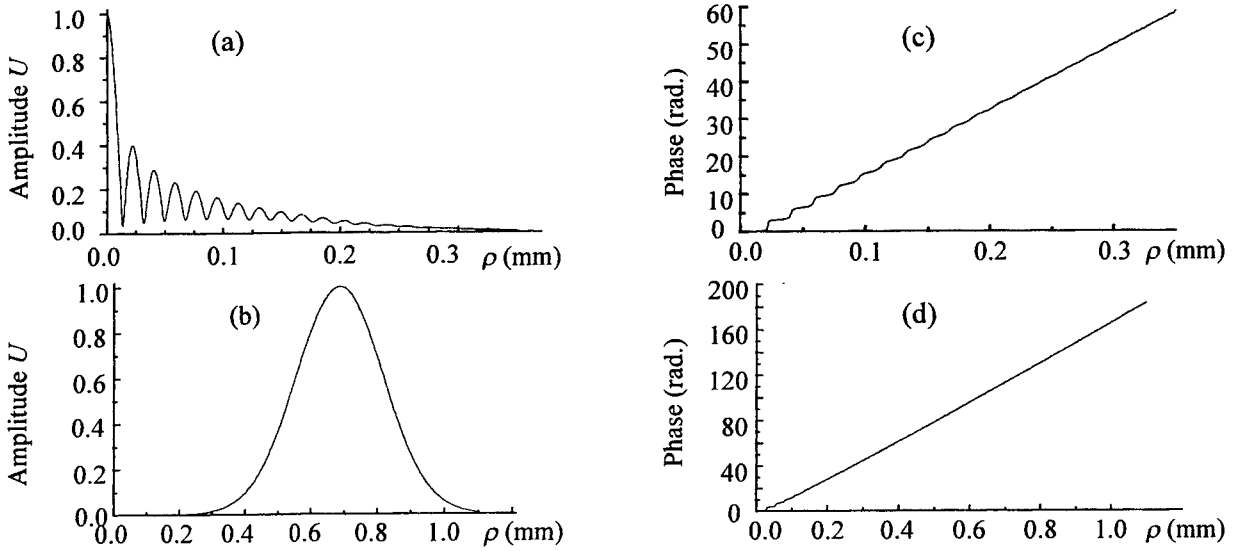


Figure 1. Amplitude and phase profiles of zero-order Bessel-Gauss light beam (γ=1 deg, w_0=0.18 mm, λ=0.633 μm). Plots on the left show field amplitude module versus radial coordinate ρ at distances (a) z=4 mm, and (b) z=40 mm. Plots on the right show radial phase distributions at these distances.

2. RESONATOR DESIGN

A concept for design of laser resonators with arbitrary modes is well described in the literature (see, for example, [20]). This concept is based on the fact if we want to build a resonator with some field being its mode, we must use mirrors that conjugate the radial phase of this field. In general case the shape of these mirrors must be aspheric, and sometimes very complex. In principle, we can make a laser resonator for generation of any field we need, if we can only manufacture mirrors with any shape we want.

We now apply this concept to design the resonator with Bessel-Gauss modes. Let the waist of zero-order Bessel-Gauss beam be situated at the plane of left resonator mirror (z =0). Since the radial phase at this plane can only be equal to 0 or π (see Eq. (2)), the mirror that conjugates such phase is a conventional plane mirror. This mirror can be made semitransparent to be used for an output of Bessel-Gauss beam from the resonator.

Let us place the second mirror at distance L from the beam waist. The reflectance function of mirror 2 can be written as

$$\tau_2(\rho) = \exp(i\varphi_2(\rho)). \tag{5}$$

To fulfill the condition that the phase of Bessel-Gauss beam is conjugated by this mirror, $\tau_2(\rho)$ must be equal to exp(-2·(phase of Bessel-Gauss beam at $z = L$)). Therefore, using Eq. 4 we obtain that the phase function $\varphi_2(\rho)$ of mirror 2 must be equal to

$$\varphi_2(\rho) = 2\Phi(z) + \frac{k\gamma^2 L^2}{R_g(L)} + \frac{k\rho^2}{R_g(L)} + 2\arg\left(J_m\left(\frac{k\gamma\rho}{1+iL/z_R}\right)\right).$$

Neglecting first two terms of this formula which does not depend on radial coordinate ρ we obtain:

$$\varphi_2(\rho) = \frac{k\rho^2}{R_g(L)} + 2\arg\left(J_m\left(\frac{k\gamma\rho}{1+iL/z_R}\right)\right). \tag{6}$$

The first term of this formula describes a spherical component of mirror 2 shape, and the second term – its aspericity.

In their article [19] Pertti Pääkkönen and Jari Turunen obtained formula (6), proposed and studied a resonator scheme on the basis of such aspheric mirror. In order to design a resonator without complex optical elements, we suggest to use the fact that the second term of (6) is approximately linear at large resonator lengths, as it can be inferred from Fig. 1(d). Then mirror 2 can be realized as a combination of usual spherical mirror, corresponding to the first term of (6), and an axicon, corresponding to the second term of (6). This combination can be manufactured as a single optical element.

The optical scheme of this resonator is shown in Fig. 2. The waist of Bessel-Gauss beam is formed in the plane of mirror 1, which has an aperture radius of $R_{1\max}$. The field in the plane of mirror 2 and axicon 3 is annular, with the maximum of intensity of the ring situated at a distance γL from resonator axis. The aperture of mirror 2 can be also annular, with the radii of reflective part equal to $R_{2\min}$ and $R_{2\max}$. Values of $R_{2\min}$ and $R_{2\max}$ affect the diffraction energy losses and resonator mode shape. For example, they can be selected to fulfill the equation $(R_{2\min} + R_{2\max})/2 = \gamma L$.

The radius R of mirror 2 and parameter α of axicon 3 ($\alpha = (n-1)\beta$, where n is a refractive index of the axicon, and β is its base angle) determine the parameters γ and w_0 of Bessel-Gauss modes. In the following section we will obtain formulas relating parameter of resonator and parameters of its Bessel-Gauss modes.

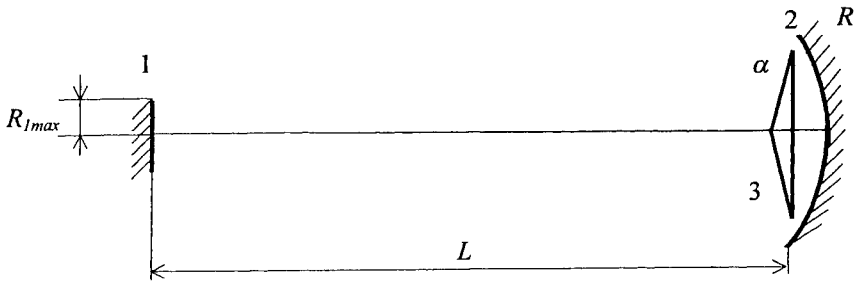


Figure 2. Design of resonator with Bessel-Gauss modes.
1 – semitransparent plane mirror with radius of aperture $R_{1\max}$, 2 – spherical mirror with radius of curvature R placed at a distance L from the plane mirror, its annular aperture has radii $R_{2\min}$ and $R_{2\max}$, 3 – axicon with parameter α.

In order to prove that the modes of proposed resonator are indeed close to Bessel-Gauss beams, we used Fox-Li algorithm of numerical calculation of resonator modes. This algorithm allows not only to determine the mode structure but also to calculate diffraction energy losses of these modes. Fig. 3 shows an example of radial amplitude distributions (solid line) for three different radii of plane mirror 1. It is clear that the resonator modes are indeed very close to Bessel-Gauss beams (dotted line), especially when energy losses are small.

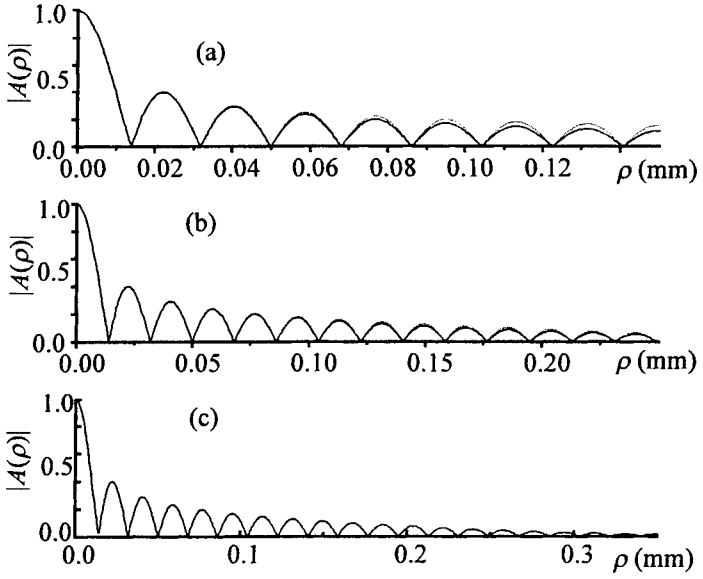


Figure 3. Transverse amplitude distribution of resonator mode (solid line) at plane mirror 1 and Bessel-Gauss light beam (dotted line) for
(a) R_{1max}=0.15mm (diffraction energy loss 55.7%),
(b) R_{1max}=0.25mm (diffraction energy loss 13.0%),
(c) R_{1max}=0.35mm (diffraction energy loss 4.31%).
(Resonator parameters: α = 0.670 deg, R = 0.835m, L=0.2 m, R_{2min}=3.1 mm, R_{2max} =3.9mm; Bessel-Gauss beam parameters: γ = 1 deg, w_0 = 424 λ, λ=643 nm.)

3. RELATIONSHIPS BETWEEN RESONATOR AND MODE PARAMETERS

Let us now proceed to deriving analytical expressions for resonator parameters required to generate a Bessel-Gauss light beam with given parameters.

It can be shown that the following approximation of the second term of (6) can be made for large L:

$$\arg\left(J_m\left(\frac{k\gamma\rho}{1+iL/z_R}\right)\right) \approx \frac{k\gamma\rho}{1+L^2/z_R^2}.$$

Then the phase function of mirror 2 is

$$\varphi_2(\rho) = \frac{k\rho^2}{R_g(L)} + 2\frac{k\gamma\rho}{1+L^2/z_R^2}.$$

The phase function of spherical mirror with radius R is $k\rho^2/R$, and that of an axicon is ($k\alpha\rho$). Taking into account that light travels two times through the axicon in this scheme, and making substituting $z_R = kw_0^2/2$, we finally arrive at the following equations:

$$R = L + \frac{(kw_0^2)^2}{4L}, \tag{7}$$

$$\alpha = \frac{\gamma}{1+4L^2/(kw_0^2)^2}. \tag{8}$$

In order to make a resonator which would generate Bessel-Gauss beam with conicity angle γ and width w_0, we must choose R and α in accordance with Eqs. (7)–(8).

Let us now analyze these formulas. First of all, consider the case of generation of Bessel (not Bessel-Gauss) light beam. It is easy to see that when $w_0 \to \infty$, the mirror radius $R \to \infty$ (flat mirror), and axicon parameter $\alpha \to \gamma$. Thus, to construct a resonator with Bessel modes, we can use just two plane mirrors and an axicon (or one plane mirror and an axicon with reflecting base).

Then we would like to underline the fact that parameter α of the axicon and conicity angle γ of the generated beam are not equal, while they are equal for the passive scheme of Bessel beam production with an axicon. In fact, the conicity angle is always larger than α. In other words, having an axicon with parameter α we cannot obtain Bessel-Gauss beam with $\gamma < \alpha$ with this resonator scheme.

The equations defining parameters of mode in a resonator with given L, α, and R follow from Eqs. (7)-(8):

$$w_0^2 = \frac{1}{2}\sqrt{\frac{(R-L)L}{k}}, \tag{9}$$

$$\gamma = \alpha\frac{R}{R-L}. \tag{10}$$

In order to illustrate these relationships we plotted functions $w_0(L)$ and $\gamma(L)$ in Fig. 4a, b. It can be inferred from Fig. 4b that the maximum resonator length for given α and R is limited by the requirement of applicability of paraxial approximation. For the parameter a under consideration, the approximate inequality $L<0.8R$ should be fulfilled. Note that Bessel-Gauss mode structure is not formed when $L>R$.

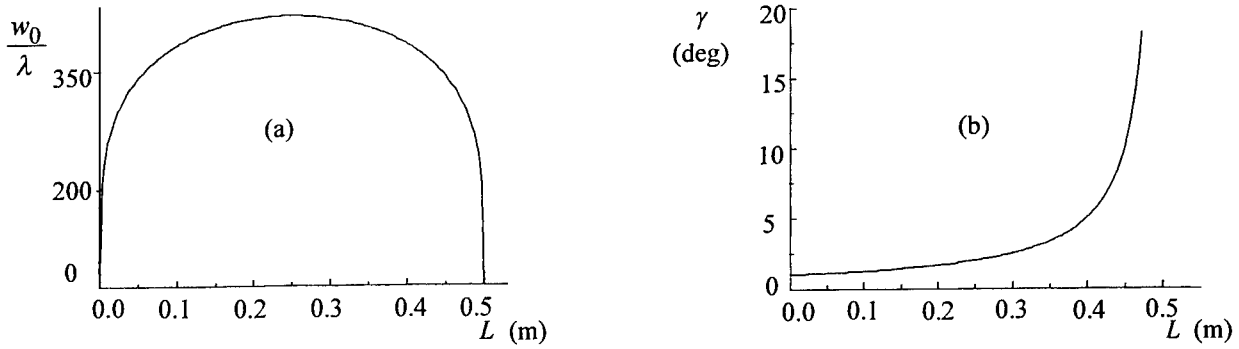


Figure 4. (a) Beam width w_0 and (b) conicity angle γ versus resonator length L. (Radius of mirror curvature R = 0.5 m and axicon parameter α = 1 deg.)

4. DIFFRACTION ENERGY LOSSES AND MODAL DISCRIMINATION

Although we dealt with zero-order Bessel-Gauss beams above, higher-order Bessel-Gauss beams are also the transverse modes of the resonator, because the radial phase of Bessel-Gauss beams of different orders is almost the same for large diffraction lengths, and a combination of mirror and axicon conjugates the radial phases of them all. It means that diffraction energy losses of resonator modes of different orders do not differ significantly. Therefore, there possible regimes when laser generates several transverse modes at a time. Sometimes it is not a problem, but there are cases when it is desirable to have a resonator operating in a single-mode regime. In this section we propose and discuss two ways of solving the problem of selection of transverse resonator modes.

The first way to select a single mode among other Bessel-Gauss modes is to use a plane mirror with properly chosen radius $R_{1\max}$. The intensity distribution at the waist of these Bessel-Gauss modes is different, which accounts for their different diffraction energy losses. Variation of aperture size of spherical mirror 2 can provide only very insignificant difference between losses of different modes because the intensity distribution at this mirror is annular regardless of the mode index m.

We used the Fox-Li algorithm for calculation of diffraction energy losses of Bessel-Gauss modes of different orders. The initial field was chosen in the form

$$U_m(\rho,\phi,z) = u_m(\rho,z)\exp(im\phi). \tag{11}$$

This allowed us to perform Fox-Li iterations using the one-dimensional Fresnel diffraction integral written for the field of type (11):

$$U_m(\rho,\phi,z) = -i^{m+1}\frac{k}{z}\exp(ikz)\exp\left(\frac{ik}{2z}\rho^2\right)\exp(im\phi)\int_0^\infty u_m(\rho',0)J_m(k\rho\rho'/z)\exp\left(\frac{ik}{2z}\rho'^2\right)\rho'^2 d\rho'. \tag{12}$$

The general two-dimensional Fresnel integral is not convenient for calculation of diffraction energy losses of individual modes for two reasons. First of all, because only the mode with minimal loss (or superposition of modes) would establish in the resonator during our calculations with two-dimensional integral, we cannot determine the losses of the other modes. The second reason is that it takes a lot of time to calculate a two-dimensional integral. Using one-dimensional integral (12) we eliminate these difficulties. The initial field $u_m(\rho',0)$ of Fox-Li algorithm was chosen random in our calculations.

Fig. 5 shows diffraction loss per one trip for $m = 0, 1, 2$ as a function of plane mirror radius R_{1max} for the resonator configuration designed to produce a Bessel beam with $\gamma = 1$ deg ($\alpha = 1$ deg, $R = \infty$, L=6 cm, R_{2min} = 0.4 mm, R_{2max} = 1.6 mm). Some values of diffraction losses are also shown in Table 1. Fig. 6 shows the ratio of diffraction loss of first mode to the loss of the zeroth mode. These results indicate that the diffraction losses are indeed different for modes of different orders, although the difference is rather small. This difference might be enough to ensure single-mode operation of the resonator, especially in low-gain laser systems.

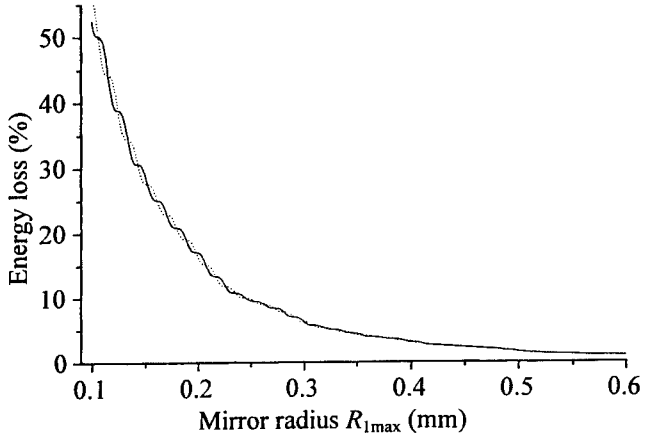


Figure 5. Diffraction loss per trip versus plane mirror radius for Bessel-Gauss modes of orders 0, 1, 2. Resonator is designed to produce a Bessel beam with $\gamma = 1$ deg ($\alpha = 1$ deg, $R = \infty$, L=6 cm, R_{2min} = 0.4 mm, R_{2max} = 1.6 mm).

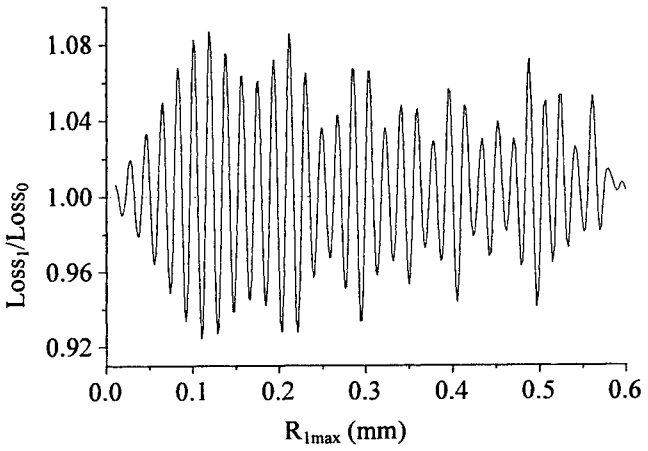


Figure 6. The ratio of diffraction losses of Bessel-Gauss modes of orders 1, 2 to the round-trip loss of mode 0 (resonator parameters are the same).

R_{1max}, mm	Loss for m=0	Loss for m=1	Loss for m=2	R_{1max}, mm	Loss for m=0	Loss for m=1	Loss for m=2
0.25	9.5152 %	9.8499 %	9.5509 %	0.2578	9.4010 %	9.0921 %	9.4329 %
0.2513	9.4851 %	9.7456 %	9.5274 %	0.2591	9.3296 %	9.0256 %	9.3558 %
0.2526	9.4779 %	9.6184 %	9.5231 %	0.2604	9.2295 %	8.9933 %	9.2503 %
0.2539	9.4773 %	9.4749 %	9.5219 %	0.2617	9.1017 %	8.9843 %	9.1182 %
0.2552	9.4698 %	9.3282 %	9.5114 %	0.2630	8.9532 %	8.9838 %	8.9679 %
0.2565	9.4464 %	9.1955 %	9.4835 %	0.2643	8.7979 %	8.9773 %	8.8142 %

Table 1. Diffraction loss per trip versus plane mirror radius for Bessel-Gauss modes of orders 0, 1, 2.

The second way to select a mode which is generated in the laser resonator is to use the plane mirror with special configuration of reflective surface.

Let us consider a superposition of Bessel-Gauss modes with m=-1 and m=1. This field is proportional to

$$J_1(k\gamma z)\cos(\phi + \phi_0)\,. \tag{13}$$

The minimums of this distribution are in directions $\phi = \pi/2$ and $\phi = 3\pi/2$ when phase shift ϕ_0=0. Let us place two nonreflecting sectors along these directions, as it is shown in Fig. 7. The losses of mode $J_1(k\gamma z)\cos(\phi)$ would be lesser than losses of other modes, which would cause this mode to be the only mode of this now single-mode-operating resonator. To confirm this idea we resorted to Fox-Li algorithm again, this time with two-dimensional Fresnel diffraction integral. Fig. 8 shows two-dimensional intensity distribution of the field (13), and Fig. 9 – of the calculated mode field (regions $\phi \in (\pi/2 - \pi/10,\ \pi/2 + \pi/10)$ and $\phi \in (3\pi/2 - \pi/10,\ 3\pi/2 + \pi/10)$ were nonreflecting). Excellent agreement between Figs. 8 and 9 indicated the validity of this method of modal selection.

In the general case, we can use the plane mirror with $2m$ nonreflecting sectors to select a mode $J_m(k\gamma z)\cos(m\phi)$.

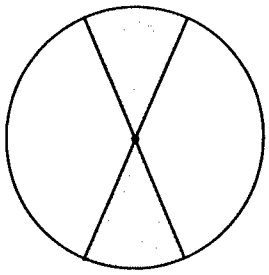


Figure 7. Mirror with two nonreflecting sectors (shown gray).



Figure 8. Intensity distribution of field (13).

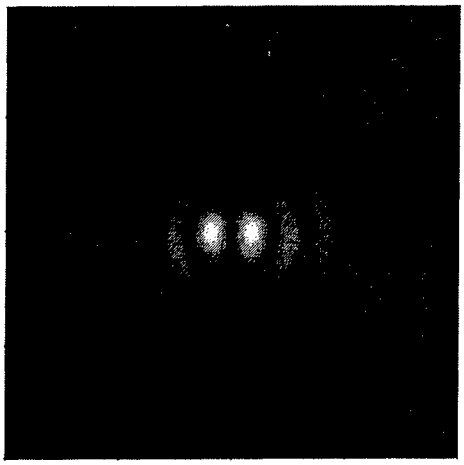


Figure 9. Calculated intensity distribution of the mode at the output mirror 1.

5. CONCLUSION

The resonator composed of plane and spherical mirrors and an axicon produces beams which are very close to Bessel-Gauss beams. Modes of the resonator with two plane mirrors and an axicon are Bessel beams. An important advantage of the proposed resonator with Bessel-Gauss modes is that its construction does not require any complex optical elements.

Properly selecting the plane mirror radius we can ensure single-mode operation of the laser resonator in low-gain laser systems. More effective method of attainment of high modal discrimination is to use the plane mirror with nonreflecting sector-shaped regions.

REFERENCES

1. J. Durnin, "Exact solutions for nondiffracting beams. I. The scalar theory.", *J. Opt. Soc. Am. A* **4**, pp. 651-654, 1987.
2. J. Durnin, J.J Miceli, Jr., J.H. Eberly, "Diffraction-free beams", *Physical Review Letters* **58**, №. 15, pp. 1499-1501, 1987.
3. T. Wulle, S. Herminghaus, "Nonlinear Optics of Bessel Beams", *Physical Review Letters* **58**, pp. 1401-1404, 1987.
4. Keisuke Shinozaki, Chang-qing Xu, Hironori Sasaki, Takeshi Kamijoh, "A comparision of optical second-harmonic generation efficiency using Bessel and Gaussian beams in bulk crystals", *Optics Communications* **133**, pp. 300-304, 1997.
5. J. Arlt, K. Dholakia, L. Allen, M.J. Padgett, "Efficiency of second-harmonic generation with Bessel beams", *Physical Review A* **60**, pp. 2438-2441, 1999.
6. B. Glushko, B. Kryzhanovsky, D. Sarkisyan, "Self-Phase-Matching Mechanism for Efficient Harmonic Generation Processes in a Ring Pump Beam Geometry", *Physical Review Letters* **71**, pp. 243-246,1993.
7. Surya P. Tewari, H. Huang, R.W. Boyd, "Theory of third-harmonic generation using Bessel beams, and self-phase-matching", *Physical Review A* **54**, pp. 2314-2325, 1996.
8. C.F.R. Caron and R.M. Potvliege, "Optimum conical angle of a Bessel-Gauss beam for low-order harmonic generation in gases", *J. Opt. Soc. Am. B* **16**, pp. 1377-1384, 1999.
9. A. Piskarskas, V. Smilgevicius, A. Stabinis, "Optical parametric oscillation excited by an incoherent conical beam" *Optics Communications* **143**, pp. 72-74, 1997.
10. R. Gadonas, A. Marcinkevicius, A. Piskarskas, V. Smilgevicius, A. Stabinis, "Travelling wave optical parametric generator pumped by a conical beam", *Optics Communications* **146**, pp. 253-256, 1997.
11. V.N. Belyi, N.S. Kazak and N.A Khilo, "Properties of parametric frequency conversion with Bessel light beams", *Optics Communications* **162**, pp. 169-176, 1999.
12. M. Florjanczyk, R. Tremblay, "Guiding of atoms in a travelling-wave laser trap formed by the axicon", *Optics Communications* **73**, pp. 448-450, 1989.
13. I. Manek, Yu.B. Ovchinnikov, R. Grimm, "Generation of a hollow laser beam for atom trapping using an axicon", *Optics Communications* **147**, pp. 67-70, 1998.
14. F. Gori, G. Guattari, "Bessel-Gauss beams", *Optics Communications* **64**, №. 6, pp. 491-495, 1987.
15. J. Arlt, K. Dholakia, "Generation of high-order Bessel beams by use of an axicon", *Optics Communications* **177**, pp. 297-301, 2000.
16. C. Paterson, R. Smith, "Higher-order Bessel waves produced by axicon-type computer-generated holograms", *Optics Communications* **124**, pp. 121-130, 1996.
17. K. Uehara, H. Kikuchi, "Generation of Nearly Diffraction-Free Laser Beams", *Applied Physics B* **48**, pp. 125-129, 1989.
18. J.K. Jabczyński, "A "diffraction-free" resonator", *Optics Communications* 77, №. 4, pp. 292-294, 1990.
19. Pertti Pääkkönen, Jari Turunen, "Resonators with Bessel-Gauss modes", *Optics Communications* **156**, pp. 359-366, 1998.
20. J.R. Leger, D. Chen, Z. Wang, "Diffractive optical element for mode shaping of a Nd:YAG laser", *Optics Letters* **19**, 108-110, 1994.

New method of formation of high-order Bessel light beams using biaxial crystals

N.S.Kazak [a], N.A.Khilo [b], E.G.Katranji [a], A.A.Ryzhevich [a]

[a] B.I.Stepanov Institute of Physics, NAS of Belarus, 70 F.Skaryna ave., 220072, Minsk, Belarus*
[b] Division for optical problems in information technologies, NAS of Belarus, 1-2 Kuprevich str., 220141, Minsk, Belarus

ABSTRACT

A new method for obtaining high-order Bessel light beams has been developed and proved theoretically and experimentally. It is based on the phenomenon of transformation of circularly polarized light beam passing through biaxial crystal along its binormal. The method can provide conversion of input Gaussian beam into Bessel beam with an almost 100% efficiency. Besides this method can be used to convert high-intensity laser beams.

The light field having the cross distribution in the form of spiral is obtained from the first order Bessel light beams. A possibility of formation of the zeroth and the first order Bessel light beam from Gaussian light beam in biaxial crystal without axicon is investigated theoretically.

Keywords: Bessel light beams, axicon, wavefront dislocations, biaxial crystals.

1. INTRODUCTION

Investigations of non-Gaussian light fields having the cylindrical symmetry of interference structure in their cross-section are recently a great interest. The most known of such fields are the Laguerre-Gaussian and Bessel light beams (LGLBs, BLBs). These beams can be applied to making microparticles and atoms optical traps [1-3]. Besides the zero and higher orders Bessel beams have diffractionless property near beam symmetry axis. Therefore BLBs can be used for precision marking of the certain direction in space [4]. Screw wavefront dislocations avail in this case because ones do not undergo diffraction blurring. As applied to BLBs having specific spatial frequencies spectrum structure can be used in a nonlinear optics problems and permits to realize different vector interactions in a nonlinear medium [5]. Both the higher orders BLBs and LGLBs interact with a new type of nonlinear interactions due to processes of formation and cancellation of dislocations [6-8].

The propagation of a light beam in a binormal direction of a biaxial crystal is accompanied by manifold effects of transformation of its cross structure. An output field can be formed as zero- and first-orders BLB and also as different ring beams depending on a degree of focusing of the input circularly polarized Gaussian beam. The case of the transformation of Gaussian beam to the one-ring field approximately coinciding with a L_{01} mode of a Laguerre-Gauss is investigated. It is important, that all output beams polarized orthogonally to input ones have a screw phase front dislocation.

2. NEW METHOD OF BESSEL LIGHT BEAM TRANSFORMATION

2.1. Theoretical Model

It is known that when the light wave propagates in the vicinity of binormals, the effect of internal conical refraction shows up when the incident field forms, inside a biaxial crystal, a cone of directions of the energy flow. On the basis of this effect, a theoretical model may be proposed, in which there is a relationship between the fields formed at internal conical refraction and BLB having a conical structure of the spectrum of spatial frequencies. The presence of such a relationship would permit obtaining higher-order BLBs by passing laser radiation through a homogeneous crystal.

* Send correspondence to Anatol Ryzhevich
E-mail: tol@dragon.bas-net.by; phone in Minsk 284-16-16

Laser Optics 2000: Control of Laser Beam Characteristics and Nonlinear Methods for Wavefront Control, Leonid N. Soms, Vladimir E. Sherstobitov, Editors, Proceedings of SPIE Vol. 4353 (2001)
© 2001 SPIE · 0277-786X/01/$15.00

It is known that in the vicinity of binormal, the section of wave vectors surface represents two coaxial coni (Fig.1). The geometrical parameters of the coni are such that the wave vectors $\mathbf{k}_p$ of two normal modes propogating with the small angle to binormal are equal

$$\mathbf{k}_p(q) = k_x\mathbf{e}_1 + k_y\mathbf{e}_2 + (k - \gamma\mathbf{k}_x - p\gamma q - q^2/2k)\mathbf{e}_3 \tag{1}$$

where $q = \sqrt{k_x^2 + k_y^2}$, $\gamma = arctg[c^2\sqrt{(\varepsilon_3^{-1} - \varepsilon_2^{-1})(\varepsilon_2^{-1} - \varepsilon_1^{-1})}/2\mathrm{v}^2]$ is the parameter of crystal anisotropy, $k=\omega/\mathrm{v}$, v is the phase velocity of waves in the direction of binormals, $\varepsilon_{1,2,3}$ are the principal values of the permittivity tensor. Indices $p = \pm 1$ enumerate the slow and the fast modes, and $\mathbf{e}_1,\mathbf{e}_2,\mathbf{e}_3$ are the unit vectors of the Cartesian coordinate system with the z-axis parallel to the binormal (Fig. 1).

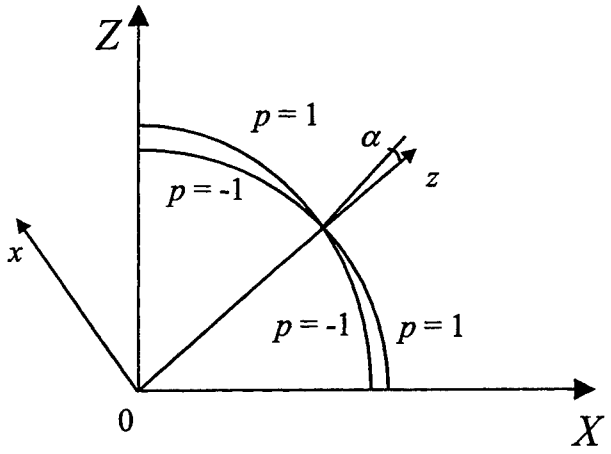


Figure 1. Cross section of the wave vector surface in the vicinity of the binormal by the crystallographic plane XZ. α is anisotropy parameter and indices $p = \pm 1$ enumerate a slow and a fast mode.

The polarization of normal waves in the vicinity of the binormal is linear, dependent of the azimuth angle $\varphi = arctg(k_y/k_x)$. As the azimuth angle is changed by the value of φ, the polarization vectors of the normal waves c_p ($p=\pm 1$) rotate by angle $\varphi/2$. These polarization vectors can be given in the form

$$\mathbf{c}_1(\varphi) = \sin(\varphi/2)\mathbf{e}_1 + \cos(\varphi/2)\mathbf{e}_2\,, \quad \mathbf{c}_{-1}(\varphi) = \cos(\varphi/2)\mathbf{e}_1 - \sin(\varphi/2)\mathbf{e}_2 \tag{2}$$

or in an alternative form in terms of vectors of the right- and left circular polarization $\mathbf{e}_\pm = (\mathbf{e}_1 \pm i\mathbf{e}_2)/\sqrt{2}$:

$$\mathbf{c}_1(\varphi) = \frac{-i}{\sqrt{2}}[\mathbf{e}_+ \exp(i\varphi/2) - \mathbf{e}_- \exp(-i\varphi/2)];$$

$$\mathbf{c}_{-1}(\varphi) = \frac{1}{\sqrt{2}}[\mathbf{e}_+ \exp(i\varphi/2) + \mathbf{e}_- \exp(-i\varphi/2)]\,. \tag{3}$$

Normally, the effect of internal conical refraction is considered for the case of linear polarization of the incident light. It should be noted that due to the azimuth dependence of the polarization direction of normal waves inside the crystal the transmitted radiation has, accordingly, the azimuthally inhomogeneous intensity distribution. From this is follows that to solve the problem of formation of azimuthally homogeneous beams, it is necessary to use circularly polarized input radiation.

Specifically, we shall assume that the incident field has, for example, right-hand circular polarization with an amplitude on the input face of the crystal equal to

$$\mathbf{a_0}(\rho,\varphi) = a_0 \mathbf{e}_+ f_{in}(\rho,\varphi), \tag{4}$$

To find the refracted waves, we represent the incident field polarization vector in the form of a linear superposition of eigen vectors (2) as follows:

$$\mathbf{e}_+ = \sum_p \alpha_p(\varphi)\mathbf{c_p}(\varphi) \tag{5}$$

with eigen values $\alpha_1(\varphi) = i\exp(-i\varphi/2)/\sqrt{2}$ и $\alpha_{-1}(\varphi) = \exp(-i\varphi/2)/\sqrt{2}$.

Then the Fourier-spectrum of the field (3) on the output crystal face can be given in the form

$$\mathbf{A}_0(q,\varphi) = a_0 \sum_{\mathbf{p}} F_{in}(q,\varphi)\alpha_p(\varphi)\mathbf{c_p}(\varphi), \tag{6}$$

where

$$F_{in}(q,\varphi) = \iint f_{in}(\rho,\varphi)\exp[iq\rho\cos(\varphi-\varphi_1)]\rho d\rho d\varphi_1 \tag{7}$$

is the Fourier-spectrum of the function $f_{in}(\rho,\varphi)$.

In a particular case of the azimuth-independent input field,

$$F_{in}(q) = 2\pi\int f_{in}(\rho)J_0(q\rho)\rho d\rho, \tag{8}$$

where $J_0(q\rho)$ is the zero-order Bessel function.

When passing over the interface, each Fourier component (5) experiences reflection depending in the general case on the quantity q. This dependence can be neglected for paraxial beams. For such a beams the Fourier component of the field inside the crystal, near its boundary, will be described by expression (4). Consequently, the field in the crystal will be of the form

$$A(\rho,\varphi,z) = \frac{a_0}{(2\pi)^2}\sum_p \iint F(q,\varphi_1,z)\alpha_p(\varphi_1)\mathbf{c_p}(\varphi_1)\exp[iq\rho\cos(\varphi-\varphi_1) - ip\gamma qz]q\,dq\,d\varphi_1, \tag{9}$$

where $F(q,\varphi_1,z) = F_{in}(q,\varphi_1)\exp(-iq^2z/2k)$.

Let the input field be azimuthally symmetric. Then, substituting into (6) the polarization vectors from (2), integrating with respect to φ_1 and summing over p, we obtain

$$\mathbf{A}(\rho,\varphi,z) = \frac{a_0}{(2\pi)}\int F(q,z)[J_0(q\rho)\mathbf{e}_+\cos(\gamma qz) - J_1(q\rho)\exp(-i\varphi)\mathbf{e}_-\sin(\gamma qz)]\,qdq, \tag{10}$$

where $\rho = \sqrt{(x-\gamma z)^2 + y^2}$.

Now let us assume that the input field is left-hand circularly polarized. In this case, in expansion (4) in terms of eigen-vectors (3), the eigen-values are equal to $\alpha_1(\varphi) = -i\exp(i\varphi/2)/\sqrt{2}$ and $\alpha_{-1}(\varphi) = \exp(i\varphi/2)/\sqrt{2}$. Calculation similar to the previous one gives

$$\mathbf{A}(\rho,\varphi,z) = \frac{a_0}{(2\pi)}\int F(q,z)[J_0(q\rho)\mathbf{e}_-\cos(\gamma qz) - J_1(q\rho)\exp(i\varphi)\mathbf{e}_+\sin(\gamma qz)]\,qdq, \tag{11}$$

As follows from equations (9), (10), the circularly polarized wave excites in the biaxial crystal the superposition of two

waves of orthogonal polarization one of which contains wavefront dislocation. The amplitude ratio of these waves depends on the distance covered in the crystal by the simple harmonic law.

Let us consider the particular case of incidence on the crystal of a zero-order BLB. Then $f_{in}(\rho) = J_0(q_{in}\rho)$. Neglect the influence of the Bessel beam transverse restriction on its Fourier-spectrum. Then $F_{in}(q) = 2\pi\delta(q - q_{in})/q_{in}$ where $\delta(x)$ is the delta-function. Integrating (10) and (11) we find the field amplitudes at the exit from a crystal of thickness L.

$$\mathbf{A}(\rho,\varphi,L) = a_0\left(J_0(q_{in}\rho)\cos(\gamma q_{in}L)\,\mathbf{e}_+ - J_1(q_{in}\rho)\exp(-i\varphi)\sin(\gamma q_{in}L)\,\mathbf{e}_-\right) \tag{12}$$

for the right-hand polarized incident beam and

$$\mathbf{A}(\rho,\varphi,L) = a_0\left(J_0(q_{in}\rho)\cos(\gamma q_{in}L)\,\mathbf{e}_- - J_1(q_{in}\rho)\exp(i\varphi)\sin(\gamma q_{in}L)\,\mathbf{e}_+\right) \tag{13}$$

for the left-hand polarized one.

Thus, the output field is the superposition of the zero-order and the first order BLBs with orthogonal polarizations. When the condition

$$\gamma q_{in}L = (2n+1)\pi/2\,, \tag{14}$$

where n=0,1... is fulfilled, the term in (12), (13) proportional to the Bessel function $J_0(q_{in}\rho)$ becomes zero. Consequently, complete conversion of the right-hand circularly polarized input zero-order Bessel beam into a left-hand circularly polarized first-order Bessel beam, and vice versa, will take place. Estimation of the oscillation period on the basis of equation (8) at $\alpha \approx 0.016$ (KTP crystal), $\lambda = 0.63$ μm, $\gamma = 0.02$ gives $L_0 \approx 0.5$ mm.

It is important to note that the procedure of increasing the Bessel function order can be continued. To do this, it is necessary to separate in output field (12), (13) a component proportional to the first-order Bessel function and realize its repeated passage through the crystal, and so on.

In the general case of incidence on the crystal of a Bessel function of order m with the phase factor $\exp(im\varphi)$, integrating (7), we find

$$F_{in}(q,\varphi) = 2\pi(i)^m \exp(im\varphi)\delta(q - q_{in})/q_{in}\,. \tag{15}$$

Substitution of (15) into (9) leads to formulas generalizing (12), (13):

$$\mathbf{A}(\rho,\varphi,L) = \frac{a_0(-1)^m}{2\pi}\left(J_m(q_{in}\rho)\cos(\gamma q_{in}L)\,\mathbf{e}_+ + J_{m-1}(q_{in}\rho)\exp[i(m-1)\varphi]\sin(\gamma q_{in}L)\,\mathbf{e}_-\right)$$

$$\mathbf{A}(\rho,\varphi,L) = \frac{a_0(-1)^m}{2\pi}\left(J_m(q_{in}\rho)\cos(\gamma q_{in}L)\,\mathbf{e}_- - J_{m+1}(q_{in}\rho)\exp[i(m+1)\varphi]\sin(\gamma q_{in}L)\,\mathbf{e}_+\right)$$

Thus, theoretical analysis points to the possibility of formation in biaxial crystals of light beams with screw dislocations and, in particular, to higher-order BLBs.

2.2. Experimental Results and Discussion

The effect of transformation of the order of a BLB was tested experimentally. The experimental setup shown in Fig. 2.

A collimated, circularly-polarized Gaussian beam of a He-Ne laser, 5 mm in diameter (1/e) was transformed into a zero-order BLB using an axicon with an angle at is cone base of $\sim 2.2^\circ$. Consequently, the cone angle γ of the resulting zero-order BLB is ~ 0.02. Then the Bessel beam is focused on a 12mm thick KTP crystal oriented perpendicularly to the binormal and

located at a distance of ~ 16 cm from the axicon. The radius of the BLB formed by the axicon, within the limits of the crystal position, is ~ 1.5 mm.

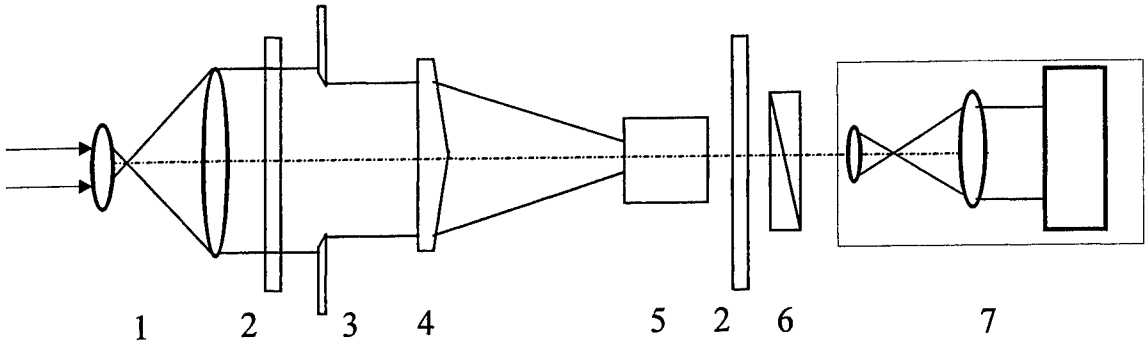


Figure 2. Optical system for transformation of the order of the Bessel beam: 1 - 16× telescope; 2 - λ/4 plate, 3 - diaphragm, 4 - axicon; 5 - KTP crystal; 6 - polarization analyzer; 7 - viewing and recording system.

In the output field, the right- and left-circularly polarized components are separated and investigated independently. The intensity distribution in their cross-section is measured and compared to squared zero- and first-order Bessel functions in accordance with equation (12). Figs. 3(a,b) show the images of the central part of the beams at the output face of the crystal.

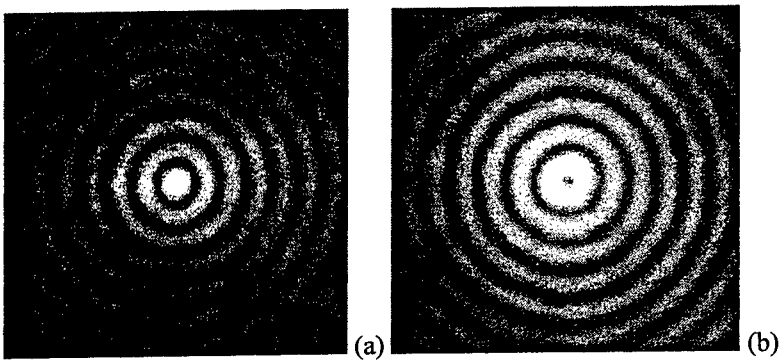


Figure 3. Images of the field at the output face of the crystal for radiation with circular polarization coinciding with the input one (zero-order BLB)(a) and orthogonal to it (first-order BLB)(b).

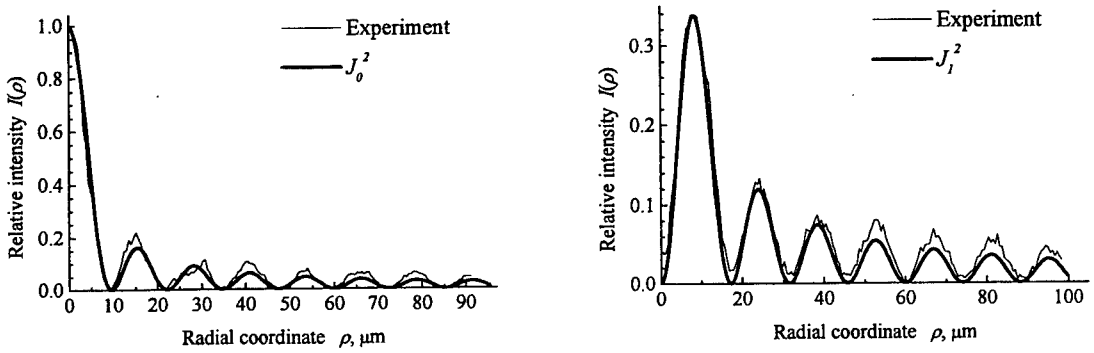
Figs. 4(a,b) give the corresponding intensity distributions in comparison with the squared Bessel functions $J_0^2(\gamma k_0 \rho)$ and $J_1^2(\gamma k_0 \rho)$. It is clear that good quantitative agreement between theoretical and experimental data is obtained.

In addition to these radial distributions of intensity, an important signature of first-order BLBs is their wave-front dislocation. To reveal this, interference of the BLB with plane and spherical reference waves have been studied. For comparison with theory in Fig. 5 the numerically calculated interference pictures is shown. It is seen that in the case of interference with a plane reference wave, a characteristic indication of dislocation is the bifurcation of the maximum at the center of the BLB and in case of interference with a spherical wave – a spiral structure. The above peculiarities have also been observed in experimental interference patterns. Images of these patterns are given in Figs.7(a,b) for plane and spherical reference waves respectively.

Note that the direction of spiraling as well as the orientation of the bifurcated maximum reverse when we change the sign of input beam circular polarization.

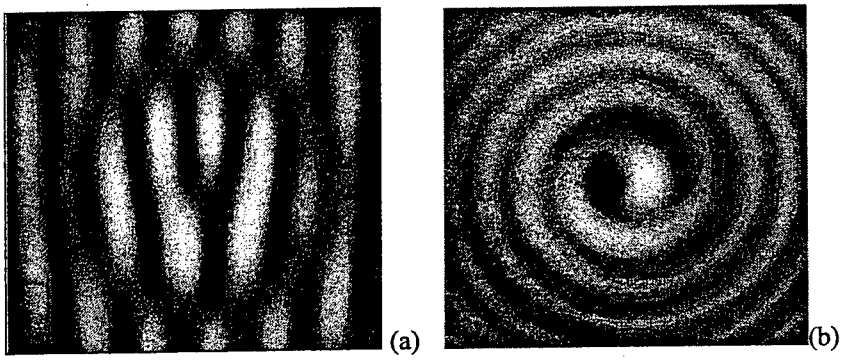
We also checked the theoretical result of section 2, indicating the possibility to stepwise increase the order of the Bessel

function under repeated passage of light through a crystal. For this purpose we used an experimental setup with two crystals in series. In the first stage a zero-order BLB, incident on the KTP crystal, is transformed into a first-order BLB, as before.



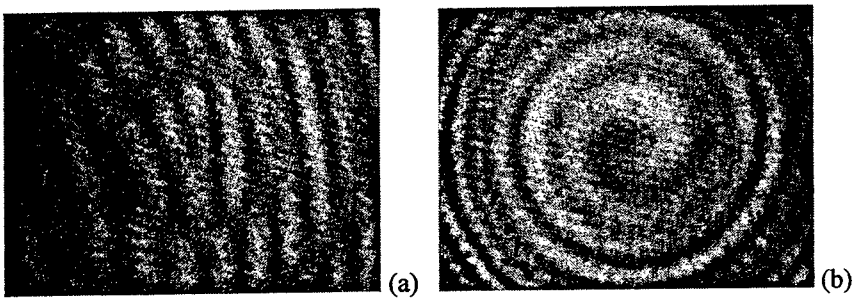
(a) (b)

Figure 4. Experimental intensity distribution of the output field with polarization equal to the input one (a) and orthogonal to it (b) as compared to design-theoretical zero- and first-order Bessel beam intensity distributions.



(a) (b)

Figure 5. Distribution of interference maxima, calculated for the case of interference of the field~ $\exp(i\varphi)$ with a plane wave (a) and a spherical wave (b).



(a) (b)

Figure 6. Images generated by interference of a first-order Bessel beam with a reference plane wave (a) and with a reference spherical wave (b).

Next the first-order beam polarization is converted from left-circular to right-circular polarization and the beam is directed to the second biaxial crystal α-HIO_3 (iodic acid) along the direction of its optical axis. According to equation (14) the output field then involves a superposition of first- and second-order BLBs. Fig. 7 shows the radial intensity distribution of the output field component with polarization orthogonal to the input polarization. It is seen that this distribution is reasonably well approximated by the squared second-order Bessel function.

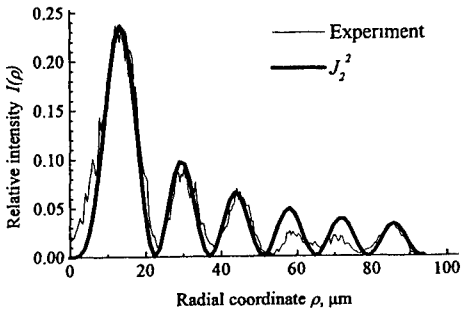


Figure 7. Experimental intensity distribution of the output field behind the second crystal with polarization orthogonal to the input field polarization as compared to design-theoretical second-order Bessel beam intensity distribution.

It can be concluded that the effect of transformation of Bessel beams when propagation along the biaxial crystal binormal as expressed by formula (14), is confirmed experimentally.

3. WAVEFRONT DISLOCATION ORDER TRANSFORMATION FOR RING LIGHT BEAMS

In this section the problem of field spatial pattern transformation in the interior conical refraction scheme is considered for an input field in a form of circularly polarized Gaussian beam.

The cylindrical co-ordinates with Z axis along binormal direction will be used below. The electric intensity vector of incident beam we represent in the form

$$\mathbf{E_{in}}(\rho,z) = f_{in}(\rho,z)\mathbf{e}_+ \exp(ik_z z), \tag{16}$$

where $\mathbf{e}_+ = (\mathbf{e}_1 + i\mathbf{e}_2)/\sqrt{2}$ is the unit vector of right-hand circular polarization. If a beam (16) is the Gaussian one that $k_z \approx k_0$, $k_0 = \omega/c$, for the Bessel beam $k_z = k_0 \sin(\gamma)$, γ is the cone angle, i.e. half-angle at the vertex of BLBs wave vectors cone. The field (16) excites inside a crystal a light wave:

$$\mathbf{A}(\rho,\varphi,z) = A_+(\rho,z)\mathbf{e}_+ + A_-(\rho,\varphi,z)\mathbf{e}_-, \tag{17}$$

where $\mathbf{e}_-$ unit vector of the left-hand circular polarization and

$$A_+(\rho,z) = \frac{1}{(2\pi)}\int F_{in}(q)J_0(q\rho)\cos(\alpha qz)\exp(-iq^2 z/2k)qdq\,, \tag{18}$$

$$A_-(\rho,\varphi,z) = \frac{-1}{(2\pi)}\int F_{in}(q)J_1(q\rho)\sin(\alpha qz)\exp(-iq^2 z/2k + i\varphi)\,qdq\,. \tag{19}$$

Here $F_{in}(q)$ - function Fourier-spectrum $f_{in}(\rho,0)$, $\rho = \sqrt{(x-\alpha z)^2 + y^2}$, $\alpha = arctg[c^2\sqrt{(\varepsilon_3^{-1} - \varepsilon_2^{-1})(\varepsilon_2^{-1} - \varepsilon_1^{-1})}/2v^2]$ is the anisotropy parameter, $k=\omega/v$, v is the wave phase velocity in the binormal direction, $\varepsilon_{1,2,3}$ is the principal values of an inductivity tensor, $J_{0,1}(q\rho)$ are the zero- and the first-order Bessel functions.

The vector field (17) is a superposition of the right and left polarized components and amplitudes of ones depend on light path length in the crystal. To define the output field it is necessary to give concrete expression of the $F_{in}(q)$ function. Let's consider incidence of the Gaussian beam with amplitude $f_{in}(\rho) = \exp(-\rho^2/2w_{in}^2 + ik_0\rho^2/2R_{in})$ on the crystal. Then

$$F_{in}(q) = \frac{2\pi w_{in}^2}{(1 - ik_0 w_{in}^2/R_{in})}\exp\left(-\frac{q^2 w_{in}^2}{2(1 - ik_0 w_{in}^2/R_{in})}\right). \tag{20}$$

The estimation of integrals (18),(19) leads to following expression of vector amplitude of the output field:

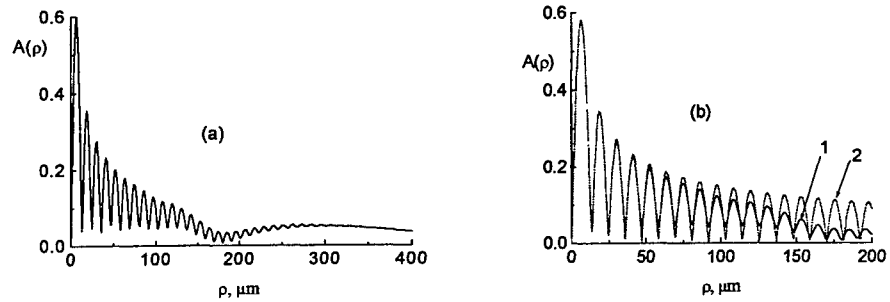
$$\mathbf{A}(\rho,\varphi,L) = C[J_0(q_{st}\rho)\mathbf{e}_+ + i\exp(i\varphi)J_1(q_{st}\rho)\mathbf{e}_-]. \quad (21)$$

where C is some stationary value.

As follows from (21) at the sharp focusing of the Gaussian beam on the input crystal face the output field is the superposition of zero and first order Bessel beams with right-hand and left-hand circular polarizations.

At that BLB obliquity parameter equals αk. For the KTP crystal it corresponds to the cone angle outside of the crystal approximately 1.6 deg.

To improve the influence of the Gaussian beam focusing degree on the output field the numerical calculations of integrals (18), (19) were made. Fig.8a,b shows the amplitude distribution of the left-handed polarized field on the output crystal face and also the Bessel function of the first order at the input Gaussian beam of radius $w_{in} \approx 6\lambda$.



(a) (b)

Figure 8. (a): Transversal distribution of amplitude module of left-hand polarized field component on the output face of the crystal. (b): Comparison amplitude in the axis region (1) with the first-order Bessel function $|J_1(\alpha\ k\ \rho)|$ (2) at w_{in}=4μm, L=12mm.

The structure of the right-hand polarized field has a similar form. As figures show, the field near the beam symmetrical axis is precisely described by the expression (21). The Bessel function and also smoothly varying pedestal having two-ring structure are general properties of these distributions. When w_{in} increases the number of Bessel function rings decreases and the pedestal level enlarges (Fig. 9a). If we magnify w_{in} still more the Bessel structure practically vanishes in comparison with the two-ring field (Fig. 9b).

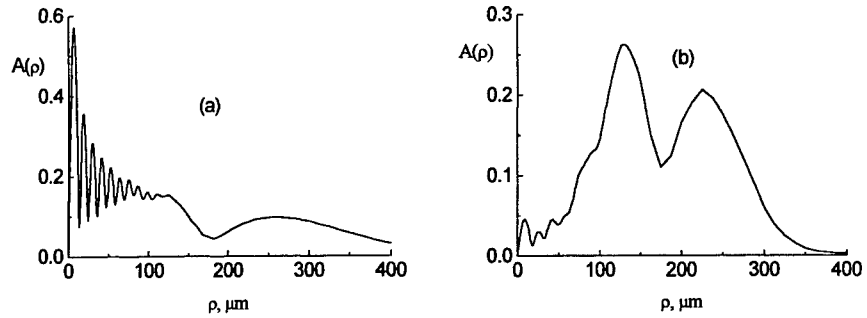


Figure 9. Amplitude distribution of left-hand polarized field component on the output crystal face at L=12mm., w_{in}=6μm (a), 12μm (b).

When light is focused sharp, diminishing of the crystal width L leads to decreasing of BLB rings number. At magnification of L the number of rings increases along with the pedestal maintaining. The behavior of the field with right-hand circular polarization is completely similar. At that in both cases dependence of output field intensity distribution on the curvature radius R_{in} is negligible.

To affirm availability of the Bessel component in the output field its profile change at a free propagation behind a crystal was explored. As a result the one-ring intensity profile typical for BLB propagation in a far-field region (Fig. 10) is formed only at aperture restriction of an output field permitting to reduce the influence of a pedestal. The divergence angle of the one-ring field equals $\alpha n k_0$ that corresponds to the formula (21). To estimate the restricting diaphragm radius we can use the expression $R_{BLB} \approx 0.3R_0$, where $R_0 \approx \alpha L$ is the dark ring radius of the two-ring field. Thus for the KTP crystal of width 12мм we have

$R_0 \approx 190\mu m$ and $R_{BLB} \approx 50\mu m$. The rather small magnification of a diaphragm radius distorts the one-ring field. At that typical input field structure formed behind a crystal is multi-ring profile.

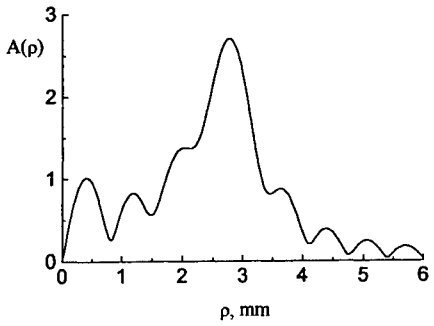


Figure 10. Amplitude distribution of left-hand polarized field component behind the crystal at L=12mm, z=10cm, R_{BLB}=50μm.

Thus to form and also separate Bessel beams by the conical refraction scheme it is necessary to restrict stringently both input beam and output field cross section dimensions.

Let's consider in detail the transformation by the crystal of more broad Gaussian beams. At values w_{in} larger 10μm the Bessel structure as is shown above is distorted and transformed to small oscillations near the field symmetrical axis against a background of the two-ring field (Fig. 9b). Behind the crystal the beam field is converted to the multi-ring high quality beam (Fig. 11b). The right-hand polarized component has a similar structure (Fig. 11a). At that the left-hand polarized component has the axial dislocation. It is important that the experimentally registered intensity distributions of these fields (Fig. 11a,b) coincide with theoretically calculated ones.

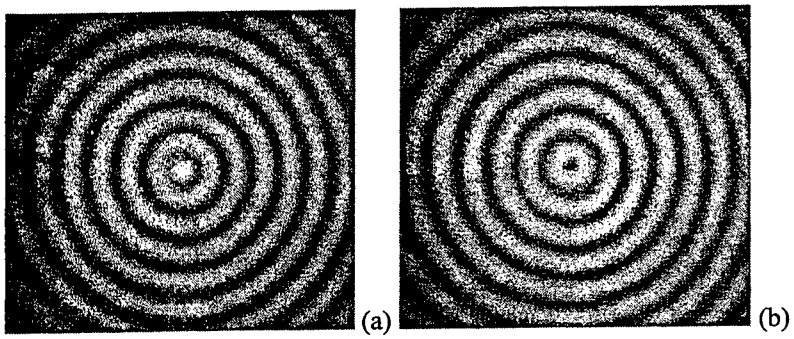


Figure 11. Multi-ring beams without dislocation (a) and with the first-order wavefront dislocation (b).

When the two-ring output field propagates at a free area its structure is invariable and the outer ring amplitude diminishes with magnification w_{in}. In the case of extreme broad input beams (w_{in}~200μm) the one-ring field behind a crystal does not change the structure. It is important that this field can be approximated by a Laguerre-Gauss mode L_{01} with a split-hair accuracy. Fig. 12 shows the experimentally registered intensity distributions of this mode.

It is of interest to investigate the propagation of beams having wave front dislocations in a crystal. To describe this case it is necessary to exchange $f_{in} \rightarrow f_{in}\exp(i\varphi)$ in the formula (16). At that the formulas (18), (19) remain valid taking into account replacements $J_0(q\rho) \rightarrow J_m(q\rho)\exp(im\varphi)$, $J_1(q\rho) \rightarrow J_{m+1}(q\rho)\exp[i(m+1)\varphi]$. Therefore it is possible to receive fields with a dislocation second and higher orders (Fig. 13) by passing through the crystal of ring or Laguerre-Gaussian modes formed from a Gaussian beam.

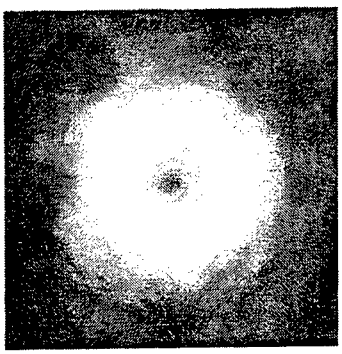
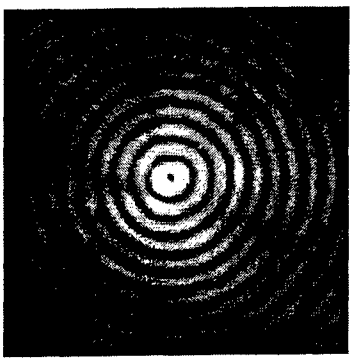


Figure 12. L_{01} Laguerre-Gaussian mode, formed at the conditions of internal conical refraction.

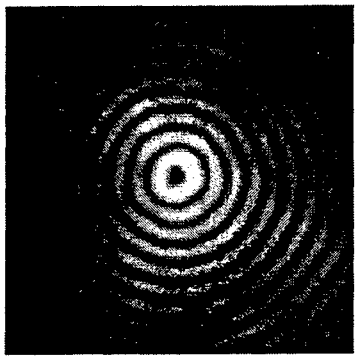


Figure 13. Ring beam with the second-order wavefront dislocation formed at L_{01} mode (Fig. 12) propagation through the crystal.

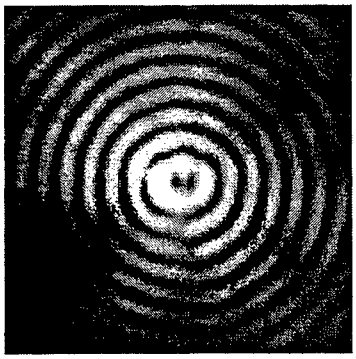
The additional opportunities to transform beams are disclosed at overlapping of the crystal and axicon in the unified. Fig. 14 shows some examples of beams experimentally obtained by means of axicon from beams with wave front dislocations. Virtues of this method of forming of light beams with higher orders dislocations are the simplicity of production and opportunity to use one for high-intensity beams transformation. The property of spatial cross invariance of the optical scheme on the base of the biaxial crystal is also important and allows to form two-dimensional arrays of beams.



(a)



(b)



(c)

Figure 14. Bessel light beams of the first (a) and the second (b) order formed by the axicon from beams showed on the Figs. 12 and 13 respectively. (c) - beam with disintegrated wavefront dislocation of the second order..

The sensitivity to different contortions of the scheme is the relevant performance of beam spatial pattern transformation processes in biaxial crystals. We studied influence of the propagation direction deflection from binormals on an output field. It is revealed, that at small rotational displacement of a crystal (~20min) the symmetry of a L_{01}-mode is disturbed (Fig. 15). If axicon is illuminated by such asymmetric beam the spiral beam is formed. Helical intensity distribution is revealed easily after passage of this beam through a short-focus (5-10cm) diverging lens (Fig. 16). In a case, when the scheme with two crystals is used and the output field contains a dislocation of the second order, the rotational displacement of a crystal leads to its decay on two first-order dislocations.

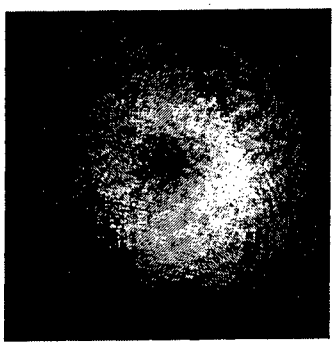


Figure 15. Asymmetric ring field formed at input beam deflection from the crystal binormal.

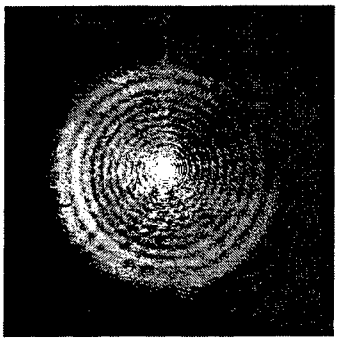


Figure 16. Helical beam formed from asymmetric ring field (Fig. 15) by passing through the axicon and diverging lens.

The observed experimentally field distortions can be explained as a result of the beam axis deflections from a binormal direction that leads to the occurrence of the small nondislocation impurity in left-hand polarized field component. The comparison of Fig.9 and results of numerical calculations of the interference of the L_{0l} mode with plane wave (axial beam), and also known effect of second order dislocation disintegration because of interference with an axial beam without dislocation [6] confirms this fact. Observed distortions of axial symmetry of a field occur if to rotate the polarizer by a little angle that uniquely results to modes intermixing. This fact confirms that similar distortions of the field spatial pattern arise because of the superposition of modes.

CONCLUSION

In this paper we have investigated and systematized amplitude-phase effects taking place when Bessel or Gaussian light beams propagate in the binormal direction of a biaxial crystal. It is shown that the circularly polarized input Gaussian beam depending on a degree focusing can be transformed to different ring fields including in Bessel beams. The singularity of a biaxial crystal optical properties in the binormal direction induces the phase front screw dislocation of the output wave polarized orthogonally to the input one. The repeated passage through the crystal allow to increase step by step the dislocation order. The mentioned above features of cylindrical light beams, such as availability of screw dislocations and conical structure of a spatial frequencies spectrum, motivate to attack problem of these light beams production and transformation. It is important that it is possible to receive the transformation ratio of beams close to 100% by selection of width of a crystal or cone angle initial BLB.

Thus on the basis of a biaxial crystal the effective scheme for production and transformation of light beam phase front dislocations has been created.

REFERENCES

1. Friese M.E.J., He H., Hockenberg N.R., Rubinsztein-Dunlop H. Transfer of angular momentum to absorbing particles from a laser beam with a phase singularity, *Proc. SPIE.*- 1998. - Vol. 2792.- P. 190.
2. Yin J., Zhu Y., Wang W., Jhe W. Optical potential for atom guidance in a dark hollow laser beam, *JOSA*- 1998.- Vol. 15.- № 1.- P. 25-33.
3. Florjańczyk M., Tremblay R. Guiding of atoms in a travelling-wave laser trap formed by the axicon, *Optics Communs.*- 1989.- Vol. 73. -№ 6. - P. 448-450.
4. Paterson C., Smith R. Higher-order Bessel waves produced by axicon-type computer-generated holograms, *Optics Communs.*- 1996.- Vol. 124.- P. 121-130.
5. Белый В.Н., Казак Н.С., Кондратюк Н.В., Хило Н.А., Шагов А.А. Генерация второй гармоники бесселевыми световыми пучками в кристалле KTP, *Квант. электроника.* 1998. -Т.25. - № 11.- С. 1037-1042.
6. Basistiy I.V., Bazhenov V.Yu., Soskin M.S., Vasnetsov M.V. Optics of light beams with screw dislocations, *Optics Communs.*- 1993.- Vol. 103.- P. 422-428.
7. Dholakia K., Simpson N.B., Padgett M.J., Allen L. Second-harmonic generation and the orbital angular momentum of light, *Phys Rev.* A.- 1996. -Vol.54.- № 5.- P. R3742-R3745.
8. BerŽanskis A., MatijoŠius A., Piskarskas A., SmilgeviČius V., Stabinis A. Engineering of optical vortices by means of parametric frequency converter, *Lithuanian J. Physics.* - 1997. - Vol. 37. - № 4. P. 327-330.

Single-frequency stabilized dye jet laser pumped with a Cu-vapour laser through a fibre

V.I.Baraulya, S.M.Kobtsev, S.V.Kukarin, A.A.Pustovskikh, V.B.Sorokin

Novosibirsk State University
Pirogova 2, Novosibirsk, 630090, Russia

ABSTRACT

Presented is a stable single-frequency master-oscillator on the basis of a pulsed dye jet laser for powerful isotope separation systems. In a simple GIG resonator without prism expanders, we obtained 170-mW single-frequency output power with an open beam pump and up to 100 mW with a fibre-guided pump. The application of a frequency stabilization system brought the short-term stability down to 50 MHz/s (at pulse duration 8 ns, 15-kHz repetition rate) and the long-term stability down to 120 MHz/hour. A smooth frequency scan within an 8 GHz region (and wider) was achieved on the basis of pivot method with newly implemented components.

Keywords: pulsed dye laser, single-frequency, GIG-resonator, smooth frequency scan

A single-frequency dye laser (SF-DL) pumped with a Cu-vapour laser (CVL) is an efficient source of tunable narrowband radiation of the visible spectrum. An important field of application of this type of lasers is that of using them as master oscillators in powerful laser isotope separation systems. The spectral characteristics of the output radiation of these systems is largely determined by those of the master oscillator. This refers to the radiation spectrum width, the radiation frequency stability, and the smooth scanning range of the frequency. The works aimed at developing and applying new methods of improving the spectral characteristics of master oscillators on the basis of SF-DL pumped with a CVL are rather numerous [1], but, to our view, the ways of improving this kind of lasers are far from exhausted.

In this paper we present a stable single-frequency dye jet laser pumped with a CVL through a light guide designed to be used as a master oscillator of a powerful laser system [2]. In designing the laser at issue particular attention has been given to improving the short-term and the long-term frequency stability, developing simpler methods of smooth frequency tuning, and to optimizing the delivery of pump radiation into the active medium.

In the designed dye laser use has been made of a GIG-type resonator (a short resonator with a grazing incidence of radiation onto a diffraction grating) with the dye cell replaced by a free-flowing dye jet (fig. 1). Longitudinal pumping was employed, the pump radiation is made through a dichroic mirror of the resonator with 89 % of the CVL green line being passed. The selecting element was a holographic diffraction grating produced by the firm "American Holographic" (2400 rulings/mm, 50 mm long) fixed at an angle of 89°30' to the resonator axis. The flow rate of the dye solution was 10 m/s, the jet cross-section is 0.5 mm x 4 mm (the jet former is a quartz nozzle), the incline of the jet to the resonator axis is 10°. The laser dye solution used was 1.3×10^{-3} M/liter Rhodamine 6G in a ethylene glycol - pure alcohol mixture (1:1). The tuning mirror was a high reflectivity dielectric coated optical flat. The duration of the SF-DL oscillation pulses did not exceed 8 ns FWHM, the duration of the CVL pulses was 12 ns FWHM, the pulse repetition rate was 15 kHz.

The dye jet laser could be pumped both with an open Cu-laser beam and through a light guide . The open beam of the CVL was focused in the dye jet laser active medium by means of a lens with 65-mm focal distance, the pumping beam waist diameter amounting to about 100 μm. Fig. 2a presents the measured pumping beam waist profile for this focusing, the measurement was made with a one dimensional photodiode array (the distance between the array elements was 25 μm).

For the 3.5 W power of the pump radiation (CVL green line) fed into the dye solution jet, the output power of the dye laser amounted to 170 mW in stable single-mode operation with the maximum output power of about 565 – 570 nm. The maximum overall efficiency of pump radiation conversion was 4.6%. It should be noted that in the short-resonator GIG laser this parameter is largely determined by the diffraction grating efficiency and that for the most efficient gratings the overall pump radiation conversion efficiency can reach 12% [3] while the typical values of the overall efficiency for GIG-dye-lasers fall within the range of 4 – 6%. A significant increase in the efficiency of a SF-DL can be expected in using combined gratings [4], their production, however, is so far connected with a number of technological problems.

Laser Optics 2000: Control of Laser Beam Characteristics and Nonlinear Methods for Wavefront Control,
Leonid N. Soms, Vladimir E. Sherstobitov, Editors, Proceedings of SPIE Vol. 4353 (2001)
© 2001 SPIE · 0277-786X/01/$15.00

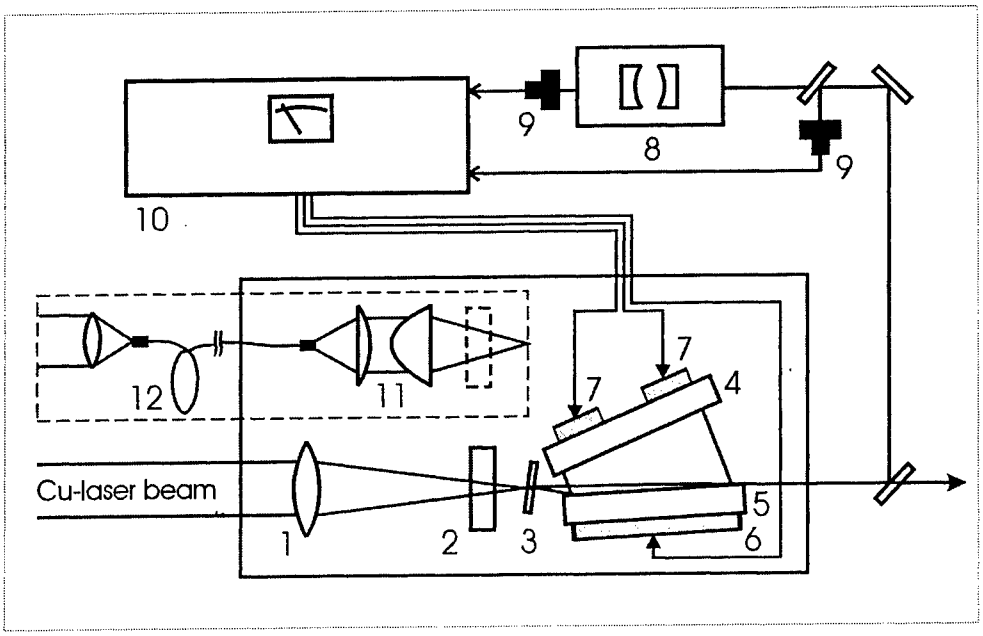
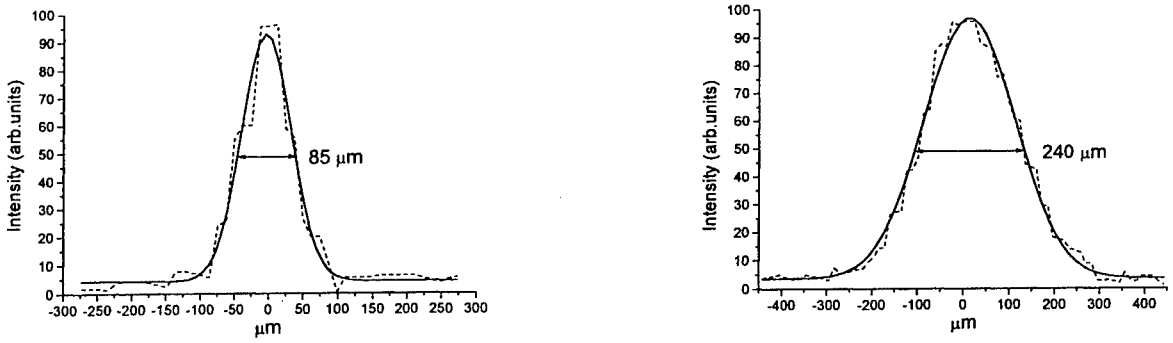


Figure 1. The schematic of the designed single-frequency dye jet laser: 1 – focusing lens, 2 - dichroic mirror of the resonator, 3 - dye solution jet, 4 - tuning mirror, 5 - holographic diffraction grating, 6 - auxiliary piezoelectric element, 7 – control piezotransducers, 8 - reference confocal interferometer, 9 – photodetectors, 10 – SF-DL electronic control unit, 11 - modified Fraunhofer objective, 12 - light guide.

The application of a fiber for delivering the pumping laser beam into the GIG-dye-laser active medium which was first accomplished in reference [5] under the conditions of longitudinal pumping makes it possible to spatially "untie" these lasers and improve the stability of the frequency and power characteristics of dye lasers. The main problem arising in using a light guide consists in obtaining a sufficiently small waist of the pump beam at the exit of the light guide. In focusing the light guide leaving beam with a spherical lens the beam waist diameter is close to that of the light guide diameter. However, the application of a light guide with a relatively small diameter, say, with that of 100 μm, creates problems in feeding a relatively powerful pump beam due to the destruction or welding off of the light guide inlet end.



a) b)

Figure 2. The measured pump beam waist profile in focusing; (a) an open beam with a spherical lens, (b) a beam at the light guide outlet with a modified Fraunhofer objective; (the dotted line denotes the experimental data, the solid line shows the approximation with a Gauss contour).

To deliver the pumping laser beam to the dye jet laser, we used a light guide of the quartz-quartz type with an inner diameter of 400 μm. The pump beam was focused into the fiber by means of a spherical lens with a 65-mm focal length. The radiation losses in passing through the light guide did not exceed 14%. To focus the pump beam at the exit of the light guide

we used a modified Fraunhofer objective with a 40-mm focal length consisting of a planoconvex and a parabolic lenses. This objective introduces relatively small spherical aberrations and makes it possible to concentrate up to 90 – 95% of the radiation in the light spot of an essentially smaller size than that of the light guide diameter. The least pump beam waist diameter obtained in the dye solution jet was that of 240 μm (Fig. 2b).

In pumping a dye jet laser through the light guide the pump power getting into the dye solution jet was equal to 2 W (510.6 nm), that of the output of the dye jet laser in single-frequency operation amounting to 80 mW (the overall exitation conversion efficiency amounts to 4%). Thus, the improved pump beam focusing at the 400 μm light guide outlet by means of a modified Fraunhofer objective makes it possible to obtain a single-frequency oscillation regime in a dye jet laser with a GIG-resonator without using any prism beam expanders and with the relatively high pump power conversion efficiency.

The short-term (for averaging times of 1 sec) dye jet laser oscillation frequency free-running jitter controled with the help of a scanning Fabri-Perot interferometer with a resolution of 30 MHz amounted to 100 – 150 MHz/sec. The external conditions of the laser service worsening (vibration, acoustic disturbances), the short-term oscillation frequency jitter could increase up to 500 – 600 MHz. Note that the range of the short-term free-running frequency jitter in similar short-resonator GIG-dye-lasers lies between 100 – 150 MHz [3] and 1 GHz [6], sometimes even more.

Systems of active stabilization of frequency generation in a dye laser pumped with a CVL are used quite seldom, and their arrangement is quite diverse. Frequency generation can be actively stabilized with the aid of a high-precision wavelength meter [7, 8], a two-element photodetector recording the change in the angular position of the output beam with changing oscillation frequency [9, 10], a reference interferometer recording the passing radiation by a linear CCD array with subsequent digital data processing [11] or a scanning reference interferometer with the digital processing of its registered passage profile [12]. Characteristic of most systems applied to actively stabilize the SF-DL is computer-based data processing as well as computer-aided elaboration of the finalizing control signal. Since the limited speed of the digital systems of the active stabilization of a pulse dye laser frequency does not permit the short-term frequency stability to be essentially improved, their application is mainly aimed at decreasing the laser's long-term frequency generation drift.

To stabilize the dye jet laser's oscillation frequency, we used the method of the frequency lock to a side of a transmission fringe of the reference cavity with an analog feedback loop control system. The reference interferometer represented a thermostatically controlled confocal Fabri-Perot interferometer (the temperature instability of the interferometer is < 0.02°) with a FSR 5 GHz, finesse 2. An actuating element of the frequency stabilization system were the piezotransducers of the tuning mirror. The response time of the feedback loop control system was 0.1 sec. The application of the frequency stabilization system made it possible to reduce the short-term oscillation frequency jitter of the dye jet laser down to 50 MHz/sec (fig. 3) an to achieve the long-term stability of the oscillation frequency of 120 MHz/ hour. Obtained short-term linewidth is of the order of the Fourier transform limit for a 8 ns laser pulse.

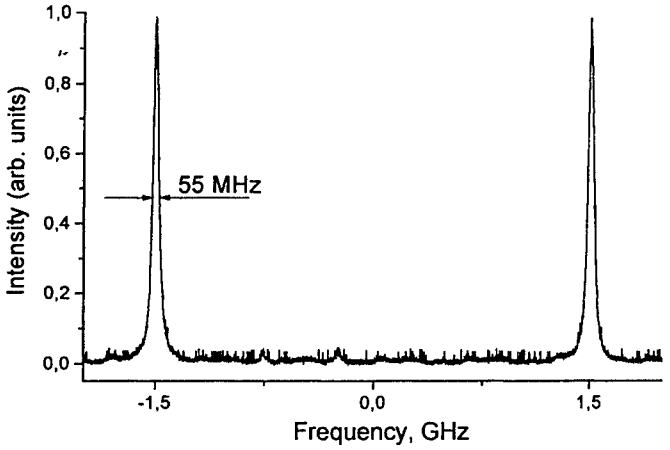


Figure 3. Single-mode stabilized dye laser output monitored by a 3 GHz FSR scanning confocal interferometer (finesse=100). Approximately $5 \cdot 10^3$ laser pulses occurred during the sweep.

The traditional method of smooth single-frequency scanning in GIG-resonators is the pivot-method [13, 14]. The gist of the method consists in that to smoothly scan the oscillation frequency of a short-resonator GIG-laser in a range exceeding that of resonator dispersion, the tuning mirror turns around a certain axis referred to as a pivot-axis. The location of this axis is determined by an intersection of the plane of the tuning mirror and that of the diffraction grating. This rotation of the tuning mirror synchronizes the rates of scan the frequency of the resonator's selected longitudinal mode and of the maximum reflection of the diffraction grating. The other method of the smooth frequency scanning in the laser with a GIG-resonator involves the application of an additional optical element: a wedge located between the diffraction grating and the rotary mirror [15, 16]. In this case the rates of scan the resonator's selected longitudinal mode frequency and the maximum reflection of the diffraction grating are synchronized when the wedge also rotates around a definitely located axis. However, the successful application of these methods to smoothly scan the oscillation frequency of a GIG-laser is rather a complicated task as it requires a high-precision actuating mechanism (say, a high-precision kinematic drive) and sufficiently accurate adjustment of the frequency scan unit.

To simplify the procedure of the smooth oscillation frequency scanning in a dye jet laser with a GIG-resonator we combined the idea of the pivot method with a new and simpler actuating mechanism of the tuning mirror rotation. For a prescribed rotation of the GIG-resonator's tuning mirror we used two piezoelectric transducers with a very simple control scheme.

If the tuning mirror of a GIG resonator is mounted on two identical piezoactuators placed at a distance $2L$ from each other (fig. 4), then for the mirror to turn through $\delta\varphi$ round the pivot-axis, the ration of the voltages fed to the piezoactuators must be equal to

$$\frac{U_2}{U_1} = \frac{h_2}{h_1} \approx \frac{d+L}{d-L}$$, where d is the distance from the pivot-axis to the middle of the tuning mirror.

This expression is true for small angles $\delta\varphi$ when h_1 and h_2 can be considered linear. In our laser the distance $2L$ between the piezoactuators was 36 mm, and d=40 mm. In our case the necessary calculated ratio of the controlling voltages U_1/U_2 for the tuning mirror to rotate around the pivot-axis is equal to 2.5. Thus, by feeding voltages to the piezoactuators from one power source through a corresponding voltage divider, one can accomplish the prescribed rotation of the tuning mirror.

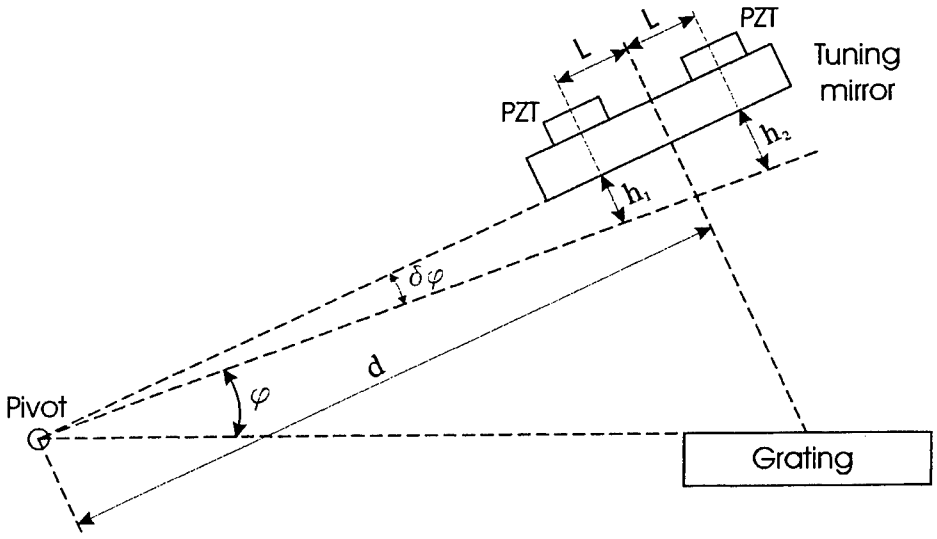


Figure 4. The scheme of controlling the rotation of the tuning mirror in a GIG-oscillator with the aid of two piezotransducers.

The width of the range of the smooth single-frequency scanning in the laser with a GIG-resonator in rotating the tuning mirror with the aid of two PZT is determined by the expression:

$$\Delta\nu = \frac{d \cdot h_2}{d + L} \cdot \frac{c}{\lambda \cdot l_{cav}}$$

For our parameters (d=40 mm, h_2=1.6 μm, L=18 mm, λ = 566 mm, l_{cav}=65 mm) the calculated value of the smooth frequency scanning range $\Delta\nu$ is 9 GHz. The value of h_2 is determined by the sensitivity of the piezoactuators and by the value of the control voltage. As piezoactuators we used nine-layer piezoceramics (15(diameter) x 5 mm size), the control voltage U_2 was equal to ± 200 V. The sensitivity of the piezoceramic transducers came to 4 μm/kV, thus the value of h_2 could not exceed 1.6 μm.

The real range of the laser's smooth single-mode scan was 8 GHz (fig. 5). The ratio of the voltages on the tuning mirror piezoactuators was close to the calculated one (2.5), the procedure of the smooth scanning of the laser's frequency was initially optimized by changing the ration of the voltages on the piezoactuators within a small range. Besides, for a more accurate initial coincidence of the maximum dispersion contour of the grating with the selected oscillation frequency the grating was mounted on an additional piezoelement which could shift in the direction perpendicular to the working surface of the grating. In the process of the smooth scanning of the laser's oscillation frequency this additional piezoelement was not used.

Note that the proposed actuating mechanism based on two piezoelements allows the oscillation frequency to be smoothly scanned in the regime of active frequency stabilization following the scan of the reference interferometer. The error signal of the frequency offsetting is fed to the piezoactuators in the same proportion (1.0:2.5). The scan rate of the laser's oscillation frequency under the conditions of the active frequency stabilization amounted to 1 GHz/sec (8-sec sweep).

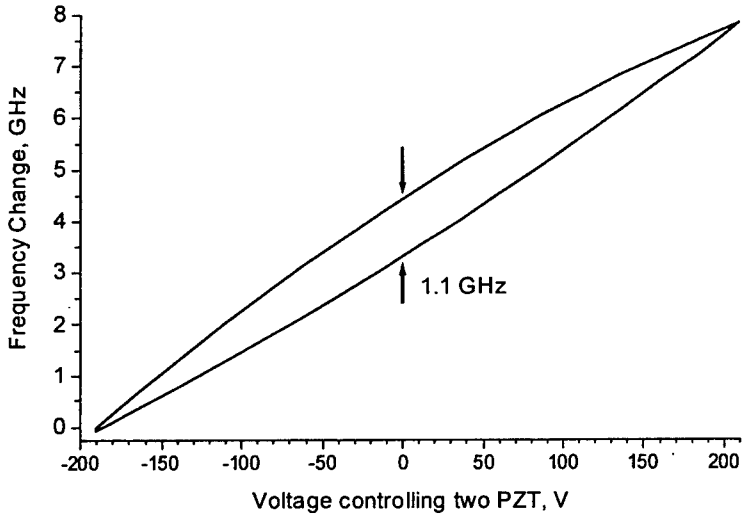


Figure 5. A 8-GHz scan of the SF-DL under two PZT tuning mirror control.

The unquestionable advantages of the advanced method of the smooth scanning of a laser's oscillation frequency are the simplicity of the actuating elements and that of the control procedure as well as the fast operation of the actuating elements – piezoactuators. One should note, however, a marked hysteresis in the dependence of the laser's oscillation frequency on the controlling voltage which is typical of piezoelectric positioners.

ACKNOWLEDGEMENTS

We thank the "Coherent Technology" JSC (Novosibirsk, Russia) for providing the necessary Cu-vapour laser. This research was partially supported by the Novosibirsk Regional Administration (contract N T-35-99), "Tekhnoscan" JSC (Novosibirsk, Russia) and company "UTAR International Ltd." (Richmond, Canada). Dr. S.Kobtsev's e-mail address is kobtsev@lab.nsu.ru.

REFERENCES

1. High-power dye lasers. Ed.: F.J.Duarte, Springer Series in Optical Sciences, **65**, 1991.
2. V.I.Baraulya, S.M.Kobtsev, S.V.Kukarin, V.B.Sorokin. "Powerful single-frequency laser system based on a Cu-laser pumped dye laser". *Proc. SPIE, "Atomic and Molecular Pulsed Lasers III"*, **4071**, pp. 219-223, 2000.
3. I.T.McKinnie, A.J.Berry, T.A.King. "Stable, efficient, single-frequency operation of a high repetition rate grazing incidence dye laser". *J. Mod. Optics,* **38**, N 9, pp. 1691-1701, 1991.
4. S.V.Vasil'ev. "Efficient difraction grating for use in a grazing-incidence configuration". *Kvantovaya Elektronika (Quant. Electronics)*, **25**, N 5, pp. 429-432, 1998.
5. S.V.Vasil'ev, V.A.Mishin, T.V.Shavrova. "Single-frequency dye laser with fibre-optic pump". *Kvantovaya Elektronika (Quant. Electronics)* , **24**, N2, pp. 131-133, 1997.
6. Y.Maruyama, M.Kato, T.Arisava. "Copper vapor laser pumped single-mode grazing incidence dye laser using dye jet". *Jap. J. Appl. Phys.*, **30**, N4B, pp. L748-750, 1991.
7. I.L.Bass, R.E.Bonanno, R.P.Hackel, P.R.Hammond. "High-average-power dye laser at Lawrennce Livermore National Laboratory". *Appl. Opt.,* **31**, N33, pp. 6993-7006, 1992.
8. S.A.Kostritsa, V.A.Mishin. 'Tunable narrow-band moderate-power laser system pumped by copper vapour lasers". *Kvantovaya Elektronika (Quant. Electronics),* **22**, N6, pp. 542-546, 1995.
9. T.D.Raymond, P.Esherick, A.V.Smith. "Widely tunable single-longitudinal-mode pulsed dye laser". *Opt. Lett.*, **14**, N 20, p. 1116-1118, 1989.
10. J.D.Corless, J.A. West, J.Bromage, C.R.Stroud. "Pulsed single-mode dye laser for coherent control experiments". *Rev. Sci. Instrum.*, **68**, N6, pp. 2259-2264, 1997.
11. P.L.Stricklin, D.C.Jacobs. "Long-term wavelength stabilization of a commercial pulsed dye laser". *Appl. Optics*, **31**, N 33, pp. 6983-6986, 1992.
12. Y.Maruyama, M.Kato, A.Sugiyama, T.Arisava. "A narrow linewidth dye laser with double-prism beam expander". *Opt. Commun.*, **81**, N 1-2, pp. 67-70, 1991.
13. K.Liu, M.G.Littman. "Novel geometry for single-mode scanning of tunable lasers". *Opt. Lett.*, **6**, N 3, pp. 117-118, 1981.
14. G.Z.Zhang, K.Hakuta. "Scanning geometry for broadly tunable single-mode pulsed dye lasers". *Opt. Lett.*, **17**, N 14, pp. 997-999, 1992.
15. A.A.Hnilo, F.A.Manzano, O.E.Martinez. "High resolution tuning system for pulsed dye lasers". *Appl. Opt.*, **30**, N 18, pp. 2481-2483, 1991.
16. D.K.Ko, S.H.Kim, J.B.Kim, J.Lee, S.A.Kostritsa, V.A.Mishin. "Accurate frequency-tuning mechanism from a wedge prism in a single-mode tunable laser". *Appl. Opt.*, **34**, N 6, pp. 983-987, 1995.

Efficient autoscanned single-frequency CW dye laser

S.M.Kobtsev, A.V.Korablev, S.V.Kukarin, V.B.Sorokin
Novosibirsk State University

ABSTRACT

We report on a CW single-frequency dye laser with a 1-W threshold power. Output power of the laser working on the Rhodamine19 dye was 100 mW out of 2.4 W of the argon ion pump. Smooth frequency scanning in a 20-GHz region with up to 20-GHz/s rate was implemented in a linear dye laser cavity. A special resonator auto-adjustment system with internal reference features the short-term radiation linewidth down to 3 MHz/s and long-term stability level of 150 MHz/hour without any external frequency stabilization systems. Explained are arrangements of original execution units included into the laser control system. The control system's features are discussed.

Keywords: CW dye laser, single-frequency, linewidth, smooth frequency scan

A single-frequency CW dye laser (SF-CW-DL) is a traditional source of a narrow-band smoothly wavelength-tuned radiation in the visible spectrum. An SF-CW-DL is widely used both directly as a radiation source in the spectroscopy of high and superhigh resolution of the visible and UV (on a doubling of radiation frequency) spectrum range, and as master oscillator whose narrow-band radiation of an assigned wavelength may increase, e.g., in technological (laser isotope separation), astrophysical (creation of artificial guide stars [1]) and other powerful laser systems.

By now the greatest acceptance has been gained by ring SF-CW-DL which provide a higher level of output radiation power and a better stability of a single-frequency oscillation regime as compared to linear SF-CW-DL. The ring SF-CW-DL, however, are distinguished for a more complicated adjustment/maintenance, and with a low level of output radiation power (e.g., 50 – 150 mW) they require a more powerful pumping because of a relatively high oscillation threshold. A typical ring SF-CW-DL contains 22 optical surfaces (8 of which have reflective coatings), and its generation threshold on effective Rhodamine 6G or DCM dyes amounts to about 3 W in pumping with polarized radiation of all the blue-green lines of an Ar-laser.

The present paper reports the results of developing a linear SF-CW-DL rated at a relatively low radiation pumping power (3 W all B-G lines Ar-laser or 2 W CW DPSS-laser, 532 nm) and providing, at this pumping, under a stable single-frequency regime, an output radiation power of up to 150 mW, a smooth radiation frequency tuning in the range of 20 GHz, a short-term radiation linewidth of 3 MHz/s with a long-term frequency drift of no more than 150 MHz/hr without any external frequency stabilization systems.

The scheme of the designed linear SF-CW-DL is presented in fig. 1. The laser's radiation wavelength selectors are: a three-component birefringent filter (the thickness of the first plate is 0.45 μm, the ratio of the plate thicknesses is 1:4:13), a thin (0.5 mm) Fabry-Perot etalon (the surface reflection coefficient $R_{1,2} = 0.3$) optimized in accordance with the recommendations of [2], and a selective reflector which contains a thin metal film and the resonator's output mirror which are aligned parallel to each other.

The possibility of selection one longitudinal mode of the laser's linear resonator by means of a thin absorbing film (TAF), the thickness of which is far less than the length of the radiation wavelength (this possibility was first demonstrated in [3]), makes it equally possible to obtain an effective single-frequency oscillation regime both in continuously operated dye lasers [4, 5] and in lasers of other types [6]. Essentially, the method of selecting longitudinal modes of the laser's linear resonator with the help of a TAF fixed perpendicular to the resonator's axis is as follows. The nodal surfaces of different longitudinal modes in a linear resonator are shifted relative to one another along the resonator axis, so of maximum Q-factor are only the modes in which the electric field nodes coincide with the TAF surface. The correct selection of the ratio of the power absorbed by the film to the laser gain as well as of the distance from the film to the resonator's nearest mirror, of the film thickness and the set of preliminary selectors provides the formation of only one mode in the laser. The TAF is a much simpler selector than the thick Fabri-Perot interferometers consisting of two Littrow prisms and traditionally used at the last stage of single-frequency dye laser mode selection. In addition, the selective reflector from a TAF possesses a higher selectivity [5] as compared with the thick Fabri-Perot interferometer.

Laser Optics 2000: Control of Laser Beam Characteristics and Nonlinear Methods for Wavefront Control,
Leonid N. Soms, Vladimir E. Sherstobitov, Editors, Proceedings of SPIE Vol. 4353 (2001)
© 2001 SPIE · 0277-786X/01/$15.00

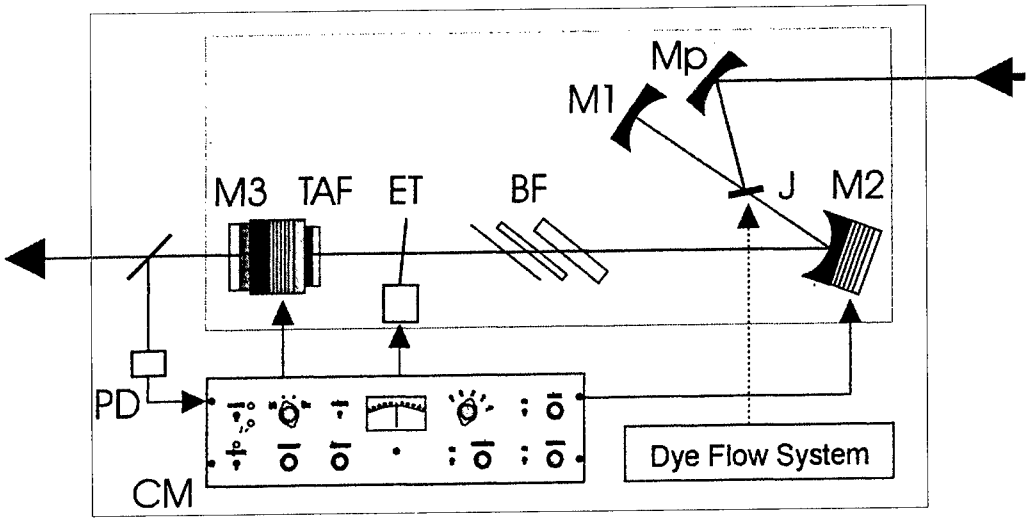


Figure 1. The optical scheme of the dye laser is a three-mirror resonator with astigmatism compensation and non-parallel pumping beam. **M3** is the coupling mirror, transmittance - 3-5%, flat; **M2** is the collimating mirror, curvature radius 50 mm; **M1** is the end mirror, curvature radius 50 mm, **Mp** is the pump mirror, curvature radius 50 mm, **J** - is the dye jet, **BF** - birefringent filter, **ET** - thin etalon, **TAF** – thin absorbing film, **PD** - photodiode with pre-amplifier, **CM** – control module.

The dispersion range of the selective reflector from a TAF is defined by the distance L between the TAF and the output mirror of the laser resonator. In order to effectively separate one longitudinal resonator mode the value of L must lie within the range of

$$4lh/\lambda < L < 2l(1 - 2h/\lambda),$$

where l is the distance from the dye solution jet to the resonator's end mirror defining the frequency interval between the modes that do not compete due to the spatial hole burning effect, λ is the radiation wavelength, h is the thickness of the absorbing film. The lower limit (0.3 cm in this instance) is defined by the condition according to which the distance between the nodes of the electric fields of the selected mode and those of the nearest noncompetitive mode must at least be greater than the thickness of the film at the point of its location. For $L = 2l$ the nodes of the electric fields of the two nearest noncompetitive modes coincide with the TAF surface, so the selection of one of the modes is impossible. At $L = l$ the suppression of the modes not competing with the selected one because of the spatial hole effect becomes the strongest.

The design of the selective reflector from the TAF developed by the present authors (Fig. 2) provides the parallel arrangement of the laser's output mirror and of the TAF at the opposite end faces of a cylindrical monolithic block made of two quartz cylinders glued to the piezoelectric transducer on either side. The inner cavity of the block (between the surfaces of the output mirror and of the TAF) is isolated from dust and air flows, which, combined with the rigidity of the monolithic structure, provides an increased stability of the selective reflector's base. The distance between the output mirror and the TAF was chosen in the above range to meet the condition of sufficiently sharp reflection peaks of this selector and that of the design compactness and amounted to 2.7 cm (FSR = 5.5 GHz).

In order to maintain the single-frequency regime of the laser oscillation for a long time it is necessary to use a system of automatic adjustment of the TAF to the node of the selected mode's electric field or vice versa: of the latter to the former. We have used the latter method which at the same time, thanks to the rigid structure of the selective reflector, has permitted us to stabilize the laser's oscillation frequency as well. The base of the selective reflector is less subject to external perturbations than that of the laser resonator, so the selective reflector of the monolithic-block structure can also play the part of an internal reference device. The automatic adjustment system applied operates as follows: the base of the selective reflector is modulated with the aid of the PZT on a frequency of 1.3 kHz, the periodic deflection of the TAF from the electric field node of the selected mode leads to the modulation of the laser's output power (for the operation of the self-tuning to be stable the amplitude of this modulation may amount to 2 - 3%), but does not cause any change in the laser's oscillation frequency. The

photoreceiver registers the output power of the laser and gives an electrical signal which is proportional of laser output power to the synchronous detector with frequency of detecting 1.3 kHz. The signal from the synchronous detector amplifies and moves to the piezoelectric package of the collimating mirror so that to reduce amplitude of modulation of the laser output power at the 1.3 kHz frequency. Thus, the automatic adjustment of the single-frequency oscillation regime proceeds concurrently with the stabilization of the laser's oscillation frequency by means of the internal reference discriminator – monolithic-block selective reflector.

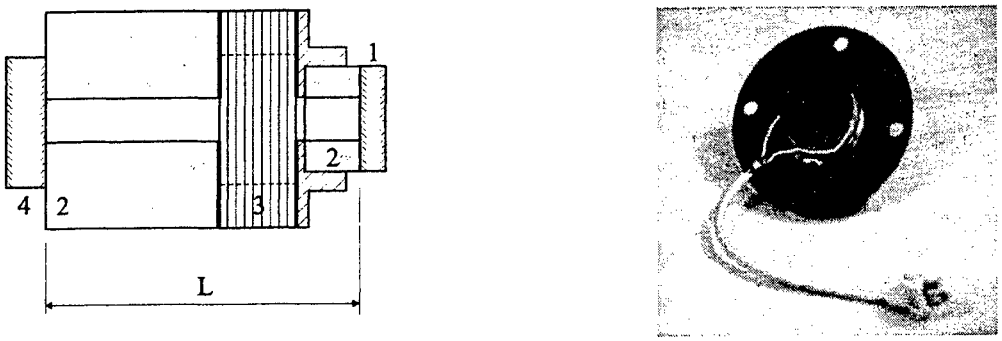


Figure 2. The structure of the designed selective reflector with a TAF. 1 – a TAF (deposed on the left-hand side of the quartz substrate is an aluminum coating with the transmission T = 65%, on the right-hand side – an anti-reflection coating), 2 – quartz cylinders, 3 – a PZT, 4 – an output mirror (deposited on the right-hand side of the quartz substrate is a dielectric coating with the transmission T = 5%, on the left-hand side – an anti-reflection coating), L – the reflector's selective base. The mounts of the output mirror and of the TAF to the monolithic block are not shown.

To measure the short-term instability of the oscillation frequency use was made of the optical heterodyning method involving two identical dye jet lasers. The radiation beams of the lasers were brought into spatial coincidence, the beatings of the lasers' frequencies were recorded by a fast-responding photodiode and by a spectrum frequency analyser CK4-56 with a view band of 0-100 MHz (Fig. 3). A typical width of the frequency beating spectrum of either laser was 8 – 10 MHz/sec FWHM which corresponds to either laser's short-term oscillation frequency instability of no more than 7 MHz/sec. In the perions of the minimum external perturbations the laser's oscillation frequency jitter amplitude per second was 3 – 5 MHz FWHM. The laser's long-term oscillation frequency drift was analyzed with the aid of a high-precision wavelength meter "Angström" to a measurement accuracy of 5×10^{-8} and with automatic temperature correction of the readings. The dye laser's oscillation frequency drift rate recorded by the oscillation wavelength meter did not exceed 150 MHz/hour, although the laser's actual frequency drift rate appears to be lower, because the radiation wavelength meter possesses its own drift of readings at a level of 50 – 100 MHz/hour.

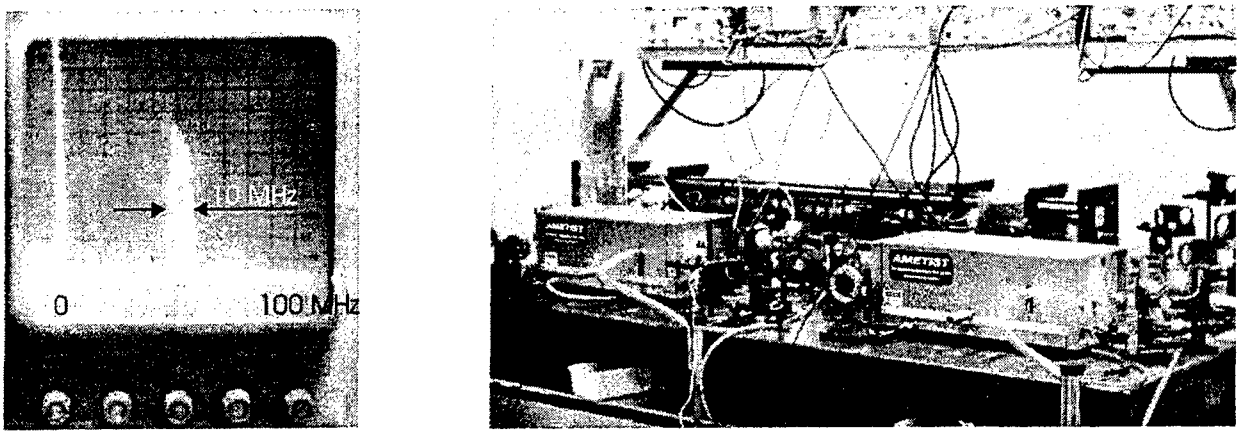


Figure 3. The outward appearance of the system which was used to measure the short-term oscillation frequency instability of the designed lasers by the method of optical frequency heterodyning. Shown from the left is the recorded spectrum of the lasers' frequency beatings (the scale of the X-axis of the frequency spectrum analyser's screen is 0 – 100 MHz)

The smooth scanning of the analyser's oscillation frequency is performed by changing the selective reflector's base followed by tuning the laser's resonator with the aid of the PZT-controlled collimmating mirror. For a fixed position of the thin etalon the range of the smooth tuning of the laser's oscillation frequency does not exceed 5 GHz. When the range of the smooth frequency tuning broadened to 20 GHz, we performed the synchronous scanning of the thin etalon using a special electro-mechanical drive and the multipiezodrive (four nine-layer PZTs) of the collimating mirror. To linearize the dependence of tuning the peak of the thin etalon transmission according to frequency on the voltage that controls the electromechanical drive, use was made of an analog electronic scheme extracting the square root of the input voltage and operating the drive with the thus obtained signal. This linearization allowed the thin etalon to be scanned concurrently with the selective reflector without using an additional feedback loop of automatic adjustment; the rates of tuning these selectors were synchronized by calculating and selecting the appropriate ratio of controlling voltages (a total amplitude of the voltage across the PZT package equal to 570 V). The maximum range of the smooth oscillation frequency tuning ran up to 21.01GHz (cf. Fig. 4), the maximum smooth tuning rate, to 20 GHz/sec.

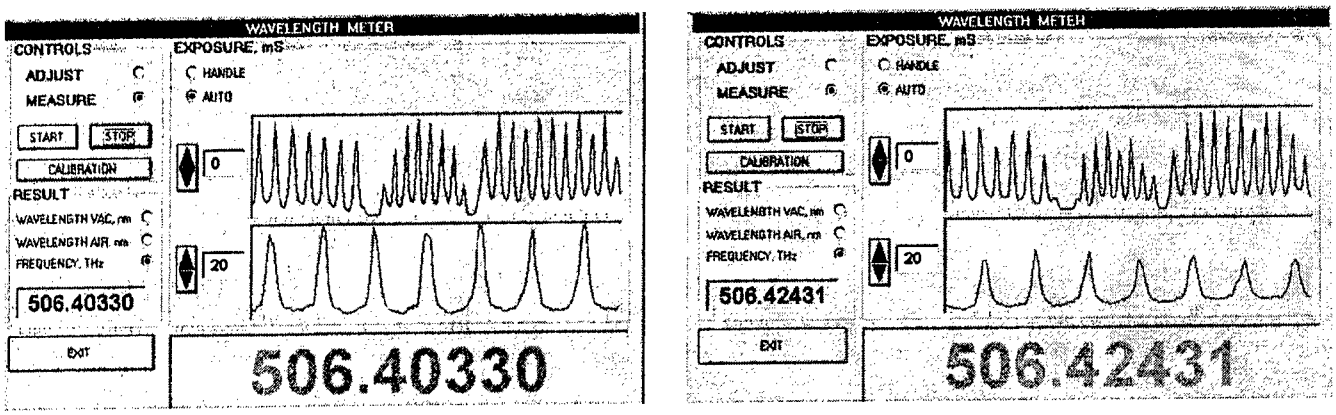


Figure 4. The frequency of the SF-CW-DL radiation in the beginning and in the end of the smooth scanning range - the difference of frequencies in the beginning and in the end of range is 21.01 GHz.

Note that the application of the multipiezoactuator of the collimating mirror for the smooth tuning of the SF-CW-DL's oscillation frequency within a wide range makes it possible to get rid of a number of problems [7] typical of the scanning Brewster plate commonly used for tuning the length of the laser resonator.

The oscillation threshold of the designed SF-CW-DL was no higher than 1 W on the dyes Rhodamine 19 and Rhodamine 6G on pumping by the polarized radiation of all the lines of an Ar-laser. The low oscillation threshold is due to the application of high-quality mirrors (the total radiation losses on a resonator's mirror do not exceed 0.15%) and to small nonselective losses introduced by the birefringent filter, the thin Fabry-Perot etalon and the selective reflector. The birefringent filter and the selective reflector are adjusted by a special technique precluding an incomplete adjustment of these selective elements, i.e. an incomplete speectral coincidence of the peaks of transmitting various plates of the 3-plate birefringent filter or the nonparallelism of the output mirror's working surfaces and of the selective reflector's TAF.

The output power of the designed SF-CW-DL is restricted by the level of 150 – 200 mW above which the absorbing film may be damaged (burnt-out) in the procedures of the laser's adjustments brining about a nonsingle-frequency oscillation regime and, accordingly, a considerable absorption of radiation not selected by the film. At a 100-mW output radiation power of a SF-CW-DL the aluminum films we use can operate for an unlimited time in any procedures of the laser adjustment. The pump radiation power required for a Rhodamine 19 dye laser and a Rhodamine 6G dye one at this output radiation power amounts to 2.4 and 2.6 W, respectively (all the Ar-laser lines)

ACKNOWLEDGEMENTS

This research was partially supported by the company ""Unified Technologies Advanced Research International Ltd." (Richmond, Canada). Dr. S.Kobtsev's e-mail address is kobtsev@lab.nsu.ru.

REFERENCES

1. Davies, R.I., W. Hackenberg, T. Ott, A. Eckart, S. Rabien, S. Anders, S. Hippler, M. Kasper, P. Kalas, A. Quirrenbach, A. Glindemann. "The Science Potential of ALFA: Adaptive Optics with Natural and Laser Guide Stars". *Astron. Astrophys. Suppl. Ser.*, **138**, pp. 345-353, 1999.
2. S.M.Kobtsev, N.A.Sventsitskay. "Application of birefringent filters in continuous-wave tunable lasers: a reviev". *Opt. Spectrosc.*, **73**, N 1, pp.114-123, 1992.
3. Y.V.Troitskii, N.D.Goldina. "Optical resonator with absorbing film as a mode selector". *J. Exp. Theor. Phys. Lett.*, **7**, pp. 309-313, 1968.
4. I.M.Beterov, Y.M.Kirin, B.Y.Yurshin. "A single-mode CW dye laser and the spatial hole burning effect". *Opt. Commun.*, **13**, N 3, pp. 238-240, 1975.
5. B.V.Bondarev, A.V.Kapitanov, S.M.Kobtsev, V.M.Lunin. "Frequency-stabilized CW dye laser with precise automatic tuning for high-resolution spectroscopy". *Atm. Opt.*, **2**, N 12, p.1132-1136, 1989.
6. J.K.Jabczynski, I.I.Peshko, J. Firak. "Single-frequency, thin-film-tuned, 0.6 W, diode-pumped Nd:YVO_4 laser". *Appl. Optics*, **36**, N 12, pp. 2484-2490, 1997.
7. H.El-Kashef, G.E.Hassan. "Studies of problems connected with wide scan dye laser spectroscopy". *Optical Materials*, **14**, pp. 19-24, 2000.

Time-resolved autocorrelation measurements of the transient ultrashort pulse formation

V.A.Zaporozhchenko

B.I.Stepanov Institute of Physics Academy of Sciences
F.Skaryna Ave., 68, Minsk 220602, Belarus
Phone: (375)-2841023, Fax: (375)-2840879, E-mail: vzap@dragon.bas-net.by.

ABSTRACT

The evolution of autocorrelation function observed at the 50 ns resolution for prelase oscillations of actively mode-locked laser evidences that an effective and fast pulse shortening begins when the intracavity radiation intensity attains the saturation level. Pulse duration decreases down to 70-75 ps value during 10 cavity roundtrips and further remains unchangeable and independent on the ultrashort pulse energy.

1. INTRODUCTION

Applications of the flashlamp pumped actively mode-locked lasers with the negative feedback stabilization of prelase as the ultrashort pulse sources synchronizable to the external events make two questions to be of particular importance: what time is necessary for the transient pulse formation after prelase starting moment and whether any correlation exists between pulse energy and duration in the prelase train. A well known results obtained by Letokhov[1] and latter by Kuizenga and Siegman[2] in frame of the first approximation of dispersion theory predicted a bandwidth limited steady-state pulse formation during first 200-300 radiation roundtrips in laser cavity (2-3 μs). Last thirty years these results were being referenced widely in all discussions on pulse formation problem but obtained only indirect experimental verification. A recent involving in consideration of the group velocity dispersion effects[3] predicts the possibility of much faster pulse shaping in the actively mode-locked laser with a feedback stabilized prelase.

The present communication performs the results of the transient pulse formation study in the actively mode-locked flashlamp pumped YAG:Nd^{3+} laser with the negative feedback prelase stabilization[4].

2. MEASUREMENT PROCEDURE

Experimental study of the transient formation of ultrashort light pulses was based on the time-resolved measurements of autocorrelation function. A schematic diagram of experimental setup is shown in Fig.1. To study a total available picture of prelase operation Q-switching and cavity dumping in laser were inhibited. A quasi-steady-state prelase oscillations were maintained by the negative feedback loop and a mode-locker drive rf-pulse was switched on much earlier of prelase starting instant.

The prelase radiation was extracted from laser cavity by polarizer due to the presence of bias voltage applied to the electrooptic DKDP crystal used for the cavity Q-control. This output beam was divided by a beam splitter and directed into a negative feedback loop and correlator. Before correlator radiation was detected by an avalanche photo-detector PhD1 with 10 ns integrating circuit. Output correlation signal provided via non-collinear second harmonic generation in $LiIO_3$ crystal was directed to a high speed amplified silicon detector PDA-155 with 20 ns rise time (PhD2).

Monitoring of ultrashort pulse formation process in laser have been organized on basis of personal computer with CAMAC interface. The detector signals were analyzed by two 8-bit analog-to-digital converters (ADC) with resolution limit of 50 ns. To provide a synchronous numbering of the detector signals both ADCs were triggered by the same sync pulse from laser timer and were gated by the common signal at the frequencies either 10 or 20 MHz.

Performed above measurement system accomplished by the corresponding computer code offers the opportunity to obtain a temporal sweep of the autocorrelation function up to 50 ns (5 cavity roundtrips) resolution. Enhanced by a negative feedback loop high reproducibility of prelase dynamics[4] made it possible to carry out measurements at the averaging of experimental data over large enough number of laser shorts. To reduce the influence of possible amplitude fluctuations on the averaging of

Laser Optics 2000: Control of Laser Beam Characteristics and Nonlinear Methods for Wavefront Control,
Leonid N. Soms, Vladimir E. Sherstobitov, Editors, Proceedings of SPIE Vol. 4353 (2001)
© 2001 SPIE · 0277-786X/01/$15.00

non-collinear second harmonic autocorrelation signal $W_{2\omega}$ a data processing code provided the calculation of $\eta(\tau,t) = W_{2\omega}(\tau,t)/W_{\omega}^{2}(t)$ ratio for every laser shot and following averaging both $W_{2\omega}(\tau,t)$ and $\eta(\tau,t)$.

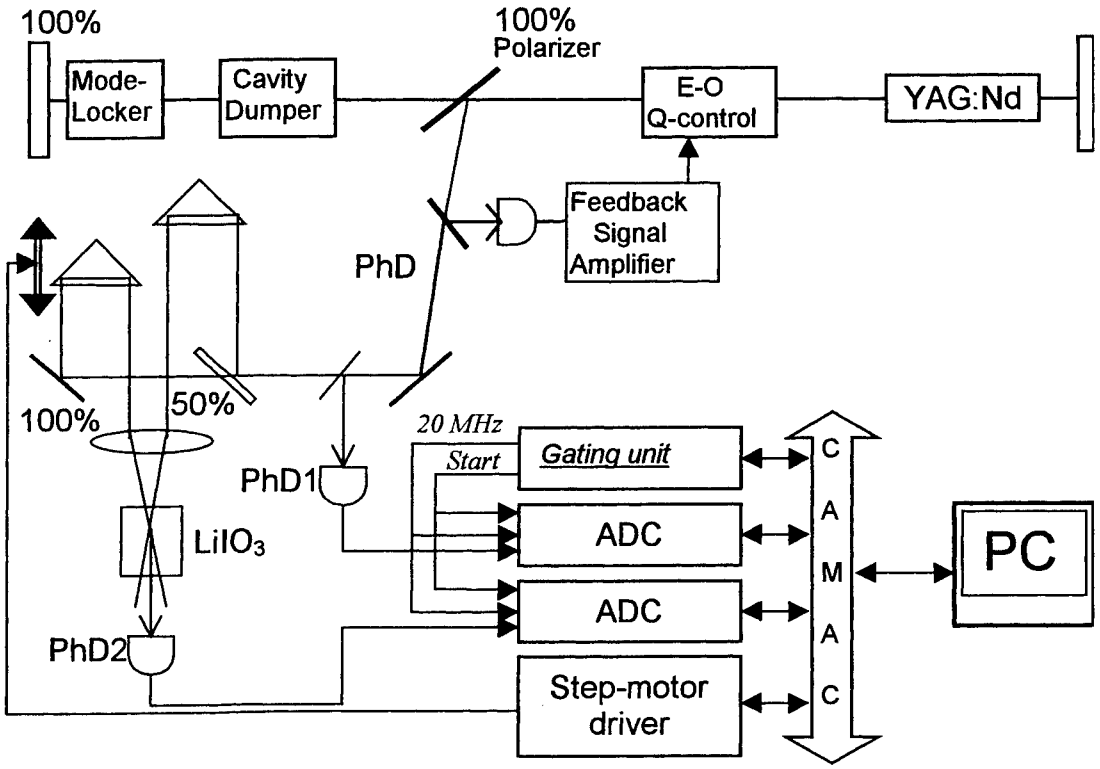


Fig.1. Experimental setup.

The main problem at the autocorrelation technique application for the transient pulse formation measurements is prelase jitter removing. It should be reminded that earlier proved[4] reproducibility of prelase dynamics is valid in time scale with floating starting point which jitter with respect to flashlamp trigger is about several microseconds. Therefore the correct measurement of the atuocorrelation function sweep requires a locking of signal envelope records involved in the statistical averaging at all values of optical delay to the common time axis origin corresponding to the prelase starting instant. Jitter removing problem has been solved via data processing[4] with the specially designed computer code simulating the oscilloscopic scan triggering by a fast comparator with adjustable threshold. For every oscilloscopic scan it have supplied a value of time delay corresponding to the instant when the intracavity radiation power attained preset level. These data have been used for a proper alignment of oscilloscopic scans at their statistical processing.

3. RESULTS AND DISCUSSION.

The sweep of normalized autocorrelation function shown in Fig.2 was obtained at the gating frequency 10 MHz and 100-shots averaging scope. It shows that the auto-correlation function on the first microsecond of prelase oscillations acquires a quasi-Gaussian shape corresponding to about 70 ps pulse duration which remains practically unchanged during a prelase. A sweep in Fig.2 corresponds to the first 48 μs of quasi-cw laser oscillations maintained by a negative feedback loop during more than 100 μs. Because of the limited ADC's RAM 100 μs sweep of autocorrelation function could be recorded at twice lower time resolution. Such records have been done and verify the uniformity of the autocorrelation function to the very end of the quasi-cw ultrashort pulse train envelope.

To obtain more detail information from the results of time-resolved autocorrelation function measurements Gaussian fit have been fulfilled for every time-cut of function shown in Fig.2. Data in every from more than 900 time-cuts contained mean values and standard deviations for 50 experimental points along the delay axes measured in result of averaging over 100 laser shots. Used algorithm of regression reconstruction was based on the least-square criterion with taking into account a standard deviations of experimental data points. The pulse duration obtained after such data processing and presented in Fig.3 *b* does not manifest any correlation with pulse amplitude shown in Fig.3 *a*. An additional evidence of pulse duration conservation is the behavior of the efficiency of second harmonic generation at zero correlator delay $\eta(0,t)$ shown in Fig.3 *c*. One can see that $\eta(0,t)$ (which is proportional to $1/\tau_p$ for the structureless pulses) remains constant in comparison with non-rectangular envelope of prelase signal (Fig.3 *a*).

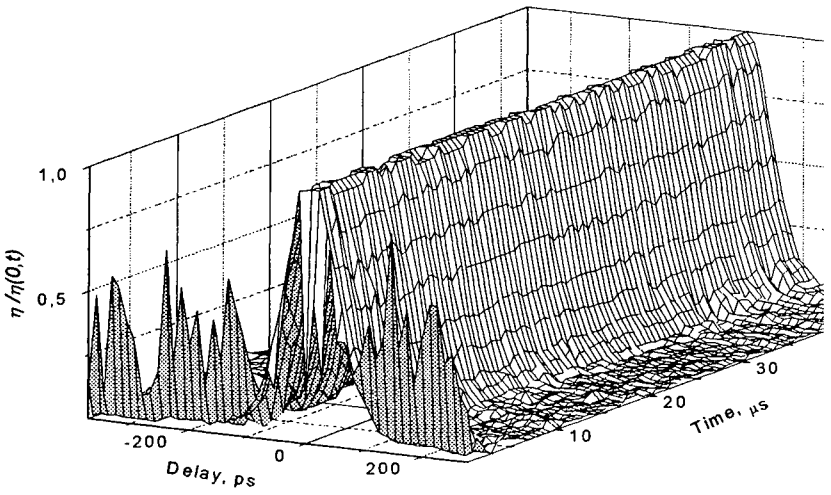


Fig.2. Temporal sweep of autocorrelation function

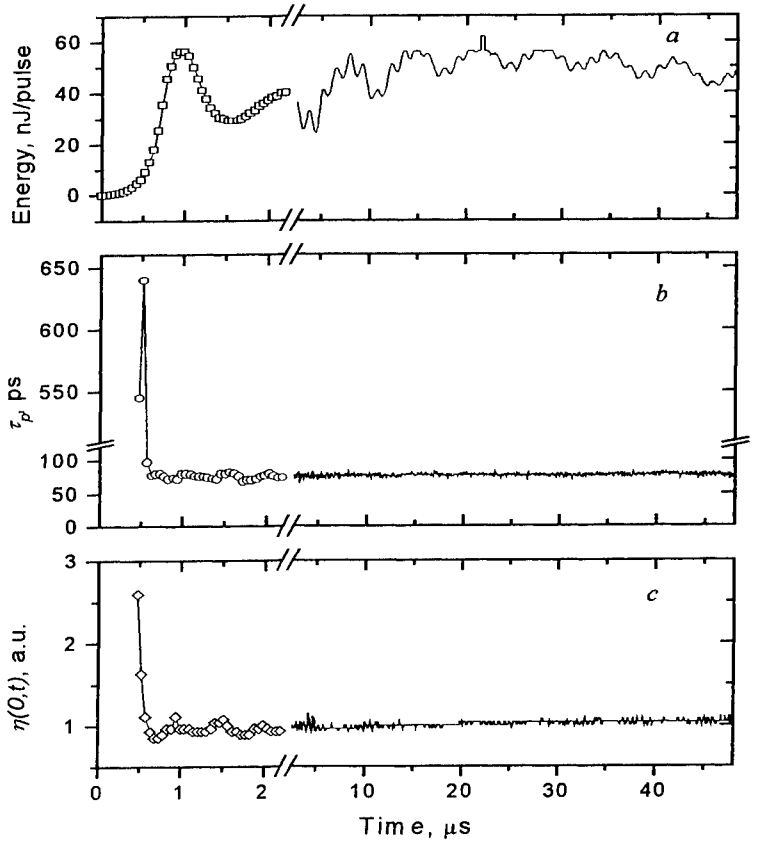


Fig.3. Evolution of pulse energy – *a*, duration – *b* and efficiency of second harmonic generation – *c* in the feedback-stabilized prelase.

For more detail consideration of the transient laser oscillations in their very beginning the initial 2 μs range of time axis in Fig.3 is scaled stretched up to perform the experimentally realized temporal resolution. It is seen that a pulse shortening takes about 10 cavity roundtrips after the attaining of the measurable level of autocorrelation signal. The front time-cut of autocorrelation function in Fig.2 is characterized by the central spike corresponding to the 30 ps pulse temporal sub-structure and high background over all range of delay time. The analysis of regression evidences a low quality of Gaussian fit for first two time-cuts of autocorrelation function. Thus the initial two points in Fig.3 *b* can be attributed to the delay variation range rather than to time interval in which spikes of valuable amplitude are present.

Higher values of the second harmonic generation efficiency $\eta(0,t)$ (Fig.3 *c*) in the sweep beginning can also

be caused by the rich temporal structure which increases the effective radiation intensity and as a consequence gives rise to $\eta(0,t)$. It should be pointed out that the presence of pulse fine structure results usually in high fluctuations level of the second harmonic generation efficiency. However the results performed in Fig.3 *c* evidence that $\eta(0,t)$ attains the value which further remains practically constant after 15-th cavity roundtrip.

It should be noticed that 0.5 μs time interval exists between the moments of the detectable level attainment for laser output power and autocorrelation signal (compare curves in Fig.3 *a* and *b*). Moreover the abrupt pulse shortening seen from Fig.3 *b* begins when the intracavity radiation intensity achieves the level of 2.2 kW/cm^2 almost exactly coinciding to the saturation intensity for lasing transition of active medium. An attempt to suppose that the pulse formation process spans also the initial 0.5 μs interval evanesced from the measurement procedure because of low signal level faces the substantial difficulties. It is inconsistent with too abrupt pulse shaping when observed sub-structure of autocorrelation function is smoothen out and wings in wide enough delay range are suppressed during about 100 ns (less than 10 cavity roundtrips).

Above results are in good agreement with the theoretical calculations fulfilled in[3] for the laser configuration similar to the experimental one. The discrepancy with[1,2] predictions can arise from a negative feedback loop action which was not taken into account in the theory but had a fast enough response to provide a certain input into the intracavity nonlinearity and dispersion.

These results are of both fundamental and practical impotence. They mean that a time interval covering 100 μs exists which begins about 0.5 μs past prelase stating moment where Q-switching providing highly reproducible output pulse parameters is available. The autocorrelation function of single output pulse extracted from resonator via cavity dumping 18 roundtrip passes latter Q-switching and its' best Gaussian fit corresponding to 62 ps pulse duration are shown in Fig.4. The low standard deviations of experimental points almost unrecognizable in picture under their graphic representations are a good confirmation of this high reproducibility.

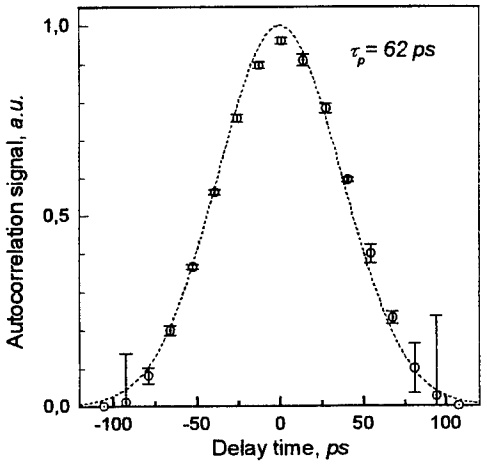


Fig.4. Autocorrelation function of the single pulse after Q-switching and cavity dumping.

4. SUMMARY

Resuming above results we can conclude that:
- ultrashort pulse formation process in the actively mode-locked laser with negative feedback stabilization begins at the intensity level in the cavity corresponding to the saturation one for laser medium;
- pulse shortening is very fast and covers about 10-20 cavity roundtrips only;
- after an initial pulse formation the duration remains constant while feedback stabilized quasi-cw laser oscillations are maintaining and no correlation between pulse duration and energy was observed.

5. ACKNOWLEDGEMENTS.

Author is grateful for the support of this work in frame of ISTC project B-078-97.

6. REFERENCES

1. V.S.Letokhov, Zh. Eksp. Teor.Fiz., Vol.54, p.1392, 1968 (Sov.Phys. JETP, Vol.27, p.746, 1968).
2. D.J.Kuizenga, D.W.Phillion, T.Lund, A.E.Siegman, Opt. Commun., Vol.9, p.221,1973.
3. R.G.Zaporozhchenko, V.A.Zaporozhchenko, Journal of Applied Spectroscopy, Vol. 67, pp. 65-68, 2000.
4. V.A.Zaporozhchenko, "Feedback timing approach to the pulse energy stabilization in the actively mode-locked laser", in Laser Optics'98: Solid State Lasers, Vladimir I. Ustyugov, Editor, Proc. of SPIE Vol.3682, pp.170-173 (1998).

Characteristics and kinetics of Ti:Sapphire oscillator pumped by SH of double pulse Nd^{3+}:YAG laser

Yury V. Zaporozhchenko

Belorussian-Japanese Joint Venture "Lotis TII", Surganova str.6, Minsk 220072, Belarus
(telephone +375-2684096, fax +375-2840621, E-mail:was@lotis.belpak.minsk.by)

ABSTRACT

The dependence of output parameters of a $Ti^{3+}:Al_2O_3$ tunable laser (an efficiency, build-up time, jitter, etc.) on the temporal delay between pump pulses of a Q-Switched double pulse Nd^{3+}:YAG laser has been investigated. The advantages of double pulse pumping of the Ti:Sapphire oscillator has been demonstrated, experimentally. New methods of output characteristics control for tunable Ti:Sapphire lasers have been proposed.

1. INTRODUCTION

The Ti:Sapphire lasers are a well known sources of a tunable radiation in visible and near-infrared spectrum range. However an attempt to obtain a valuable output energy in narrow line from $Ti^{3+}:Al_2O_3$ laser requires the application of selective elements bringing high intracavity losses that results in the increase of threshold pump energy and the generation build-up time and also decrease of laser efficiency. To achieve a high output energy at a narrow generation line, the laser oscillator-amplifier combination or a special seeding technique [1,2] is usually used for tunable $Ti^{3+}:Al_2O_3$ lasers.

The double pulse pump was proposed and investigated successfully for the improvement of the tunable dye laser output characteristics [3]. With pumping by the double pulse laser, the first weak pulse excites the active medium at the small exceeds above threshold, while the second (powerful) pump pulse arrives into exited active element by the time the generation starts. Such pump method increased the efficiency of dye laser up to ~ 30% with about two times narrowing of the generated linewidth in the center of the dye tuning curve.

The main difference of Ti:Sapphire from dye in this aspect is the high fluorescence lifetime of Ti^{3+} in Al_2O_3 ~ 3,2 μs and relatively low stimulated emission cross-section $\sigma \sim 10^{-19}$ cm^2 [4]. These parameters lead to increase temporal instability and a generation build-up time in comparison with typical Q-Switched pump pulse duration ~ 10 ns.

The goal of this work is an investigation of the possibility to improve and to control output parameters of the tunable Ti:Sapphire laser using the double pulse pumping.

2. EXPERIMENT

The pumping of the $Ti^{3+}:Al_2O_3$ laser was carried out by the doubled radiation of the Nd:YAG laser LS-2134D, by "Lotis-TII" production, with the dual pulses of radiation. LS-2134D has the following characteristics at the pump wavelength (532 nm): dual pulses repetition rate - 10 Hz, energy per each pulse is ~ 150 mJ, beam diameter - 6 mm, pulse duration (on FWHM) ~ 10-12 ns, divergency of laser radiation on a 0,5 level ~ 2,5 mrad.

The special design of the LS-2134D pump chamber is used to make pump of two Nd:YAG active elements by one pump lamp. Both active elements are placed in their own identical Q-Switched laser resonators. Each laser resonator generates pulses of 1,064 μm radiation. The delay between pulses is determined by the Q-Switches triggering moments and can be varied in 0-80 μs range with step 1 μs. Moreover, there is a possibility of slight delay adjustment with accuracy ~ 2 ns. Special polarizer unit is utilized for coincidence of these pulses in common beam. The output double-pulse fundamental frequency radiation falls on to the nonlinear KTP crystal, cut according to type II of phase matching (oee) for the second harmonic conversion. Wavelength separator mirrors placed after KTP crystal are used for spectral separation of second harmonic generation.

Laser Optics 2000: Control of Laser Beam Characteristics and Nonlinear Methods for Wavefront Control,
Leonid N. Soms, Vladimir E. Sherstobitov, Editors, Proceedings of SPIE Vol. 4353 (2001)
© 2001 SPIE · 0277-786X/01/$15.00

The optical scheme of the Ti:Sapphire laser is shown in Fig.1. Two identical Brewster–cut active elements $Ti^{3+}:Al_2O_3$ were used in this experiment. They have had following parameters: length 9 mm, transmittance at the 532 nm ~ 22%, FOM – factor (a532/a800) ~ 100. Pump radiation is focused by lens *3* (f ~ 500 mm). The optical resonator length is about 400 mm.

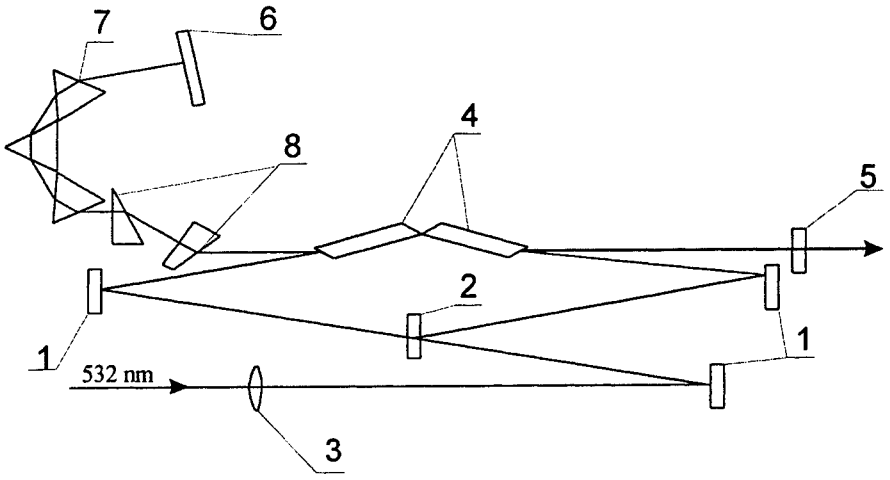


Fig.1. Optical scheme of tunable Ti:Sapphire laser:
1-mirrors R = 99,9 % (532nm); 2- beam splitting mirror R = 50 % (532nm); 3-focusing lens; 4-active elements; 5-output coupler R ~ 80 % (770 nm); 6 - wideband "rear" mirror; 7-dispersion prism assembly; 8-prism beam expander

Laser parameters have been measured by pyroelectric energymeter Rm-3700 by "Laser Probe", oscilloscope C1-75 with avalanche photodiode, monochromator MSD-1000 by "Solar TII".

3. RESULTS AND DISCUSSIONS

The results obtained with the single-pulse and the double-pulse pumping have been compared. The use of two λ=532nm pump pulses (~ 75 mJ, 10 ns) separated by a delay $\Delta\tau$ ~ 40ns allowed to obtain a ~ 33 % efficiency (instead of a ~ 22,5 % for a single (150 mJ, 10 ns) pump pulse) at the λ=770nm generation (see Fig.2). The linewidth of the Ti:Sapphire laser generation at the single- and double-pulse pumping was ~ 0,08 nm. The delay between pulses was determined as time difference between pulses peaks. In the double-pulse pump regime pump energy is determined as sum of both pulses energies.

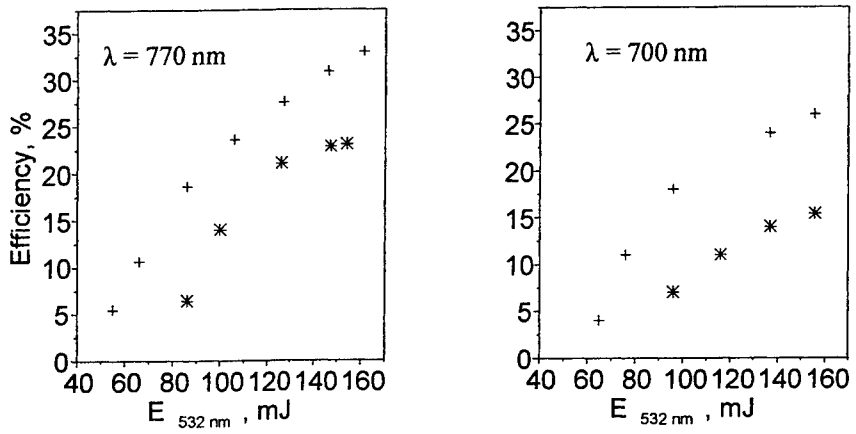


Fig. 2. Slope efficiency of the Ti:Sapphire laser with the single- (*) and double- (+) pulse pumping.

The decrease of the generation thresholds (see Fig.2) at the double-pulse pumping allows to extend the Ti:Sapphire laser tuning range. In the present work the expansion of a tuning range from 675-980 nm to 660-1015 nm was achieved.

As is illustrated in Fig. 2, the pump energy is utilized more effective in the double-pulse case. The decrease of the generation thresholds conducts to growth of efficiency and faster generation development. The stronger effect of the efficiency increasing is appeared close to the edges of the Ti:Sapphire

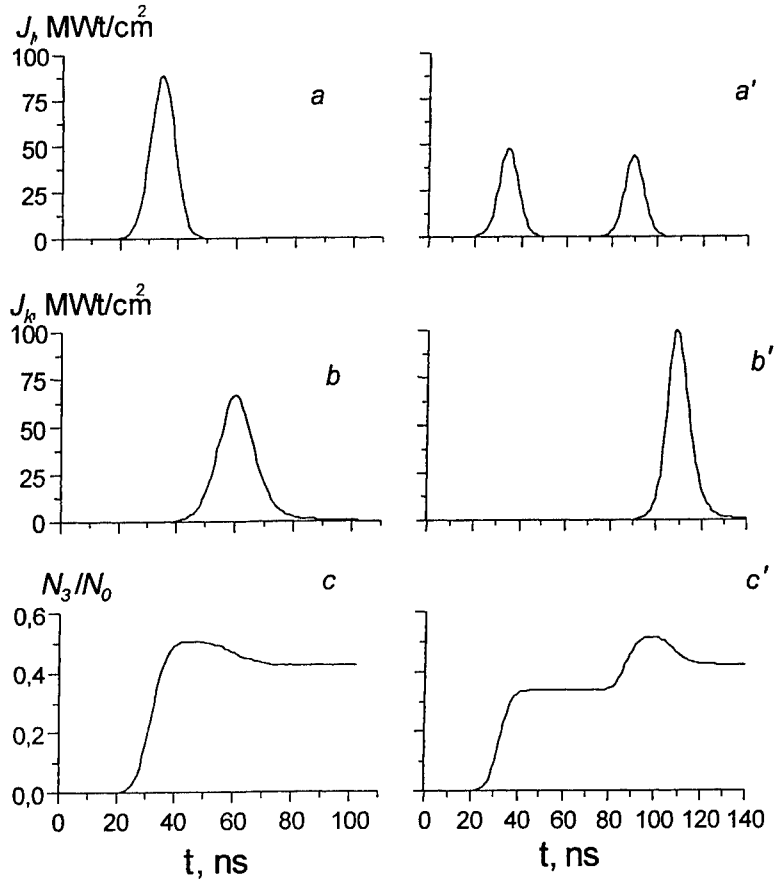


Fig. 3. Envelopes of the transmitted pump intensities (a, a'), generation intensities (b, b') and working level population N_3 normalized on full number of Ti^{3+} ions N_0 (c, c').

tuning curve (see Fig.2 at λ = 700 nm). In this case the proportion between the efficiencies of the double- and single-pulse pumping is higher than that at the maximum of a $Ti^{3+}:Al_2O_3$ tuning curve apparently because of affinity to threshold mode. Moreover, the efficiency curve for the double-pulse pumping doesn't show such absorption at high pump energies as in the single-pulse pumping regime.

The mathematical modeling of the experiment was carried out for the experimental scheme (Fig. 1). The $Ti^{3+}:Al_2O_3$ levels population dynamics was simulated by a four level model with quasi-stationary assumption, since the pump pulse duration ~ 10 ns is much longer than the phase relaxation time [4]. The temporal envelopes calculated on the basis of algorithm from [5] are illustrated in Fig.3. The left side of Fig.3 corresponds to a single-pulse pumping, the right side corresponds to a double-pulse pumping. Transmitted pump radiation intensities J_l (a, a'), intensities of a Ti:Sapphire generation J_k (b, b') at 770 nm and normalized working level population N_3/N_0 (c, c') (see Fig. 3) were calculated at parameters appropriate to the carried out experiment. They are of the following values: pump intensity J_l = 400 MWt/cm^2 (corresponds to pump pulse energy ~ 150 mJ or 80 mJ + 70 mJ (first and second pump pulses) at ~ 10 ns pulse duration); resonator length 400 mm; output coupler transmittance 80 %; rear mirror reflectance 99,9 %, delay between pump pulses $\Delta\tau$ = 40 ns. The calculated data are in a good agreement with experiment. So, Ti:Sapphire build-up time (at the 770 nm) measured at the single-pulse pumping (150 mJ, 10 ns) is equal 28 ns with pulse duration ~ 12 ns and efficiency ~ 22,5 %, while the calculated build-up time equals 25 ns with pulse duration 13,5 ns and efficiency 25 % (see Fig. 3a, 3b). For the double-pulse pumping experimental results have following values: the build-up time (relative to a second pump pulse) equals ~ 18 ns, generation pulse duration ~ 10 ns. As is indicated in Fig. 3 (b, b') the intensity of the $Ti^{3+}:Al_2O_3$ generation at the double-pulse pumping in ~ 1,3 times exceeds that at the single-pulse pumping, while the experimental result is ~ 1,45 times (see Fig. 2 at the 770 nm). The envelopes in Fig. 3 (c, c') indicates that the working level population grows quickly enough at submission of a second pump pulse and achieves higher value than that at the single-pulse pumping. This results in the faster generation dynamics. As the generation develops from the "prelase" initiated by the first pulse, the amplification it on the resonator roundtrip achieves higher value, that results in more effective stored energy utilization. For a single-pulse pumping the saturation occurs with pump intensity increasing, while the division of pulses in time provides more linear absorption mode.

It is important to note an opportunity of the Ti:Sapphire laser generation stability increasing with temporal jitter reducing. The signed above results on build-up time reduction (with respect to second pump pulse) allow to assume an opportunity of jitter control using double-pulse pumping. It is especially important at the edges of the Ti:Sapphire tuning curve, while the jitter in these region is inappropriately great as a rule. Shown in Fig. 4 results on Ti:Sapphire generation jitter was measured with respect to a pump laser Q-Switch triggering pulse as a jitter of pulse leading edge at the half-maximum level on set of ~ 100 pulses, while the pump pulses (532 nm) jitter was ~ ±1 ns. The dash line shows the Ti:Sapphire jitter (at 690 nm) at the single 150 mJ pulse pumping. Curves (▲) and (■) differ by the first pump pulse energies: ▲ -first pump pulse

energy equals ~1.1 threshold energy, ■ - 1.2 threshold energy. The second pump pulse is 80 mJ, that equals ~1,3 threshold energy for the 690 nm generated pulse. The build-up time at the single-pulse pumping is ~ 100 ns, at the double-pulse pumping it changes from ~ 120 ns (at $\Delta\tau$ =50 ns) to ~ 40 ns (at $\Delta\tau$ =250 ns). It is important to say that change of the delay between pump pulses practically doesn't influence on the generated pulse energy. The shaded area in Fig. 4 corresponds to the probable moment of the generation pulse occurrence, if the first pump pulse only comes in to action. As is illustrated in Fig. 4, increase of the first pump pulse energy conducts to improvement of the generation jitter and by appropriate choose of the delay between pulses it can be reduced substantially. But at approaching of $\Delta\tau$ to the instant of the generation pulse occurrence under the first pump pulse action, the jitter grows sharply. It is a consequence of the generation build-up process (affected by the first pulse) transition from linear to the exponential mode of pulse development. The jitter of the 770 nm generation pulses measured at the single-pulse pumping with parameters according Fig.3 ~ twice exceeds that at the double-pulse pumping (± 3 ns and ± 1,5 accordingly).

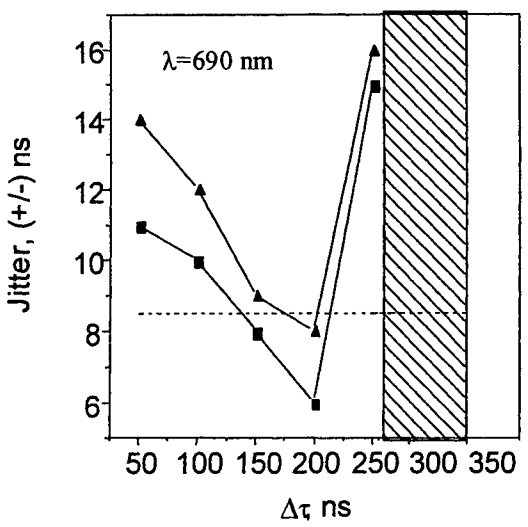


Fig. 4. Dependence of the generation temporal jitter on the delay between pump pulses at the different pump intensities.

On a basis of the above results it is possible to make a conclusion about an opportunity to control Ti:Sapphire laser parameters using double-pulse pumping. It is needed to excite $Ti^{3+}:Al_2O_3$ on the high level above threshold by the first pump pulse and at the corresponding delay $\Delta\tau$ the second pump pulse will provide the reliable pulse building-up. The reducing of the Ti:Sapphire laser jitter and build-up time in wide tuning range, using the double-pulse pumping, opens new opportunities of synchronization $Ti^{3+}:Al_2O_3$ generation with that from other laser sources.

4. CONCLUSION

Resuming advantages of the Ti:Sapphire double-pulse pumping we can conclude that:
- at the double-pulse pumping the pump energy is utilized more effective due to the acceleration of the generation development rate and reduction of the saturation in the absorption channel;
- the extending of the tuning range can be achieved easily as a consequence of the threshold energy decrease;
- high reliable Ti:Sapphire generation can be achieved in wide tuning range by changing the delay between pump pulses and their energies proportion;
- the possibility of the reliable generation pulses timing to that from the other laser sources takes place in wide Ti:Sapphire tuning range.

5. REFERENCES

1. P. Brockman, C.H. Bair, J.C. Barnes, R.V. Hess, E.V. Browell, "Pulsed injection control of a titanium-doped sapphire laser", *Opt. Lett.*, Vol.11, pp. 712-714, November 1986.
2. A.J Merriam, G.Y. Yin, "Efficient self-seeding of a pulsed $Ti^{3+}:Al_2O_3$ laser", *Opt. Lett.,* Vol. 23, pp. 1034-1036, July 1998.
3. N.M. Buzinov, V.I. Eliseenkov, I.Ya. Ickhoki, L.K. Mikhailov, S.L. Seregin, O.B. Cheridnichenko, *Electron. Techn., Ser. 11, Las.techn. and electron.*, N 4, pp. 32-43, 1983.
4. P. F. Moulton, "Spectroscopic and laser characteristics of $Ti^{3+}:Al_2O_3$", *J. Opt. Soc. Am.B*, Vol-3, no.1, pp.125-133, 1986.
5. R.G. Zaporozhchenko, I.V. Pilipovich, A.V. Kachinskii, "Generation dynamics of ultrashot pulses in the $Ti^{3+}:Al_2O_3$ laser synchronously pumped by time-limited train of mode-locked laser", *Experimentelle Technik der Physik*, 39, pp. 427-430, 1991.

Superhigh fidelity of phase conjugation at SBS with using the kinoform optics of new generation

F. A. Starikov, Yu. V. Dolgopolov, S. A. Kovaldov, G. G. Kochemasov, A. V. Kopalkin, S. M. Kulikov, V. K. Ladagin, S. A. Sukharev, N. N. Gerasimenko

Russian Federal Nuclear Center – Institute of Experimental Physics
607190 Sarov (Arzamas-16), Nizhny Novgorod Reg., Russia

ABSTRACT

Using the most complete in literature physical model of the non-steady-state stimulated Brillouin scattering (SBS), the numerical study is carried out of phase conjugation (PC) in the SBS-mirror that consists of an angular selector of Stokes radiation, an ordered raster of small lenses, a main focusing lens, and an SBS-cell. The ordered raster with controlled varying of its parameters allows to perform the effective angular filtering of non-conjugated Stokes component, to reduce the local light loads, and to avoid the competitive nonlinear effects. An optimal configuration of such SBS-mirror has been determined. It has the unique properties as compared with the current SBS-mirrors. It fixedly yields the PC quality that is near to an ideal (the PC coefficient is about of or more than 95%) at the selector transmittance 50-70% and any level of SBS saturation, i.e. any reflection coefficient. In the SBS-mirrors of different types the high PC quality in the focused beams takes place at the high reflection coefficients only that is difficult to realize as a rule. The experimental data obtained at a Nd laser facility show the validity of the simulation results. The developed conception of SBS-mirror with unique properties can be applied for the improvement of wide class of industrial lasers.

Key words: phase conjugation, stimulated Brillouin scattering.

1. INTRODUCTION

The phase conjugation (PC) based on stimulated Brillouin scattering (SBS) has been widely used in double-pass laser amplifiers. After the first pass, the amplified laser beam, distorted due to various optical inhomogeneities in the amplifier, is incident on the PC-mirror. The purpose of PC-mirror is to create a reflected Stokes beam with the wave front being a conjugate to the incident one and, thus, to compensate the optical inhomogeneities of amplifier during the reverse pass. The PC fidelity and reflectivity of PC-mirror have a crucial influence on the performance of such system.[1-4]

The main component of PC-mirror is an SBS-cell. It was also a usual way to use a random phase plate located ahead of SBS-cell. The aberrated laser beam after passing through the random phase plate acquires a small-scale speckled structure. This promotes the reduction of "snake-like" distortions of the Stokes wave in the SBS-cell and increases the PC fidelity. Then the use of SBS-cell in the form of a rather long light waveguide allows obtaining a practically perfect PC fidelity of the statistically uniform speckled beam, but unfortunately at substantial laser intensities the lightguide damage resistance is a challenge. In order to avoid this and to solve the problem of exceeding an experimental SBS threshold, the speckled laser beam is tightly focused by a lens into the cell with a gaseous or liquid SBS-medium. However, the focused speckled laser beam becomes a statistically nonuniform one, and its bell-shaped mean envelope being more pronounced in the Stokes beam. This leads to a decrease in the PC fidelity. For example, in the SBS steady-state linear mode, when the Stokes beam weakly affects the laser beam, the PC coefficient does not exceed 30%.

On the other side, there are a few experimental investigations of double-pass amplifiers where the aberrated laser beam experience ordered spatial distortions after or during the first pass. First, the ordered distortions may be introduced into the laser beam through the use of an ordered phase plate in the PC-mirror scheme instead of the random one. In this case the phase plate is a raster of identical Fresnel lenses.[5-8] Second, the ordered distortions can appear in the laser beam during its first pass because of a specific construction of the amplifier, for example, if the amplifier is made as an ordered fibre bundle.[9]

We have carried out a numerical investigation[10] of PC at the steady-state SBS of an aberrated laser beam in the case of PC-mirror composed of an angular selector of Stokes radiation, an ordered raster of small lenses, a main focusing lens and an SBS-cell. As a result of the investigation, a new effect of extremely low noising of Stokes beam has been found. Its essence

Laser Optics 2000: Control of Laser Beam Characteristics and Nonlinear Methods for Wavefront Control, Leonid N. Soms, Vladimir E. Sherstobitov, Editors, Proceedings of SPIE Vol. 4353 (2001)
© 2001 SPIE · 0277-786X/01/$15.00

is in the fact that the angular selection of Stokes radiation leads to the nearly perfect PC when the SBS-mirror arrangement is optimal. For this purpose the input window of SBS-cell should be placed in a certain intermediate region between the focal plane of rasher's lenses and the focal plane of main lens. It has been shown also that the usage of the Gaussian random phase plate, which was traditional in the PC research, instead of ordered one results in the substantially poorer PC fidelity and unprincipled role of angular selection.

Calculation[10] have been performed in an approximation of steady-state linear (unsaturated) SBS when the Stokes field does not affect the laser pump one. But in the experiments the SBS saturation shows itself in any event. Moreover, the operation in the saturated regime of SBS is one of the aims of the experiment as it leads to an increase of the SBS-mirror reflection coefficient. Further, for modeling the experiments on PC at SBS of pulsed laser beams it is needed to additionally allow for the non-steady-state transient processes related to the finite time of hyper-sound relaxation in the SBS-medium. The usage of simplified models of SBS often results in the problems of interpretation of the experimental data or in the failure of quantitative comparison with the experiment. The numerical simulations taking into account the non-steady-state saturated SBS and experiments have been recently begun. [11] For this purpose the most complete in literature physical and numerical model of non-steady-state transient SBS has been developed that takes into account all main physical effects and is more close to experimental situation. Carrying on our recent paper,[11] we describe new numerical as well as experimental results of the study of PC at SBS of laser beam passed through an ordered raster of small lenses in the SBS-mirror. Main attention is paid to the determination of the SBS-mirror arrangement giving near-to-ideal PC quality in the wide range of laser power.

2. TRANSIENT SBS MODEL

The SBS is described by the set of equations:[11]

$$\frac{n_0}{c}\frac{\partial A_L}{\partial t}+\frac{\partial A_L}{\partial z}-\frac{1}{2ik}\Delta_\perp A_L+\frac{ik}{2}\left(\frac{n^2}{n_0^2}-1\right)A_L=-\frac{i}{2}pA_S, \tag{1}$$

$$\frac{n_0}{c}\frac{\partial A_S}{\partial t}-\frac{\partial A_S}{\partial z}-\frac{1}{2ik}\Delta_\perp A_S+\frac{ik}{2}\left(\frac{n^2}{n_0^2}-1\right)A_S=-\frac{i}{2}p^*A_L, \tag{2}$$

$$\frac{\partial^2 p}{\partial t^2}+2\left(\frac{1}{\tau}+i\Omega\right)\frac{\partial p}{\partial t}+\frac{2i\Omega}{\tau}p=\frac{2g\Omega}{\tau}A_LA_S^*+2i\Omega S, \tag{3}$$

where A_L, A_S and p are slowly varying laser, Stokes and hypersonic complex amplitudes, respectively, $g=\omega_0\tau\Omega/[4\beta_S n_0^2c^2]$ is the SBS gain coefficient, $\tau=2/(q^2\Gamma)^2$ is the hyper-sound relaxation time (phonon lifetime), $\Omega=\omega_L-\omega_S$ and $q\cong 2k_L$ are the frequency and wave number of hyper-sound, n_0 is the mean refractive index defined by the relationship $k=n_0\omega_0/c$, $\beta_s=1/(\rho^0 v_s^2)$ is the compressibility of the medium, v_s is the adiabatic hyper-sound speed, $\Gamma=(4\eta/3+\eta')/\rho^0$ is the damping constant, η and η' are the shear and bulk viscosity, ρ^0 is the mean density. The frequencies and wave numbers of laser and Stokes waves are considered to coincide. The field amplitudes are normalized so that the radiation density fluxes are equal to $J_L=|A_L|^2$, $J_S=|A_S|^2$. Below in calculations the time of varying A_L (the pulse duration) is considerably more than the hypersonic period $T=2\pi/\Omega$ then the equation (3) can be simplified:

$$\frac{\partial p}{\partial t}+\frac{p}{\tau}=-i\frac{g}{\tau}A_LA_S^*+S. \tag{4}$$

In the equations (1) and (2) the refraction due to non-uniformity of refractive index n not related to density variations in hypersonic wave is taken into account together with the amplification owing to the parametric build-up of hypersonic wave. This refraction can be linear as well as nonlinear when n depends on the laser and Stokes intensities. In the present work the refraction is neglected. The fluctuation Langevin force S is delta-correlated in time. Its modeling has been considered in detail in Ref.11. The test calculations show a good accuracy of the numerical method.[11]

3. CALCULATIONS OF PC OF GAUSSIAN BEAM AT SATURATED SBS

In all actual experiments the role of SBS saturation is noticeable in a varying degree. The SBS saturation and reflection coefficient rise are considered [1-4] to favour the PC fidelity improvement. We will obtain here the dependence of PC quality on SBS saturation depth. Let's consider an ideal Gaussian laser beam $A_L=A_{L0}\exp(-r^2/a^2)$, where $a=0.047$ cm. The input laser amplitude does not vary in time. We take the following parameters of SBS-medium: the spontaneous Brillouin scattering coefficient $\kappa=10^{-5}$ cm^{-1}sr^{-1}, $\tau=5$ ns, $g=23$ cm/GW, the SBS-cell length $L=80$ cm. The laser beam is focused into SBS-cell with the help of a lens with focal length $z_f=50$ cm. In this case the SBS threshold power [11] equals $P_L^{th}\approx 6.4\lambda/g=1.5\times10^{-5}$ GW.

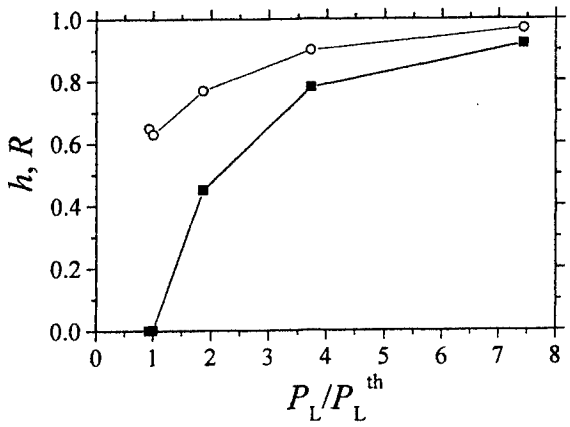


Fig.1. Reflection coefficient R (■) and asymptotic PC coefficient h (O) against the laser power.

To evaluate the PC quality we introduce the PC coefficient $h(z, t)=|\iint A_L(\mathbf{r}, z, t)A_S(\mathbf{r}, z, t)d\mathbf{r}|^2/[P_S(z, t)P_L(z, t)]$, where $P_L(z, t)=\iint|A_L(\mathbf{r}, z, t)|^2d\mathbf{r}$ and $P_S(z, t)=\iint|A_S(\mathbf{r}, z, t)|^2d\mathbf{r}$ are the laser and Stokes powers. At an ideal PC we have h=1. In Fig.1 are shown the asymptotic PC coefficient at the SBS-cell input and the reflection coefficient (the ratio of asymptotic Stokes power at the SBS-cell input to the input laser power) as functions of laser power. The PC coefficient value obtained under the near-threshold SBS conditions agrees with the theory[2] and calculations[10,12] of the linear steady-state SBS. The PC quality with h<90% can not be considered as satisfactory. As it is seen from Fig.1, the PC fidelity that is near to the ideal with h>90% occurs at the laser radiation reflection that is more than 80%.

Fig.2 demonstrates the laser and Stokes density flux distributions in the longitudinal section of SBS-cell at $J_{L0}=3.2\times10^{-2}$ GW/cm^2 at three temporal moments. It is seen how the Stokes radiation begins to form from noises (Fig.2(d)), experiences a linear SBS stage (Fig.2(e)) and is "attracted" to the input window of SBS-cell under the deep SBS saturation (Fig.2(f)). SBS saturation changes considerably the spatial structure of laser intensity in the SBS-cell (Fig.4(c)). The transverse distributions of the laser and Stokes density fluxes at those three temporal moments are given in Fig.3. They show demonstrably the temporal rising of the PC quality. With the validation purpose, the calculations have been made in the case of $J_{L0}=3.2\times10^{-2}$ GW/cm^2 for three steps Δz so that $gJ_{L0}\Delta z$=0.49, 0.98, and 1.96. The calculations give that the noted variation of the step Δz does not practically affect the Stokes power and the PC quality. The energy balance takes place (i.e. the incident laser energy is equal to the sum of the laser energy passed through the SBS-cell and the output Stokes energy) with the accuracy of 0.15, 0.58, and 2.4%, respectively.

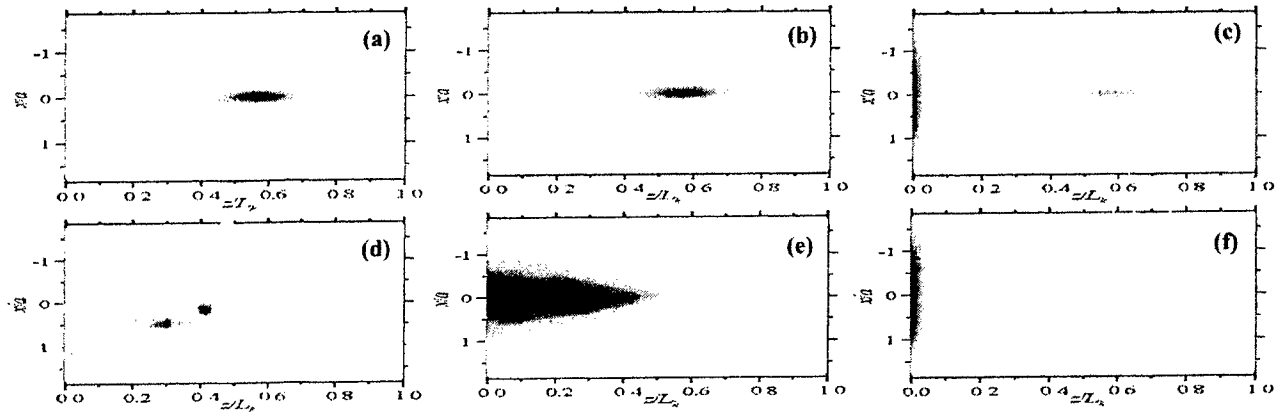


Fig.2. Longitudinal distributions of laser J_L (a-c) and Stokes J_S (d-f) density flux in the SBS-cell at t/τ=0.01 (a, d), 1 (b, e) and 6 (c, f) obtained for J_{L0}=0.032 GW/cm^2.

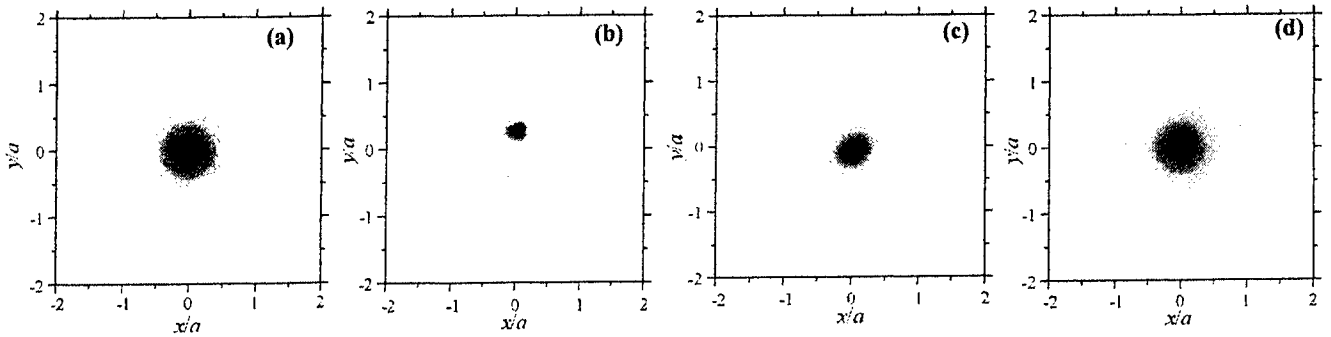


Fig.3. Transverse distributions of density flux of the laser radiation J_L (a) and Stokes radiation J_S at the SBS-cell input at t/τ=0.01 (b), 1 (c) and 6 (d) obtained for J_{L0}=0.032 GW/cm^2.

4. CALCULATIONS OF PC IN THE CASE OF SBS-MIRROR WITH THE RASTER OF SMALL LENSES

We have shown above that one can reach the high PC fidelity in the case of SBS-mirror, including the focusing lens and SBS-cell, only at the great reflection coefficients of the laser radiation from the SBS-mirror. But often it is not feasible since the considerable light loads result in the growth of parasitic competitive non-linear processes in the SBS-active medium (the thermal self-defocusing, the electrostriction self-focusing, the optical breakdown), which exert the negative influence on the SBS process to the point of its destruction. Therefore it is actual to obtain the near-to-ideal PC quality for the relatively small laser powers. With this purpose we will consider below more complicated SBS-mirror with an ordered phase plate in the form of a raster of small lenses and an angular selector of the Stokes radiation. As it recently shown under conditions of the linear steady-state SBS,[10] the raster is more preferable in comparison with the random phase plate.

The principal schematic arrangement of SBS-mirror with the raster of small lenses is shown in Fig.4. We suppose that the laser beam after its first pass in the amplifier has a half-width a and angular divergence θ_L. Its undesirable excess over the diffraction limit results from the optical nonuniformities in the actual amplifiers. According to Fig.4, the laser radiation is coupled into the angular selector consisting of two lenses and a pinhole situated between them. The pinhole plane is the place where the angular selection of radiation can occur. The angular spectrum of the radiation is cut in the selector by a value of the transmission angle θ_{sel}. The condition $\theta_{sel}>\theta_L$ is satisfied. After passing through the selector, the laser beam goes through the ordered raster of identical small lenses with a focal length f and a size d. Optical properties of the multiple Fresnel lens [7,8] do not differ practically from the conventional one. The distance between the phase plate and the main focusing lens is L_0. The main lens with focal length F focuses the aberrated and orderly disturbed laser radiation field into the SBS-cell of length L. The distance between the main lens and the input window of the SBS-cell is L_1.

The laser intensity after passing through the raster has the specific distributions in the zones I and II, where the laser beam is broken up into the ordered arrays of beamlets. One of them, zone I, is the focal region of main focusing lens (see Fig.4). An ordered spotted picture is formed in zone I. Each peak of this picture has a structure of angular distribution of the laser intensity incident on the raster. The angular interval between the peaks is equal to $\theta_d=\lambda/d$. The smooth envelop of the peaks depends on the amplitude transmission coefficient of the raster's cell and does not depend on the incident laser field under its large-scale nonuniformity. We take d=0.1 cm, f=16 cm. At λ=1.315 μm it gives 3×3 main peaks of the equal intensity in the zone I.[10] The other specific distribution of the laser intensity is in the zone II, i.e. the focal region of the raster's small lenses. Unlike the zone I, the envelope of small focal peaks in the zone II is proportional to the laser intensity incident on the raster.

The steady-state linear SBS calculations[10] have shown that the distribution of Stokes intensity in the pinhole plane consists of a discrete set of peaks or diffraction orders that is consistent with the experiments.[5-9]. The angular separation between them equals θ_d like that in the laser pattern in the zone I. A perfect PC requires only the central Stokes order of diffraction conjugated to the laser beam. Angular selection in the pinhole plane removes the non-zero orders of diffraction, thereby increasing the PC fidelity. A novel encouraging effect of extremely low noising of the Stokes field was found.[10] Its essence is in the fact that the angular selection of central Stokes mode allows achieving a nearly perfect PC. For this purpose the input window of the SBS-cell should be placed in a certain region between the zone I and zone II, where the quasi-lightguide mosaic zones with the periodical distribution of the laser intensity are formed. If the arrangement of PC-mirror is optimal, the PC coefficient is more than 90-95% whereas the PC coefficient before the selection does not exceed the value of 30%. To increase the selector transmission coefficient, the SBS-cell should be moved towards the main focusing lens so that the zone II would be put within the SBS-cell. However, this increase of selection coefficient is accompanied by a noticeable decrease of PC fidelity after the selection.

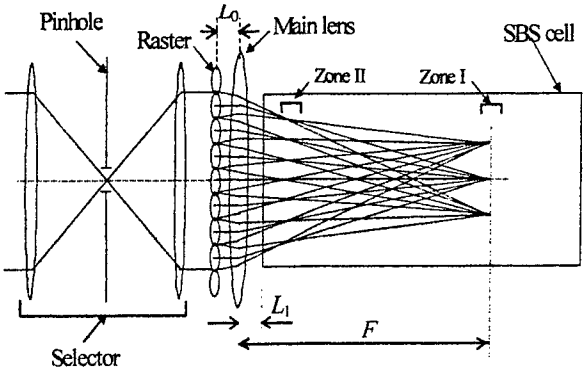


Fig.4. Schematic of the SBS-mirror with the raster of small lenses.

To explore an effect of SBS saturation on the performance of the aforesaid SBS-mirror, we carry out the calculations in the 2D approximation that reduces the calculation time considerably. As it has been shown earlier,[10] the 2D approximation describes all the principal features of working the SBS-mirror considered. In this case the PC and selection coefficients for the 3D medium are close to the squared corresponding values obtained in the 2D approximation. We use the Gaussian laser intensity distribution at a=0.4 cm. In the experiments one registers, as a rule, not instantaneous but temporally integrated data. For modeling the actual experimental situations it is needed to

take into account a concrete temporal profile of the laser power and a non-steady-state effect. Calculations are conducted at the Gaussian temporal profile of laser power is taken. The profile width is about 4τ, and the non-steady-state effects being showing themselves. The calculations with the same laser intensity but with the different realizations of the hyper-sound noise are analogous to a series of flashes of a pulsed laser in the experiment. The calculations are conducted at F=100 cm, $\theta_{sel}=\theta_d/2$, L_0=1 cm and two distances L_1. At L_1=1 cm, when the both zones I and II are within the SBS-cell, the SBS-cell length is L=200 cm. At L_1=68 cm, when the only zone I is within the SBS-cell, the SBS-cell is shorter, L=132 cm. In the calculations the axial laser intensity $J_{L0}=|A_{L0}|^2$ varies. The typical instantaneous distributions of the laser and Stokes density flux in the longitudinal section of the SBS-cell are shown in Fig.5 for L_1=1 cm и 68 cm. The quasi-lightguide zones, which are formed in the place of intersection of the neighboring laser beamlets existing in the zone I, are distinctly seen. At L_1=68 cm the region of the quasi-lightguide zones is situated in the vicinity of the input window of SBS-cell (see Fig.5(b)), ensuring an optimal SBS-mirror arrangement in terms of achieving the highest PC fidelity under the linear steady-state SBS conditions.[10]

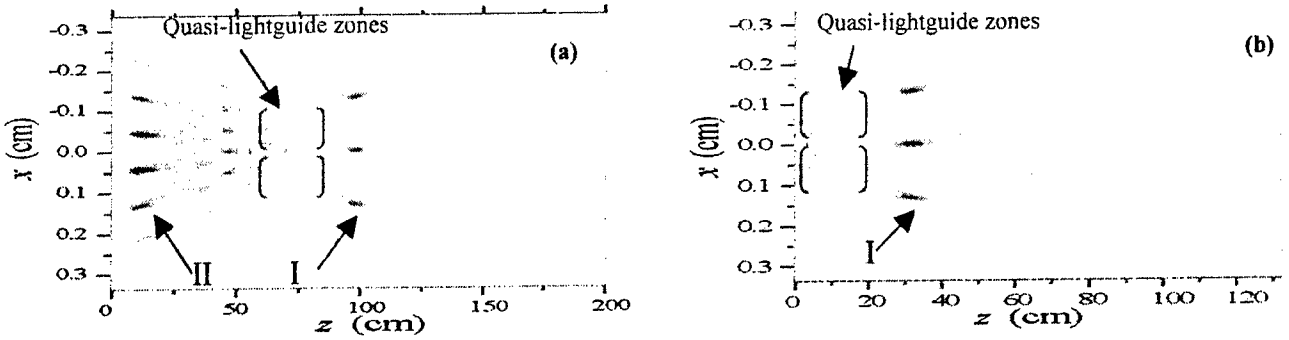


Fig.5. Longitudinal distributions of laser density flux J_L in the SBS-cell obtained for (a) L=200 cm, L_1=1 cm and (b) L=132 cm, L_1=68 cm.

The typical dynamics of the laser power at the input and output of SBS-cell and the Stokes power at the input of SBS-cell is shown in Fig.6. Fig.7 illustrates the dynamics of the PC coefficient at the input of SBS-cell h and after the angular selection h_{sel} as well as the selection coefficient k_{sel} (i.e. the Stokes energy fraction passed through the pinhole).

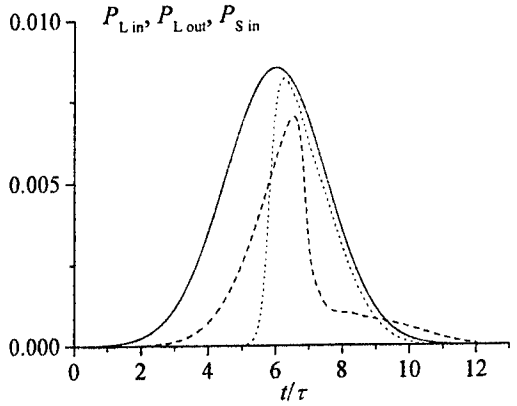


Fig.6. The dynamics of laser power at the input (—) and output (- - -) and Stokes power at the input (····) of the SBS-cell at L_1=1 cm, J_{L0}=24 a.u.

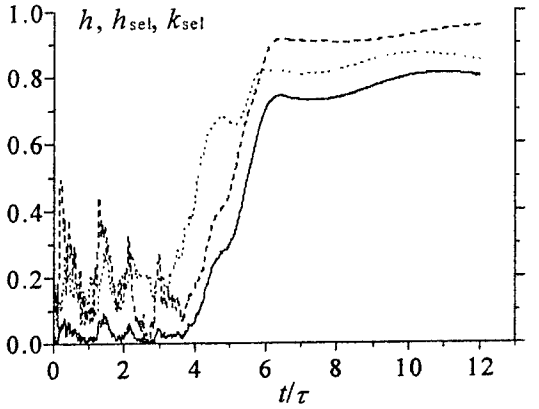


Fig.7. The dynamics of the PC coefficient at the SBS-cell input h (—) and after the angular selection h_{sel} (- - -) and the selection coefficient k_{sel} (····) at L_1=1 cm, J_{L0}=24 a.u.

Fig.8 gives the numerical dependence of the reflection coefficient from the SBS–mirror R (i.e. the ratio of the Stokes energy to the incident laser energy), the selection coefficient k_{sel} and the PC coefficient after selection h_{sel} on the maximal axial laser intensity J_{L0} for the both arrangements of the SBS-mirror. For the PC coefficient at the SBS-cell input (unselected) the relationship $h=h_{sel}k_{sel}$ is fulfilled. Here are given the h_{sel} and k_{sel} values, which have been averaged over the pulse (i.e. the values time-integrated with a weight of the output Stokes power and divided by the Stokes energy). The R fluctuations are rather small under the both arrangements of SBS-mirror. At L_1=1 cm the SBS threshold is less than that is at L_1=68 cm due to the longer SBS-cell length and the additional presence of bright zone II within the SBS-cell.

At L_1=1 cm near the SBS threshold the PC quality is low but the selection losses are less than at L_1=68 cm. With increasing the reflection coefficient, the both h_{sel} and k_{sel} rise, nevertheless the PC quality is far from an ideal. The value h_{sel} is less than 90% at R=60%. The cause of spread in of h_{sel} and k_{sel} consists in the fluctuations of their instantaneous values within an initial stage of the Stokes beam amplification (although their maximal asymptotic values in the different trials are much more close each other).

At L_1=68 cm, h_{sel} is more than 90% near the SBS threshold that has been the most substantial result of the steady-state linear SBS calculations.[10] It is extremely important that the effect of SBS saturation does not deteriorate this result, moreover, with increasing the laser power the PC quality rises yet more approaching to the ideal. The fluctuations of PC coefficient are very small. But there is a considerable spread in the k_{sel} value that is explained as follows. The PC coefficient is near to the ideal in any quasi-lightguide zone.[10] As it is seen from Fig.5, each quasi-lightguide zone is formed by two neighboring laser beamlets existing in zone I. In each laser beamlet in the zone I the Stokes radiation is amplified practically independently, therefore the Stokes fields in the quasi-lightguide zones are not phased. In other words, there is no complete diffraction mixing of the Stokes radiation in the transverse section of the beam. Contra, at L_1=1 cm the output Stokes radiation, passed from the far field to the near one in the medium with considerable gain, is transversely coherentized that leads to less spread in value of k_{sel}.

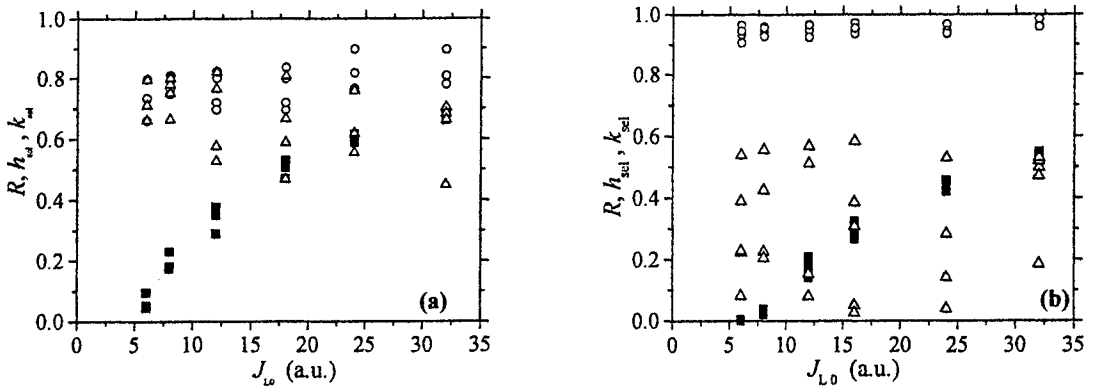


Fig.8. Numerical dependence of the reflection coefficient R (■), the time-integrated PC coefficient after selection h_{sel} (○) and the time-integrated selection coefficient k_{sel} (Δ) on the laser intensity at L_1=1 cm (a) and 68 cm (b).

In Fig.9 we compare the results shown in Fig.8(b) at L_1=68 cm with those obtained with no raster in the SBS-mirror scheme. It is seen from Fig.9(a) that presence of the raster increases the SBS threshold but, as it follows from Fig.9(b), considerably improves PC quality. In the absence of the raster the PC fidelity is poor at small reflection coefficients (see Fig.1 also). PC coefficient increases with laser intensity increasing when reflection coefficient rises but its values are lower than those in the raster case. In addition, in the absence of the raster the large reflection coefficients are connected with considerable light loads resulting in the growth of parasitic non-linear processes in the SBS-medium. Note that enhancement of PC coefficient from 0.9 to 0.95 is very important (for example, six-fold differences in the reflected intensity pattern can be observed at PC coefficient 0.85).[2] This means the obtaining of the super-high PC fidelity. We believe that in the case of distorted laser beam, an advantage of SBS-mirror with the raster will show itself still more appreciably. This question will be considered in the near future.

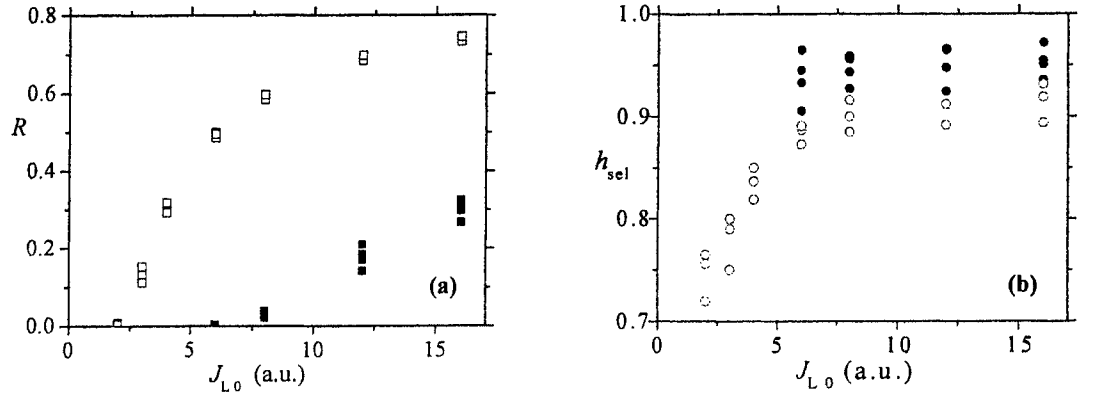


Fig.9. Numerical dependence of the time-integrated PC coefficient after selection h_{sel} (a) and the reflection coefficient R (b) with (solid) and with no (open) raster in the SBS-mirror scheme at L_1=68 cm.

For the purpose of increasing and stabilizing k_{sel} at keeping the high PC quality we propose to modify the SBS-mirror configuration. As it follows from Fig.8, we must fulfil two conditions. First, the input window of the SBS-cell should be set in the field of quasi-waveguide zones for achieving the high PC quality. Second, the zones I and II should be within the SBS-cell for reaching more high and stable values of k_{sel}. Both the conditions can be satisfied at placing the zone II in the SBS-cell behind the zone I. In order to realize this, we move the raster away the main lens so that L_0 exceeds the distance $(F+f)$ (see Fig.10).

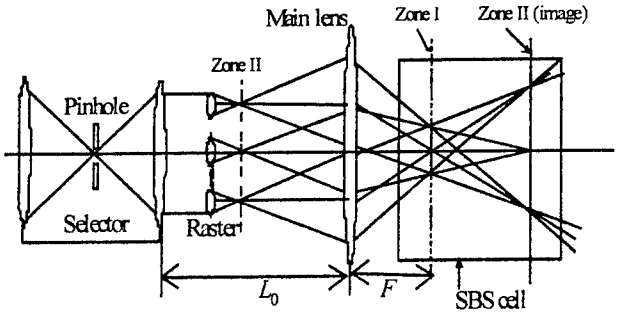


Fig.10. Modified scheme of SBS-mirror with the raster.

In this case the zone II is outside of the SBS-cell but its image, which is $F[1+F/(L_0-F-f)]$ distant from the main lens, can fall within the SBS-cell behind the zone I. In the calculations we put L_0=241 cm, L_1=1 cm, therefore the zone I and the image of zone II are at the distance of 100 и 180 cm, respectively, from the main length, and at L=200 cm they being within the SBS-cell. The distribution of the laser density flux in the longitudinal section of the SBS-cell for the zone I+zone II arrangement within the SBS-cell are shown in Fig.11. As the calculations show (see Fig.12), such the SBS-mirror arrangement allows to ensure the excellent PC quality and to increase the selection level and stability.

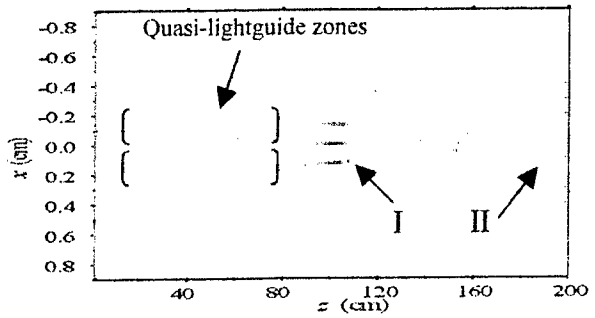


Fig.11. The longitudinal distributions of laser radiation density flux J_L in the SBS-cell at t/τ=1 obtained for L=200 cm, L_0=241 cm, L_1=0.

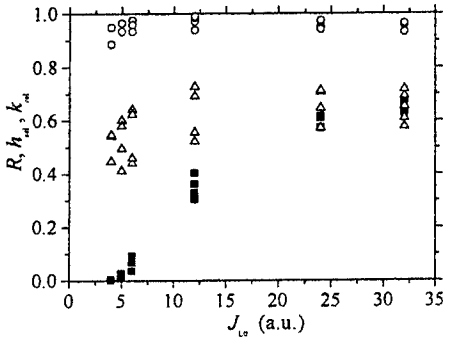


Fig.12. Numerical dependence of the reflection coefficient R (v), the time-integrated PC coefficient after selection h_{sel} (o) and the time-integrated selection coefficient k_{sel} (Δ) on the laser intensity for L=200 cm, L_0=241 cm, L_1=0.

5. EXPERIMENTAL RESULTS AND COMPARISON WITH CALCULATIONS

To carry out experiments on exciting SBS in gaseous mixtures, special gas-filled cells have been manufactured. Design philosophy and technology of the cell manufacture permit to keep the initial purity of the gas introduced into the cell. For this purpose, mechanical and electrical polishing is used, which permits to obtain a high degree of finish of the inner walls and separate parts of the cell (surface roughness ≤ 0.32 μm). Separate parts in the cell are joined by of copper and indium gaskets; welding works are carried out by means of electron beam welding.

The PC fidelity is significantly affected by competitive with SBS non linear optical processes, in particular heating and optical breakdown of SBS-medium. Since both these processes are considerably determined by the degree of the impurities removal from the gas, a special system for gas cleaning from dispersed micro-impurities and filling it into the cell has been manufactured. The main part of this system is a filtering system designed for the treatment of working gas (xenon). The treatment system enables not only remove solid impurities from gases, but filling in SBS-cells with gaseous mixtures with a component content at given partial pressures. Two stages of gas cleaning are used in the system. The first is located directly

after the gas cylinders, and the second is located in front of the cell. The second stage of treatment is equipped with special fine filters. As a filtering element in the fine filter nickel powder of the given particle size is used. Depending on the pore size of the filtering element specific degree of gas cleaning can be attained. Filters of the system developed allow to clean gases from particles with the size of more than 0.1 μm with the efficiency of ~99.9999%. In order not to pollute filter during the evacuation, the latter and filling in SBS-cell are carried out by different routes.

We have carried out the detailed experimental verification of the numerical results. The schematic of experimental setup is shown in Fig.13. The Nd laser consists of master oscillator and two amplifiers. At the output of the second amplifier a practically diffraction-limited laser beam is formed with λ=1.06 μm, energy 1.5 J and pulse duration 25 ns. The laser radiation is sent to a KD*P crystal where its frequency is doubled. Energy of the second harmonic radiation is ≤300 mJ, the pulse duration is 25 ns, the divergence is $3\cdot10^{-4}$ rad. On going to the second harmonic, the laser setup is isolated from the back-scattered SBS component. SBS is excited in the regime very near to the steady-state in a superclean cell filled with a mixture of SF_6 and Xe. The SF_6 partial pressure is 1.5 atm and the total mixture pressure is 28 atm. The SBS gain coefficient in such a medium is g=0.023 cm/MW, the hypersound relaxation time is $\tau\approx$5 ns. Gas filling into the SBS cell is realized through the aforesaid special system containing a filter for purifying gases from dispersion micro-impurities and aerosol particles with a diameter that is not less than 0.1 μm. In the experiments we use an eight-level kinoform raster of closely packed diffraction Fresnel lenses with the diffraction efficiency of 95%. The size of a separate lens d=0.5 mm and focal length f=6 cm so that $N_F=d^2/(2\lambda f)$=3.93. A photographic image of the raster fragment is shown in Fig.14.

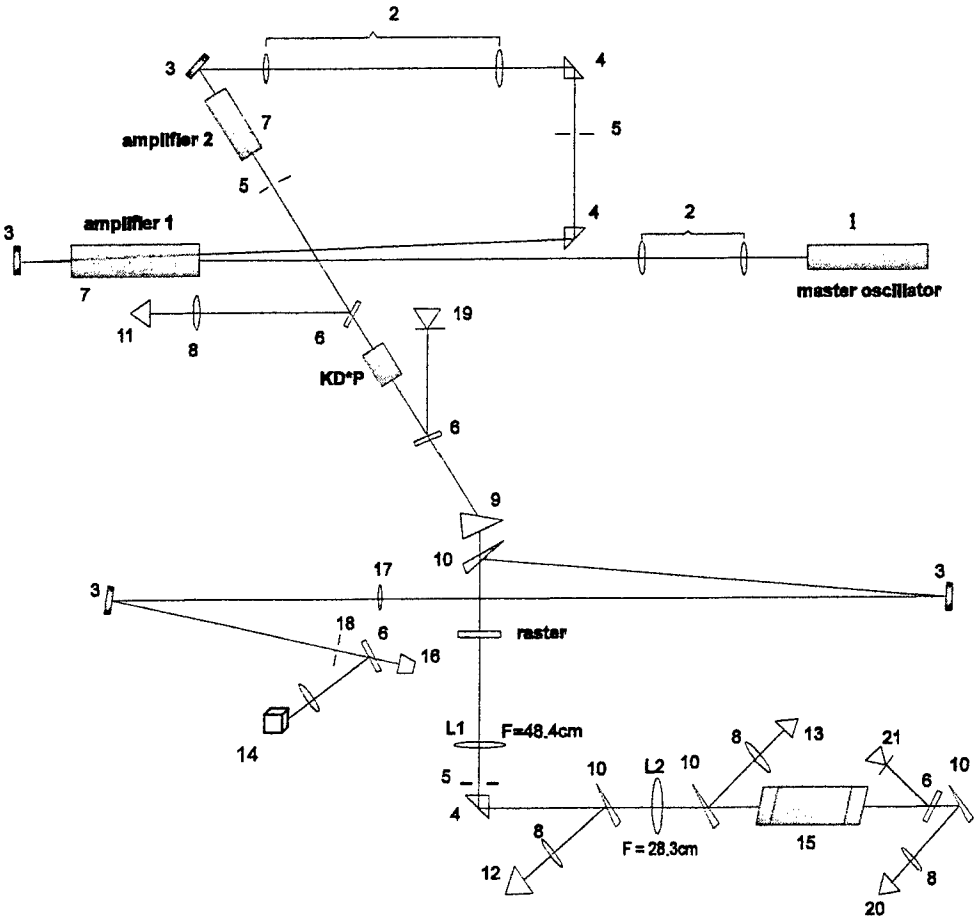


Fig.13. Schematic of the experimental setup:
(1) master oscillator; (2) matching telescopes; (3) dielectric mirrors; (4) turning prisms; (5) pinhole; (6) glass plates; (7) amplifiers; (8) focusing lenses; (9) dispersion prism; (10) glass wedges; (11-13, 20) calorimeters; (14) CCD camera; (15) SBS cell; (16) pyrocalorimeter; (17) measuring lens; (18) measuring diaphragm; (19, 21) coaxial photodetectors (CPDs); (L1 and L2) lenses focusing the pump radiation into the cell.

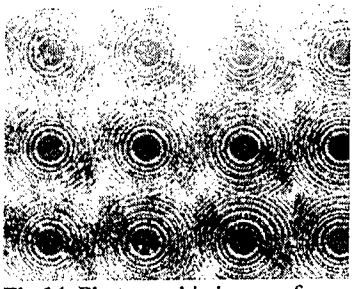


Fig.14. Photographic image of a fragment of the kinoform raster.

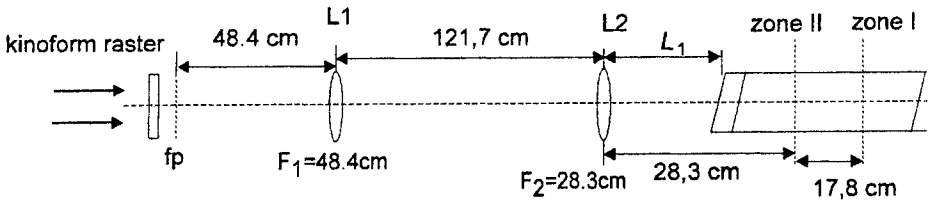


Fig.15. Scheme of focusing of laser radiation into the SBS-cell.

In experiments a version of the focusing scheme shown in Fig.15 is used. In such a scheme all characteristic zones of the laser beam may be located in the cell. According to the beam path these zones are located as follows: the zone II and the zone I. This location of zones is achieved by the following way: after the raster a two-lens-system consisting of lenses L1 and L2 is placed (see Fig.15). The lens foci plane forming the raster is placed at a front focal plane of lens L1. Their image is transferred to the focal plane of lens L2. The zone I is formed at an equivalent focus of the two-lens system and located at a distance of 17.8 cm from the zone II. The beam diameter on the raster is 0.8 cm. By changing distance L_1 between lens L2 and the input window of the SBS cell, it is possible to realize various regimes of exciting SBS. In Fig.16 are shown the distributions of laser energy in zones I and II, which are in good agreement with the results of calculations.[10]

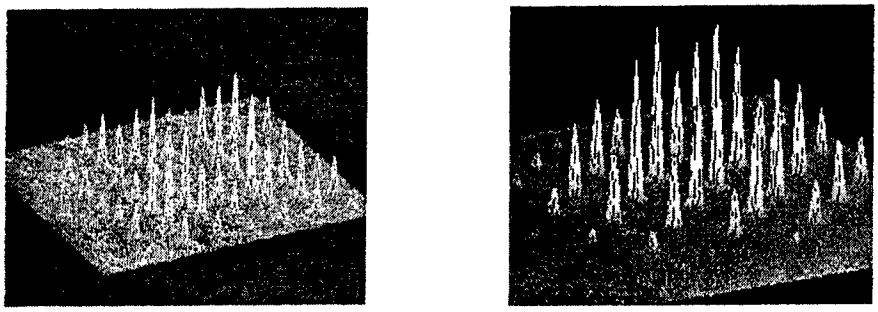


Fig.16. Experimental distributions of laser intensity in zone II (left) and zone I (right).

The process of forming a conjugated Stokes wave in the scheme with the kinoform raster inserted may be represented as consisting of two phases. During the first phase in the zone I independent of each other there occurs generation of Stokes radiation at various orders of diffraction. In the zone of total waist and in the zone II (imaging foci of separate lenses of the raster) there occurs coherentization of radiation of separate beams and prevailing amplification (separation) of the conjugated Stokes component.

In experiments measurements are made of the reflection and selection coefficients and threshold energy of SBS excitation. The reflection coefficient $R=E_S/E_L$ was determined as the ratio of Stokes radiation total energy (E_S) to the laser pump energy (E_L). The laser and Stokes energy are measured by calorimeters 12 and 13, respectively. Selection coefficient (portion of the selected Stokes energy) is measured by pyrodetector 16, located after diaphragm 18 residing at focus of lens 17 and selecting this portion of energy from the scattered Stokes energy. The directivity diagram of Stokes beam reflected out of the SBS cell and passed through the raster in a general case consists of a discrete set of maxima in agreement with the theory prediction. During this the conjugated component of scattered radiation passing through the raster restores its phase front and forms the central maximum transmitted by diaphragm 18.

Two configurations of SBS-mirror have been considered. In the first, the value L_1 equals about 10 cm, i.e. in the SBS-cell the both bright zones are situated in the sequence II+I as in Fig.5(a). In the second, the value L_1 equals about 40 cm, i.e. in the SBS-cell the only zone I is situated so that the region of quazi-lightguide zones is close to input window of SBS-cell (see Fig.5(b)). Experimental dependencies of reflection coefficient R in both configurations of SBS-mirror are shown in Fig.17. They are in full agreement with the results of calculations. Experimental SBS threshold is E_{th}=0.08 J.

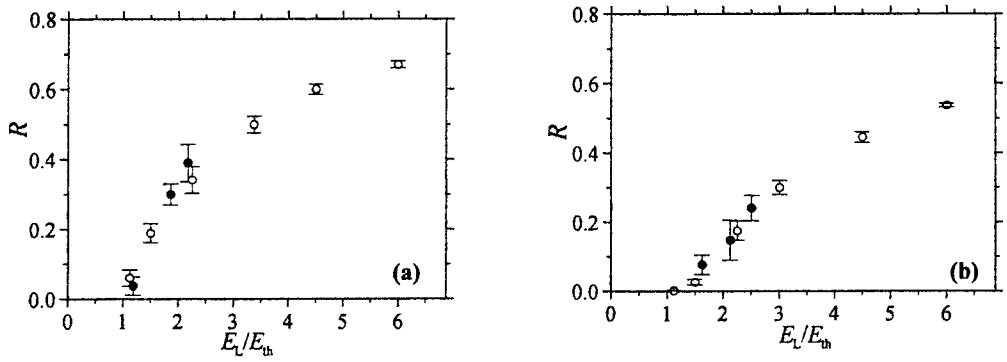


Fig.17. The dependence of the reflection coefficient R in experiment (●) and calculations (O) on the laser energy at the arrangement of the zone II+zone I (a) and the zone I (b) within the SBS-cell. E_{th}=0.08 J.

Fig.18 gives the experimental and numerical dependencies of the time-integrated selection coefficient k_{sel} on the laser energy E_L for two arrangements of the SBS-mirror. In the case when only zone I is put into the SBS-cell, but zone II is out of SBS-cell (see Fig.18(b)), the great spread of selection coefficient ($0.16<k_{sel}<0.49$) takes place with rms deviation 0.035. Its mean value is relatively small (k_{sel}=0.3). Putting into SBS-cell of zone II leads to a significant increase of selection coefficient (k_{sel}=0.7) and to a decrease of spread in its value (Fig.18(a)). The mean value k_{sel} increases up to 0.69, rms deviation of value k_{sel} decreases to 0.025. It is important that results of calculations are in excellent quantitative agreement with the experimental data as regards to the mean value of k_{sel} as well as its spread.

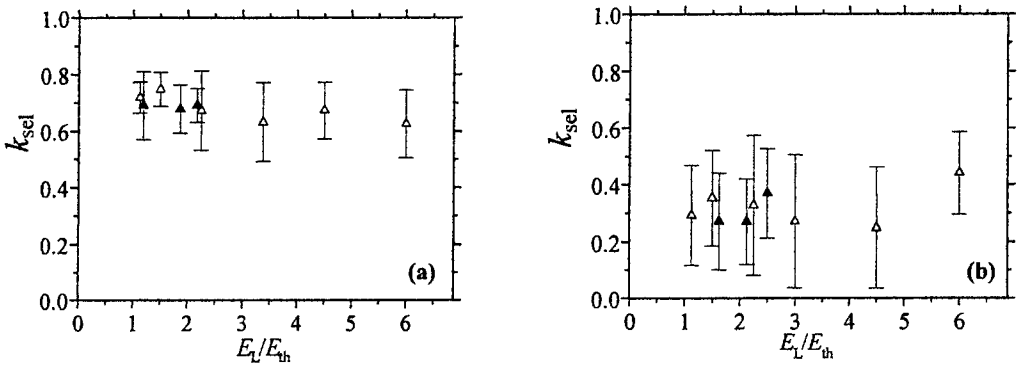


Fig.18. The dependence of the time-integrated selection coefficient k_{sel} in experiment (▲) and calculations (Δ) on the laser energy at the arrangement of the zone II+zone I (a) and the zone I (b) within the SBS-cell.

It is impossible to conduct the comparison of calculations with experiment on parameter h_{sel} in view of impossibility of its direct measurement. There has been conducted the detailed measurement and comparison of laser and Stokes energy distributions in front of the raster, i.e. in near field (see Fig.4). In Fig.19 are shown the experimental dependencies of energy part in the circle of radius r for laser and Stokes beams at both configurations of SBS-mirror. Under processing CCD-camera images the optical axis (r=0) is referred to "center of gravity" of the beam. At each SBS-mirror geometry 5-10 experimental curves are presented for laser and Stokes signals, from which conclusions can be done about the spread of experimental data from flash to flash. Reflection coefficient in these experiments is in the interval from 5 to 38%. The distribution of laser energy weakly fluctuates from flash to flash whereas the distribution of Stokes energy is characterized by greater spread. It is seen that the configuration with zones II and I in the SBS-cell results in narrower distribution of Stokes energy in near field (see Fig.18(a)) that is intrinsic for PC, which is far from the ideal.[10] At SBS-mirror configuration with the only zone I in the SBS-cell, a close agreement of laser and Stokes energy distributions takes place (see Fig.19(b)). It conforms to calculations of PC coefficient, results of which are shown in Fig.20. In Fig.21 we demonstrate the examples of transverse laser and Stokes energy distributions registered by CCD-camera in near field under both SBS-mirror configurations. They illustrate the superhigh PC quality at the SBS-mirror arrangement with the only zone I in the SBS-cell.

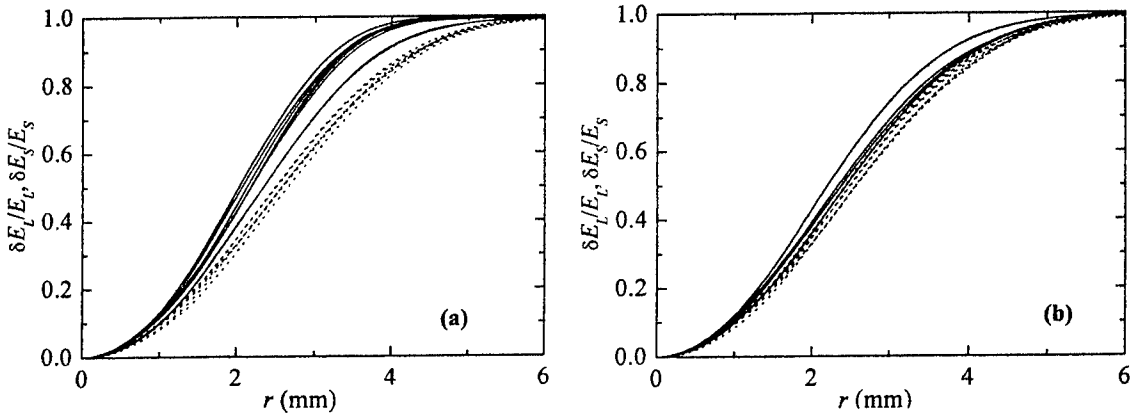


Fig.19. Experimental dependence of energy fraction in the circle of radius r in the near field for laser (dotted curves) and Stokes (solid curves) beam under the configuration "zone II+zone I" (a) and "zone I" (b) in the SBS-cell.

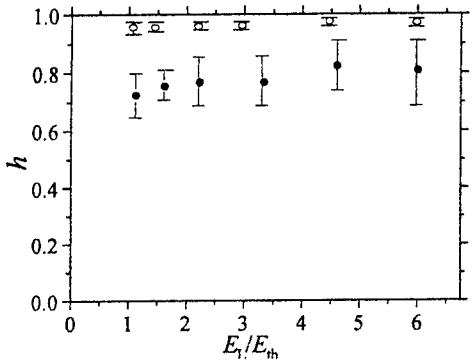


Fig.20. Numerical dependence of the time-integrated PC coefficient after selection h_{sel} on the laser energy at the arrangement of the zone II+zone I (●) and the zone I (O) within the SBS-cell.

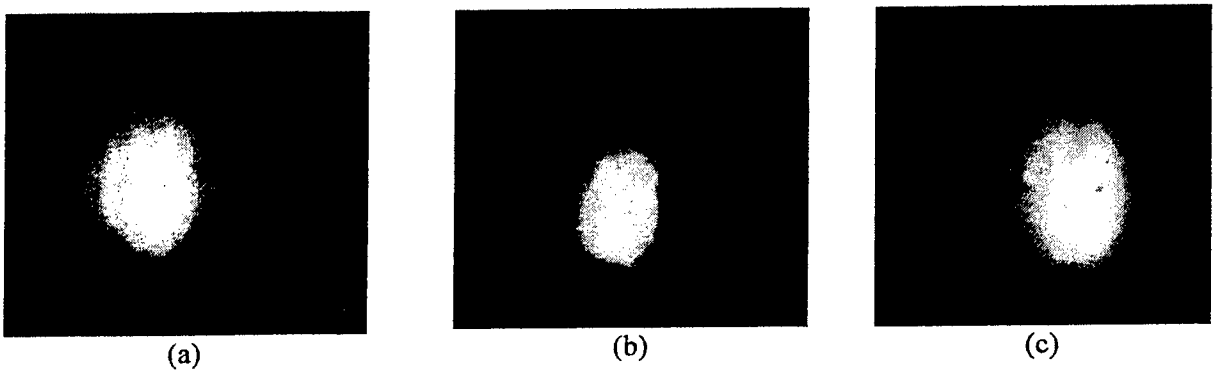


Fig.21 Intensity pattern of laser (a) and Stokes radiation under the configuration "zone II+зона I" (b) and "zone I" (c) in the SBS-cell.

It should be noted that the purity extent of SBS-medium has greatly affected the PC quality. In the experiments that have been conducted under quite identical conditions but using the gas mixture, which has not subjected to special cleaning, the trend of behavior of k_{sel} is radically different from that shown in Fig.18, namely, as zone II begins to be placed into SBS-cell then k_{sel} decreases. The possible cause of this can be an influence of parasitic nonlinear effects dealt with medium heating, which shows itself the more considerable, the more bright zones are within the SBS-cell.

6. CONCLUSIONS

With the help of the most complete in literature physical model and computer code of the non-steady-state SBS, the 3D calculations have been carried out of the PC of a Gaussian beam of the long duration in the simplest SBS-mirror including the focusing lens and the SBS-cell. The dependencies of the reflection coefficient from the SBS-mirror and the PC fidelity on the laser intensity have been obtained. The improvement of PC quality takes place with rising the reflection coefficient. It has been found that the PC quality with the PC coefficient that is more than 90%, i.e. that is near to the ideal, can be obtained at the reflection coefficient that is more than 80%. This is usually intractable in the experiments due to growing the competitive nonlinear processes in the SBS-medium under the high laser powers.

The PC has been studied of the Gaussian focusing laser beam with the pulse duration about 4τ, where τ is the hyper-sound relaxation time, in the SBS-mirror that includes additionally the ordered raster of small lenses and the angular selector of Stokes radiation. The raster allows to perform the effective angular filtration of non-conjugated Stokes component, to reduce the local light loads in the SBS-medium and to avoid the influence of undesirable nonlinear effects. Unlike the random phase plate, in the case of using the raster there are more possibilities to controllably change its characteristics. This allows to expand the spectrum of conditions of focusing the laser beam into the SBS-cell and to determine the most optimal ones. As a result of the calculations, an optimal arrangement of the SBS-mirror has been found with the unique properties. It gives the superhigh PC fidelity with PC coefficient that is more than 90-95% at the selection coefficient 50-70% and any laser power (beginning from the threshold one), i.e. at any reflection coefficient. The experimental data obtained at the Nd laser facility have shown the validity of the simulation results. Measured reflection and selection coefficients and SBS threshold energy are in an excellent agreement with calculations. Measured near-field laser and Stokes energy distribution are very close to each other in the case when calculations give near-to-ideal PC fidelity. The developed conception of SBS-mirror with the unique properties after the complete experimental verification can be applied for the improvement of wide class of industrial lasers.

ACKNOWLEDGEMENT

The present work was financially supported by ISTC within the framework of the project #591-98.

REFERENCES

1. *Optical Phase Conjugation*, R. Fisher, ed., Academic Press, N.Y., 1983.
2. B. Ya. Zel'dovich, N. F. Pilipetskii and V. V. Shkunov, *Principles of Phase Conjugation*, Springer-Verlag, Berlin, 1985.
3. V. I. Bespalov and G. A. Pasmanik, *Nonlinear Optics and Adaptive Laser System*, Nauka, Moscow, 1985.
4. V. V. Ragul'skii, *Wave Front Reversal at Stimulated Scattering of Light*, Nauka, Moscow, 1990.
5. S. T. Bobrov, K. V. Gratsianov, A. F. Kornev et al., "*Investigation* of possibility of phase conjugation fidelity improvement of SBS-mirrors at smooth aberrations", *Optics Spectrosc.* **62**, pp. 402-406, 1987.
6. K. V. Gratsianov, A. F. Kornev, V. V. Lyubimov , V. G. Pankov, "Phasing of laser beams at phase conjugation by SBS", *Optics Spectrosc.* **68**, pp. 617-619, 1990.
7. Yu. V. Dolgopolov, G. A. Kirillov, G. G. Kochemasov et al, "Iodine laser with SBS-mirror" *Proc. SPIE*, **1980**, pp. 23-30, 1992.
8. Yu. V. Dolgopolov, A. M. Dudov, L. I. Zykov, G. A. Kirillov, G. G. Kochemasov, S. M. Kulikov, V. M. Murugov, S. A. Sukharev and A. F. Shkapa, "High power iodine laser with high quality phase conjugation" *Izv. AN USSR ser. fiz.* **58**, pp. 35-40, 1994.
9. H. J. Eichler, B. Liu, M. Duelk, Z. Lu and J. Chen, "Phase conjugation behind an ordered multimode fibre bundle", *Optics Communications* **123**, pp. 412-422, 1996.
10. G.G.Kochemasov and F.A.Starikov, "Novel features of phase conjugation at SBS of beams passed through an ordered phase plate ", *Optics Communications* **170**, pp.161-174, 1999.
11. F.A.Starikov, Yu.V.Dolgopolov, G.G.Kochemasov, S.M.Kulikov, V.K.Ladagin, S.A.Sukharev, "Phase conjugation at SBS of pulse laser radiation with using the kinoform optics", *Proc. SPIE* **3930**, pp. 12-23, 2000.
12. V. P. Kandidov, V. I. Ledenev, "Numerical modeling of random field of dielectric permittivity of turbulent atmosphere", Vestnik MGU, ser. fiz. **23**, 3 (1982); V. K. Ladagin, F. A. Starikov, and V. A. Volkov, "Amplified spontaneous emission at gain saturation: two investigation approaches", in *Advances in Laser Interaction with Matter and Inertial Fusion*, eds. G.Velarde, J.M.Martinez-Val, E.Minguez, J.M.Perlado (World Scientific, London, 1997), pp.546-549.

Powerful Neodymium Lasers with the Self–Phase–Conjugation

Tasoltan T. Basiev [*a], Alexander V. Fedin [**b], Andrey V. Gavrilov [b], Andrey V. Ruliov [b], Sergey N. Smetanin [b], Svetlana A. Kyalbieva [b]

[a] Laser Materials and Technology Research Center of GPI, Moscow, Russia

[b] Kovrov State Technological Academy, Kovrov, Russia

ABSTRACT

The powerful neodymium lasers with the self–phase–conjugation (SPC) and passive Q–swither are submitted. It is shown, that the application of a LiF:F_2^- crystal as Q–swither and SPC–mirror simultaneously, and also a Sagnac interferometer as end reflector of the cavity allows to increase efficiency and quality SPC–radiation. High power and spatial laser characteristics are obtained: Nd:YAG laser – 114 W average power at 0.5 mrad beam divergence; Nd:YAP laser – 51 W average power at 1.2 mrad beam divergence; Nd:Glass laser – 18 J in pulse train at 1 mrad beam divergence.
Keywords: self–phase–conjugation, holographic gratings, adaptive cavity, passive Q–switcher.

1. INTRODUCTION

Low–threshould self–phase–conjugation (SPC) in loop laser cavity based on four wave mixing of intersecting beams in resonant absorber [1–3], and also in active laser medium [4–6] is very interesting and promising field in laser physics. It allows decreasing thermal beam distortions and obtaining single–mode radiation of SPC–lasers under high power flashlamp pumping. However, a big number of such lasers has unsufficiently high power characteristics for its application in material processing. SPC–multiloop Nd:YAG laser system with high power and spatial characteristics was developed earlier and was applied for effective hole drilling.[7] The results have shown that this laser is more acceptable than traditional linear technological lasers.

In the present paper we investigate multiloop laser schemes with different active media Nd:YAG, Nd:YAP and Nd:Glass, what are perspective for application.

2. SINGLE–MODE Nd–CRYSTAL LASERS WITH SELF–PHASE–CONJUGATION

The optical scheme of the laser is presented in Fig. 1. The laser consists of three active rods (1, 2, and 3) by 6.3 mm dia and 100 mm long, passive LiF:F_2^- Q–switcher (4), four 100 % reflective mirrors (5–10), a high selective rear reflector based on a Sagnac interferometer (SI) formed by beam splitter (11) and two 100 % reflective mirrors (12 and 13), and $\lambda/2$ plate (14) inside SI. The optical pumping was realized by DNP–6/90 krypton flashlamps, which were connected to a power supply of 13 GDN type, which done to change the pulse repetition rate from 1 up to 30 Hz. The pump pulse duration was 200 μs.

Laser generation starts from the spontaneous noise amplified in active rods (1–3), reflected by the rear reflector ensuring the initial spatial–angular beam selection. As the generation develops, pairs of the crossed intracavity beams write dynamic holographic gratings inside the active rods, forming reciprocal feedback and a self–adjusted adaptive loop laser cavity On the gratings formed in active rods (AR) and passive Q–switcher (PQS), the radiation field redistribution and the lowest order TEM_{00} mode self–phase–conjugation occur, which improves spectral, spatial and power characteristics of output radiation. The $\lambda/2$ plate provides polarization bypass of the collision waves in the AR and PQS. It results in more favorable redistribution of contributions of various holographic gratings to the laser field forming in the cavity, practically excludes formation of standing waves and prevents spatial hole burning of the inversion.

For high effective passive Q–switching [8] of Nd:YAG laser, we used a LiF:F_2^- crystal with initial transmittance of 58 % and placed it in the beam intersection point. It allows us to realize Q–switching regime with repetitive trains about of equidistant

* Correspondence: Email: basiev@lst.gpi.ru; Telephone: +7(8095)1350267; Fax: +7(8095)1350267
** Correspondence: Email: kasapr@kc.ru; Telephone: +7(809232) 31347; Fax: +7(809232)32533

Laser Optics 2000: Control of Laser Beam Characteristics and Nonlinear Methods for Wavefront Control, Leonid N. Soms, Vladimir E. Sherstobitov, Editors, Proceedings of SPIE Vol. 4353 (2001)
© 2001 SPIE · 0277-786X/01/$15.00

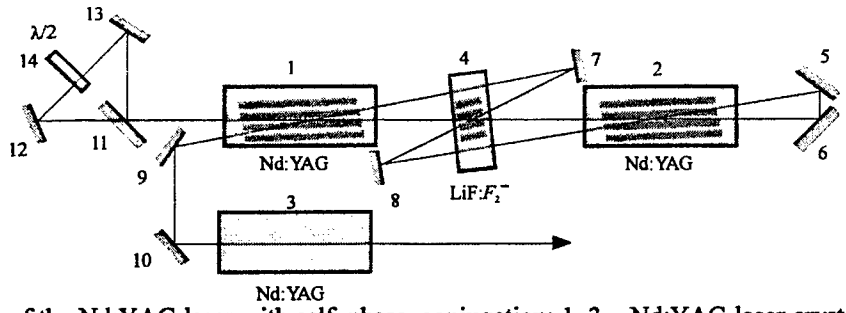


Fig. 1. Optical scheme of the Nd:YAG laser with self–phase–conjugation: 1–3 – Nd:YAG laser crystals; 4 –passive LiF:F_2^- Q–switcher; 5–10 – laser cavity mirrors; 11 – beam splitter; 12, 13 – Sagnac interferometer mirrors; 14 – half–wave plate

giant pulses. The duration of giant pulses, defined by initial PQS transmittance, was 50 ns and within a measurement error didn't depend on the energy of pump pulses. All giant laser pulses recorded with the help of an avalanche photodiode LFD–2A and a high–speed oscilloscope C1–75 had a smooth temporal profile, that testifies to the single–mode character of output radiation [9,10].

Fig. 2 shows output power (a, b) and temporal (c) characteristics of Nd:YAG laser radiation versus total pulse energy at the fixed repetition rate of 30 Hz. As one can see, overall efficiency of generation, the repetition rate of generation pulses in the train, number of pulses in the train, individual pulse energy and its peak power increases with the pump pulse energy growing. At the maximum pump pulse energy of 63.5 J for each pump cavity, the individual output pulse energy and peak power were 345 mJ and 7 MW accordingly; overall efficiency achieved 2 %. An increase of the individual pulse peak power results in saturation level and substraction energy increasing. The maximum output pulse train energy was as high as 3.79 J and the average radiation power attained 114 W.

The output laser beam divergence slightly increased with the increase of pump pulse energy. At the maximum pump pulse energy (63.5 J per each pump cavity), the radiation divergence at e^{-2} level didn't exceed two diffraction limits and was 0.5 mrad (beam quality factor $M^2 = 1.33$). The laser radiation coherence length determined by a Michelson interferometer was more than 15 m (oscillation spectrum width of 0.07 pm). The spatial brightness as high as $8.6 \cdot 10^{13}$ W/(cm^2·sr) was achieved.

At present paper we additionally investigated the similar multiloop Nd:YAP laser schemes with flashlamp pumping by the same power supply unit. The interest to this active medium was caused by its higher gain saturation in comparison with Nd:YAG. Fact that the thermo–physical characteristics of Nd:YAP is poor than that of Nd:YAG, usually result in higher thermo–optical wavefront phase aberrations. It usually complicates realization of the single–mode radiation with large average output power and small beam divergence.

In the beginning, the optical scheme with two Nd:YAP rods (6.3 mm dia and 100 mm long), and 58 % PQS (Fig. 1), without AR 3 and λ/2 plate was investigated. In this case, at the maximum pump energy 63.5 J per flashlamp pump cavity, and

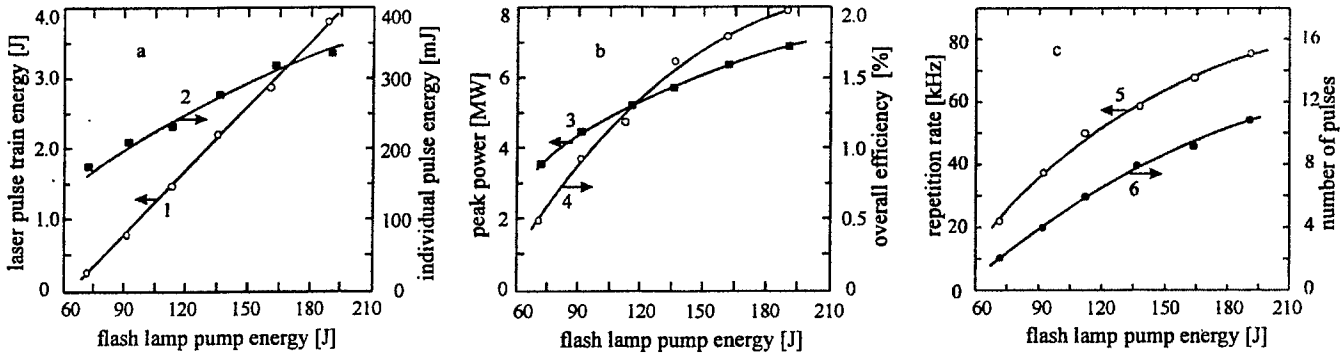


Fig. 2. Output characteristics of investigated Nd:YAG laser radiation versus pump pulse energy on each pump cavity at 30 Hz repetition rate: 1 – free running mode pulse energy; 2 – pulse train energy; 3 – individual pulse peak power; 4 – individual pulse energy; 5 – repetition rate of pulses in the train; 6 – number of pulses in the train

30 Hz repetition rate of pump pulses, the output beam divergence at the e^{-2} level was 1.5 mrad. The total energy of 30 pulses train was 1.6 J. We found out, that to obtain the single–mode radiation with small divergence it is necessary to match the thermolenses and in such a way to form the telescopic system. The best output parameters were received when the single–loop scheme was realized in AR 2 (Fig. 1) and AR 3 was applied as the single–pass amplifier (AR 1 was removed from cavity). At the optimum AR 3 position (distance between two AR was two times higher than focal length of AR thermal lens), the single–mode radiation with 1.2 mrad beam divergence was received. The 1.7 J train of output radiation consists of 14 pulses with an individual pulse energy of 120 mJ and peak power of 2.4 MW. The higher power and spatial characteristics of output radiation, obtained in the latter case, are explained by the best compensation of thermal aberrations in AR, and also more optimum positive feedback in the holographic oscillator.

Thus, investigated multiloop Nd:YAG laser system with dynamic cavity, passive LiF:F_2^- Q–switch and self–phase–conjugation has allowed to receive single–mode laser radiation with high spatial brightness reached 10^{14} W/(cm^2·sr) and radiation divergence close to diffraction limit for output energy 3.79 J in train of 11 pulses with individual pulse energy 345 mJ, peak power 7 MW, average power 114 W and overall efficiency 2 %. In case of Nd:YAP active rods, in view of poor thermo–physical properties of the medium, the beam quality is approximately two times poor than for Nd:YAG, but the power characteristics are also high.

3. SINGLE–MODE Nd:GLASS LASER WITH SELF–PHASE–CONJUGATION

The interest to Nd:Glass lasers is explained by possibility to get a laser pulse energy much more than from lasers on Nd:crystals owing to large volume and high homogeneity of active glass medium. This advantage is successfully used for material processing. However, wider gain width of Nd:Glass than that for Nd:crystals results in essentially multimode character of output radiation.

An application of four-wave mixing for SPC in active Nd:Glass and passive LiF:F_2^- Q-switcher medium allowed to realize a single-mode radiation with spectrum width less than $8\cdot10^{-3}$ cm^{-1} and coherence length more than 0.9 m. The optical scheme of the multiloop Nd:Glass laser based on the laser pump system of type "Kvant–16" is presented in Fig. 3. The laser cavity consists of end 100 % reflective mirror 1, output coupling 53 % reflective mirror 2, and 100 % reflective mirrors 3–5 that form intracavity loops. In crossing points of loops the active element on Nd:Glass of GLS–6 type by size ∅12×260 mm and PQS 7 by size 8×18×65 mm are placed. The PQS has initial transmittance linearly varying from 60 to 90 % along the perpendicular to the crystal optical axis.

In Fig. 4 the power and temporal characteristics of the laser radiation versus PQS initial transmittance at pump pulse energy 1626 J, duration 4 ms and repetition rate 0.1 Hz are shown. Energy meter of IKT-1N type defined the laser power characteristics. The maximum of pulse train energy reaches 2.23 J. Decrease of initial PQS transmittance from 80 to 60 % results in increase of individual pulse energy (curve 2) and peak power (curve 1), and also pulse repetition period in train (curve 4). Thus the complete pulse train energy (curve 3) and duration of each pulse (curve 5) are reduced. Increasing the power characteristics of an individual pulse is explained by growth of radiation losses at the PQS saturation. It results in increase of threshold population inversion of AR that causes increasing the peak power up to 0.5 MW, energy up to 127 mJ, and decreasing the duration of individual pulses down to 250 ns, and also it is accompanied by increase of pulse repetition period in train.

In Fig. 5 the laser output radiation characteristics versus pump pulse energy at the PQS initial transmittance of 60 % are shown. As one can see, the pulse repetition period in train (curve 4), determined by time of achievement of threshold population inversion, is reduced at an increase of pump pulse energy. It results in increasing the number of pulses in train from 2 to 13 (curve 5) and the individual pulse energy (curve 3). At maximum pump pulse energy of 1626 J the radiation

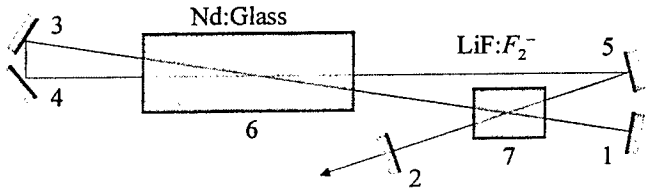


Fig. 3. Optical scheme of the laser: 1 – end mirror; 2 – output coupling mirror; 3–5 – 100 % reflective mirrors; 6 – active Nd:Glass element; 7 – passive LiF:F_2^- Q-switcher

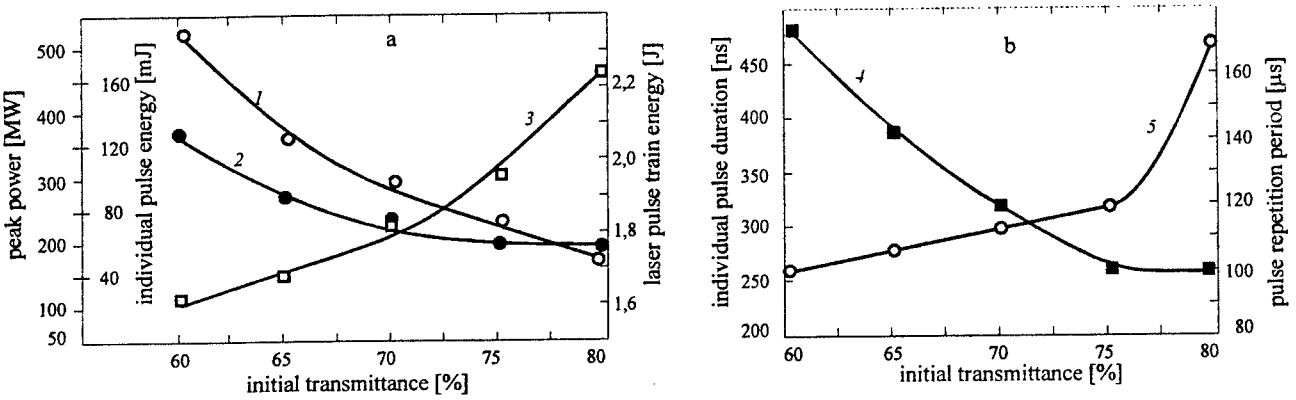


Fig. 4. Power and temporal characteristics of the laser radiation versus initial transmittance of the LiF:F_2^- Q-switcher at pump pulse energy of 1626 J, duration of 4 ms and repetition rate of 0.1 Hz: 1 – individual pulse peak power; 2 – individual pulse energy; 3 – pulse train energy; 4 – individual pulse duration; 5 – pulse repetition period in train

pulse train energy reaches 1,62 J. Peculiarity of the received generation regime as against investigated by us early at continuous [11,12] and repetitively pulsed [13] pumping is the fact that the individual pulse peak power (curve 1) and energy (curve 2) are increased only in narrow interval of changing the pump pulse energy from 810 to 1000 J. This growth can be caused by increasing the TEM_{00} mode volume and efficiency of holographic gratings recorded both inside AR and LiF:F_2^- crystal. At further increase of pump energy from 1000 to 1626 J the power characteristics of an individual pulse are practically constant (peak power of 520 kW and individual pulse energy of 127 mJ) that testifies to maximum use of reserved pump energy and her transformation in output radiation[14] at four-wave mixing in AR medium.

However as one see the generation efficiency was low. The pulse train energy of Q-switched radiation was 1.62 J at pump pulse energy of 1.6 kJ. Thus, in order to achieve maximum energy of basic waves for FWM and maximum pulse train energy of output radiation it was necessary to increase the output coupler reflection from 0.30 to 0.53. In turn, it resulted in amplification of feedback in the static plainly-parallel resonator, which reduced quality of basic waves, and as the consequence, diffraction efficiency of holographic gratings forming the dynamic SPC–cavity, and became the reason of restriction of generation efficiency.

In order to essentially increase the generation efficiency of the holographic Nd:Glass laser we applied a spatial-angular selector based on SI together with additional amplifying pass. The optical scheme of the multiloop Nd:Glass laser is presented in Fig. 6. The laser cavity consists of high selective rear reflector based on SI, 10 % output coupler and five 100 % reflective mirrors, which form the intracavity loops.

Decreasing the output coupler reflection from 0.30 to 0.10 reduced negative influence of the stationary cavity. To increase

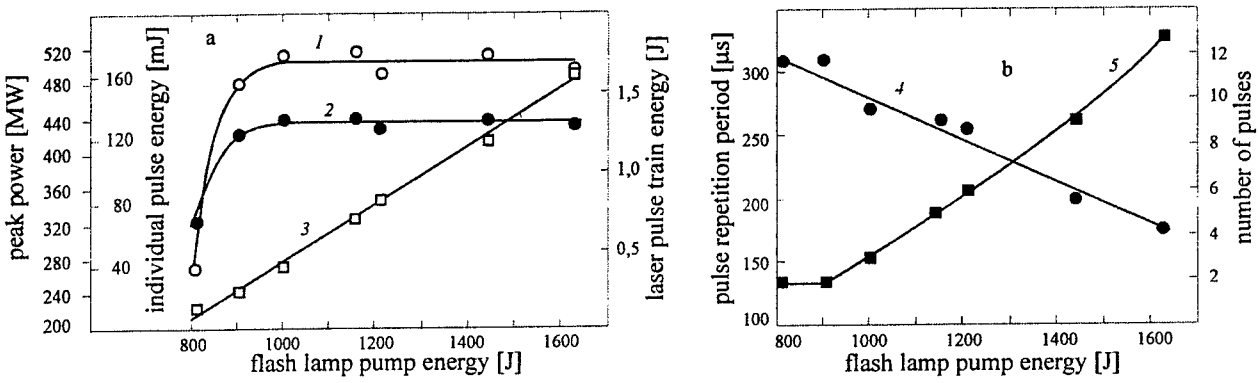


Fig. 5. Power and temporal characteristics of the laser radiation versus pump pulse energy at 60 % initial transmittance of the LiF:F_2^- Q-switcher, pump pulse duration of 4 ms and repetition rate of 0.1 Hz: 1 – individual pulse peak power; 2 – individual pulse energy; 3 – pulse train energy; 4 – pulse repetition period in train; 5 – pulse number in train

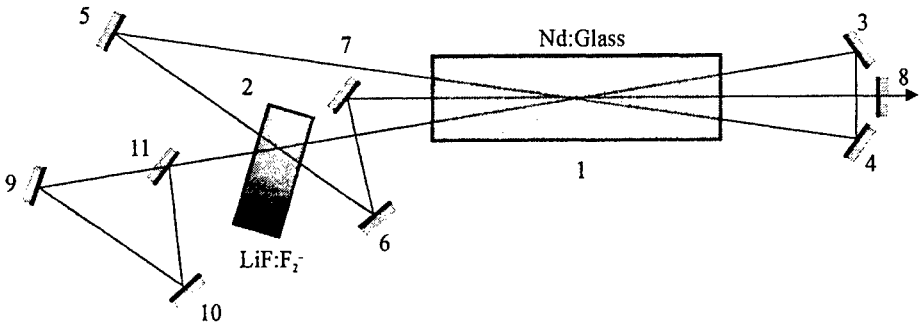


Fig. 6. Optical scheme of the Nd:Glass laser with self–phase–conjugation: 1 – Nd:Glass laser rod; 2 – passive LiF:F_2^- Q–switcher; 3–7 – laser cavity mirrors; 8 – output coupler; 9 and 10 – Sagnac interferometer mirrors; 11 – beam splitter

the positive feedback ensuring generation of conjugated radiation in the loop SPC–cavity, we applied an additional amplification in the same AR 1. Highest power characteristics of the Q-switched radiation were received in a case of using the output coupler with reflection of 0.10. Thus in free-running mode, the energy of laser radiation was 20.5 J at the maximum pump energy of 3.2 kJ. Application of PQS of initial transmittance $T_0 > 90$ % placed in intersection of intracavity beams resulted in failure of generation. The generation renewed at decreasing T_0, when in medium of the LiF:F_2^- crystal the additional SPC–mirror was created at FWM. Thus, an influence of the stationary cavity on generation development becomes minimum, and its mirrors practically participate only in creation of basic waves at FWM.

Power and temporal characteristics of the laser radiation versus PQS initial transmittance in an interval of T_0 from 90 to 60 % at pump pulse energy 3.2 kJ, duration 4 ms and repetition rate 0.1 Hz are shown in Fig. 7. As one sees from the given data, the individual pulse energy (curve 3) and peak power (curve 2) grow approximately in 2 and 6 times accordingly with decreasing initial transmittance of PQS from 80 to 65 %. Namely in this interval of PQS initial transmittance there is maximum pulse train energy of 15.4 J (curve 1). It is possible to explain the received results as follows. Increasing the PQS optical density results in increasing the threshold value of AR population inversion that causes decrease of pulse duration (curve 5) and increase of pulse repetition period in train (curve 4). Thereof the reduction of PQS initial transmittance is accompanied by increasing energy and power of individual pulses. It results in increase of diffraction efficiency of the holographic gratings in AR and PQS, and as a consequence, pulse train energy growth. On the other hand, increasing the PQS optical density causes increasing losses of radiation at PQS saturation and inactive losses in a LiF:F_2^- crystal. It becomes the reason of falling pulse train energy and delaying growth of individual pulse energy and peak power.

In the laser investigated by us earlier (Fig. 3), threshold value of pump energy was about 800 J. Such rather low value of threshold pump energy is caused by high reflection (0.53) of output coupler of the stationary cavity. However, the increase of pump energy resulted in growth of radiation power characteristics only in a narrow interval from 800 to 1000 J. At the further increase of pump energy, only pulse train energy grew due to reduction of time of achievement of threshold population inversion and growth of number of pulses in train. An individual pulse energy and peak power remained constant.

In the laser scheme of Fig. 6, threshold value of pump energy appeared almost twice more, but the domination of the dynamic SPC-cavity above stationary cavity allowed us to receive higher power characteristics of radiation in comparison with laser (Fig. 3). In Fig. 8, the dependences of the laser radiation characteristics on energy of pump pulses are shown at PQS initial transmittance of 60 % and output coupler reflection of 0.1. As one can see, the pulse repetition period in train (curve 4), determined by time of achievement of threshold population inversion is reduced at increase of pump pulse energy. It results in increasing the number of pulses in train from 2 to 35 (curve 5), growing the individual pulse energy (curve 3) and peak power (curve 2), and also increasing the train energy (curve 1). An application of PQS with initial transmittance of 60 % allows getting laser pulses with maximum energy (more than 370 mJ) and peak power (more than 1.35 MW) at pump pulse of 3.2 kJ. And an absence of saturation in the dependence of radiation power characteristics (train energy, individual pulse energy and peak power) on pump pulse energy specifies an opportunity of their further growth with increase of pump pulse energy. Growth of the laser power characteristics can be caused by increase of volume of fundamental mode in AR, length and diffraction efficiency of holographic gratings, which are written both in AR and PQS media.

Really, the application of SI as an end reflector allows to carry out soft full-aperture spatial-angular selection of radiation [15] and to create basic waves with front close to flat.[16] It enables to avoid essential narrowing of the conjugated wave in

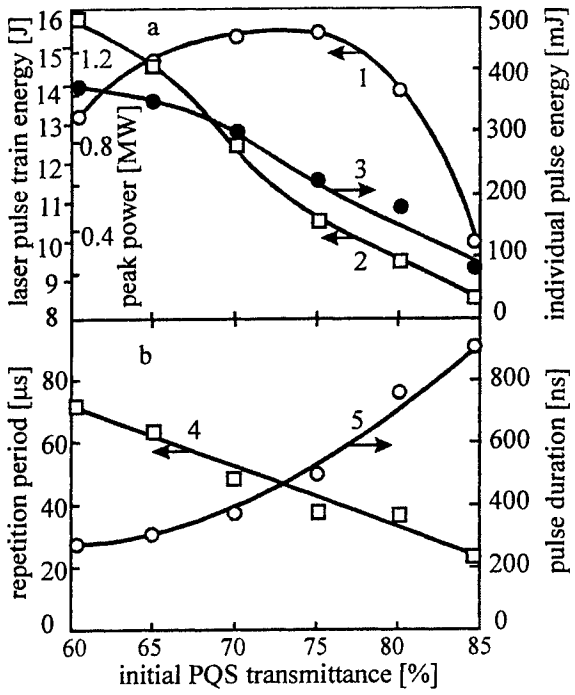


Fig. 7. Output characteristics of investigated Nd:Glass laser radiation versus PQS initial transmittance at 3.2 kJ pump energy:
1 – pulse train energy; 2 – individual pulse peak power; 3 – individual pulse energy; 4 – pulse repetition period in the train of pulses; 5 - individual pulse duration.

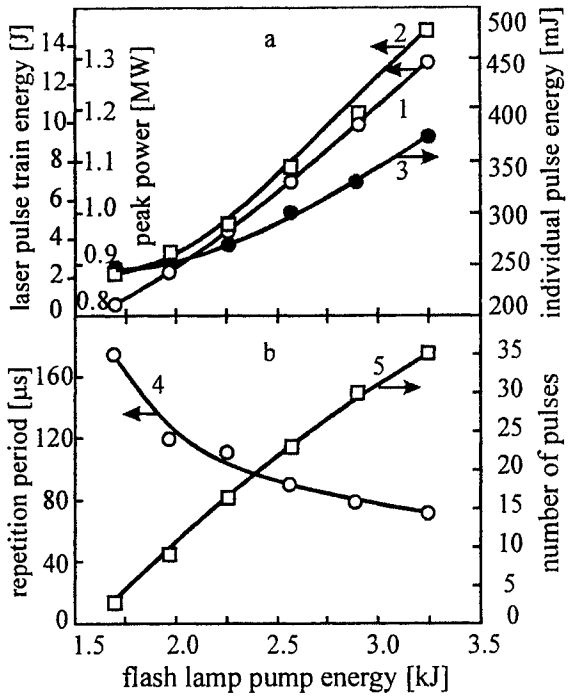


Fig. 8. Output characteristics of investigated Nd:Glass laser radiation versus pump pulse energy at 60 % LiF:F_2^- crystal initial transmittance:
1 – pulse train energy; 2 – individual pulse peak power; 3 –individual pulse energy; 4 – repetition period of pulses in the train; 5 – number of pulses in the train.

comparison with signal wave, and also her phase distortions[17]. As result, the maximal diameter d_{out} of output beam achieves 9 mm, that is $d_{out} = 0.75 \cdot d_{AR}$. It almost twice is more than at the laser (Fig. 3), where $d_{out} = 0.42 \cdot d_{AR} = 5$ mm. It is necessary to note that for gauss beams $d_{out} \approx 0.58 \cdot d_{AR} \approx 7$ mm.[17] Hence, an application of a SI end reflector allows raising uniformity of basic waves in the field of localization in AR and PQS media, so also quality of SPC.

The output beam divergence, determined in focus of a lens with a focal length of 1 m at the maximum pump pulse energy, did not exceed 0.8 mrad at e^{-2} level, which corresponds to quality factor $M^2 = 5.3$. The spatial brightness of a Q-switched pulse achieved $1.1 \cdot 10^{14}$ W/cm^2·sr. The laser radiation coherence length determined by a Michelson interferometer was 5.2 m, and oscillation spectrum width determined with the a help of Fabry-Perot interferometer did not exceed $6 \cdot 10^{-3}$ cm^{-1}. Thus, due to spatial-angular selection and additional amplification the investigated Nd:Glass laser with dynamic loop cavity has shown efficiency of generation much more than laser, in which alongside with a reciprocal feedback on holographic gratings the strong enough feedback of the static resonator is used. An application of a LiF:F_2^- crystal as both passive Q-switcher and self-phase-conjugated mirror has allowed to lower diffraction losses of laser radiation, to raise self-compensation of phase distortions of wavefront and spectral selectivity of the dynamic resonator. It has enabled to increase in 4-5 times the laser generation efficiency, and also to raise the radiation spatial and power characteristics in 5-10 times at optimum transmittance of a LiF:F_2^- crystal.

5. CONCLUSION

The realization of SPC in Nd:Glass, Nd:YAG, Nd:YAP, and LiF:F_2^- crystals has allowed to receive a laser radiation with high power and spatial characteristics. Such laser systems have a rather simple design. It considerably expands possibilities of technological solid–state lasers with loop dynamic cavity and passive LiF:F_2^- Q–switching.

ACKNOWLEDGEMENTS

This research was supported in part by the Science for Peace Programme (Grant SfP-974143).

REFERENCES

1. T.T. Basiev, Yu.N. Voron'ko, P.G. Zverev, S.B. Mirov, and A.M. Prochorov, "Four–wave mixing in LiF crystals with F_2, F_2^+, F_2^- colour centers," *Letters in JTP*, **8**, pp. 1532–1535, 1982.
2. T.T. Basiev, P.G. Zverev, S.B. Mirov, and S. Pack, "Phase conjugation in LiF and NaF crystals with colour centers," *II konf. "Phase conjugation of laser beam in nonlinear medium"*, Minsk, USSR, pp. 21–26, 1990.
3. T. Zhang, L. Wan, and Y. Ruan, "Nonlinear optical phase conjugate effect caused by F_2^- colour centers in LiF crystals," *Chines Phys.Lett.* **2**, pp.369–372, 1985.
4. A. Tomita, "Phase conjugation using gain saturation of a Nd:YAG laser," *Appl. Phys. Lett.* **34**, pp. 463–464, 1979.
5. I.M. Bel'dyugin, V.A. Berenberg, A.V. Vasil'ev, I.V. Mochalov, V.M. Petnikova, G.T. Petrovskii, M.A. Harchenko, and V.V. Shuvaliv, "Solid–state lasers with self–pumped phase–conjugate mirrors in active medium," *Sov J. Quantum Electron.*, **16**, pp. 1142–1145, 1989.
6. R.P.M. Green, D. Udaiyan, G.J. Crofts, D.H. Kim, and M.J. Damzen, "Holographic laser oscillator which adaptively corrects for polarization and phase distortions," *Physical Review Letters*, 77, pp. 3533–3536, 1996.
7. A.V. Fedin, T.T. Basiev, A.V. Gavrilov, and S.N. Smetanin, "Single–mode Nd:YAG laser with self–phase–conjugation and its application," *Izvestia A N. Seria fizicheskaya (Russian)*, **63**, pp. 1909–1913, 1999.
8. A.V. Fedin, T.T. Basiev, A.V. Gavrilov, O.L. Antipov, A.S. Kuzhelev, and S.N. Smetanin, "Single–mode Nd:YAG laser with cavity formed by population gratings," *Proceedings of SPIE*, **3684**, pp. 59–63, 1999.
9. T.T. Basiev, A.N. Kravets, S.V. Mirov, A.V. Fedin, and V.A. Konjushkin, "Technological Nd:YAG laser Q–switching by LiF:F_2^- crystals," *Sov. J. Quantum Electron.*, **18** (2), pp. 223–224, 1991.
10. V.V. Grabovskii, V.I. Prokhorenko, and D.Ya. Yatskiv, "Characteristics of single–frequency emission from a laser with a cavity based on a Sagnac interferometer," *Sov J. Quantum Electron.*, **22**, pp. 361–364, 1995.
11. T.T. Basiev, A.N. Kravets, S.V. Mirov, A.V. Fedin, "Technological Nd:YAG laser with the passive Q–switching on a LiF:F_2^- crystal," *Letters in JTP* **17** (9), pp. 16–22, 1991.
12. T.T. Basiev, A.N. Kravets, S.V. Mirov, A.V. Fedin, "Three-cascade amplifier of the single-mode radiation of Nd:YAG laser with the passive Q–switcher on a LiF:F_2^- crystal," *Sov. J. Quantum Electron.*, **18** (7), pp. 822–824, 1991.
13. T.T. Basiev, A.N. Kravets, S.V. Mirov, A.V. Fedin, "Passive Q–switching of a technological Nd:YAG laser by LiF:F_2^- crystal," *Sov. J. Quantum Electron.*, **20** (6), pp. 594–596, 1993.
14. S.G. Odulov, M.S. Soskin, A.I. Hijniak, *Lasers on a dynamic gratings,* 272 p., Nauka, Moscow, 1990.
15. A.V. Fedin, T.T. Basiev, A.V. Gavrilov, et all., "Passive Q–switching of a self–pumped phase–conjugate Nd:YAG loop resonator," *Laser Physics*, 9 (2), pp. 433–436, 1999.
16. A.N. Kravets, I.N. Kompanets, A.V. Fedin, Patent of Russia 331451, 1991.
17. B.Ya. Zeldovitch, N.F. Pilipetsky, V.V. Shkunov, *Wave front conjugation*, Nauka, Moscow, 1985.

Role of resonant refractive-index grating in a nonreciprocal Nd:YAG self-pumped phase conjugator

O.L. Antipov[+], D.V. Chausov, V.V. Yarovoy
Institute of Applied Physics of the Russian Academy of Science, 46 Uljanov St., Nizhny Novgorod, 603600 Russia, Tel.: +7(8312)384547; Fax: +7(8312)363792;
[+] e-mail: antipov@appl.sci-nnov.ru

ABSTRACT

We have studied both experimentally and numerically the role of resonant refractive index gratings in a self-pumped phase conjugate mirror based on an Nd:YAG amplifier with nonreciprocal feedback loop. In experiment the generation of the phase-conjugating laser was delayed with respect to recording of a holographic nonlinear mirror by an external beam. An increase in the phase-conjugate reflectivity at a delay time of about 3 μs was measured. The numerical calculation confirmed the additional contribution of the resonant refractive-index grating, which is formed in the pumped Nd:YAG crystal due to excitation of a higher-lying level of Nd^{3+} ions, to efficiency of phase conjugation.

Key words: phase conjugation, holographic gratings of refractive index and gain, Nd:YAG laser oscillator, cavity with nonlinear dynamic mirrors

1. INTRODUCTION

The main idea of the paper is to study the influence of resonant refractive index gratings (RIG's) on generation conditions in a laser with a holographic mirror induced by an external optical pulse. It was shown that this holographic laser can provide phase conjugation (PC) of the optical signal writing the holographic mirror [1-3]. As it was supposed, this laser operates due to gain gratings (GG's) which accompany population gratings (PG's) induced by incident optical beams in the Nd:YAG amplifier. Positive feedback for this PC oscillator is realized due to π-phase nonreciprocity of the cavity.

An alternative approach to realization of the self-pumped PC in the amplifying laser crystal is mutual scattering of two intersecting optical beams, an incident wave and a wave passed through feedback loop [4,5]. As it was shown, oscillation of the PC wave in this scheme can be realized by two kinds of gratings, the GG and the RIG. The latter gratings play a key role in the reciprocal loop scheme [5].

Previous investigations have shown that the PG's in Nd:YAG amplifiers are accompanied not only by GG's but also by RIG's [6,7]. This RIG formation is caused by the difference in polarizability of excited and unexcited Nd^{3+} ions under flash-lamp pumping and can be explained by population and depopulation of the higher lying level $^2(F2)_{5/2}$. The diffraction efficiency of the RIG was found to be higher than that of the GG. The characteristic time of the RIG formation was measured to be about 3 μs. It means that the RIG follows the PG with a delay time of 3 μs, and after this delay it is possible to expect an increase in the reflection coefficient of the nonlinear mirror.

The aim of our investigation is to verify the role of RIG's in the nonreciprocal PC laser oscillator (with cavity formed by an external signal). Measurements of the PC-pulse energy as a function of the delay time of the laser cavity switch with respect to the PG formation by an external optical signal were performed in combination with numerical calculations of an oscillator model.

2. EXPERIMENTS

A linearly polarized optical beam (TEM_{00} single-longitudinal mode) from a Nd:YAG master oscillator was launched to a phase conjugator (PC) (Fig. 1). Duration of the Q-switched pulse of the beam was 30 ns. The

Laser Optics 2000: Control of Laser Beam Characteristics and Nonlinear Methods for Wavefront Control, Leonid N. Soms, Vladimir E. Sherstobitov, Editors, Proceedings of SPIE Vol. 4353 (2001)
© 2001 SPIE · 0277-786X/01/$15.00

incident wave (E_1) propagated in the scheme and transformed into a wave E_3 inside the Nd:YAG amplifier. The interference field of the waves E_1 and E_3 induced a PG in the laser amplifier.

The PC scheme comprised an additional polarization device which included two cross-polarized Glan prisms (3 and 5) and an electro-optical Pockels cell (4). This device played two roles. It decreased the signal wave to prevent saturation of amplifiers 6 which had large gain (of about 10^4) and to provide equal intensities of the intersecting writing waves E_1 and E_3 in order to maximize the induction of PG. The second function of the polarization device was to control Q switch of the cavity. The switch-on time (due to switch-on of the Pockels cell) was synchronized with an external signal pulse with a delay time τ, which was varied from several tens of nanosecond to several hundreds of microseconds. This delay provides for the formation of the RIG which accompanies the PG with a delay of 3 μs [6,7]. An optical diode 7 (based on a Faraday rotator and two crossed polarizers) provided one-way generation by suppressing a backward-propagating wave of another-way generation.

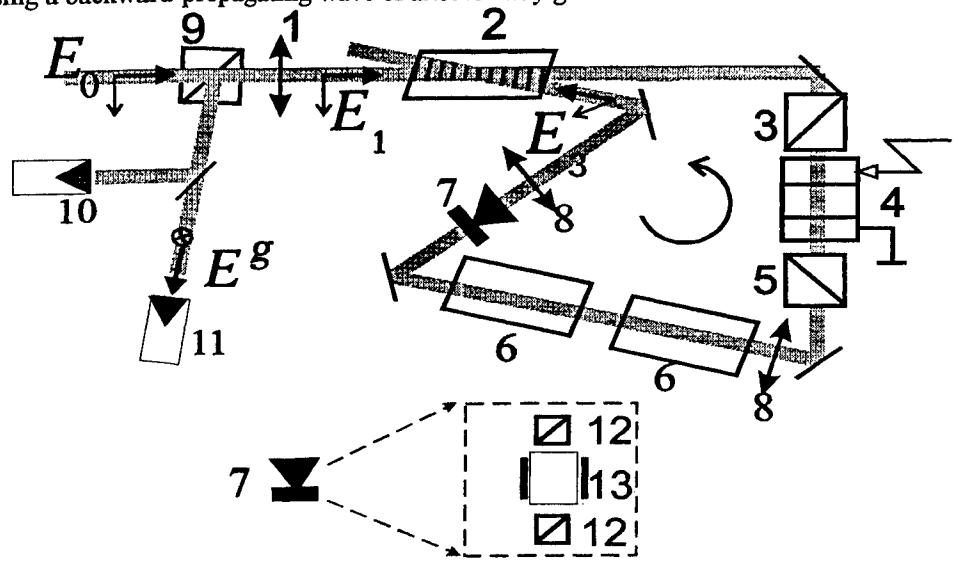


Fig. 1. A schematic of the loop holographic laser: 1,8 – lenses ; 2 – holographic amplifier; 3,5,9,12 – Glan polarizers; 4 – electro-optical Pockels cell; 6 – Nd:YAG amplifier; 7 – Faraday rotator; 10,11 – energy meters; 13 – 45^0 Faraday rotator on permanent magnet.

The small-signal gain of the holographic amplifier 2 was 60-70 and the pump-pulse duration was about 600 μs. This temporal regime ensured the stability of the amplifier gain within the delay time (from the writing signal to the generated pulse).

The energy of the generated pulse was measured in experiment as a function of the delay. The measurement showed an increase in the output beam energy with increasing delay time (up to several microsecond) (Fig. 2). The highest rise in the generated energy was observed at the delay time from 1.5 μs ($W_g(\tau = 1.5) \sim 11\,\text{mJ}$) to 6 μs ($W_g(\tau = 6) \sim 14\,\text{mJ}$). The generated-pulse energy decreased after a delay of 40-50 μs due to relaxation of the population inversion.

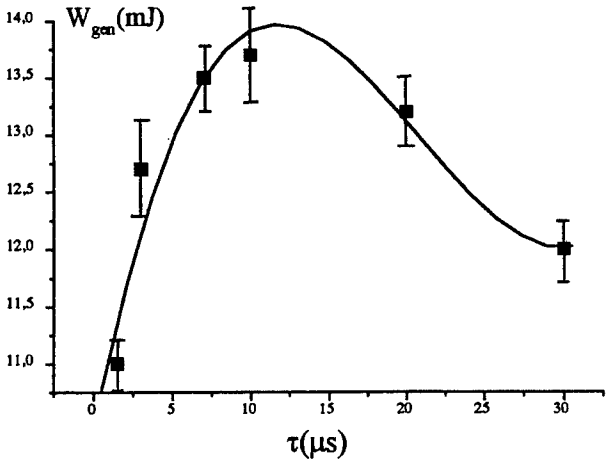


Fig. 2. The energy of the generated beam (W_g) vs delay time of the optical device (Pockels-cell) opening (τ).

To prevent the influence of pump instability (of about 5%), the measurement of $W_g(\tau)$ was averaged over 100 pump pulses. The measured increase of the PC reflection coefficient was found to be about 30-40%. So, the result of the experiments was independent of any technical instabilities and fluctuations.

Thus the experiments confirmed that generated pulse energy increases with increasing delay time. The characteristic time (3-10 μs) was comparable with the time of RIG formation.

3. NUMERICAL CALCULATIONS

For numerical calculations we used a schematic of the PC system shown in Fig. 3.

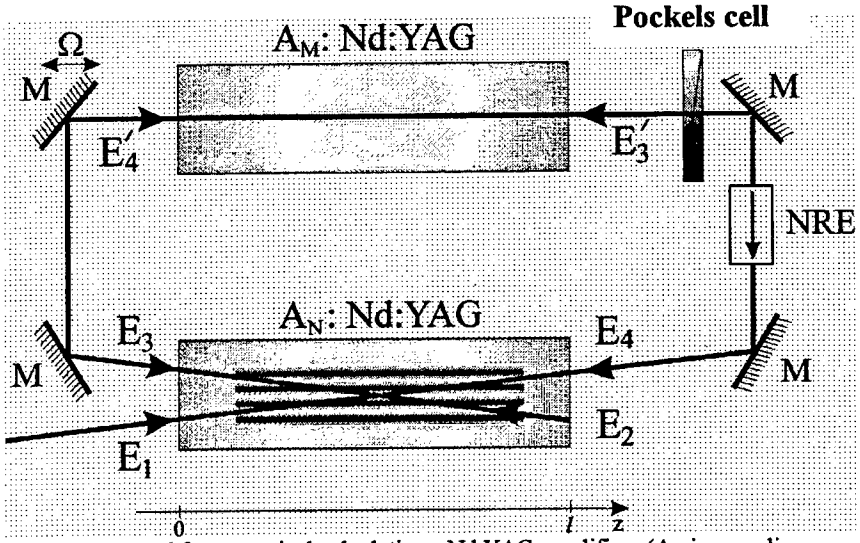


Fig. 3. The scheme used for numerical calculations: Nd:YAG amplifiers (A_N is a nonlinear amplifier; A_M is an additional intracavity amplifier); NRE is a nonreciprocal transmitting element; M are mirrors; E_1-E_4 are optical waves

3.1. Set of equations

To describe the system we used approximations of plane and monochromatic optical waves.

For the **first time interval** when **the incident beams write the population grating** (0<t<30ns) the set of equations for the writing-wave amplitudes E_1 and E_3 was as follows

A set of equations for amplifier A_N:

$$\mu\frac{\partial E_1}{\partial t}+\frac{\partial E_1}{\partial z}=(\sigma_1 N_0+i\beta_2\sigma_0 N_0^{'})E_1+(\sigma_1 N_{13}+i\beta_2\sigma_0 N_{13}^{'})E_3$$
$$\mu\frac{\partial E_3}{\partial t}+\frac{\partial E_3}{\partial z}=(\sigma_1 N_0+i\beta_2\sigma_0 N_0^{'})E_3+(\sigma_1 N_{13}^{*}+i\beta_2\sigma_0 N_{13}^{'*})E_1 \quad , \qquad (1.1)$$

$$\frac{\partial N_0}{\partial t}+N_0=-N_0(|E_1|^2+|E_3|^2),\frac{\partial N_{13}}{\partial t}+N_{13}=-N_0E_1E_3^{*}-N_{13}(|E_1|^2+|E_3|^2)$$
$$\frac{\partial N_0^{'}}{\partial t}+\frac{N_0^{'}}{T_2}=\frac{N_0}{T_2},\frac{\partial N_{13}^{'}}{\partial t}+\frac{N_{13}^{'}}{T_2}=\frac{N_{13}}{T_2} \quad , \qquad (1.2)$$

where $E_1 - E_4$ are the complex amplitudes of the optical waves normalized to the saturation amplitude ($\sqrt{I_S}$, I_S is the saturation intensity, $\sigma_1 = \sigma_0\cdot(1+i\beta_1)$, $\sigma_1 = \sigma_0\cdot(1+i\beta_1)$, σ_0 is the cross-section of the resonant transition ($\sigma_0 = 2$), β_1=0.15, β_2=2.5, z-coordinate is normalized to the total length of Nd:YAG crystal (l=10cm), N_0 and N_{ij} are the average-in-space population and the gratings of population of the $^4F_{3/2}$ level, respectively, for the A_N-amplifier; $N_0^{'}$ and $N_{ij}^{'}$ are the average-in-space population and the gratings of population of the $^2F(2)_{5/2}$ level, respectively (see Fig. 4); T_2=0.014 is the longitudinal relaxation time of the $^2F(2)_{5/2}$ level, which is normalized to the relaxation time of the working transition (T_1).

The changes in population of the $^2F(2)_{5/2}$ and $^4F_{3/2}$ levels determined the resonant changes of the refractive index of the Nd:YAG crystals, which can be described by the following expression: $\Delta n^e(\nu)=\frac{2\pi F_L^{\,2}}{n_0}(N\cdot\Delta p_n+N^{'}\cdot\Delta p_h)$, where $F_L=(n^2+2)/3$ is the factor of a local field (Lorentz factor), n_0 is the linear index of refraction, Δp_n and Δp_h are the polarizability difference of the active Nd^{3+} ions in the ground state ($^4I_{9/2}$) and in the excited $^4F_{3/2}$ and $^2F(2)_{5/2}$ levels, respectively.

The existence of the RIG and GG was assumed for description of the nonlinear amplifier (A_N). The complex cross-section σ_1 and the parameter β_2 indicate the RIG and GG which accompany the PG of the metastable level of the working transition ($^4F_{3/2}$) and the higher-lying level ($^2(F2)_{5/2}$) of the 4f-electron shell of the Nd^{3+} ions in the laser crystal Nd:YAG.

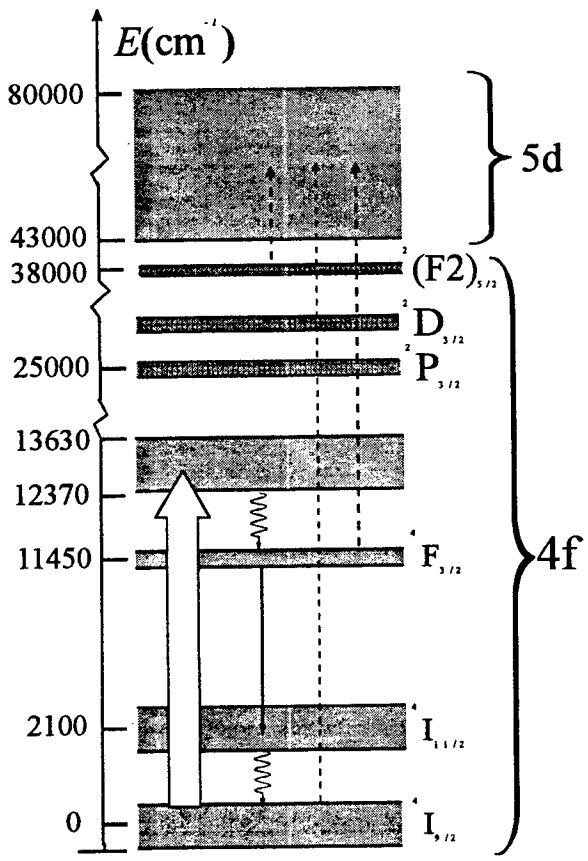


Fig. 4. Diagram of energy levels of Nd^{3+} -ion in a Nd:YAG crystal (white arrow indicates the pump-induced transitions, black arrow indicates the working laser transition, dashed arrow indicates the virtual transitions determining the polarizability of metastable levels, and sinuous arrows indicate non-radiative transitions).

A set of equations for amplifier A_M:

$$\mu\frac{\partial E_3'}{\partial t}+\frac{\partial E_3'}{\partial t}=(\sigma_1^M M_0+i\beta_2\sigma_0^M M_0')E_3',$$

$$\frac{\partial M_0}{\partial t}+M_0=-M_0(|E_3'|^2),\frac{\partial M_0'}{\partial t}+\frac{M_0'}{T_2}=\frac{M_0}{T_2}, \qquad (1.3)$$

where $\sigma_1^M=\sigma_0^M(1+i\beta_1)$, σ_0^M is the cross section of the resonant transition of the "M"-amplifier, M_0 and M_0' are the average-in-space populations of the $^4F_{3/2}$ and $^2(F2)_{5/2}$ levels in the "M"-amplifier.

The zero initial conditions for the optical waves was used for this stage of the process

$$E_1(z,\ t=0)=E_2(z,\ t=0)=E_3(z,\ t=0)=E_4(z,\ t=0)=0. \qquad (1.4)$$

The initial condition of the populations in the laser amplifier assumed the previous pumping

$$N_0(z,\ t=0)=N_0'(z,\ t=0)=M_0(z,\ t=0)=M_0'(z,\ t=0)=1,$$
$$N_{13}(z,\ t=0)=N_{13}'(z,\ t=0)=0, \qquad (1.5)$$

The boundary conditions assumed the existence of the input optical pulse, the transmission of the pulse through the scheme, the loop phase nonreciprocity ($\varphi(A_N)$ and $\varphi(A_M)$) and frequency detuning of the writing and generated pulses

$$E_1(0,t)=E_{10}\cdot\exp(-\frac{(t-t_0)^2}{t_0^2});\ t<30ns;\ \ t_0=20ns$$

$$E_2(l,t)=0, E_3(0,t)=|E_1(0,t)|\cdot e^{ik_0L+i\varphi(A_N)+i\varphi(A_M)},$$
$$E_4'(0,t)=E_2(0,t)\cdot e^{i\Omega t}, E_4(l,t)=E_4'(0,t)\cdot e^{ik_0L}\cdot K(A_M), E_4(l,t)=E_4'(l,t) \quad (1.6)$$

During **the second time interval** (30 ns < t < τ), when the writing beams were absent and the Pockels cell closed, the population grating relaxed. The set of equations for the amplifiers was as follows

$$\frac{\partial N_0}{\partial t}+N_0=0 \qquad \frac{\partial N_0'}{\partial t}+\frac{N_0'}{T_2}=0 \qquad \frac{\partial M_0}{\partial t}+M_0=0$$
$$\frac{\partial N_{13}}{\partial t}+N_{13}=0 \qquad \frac{\partial N_{13}'}{\partial t}+\frac{N_{13}'}{T_2}=0 \qquad \frac{\partial M_0'}{\partial t}+\frac{M_0'}{T_2}=0 \quad (1.7)$$

During **the third time interval** (t > τ), when the optical device (Pockels cell) is open; the generation starts. The set of equations for this stage was as follows.

A set of equations for amplifier A_N was as follows

$$\mu\frac{\partial E_2}{\partial t}-\frac{\partial E_2}{\partial z}=(\sigma_1N_0+i\beta_2\sigma_0N_0')(E_2+E_{noise})+(\sigma_1N_{13}+i\beta_2\sigma_0N_{13}')E_4$$
$$\mu\frac{\partial E_4}{\partial t}-\frac{\partial E_4}{\partial z}=(\sigma_1N_0+i\beta_2\sigma_0N_0')E_4+(\sigma_1N_{13}^*+i\beta_2\sigma_0N_{13}'^*)E_2 \quad (1.8)$$
$$\frac{\partial N_0}{\partial t}+N_0=-N_0(|E_2|^2+|E_4|^2), \frac{\partial N_{13}}{\partial t}+N_{13}=-N_0E_2E_4^*-N_{13}(|E_2|^2+|E_4|^2)$$
$$\frac{\partial N_0'}{\partial t}+\frac{N_0'}{T_2}=\frac{N_0}{T_2}, \frac{\partial N_{13}'}{\partial t}+\frac{N_{13}'}{T_2}=\frac{N_{13}}{T_2} \quad (1.9)$$

A set of equations for amplifier A_M was as follows

$$\mu\frac{\partial E_4'}{\partial t}+\frac{\partial E_4'}{\partial t}=(\sigma_1^MM_0+i\beta_2\sigma_0^MM_0')\cdot E_4'$$
$$\frac{\partial M_0}{\partial t}+M_0=-M_0(|E_4'|^2), \frac{\partial M_0'}{\partial t}+\frac{M_0'}{T_2}=\frac{M_0}{T_2}. \quad (1.10)$$

where E'_{noise} is the spatio-temporal random noise source.

3.2. Results of numerical calculations

Set of Eqs. (1.1)-(1.10) was numerically calculated for the parameter which corresponded to experimental conditions. Generation of the optical pulses was calculated. The generated pulse duration and the generation pulse delay (with respect to the Pockels switch-on-time) were calculated to decrease with an increase in the delay time between grating formation and opening of the Pockels cell (Fig. 5). The noised oscillations on the curves indicated the presence of a random source of the optical wave in Eq. (1.8).

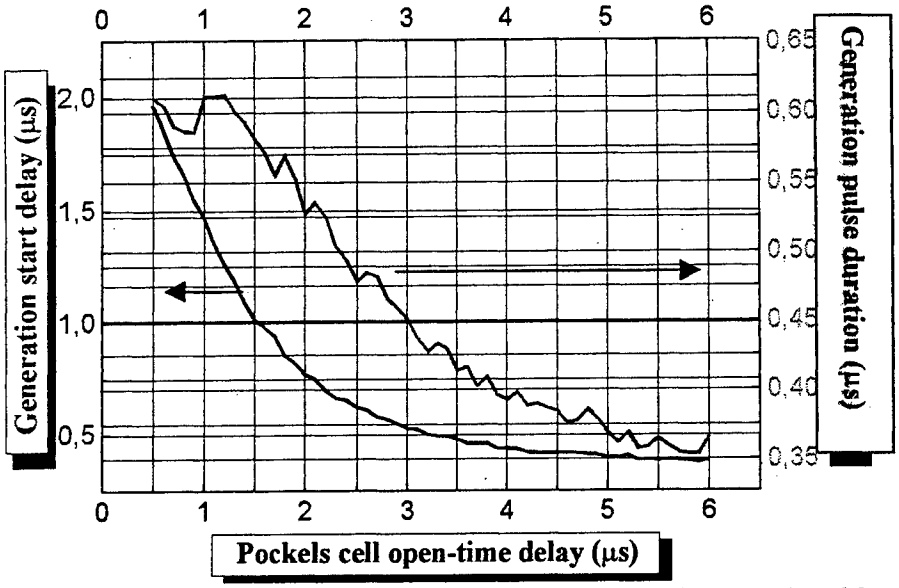


Fig. 5. Generation start delay (below curve) and generated pulse duration (above curve) vs delay time (a time delay between the moments when grating is written and the optical device is open) for intracavity frequency detuning $\Omega T_1=1.25$ and writing beam intensities $|E_{10}|^2=144 \cdot I_{sat}$.

The energy of the generated pulses increased with increasing delay time of the Pockes opening. This result is in good accord with experiment (compare Fig. 7 and Fig. 2).

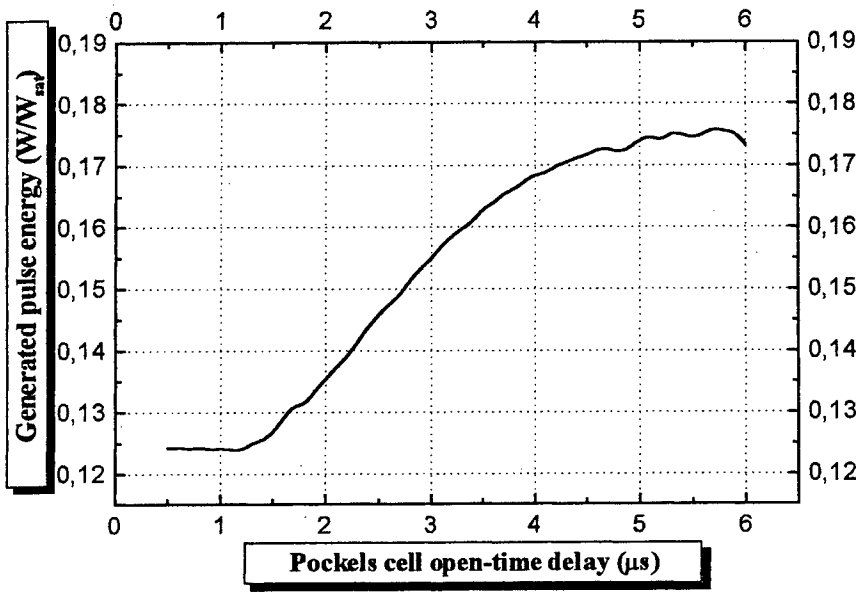


Fig. 6. Generated pulse energy vs delay time (a time delay between the moments when the grating is written and the optical device is open) for intracavity frequency detuning $\Omega T_1=1.25$ and writing beam intensities $|E_{10}|^2=144 \cdot I_{sat}$.

The generation start delay was found to be dependent on the nonreciprocal phase shift in the loop ($\varphi(A_N)$ + $\varphi(A_M)$). It is very interesting that minimum delay correspondes to the π phase nonreciprocity (Fig. 7).

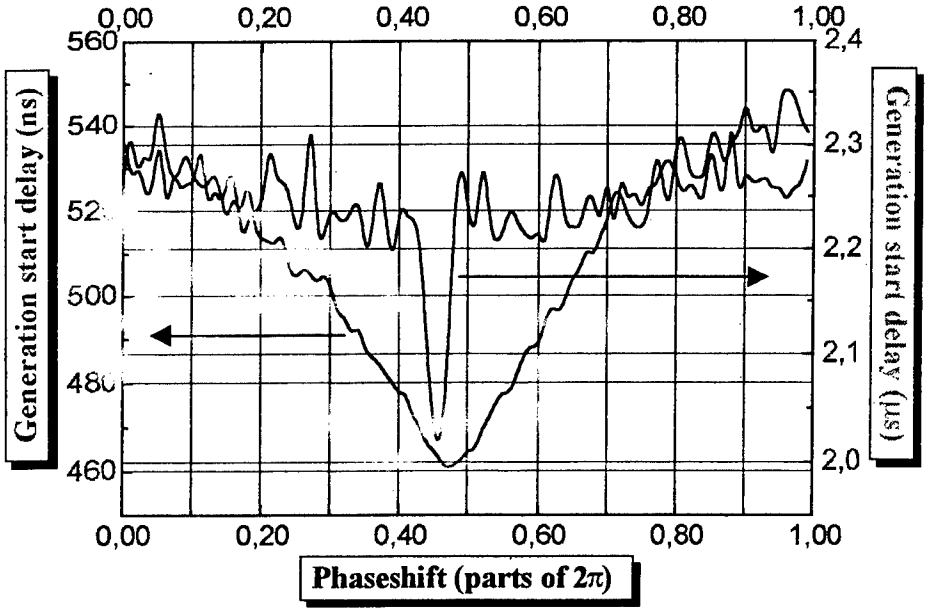


Fig. 7. Generation start delay vs intracavity phase shift for the delay time of the diode opening τ = 3μs (below curve) and τ = 200ns (above curve) for intracavity frequency detuning ΩT_1=1.25 and writing beam intensities $|E_{10}|^2$=144·I_s.

The generated pulse duration was also dependent on phase nonreciprocity (Fig. 8).

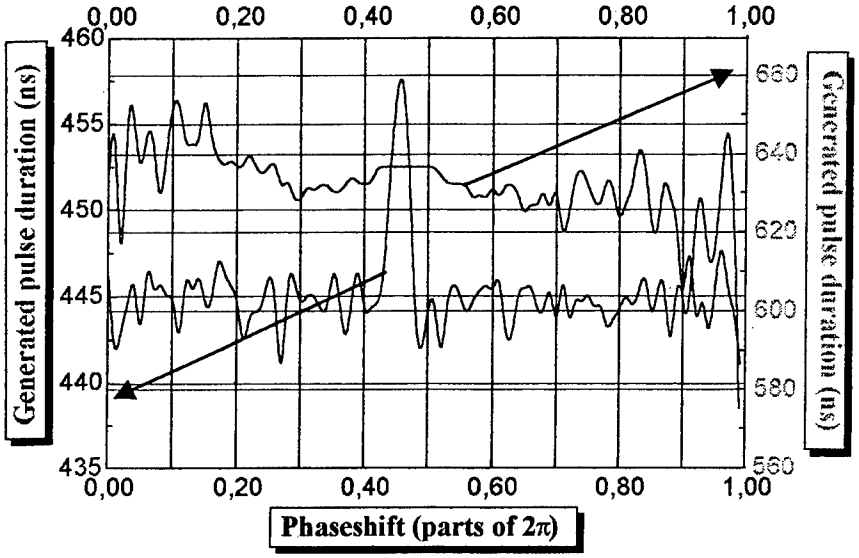


Fig. 8. Generated pulse duration vs intracavity phase shift for the delay time of the diode opening τ = 3μs (above curve) and τ = 200ns (below curve) for intracavity frequency detuning ΩT_1=1.25 and writing beam intensities $|E_{10}|^2$=144·I_s.

4. CONCLUSION

The experimental investigation and numerical calculation confirmed the participation of the resonant RIG in the cavity formation of a nonreciprocal holographic laser with PG formed by the external signal beam in a Nd:YAG flash-lamp pumped laser crystal. An increase in output energy of the generated pulse by about 25 % was measured and calculated. An additional growth of energy is prevented by gain saturation of the amplifiers.

Therefore, the resonant RIG must be taken into consideration in analysis of the holographic phase conjugators and laser oscillators at least under flash-lamp pumping. The resonant refractive index grating can improve the effective reflection coefficient of the holographic grating and total phase-conjugated reflection of the full optical scheme.

Acknowledgements

This work was supported in part by the INTAS through grant I971-12112 , NATO "Science for Peace" through grant SfP 974143, and RFBR through grant 00-02-17243.

References

1. M.J. Damzen, R.P.M. Green, G.F. Crofts, "Spatial characteristics of a laser oscillator formed by optically-written holographic gain-grating", *Optics Communications* **110**, 152-156 (1994).
2. P. Sillard, A. Brignon, and J.-P. Huignard, "Loop resonators with self-pumped phase-conjugate mirrors in solid-state saturable amplifiers", *J. Opt. Soc. Amer. B* **14**, 2049-2058 (1997).
3. A.V. Kirsanov and V.V. Yarovoy, "Selection of a wave phase-conjugated to an input speckled beam in an FWMF-oscillator with a "short" hologram", *Optics Communications* **138**, 235-241 (1997).
4. O.L. Antipov, S.I. Belyaev, A.S. Kuzhelev, "Self-pumped phase conjugation of the heterogeneous light beam in the inverted Nd:YAG-rod with nonreciprocal feedback", Optics Communications **117**, 290-294 (1995).
5. O.L. Antipov, S.I. Belyaev, A.S. Kuzhelev, "Phase conjugator of the light beam based on Nd:YAG-rod with the reciprocal feedback," *OSA TOPS* on Advanced Solid-State Lasers, v. 1, Stephen A. Payne and Clifford Pollock (Eds.), 1996 Optical Society of America, 411-416 (1996).
6. O.L. Antipov, A.S. Kuzhelev, D.V. Chausov, and A.P. Zinov'ev, "Dynamics of refractive index changes in a Nd:YAG laser crystal under Nd^{3+}-ions excitation," *J. Opt. Soc. Am. B* **16**, 1072-1079 (1999).
7. O.L. Antipov, A.S. Kuzhelev, A.Yu. Luk'yanov, A.P. Zinov'ev, "Changes in the refractive index of an Nd:YAG laser crystal on excitation of the Nd^{3+} ions," *Quant. Electronics* **28**, 867-874 (1998).

Simulations of wavefront correction of distorted laser beams

H.H. Klingenberg, Th. Hall, G. Spindler

Institut fuer Technische Physik, Deutsches Zentrum fuer Luft- und Raumfahrt e.V. (DLR),
Pfaffenwaldring 38 – 40, D-70569 Stuttgart, Germany

Abstract

The transverse beam profile of solid-state lasers is a key issue for determining its propagation properties. Herein, we address laser beam distortions caused by thermal lensing and birefringence. For the simulations a finite difference method is used for the description of beam propagation problems. The method is an improved approach to the solution of the wave equation in paraxial approximation. Provided that steady-state conditions prevail, in comparison with the Fresnel-Kirchhoff integral description this method allows for a fully 3 D treatment of the aforementioned laser-optical phenomena.

Introduction

For lasers with high output power an efficient utilization of the active medium needs a larger size of the gain medium itself. In the case of solid-state lasers rods with large cross sections are used. Another realization means for scaling up the output power is a setup employing a master oscillator power amplifier (MOPA) configuration. Applications of high average and high peak power solid-state lasers in the field of science and material processing require a nearly Gaussian or flat-top beam profile. Furthermore, e.g. the divergence of the laser beam or the depolarization losses have to be considered by analyzing the evolution of the phase- and intensity distribution of a wavefront propagating through a dispersive laser medium. So far, optimization of the resonator of one or the other scheme is provided by using the well known Fox-Li method[1] (Fresnel-Kirchhoff integral method).

In the following, we briefly summarize some experimental means for the compensation of thermal lensing and stress induced birefringence. The main emphasis is however placed on the simulation of these beam distortion features.

Means for correcting beam distortions

In optically pumped materials, for example in a Nd:YAG rod, the index of refraction is changed mainly by temperature variations and thermally induced stress. The resulting effect on the evolving laser beam are phase front distortions which need to be compensated. Various experimental means for compensating either thermal lensing or the induced birefringence are described in the literature.[2] One way to correct the distorted intensity distribution caused by the thermal lensing effect in a continuously operating transversely diode-pumped Nd:YAG laser is the incorporation of an adjustable curvature mirror (ACM) as a high reflector (HR) in the cavity.[3] The thin substrate of the HR mirror was deformed using a micrometer screw with a ball tip placed at the center of the substrate. A deformation of 40 μm off the center of the initial plane mirror into a convex curved mirror was needed to compensate for the thermal lensing effect evolving from lasing threshold up to the full pump power level. For the rod used with a diameter of 2 mm and a length of 40 mm, a focal length of the thermal lens of 35 cm was observed at full pump power. By simultaneously monitoring the transverse beam profile a nearly Gaussian profile was kept up to the available pump power of 60 W. A maximum output power of 12 W was achieved.

Another possibility for reducing the thermal lensing effect of a laser rod comprises the installation of a Galilean telescope inside the cavity.[4,5] Successful compensation can be achieved for a weak thermal load. At higher pump power levels the

Laser Optics 2000: Control of Laser Beam Characteristics and Nonlinear Methods for Wavefront Control,
Leonid N. Soms, Vladimir E. Sherstobitov, Editors, Proceedings of SPIE Vol. 4353 (2001)
© 2001 SPIE · 0277-786X/01/$15.00

laser rod exhibits an additional spherical aberration which cannot be compensated for by the described conventional means. One other option exists however. Some few crystals like Nd:YLF, for example, have a small optothermal coefficient, yielding a smaller thermal lens under comparable pumping conditions.

For the development of high power lasers the available glasses or crystals are rather limited. That is why the standard way to go is a Nd:YAG master oscillator power amplifier (MOPA) setup or an amplifier chain with the inclusion of optical phase conjugate (PC)[2,6] mirrors. Such a setup takes care for the compensation of thermal lensing. To compensate for the induced birefringence polarization schemes are used[7] for the resonators with or without the inclusion of PC.[8]

In a following section, we numerically evaluate the Y-cavity configuration[9,2] for birefringence compensation as an example to demonstrate the power of the finite difference method.[10]

Numerical method

The method is an improved finite difference approach to the solution of the wave equation in paraxial approximation. Under steady-state conditions, it yields a fully 3 D representation of the optical field because, for given discretizations in the transverse directions, axial propagation steps of any small size are possible. To begin with, the underlying assumptions for this equation are briefly sketched.

Paraxial wave equation

A solution ansatz with slowly varying amplitude in z-direction and time,

$$U(x,y,z,t) = u(x,y,z,t)\exp[i(\omega t - k z)] ,$$

of the free-space wave equation,

$$\frac{\partial^2 U}{\partial x^2} + \frac{\partial^2 U}{\partial y^2} + \frac{\partial^2 U}{\partial z^2} - \frac{1}{c^2}\frac{\partial^2 U}{\partial t^2} = 0 ,$$

together with the paraxial approximation,

$$\left|\frac{\partial^2 u}{\partial z^2}\right| << \left|k\frac{\partial u}{\partial z}\right| \quad \text{and} \quad \left|\frac{\partial^2 u}{\partial z^2}\right| << \left|\frac{\partial^2 u}{\partial x^2}\right| , \quad \left|\frac{\partial^2 u}{\partial y^2}\right|$$

as well as $\left|\frac{\partial^2 u}{\partial t^2}\right| << \left|\omega\frac{\partial u}{\partial t}\right|$,

yields the paraxial wave equation as

$$\left(-2ik\left[\frac{\partial}{\partial z} + \frac{1}{c}\frac{\partial}{\partial t}\right] + \frac{\partial^2}{\partial x^2} + \frac{\partial^2}{\partial y^2}\right) u(x,y,z,t) = 0 .$$

The term in the brackets represents the total derivative of the complex field amplitude with respect to the z-direction including a part which considers a possible unsteady behavior of the wave front.

Representing a Schroedinger-type partial differential equation, the paraxial wave equation constitutes a diffusion problem with an imaginary diffusion constant.

Numerical scheme

The numerical solution is provided by a finite difference scheme, well proved for 2 D heat conduction problems in the time domain, i.e., the *Alternating Direction Implicit Method* (ADIM).[11] ADIM allows for a flexible variation of the incremental axial propagation steps with a high degree of computational stability and (phase) accuracy at the same time. The boundary conditions for the field amplitude in the x-y – plane may be either given by $u = 0$ or $\partial u / \partial x = \partial u / \partial y = 0$, supposing that the computational domain is wide enough to have the amplitude nearly faded at the boundaries.

Treatment of 3 D laser medium effects and mirror phases

The stepwise propagation of the field is performed according to the following prescription[10]:

$$u(x, y, z + \Delta z) = u^f(x, y, z + \Delta z) \exp\{[g(x, y, z)/2 - i\, k\, \Delta n(x, y, z)]\, \Delta z\} ,$$

where $u^f(x, y, z + \Delta z)$ is the field after free-space propagation from z to $z + \Delta z$, $g(x, y, z)$ is the gain and $\Delta n(x, y, z) = n(x, y, z) - 1$ is given by the spatial variation of the refractive index of the respective medium; cf. Fig 1.

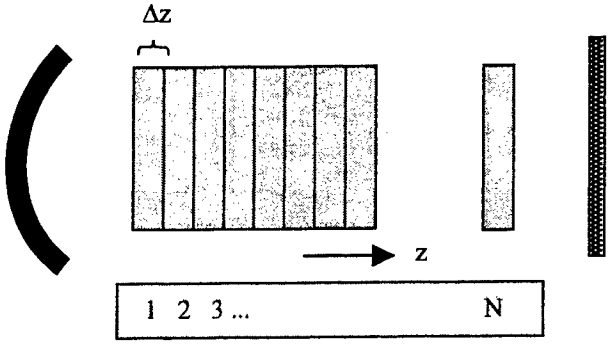


Fig. 1. Stepwise propagation of the field through a (gain) medium with spatially varying refractive index. In the axial direction, the medium is divided into N increments having the width Δz.

Additional optical elements like mirrors or thin lenses are considered in a similar way by simply correcting the complex field $u(x, y, z)$ for the respective transverse phase variation.

Thermal lensing and stress induced birefringence in laser crystals

Allowing propagation steps in the axial direction of any small size, the method is best qualified for the modeling of thermal lensing and stress induced birefringence. Thus a distributed thermal lens can be considered as an axial series of many (several 10) thin lenses.

Polarization effects are accounted for by the propagation of two scalar fields representing the p- and s-polarized states. Changes in polarization due to certain optical elements are described by a 2x2 matrix (Jones Matrix) acting on the vector consisting of the two field components. As an example, the treatment of stress induced birefringence of a laser rod (Nd:YAG) and the resulting depolarization is briefly sketched.

In a cylindrical coordinate system (system of principal axes of the indicatrix) the change of the polarization state for an incremental axial propagation step Δz is given by:

$$\begin{pmatrix} E_r(x,y,z+\Delta z) \\ E_\varphi(x,y,z+\Delta z) \end{pmatrix} = M_{Jones} \begin{pmatrix} E_r(x,y,z) \\ E_\varphi(x,y,z) \end{pmatrix},$$

with the Jones Matrix

$$M_{Jones}(r) = \begin{pmatrix} \exp[ik\Delta n_r(r)\Delta z] & 0 \\ 0 & \exp[ik\Delta n_\varphi(r)\Delta z] \end{pmatrix}.$$

Within the framework of a simple analytical photoelastic model[2] the variations of the refractive index scale as

$$\Delta n_r(r) = -2.8\times10^{-6}\, Q[\text{Watt/cm}^3]\, r[\text{cm}]^2 \;, \quad \Delta n_\varphi(r) = +0.4\times10^{-6} Q[\text{Watt/cm}^3]\, r[\text{cm}]^2 \;,$$

where Q denotes the heat deposited in the crystal. It should be stressed, in this context, that the numerical method not only predicts the change of the polarization state but also reflects the individual refraction of the r- and φ-component of the field (birefringence).

Simulation of the Y-cavity resonator

For the simulations of thermal lensing and birefringence compensation we evaluate, as an example, the Y-cavity resonator[9,2] to demonstrate the ability of the finite difference numerical method.

The Y-cavity resonator, depicted in Fig. 2, compensates for birefringence by double-pass retracing the beam through the thermally distorted laser rod. A p-polarized beam coming from the left passes the polarizer, laser rod and 45° Faraday rotator. Being orthogonally polarized on its return pass, the beam is deflected by the polarizer towards the HR re-entrant mirror. The s-polarized beam once more double-passes the rod and Faraday rotator and, being p-polarized again, passes the polarizer to reach the output coupler. Position and focal length of the rear mirror for optimum compensation of birefringence are related by[7]

$$d = f - \frac{s}{2n_0} + \sqrt{f^2 - \left(\frac{s}{2n_0}\right)^2} \quad ; \quad f \geq \frac{s}{2n_0} \;,$$

with d distance between rear mirror and rod, f focal length of the rear mirror, s active length of the laser rod, and n_0 refractive index at the center of the rod.

An additional feature of the Y-cavity resonator are the four passes of the beam through the active medium before it reaches the output coupler.

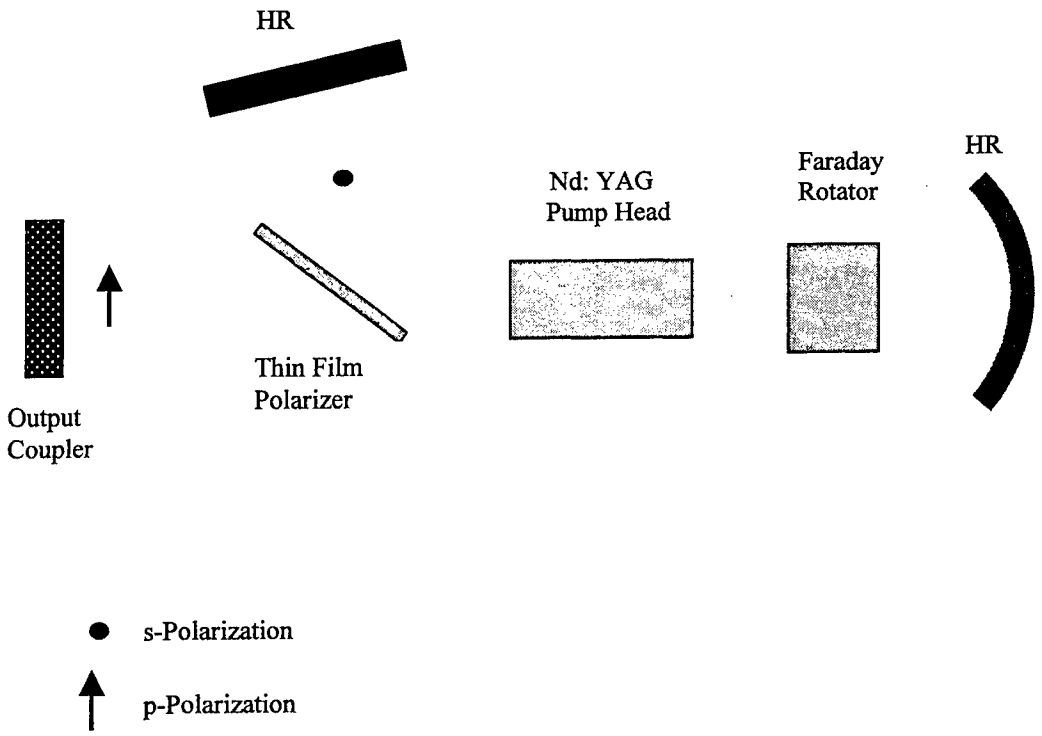


Fig. 2. Principle of the Y-cavity resonator for birefringence compensation by double-pass retracing the beam through the thermally distorted laser rod (Nd:YAG pump head).

The computations of the steady-state field distribution along the optical axis of the Y-cavity for two passes are shown in Fig. 3. The r-polarization and φ-polarization states are represented in the upper and lower part of Fig. 3. The axial positions of the output coupler and the rear curved mirror are at the left hand side and at the center, respectively. The HR re-entrant mirror is located at the right hand side; the deflection of the beam due to the thin film polarizer is ignored. The beam partially returning from the output coupler is p-polarized which means r-polarized in the selected meridian plane. When the beam passes the 45° Faraday rotator a s-polarized (φ-polarized) component appears for the first time, (lower picture in Fig. 3). In the upper picture, after the second encounter with the Faraday rotator the beam has no longer a p-polarized component, i.e., the intensity profiles terminate. The intensity peaks are due to a complex interplay of the curved rear mirror and the thermal lens of the laser rod.

The simulations indicate that without birefringence compensation (re-entrant mirror and Faraday rotator removed) the laser has an approximate depolarization loss of 25 percent. The introduction of optimum compensation reduces the loss below 0.1 percent.

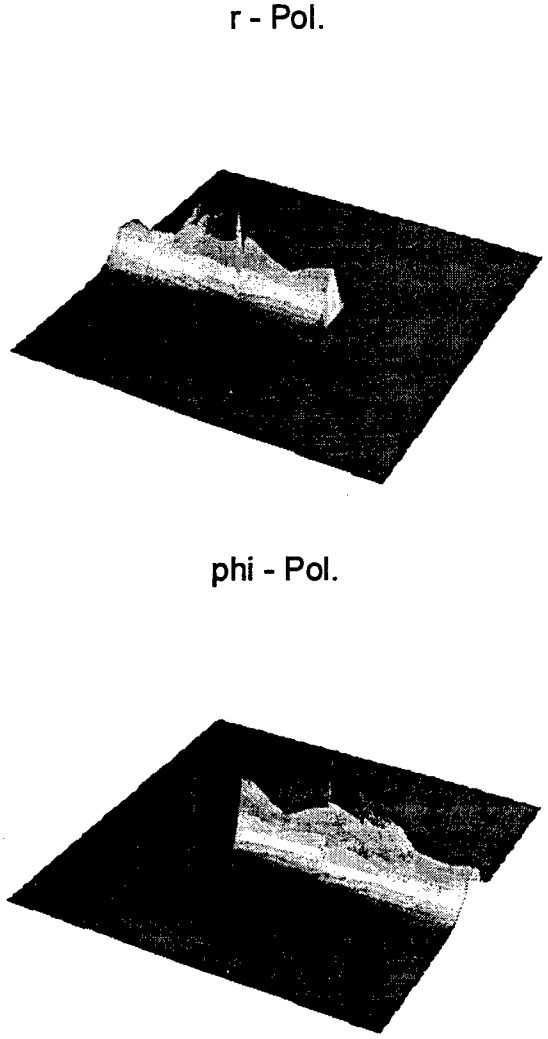


Fig. 3. Intensity profiles along the laser axis (two passes) for r- and φ-polarization states. The axial positions of the output coupler and the rear curved mirror are at the left hand side and at the center, respectively. The HR re-entrant mirror is located at the right hand side. After the second encounter with the 45° Faraday rotator the beam has no longer an r-component, i.e., the intensity profiles in the upper picture terminate. In the lower picture, a φ-polarization component appears after the beam passed the rotator for the first time.

Conclusions

In this paper, we focused on thermally induced stress birefringence and lensing constituting key issues of high power solid-state lasers. After the discussion of some experimental means for the compensation of these beam distortions, a novel approach to the solution of the paraxial wave equation, utilizing the *Alternating Direction Implicit Method* (ADIM) was introduced. Allowing for field propagation steps of any small size, the method proved to be best fitted for the (3 D) simulation of spatially distributed medium effects which cannot be addressed by the Fresnel-Kirchhoff integral procedure.

References

1. A. G. Fox, T. Li, Bell Sys. Tech. J. **40**, 453 (1961).
2. W. Koechner, *Solid-State Laser Engineering* (Springer-Verlag Berlin Heidelberg 1999).
3. U. J. Greiner, H. H. Klingenberg, Opt. Lett. **19**, 1207 (1994).
4. P. H. Sarkies, Opt. Commun. **31**, 189, (1979).
5. D. C. Hanna, C. G. Sawyer, M. A. Yuratich, Opt. Quantum Electron. **13**, 493 (1981).
6. H. J. Eichler, R. Menzel, D. Schumann, Appl. Opt. **31**, 5038 (1992).
7. N. Kugler, S. Dong, Q. Lü, H. Weber, Appl. Optics **36**, 9359 (1997).
8. I. D. Carr, D. C. Hanna, Appl. Phys. B **36**, 83 (1985).
9. G. Giuliani, P. Ristori, Opt. Commun. **35**, 109 (1980).
10. D. B. Rensch, Appl. Optics **13**, 2546 (1974).
11. R. D. Richtmyer, K. W. Morton, *Difference Methods for Initial-Value Problems* (Interscience Publishers John Wiley, New York 1967).

Spiral laser beams

Eugeny G. Abramochkin and Vladimir G. Volostnikov

P. N. Lebedev Physics Institute, Russian Academy of Sciences (Samara Branch)
Novo-Sadovaya str. 221, Samara 443011, Russia

ABSTRACT

In this review some results on spiral beam optics are considered. Spiral beams keep their intensity structure unchanged under propagation except its scale and rotation. Some theoretically calculated spiral beams and the ways of their experimental constructing are presented. A comparison between an example of nonrotating but structurally stable beam and a corresponding spiral beam is performed.

Keywords: Keywords: spiral beams, structurally stable beams, Laguerre-Gaussian beams, astigmatic transformation.

1. INTRODUCTION

The theme of this article is so called spiral laser beams. The characteristic feature of these wavefields is that they are remaining unchanged under propagation and focusing if we neglect a scaling and rotational changes. In other words under propagation these beams keep their structure and are rotating only.

The name of these beams is a consequence of their rotating and phase properties. Namely, the trajectories of corresponding points of their intensity distributions under propagation are in general some spirals. On the other hand the equiphase lines of their phase distributions outside of the waist are spirals also.

It is known that from formal point of view any coherent light field may be presented as superposition of well known class of Gaussian beams: Hermite- and Laguerre beams. For this reason a question arises: what are the arguments in favor of introducing of a spiral beam conception?

There are two aspects of this question. At first [1], the spiral beam representation of wavefields is sometimes very compact and descriptive as we will see below. And secondly [2], the proposed approach gives a new possibility to study the ways of shaping and transformation of coherent wavefields.

2. SPIRAL BEAMS

We start with an ordinary Laguerre-Gaussian mode definition:

$$L_{n,\pm m}(x,y) = \exp(-x^2 - y^2)(x \pm iy)^m L_n^m(2x^2 + 2y^2), \quad n,m = 0,1,\ldots .$$

Here index n defines a number of rings in the intensity distribution and index $\pm m$ defines an order of central zero and its sign. Below we will say that a prime zero is positive one if under counterclockwise motion around it the beam phase changes from 0 to 2π, in otherwise a zero is negative. Nonprime zeros are classified analogously.

What a combination of Laguerre-Gaussian modes describes a spiral laser beam? It may be shown that a sum of Laguerre-Gaussian modes be a spiral beam if the following condition for mode indices n,m takes place:

$$2n + |m| + \theta_0 m = \text{const}.$$

Here θ_0 is the rotation parameter and the corresponding beam rotates under propagation according to the law:

$$q(l) = q_0 \arctan\left(\frac{2l}{k r^2}\right).$$

Here l is a distance along the direction of propagation of the beam, k is a wave number, and $\rho = \text{const}$. From the index condition it is seen that any sum of Laguerre-Gaussian modes with zero n and positive m's is always a spiral beam for the rotation parameter $\theta_0 = -1$. In this case a polynomial structure of all Laguerre-Gaussian modes reduces to a single term z^m and the sum of these beams may be rewritten as the following:

Laser Optics 2000: Control of Laser Beam Characteristics and Nonlinear Methods for Wavefront Control,
Leonid N. Soms, Vladimir E. Sherstobitov, Editors, Proceedings of SPIE Vol. 4353 (2001)
© 2001 SPIE · 0277-786X/01/$15.00

$$F(x,y,l)=\frac{1}{\sigma}\exp\left(-\frac{x^2+y^2}{\rho^2\sigma}\right)f\left(\frac{x+iy}{\rho\sigma}\right).$$

Here $s=1+2il/kr^2$ and an arbitrary entire analytic function of one complex variable $f(z)$ is defined by its own zeroes and their positions. So, the beam evolution under propagation looks like a rotation of the isolated zero set with some angular velocity.

It should be noted here that the Gaussian beams known before have a rectangular or circular symmetry and a rigid distribution of their intensities. In contrast with them the spiral beams due to representation containing an arbitrary analytic function give us a wide range of possibilities to synthesize structurally stable wavefields of various topology. For example, it may be shown [2] that a spiral beam whose intensity is visually similar to a predetermined planar curve has the form

$$S(z,\bar{z}\,|z)=\exp\left(-\frac{z\bar{z}}{r^2}\right)\int_0^T\exp\left(-\frac{z\bar{z}}{r^2}+\frac{2z\bar{z}}{r^2}+\frac{1}{r^2}\int_0^t(z'\bar{z}-z\bar{z}')d\tau\right)|z'|\,dt\,.$$

Here $\zeta(t)$, $t\in[0,T]$ is a parametric complex-valued representation of the curve on the plane and $z=x+iy$ is complex variable. The base of these beams is a set of isolated zeroes or optical vortices. For this reason the beams found have a vortical nature and nonzero angular momentum. This property permits to use spiral beams as tweezers and spanners for micromanipulation purposes.

Examples of spiral beams constructed for some planar curves are shown in figs.1-4.

The importance of the zero locations and their signs are extremely high. With the aim to illustrate this let us consider the field on fig.5. This beam conserves its structure under propagation but has no any rotation. Intensity distribution of this beam is almost the same as for the spiral beam in fig.4. The comparison of the phase structures of both beams shows that the zero set dispositions inside of two maximal intensity contours are very similar to each other except the rotation over $\pi/4$ angle. But zeroes located outside of the square domains are rather different. All zeroes of the spiral beam in fig.4 are positive but outside zeroes of the beam in fig.5 are negative So, dissimilarity between peripheral zeroes of both beams determines a radical difference between behaviour of these beams under propagation.

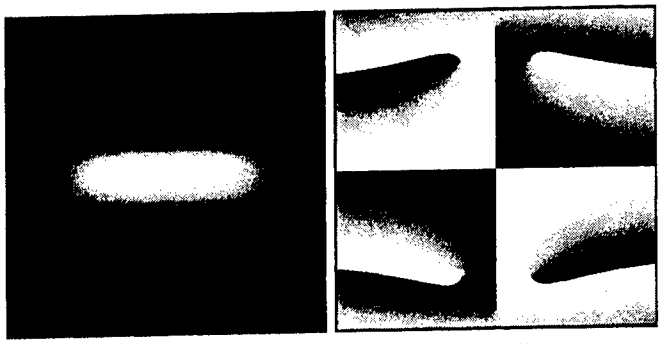


Fig.1. Intensity and phase for a spiral beam shaped like a segment. In the phase pattern black corresponds to 0, and white to 2π. Six positive zeros are seen in the left. Central region contains a saddle point but not a zero because of $\exp(i0) = \exp(2\pi i)$.

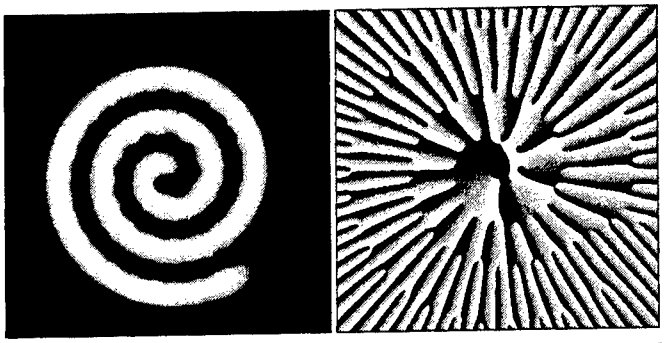


Fig.2. Intensity and phase for a spiral beam shaped like a spiral of Archimedes $\zeta(t)=te^{ict}$. The parameter c was selected to demonstrate the interference between coils.

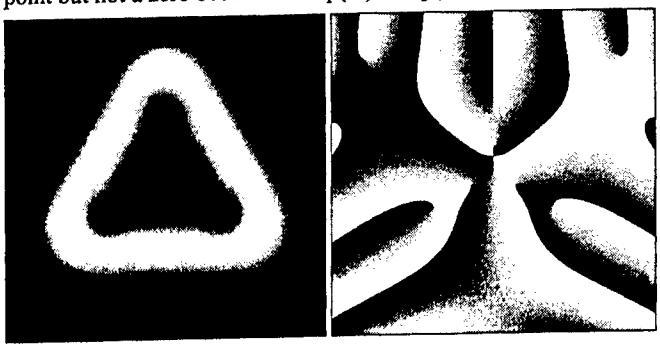


Fig.3. Intensity and phase for a spiral beam $S(z,\bar{z}\,|\Delta_7)$ shaped like a triangular boundary.

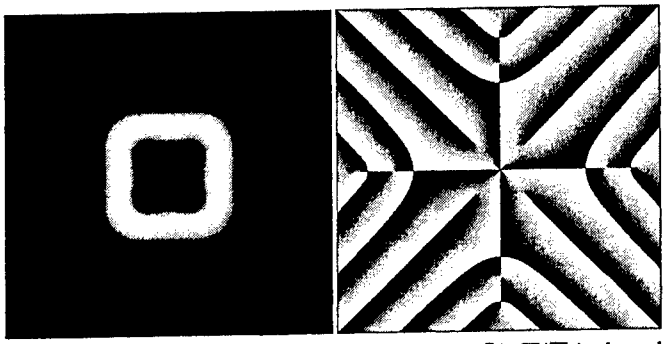
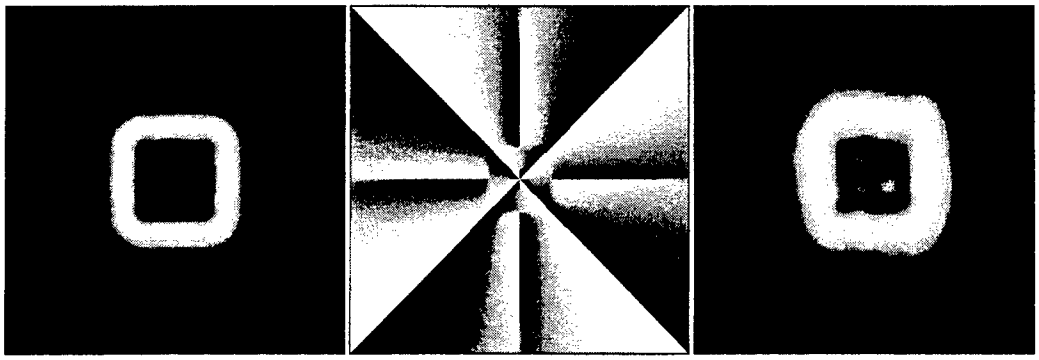


Fig.4. Intensity and phase for a spiral beam $S(z,\bar{z}\,|\square_8)$ shaped like a square boundary.



a b c

Fig.5. Intensity (a) and phase (b) of nonrotating structurally stable beam, and its experimental realization (c). Eight positive zeroes are seen inside a maximal intensity contour and four negative zeroes are placed outside the contour.

As has been mentioned above the spiral laser beams have in general nonzero angular momentum and nonzero rotor of their energy flux field. Without intention to consider this connection in details let us present a new relation between these characteristics of a coherent wavefield. It may be shown that a longitudinal component of angular momentum and a longitudinal component of rotor of a light energy flux field are connected by the following relation:

$$\underbrace{\iint_{R^2} \mathrm{Im}\left(\bar{F}\left(x\frac{\partial F}{\partial y} - y\frac{\partial F}{\partial x}\right)\right)dxdy}_{(k\sqrt{\varepsilon\mu})M_l} = -\frac{1}{2}\underbrace{\iint_{R^2}(x^2+y^2)\,\mathrm{Im}\left(\frac{\partial \bar{F}}{\partial x}\frac{\partial F}{\partial y} - \frac{\partial \bar{F}}{\partial y}\frac{\partial F}{\partial x}\right)dxdy}_{k\cdot \mathrm{rot}_0\mathbf{j}(x,y)}.$$

Like an intensity both characteristics – M_l and $\mathrm{rot}_0\mathbf{j}$ – are integral invariants for any light field, i.e. as the energy conserves itself unchanged under the field propagation as analogous integrals for M_l and $\mathrm{rot}_0\mathbf{j}$ do.

3. EXPERIMENTAL REALIZATION OF SPIRAL BEAMS

There are various methods to synthesize spiral beams. The most obvious one is connected with the usage of amplitude-phase masks. In this case the requested distribution of complex amplitude in a predetermined plane may be obtained by combination of two fabricated transparants: amplitude one and phase one. If ordinary Gaussian beam illuminates this sandwich then spiral beam amplitude is realized behind it. The example of such experiment is shown in fig.6. This beam rotates under propagation keeping its structure, and the angle of complete rotation between the waist and far zone is $\pi/2$.

Another way for constructing of a spiral beam is based on the possibility of a beam generation directly inside a laser resonator [3]. The type of resonators used for this purpose is a specific ring resonator with a field rotation. The example of experimental set-up is shown in fig.7. A Dove prism was used in this experiment as a rotator. It has been shown theoretically and experimentally that the rotation of the prism on some angle leads to generation of a spiral beam. Results of some experiments are shown in figs.8,9.

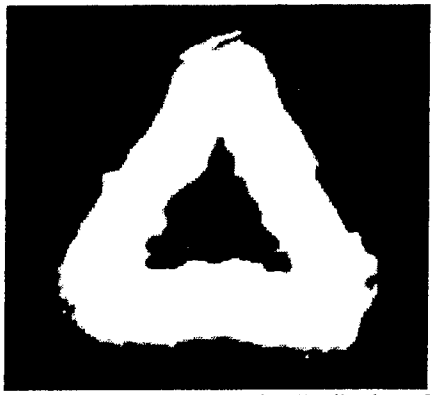


Fig.6. Experimental intensity distribution of triangle-line spiral beam (see theoretical one in fig.3).

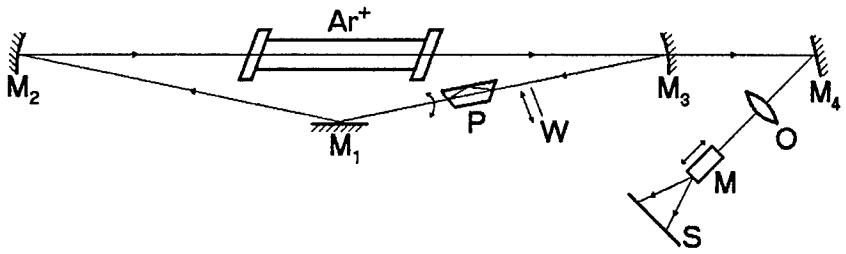


Fig.7. Experimental set-up on the base of argon ion ring laser. M_1 is plane mirror, M_2, M_3 are spherical mirrors, P is Dove prism. The resonator scheme shaped as an obtuse-angled triangle was selected in order to reduce the influence of astigmatism of the mirrors M_2, M_3. The beam generated by the laser was observed and registered after partially passing mirror M_3 with the help of objective O and microscope M in the plane of the screen S. Transverse-mode selection was realized by inserting a thin wire W into the beam zone.

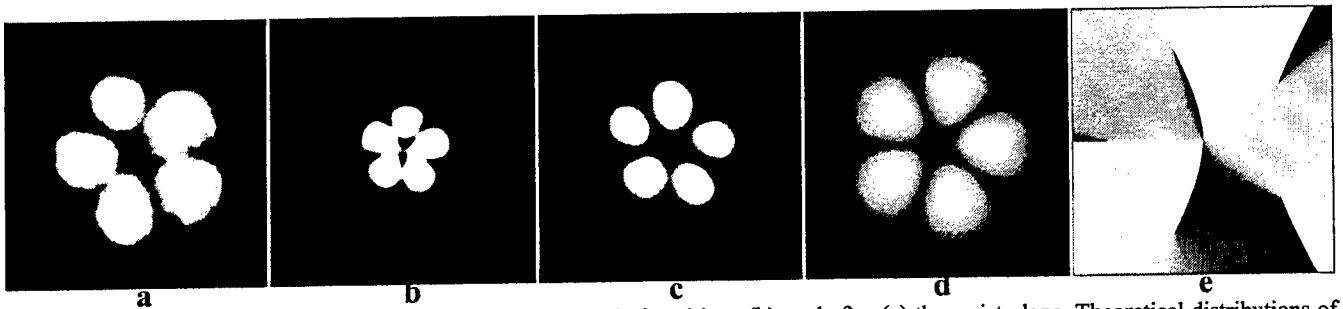


Fig.8. Experimentally registered intensities of the spiral beam before (a), at (b), and after (c) the waist plane. Theoretical distributions of intensity (d) and phase (e) of spiral beam $\mathcal{L}_{0,-3}(x,y)+2\mathcal{L}_{0,2}(x,y)$ with the rotation parameter $\theta_0=1/5$.

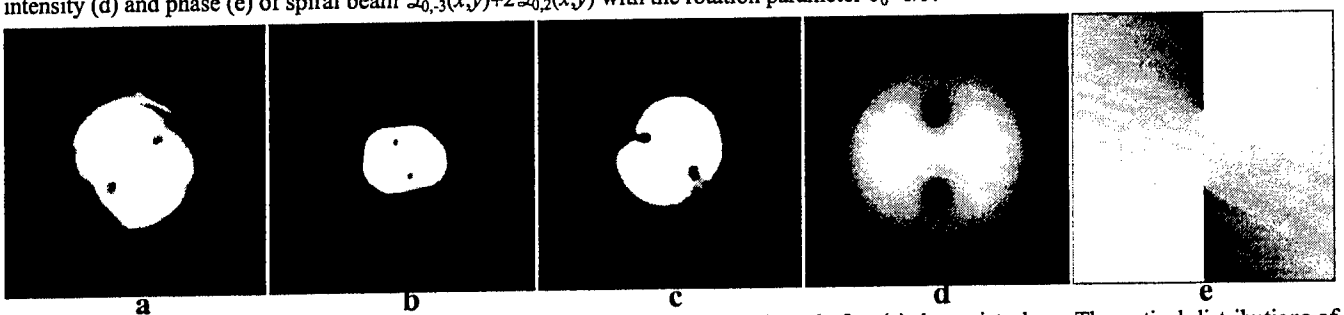


Fig.9. Experimentally registered intensities of the spiral beam before (a), at (b), and after (c) the waist plane. Theoretical distributions of intensity (d) and phase (e) of spiral beam $\mathcal{L}_{0,0}(x,y)+2\mathcal{L}_{0,2}(x,y)$ with the rotation parameter $\theta_0=-1$.

The last and not so evident way of spiral beam synthesis is based on our earlier results concerning Gaussian beam transformations. It has been shown [4], that any Hermite-Gaussian beam may be transformed into some Laguerre-Gaussian beam by means of astigmatic optics. At first this transformation was detected in experiment and later it was proven in theory. Experimentally this transformation may be realized by combination of some spherical and cylindrical lenses. Using this result any sum of Hermite-Gaussian beams may be converted into a sum of corresponding Laguerre-Gaussian beams. On the other hand, it is known that in a stable resonator the mode time frequences are

$$w_{qg} = \left(pq + g\arccos\sqrt{g_1 g_2}\right)\frac{c}{2l},$$

where l is a resonator length, g_1,g_2 are configuration parameters and $\gamma=n+m+1$ for Hermite-Gaussian beams. If the equality

$$\arccos\sqrt{g_1 g_2} = pP/Q$$

takes place, where P,Q are coprime numbers, then there exists an additional frequency degeneration for modes that satisfy the condition $\gamma P/Q = N$. The sum of these modes is the time stationary process but the total wavefield changes under propagation. Let us consider an example $P/Q = 1/3$ (resonator: R_1=2 m, R_2=∞, l=1.5 m). There is a frequency degeneration for the sum of Hermite-Gaussian modes $\sum_k c_k H_{0,3k}(x,y)$ or $\sum_k c_k H_{0,3k+1}(x,y)$ in such resonator (see fig.10). This combination can be produced by inserting a thin wire into the resonator field. The astigmatic transformation of the obtained wavefield is a spiral beam with $2\pi/3$-symmetry. The results of the experiment are shown in fig.11.

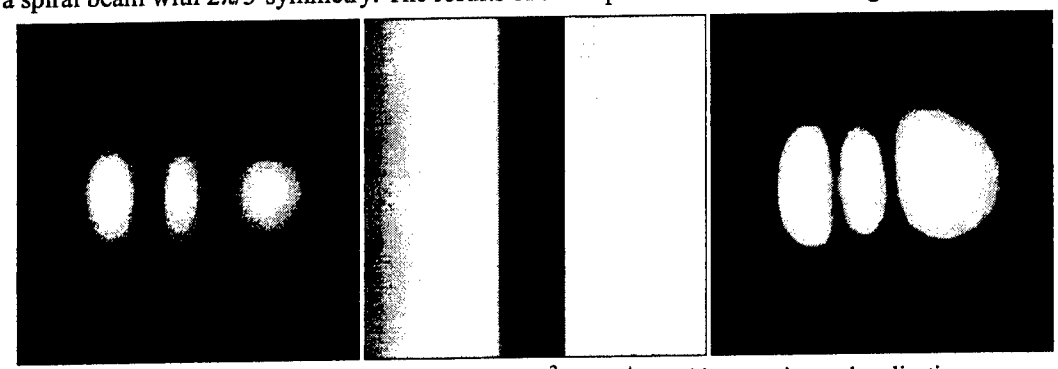


Fig.10. Intensity and phase of the field $\exp(-x^2/8)h(y|\Delta_2)$ and its experimental realization.

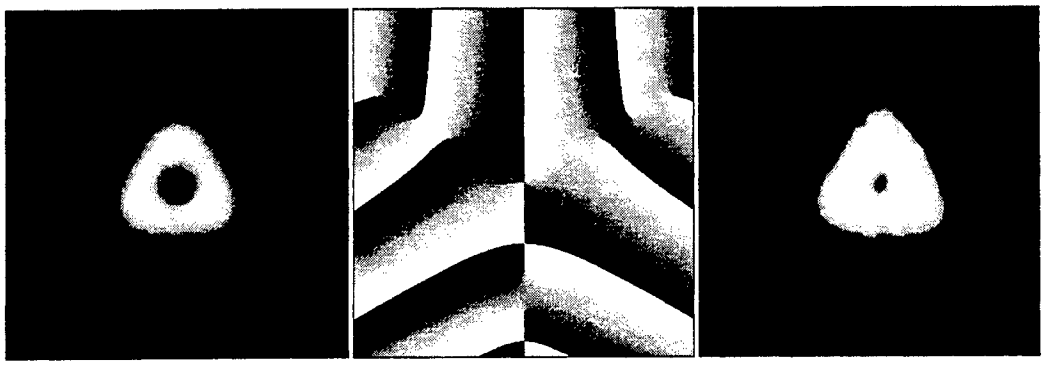


Fig.11. Intensity and phase of spiral beam $S(z, \overline{z}\,|\Delta_2)$ and its experimental realization.

4. CONCLUSIONS

Finally, it should be noted that there are spiral beam aspects which have not been discussed here. Some of them are so called derived spiral beams [5], the connection between spiral beams and quantum mechanics [2], the spiral beam usage for beam shaping problem and some others [6,7]. But the basic spiral beam features and some new results have been presented.

ACKNOWLEDGEMENTS

This work is supported by the Russian Fund for Basic Research (grant 99-02-16513).

REFERENCES

1. E.Abramochkin and V.Volostnikov. "Spiral-type beams", *Opt.Comm.*, **102**, 336-350 (1993).
2. E.Abramochkin and V.Volostnikov. "Spiral-type beams: optical and quantum aspects", *Opt.Comm.*, **125**, 302-323 (1996).
3. E.Abramochkin, N.Losevsky and V.Volostnikov. "Generation of spiral-type laser beams", *Opt.Comm.*, **141**, 59-64 (1997).
4. E.Abramochkin and V.Volostnikov. "Beam transformations and non-transformed beams", *Opt.Comm.*, **83**, 123-135 (1991).
5. E.Abramochkin, V.Volostnikov. "Structurally stable singular wavefields", *Proc. of SPIE*, **3487**, 20-28 (1998).
6. M.Loktev, V.Volostnikov. "Singular wavefields and phase retrieval problem", *Proc. of SPIE*, **3487**, 141-147 (1998).
7. M.Loktev, N.Losevsky, V.Volostnikov. "Beam synthesis with predetermined intensity", *Proc. of SPIE*, **3487**, 123-129 (1998).

The real time control of the rotation rate of a particle trapped in a focused laser beam.

M.A. Rakhmatulin, S.P. Kotova, V.G. Volostnikov

Lebedev Physical Institute of Russian Academy of Sciences,
Novo-Sadovaya Street 221, Samara 443011, Russia. E-mail: malik@fian.samara.ru.

ABSTRACT

The real time control of the rotation rate of a microscopic particle trapped in a focused laser beam by mean of polarization ellipticity of laser radiation has been studied. The ellipticity change was carried out with the modulator using orientational S-effect in nematic liquid crystals. The dependence of the particle rotation speed on the state of polarization ellipticity was determined. The calculation of an angular momentum of rotation per a unit of energy of the light field is shown.

Keywords: laser trap, real time control, liquid crystal modulator

1. INTRODUCTION

It was A. Sadowsky who calculated the optical torque of elliptically polarized light in 1900 for the first time [1]. It was considered too small for experimental detection, while R.A. Beth in 1936 in his famous difficult experiment had measured it [2]. He observed the deflection of a quartz wave plate suspended from a thin quartz fiber when circularly polarized light passed through it. Nowadays with the help of such tool as the optical trap it is possible to observe transfer of an optical torque at a microscopic level. The result of optical torque calculation in papers [3-5] indicates that its transfer to an absorptive particle will put it to rotation with speed in some hertz. Light transfers the angular momentum from the polarized Gaussian mode of a laser beam to absorptive microscopic particle. The angular momentum carried by light can be characterized by the "spin" angular momentum associated with the circular polarization. Changing the polarization degree of laser radiation, it is possible to change the rotation rate of a microscopic particle. The authors of the article [6] have shown theoretically and experimentally a capability of two-dimensional trapping and manipulations above absorptive particles by a tightly focused Gaussian laser beam. Moreover, they have shown that the use of a Gaussian mode gives new capabilities for the study of the transfer of an optical rotary moment caused by elliptical polarization of light to absorptive particles. In articles [7-9] for demonstrating microscopic station of the transfer of orbital and spin angular momentums from a laser mode to the trapped particle the Laguerre-Gaussian mode was used.

The presented work intends to develop a method to control rotation rate of a microscopic particle trapped in a focal point of the laser, with the help of optoelectronic modulator without mechanical movements in real time. Now movement and rotation are accessible for microparticles manipulations. The movement of particles has been realized by scanning of a focused laser beam in image plane [7], and by moving of an object table [9]. In the latter case a focused beam keeps the particle, and environment ambient are moves. The rotation of particles is possible by the use of circular polarization of a laser beam [6] or by the use of laser modes with spiral wave front [7-9]. In all papers [6-9] the control of the rotation rate in real time was implemented by change of an ellipticity polarization degree of a laser beam with the help of rotation of a $\lambda/4$ plate. In the given article the real time control of rotation rate of a particle trapped by a focused laser beam was performed with the help of the liquid crystal modulator (LCM), capable to change a degree of an ellipticity polarization of laser radiation without mechanical movements.

2. THEORY

Let's find an angular momentum comes per unit of energy of a light field. The electric field of an elliptically polarized beam is:

$$\varepsilon_x = \mathbf{E}(x,y,l)\cos\theta e^{ikl-i\omega t},$$
$$\varepsilon_y = i\mathbf{E}(x,y,l)\sin\theta e^{ikl-i\omega t}, \quad (1)$$

Laser Optics 2000: Control of Laser Beam Characteristics and Nonlinear Methods for Wavefront Control,
Leonid N. Soms, Vladimir E. Sherstobitov, Editors, Proceedings of SPIE Vol. 4353 (2001)
© 2001 SPIE · 0277-786X/01/$15.00

$\varepsilon_l = g(x,y,l)e^{ikl-i\omega t}$,

where $k = k_0\sqrt{\varepsilon\mu} = \frac{\omega}{c}\sqrt{\varepsilon\mu}$

Then from the Maxwell's equation $divE=0$ the connection between longitudinal and transversal components of electrical vector is discovered:

$$E_x' \cos\theta + iE_y' \sin\theta + igk + \frac{\partial g}{\partial l} = 0 \Rightarrow$$
$$g = -e^{-ikl}\int e^{ikl}(E_x' \cos\theta + iE_y' \sin\theta)dl \approx \frac{i}{k}(E_x' \cos\theta + iE_y' \sin\theta) = \varepsilon_l \quad (2)$$

where $f_x' = \frac{\partial f}{\partial x}$, $f_y' = \frac{\partial f}{\partial y}$. From the Maxwell's equation $\mathbf{B} = \frac{1}{ik_0}\mathrm{rot}\mathbf{E}$ matching components of a magnetic field is discovered:

$$\mathcal{B}_x = -i\frac{k}{k_0}E\sin\theta$$
$$\mathcal{B}_y = \frac{k}{k_0}E\cos\theta \quad (3)$$
$$\mathcal{B}_l = \frac{1}{k_0}(E_x' \sin\theta + iE_y' \cos\theta)$$

The time-average angular density of a moment is determined by following expression:

$$\mathbf{M}_l = \frac{1}{8\pi c}\mathrm{Re}[\mathbf{r}\times[\varepsilon\mathbf{E}\times\bar{\mathbf{B}}]]_l, \quad (4)$$

Where the badge $\bar{}$ is marks conjugate values. Substituting in this expression (1) and (3) for volumetric density of an angular momentum we shall receive:

$$M_l = \mathrm{Re}[-x(\varepsilon\varepsilon_x\overline{\mathcal{B}_l} - \overline{\mathcal{B}_x}\varepsilon\varepsilon_l) - y(\varepsilon\varepsilon_y\overline{\mathcal{B}_l} - \varepsilon\varepsilon_l\overline{\mathcal{B}_y})] =$$
$$= -\frac{1}{8\pi c}\frac{\varepsilon x(E\bar{E})_x' + \varepsilon y(E\bar{E})_y'}{2k_0}\sin 2\theta + \frac{1}{8\pi c k_0}\left(\frac{x\varepsilon(\bar{E}E_y' - E\overline{E_y'})}{2i} - \frac{y\varepsilon(\bar{E}E_x' - E\overline{E_x'})}{2i}\right) \quad (5)$$

Here first member depending on θ is a polarizing component of an angular momentum.

Volumetric density of energy of a light field W is determined as $W = \frac{\varepsilon}{8\pi}E\bar{E}$. Then we receive the specific polarizing moment per energy unit of light field

$$L_\sigma = -\frac{\frac{\varepsilon\sin 2\theta}{8\pi c}\iiint\frac{x(E\bar{E})_x' + y(E\bar{E})_y'}{2k_0}dxdydl}{\frac{\varepsilon}{8\pi}\iiint E\bar{E}dxdydl} \quad (6)$$

The integrals in (6) will be reduced to two-dimensional one if a layer thickness Δl corresponds the condition $I(x,y,l)\approx I(x\ y)$ at $l\in(l_0\pm\Delta l)$. Then

$$L_\sigma = -\frac{\sin 2\theta}{2\omega}\frac{\iint(xI'_x + yI'_y)dxdy}{\iint Idxdy}, \quad (7)$$

where ω - angular frequency of light.

Supposing $\iint(xI_x + yI_y)dxdy = -\iint 2Idxdy$ we shall receive:

$$L_\sigma = \frac{\sin 2\theta}{\omega} \quad (8)$$

The polarizing moment L (8) versus ellipticity β=tgθ for $\omega = 3 \cdot 10^{15}$ s^{-1} is shown on Figure 1. The β was determined as the ratio of small and large semi-axis components of a polarization vector.

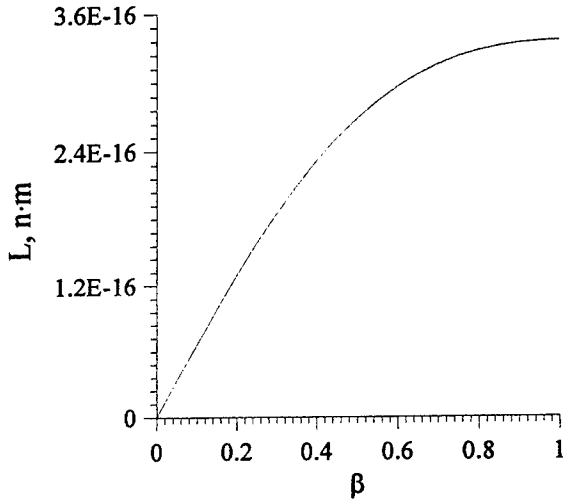


Fig. 1. Dependence of a polarizing moment L on an ellipticity of polarization β.

Thus, the rotary moment M on the part of elliptically polarized light that effects a particle of the radius r and the absorptive ability α, trapped by a laser beam of a radius w(z) and power P, is described by the formula

$$M = \frac{P\alpha}{\omega}\frac{2\beta}{1+\beta^2}\left(1 - \exp\left\{\frac{-2r^2}{w^2(z)}\right\}\right), \quad (9)$$

3. EXPERIMENT

The experimental setup for the real time rotation of particles is shown on Figure 2. He-Ne laser (LGN-215) (1) was used with the maximum power output ≈ 70 mW. To perform the single-beam gradient optical trap the laser beam was directed by the beam splitter (6) into the polarization microscope MIN-8 with an immersion microobjective (90x, NA=1.25) (7). For an image plane adjustment with a focal plane of the microobjective the assembling lens (5) with a focal length of 0.1 m was placed in the front of the microobjective. This system allows forming a laser beam with a waist diameter about 1.5 microns. The maximum power of focused light irradiating a particle was 10 mW. Suspended in spirit Teflon particles (diameter 0,5 microns) were used as absorptive particles. These particles form larger particles of the various sizes and shapes by mean of the agglutination. The dredge of these particles was placed in cell (8). The frequency of trapped Teflon particles rotation in a focal point of a Gaussian laser beam was measured for various degrees of an ellipticity of polarization of an irradiating beam after installing of a fixed mode. For the real time control of the polarization degree the liquid crystal modulator (LCM) (3) working on S-effect [10] was developed. The nematic liquid crystal 1348 with a birefringence Δn=0.227 for λ=0.6328 μm was used in this modulator. The modulator was placed on an optical axis before a lens (5). The modulator was controlled by the low-frequency generator (4). The initial orientation of the director of a layer LC was 45^0 in relation to polarization of an incident radiation.

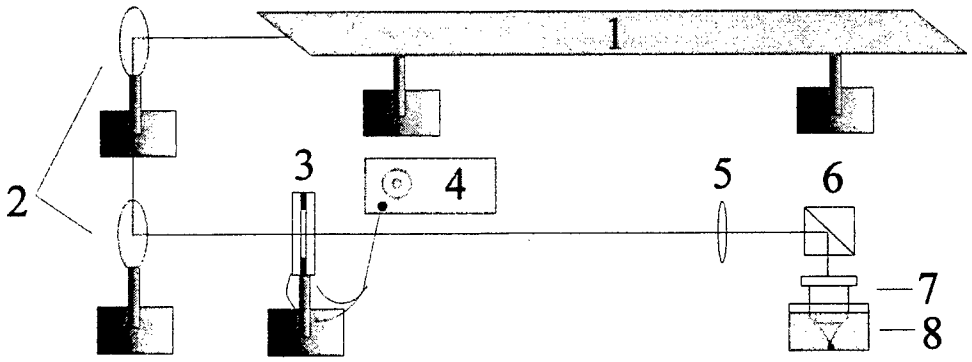


Fig. 2. The experimental setup: 1 - He-Ne laser; 2 - mirrors; 3 - LCM; 4 - low-frequency generator; 5 - assembling lens; 6 – beam splitter; 7 - microobjective; 8 - cell with particles.

On Figure 3 the fragment of the dependence of the intensity of passing through LCM laser beam, located between crossed (X) and parallel (II) polarizes on the supplied control voltage of 10 kHz frequency is shown. This fragment of the dependence is the most convenient for using in the experiments because of smaller sensitivity relative to controlling voltage. From this graph the state of light polarization behind the modulator was determined.

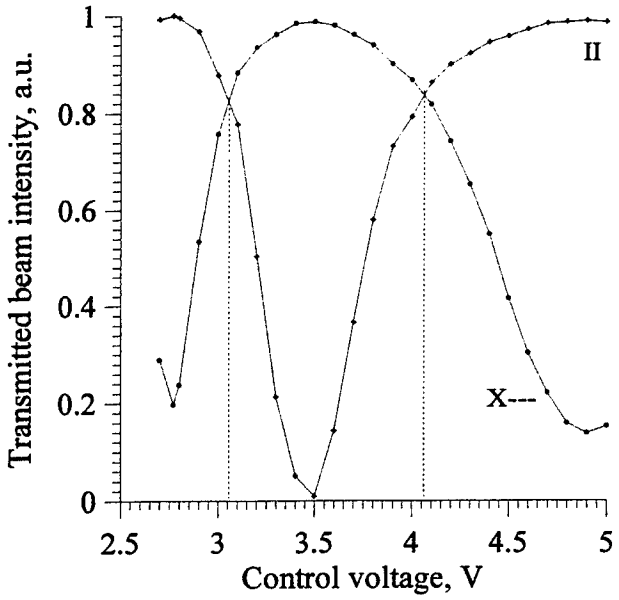


Fig. 3. The characteristic LCM, removed in crossed - X and parallel - II polarizers

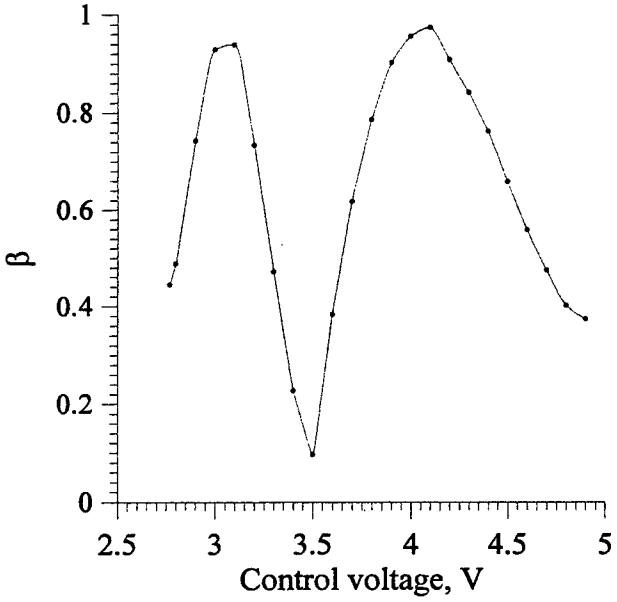


Fig. 4. The dependence of a degree of an ellipticity of polarization of light, past through LCM, on the control voltage.

The control voltage about 3 V and 4 V corresponds to circularly polarized light and about 3.5 V - linearly polarized. The polarization of the light passing through was varied from circular up to linear by mean of the LCM control voltage variation. And, accordingly, frequency of rotation of the trapped particle was varied. On Figure 4 the dependence of the polarization ellipticity of the light passing through LCM on control voltage is shown for a selected part of the curve.

On Figure 5 dependence of the rotation frequency of a Teflon particle on control voltage on LCM is shown. The rotation was observed up to a full stop of a particle. A particle stayed, when the angular momentum became insufficient or other particle adhered to it. On a voltage from 2.8 V up to 3.5 V the particle rotated clockwise with maximum speed at control voltage equal 2.91 V. With further voltage increasing to the state of linear polarization (3.5 V) and higher, the particle began to rotate counter-clockwise and the maximum rotation rate was achieved at controlling voltage equal 4.015 V. Using the

data shown on Figures 4 and 5, it is possible to obtain the experimental dependence of rotation frequency of a Teflon particle on ellipticity of polarization of laser radiation (Fig. 6).

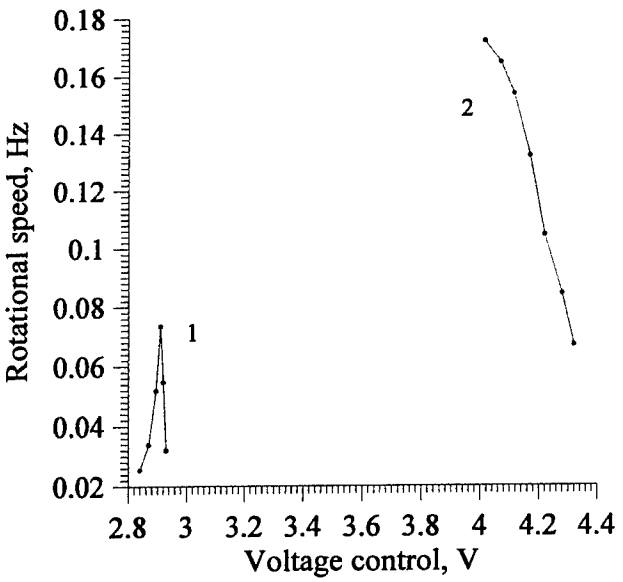


Fig. 5. The dependence of frequency of rotation on control voltage: 1 - rotation clockwise; 2 - rotation counter-clockwise.

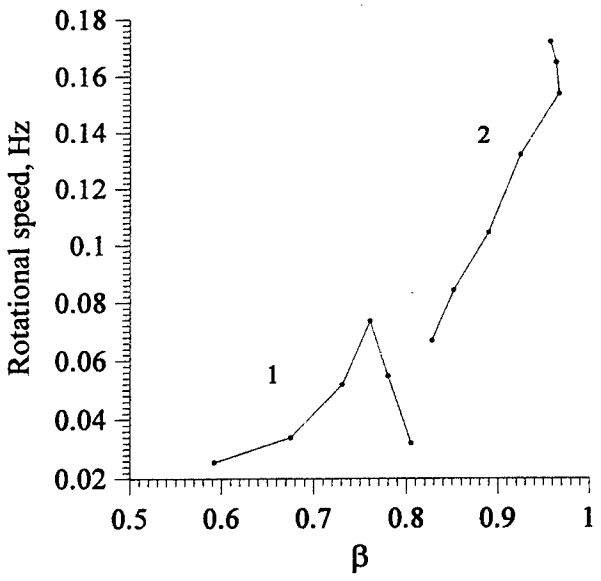


Fig. 6. The dependence of the frequency of rotation of a Teflon particle on a degree of an ellipticity of polarization of the laser radiation.

The work was made at support FPP "Integration" (project 2.1 - 235) and RFFI (grant № 99-02-16513).

4. REFERENCES

1. A. Sadowsky. Acta Comment. Imp. // Universit. Jurievensis 7, 1, 1899; 8, 1, 1900.
2. R.A. Beth, Phys. Rev. 50, 115, 1936.
3. P.L. Marston, J. H. Crichton, Phys. Rev A 30, 2508, 1984.
4. S. Chang, S.S. Lee, J. Opt. Soc. Am. B 2, 1853, 1985.
5. J.P. Barton, D.R. Alexander, S.A. Schaub, "Theoretical determination of net radiation force and torque for a spherical particle illuminated by a focused laser beam", J. Appl. Phys. 66, pp. 4594-4602, 1989.
6. M.E.J. Friese, T.A. Nieminen, N.R. Heckenberg, H. Rubinsztein-Dunlop, "Optical torque controlled by elliptical polarization", Optics Letters, Vol. 23, № 1, pp. 1-3, 1998.
7. N.B. Simpson, K. Dholakia, L. Allen, M.J. Padgett, "Mechanical equivalence of spin and orbital angular momentum of light: an optical spanner", Optics Letters, Vol. 22, № 1, pp.52-54, 1997.
8. M.E.J. Friese, J. Enger, H. Rubinsztein-Dunlop, N.R. Heckenberg, "Optical angular-momentum transfer to trapped absorbing particles", Phys. Rev A. Vol. 54, № 2, pp. 1593-1596, 1996.
9. M.J. Padgett, L. Allen, "Optical tweezers and spanners", Phys. World, pp. 35-38, September 1997.
10. L.M. Blinov. M.: Nauka. 1978.

Photorefractive four-wave mixing for optical image restoration

Yoshihisa Takayama [a], Atsushi Okamoto [b], and Kenichi Araki [a]
[a] Communications Research Laboratory, 4-2-1 Nukui-Kita
Koganei, Tokyo 184-8795 Japan
[b] Faculty of Engineering, Hokkaido University, Kita 13 Nishi 8, Kita-ku
Sapporo, Hokkaido 060-0813 Japan

ABSTRACT

We describe an optical image restoration by using holographic filtering and photorefractive four-wave mixing. A beam generated by four-wave mixing, that is, the phase conjugate beam, reads a hologram recorded by a blurred image and blur function, where the four-wave mixing process is influenced by an erase beam which has the information of the blur function. We calculate the generation efficiency of the phase conjugate beam and show that the amplitude of the phase conjugate beam can be inversely proportional to the intensity of the erase beam. We also simulate the image restoration by preparing sample images and show that the blur effect can be removed from the distorted image by this method.

Keywords: photorefractive, four-wave mixing, image restoration, deconvolution, holographic filtering

1. INTRODUCTION

Optical information processing by means of the Fourier transform has been actively studied and many applications of this kind of processing have been proposed [1-3]. Spatial filtering techniques using the holograms and the Fourier transforms have been employed in various applications such as the joint transform correlation, associative memory, and image encryption. Especially image restoration removing the distortion from a blurred image has been widely discussed and improvements in this technique have been reported [4-8].

Optical image restoration requires a filter, so-called inverse filter, whose amplitude transmittance is inversely proportional to the power spectrum of the blur function. Such a filter can be obtained by, for example, preparing a suitable photographic film by the appropriate exposure, development, and fixing processes [9]. But the time taken to complete all of these processes is of the order of minutes. This is so long that a filter prepared by this way is of little use in real-time image restoration. It has recently become possible to obtain the desired image quality by using image detectors and computers [10], but even efficient algorithms and high-performance computers cannot always restore large images quickly enough when high resolution is needed.

Photorefractive effect has attracted much interest because of its potential in recording holograms in real-time, and many applications of photorefractive effect have been proposed [11-13]. Four-wave mixing using a photorefractive medium is one of the methods to generate the phase conjugate beam, and detailed investigations on generating the phase conjugate beam have been done. The amplitude of a phase conjugate beam is known to decrease when a beam incoherent to any other beams used in the four-wave mixing process is applied to the photorefractive medium [14]. This incoherent beam is

Laser Optics 2000: Control of Laser Beam Characteristics and Nonlinear Methods for Wavefront Control,
Leonid N. Soms, Vladimir E. Sherstobitov, Editors, Proceedings of SPIE Vol. 4353 (2001)
© 2001 SPIE · 0277-786X/01/$15.00

called the erase beam because it attenuates the amplitude of the grating induced by the four-wave mixing in the photorefractive medium. If the decrease in the amplitude of the phase conjugate beam is inversely proportional to the intensity of the erase beam, photorefractive four-wave mixing can be used as a function of the inverse filter and the image restoration will be advanced to the real-time processing. Besides the four-wave mixing process has an advantage over computational techniques because the response time is independent of the size and resolution of the image to be treated.

In this paper we show that photorefractive four-wave mixing is useful for real-time image restoration when the Fourier transform of the blur function is used as the erase beam. We derive an expression for the amplitude of the phase conjugate beam and perform the numerical estimation to determine the required range of the intensity of the erase beam in which the amplitude of the phase conjugate beam is inversely proportional to the intensity of the erase beam. We indicate an optical setup for the image restoration by using the four-wave mixing and show the result of simulation of the image restoration.

2. PHOTOREFRACTIVE FOUR-WAVE MIXING

A schematic drawing of photorefractive four-wave mixing is shown in Fig. 1, where A_1 is the probe beam, A_2 is the forward pump beam, A_3 is the backward pump beam, and A_4 is the phase conjugate beam. The beams are mutually coherent, but only interference between A_1 and A_2 and interference between A_3 and A_4 are taken into consideration, because we assume here that the crossing angles between the other pair of beams are so large that the photorefractive effects induced by interference between those pairs are so weak as to be negligible [11]. The beam A_e is the erase beam, which does not interfere with any other beams and attenuates the induced photorefractive grating. $z = 0$ and $z = L$ represent the boundaries of the medium.

This four-wave mixing process can be described by a well-known set of equations:

$$\frac{dA_1(z)}{dz} = \frac{\gamma A_2(z)}{2(I_0 + I_e)}\left\{A_1(z)A_2(z)^* + A_3(z)A_4(z)^*\right\} \tag{1a}$$

$$\frac{dA_2(z)^*}{dz} = \frac{-\gamma A_1(z)^*}{2(I_0 + I_e)}\left\{A_1(z)A_2(z)^* + A_3(z)A_4(z)^*\right\} \tag{1b}$$

$$\frac{dA_3(z)}{dz} = \frac{-\gamma A_4(z)}{2(I_0 + I_e)}\left\{A_1(z)A_2(z)^* + A_3(z)A_4(z)^*\right\} \tag{1c}$$

$$\frac{dA_4(z)^*}{dz} = \frac{\gamma A_3(z)^*}{2(I_0 + I_e)}\left\{A_1(z)A_2(z)^* + A_3(z)A_4(z)^*\right\}, \tag{1d}$$

where $I_0 = \sum_{j=1}^{4} I_j$, $I_j = |A_j|^2$, $I_e = |A_e|^2$, and γ is the coupling coefficient for the interaction between the beams. The asterisks denote complex conjugates. Although any A_j (j=1-4) is a function of z, I_0 is independent of z [11,12]. A given I_e is also constant for any value of z because the erase beam simply passes through the medium. The coupling coefficient is in general a complex number, but it can be a real number if no external field is applied to the medium. In the photorefractive four-wave mixing process, both pairs of A_1 and A_2, and A_3 and A_4 contribute to

writing the photorefractive grating. However we assume here that the pair of A_1 and A_2 is dominant in writing the grating, and adopt the condition of

$$\left|A_3 A_4^*\right| << \left|A_1 A_2^*\right| \tag{2}$$

in Eqs. (1a)-(1d) [11]. When each beam is described as $A_j(z) = \sqrt{I_j(z)}\exp\{i\varphi_j(z)\}$ for j=1, 2, 3, 4, and e, we obtain

$$A_1(z) = \sqrt{\frac{I_1(0)(1+m)}{m+\exp\left[-\dfrac{(1+m)\gamma z}{1+m+n+mr_e}\right]}}\exp\{i\varphi_1(0)\} \tag{3a}$$

$$A_2(z) = \sqrt{\frac{I_1(0)(1+m^{-1})}{1+m\exp\left[\dfrac{(1+m)\gamma z}{1+m+n+mr_e}\right]}}\exp\{i\varphi_2(0)\} \tag{3b}$$

$$A_3(z) = \sqrt{\frac{n}{m}I_1(0)}\exp\{i\varphi_3(L)\}\cos\{\nu(z)\} \tag{3c}$$

$$A_4(z) = \sqrt{\frac{n}{m}I_1(0)}\exp\{-i\varphi_1(0)\}\exp[i\{\varphi_2(0)+\varphi_3(L)\}]\sin\{\nu(z)\}, \tag{3d}$$

where

$$\nu(z) = \tan^{-1}\left[\sqrt{m}\exp\left\{\frac{(1+m)\gamma z}{1+m+n+mr_e}\right\}\right] - \tan^{-1}\left[\sqrt{m}\exp\left\{\frac{(1+m)\gamma L}{1+m+n+mr_e}\right\}\right] \tag{4a}$$

$$m = \frac{I_1(0)}{I_2(0)} \tag{4b}$$

$$n = \frac{I_3(L)}{I_2(0)} \tag{4c}$$

$$r_e = \frac{I_e}{I_1(0)} \tag{4d}$$

and φ_j is the phase of the j-th beam. In deriving Eqs. (3a)-(3d), we have assumed that the incident intensities of the probe beam, forward pump beam, and backward pump beam on the medium are already known and are respectively represented by $I_1(0)$, $I_2(0)$, and $I_3(L)$. We have also adopted a boundary condition for the phase conjugate beam $I_4(L) = 0$.

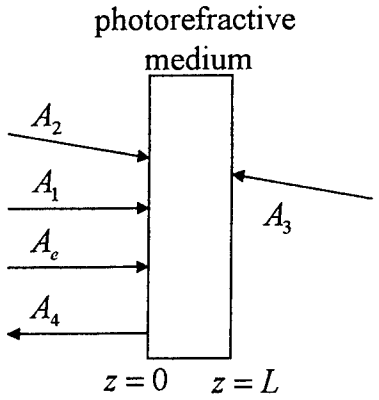


Figure 1. Schematic drawing of photorefractive four-wave mixing

3. NUMERICAL ESTIMATION OF FOUR-WAVE MIXING

We calculate the relation between the amplitude of the phase conjugate beam and the intensity of the erase beam. Here we use criteria analogous to the ones used to describe the characteristics of photographic films, the photographic density and the photographic development factor.

In the case of photographic films, the relation between the incident intensity I_{in} and the transparent intensity I_{tr} for a film after development depends on the exposure E of the film. This relation is generally represented as a photographic characteristic curve by plotting the photographic density $D=\log(I_{in}/I_{tr})$ against $\log(E)$. The inclination of the linear portion of the photographic characteristic curve is the development factor, so-called gamma. When the value of the development factor is 2, the amplitude transparency of the film after development is inversely proportional to the intensity used to expose the film. In this case, by using the Fourier transform of the blur function of the distorted image to expose the photographic film, we can obtain the inverse filter used in image restoration.

In the case of photorefractive four-wave mixing, the relation between the incident intensity of the probe beam $I_1(0)$ and the generated intensity of the phase conjugate beam $I_4(0)$ depends on the ratio of the erase beam intensity to the probe beam intensity r_e described in Eq. (4d). Therefore we define a criterion correspondent to the photographic density D as

$$D_{PR}=\log\left\{\frac{I_1(0)}{I_4(0)}\right\}. \tag{5}$$

By plotting D_{PR} against $\log(r_e)$, we can obtain the value of the inclination of the curve as γ_{ph} which is analogous to the development factor gamma. The calculated result of D_{PR} against $\log(r_e)$ is shown in Fig. 2, where the values of m, n, and γL are respectively given as 1, 0.1 and 1, and the value of $I_1(0)$ is given as 1 for normalization. The inclination of this curve was calculated and is shown in Fig. 3. We note that the value of γ_{ph} becomes 2 in the range of $\log(r_e)\geq 2.5$, or $I_e\geq 10^{2.5}$. By using the Fourier transform of the blur function of the distorted image as the erase beam and maintaining the condition $I_e\geq 10^{2.5}$, we can employ the four-wave mixing as the inverse filter for image restoration.

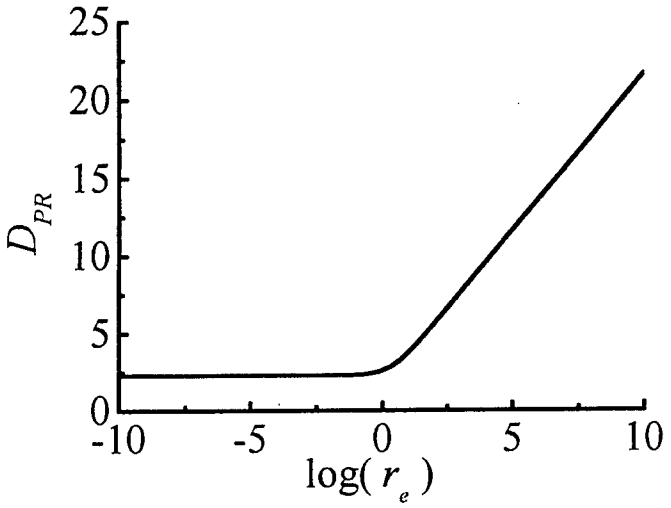


Figure 2. The intensity of phase conjugate beam against the intensity of the erase beam.

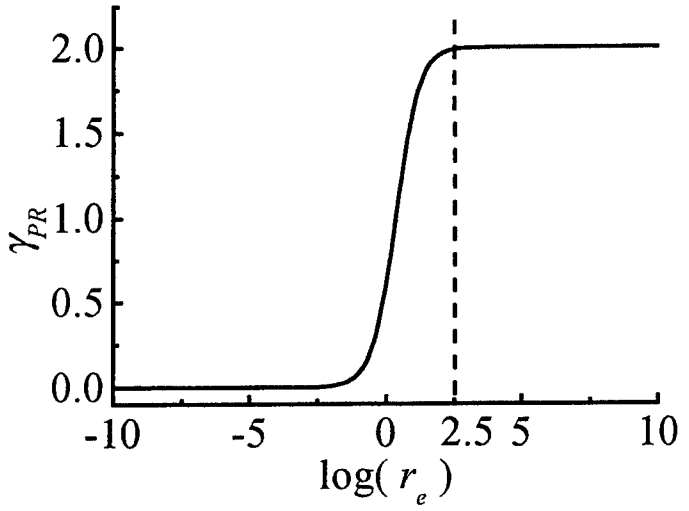


Figure 3. The inclination of the curve shown in Fig. 2.

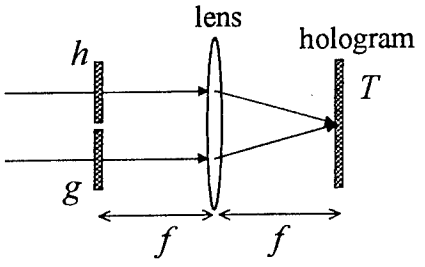
4. IMAGE RESTORATION

The optical setup for the image restoration employing photorefractive four-wave mixing is shown in Fig. 4. Figure 4(a) is the writing process of a hologram and (b) is the reading process of the hologram. Photorefractive four-wave mixing is used in the reading process. In these figures, we respectively represent the amplitude transparencies proportional to the blurred image and blur function as g and h, where g is given by the convolution of the original object o and h. The amplitude transparency of the recorded hologram is proportional to $|aG+bH|^2$, where G and H is the Fourier transforms of g and h, and a and b are complex constants dependent on the locations of the images.

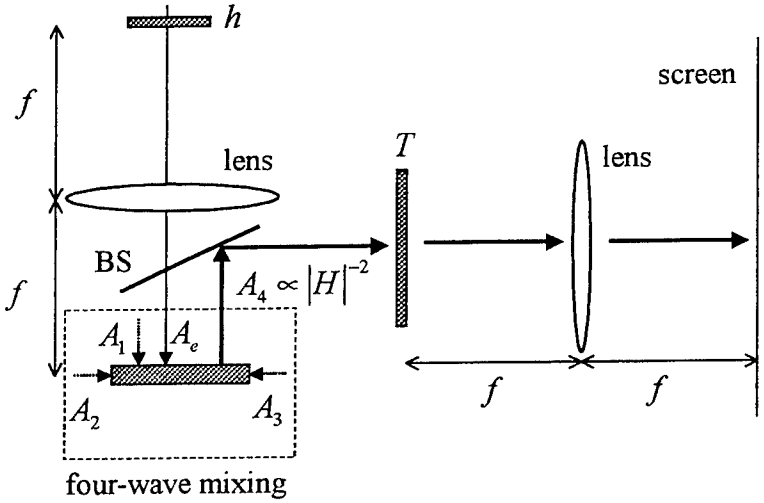
In the reading process of the hologram, we use the Fourier transform of h as the erase beam to the four-wave mixing. When the intensity of the erase beam keeps the condition indicated in Fig. 3, the amplitude of the phase conjugate beam is inversely proportional to the intensity of the erase beam $|H|^2$. The amplitude of the phase conjugate beam after passing through the hologram is proportional to

$$|aG+bH|^2|H|^{-2} = \left(|aG|^2 + |bH|^2 + a^*bG^*H + ab^*GH^*\right)|H|^{-2}, \tag{5}$$

where the asterisks denote the complex conjugate. Since the Fourier transform of g is given by $G=OH$, the fourth term of Eq. (5) is ab^*O, and the Fourier transform of this term yields the original object o. Although the constant ab^* accompanies, this constant will only shift the location at which the object o appears and will not affect its quality. Thus the original object o can be restored from the distorted image g.



(a)



(b)

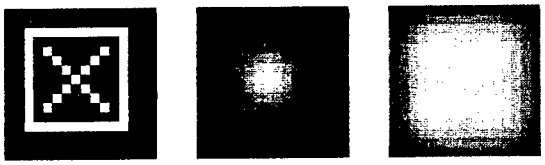
Figure 4. Schematic drawing of image restoration. (a) Writing process, and (b) reading process of hologram.

5. SIMULATION

We simulate the image restoration based on our method with the sample images shown in Fig. 5. Figures 5(a), (b), and (c) are respectively the distorted image g, the blur function h, and the original object o, where h has a Gaussian

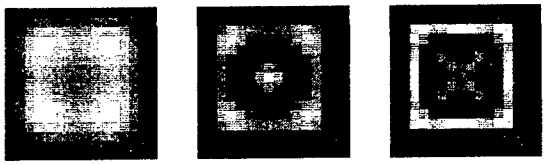
profile and g is given by the convolution of o and h. The Fourier transforms of g and h are recorded as a hologram, and the hologram is read by the beam coming from photorefractive four-wave mixing in which the Fourier transform of h is used as the erase beam. The condition of four-wave mixing assumed for calculation is the same as that used in Fig. 2; $m=1$, $n=0.1$, and $\gamma L=1$. We also use the normalized intensity $I_1(0)=1$.

We define I_h as the intensity of a beam used to illuminate h in Fig. 4(b). The restored images are shown in Fig. 6, where (a), (b), and (c) correspond to the cases of I_h=10^3, 10^6, and 10^9, respectively. Figure 7 is a schematic drawing of the relation between the power spectrum of h denoted by the solid line and the required intensity of the erase beam $I_e=10^{2.5}$ denoted by the dotted lines, where the dotted lines A, B, and C respectively correspond to the cases of I_h=10^3, 10^6, and 10^9. In the case of Fig. 6(a), the power spectrum of the erase beam is under the line A and an accurate image restoration is not performed. In the case of Fig. 6(b), part of the power spectrum is over the line B. Image restoration for this part is carried out and the structure of the object slightly appears. In the case of Fig. 6(c), most of the power spectrum is over the line C, and the structure of the original object emerges rather clearly. But even in this case, the restored image is not completely the same as the original object o, because the region of high spatial frequency is still under the line C and an accurate restoration is not performed for this portion. If the intensity used to illuminate h in Fig. 4(b) becomes larger, the region of spatial frequency for accurate image restoration extends due to the lowering of the relative position of the dotted line in Fig. 7, and a more clearly restored image will be obtained.



(a) (b) (c)

Figure 5. Sample images for simulation. (a) original object, (b) blur function, (c) distorted image.



(a) (b) (c)

Figure 6. Simulation result of image restoration. The blur function h in Fig. 4(b) is illuminated with the intensity (a) I_h=10^3, (b) 10^6, and (c) 10^9.

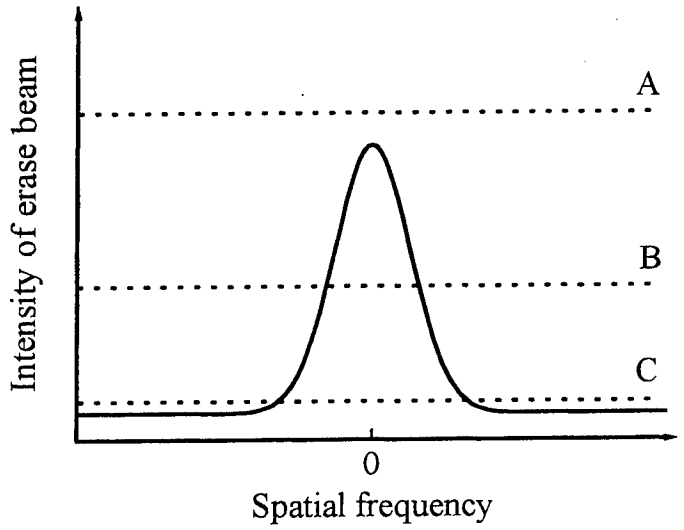


Figure 7. Schematic drawing of the relation between the power spectrum of the blur function and the required intensity of the erase beam for accurate image restoration.

6. CONCLUSION

We have attempted to use photorefractive four-wave mixing in image restoration as a function of the inverse filter used in the reading process of the recorded hologram. We have shown that the amplitude of the generated phase conjugate beam can be inversely proportional to the intensity of the erase beam when the intensity of the erase beam is much stronger than other beams contributing to four-wave mixing process. We have simulated the image restoration by our method and shown that the structure of the object gradually emerges as the intensity of the erase beam increases.

REFERENCES

1. J. W. Goodman, *Introduction to Fourier Optics*, McGraw-Hill, New York, 1980.
2. A. Vanderlugt, *Optical Signal Processing*, John Wiley & Sons, Inc. New York, 1992.
3. K. Iizuka, *Engineering Optics*, Springer-Verlag, Berlin, 1987.
4. F. T. S. Yu, Q. W. Song, Y. S. Cheng, and D. A. Gregory, "Comparison of detection efficiency for VanderLugt and joint transform correlators," Appl. Opt. **29**, 2, pp. 225-232, 1990.
5. Y. Owechko, G. J. Dunning, E. Marom, and B. H. Soffer, "Holographic associative memory with nonlinearities in the correlation domain," Appl. Opt. **26**, 10, pp. 1900-1919, 1987.
6. B. Javidi, G. Zhang, and J. Li, "Encrypted optical memory using double-random phase encoding," Appl. Opt. **36**, 5, pp. 1054-1058, 1997.
7. J.-M. Conan, L. M. Mugnier, T. Fusco, V. Michau, and G. Rousset, "Myopic deconvolution of adaptive optics images by use of object and point-spread function power spectra," Appl. Opt. **37**, 21, pp. 4614-4622, 1998.

8. B. Javidi, H. J. Caulfield, and J. L. Horner, "Image deconvolution by nonlinear signal processing," Appl. Opt. **28**, 15, pp. 3106-3111, 1989, Chap. 20.
9. M. Bass, ed., *Handbook of Optics Fundamentals, Techniques, and Design Volume I*, McGraw-Hill, Inc. New York, 1995.
10. N. A. Bezina, A. A. Leshchev, M. V. Vasil'ev, and V. Yu. Venediktov, "Numerical simulation of observational telescope with the dynamic holographic correction," *Adaptive Optical System Technologies*, D. Bonaccini and R. K. Tyson, ed., Proc. SPIE **3353**, pp. 210-214, 1998.
11. P. Yeh, Introduction to Photorefractive Nonlinear Optics, John Wiley & Sons, Inc. New York, 1993.
12. M. Cronin-Golomb, B. Fischer, J. O. White, and A. Yariv, "Theory and applications of four-wave mixing in photorefractive media," IEEE J. Quantum Electron. **QE-20**, 1, pp. 12-30, 1984.
13. M. H. Farzad and M. T. Tavassoly, "Degenerate four-wave mixing without slowly varying amplitude approximation," J. Opt. Soc. Am. B, **14**, 7, pp. 1707-1715, 1997.
14. J. Zhang, H. Gao, Y. Zhu, and P. Ye, "Reduction of fanning influence in two-wave mixing coefficient measurement in thick crystals," Appl. Phys. Lett. **68**, 16, pp. 2174-2176, 1996.

On relation between the wave aberration function and the phase transfer function in an adaptive optical system for earth observation

A. J. Smirnov[a] and A. B. Utkin[b*]

[a] Universidade da Beira Interior, Covilhã 6200, Portugal
[b] Institute for Laser Physics, St. Petersburg 199034, Russia

ABSTRACT

We demonstrate how to correct odd-order aberrations (tilt, coma, etc.) of the imaging system on the basis of information containing in the phase transfer function. For earth-observation systems this information can be obtained just by accumulation of the detected images, without source of the reference beam or wavefront detector. This technique is beneficial for elaborating robust equipment for long-term operation in autonomous conditions.

Keywords: remote sensing, adaptive optics, wavefront correction, Fourier optics, wave aberration, optical transfer function, pupil function.

1. INTRODUCTION

According to the principles of the wave optics, the phase distortion of an initially plane transverse reference wave by an optical system can be quantitatively represented by the *wave aberration* function Ψ describing the phase distribution at the exit pupil plane XY. Thus, in the presence of wave aberrations the *generalized pupil function*[1] $P(x,y)$ is characterized by the complex value

$$P(x,y) = A(x,y)e^{i\Psi(x,y)} \tag{1}$$

where the amplitude $A(x,y)$ is unity inside and zero outside the pupil aperture. The distorted wavefront produces the *coherent impulse response* $H_c(x_{im}, y_{im})$ in the image plane $X_{im}Y_{im}$

$$H_c(x_{im}, y_{im}) = \frac{A_c}{\lambda z_{ei}} \iint_{-\infty}^{+\infty} P(x,y) e^{-i\frac{2\pi}{\lambda z_{ei}}(x_{im}x + y_{im}y)} dxdy \tag{2}$$

where λ is the operating wavelength of the image detector, z_{ei} is the distance between the exit pupil and the image, and A_c is a constant amplitude.

Optical properties of the incoherent-light imaging system is defined by the light intensity, rather than the amplitude, distribution at the image plane, that is, by the *incoherent (intensity) impulse response* $H(x_{im}, y_{im})$

$$H(x_{im}, y_{im}) = \left|H_c(x_{im}, y_{im})\right|^2 = H_c(x_{im}, y_{im}) H_c^*(x_{im}, y_{im}) \tag{3}$$

The complex optical *transfer function* (OTF) H_f is defined in the space of the spatial frequencies u and v along x_{im} and y_{im} axes as a Fourier image of the impulse response

* Further author information:
A. J. S.: E-mail: smirnov@ubista.ubi.pt
A.B.U.: E-mail: anoutkine@yahoo.com

Laser Optics 2000: Control of Laser Beam Characteristics and Nonlinear Methods for Wavefront Control, Leonid N. Soms, Vladimir E. Sherstobitov, Editors, Proceedings of SPIE Vol. 4353 (2001)
© 2001 SPIE · 0277-786X/01/$15.00

$$H_f(u,v)=\frac{\int\limits_{-\infty}^{+\infty}\iint H(x_{im},y_{im})e^{-i2\pi(x_{im}u+y_{im}v)}dx_{im}dy_{im}}{\int\limits_{-\infty}^{+\infty}\iint H(x_{im},y_{im})dx_{im}dy_{im}} \tag{4}$$

This function can be represented in the modulus-argument notation as follows

$$H_f(u,v)=B(u,v)e^{i\Phi(u,v)} \qquad B(u,v)=\left|H(u,v)\right|, \quad \Phi(u,v)=arg\left(H(u,v)\right) \tag{5}$$

where the real functions $B(u,v)$ and $\Phi(u,v)$ are referred to as the *modulation transfer function* and the *phase transfer function* respectively (for detailed discussion on the above definitions see Ref. 1 and references therein).

As it has been shown previously,[2] the phase transfer function may be obtained without additional measuring equipment, just via the statistical analysis of spatial spectra of the sufficiently large set of monochromatic images produced by the optical system in question. Being separated from the initial wave aberration function Ψ by rather long chain of transforms (2)-(5), the phase transfer function still contains some information about the phase distortions introduced by the optical train. Thus, it is possible to create very simple adaptive control loop that uses this information for improvement of the imaging quality. In principle, such a loop consists of nothing but a numerical processor that analyzes the output-channel information, restores the wave aberration function, and finally constructs a set of the driving signals for the adaptive optical element. Neither the source of the reference beam nor the wavefront sensor is needed. Application of this technique would be extremely beneficial for robust autonomous systems, such as aircraft- and satellite-based optical trains for earth observation.

The straightforward algorithm for the wave aberration restoration is based upon representation of Ψ as a finite set of conventional aberration terms described mathematically by the Zernike polynomials

$$\Psi(x,y)=\Psi_p(r,\varphi)=\sum_n\sum_m \Psi_{n,m}Z_n^m(r,\varphi) \tag{6}$$

where $\Psi_p(r,\varphi)$ is representation of $\Psi(x,y)$ in polar coordinates r,φ derived from the initial Cartesian system XY. The first ten Zernike polynomials are depicted in Table 1.

Then some initial values of the sought coefficients $\left\{\Psi_{n,m}^{(0)}\right\}$ are specified and corresponding phase transfer function $\Phi^{(0)}(u,v)$ is constructed with the help of relations (2)-(5). The set of desired coefficients to the expansion (6) (and, correspondingly, estimation to the wave aberration function) is obtained in the course of iterative variations

$$\left\{\Psi_{n,m}^{(k-1)}\right\} \mapsto \left\{\Psi_{n,m}^{(k)}=\Psi_{n,m}^{(k-1)}+\Delta\Psi_{n,m}^{(k)}\right\} \tag{7}$$

of the initial set in order to minimize some criterion function $\Xi=\Xi\left(\left\{\Psi_{n,m}\right\}\right)$ that is the measure of difference between the constructed dependence $\Phi^{(k)}(u,v)$ and the phase transfer function $\Phi(u,v)$ obtained by statistical analysis of the detected images. The classical example implies combination of the mean-square criterion function

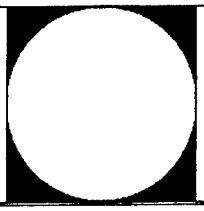
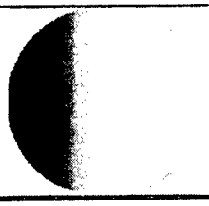
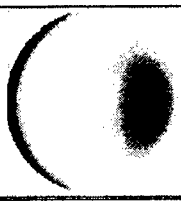
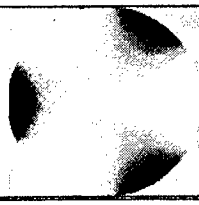
$$\Xi=\int\limits_{-\infty}^{+\infty}\iint\left(\Phi^{(k)}(u,v)-\Phi(u,v)\right)^2 dudv \tag{8}$$

and the gradient method for the coefficient variation (7).

It should be noted, however, that applicability of the above straightforward numerical methods needs additional theoretical proof, as there is no confidence in the fact that all information about the initial wave aberration is preserved in the phase transfer function after the chain of transformations (2)-(7). The second (complex modulus) and the last (complex argument) irreversible operations are a priori suspicious in point of the information loss. It is revealed in poor convergence of the iterative process (7) and unsatisfactory accuracy of the final result. These shortcomings cannot be cured with intricate numerical techniques as they are originated from the underlying physics. As a result, for the case in question unconcerned application of the standard variational methods leads to ineffective control algorithms and dysfunction of the adaptive control loop as a whole.

In the present work we derive a quadrature formula that links the wave aberration function and the phase transfer function of the imaging system with the circular pupil. Analysis of this relation with respect to the information loss enables us to evolve a subset of the conventional aberration terms that effectively add to the phase transfer function.

Table 1. First ten Zernike polynomials

		m = 0	**m = ±1**	**m = ±2**	**m = ±3**
n = 0	name	piston			
	angular part	1			
	radial part ($R_n^{\lvert m \rvert}$)	1			
	grayscale plot				
n = 1	name		tilt		
	angular part		$(+)\cos\varphi$ $(-)\sin\varphi$		
	radial part ($R_n^{\lvert m \rvert}$)		r		
	grayscale plot				
n = 2	name	defocus		astigmatism	
	angular part	1		$(+)\cos(2\varphi)$ $(-)\sin(2\varphi)$	
	radial part ($R_n^{\lvert m \rvert}$)	$2r^2-1$		r^2	
	grayscale plot				
n = 3	name		lateral coma		three-leaf clover
	angular part		$(+)\cos\varphi$ $(-)\sin\varphi$		$(+)\cos(3\varphi)$ $(-)\sin(3\varphi)$
	radial part ($R_n^{\lvert m \rvert}$)		$3r^3-2r$		r^3
	grayscale plot				

2. BASIC RELATION

Substituting (2) into (3) yields the explicit relation for the impulse response

$$H(x_{im},y_{im}) = H_c(x_{im},y_{im})H_c^*(x_{im},y_{im}) = \frac{|A_c|^2}{\lambda^2 z_{ei}^2}\int_{-\infty}^{+\infty}\iiint A(x_1,y_1)A(x_2,y_2)e^{i(\Psi(x_1,y_1)-\Psi(x_2,y_2))}e^{i\frac{2\pi}{\lambda z_{ei}}(x_{im}(x_2-x_1)+y_{im}(y_2-y_1))}dx_1dy_1dx_2dy_2 \tag{9}$$

and the OTF

$$H_f(u,v) = A_f\int_{-\infty}^{+\infty}\iiint A(x_1,y_1)A(x_2,y_2)e^{i(\Psi(x_1,y_1)-\Psi(x_2,y_2))}e^{i2\pi x_{im}\left(\frac{x_2-x_1}{\lambda z_{ei}}-u\right)}e^{i2\pi y_{im}\left(\frac{y_2-y_1}{\lambda z_{ei}}-v\right)}dx_1dy_1\,dx_2dy_2\,dx_{im}dy_{im} \tag{10}$$

where A_f is the scaling coefficient defined by (4) so that $H_f(0,0)=1$. Using the well-known Fourier-integral representation of the Dirac delta function

$$\int_{-\infty}^{+\infty}e^{i2\pi x\varsigma}dx = \delta(\varsigma) \tag{11}$$

one has

$$H_f(u,v) = A_f\int_{-\infty}^{+\infty}\iint A(x_1,y_1)A(x_2,y_2)\,e^{i(\Psi(x_1,y_1)-\Psi(x_2,y_2))}\,\delta\left(\frac{x_2-x_1}{\lambda z_{ei}}-u\right)\delta\left(\frac{y_2-y_1}{\lambda z_{ei}}-v\right)dx_1dy_1\,dx_2dy_2 \tag{12}$$

Change of variables $x_2 \mapsto \frac{x_2-x_1}{\lambda z_{ei}}$, $y_2 \mapsto \frac{y_2-y_1}{\lambda z_{ei}}$ leads immediately to

$$H_f(u,v) = \lambda^2 z_{ei}^2 A_f\int_{-\infty}^{+\infty}\iint A(x,y)A(x+\lambda z_{ei}u,y+\lambda z_{ei}v)\,e^{i(\Psi(x,y)-\Psi(x+\lambda z_{ei}u,y+\lambda z_{ei}v))}\,dxdy \tag{13}$$

Employing the relation $H_f(0,0)=1$ yields

$$A_f = \left(\lambda^2 z_{ei}^2\int_{-\infty}^{+\infty}\iint A^2(x,y)dxdy\right)^{-1} = \left(\lambda^2 z_{ei}^2\int_{-\infty}^{+\infty}\iint A(x,y)dxdy\right)^{-1} = \frac{1}{\lambda^2 z_{ei}^2 S_p} \tag{14}$$

where S_p is the area of the exit pupil. Thus, the basic relation between the wave aberration function $\Psi(x,y)$ and the OTF $H_f(u,v)$ takes the form

$$H_f(u,v) = \frac{1}{S_p}\int_{-\infty}^{+\infty}\iint A(x,y)A(x+\lambda z_{ei}u,y+\lambda z_{ei}v)\,e^{i(\Psi(x,y)-\Psi(x+\lambda z_{ei}u,y+\lambda z_{ei}v))}\,dxdy \tag{15}$$

Change of variables $x \mapsto x-\frac{1}{2}\lambda z_{ei}u$, $y \mapsto y-\frac{1}{2}\lambda z_{ei}v$ enables us to write the symmetric expression

$$H_f(u,v) = \frac{1}{S_p}\int_{-\infty}^{+\infty}\iint A\left(x-\frac{1}{2}\lambda z_{ei}u,y-\frac{1}{2}\lambda z_{ei}v\right)A\left(x+\frac{1}{2}\lambda z_{ei}u,y+\frac{1}{2}\lambda z_{ei}v\right) \times e^{i\left(\Psi\left(x-\frac{1}{2}\lambda z_{ei}u,y-\frac{1}{2}\lambda z_{ei}v\right)-\Psi\left(x+\frac{1}{2}\lambda z_{ei}u,y+\frac{1}{2}\lambda z_{ei}v\right)\right)}\,dxdy \tag{16}$$

3. OPTICAL TRANSFER FUNCTION FOR IMAGING SYSTEM WITH CIRCULAR PUPIL

For the imaging system with circular exit pupil of the radius R the amplitude part of the pupil function is

$$A(x,y)=h\left(1-\frac{\sqrt{x^2+y^2}}{R}\right), \qquad h(\varsigma)=\begin{cases}0 & \text{for } \varsigma<0\\ 1/2 & \text{for } \varsigma=0\\ 1 & \text{for } \varsigma>0\end{cases} \tag{17}$$

To evaluate further the OTF, we must explicitly represent (16) as an integral over the actual domain of integration, which is the intersection of two circles shown in Fig. 1. To do this, let us first express the OTF via dimensionless polar coordinates of the spatial frequencies ρ,α as follows

$$u=\frac{2R}{\lambda z_{ei}}\cdot\rho\cos\alpha, \quad v=\frac{2R}{\lambda z_{ei}}\cdot\rho\sin\alpha \tag{18}$$

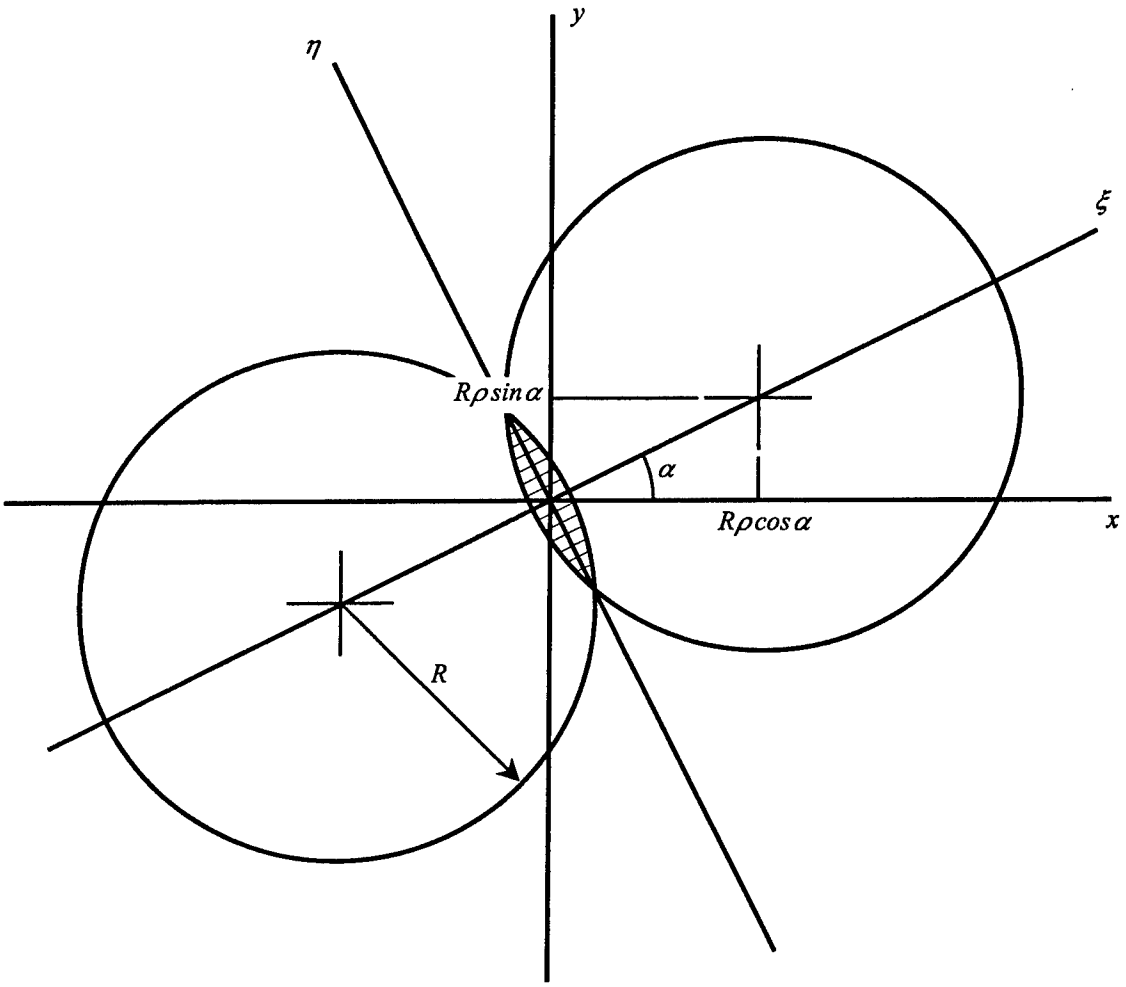


Figure 1. Calculation of the optical transfer function: coordinate systems and the domain of integration.

and, then, pass to the dimensionless Cartesian coordinates

$$\xi=\frac{x}{R}\cos\alpha+\frac{y}{R}\sin\alpha, \quad \eta=-\frac{x}{R}\sin\alpha+\frac{y}{R}\cos\alpha \tag{19}$$

that coincide with the axes of symmetry to the domain of integration (see Fig. 1.). Now $H_f(u,v)$ can be represented via its polar-coordinate counterpart $H_{fp}(\rho,\alpha)$ as follows

$$
\begin{aligned}
H_f(u,v) &= H_{fp}\left(\rho=\frac{\lambda z_{ei}}{2R}\sqrt{u^2+v^2},\alpha=arg(u+iv)\right)\\
&=\frac{1}{\pi}\int_{-\sqrt{1-\rho^2}}^{\sqrt{1-\rho^2}}\int_{-\left(\sqrt{1-\eta^2}-\rho\right)}^{\sqrt{1-\eta^2}-\rho} e^{i(\Psi_\alpha(\xi,-\rho,\eta)-\Psi_\alpha(\xi,\rho,\eta))}\,d\xi\,d\eta\\
&=\frac{1}{\pi}\int_{0}^{\sqrt{1-\rho^2}}\int_{-\left(\sqrt{1-\eta^2}-\rho\right)}^{\sqrt{1-\eta^2}-\rho} e^{i(\Psi_\alpha(\xi,-\rho,\eta)-\Psi_\alpha(\xi,\rho,\eta))}\,d\xi\,d\eta\\
&+\frac{1}{\pi}\int_{-\sqrt{1-\rho^2}}^{0}\int_{-\left(\sqrt{1-\eta^2}-\rho\right)}^{\sqrt{1-\eta^2}-\rho} e^{i(\Psi_\alpha(\xi,-\rho,\eta)-\Psi_\alpha(\xi,\rho,\eta))}\,d\xi\,d\eta
\end{aligned}
\tag{20}
$$

where

$$
\Psi_\alpha(\xi,\rho,\eta)=\Psi(x=((\xi+\rho)\cos\alpha-\eta\sin\alpha)R,\ y=((\xi+\rho)\sin\alpha+\eta\cos\alpha)R) \tag{21}
$$

and ρ is supposed to vary within the range $0\le\rho<1$ as for $\rho\ge1$ the area of the integrand carrier is zero, so the value of $H_{fp}(\rho,\alpha)$ is also zero. Change of variables $\eta\mapsto-\eta,\xi\mapsto-\xi$ in the last integral leads us to

$$
\begin{aligned}
H_{fp}(\rho,\alpha)&=\frac{1}{\pi}\int_{0}^{\sqrt{1-\rho^2}}\int_{-\left(\sqrt{1-\eta^2}-\rho\right)}^{\sqrt{1-\eta^2}-\rho} e^{i(\Psi_\alpha(\xi,-\rho,\eta)-\Psi_\alpha(\xi,\rho,\eta))}\,d\xi\,d\eta\\
&+\frac{1}{\pi}\int_{0}^{\sqrt{1-\rho^2}}\int_{-\left(\sqrt{1-\eta^2}-\rho\right)}^{\sqrt{1-\eta^2}-\rho} e^{i(\Psi_\alpha(-\xi,-\rho,-\eta)-\Psi_\alpha(-\xi,\rho,-\eta))}\,d\xi\,d\eta
\end{aligned}
\tag{22}
$$

Combining two integrals into one, we get representation of the OTF in the dimensionless polar coordinates that possess more symmetry than initial expression (16)

$$
H_{fp}(\rho,\alpha)=\frac{1}{\pi}\int_{0}^{\sqrt{1-\rho^2}}\int_{-\left(\sqrt{1-\eta^2}-\rho\right)}^{\sqrt{1-\eta^2}-\rho}\left(e^{i(\Psi_\alpha(\xi,-\rho,\eta)-\Psi_\alpha(\xi,\rho,\eta))}+e^{-i(\Psi_\alpha(-\xi,\rho,-\eta)-\Psi_\alpha(-\xi,-\rho,-\eta))}\right)d\xi\,d\eta \tag{23}
$$

4. REPRESENTATION OF OPTICAL TRANSFER FUNCTION VIA ABERRATION TERMS

To investigate the linkage between the OTF and the aberration terms representing phase distortion at the exit pupil plane, we should first pass to the polar-coordinate representation

$$
\Psi(x,y)=\Psi_p\left(r=\frac{\sqrt{x^2+y^2}}{R},\varphi=\arg(x+iy)\right)=\sum_n\sum_m\Psi_{nm}Z_n^m(r,\varphi) \tag{24}
$$

where r,φ are dimensionless polar coordinates of the point x,y and $Z_n^m(r,\varphi)$ are the Zernike polynomials, $n\le0$, $-n\le m\le n$, $n-|m|$ is even. There are several representations of the Zernike polynomials reported in literature; in order to avoid nested complex-number notation, here we use the real-valued form

$$
Z_n^m(r,\varphi)=\begin{cases}R_n^m(r)\cos(m\varphi) & \text{for}\quad m\ge0\\ R_n^{|m|}(r)\sin(m\varphi) & \text{for}\quad m<0\end{cases}
\qquad
R_n^m(r)=\sum_{k=0}^{\frac{n-m}{2}}\frac{(-1)^k(n-k)!}{k!\left(\frac{n+m}{2}-k\right)!\left(\frac{n-m}{2}-k\right)!}r^{n-2k} \tag{25}
$$

Explicit form of the expansion (24) is

$$\Psi_p(r,\varphi)=V_e(r,\varphi)+V_o(r,\varphi)$$
$$V_e(r,\varphi)=\sum_{n=0}^{\infty}\sum_{m=-n}^{n}\Psi_{2n,2m}Z_{2n}^{2m}(r,\varphi),\quad V_o(r,\varphi)=\sum_{n=0}^{\infty}\sum_{m=-n-1}^{n}\Psi_{2n+1,2m+1}Z_{2n+1}^{2m+1}(r,\varphi) \tag{26}$$

One can check by direct calculations or geometrical constructions based on Fig. 1 that the phase components presenting in the integrand of the relation for the OTF (23) are expressed in terms of polar-coordinate function $\Psi_p(r,\varphi)$ as follows

$$\begin{aligned}
\Psi_\alpha(\xi,-\rho,\eta) &= \Psi(((\xi-\rho)\cos\alpha-\eta\sin\alpha)R,((\xi-\rho)\sin\alpha+\eta\cos\alpha)R) &&= \Psi_p(r_-,\varphi_-)\\
\Psi_\alpha(\xi,\rho,\eta) &= \Psi(((\xi+\rho)\cos\alpha-\eta\sin\alpha)R,((\xi+\rho)\sin\alpha+\eta\cos\alpha)R) &&= \Psi_p(r_+,\varphi_+)\\
\Psi_\alpha(-\xi,\rho,-\eta) &= \Psi(-((\xi-\rho)\cos\alpha-\eta\sin\alpha)R,-((\xi-\rho)\sin\alpha+\eta\cos\alpha)R) &&= \Psi_p(r_-,\varphi_-+\pi)\\
\Psi_\alpha(-\xi,-\rho,-\eta) &= \Psi(-((\xi+\rho)\cos\alpha-\eta\sin\alpha)R,-((\xi+\rho)\sin\alpha+\eta\cos\alpha)R) &&= \Psi_p(r_+,\varphi_++\pi)
\end{aligned} \tag{27}$$

where $r_\pm=\sqrt{(\xi\pm\rho)^2+\eta^2}$, $\varphi_\pm=arg(\xi\pm\rho+i\eta)+\alpha$. Thus we get the following representation of the OTF in terms of the classical aberrations

$$\begin{aligned}
H_{fp}(\rho,\alpha)=\frac{1}{\pi}\int_0^{\sqrt{1-\rho^2}}\int_{-\left(\sqrt{1-\eta^2}-\rho\right)}^{\sqrt{1-\eta^2}-\rho}&\left(e^{i(V_e(r_-,\varphi_-)+V_o(r_-,\varphi_-)-V_e(r_+,\varphi_+)-V_o(r_+,\varphi_+))}\right.\\
&\left.+e^{-i(V_e(r_-,\varphi_-+\pi)+V_o(r_-,\varphi_-+\pi)-V_e(r_+,\varphi_++\pi)-V_o(r_+,\varphi_++\pi))}\right)d\xi\,d\eta
\end{aligned} \tag{28}$$

Noticing that

$$\begin{aligned}
V_e(r,\varphi+\pi)&=\sum_{n=0}^{\infty}\sum_{m=-n}^{n}\Psi_{2n,2m}Z_{2n}^{2m}(r,\varphi+\pi)=\sum_{n=0}^{\infty}\sum_{m=-n}^{n}\Psi_{2n,2m}R_{2n}^{2m}(r)\begin{pmatrix}\cos(2m\varphi+2m\pi)\\ \sin(2m\varphi+2m\pi)\end{pmatrix}\\
&=\sum_{n=0}^{\infty}\sum_{m=-n}^{n}\Psi_{2n,2m}R_{2n}^{2m}(r)\begin{pmatrix}\cos(2m\varphi)\\ \sin(2m\varphi)\end{pmatrix}=\sum_{n=0}^{\infty}\sum_{m=-n}^{n}\Psi_{2n,2m}Z_{2n}^{2m}(r,\varphi)=V_e(r,\varphi)
\end{aligned} \tag{29}$$

and

$$\begin{aligned}
V_o(r,\varphi+\pi)&=\sum_{n=0}^{\infty}\sum_{m=-n-1}^{n}\Psi_{2n+1,2m+1}Z_{2n+1}^{2m+1}(r,\varphi+\pi)\\
&=\sum_{n=0}^{\infty}\sum_{m=-n-1}^{n}\Psi_{2n+1,2m+1}R_{2n+1}^{2m+1}(r)\begin{pmatrix}\cos((2m+1)\varphi+(2m+1)\pi)\\ \sin((2m+1)\varphi+(2m+1)\pi)\end{pmatrix}\\
&=\sum_{n=0}^{\infty}\sum_{m=-n-1}^{n}\Psi_{2n+1,2m+1}R_{2n+1}^{2m+1}(r)\begin{pmatrix}-\cos((2m+1)\varphi)\\ -\sin((2m+1)\varphi)\end{pmatrix}=-V_o(r,\varphi)
\end{aligned} \tag{30}$$

one can reduce (28) to

$$\begin{aligned}
H_{fp}(\rho,\alpha)=\frac{1}{\pi}\int_0^{\sqrt{1-\rho^2}}\int_{-\left(\sqrt{1-\eta^2}-\rho\right)}^{\sqrt{1-\eta^2}-\rho}&\left(e^{i(V_e(r_-,\varphi_-)-V_e(r_+,\varphi_+))}+e^{-i(V_e(r_-,\varphi_-)-V_e(r_+,\varphi_+))}\right)\\
&\times e^{-i(V_o(r_+,\varphi_+)-V_o(r_-,\varphi_-))}d\xi\,d\eta
\end{aligned} \tag{31}$$

and get final polar-coordinate representations of the OTF and the phase transfer function via classical aberration terms

$$H_{fp}(\rho,\alpha)=\frac{2}{\pi}\int_0^{\sqrt{1-\rho^2}}\int_{-\left(\sqrt{1-\eta^2}-\rho\right)}^{\sqrt{1-\eta^2}-\rho}\cos(V_e(r_+,\varphi_+)-V_e(r_-,\varphi_-))e^{-i(V_o(r_+,\varphi_+)-V_o(r_-,\varphi_-))}d\xi\,d\eta \tag{32}$$

$$\Phi(u,v)=\Phi_p\left(\rho=\frac{\lambda z_{ei}}{2R}\sqrt{u^2+v^2},\alpha=arg(u+iv)\right)$$
$$=arg\left(\int_0^{\sqrt{1-\rho^2}}\int_{-\left(\sqrt{1-\eta^2}-\rho\right)}^{\sqrt{1-\eta^2}-\rho}cos\left(V_e(r_+,\varphi_+)-V_e(r_-,\varphi_-)\right)e^{-i\left(V_o(r_+,\varphi_+)-V_o(r_-,\varphi_-)\right)}d\xi\,d\eta\right) \tag{33}$$

5. RESTORATION OF THE WAVE ABERRATION FUNCTION

General quadrature formula (33) obtained for the imaging system with the circular pupil do not provide explicit relation between the phase transfer function $\Phi_p(\rho,\alpha)$ and the wave aberration function $\Psi_p(r,\varphi)$ that is needed for data processing in the adaptive control loop. However, the results obtained enable us to make the following conclusions:

(i) An inherent limitation is imposed into any adaptive control technique based entirely on the phase transfer function information: only odd-order aberrations can be corrected. In the absence of these aberrations the OTF becomes purely real

$$H_{fp}(\rho,\alpha)=\frac{2}{\pi}\int_0^{\sqrt{1-\rho^2}}\int_{-\left(\sqrt{1-\eta^2}-\rho\right)}^{\sqrt{1-\eta^2}-\rho}cos\left(V_e(r_+,\varphi_+)-V_e(r_-,\varphi_-)\right)d\xi\,d\eta$$

Thus, in condition of small phase perturbations $\Phi_p(\rho,\alpha)\equiv 0$ while for Ψ it jumps abruptly between two fixed values, 0 and π, following the sign of the OTF.

(ii) The even aberration terms V_e represent the only inherent information loss in the chain of transformations (3)-(5) of the wave aberration function into the phase transfer function. That is, in principle, in the absence of noise and detection discretization errors all remaining aberrations V_o can be restored.

To illustrate the latter statement, let us turn to one more representation of the phase transfer function, $\Phi_\varepsilon(\varepsilon,\alpha)$, this time via the variable $\varepsilon=\sqrt{1-\rho^2}$

$$\Phi_p(\rho,\alpha)=\Phi_\varepsilon\left(\varepsilon=\sqrt{1-\rho^2},\alpha\right) \tag{34}$$

and suppose that the wave aberration function can be represented with enough accuracy via the first decade of the Zernike polynomials, that is

$$V_e(r,\varphi)\approx\Psi_{0,0}+\Psi_{2,-2}r^2\sin(2\varphi)+\Psi_{2,0}\left(2r^2-1\right)+\Psi_{2,2}r^2\cos(2\varphi)$$
$$V_o(r,\varphi)\approx\Psi_{1,-1}r\sin\varphi+\Psi_{1,1}r\cos\varphi+\Psi_{3,-3}r^3\sin(3\varphi)+\Psi_{3,-1}\left(3r^3-2r\right)\sin\varphi \tag{35}$$
$$+\Psi_{3,1}\left(3r^3-2r\right)\cos\varphi+\Psi_{3,3}r^3\cos(3\varphi)$$

Then the algorithm of restoration of the odd-order terms (defined by their coefficients $\{\Psi_{2\beta+1,2\mu+1}\}$) to the wave aberration function from the phase transfer function $\Phi(u,v)$ consists of the following stages:

(i) The dimensionless coordinate system $\varepsilon\in[0,1],\ \alpha\in[0,2\pi]$ is introduced according to formulas (18) and (34)

$$\varepsilon=\sqrt{1-\rho^2}=\sqrt{1-\left(\frac{\lambda z_{ei}}{2R}\right)\left(u^2+v^2\right)},\quad \alpha=arg(u+iv) \tag{36}$$

and the initial phase transfer function $\Phi(u,v)$ is represented in this coordinate system

$$\Phi_\varepsilon(\varepsilon,\alpha)=\Phi_p\left(\rho=\sqrt{1-\varepsilon^2},\alpha\right)=\Phi\left(u=\frac{2R}{\lambda z_{ei}}\sqrt{1-\varepsilon^2}\cos\alpha,\ v=\frac{2R}{\lambda z_{ei}}\sqrt{1-\varepsilon^2}\sin\alpha\right) \tag{37}$$

(ii) Using interpolating procedures (see, for example, Ref. 3), the obtained function $\Phi_\varepsilon(\varepsilon,\alpha)$ is expanded into the Taylor series with respect to ε^2 in the vicinity of $\varepsilon = 0$

$$\Phi_\varepsilon(\varepsilon,\alpha) = \Phi_0(\alpha) + \Phi_1(\alpha)\varepsilon^2 + \Phi_2(\alpha)\varepsilon^4 + \ldots \tag{38}$$

that yields functions $\Phi_0(\alpha)$ and $\Phi_1(\alpha)$ of only one argument.

(iii) The above functions are further reduced to a set of six constant coefficients

$$\begin{aligned}
\Phi_{0,-3} &= \frac{1}{\pi}\int_0^{2\pi}\Phi_0(\alpha)\sin(3\alpha)\,d\alpha \quad & \Phi_{0,3} &= \frac{1}{\pi}\int_0^{2\pi}\Phi_0(\alpha)\cos(3\alpha)\,d\alpha \\
\Phi_{0,-1} &= \frac{1}{\pi}\int_0^{2\pi}\Phi_0(\alpha)\sin\alpha\,d\alpha & \Phi_{0,1} &= \frac{1}{\pi}\int_0^{2\pi}\Phi_0(\alpha)\cos\alpha\,d\alpha \\
\Phi_{1,-1} &= \frac{1}{\pi}\int_0^{2\pi}\Phi_1(\alpha)\sin\alpha\,d\alpha & \Phi_{1,1} &= \frac{1}{\pi}\int_0^{2\pi}\Phi_1(\alpha)\cos\alpha\,d\alpha
\end{aligned} \tag{39}$$

(iv) Desired six odd-order Zernike-polynomial coefficients are calculated according to the formulas

$$\Psi_{1,\pm1} = -\frac{1}{48}\left(29\Phi_{0,\pm1} + 10\Phi_{1,\pm1}\right), \quad \Psi_{3,\pm1} = \frac{5}{48}\left(\Phi_{0,\pm1} + 2\Phi_{1,\pm1}\right), \quad \Psi_{3,\pm3} = -\frac{1}{2}\Phi_{0,\pm3} \tag{40}$$

To prove the aberration restoration technique (37)-(40), note that after the change of variables $\rho \mapsto \sqrt{1-\varepsilon^2}$, $\eta \mapsto \varepsilon\mu$, $\xi \mapsto \varepsilon^2\gamma$ expression for the phase transfer function (33) in the vicinity of $\varepsilon = 0$ becomes

$$\begin{aligned}
\Phi_\varepsilon(\varepsilon,\alpha) &= \arg\left(\int_0^1\int_{-\gamma_0}^{\gamma_0}\cos\left(V_e(r_+,\varphi_+) - V_e(r_-,\varphi_-)\right)e^{-i\left(V_o(r_+,\varphi_+) - V_o(r_-,\varphi_-)\right)}d\gamma\,d\mu\right) \\
\gamma_0 &= \frac{\sqrt{1-(\varepsilon\mu)^2} - \sqrt{1-\varepsilon^2}}{\varepsilon^2} = \frac{1}{2}\left(1-\mu^2\right) + \frac{1}{8}\left(1-\mu^4\right)\varepsilon^2 + O\left(\varepsilon^4\right), \quad r_\pm = \sqrt{\left(\varepsilon^2\gamma \pm \sqrt{1-\varepsilon^2}\right)^2 + \varepsilon^2\mu^2} \\
\varphi_+ &= \arctan\left(\frac{\varepsilon\mu}{\sqrt{1-\varepsilon^2} + \varepsilon^2\gamma}\right) + \alpha, \quad \varphi_- = \pi - \arctan\left(\frac{\varepsilon\mu}{\sqrt{1-\varepsilon^2} - \varepsilon^2\gamma}\right) + \alpha
\end{aligned} \tag{41}$$

that yields the expansion

$$\Phi_\varepsilon(\varepsilon,\alpha) = -2V_o(1,\alpha) + \frac{1}{5}\left(4\frac{\partial V_o}{\partial r}(1,\alpha) - \frac{\partial^2 V_o}{\partial\varphi^2}(1,\alpha)\right)\varepsilon^2 + O\left(\varepsilon^4\right) \tag{42}$$

Comparing (42) with (38) one gets

$$\Phi_0(\alpha) = -2V_o(1,\alpha), \quad \Phi_1(\alpha) = \frac{1}{5}\left(4\frac{\partial V_o}{\partial r}(1,\alpha) - \frac{\partial^2 V_o}{\partial\varphi^2}(1,\alpha)\right) \tag{43}$$

Substitution of (43) into (39) and use of explicit representation (35) as well as orthogonality of the angular terms lead us to the system of linear equations

$$\Phi_{0,\pm3} = -2\Psi_{3,\pm3}, \quad \Phi_{0,\pm1} = -2\left(\Psi_{1,\pm1} + \Psi_{3,\pm1}\right), \quad \Phi_{1,\pm1} = \frac{1}{5}\left(5\Psi_{1,\pm1} + 29\Psi_{3,\pm1}\right) \tag{44}$$

whose solution is represented by (40).

Taking more terms of the expansion (42), one can get additional phase transfer function parameters $\{\Phi_{q,l}\}$ and, correspondingly, extra equations for the coefficients $\{\Psi_{2n+1,2m+1}\}$ of the higher-order Zernike polynomials that may be added to series (35).

6. CONCLUSION

This work demonstrates possibility of correction of the odd-order wave aberrations (tilt and coma) on the basis of information containing in the phase transfer function. As it was shown in Ref. 2, for the earth observation satellite systems this information can be readily obtained just by accumulation of the detected images. Correction of the even-order aberrations, mostly defocus, may require separate loop of the adaptive control. Additional investigations are required for definition of the precision and stability of the restoration algorithms. The quasi-analytical algorithm discussed here clearly demonstrates that all odd-order aberrations influence the behavior of the phase transfer function near the limit of circular area of its definition. In the deeper-laid parts of the area (except for the very center where the phase transfer function tends to zero) the influence is believed to be strong as well. However, large integration domain does not enable us to obtain as analyzable relations as in the case above. Thus, in the presence of substantial noise the numerical prediction-correction algorithms discussed in the Introduction may turn out to be more accurate, as they cover all domain of definition of the phase transfer function. Here the coefficient estimation (40) can serve as an initial prediction $\left\{\varphi_{n,m}^{(0)}\right\}$, while the criterion function should allow for nearly zero sensitivity of the phase transfer function to the even-order aberrations.

ACKNOWLEDGMENTS

This work was carried out within the framework of Contract 3/3.1/CTAE/1929/95 (Program PRAXIS-XXI).

REFERENCES

1. J. W. Goodman, *Introduction to Fourier Optics*, McGrow-Hill, New York, 2nd ed., 1996.
2. A. J. Smirnov, J. A. R. Pacheco de Carvalho, Utkin A. B., "Dynamic aberration measurement in earth observation adaptive optics systems," in *Sensors, Systems, and Next-Generation Satellites II*, H. Fujisada, ed., *Proc. SPIE*, **3498**, pp. 471-482, 1998.
3. W. H. Press, S. A. Teukolsky, W. T. Vetterling, and B. P. Flannerly, *Numerical Recipes in C: The Art of Scientific Computing*. Cambridge University. Press, Cambridge, New York, etc., 2nd ed., 1997 (on-line Internet access: www.nr.com).

Brillouin nonlinearity as a mechanism of dynamic holography

Oleg Kotiaev[a], Shigeaki Uchida[a], Hiroshi Sawada[b]

[a]Institute for Laser Technology, 2-6 Yamada-oka, Suita, 565-0871, Osaka, Japan
[b]Kinki University, 3-4-1 Kowakae, Higashi-Osaka, 577-0818, Osaka, Japan

ABSTRACT

The dynamic holography is considered as the most perspective technique of correction for dynamic aberrations of large-aperture optical elements when operating in near IR range. The use of fluorocarbon Flourinert FC-72, characterized by Brillouin nonlinearity, for recording the dynamic hologram has been demonstrated experimentally. Resonant enhancement of the hologram's diffraction efficiency resulting in 10 times growth has been shown. Diffraction efficiency over 50% has been obtained. Different behavior of diffraction efficiency in dependence on intensity of recording beams and length of nonlinear medium has been shown. Capability of correction of laser beam distortions as well as dynamic behavior of recorded hologram have been tested. The random phase distortions bringing about 20 times increase of the laser beam divergence have been corrected resulting in near-diffraction quality of a point object image. It has been shown that lifetime of the hologram does not exceed 10^{-9} sec. Perspective of the use of Brillouin enhanced dynamic holography for nonlinear compensation of optical aberrations has been presented.

Keywords: dynamic holography, Brillouin nonlinearity, correction for aberrations

1. INTRODUCTION

The dynamic holography[1-3] is considered as the most perspective technique of correction for dynamic aberrations of large-aperture optical elements. Figure 1 shows the use of dynamic holography for imaging the remote object.

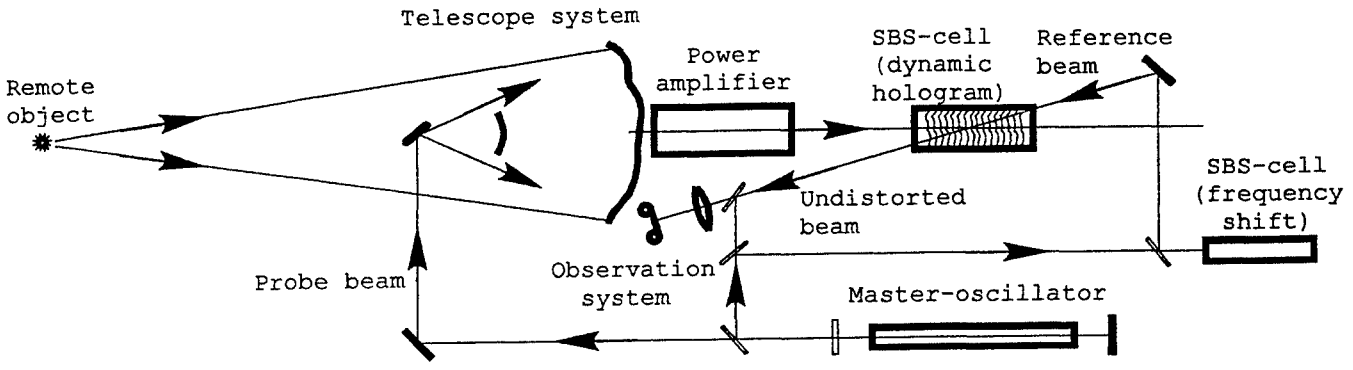


Fig.1 The use of dynamic holography for imaging the remote object

Imagine there is a telescope system with primary mirror of poor quality, for example lightweight deployable membrane, and it is necessary to obtain image of the remote object. The use of dynamic holography will help to improve this image up to

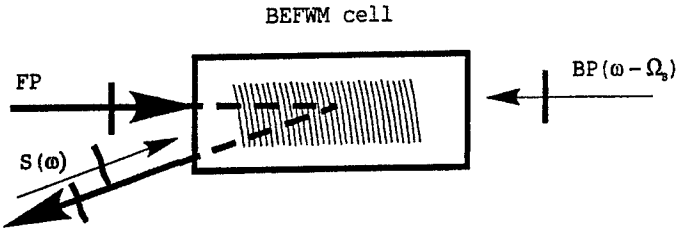
*Correspondence: Tel.: +81-6-6879-8737, Fax: +81-6-6878-1568, E-mail: oleg@ile.osaka-u.ac.jp

Laser Optics 2000: Control of Laser Beam Characteristics and Nonlinear Methods for Wavefront Control, Leonid N. Soms, Vladimir E. Sherstobitov, Editors, Proceedings of SPIE Vol. 4353 (2001)
© 2001 SPIE · 0277-786X/01/$15.00

diffraction quality. The following is the principal of operation. Dynamic hologram is recorded inside the cell filled with special nonlinear medium. The two beams record the hologram: high quality reference beam and probe beam passed through optical system and containing information about aberrations. Radiation coming from the remote object is subjected to the same distortions as the probe beam. This radiation reads out the recorded dynamic holography producing undistorted beam. As a result, corrected image of the remote object can be observed. Dynamic holography allows developing and using the telescope systems with large-aperture or segmented primary mirrors of lower weight and lower cost.

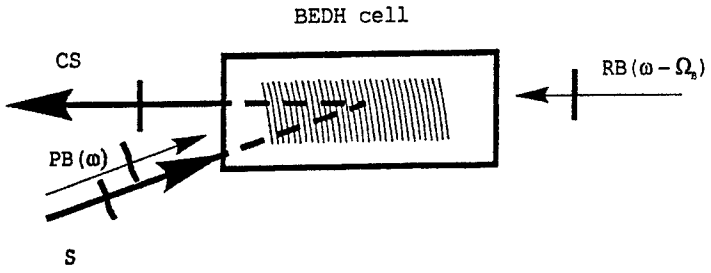
2. BRILLOUIN ENHANCED FOUR WAVE MIXING AND BRILLOUIN ENHANCED DYNAMIC HOLOGRAPHY

However, in the near infrared range (~1 μm), the use of dynamic holography is restricted by low diffraction efficiency of the hologram recorded under degenerate interaction. We suggest using the well-known effect of Brillouin Enhanced Four Wave Mixing[4-6] for increasing the diffraction efficiency. The effect is known by Phase Conjugation ability of extremely weak signals with a large reflection coefficient.



S(ω)	Signal to be conjugated
BP(ω − Ω_B)	Backward Pump with Brillouin frequency shift
FP	Forward pump
PC	Phase Conjugated signal

Fig.2-a. Brillouin Enhanced Four-Wave Mixing



PB(ω)	Probe Beam
RB(ω − Ω_B)	Reference Beam with Brillouin frequency shift
S	Signal to be corrected
CS	Corrected Signal

Fig.2-b. Brillouin Enhanced Dynamic Holography

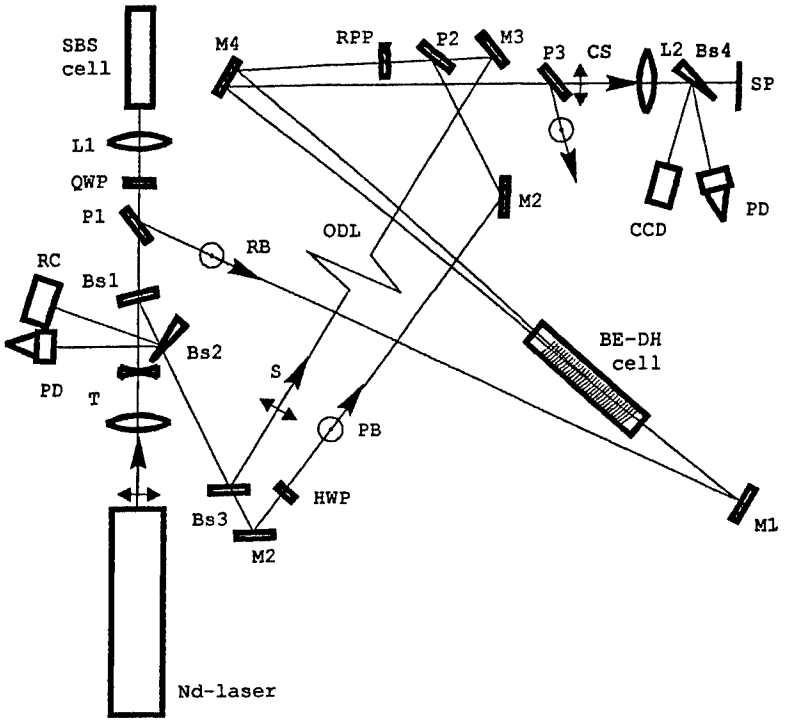
As you know, the technique of Brillouin Enhanced Four Wave Mixing is just a form of nearly degenerate four wave mixing (Figure 2-a). Mixing and interaction occur inside a cell filled with nonlinear medium which is characterized by Brillouin nonlinearity.

The incoming signal to be conjugated interacts with coherent backward pump beam which has a Brillouin frequency shift with respect to the incoming signal, so that the produced interference pattern moves at close to acoustic velocity and drives an acoustic (hypersonic) wave. This wave scatters the forward pump beam to form the conjugate beam. Additional interference between scattered (conjugated) beam and forward pump results in amplification of the acoustic wave and increase of its efficiency in scattering. This increase takes place until a significant fraction of available power is extracted from the forward pump beam into the conjugated beam. As a result, power of the conjugated beam can achieve the order of the forward pump power magnitude which is much more than power of the incoming signal to be conjugated.

The mentioned above acoustic wave can be considered as a dynamic hologram and efficiency in scattering is just diffraction efficiency. In our experiment, we used Brillouin scattering for increasing the diffraction efficiency. In our case, the dynamic hologram was recorded by probe and reference beams (see Figure 2-b). Then it was read out by signal to be corrected, which propagated in the same direction as the probe beam. This signal was scattered effectively by the hologram (acoustic wave). As a result, the high quality beam arose, which was used for image formation.

3. EXPERIMENTAL SETUP

Figure 3 shows the experimental setup. Experimental setup allowed to determine energetic, spatial and temporal characteristics of laser signals. The main parameters subject to study were diffraction efficiency of dynamic hologram, correction fidelity and life time of dynamic hologram.



Equipment:

Nd-laser: MOPA,
E = 1 J, t = 20 ns, d = 15 mm
SBS cell - Stimulated Brillouin Scattering cell
BE-DH cell - Brillouin Enhanced Dynamic Hologram cell
Nonlinear medium - liquid fluorocarbon
Flourinert FC-72 refractive index n = 1.248
sound velocity v_s = 512 m/sec
Brillouin frequency Dn_B = 1.2 GHz
QWP - Quarter Wave Plate
HWP - Half Wave Plate
T - Telescope, M = 0.4
P - Polarizer
L - Lens
BS - Beamsplitter
M - Mirror
RC - Reference Calorimeter
PD - Pin-diode
CCD - Video camera
SP - Sensitive paper
RPP - Random Phase Plate
ODL - Optical Delay Line

Signals and energy:

S - Signal to be corrected	40 mJ
PB - Probe Beam	500 mJ
RB - Reference Beam	100 mJ
CS - Corrected Signal	20 mJ

Fig.3. Schematic diagram of experimental setup

Nd laser assembled on the Master-Oscillator – Power Amplifier (MOPA) scheme was used as a source of laser radiation. Output radiation energy achieved 1 J, pulse duration was equal to 20 ns (FWHM). Beam size was equal to 15 mm. Output telescope with magnification M = 0.4 was used for reducing the beam size and collimating the output radiation. Output radiation was polarized in a horizontal plane.

Fraction of the radiation was used for forming the probe beam PB and the signal to be corrected S. The rest radiation was brought into an SBS cell for forming the reference beam with frequency shift RB. Liquid fluorocarbon[7, 8] FC-72 was used as an SBS medium. Here you can see the main properties of the medium are the following.

The Brillouin Enhanced Dynamic Hologram cell was filled with the same medium. Inside this sell, probe and reference beams (polarized in a vertical plane) intersect each other producing an interference pattern. Intersection angle θ was equal to (π - 0.014) rad. That means that the beams formed an interference pattern with spatial period of about $d = \lambda / 2n\sin(\theta/2) = 0.43$ μm. Because of frequency shift this pattern was moving at close to sound velocity and induced an appropriate acoustic wave. The acoustic wave functioned as a dynamic hologram. The signal to be corrected (polarized in a horizontal plane) was scattered by this hologram producing a corrected beam which was free of any aberration. The aberration was simulated by random phase plate which was installed at the common optical path of the signal and the probe beam. Optical delay line was used for measuring life time of the recorded hologram.

The corrected signal was brought into detecting scheme which included CCD-camera, Pin-diode PD and thermal sensitive paper SP. Lens L2 formed a far field zone at the sensing head of the CCD-camera. The detecting scheme was isolated from the reference beam by polarizer P3.

Energy of the signals was measured by the reference calorimeter RC.

4. EXPERIMENTAL RESULTS

The main purpose of the experiments was studying of Brillouin enhancement of diffraction efficiency of dynamic hologram. We considered diffraction efficiency as a ratio of energy of corrected signal to the energy of the signal to be corrected. Up to 53% diffraction efficiency were achieved. This is in a very good agreement with our previous experiment on Brillouin Enhanced Four-Wave Mixing. You can see, that we obtained more than 10 times increase of diffraction efficiency in comparison with the case of degenerate interaction.

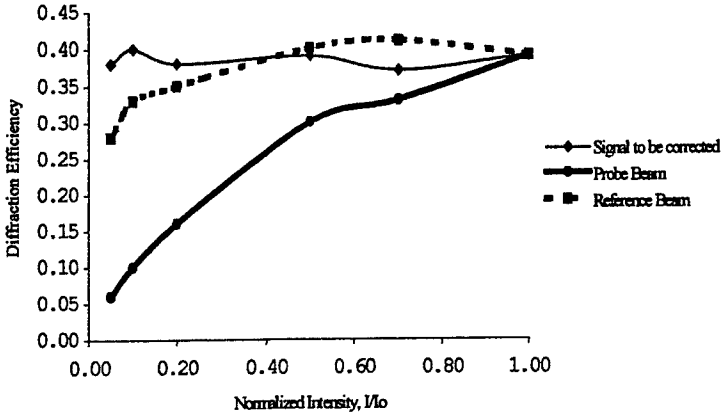


Fig.4. Dependence of Diffraction Efficiency on radiation energy

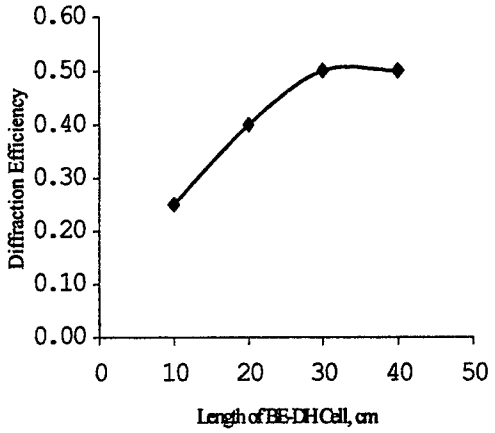
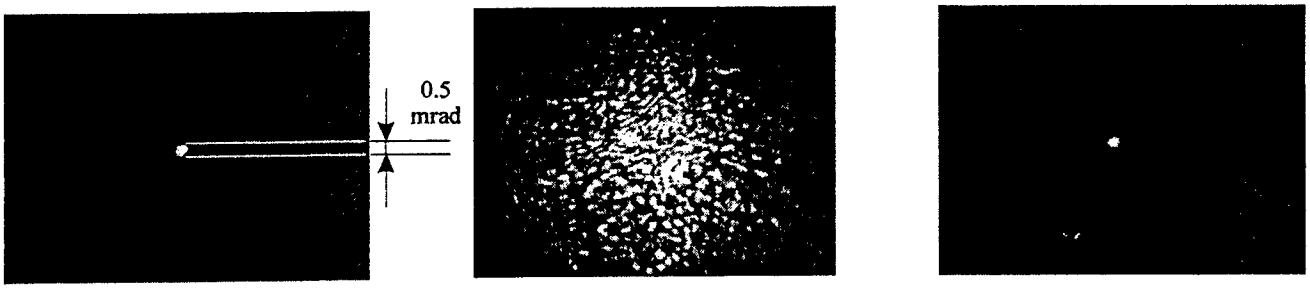


Fig.5. Dependence of Diffraction Efficiency on length of BE-DH Cell

We studied the dependence of diffraction efficiency on intensity of interacting beams and length of nonlinear medium (Figure 4). As it was expected, efficiency did not depend on intensity of signal to be corrected, but weakly depended on reference beam intensity and strongly depended on probe beam intensity. The use of longer nonlinear medium cells resulted in increasing the diffraction efficiency approximately up to 50% (Figure 5).



a) Initial signal

b) Distorted signal

c) Corrected signal

Fig.6. Illustration of correction for laser beam distortions. Initial (a), distorted (b) and corrected (c) signals are characterized by the following magnitudes of fraction of energy propagating within diffraction limited solid angle: 0.81, 0.08 and 0.74, respectively. Fidelity of correction for laser beam distortions - over 90 %

Then we tested capability of correction for laser beam distortions (Figure 6). Estimation of correction fidelity was made in terms of fraction of laser energy propagating within diffraction-limited solid angle. Spyglass application was used for processing the CCD-camera data and Excel application was used for evaluating the energy fraction. To introduce laser beam distortions we used a random phase plate bringing about 20 times increase of the laser beam divergence. Initial (a), distorted (b) and corrected (c) signals are characterized by the following magnitudes of fraction of energy propagating within diffraction limited solid angle: 0.81, 0.08 and 0.74, respectively. You can see, the dynamic hologram allowed to correct this distorted image with 90% fidelity.

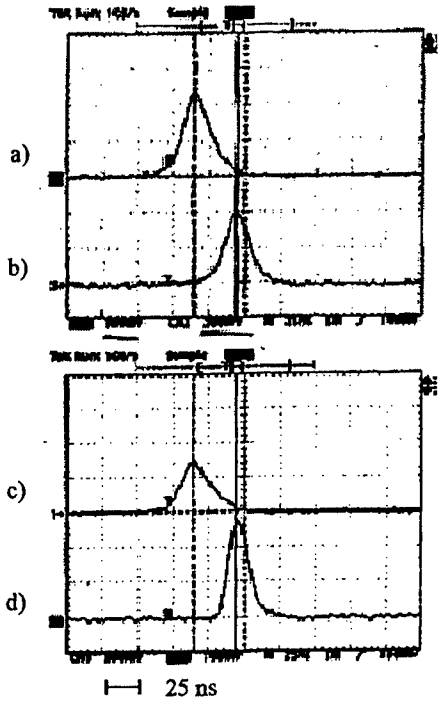


Fig7. Time location of laser pulses when no time delay between the signal to be corrected and probe or reference beam $t_d = 0$: a) output laser pulse, b) signal to be corrected in front of the BE-DH cell, as well as time location of probe and reference beams recording the hologram, c) output laser pulse, d) corrected signal.

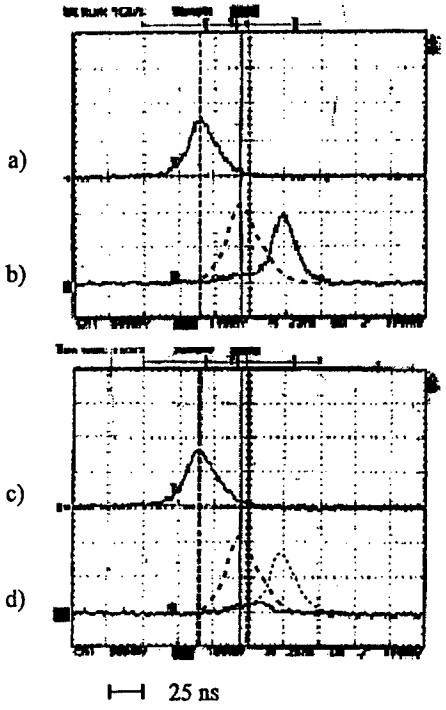


Fig8. Time location of laser pulses when time delay between the signal to be corrected and probe or reference beam $t_d = 25$ nc: a) output laser pulse, b) signal to be corrected in front of the BE-DH cell, dotted line represents time location of probe and reference beams recording the hologram, c) output laser pulse, d) corrected signal, dotted lines represent time location of probe and reference beams and signal to be corrected in front of the BE-DH cell.

One of the important parameters of dynamic hologram is its lifetime. As estimation showed, lifetime of such a kind of dynamic hologram should not to exceed 1 ns. Actually, that means that efficient scattering of laser radiation by the hologram takes place (Figures 7) only at the present of the recording beams (probe and reference ones). We tried to introduce additional optical path into the signal to be corrected (Figures 8). As a result, the signal was delayed by 25 ns in relative to the probe and reference beams. And you can see the pulse of scattered radiation located at the end of the recording beams. There is no hologram without recording beams. That means that such a kind of dynamic hologram can be re-recorded with very high rate and this fact allows the effective using of dynamic holography technique in a high pulse repetition mode of operation.

5. A TELESCOPE SYSTEM WITH NON-RECIPROCAL ELEMENT

To realize good performance of correction for phase distortions via dynamic holography it is necessary to provide similarity of wave front shapes of probe beam and signal to be corrected. For that purpose, both probe beam and signal to be corrected should propagate in one and the same direction and undergo the same phase distortions. In the case of small-scale optical elements as in the experiment described above, the use of beamsplitter or polarizer is the simplest way. But in the case of real telescope system with large primary mirror, the use of beamsplitter or polarizer is not a good idea because it would be necessary to design large-scale beamsplitter or polarizer characterized by high optical quality. Moreover, it would be necessary to develop additional large aperture optical system intended for producing the probe beam.

It is possible to use the technique based on illumination of primary mirror from the center of its curvature by probe beam and collection of reflected radiation for recording the dynamic hologram[2, 9]. But in this technique, probe beam and signal to be corrected propagated in different optical paths after reflection off primary mirror. If these optical paths have another sources of distortions (vibration, thermal deformation, inhomogeneities of power amplifier active medium etc), probe beam and signal to be corrected passing through different sources of distortions will have different shapes of wave front. This will result in reducing correction quality. In our opinion, much more attractive are the systems with non-reciprocal elements. For example, telescope system equipped with counterreflector with annular diffraction structure (see Figure 9) developed as a forming optical system with non-linear correction for phase distortions[10] (TENOCOM - TElescope system with NOn-linear-optic COMpensation of aberrations).

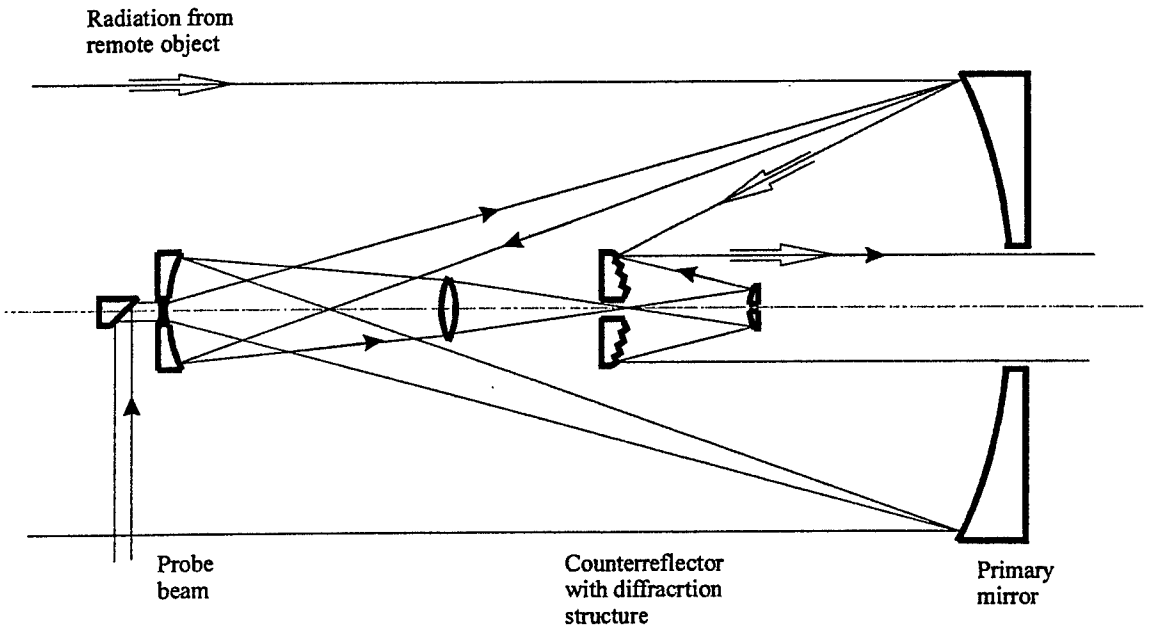


Fig.9. A telescope system with non-reciprocal element

In TENOCOM system, primary mirror is illuminated by probe beam from the point close to the center of curvature. Reflected radiation is collected and directed to counterreflector with annular diffraction structure. Radiation propagating in the first order of diffraction as well as remote object radiation reflected off the counterreflector have similar shapes of wave front and propagating in one and the same direction. Optical system is designed in such a way that not only shapes of wave front are similar, but also planes of primary mirror image are coincide in the probe beam and signal to be corrected. Coincidence of planes of primary mirror image and similarity in direction of propagating should result in the best performance of dynamic holography technique. Combination of telescope system with non-reciprocal element and Brillouin enhanced dynamic holography can be considered as the most attractive realization of systems providing distortion-free image in near IR spectral range.

CONCLUSION

Physical mechanism of recording the dynamic hologram based on Brillouin nonlinearity has been studied experimentally.

- Up to 53% diffraction efficiency has been obtained.
- Efficiency does not depend on intensity of signal to be corrected, but weakly depends on reference beam intensity and strongly depends on probe beam intensity.
- The use of longer nonlinear medium cells results in increasing the diffraction efficiency.
- The random phase distortions bringing about 20 times increase of the laser beam divergence have been corrected resulting in near-diffraction quality of a point object image.
- Lifetime of the hologram does not exceed 10^{-9} sec. This fact allows the effective using of dynamic holography technique in a high pulse repetition mode of operation.
- Combination of telescope system with non-reciprocal element and Brillouin enhanced dynamic holography can be considered as the most attractive realization of systems providing distortion-free image.

As the next step of study we plan to investigate field of view of such a kind of dynamic hologram.

ACKNOWLEDGEMENTS

We would like to thank Dr. H. Yoshida for his laser facility and very useful discussions.

REFERENCES

1. A. A. Ageichik, S. A. Dimakov, O. G. Kotyayev, A. A. Leshchev, Yu. A. Rezunkov, A. L. Safronov, and V. E. Sherstobitov. "The use of dynamic holography technique for correction of aberrations in telescopes". Proceedings of SPIE, **2771**, pp. 156-163, (1996).
2. N. V. Kukhtarev, H. J. Caulfield. "Status of dynamic holography". Proceedings of SPIE, **2532**, pp. 284-289 (1995).
3. M. T. Gruneisen, D. V. Wick, Ty Martinez, and J. M. Wilkes. "Correction of large dynamic aberrations by real-time holography using electro-optical devices and nonlinear optical media". Proceedings of SPIE, **3432**, pp. 137-150 (1998).
4. N. F. Andreev, V. I. Bespalov, A. M. Kiselev, A. Z. Matveev, G. A. Pasamanik, and A. A. Shilov. "Wavefront inversion of weak optical signals with a large reflection coefficient". Sov. Phys. JETP Letters, **32**, pp. 625-629 (1981)
5. N. F. Andreev, V. I. Bespalov, M. A. Dvoretskii, and G. A. Pasamanik. "Four-wave hypersonic reversing mirrors in the saturation regime". Sov. J. of Quantum Electronics, **14**, pp. 999-1000, (1984).
6. A. M. Scott, K. D. Ridley. "A review of Brillouin enhanced four-wave mixing". IEEE J. of Quantum Electronics, **25**, pp. 438-459 (1989).
7. V. Kmetik, H. Fiedorovicz, A. A. Andreev, K. J. Witte, H. Diado, H. Fujita, M. Nakatsuka, and T. Yamanaka. "Reliable stimulated Brillouin scattering of Nd:YAG laser pulses with liquid fluorocarbon for long time operation at 10 Hz". Applied Optics Letters, **37**, pp. 7085-7090 (1998).
8. V. Kmetik, T. Kanabe, H. Fujita, M. Nakatsuka, and T. Yamanaka. "The optical absorption in fluorocarbon liquids for the high energy stimulated Brillouin scattering phase conjugation and compression". The Review of Laser Engineering, **26**, pp. 322-327 (1998).
9. G. Andersen, J. Munch, and P. Veitch. "Holographic correction of large telescope primaries by proximal, off-axis beacons". Applied Optics, **35**, pp. 603-608 (1996).
10. M. V. Vasil'ev, V. Yu. Venediktov, A. A. Leshchev, and P. M. Semenov. Laser beam forming telescopic system with output tract compensation via phase conjugation. Kvantovaya Elektronoka, **20**, pp. 317-319 (1993)

Dual-conjugate adaptive optics

Thu-Lan Kelly, David F. Buscher[a], Paul Clark, Colin N. Dunlop,
Gordon D. Love, Richard M. Myers, Ray M. Sharples and Andrew Zadrozny

Dept of Physics, University of Durham, Durham UK DH1 3LE
[a]Dept of Physics, University of Cambridge, Cambridge UK

ABSTRACT

Conventional adaptive optics systems using a single wavefront corrector suffer from a limited field of view. Multi-conjugate adaptive optics use two or more correctors to improve off-axis correction. We describe an experimental system which simulates dual-layer turbulence, and present results using a single corrector showing anisoplanatic effects. Future experiments using a second corrector are also discussed.

Keywords: multi-conjugate adaptive optics

1. INTRODUCTION

The limitations of conventional adaptive optics (AO) in correcting large areas of the sky are well-known.[1] Light from a natural guide star is well-corrected by an AO system, but a problem occurs when the science object does not have a suitable natural guide star nearby. The science object does not pass through the same upper layers of the atmosphere as the beacon, and hence turbulence experienced by the science object will not be well compensated (Fig 1).

We have designed a dual-conjugate experiment to investigate off-axis effects of AO systems, consisting of a ferroelectric liquid crystal spatial light modulator (FLC SLM) turbulence generator and a deformable mirror (DM) adaptive optics system. The turbulence generator was based on a technique described in Ref 2 for binary SLMs, and was expanded to produce three-dimensional turbulence by using two FLC SLMs to represent two turbulent layers in the atmosphere separated by a height h. Initially, the adaptive optics system consisted of a single DM corrector with dual layer turbulence. In future work, the system will be modified to allow the insertion of a second corrector.

2. DESIGN OF THE MCAO TURBULENCE GENERATOR

The turbulence generator described in Ref 2 used a holographic technique to produce an analogue phase from a binary SLM. Tilt was added to the desired wavefront, which was then binarized. Laser light modulated by the binary FLC SLM was Fourier transformed by a lens and spatially filtered to remove unwanted higher orders, and inverse Fourier transformed by a second lens to produce the desired phase.

Modifications to the original design for dual-conjugate wavefront generation needed to ensure that the turbulence generator accurately represented the different paths through the upper atmosphere followed by the on and off axis beams. Some of the issues considered are discussed in the following sections.

2.1. Design Issues

1. The upper layer should be oversized with respect to the lower layer (see Fig 1) so that the on and off-axis beams pass through different areas of turbulence in the upper layer.
2. The off-axis beam should not be vignetted by the SLMs, spatial filters or lens apertures.
3. Consider the maximum off axis angle allowed, including demagnification of angles at SLM. If d is the SLM aperture size, D is the telescope aperture , θ is the off-axis angle in the sky and β is the off-axis angle at the lower SLM

$$\beta = \theta(D/d) \tag{1}$$

4. Allow for the magnification of distance between SLMs to represent distance between layers in atmosphere.
5. Consider the loss of resolution of the upper atmosphere.

Corresponding author: Gordon D. Love, email g.d.love@durham.ac.uk

Laser Optics 2000: Control of Laser Beam Characteristics and Nonlinear Methods for Wavefront Control,
Leonid N. Soms, Vladimir E. Sherstobitov, Editors, Proceedings of SPIE Vol. 4353 (2001)
© 2001 SPIE · 0277-786X/01/$15.00

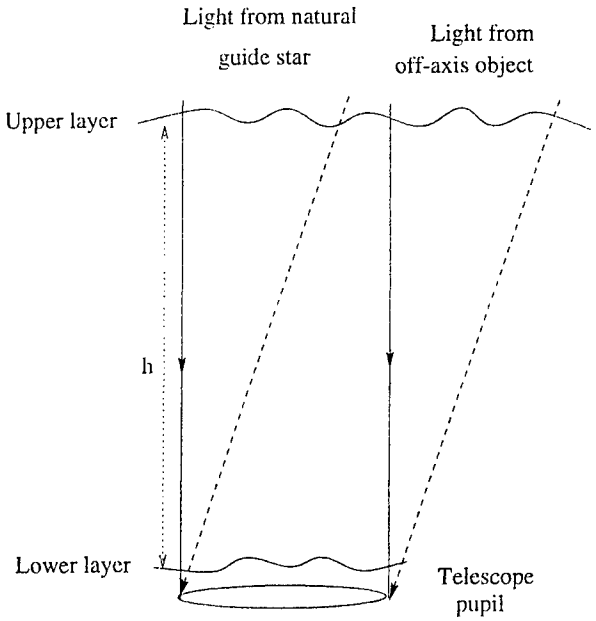


Figure 1.

2.2. Solution

1. Ensure the beam incident on both SLMs is oversized by using a beam expander on the laser and by magnifying the beam incident on the lower SLM. Also ensure that the upper layer turbulence is increased by the magnification factor to account for the fact that only part of the beam is reflected by the lower SLM.

2. The simulated telescope diameter D must not be too large or the angles incident on the SLM will be unfeasibly large.

3. Calculate the focal length of lenses and the maximum off-axis angle, which are interrelated. See Section 3 for derivation. Account for vignetting by lenses. Replace the spatial filters by slits to allow off-axis tilt in one dimension.

4. If h is the distance between layers in the atmosphere, then the distance x between image of SLM1 and SLM2 is

$$x = (\frac{d}{D})^2 h \tag{2}$$

5. The resolution of the upper atmosphere will be reduced by a factor M^2, where M is the magnification of the upper SLM onto the lower SLM. This should be large enough to allow a range of off-axis angles, but not too large to reduce unacceptably the resolution of the upper atmosphere.

3. CALCULATIONS OF ANGLES

Ideally, large off-axis angles would be produced by the modified design. However, since the aperture of the SLM $d \ll D$, where D is the telescope aperture, then from Eqn 1, the required angles of incidence required by the turbulence generator may not be feasible, especially if D is large.

Fig 2 was used for calculating the optimal angles and focal lengths. The angles to consider are the angle of incidence onto lens L1 α, and the angle of incidence onto the lower SLM β. These angles are related by

$$\frac{\tan\alpha}{\tan\beta} = \frac{f_2}{f_1} = M \tag{3}$$

where f_1, f_2 are the focal lengths of lenses L1 and L2, respectively. d_{L1},d_{L2},d are the apertures of L1, L2 and the SLMs, respectively.

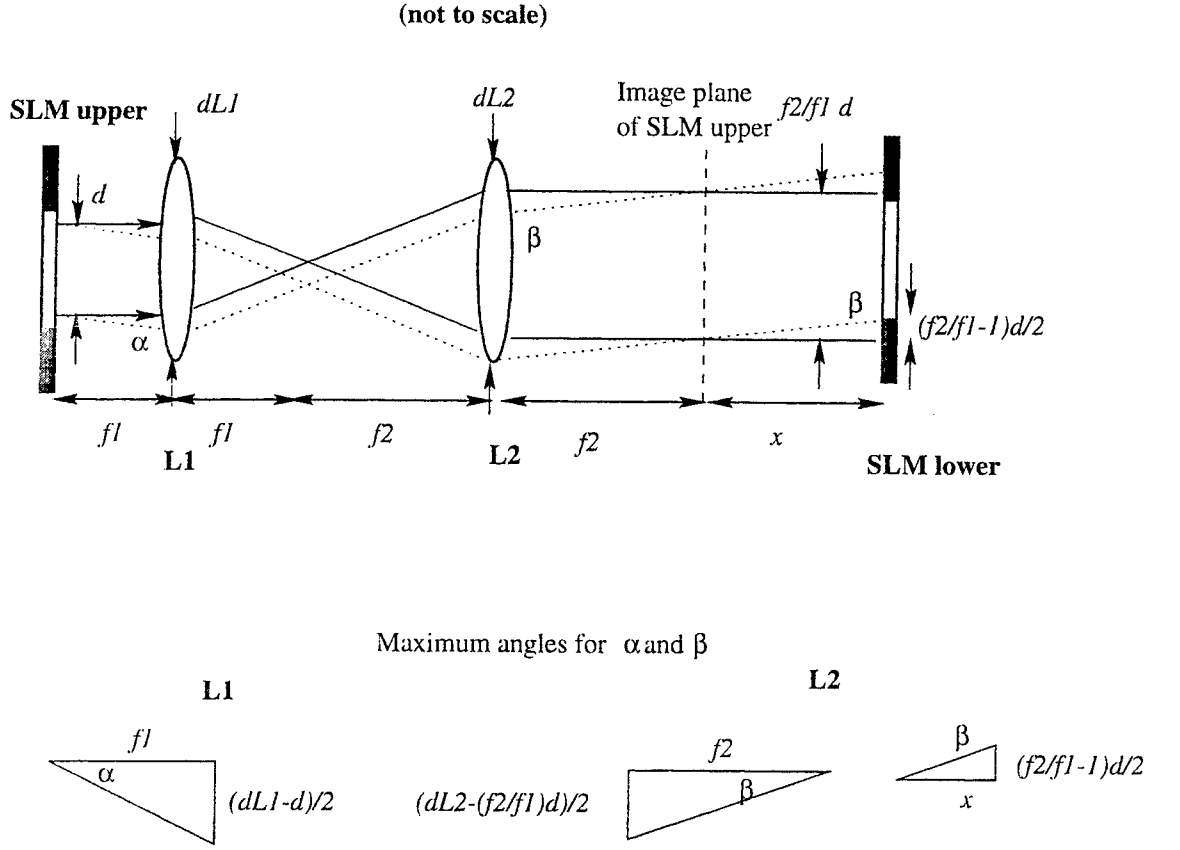


Figure 2. Diagram for calculation of angles α and β.

α and β are limited by the focal lengths and aperture sizes of L1 and L2. In addition, β is dependent on x, the effective distance between the two SLMs.

Referring to Fig 2, the maximum value of α is calculated by

$$\tan\alpha = \frac{d_{L1} - d}{2f_1} \tag{4}$$

β is determined by two factors. The first is dependent on the magnification by L1 and L2, as well as x, the effective distance between the two SLMs. From Fig 2

$$\tan\beta = \frac{(f_2/f_1 - 1)d}{2x} \tag{5}$$

The second condition is similar to Eqn 4, depending on the aperture size and focal length of L2.

$$\tan\beta = \frac{d_{L2} - (f_2/f_1)d}{2f_2} \tag{6}$$

First, try to maximise α. Choose L1 to have a fairly small focal length and relatively large aperture (a fast lens with a small f/#). Calculate the maximum value of α using Eqn 4. Choose a fast lens as L2 to give a sufficient magnification. β will the minimum value given by Eqns 3, 5 and 6.

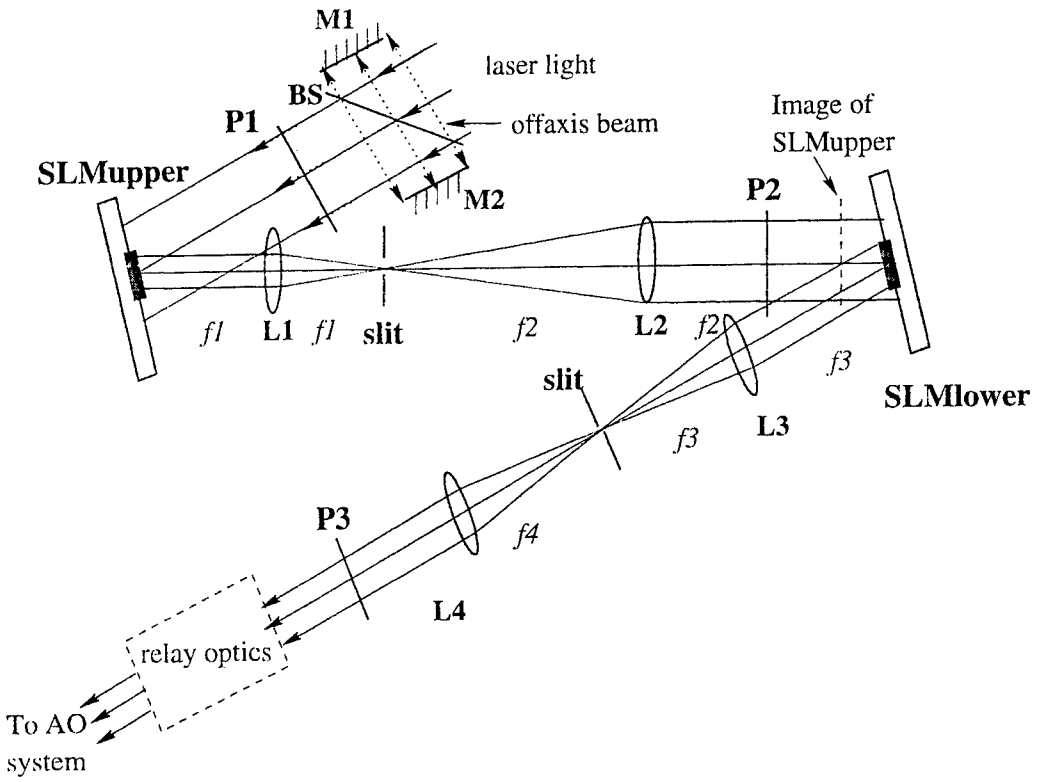


Figure 3. Optical setup for dual-conjugate wavefront generation. P1 to P3 polarizers; BS, beamsplitter; M1 and M2 mirrors. *f1* to *f4* are the focal lengths of lenses L1 to L4.

3.1. D/r_0 considerations

The maximum off-axis angle produced by the turbulence generator should be larger than the isoplanatic angle.

$$\theta_0 = 0.31 r_0 / \overline{h} \tag{7}$$

where r_0 is the Fried parameter for the turbulence given by

$$r_0 = [\sum r_i^{-5/3}]^{-3/5} \tag{8}$$

and r_i is calculated from the D/r_0 values for each layer. Then

$$\overline{h} = \left[\frac{\int_0^\infty h^{5/3} C_n^2(h)\, dh}{\int_0^\infty C_n^2(h)\, dh} \right]^{3/5} \tag{9}$$

If the lower layer is at $h = 0$, then $\overline{h}$ is equal to the height of the upper layer, and r_0 is also due entirely to the upper layer.

A maximum angle of about $5 - 10\theta_0$ should be sufficient to show anisoplanatic effects in the AO system i.e. θ_0 should be compared with β.

3.2. Calculations for $D = 1$ m

Due to the magnification of angles from the relative sizes of SLM and telescope apertures (Eqn 1), the size of the simulated telescope aperture should not be too large. We chose $D = 1$ m for a SLM aperture of $d = 3.84$ mm.

First step: From Eqn 1, $D = 1$ m requires an angle at the SLM $\beta = 4.3°$ to represent an off-axis angle of 60 arcseconds in the sky, which is feasible.

Second step: Choose the first lens L1 so that α is as large as possible (Eqn 4). We chose a lens with $f_1 = 50$ mm, $d_{L1} = 25$ mm, giving $\alpha = 11.9°$.

Third step: Calculate the maximum magnification from Eqn 3.

$$M = \frac{\tan 11.9}{\tan 4.34} = 2.78$$

So $f_2 = M \times f_1 \leq 2.78 \times 50 = 139$ mm. We chose L2 to have $f_2 = 125$ mm, $d_{L2} = 25$ mm. Then $M = 2.5$.

Fourth step: Check vignetting by L2, using Eqn 6 to find the maximum angle allowed through L2 and compare with β in step 1. $\arctan((25 - 2.5 \times 3.84)/(2 \times 125)) = 3.5° < 4.3°$. So L2 does cause vignetting, limiting β.

There are a number of alternative approaches to the problem. One is to set β at 3.5°, which is equivalent to 49 arcsecs in the sky for a 1m diameter telescope. Another approach is to reduce the magnification and keep $\beta = 4.3°$. For example if L2 has $f_2 = 100$ mm and $d_{L2} = 25$ mm, the maximum angle through L2 is 4.9°, so $\beta = 4.3°$ would be possible. However, from Eqn 5, this has the effect of reducing x, and hence the distance between layers in the sky. The best approach would be to accept the reduction of the angle in the sky to 49 arcsecs (reduced from 1 arcmin), although the alternative method of reducing the magnification will also be considered.

Fifth step: Calculate x from Eqn 5. For $M = 2.5$, $\beta = 3.5°$and $f_2 = 125$ mm, $x = 47.1$ mm. (Alternatively, if $f_2 = 100$ mm, $M = 2$ and $\beta = 4.3°$, then $x = 25.3$ mm).

Sixth step: Calculate h from Eqn 2. For $x = 47.1$ mm, $h = 3.2$ km. (Alternatively, if $x = 25.3$, then $h = 1.7$ km, which is too low.)

The final optical setup is shown in Fig 3. Lenses L3 and L4 are identical 100 mm focal length lenses. The lens apertures are 25 mm, and do not cause vignetting of the off-axis beam. The off-axis beam is produced via the pellicle beamsplitter BS and the two mirrors M1 and M2. The off-axis angle can be varied by adjusting either of these 2 mirrors. The SLMs were two Displaytech ferroelectric LC SLMs, which are binary reflective devices, each consisting of 256 X 256 pixels with a pixel size of 15 μm X 15 μm. They could operate at frame rates of up to 2.5 kHz.

3.3. Variation of conjugate planes

The height of the upper and lower layers is not fixed with respect to the corrector planes, but can be altered. To alter the height of the upper layer, lenses L1 and L2 can be moved while keeping the distance between them fixed, and similarly to vary the height of the lower layer, lenses L3 and L4 can be moved. The magnification of distances by lenses L1 and L2 must be taken into account when calculating the distance moved.

4. EXPERIMENT

The experiment was performed using a single DM corrector and both single and dual layer turbulence. The off-axis angle ranged from a minimum of about 3.5 arcsecs to a maximum of about 13 arcsecs (equivalent angles in the sky for a $D = 1$ m telescope). We could not increase the maximum off-angle angle significantly beyond 13 arcsecs, as it was limited by the resolution of the SBIG camera used to capture the images. For the turbulence we used the maximum angle was equivalent to $3 - 4\theta_0$, which is slightly less than desired. The range of angles can be increased by using a higher resolution camera, or by changing the turbulence to decrease θ_0.

The corrector was placed approximately in the conjugate layer of the lower plane of turbulence. Single layer turbulence was generated in the telescope pupil plane, while the upper plane of turbulence was approximately 3.2 km above the lower layer (for a $D = 1$ m telescope). The turbulence applied to the upper SLM was actually 2.5 times the desired turbulence, to account for the magnification of the upper layer with respect to the lower layer. TIp-tilt in the turbulence was removed to prevent vignetting by the slits.

The values of turbulence generated were

1. single layer turbulence, $D/r_0 = 6$
2. single layer turbulence, $D/r_0 = 7.7$.

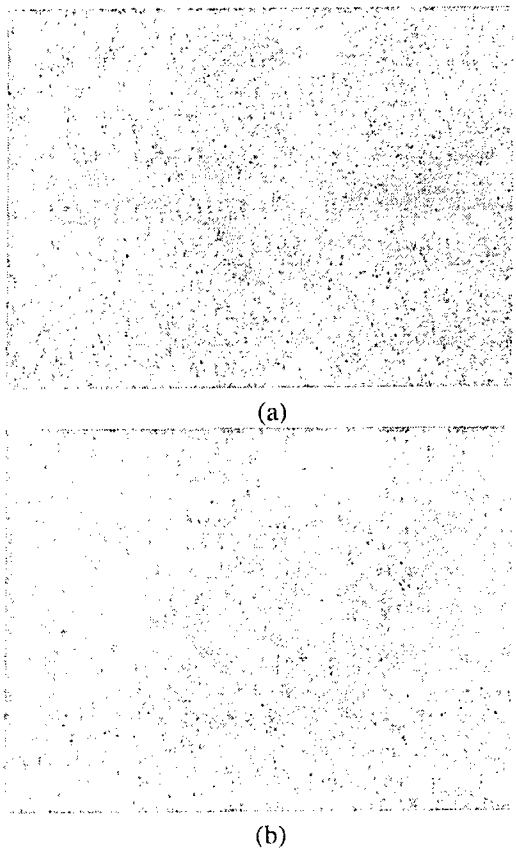


Figure 4. (a) single layer and (b) dual layer corrected point spread functions, imaged using a logarithmic scale. The on axis PSF is to the left, while the off axis PSF is to the far right.

3. dual layer turbulence, lower layer with $D/r_0 = 6$, and the upper layer with $D/r_0 = 4$, which is equivalent to a total turbulence of $D/r_0 = 7.7$.
4. dual layer turbulence, both upper and lower layer with $D/r_0 = 6$ (equivalent to a total turbulence $D/r_0 = 9.1$)

The Strehl ratio of the on and off-axis beams were calculated by dividing the peak intensity of the point spread function (PSF) with that of a near diffraction limited reference beam. The reference beam was produced by removing the static aberrations of the system using a Simplex algorithm.[3]

Theory[4] predicts that, for small off-axis angles θ, the proportional decrease in Strehl R is given by

$$R \propto \exp[-(\frac{\theta}{\theta_0})^{5/3}] \tag{10}$$

From the above relationship, we can find θ_0 from the graph by determining θ for which the Strehl ratio falls to $1/e$ of the maximum value, which corresponds to $\theta = \theta_0$. Then we can compare this value of θ_0 to the predicted value calculated by Eqn 7.

5. RESULTS

Fig 4 shows images of corrected point spread functions for (a) single layer turbulence with $D/r_0 = 6$ and (b) dual layer turbulence, with both upper and lower layer having $D/r_0 = 6$. The bright on axis beam is to the left of the image, while the off-axis beam is to the right. In both cases, the on axis beam is well-corrected, but the off-axis beam is much better corrected for the single layer turbulence than for the dual-layer turbulence. Similar images were taken for varying off-axis angles, and the Strehl ratios calculated. The experimental results in Fig 5 show that

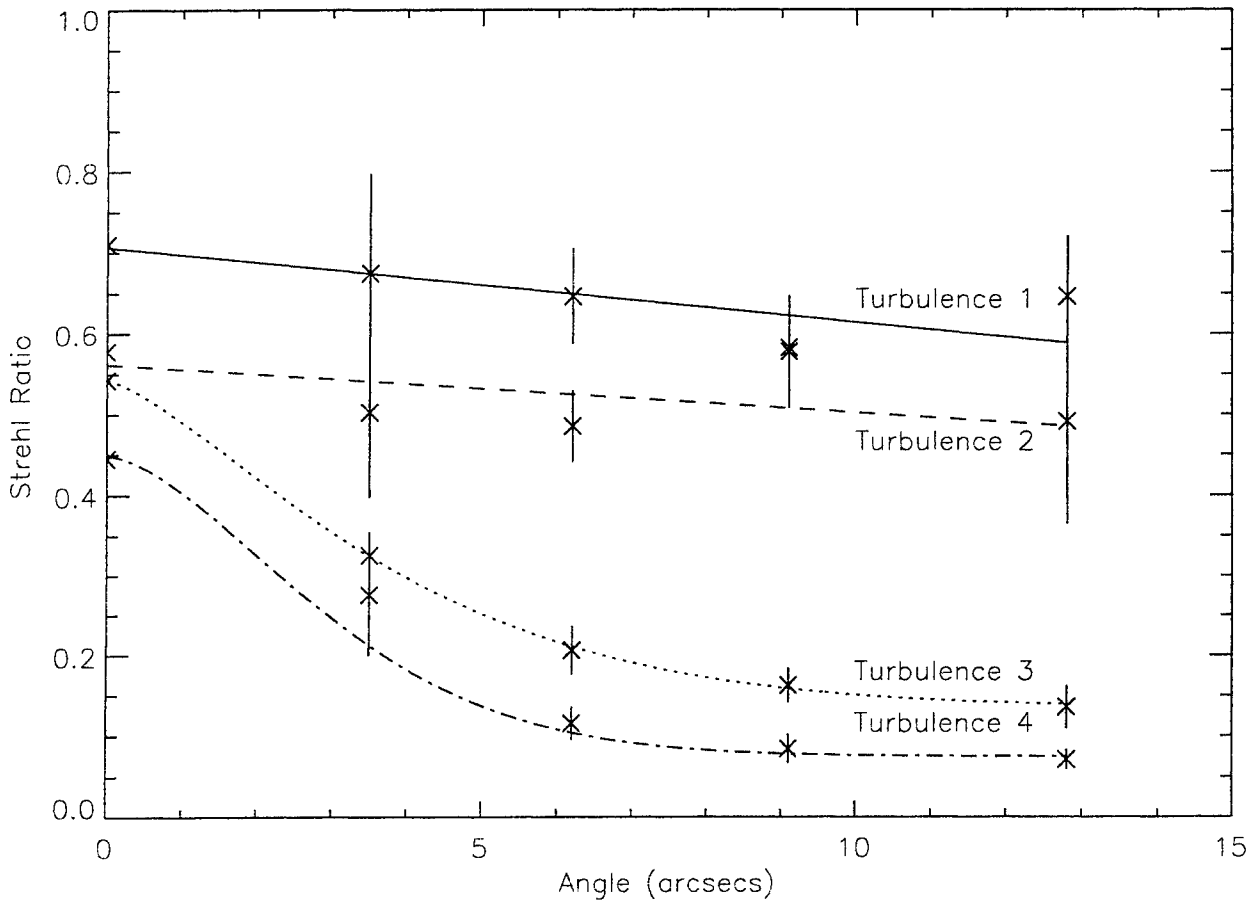


Figure 5. Experimental results

1. for single layer turbulence, the off-axis corrected Strehl is almost constant with angle;
2. for dual layer turbulence, the corrected Strehl degrades with increasing angle. The higher the effective turbulence, the faster the degradation.

The positions of the layers relative to the DM were measured and found to be 114m above the DM for the first layer, with the second layer 3.2km above the first (equivalent distances in the sky for a $D = 1$ m telescope). The slight misalignment of the DM to the conjugate plane of the lower layer explains the slight drop off in Strehl ratio with angle for turbulence 1 and 2.

By fitting curves of the form $y = A\exp(Bx^C) + D$ (similarly to Eqn 10) to the curves for turbulence 3 and 4, we could find the experimental values of θ_0 by finding the point where the graphs fall to $1/e$ of their maximum value. The parameters A to D as well as the calculated and measured values of θ_0 are shown in Table 1. Uncertainty in the calculated values is due to measurement error in determining the distance between the 2 layers. In the experimental values, the error was estimated by using the uncertainty in the fitted parameters A to D. The experimental values are slightly higher than the calculated values in column 1 by a constant factor, suggesting a systematic error, which is most likely due to the removal of tip-tilt in the turbulence. Further calculations were performed to determine the effect of the tip-tilt removal, and the results shown in Column 6 of Table 1. The tip-tilt adjusted results show much better agreement with the experimental results.

6. CONCLUSION

We have described a dual-conjugate turbulence generator which we have used to investigate off-axis effects in conventional AO systems. Experimental results show good agreement with theoretical predictions for both single and dual-layer turbulence. In

dual-layer turbulence	A	B	C	D	calculated θ_0 (arcsecs)	tip-tilt removed	experimental θ_0 (arcsecs)
turbulence 3	0.41	-0.14	1.4	0.13	4.7 ± 0.5	6.1 ± 0.6	6.6 ± 0.6
turbulence 4	0.37	-0.13	1.63	0.075	3.2 ± 0.3	4.2 ± 0.4	4.4 ± 0.5

Table 1. Fit parameters and calculated and experimental values of θ_0 for dual layer turbulence (arcsecs).

future work the turbulence generator will be used with a dual-conjugate AO system. The second corrector should increase the size of the isoplanatic patch which is corrected by the AO system.

This project was in part supported by INTAS grant INTAS-ESA 99-523.

REFERENCES

1. J. M. Beckers, "Increasing the size of the isoplanatic patch with multi-conjugate adaptive optics", in *ESO Symposium on Large Telescopes and Their Instrumentation,* M.-H. Ulrich, ed, pp. 693-703, ESO Proc, Garching,1988
2. M. A. A. Neil, M. J. Booth, T. Wilson, "Dynamic wave-front generation for the characterization and testing of optical systems", *Opt. Lett.* **23**, pp. 1849-1851, 1998
3. N.Doble, Gordon Love, D.F. Buscher, R.M. Myers, and Alan Purvis. "The use of image quality metrics for correction of non-common path errors in the ELECTRA adaptive optics system." *Proc. Soc. Photo. Opt. Instrum. Eng.* **3749,** pp 785, ICO 18th Congress, 1999
4. M. Roggeman and B. M. Welsh, *Imaging through turbulence*, CRC press, 1996

Analysis of the spectral modulated interferograms by recurrence non-linear filtering method

Igor Gurov*) and Petr Hlubina**)

*) Institute of Fine Mechnics and Optics (Technical University)
14 Sablinskaya st., Saint-Petersburg, 197101, Russia
E-mail: ig@spb.runnet.ru

**) Institute of Physics, Silesian University at Opava
Bezruèovo nám. 13, 746 01 Opava, Czech Republic
E-mail: petr.hlubina@fpf.slu.cz

ABSTRACT

Interferometric radar technique is an important tool for a surface topography reconstruction of optically rough surfaces. Spectral interferometric radar is based on optical interference phenomenon that is observed in the form of the periodical modulation of broadband spectrum at the output of interferometer. Group optical path difference of interfering light waves corresponding to the distance from the surface to be measured is characterized by the phase function or fringe frequency of the spectral modulated interferogram. To measure fringe frequency a noise-immune recurrence non-linear filtering method was used where interferometric data are assumed to be a series of samples of the spectral interferometric signal defined by a known model. It is predicted the signal value from previous step of discretization to the next step. The prediction error is used for signal parameters correction. Recurrence non-linear filtering generally gives the optimal dynamic estimate of the phase function, frequency and visibility maximum position of the interferogram. Method was verified experimentally with application to the analysis of the spectral modulated interferograms inherent to Michelson interferometer excited by low-coherent source with a subsequent spectrometer

Keywords: spectral interference, group optical path difference, recurrence data processing

1. INTRODUCTION

Interferometric radar technique is an important tool for a surface topography reconstruction of optically rough surfaces. Conventional low-coherent radar technique[1,2] is based on the principle of white-light interferometry in individual speckles, where the maximum position of the fringe visibility is found with mechanical scan of optical path difference (OPD) in interferometer. Spectral radar consists of two-beam interferometer excited by broadband light source with a subsequent spectrometer [3,4]. Spectral modulated interference fringes in the simplest consideration are similar to those that obtained in unbalanced two-beam interferometer illuminated by monochromatic light source with linearly varied wavelength without OPD mechanical scan.

It has been revealed, in agreement with previous works,[5,6] that in the case of a two-beam interference experiment the sinusoidal modulation of broad bandwidth spectra takes place.[7-9] Theoretical and experimental investigations of the interference effects in the spectral domain have revealed their great impact on the progress of new optical diagnostics methods. [3,4,7-10] Thus, the spectral modulation of white light in a Michelson interferometer is an useful method for measuring distances and displacements ranging up to hundreds of micrometers.

The intensity distribution in the spectral modulated interferogram may be presented as a sum of essentially non-uniform background component defined by the form of the power spectrum of light source and useful component of interference fringe with varied envelope. The information about the OPD to be measured is contained in the phase function and spatial frequency of the spectral interference fringe. The problem of interferometric data analysis is that

Laser Optics 2000: Control of Laser Beam Characteristics and Nonlinear Methods for Wavefront Control,
Leonid N. Soms, Vladimir E. Sherstobitov, Editors, Proceedings of SPIE Vol. 4353 (2001)
© 2001 SPIE · 0277-786X/01/$15.00

the intensity of interferogram depends on phase, frequency or visibility maximum position non-linearly and it is difficult to optimize the interference fringe processing procedure on general totality of interferometric data.

Proposed analysis method of spectral interference fringes based on recurrence non-linear filtering methodology [14,15] gives the optimal estimate of parameters pointed out above dynamically. Interferometric data are assumed to be a series of samples of the interferometric signal defined by known model of the spectral interferogram. It is predicted the signal value from previous step to the next step. The prediction error is used for signal parameters correction taking into account the particularities of interference fringe. Thus it is recovered the dynamic evolution of phase function, frequency and envelope maximum position at each data sample. The phase unwrapping problem is solved automatically because of recurrence calculation of the phase function.

2. THEORY

Recurrence non-linear data processing procedure is based on the knowledge of the parametric model of interference fringe. It is necessary at first to consider the physical forming process of spectral interferogram. Using adequate model of interference fringes and some *a priori* information about its parameters it is possible to apply the non-linear data processing algorithm to real observed data.

2.1. Forming of the spectral modulated interferogram

The mutual interference of two beams at an arbitrary point with transverse position vector **R** at the output of the uncompensated Michelson interferometer is governed at the wavelength λ by the spectral interference law [5,6]

$$G(\mathbf{R};\lambda) = G_0(\mathbf{R};\lambda) + G_1(\mathbf{R};\lambda) + 2\sqrt{G_0(\mathbf{R};\lambda)G_1(\mathbf{R};\lambda)}\cos[(2\pi/\lambda)\Delta_M(\mathbf{R};\lambda)], \quad (1)$$

where $G_0(\mathbf{R};\lambda)$ and $G_1(\mathbf{R};\lambda)$ are contributions of both beams to the resultant spectral power density $G(\mathbf{R};\lambda)$ and $\Delta_M(\mathbf{R};\lambda)$ is the spatially and spectrally dependent OPD realized between both beams at the output of the uncompensated two-beam interferometer. The dependence of the OPD on the transverse position vector **R** means that two superimposed and slightly tilted wavefronts of beams give rise at the output of the Michelson interferometer to interference fringes whose spatial frequency is determined by the tilt of the wavefronts, that is by the tilt of the mirrors.

Let us consider now that the detecting optical fiber is used at the output of the Michelson interferometer to launch the optical power into a subsequent spectrometer. After averaging over the aperture function of the input end of the detecting optical fiber we obtain the expression

$$I(\lambda) = I_0(\lambda) + I_1(\lambda) + 2V_R V_A\sqrt{I_0(\lambda)I_1(\lambda)}\cos[(2\pi/\lambda)\Delta_M(\lambda)], \quad (2)$$

where $I_0(\lambda)$ and $I_1(\lambda)$ are contributions of both beams to the resultant spectral power (spectrum) $I(\lambda)$, V_R is the visibility of the spectral interference fringes in which only the effect of the limited resolving power of the spectrometer, that is the effect of the spectral integration on the spectral modulation, is included, and V_A is the visibility of the spectral interference fringes at the output of the detecting optical fiber and $\Delta_M(\lambda)$ is the wavelength-dependent OPD between two beams in the Michelson interferometer.

One may conclude from Eq. (2) that the spectral modulation with the wavelength-dependent period of modulation

$$\Lambda(\lambda) = \lambda^2 / \Delta^g_M(\lambda), \quad (3)$$

is to be expected whenever the spectral analysis is performed with a spectrometer of a suitable resolution. Consequently, the highest visibility of the measured interference fringes can be achieved using a spectrometer whose width of response function is small compared with the period of the spectral modulation. In Eq. (3), $\Delta^g_M(\lambda)$ represents the group OPD between both beams in the uncompensated Michelson interferometer defined by the well-known relation

$$\Delta^g_M(\lambda) = \Delta_M(\lambda) - \lambda[d\Delta_M(\lambda)/d\lambda]. \quad (4)$$

It is clear that, the larger the group OPD in the Michelson interferometer, the smaller is the period (the higher is the fringe frequency) of spectral modulation, and vice versa.

If the overall visibility of spectral interference fringes is introduced by the relation

$$V_I(\lambda) = 2V_R V_A\sqrt{I_0(\lambda)I_1(\lambda)} / [I_0(\lambda) + I_1(\lambda)], \quad (5)$$

from which the effect of both the spatial and the spectral integration as well as the effect of different contributions of both beams on the visibility of the measured spectral interference fringes in a two-beam interference experiment is clarified, Eq. (2) can be rewritten into the most used form

$$I(\lambda) = I^{(0)}(\lambda)\{1 + V_I(\lambda)\cos[(2\pi / \lambda)\Delta_M(\lambda)]\}, \quad (6)$$

where $I^{(0)}(\lambda)$ is the reference spectral power, that is the reference spectrum, in which the effect of both the source spectrum and the response function of the spectrometer is inscribed. Using recurrence non-linear filtering method the wavelength dependence of both the group OPD and the envelope maximum position of the spectral fringes can be extracted from the measured spectral interferogram. Model Eq.(6) is the basic for the following data processing.

2.2. Recurrence non-linear data processing

Real interferometric signal is proportional to the intensity value Eq.(6) and is distorted by noise influence, so the data samples series must be presented in the form

$$S_k = S_0 [1 + V_k \cos(\Phi_k + N_{ph_k})] + N_{ak}, \quad (7)$$

where k=0,..., K-1, Φ_k are the samples of the phase function,

$$\Phi_k = \sum_{i=0}^{k} U_i \Delta\lambda, \quad (8)$$

U_i are the samples of circular local fringe frequency, $\Delta\lambda$ is the wavelength step of the discretisized spectral interferogram Eq.(6), N_{ph} and N_a are the phase fluctuations and additive observation noise correspondingly, M[N_{ph}]=M[N_a]=0, M[N^2_{ph}]=σ^2_{ph}, M[N^2_a]= σ^2_a, M[.] denotes the mathematical average operation. Model presented by Eqs.(7),(8) includes the vector of parameters $\Theta = \left(V, \Phi, U, N_{ph}\right)^T$.

It is well-known the Fourier transform method (FTM) of fringe analysis[12] that is widely used for recovering of the fringe phase Φ. The accuracy limitations of FTM were investigated in detail (see, for example, the paper[13]). The main disadvantages of FTM are the edge effect that caused by the limited extent of the fringe pattern, instability of the phase calculation with the influence of noises N_{ph_k}, N_{ak} and necessity to solve a phase unwrapping problem. Now we give the solution of the problem of the noise-immune estimation of the fringe frequency by non-linear recurrence filtering method using the results published[14-16] with application to spectral modulated interferograms.

Let us suppose that envelope variation Eq.(7) is approximated by exponential function, namely

$$V_k \approx V \exp\left(-C_k^2\right), \quad (9)$$

where $C_k = \left(\lambda_k - \lambda_m\right)B$, λ_m is the envelope maximum position, B is the parameter that defines the envelope width. So vector of informative parameters includes three components, $\Theta = \left(U, \Phi, C\right)^T$. The first component gives the information about group OPD. Calculation of the second parameter gives the possibility to recover if necessary the unwrapped phase function by Eq.(8). The third component characterizes the visibility maximum position.[14]

In the paper[15] were presented the equations that may be applied to recurrence non-linear filtering of vector of parameters of the spectral interferogram in the form:

$$\Theta_k = \Theta_k^{k-1} + \mathbf{R}_k^{k-1}\mathbf{D}_k\left[\Xi_k - S\left(\lambda_k, \Theta_k^{k-1}\right) - B_2 / 2\right]L_k^{-1}, \quad (10)$$

$$\mathbf{R}_k = \mathbf{R}_k^{k-1}\left(\mathbf{I} - \mathbf{D}_k\mathbf{D}_k^T\mathbf{R}_k^{k-1}L_k^{-1}\right), \quad (11)$$

where $\mathbf{R}$ is the correlation matrix of parameters, $\mathbf{D}$ is known sensitivity vector (i.e. vector of derivatives of ideal model by parameters), Ξ_k is the series of observed scalar interferometric data, $S\left(\lambda_k, \Theta_k^{k-1}\right)$ is the series of modeled values of the signal Eqs.(8),(9), B_2/2 is the correction component by Gaussian approximation of parameters probability density function of the 2-nd order[15], L_k^{-1} is the dynamic filter amplification factor dependent on the value $S\left(\lambda_k, \Theta_k^{k-1}\right)$ and on the additive noise dispersion σ^2_a, $\mathbf{I}$ is the unit matrix, upper index k-1 denotes the prediction from the previous step.

Using coarse *a priori* estimate Θ_0 of vector Θ one can calculate the value $S(\lambda_0, \Theta_0)$ and predict values Θ_1^0 and $S(\lambda_1, \Theta_1^0)$ to the next step. Difference between observed Ξ_k and predicted $S(\lambda_k, \Theta_k^{k-1})$ values is used at each step in Eq.(10) for non-linear correction of predicted vector of parameters Θ_k^{k-1}. For this purpose are used known sensitivity vector $\mathbf{D}_k$ and correlation matrix of parameters $\mathbf{R}_k$ recalculated at each step in Eq.(11). It was shown[15] that such a procedure is equivalent to optimal filtering of each component included in vector Θ. In particular it can be recovered the fringe frequency corresponding to the spectral modulated interferogram Eq.(6).

3. EXPERIMENTAL SETUP

The experimental setup[11] used in the investigation of the spectral interference between two beams at the output of the uncompensated Michelson interferometer is shown schematically in Fig. 1. A Toshiba TOLD 9140 laser diode (LD) with a collimator is used as a source of a low-coherence optical radiation. The TOLD serves as a variable coherence length source whose spectrum can be varied by varying a drive current. Consequently, a drive connected with the LD allows both the desired width of the spectrum and the output optical power of the LD to be obtained. The light from the LD is launched into a Michelson interferometer which consists of two mirrors and a beamsplitter. The wavelength dependence of the OPD results from different path lengths of both beams through the dispersive medium of a beamsplitter. Beams are combined at the output of the interferometer giving for a suitable OPD, that is for the OPD shorter than the source coherence length, spatial interference fringes. When the OPD is substantially magnified, the spatial interference fringes disappear. The position of mirror 1 is controlled by a micropositioner, which enables to adjust the desired fine change in the OPD with nearly micrometer accuracy.

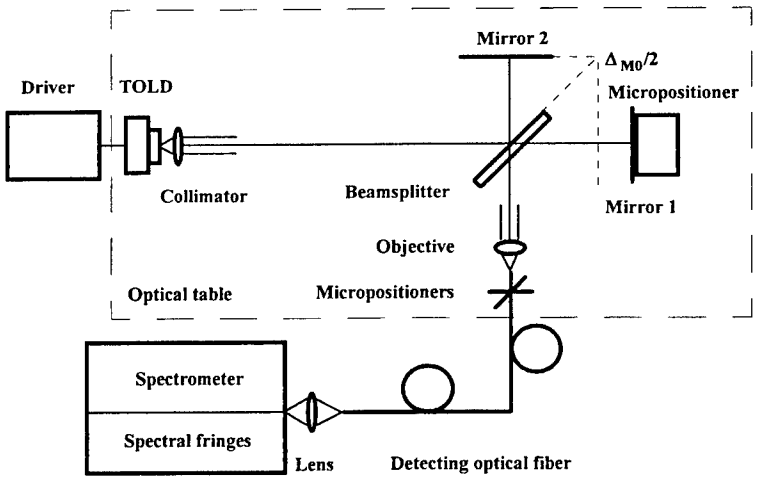


Figure 1. Experimental setup for the investigation of the spectral interference between two beams in a Michelson interferometer

The Michelson interferometer configuration is placed on the optical table which supports a vibrational isolation. Because the spectrometer is placed in a different room from the Michelson interferometer configuration, a multimode optical fiber acting as the detecting optical fiber is used to launch the optical power from the output of the interferometer into the entrance slit of the monochromator. Moreover, the multimode optical fiber whose core diameter is approximately 200 μm serves as a spatial filter. A microscopic objective and micropositioners are used to launch the light from the interferometer into the detecting optical fiber.

The light from the detecting optical fiber is focused by a lens into a Carl Zeiss SPM 2 grating monochromator. A variable width of the entrance slit of this monochromator enables the desired resolving power of the monochromator to be adjusted. The monochromator is controlled by a stepper motor. At the output of the monochromator, a semiconductor *p-i-n* photodetector with an amplifier is used. The stepper motor and the amplifier coupled with an IBM personal computer. By this system, the range of measured wavelengths, the wavelength step $\Delta\lambda$ between two

measurements can be controlled. Recurrence data processing method yields the parameters of the spectral interferogram synchronically with the data samlpling in dynamic regime.

4. EXPERIMENTAL RESULTS AND DISCUSSION

Recurrence non-linear filtering method was applied to the analysis of the spectral interferograms observed in the scheme Fig.1 in previous work [11]. The example of the series of data samples is presented in Fig. 2*a*. The whole number of discrete samples K was equal to 150 points in the wavelength range 30 nm and the wavelengh step between two points was $\Delta\lambda \approx 0{,}2$ nm .

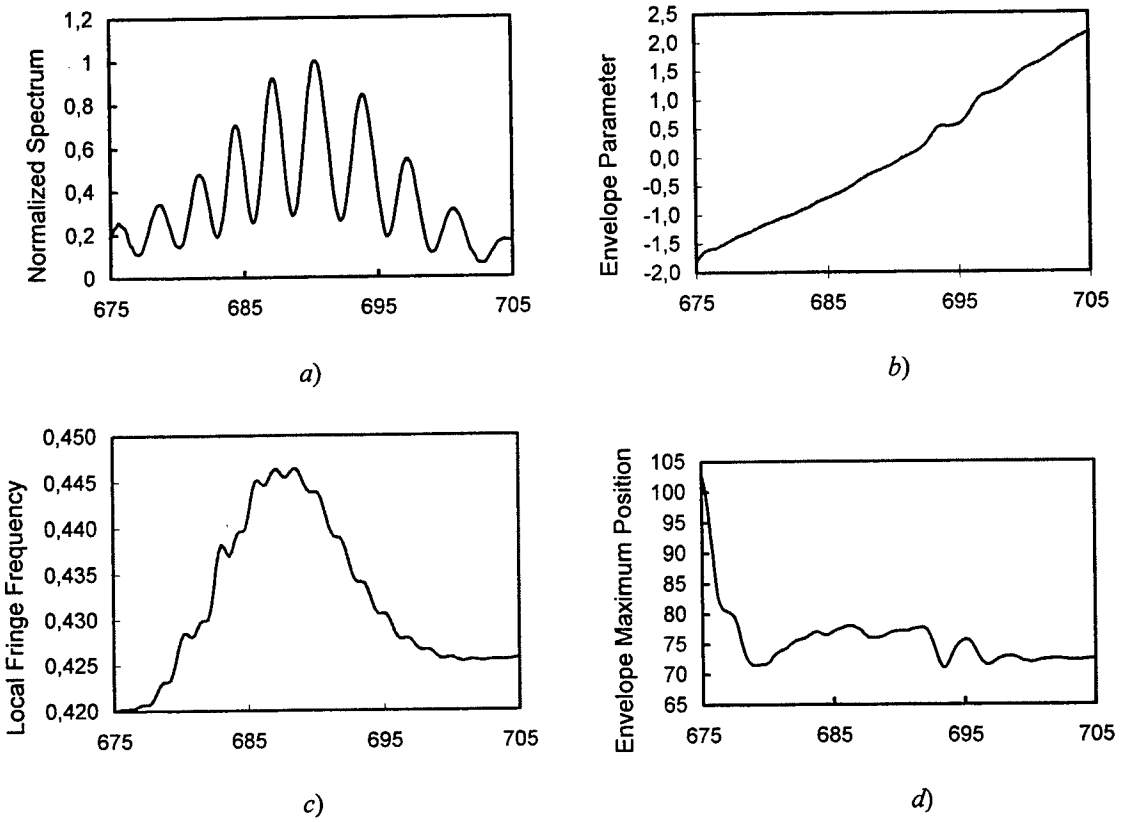


Figure 2. Initial spectral interferogram and the dynamic recurrence estimates of its local parameters dependent on the wavelength value (nm)

The results of data processing are shown in Figs. 2*b-d*, where are presented correspondingly the evolution of dynamic estimates of the envelope parameter C, local circular fringe frequency U and the fringe envelope maximum position λ_m. All the parameters were calculated simultaneously according to the Eqs. (10),(11) at each step. Estimates of the local fringe frequency give the possibility to calculate the group OPD by the evident formula (see Eq. (3) and Ref.[16])

$$\Delta^{g}_{M}(\lambda) = (1 / 2\pi)\, U(\lambda) / \lambda^2 . \qquad (12)$$

Thus the distance measurement is transformed to the frequency measurement. Selecting the middle value of U = 0,435 rad/step one can find from Eq. (12) the group OPD estimate as $\Delta^{g}_{M}(\lambda)$ = 160μm (λ =680 nm) that is in good agreement with the result found ealier.[11] The accuracy of this estimate is defined by the range of the local fringe frequency deviation. The error can be easily assessed according to the data Fig. 2*c* and the relative RMS error (2σ) of OPD is less than 1,5%. Using the data Fig. 2*b* and *d* one can assess as well the spectral power density (spectrum) of the light source that is described by the exponential model Eq. (6) with the locally variable parameters. True maximum position of the power spectrum at the 73-rd point (λ=690 nm) was found already at the15-th step, λ=678 nm,

(see Fig. 2*d*) with the accuracy of 1 nm (5 points). Note that *a priori* estimate of this parameter, the 103-rd point, was very coarse and proposed algorithm had provided the stable dynamic estimate with the quick convergence.

5. CONCLUSION

The mutual interference of two beams in the spectral domain has been demonstrated experimentally at the output of the uncompensated Michelson interferometer excited by a low-coherence source when the OPD between both beams exceeds the coherence length of the source. Spectral interferograms have been successfully analyzed using recurrence non-linear data processing method. The wavelength dependencies of the group OPDs have been expressed by the local spectral fringe frequency variations. It is clear the advantage of the proposed approach with respect to known FTM, where the local fringe frequency could not be found directly because of global character of data processing. Recurrence vector signal processing gives the optimal estimates of all the parameters of spectral interference fringes that were included in vector Θ. Method yields the spectrum estimate of the light source as well as fringe frequency. Recurrence character of calculation is convenient for any step-controlled spectrometer. As a rule the whole steps number in data series and full measurement interval may be decreased essentially with respect to FTM. High noise-immunity of the non-linear filtering method provides the measurement with very small wavelengh step and high resolution that extends the OPD measurement range. The general advantages of non-linear recurrence filtering are: optimal estimation of useful parameters that depend on intensity non-linearly; noise-immunity; solving the phase unwrapping problem automatically by recurrence calculations and using Eq. (8); possibility to use the algorithm with changing of signal parameters because of adaptive character of algorithm. Stability, accuracy and quickness of non-linear recurrence filtering are increased when *a priori* information about interferometric data is enough reliable.

6. REFERENCES

1. T. Dresel, G. Hausler and H. Ventzke, "Three-dimensional sensing of rough surfaces by coherence radar", *Appl. Opt.* **31**, pp.919-925, 1992.
2. T. Yoshimura, K. Kida and N. Masazumi, "Development of an image-processing system for a low coherence interferometer", *Opt. Commun.* **117**, pp. 207-212, 1995.
3. J.-C. Vienot, J.-P. Goedgebuer and A. Lacourt, "Space and time variables in optics and holography: recent experimental aspects", *Appl. Opt.* **16**, pp. 454-461, 1977.
4. P. Hlubina, "Experimental demonstration of the spectral interference between two beams of a low-coherence source at the output of a Michelson interferometer", *J. Mod. Opt.* **44**, pp. 1049-1059, 1997.
5. L. Mandel and E. Wolf, *Optical Coherence and Quantum Optics*, Cambridge University Press, Cambridge,1995.
6. M. Born and E. Wolf, *Principles of Optics*, Pergamon Press, Oxford, 1985.
7. L. M. Smith and C. C. Dobson, "Absolute displacement measurement using modulation of the spectrum of white light in a Michelson interferometer," *Appl. Opt.* **28**, pp. 3339-3342,1989.
8. U.Schnell, E. Zimmermann and R. Dändliker, "Absolute distance measurement with synchronously sampled white-light channelled spectrum interferometry," *Pure Appl. Opt.* **4**, pp. 643-651, 1995.
9. U. Schnell, R. Dändliker and S. Gray, "Dispersive white-light interferometry for absolute distance measurement with dielectric multilayer systems on the target," *Opt. Lett.* **21**, pp. 528-530, 1996.
10. C. Sáinz, P. Jourdain, R. Escalona and J. Calatroni, "Real time interferometric measurements of dispersion curves," *Opt. Commun.* **110**, pp. 381-390, 1994.
11. P. Hlubina, "Fourier transform analysis of the spectral modulations obtained at the output of the uncompensated Michelson interferometer", *Opto-Electr. Rev.* **5**, pp. 117-122, 1997.
12. M. Takeda, H. Ina and K. Kobayashi, "Fourier-transform method of fringe pattern analysis for computer-based topography and interferometry," *J. Opt. Soc. Amer.* **72**, pp. 156-160, 1982.
13. C.Roddier and F.Roddier, "Interferogram analysis using Fourier transform techniques", *Appl.Opt.* **26**, pp. 1668-1673, 1987.
14. I.Gurov and A.Djabiev, "3-D surface reconstruction by vector non-linear Markov filtering of white-light interference fringes visibility", BiOS'98 (Stockholm, Sweden, 8-12 Sept., 1998), *Proc.SPIE* **3568**, pp. 178-184, 1998.
15. I.Gurov and D Sheynihovich, "Interferometric data analysis based on Markov non-linear filtering methodology", *J. Opt. Soc. Amer.* A **17**, pp.21-27, 2000.
16. I.Gurov and A Kirienko, "Interferometric distance assessment by recurrence multiwavelength method", *Proc. ODIMAP II* Topical Meeting on Optoelectronic Distance/Displacement Measurements and Applications (Pavia, Italy, May 20-22, 1999), pp.48-53 (1999).

Processing of noisy signals by four-wave mixing

Vladimir V. Kabanov

Institute of Physics, National Academy of Sciences of Belarus
F. Skarina Ave. 68, Minsk 220072, Belarus

ABSTRACT

Possibilities are considered of noisy signals processing by four-wave mixing (FWM) of laser radiation in a two-level medium with taking into account of the combined influence of spatial phase matching, nonlinear response inertia, and phase cross-modulation. Regularities of time behavior transformation of randomly modulated signal are collated with particularities of FWM-reflectivity of deterministic pulses. Results are discussed of correlation analysis of FWM with partaking in a random way amplitude (or phase) modulated signals.

Keywords: four-wave mixing, phase conjugation, noisy signals, random process, autocorrelation function, and spectral density.

1. INTRODUCTION

A characteristics of actual laser systems is that the amplitude and phase of their radiation are subjected to fluctuations that significantly influence the stability of reproduction of the required characteristics of light pulses.[1] As a consequence, the parameters of the output radiation of such systems are also subjected to fluctuations. The present repot is devoted to the investigation of the specific features of the four-wave mixing (FWM) of random signals with bandwidth-limited pump pulses. The actual possibilities of processing of chirped signals with the use of the methods of dynamic gratings are considered for the FWM of laser radiation in a two-level medium with regard to the combined action of the mechanisms of spatial phase matching, finite nonlinear response time, and phase cross-modulation. The time behaviour of signal waves at the exit of a nonlinear medium in specific realizations and their statistic characteristics (autocorrelation function and spectral density) are analyzed. The regularities of the transformation of the time behaviour of the amplitude and the phase of randomly modulated initial signal in specific realizations are compared with the features of the FWM reflection of a deterministic signal. The results of the correlation of randomly amplitude- and phase-modulated signals (A(P)MS) are discussed.

2. BASIC MODEL

The possibilities of processing of deterministic signals and realization phase conjugation at FWM in different nonlinear media are sufficiently investigated.[2-4] In particular, the combined action of series of mechanisms (spatial phase matching, nonlinear response inertia, and phase cross-modulation) can markedly distort the spectral-temporal parameters of the initial signal.[5] Because of this, a phase conjugation free from marked distortions of deterministic PMS can be realized in the case were certain conditions are fulfilled and it is accompanied by a shortening of the envelope of the conjugate wave and a narrowing of its spectrum.

Reduced below analysis is based on the methods of numerical simulation of the process and on the theoretical model of a transient FWM described by the integrodifferential system of equations[4,6] for the nonlinear susceptibility of the medium

$$p_{21}^{-1}\partial_t \chi_{Nl} + (1+\underline{\alpha}\left|\vec{\mathcal{E}}\right|^2)\chi_{Nl} = -n_0 c_0 \underline{\hat{\alpha}}\left|\vec{\mathcal{E}}\right|^2 / 2\pi\,, \tag{1}$$

and the electric field of the interactive waves

$$(\mathrm{v}^{-1}\partial_t \pm \partial_z)E_{1,2} = -(i2\pi\omega / n_0 c)(\chi_0 E_{1,2} + \chi_{\pm 1} E_{3,4})\,,$$

Laser Optics 2000: Control of Laser Beam Characteristics and Nonlinear Methods for Wavefront Control,
Leonid N. Soms, Vladimir E. Sherstobitov, Editors, Proceedings of SPIE Vol. 4353 (2001)
© 2001 SPIE · 0277-786X/01/$15.00

$$(\mathrm{v}^{-1}\partial_t \pm \partial_z)E_{3,4} = -(i2\pi\omega/n_0 c)(\chi_0 E_{3,4} + \chi_{\pm 1}E_{1,2}), \tag{2}$$

$$\chi_q = (2\pi)^{-1}\int_{-\pi}^{\pi}\chi_{Nl}\exp(-iq\vec{K}_-\vec{r})d(\vec{K}_-\vec{r}),(q=0,\pm 1),$$

where n_0, $æ_0$ are, respectively, the refractive index and the extinction coefficient of an unexcited medium; $\hat{\alpha} = a + i\alpha$ is a complex nonlinear parameter; p_{21} is the total probability of spontaneous and nonradiative transitions; $\underline{\hat{\alpha}} = cn_0\hat{\alpha}/8\pi$; v is the velocity of light in the medium; $\vec{E}_i = \vec{A}_i\exp(i\varphi_i)$ are the slowly varying amplitudes; $\vec{K}_\pm = \vec{k}_1 \pm \vec{k}_3$ are vectors of dynamic gratings induced in a two-level resonant medium. The closed system of integrodifferential equations (1) - (2) corresponds to the approximation, when the large-scale dynamic gratings $\vec{K}_-$ are took part in to account only. The system of equations (1) - (2) makes possible to investigate FWM with taking into account the depletion of the pump fields, the nonlinear absorption of all interactive waves, and the appearance of a finite nonlinear response time of the medium.

Series of mechanisms can sufficiently influence on the spectral-temporal parameters of initial signals. The wave-vector mismatch of interactive waves Δk reduces the efficiency of formation of the fourth wave E_4, the amplitude of which falls by a factor of two for $\Delta kL/2 \approx 2$. The width of the spectrum, within the limits of which the phase-conjugate pulse can effectively reproduce the spectral components of the initial signal is:

$$\Delta\omega_{4c} = 2\omega_0/kL. \tag{3}$$

The spectral width $\Delta\omega_{4c}$ of an FWM-filter, determined by the spatial phase matching mechanism, is related to the transit time of the radiation in the medium $\tau_{fwm} = L/\mathrm{v}$ by $\tau_{fwm}\Delta\omega_{4c} = 2$. If the radiation frequency is $\nu = 5\times10^{14}$ Hz and if $k = 1.3\times10^5$ cm^{-1}, L=1 cm, and n_0=1.25, we find that $\tau_{fwm} \approx 4.2\times10^{-11}$ s and the bandwidth, determined by the spatial phase matching, is estimated as $\Delta\nu_{4c} = \Delta\omega_{4c}/2\pi \approx 7.6\times10^9$ Hz.

The finite nonlinear response time can be responsible for the frequency filtering of the input signal during the formation of conjugate wave with the central frequency $\omega_3 = \omega_0$ and with the half-width

$$\Delta\omega_{4m} = 2\tau_m^{-1}, \tag{4}$$

where $\tau_m = [(1+\underline{\alpha}J_0)p_{21}]^{-1}$ is the effective relaxation time of the nonlinear response, $J_0 = \sum_{i=1}^{4}|E_i|^2$. If $p_{21} = 10^9$ s, and the total intensity varies in the range $1 >> \underline{\alpha}J_0 = 1$, the quantity $\Delta\omega_{4m}/2\pi$ fluctuates within the limits $3.2\times10^8 \div 6\times10^8$ Hz.

Strong pump waves give rise to phase cross-modulation of the fourth wave. A sufficiently high level of the cross-modulation can distort the initial phase of the signal and can significantly act on the spectral composition of the conjugate and signal pulses.[6] The spectral broadening of the conjugate pulse as a result of cross-modulation can be estimated as

$$\Delta\omega_{cm} \approx \phi_{max}\Delta\omega_g, \quad \Delta\omega_g = 2\sqrt{\ln 2}\cdot\tau_0^{-1}, \tag{5}$$

where $\phi_{max} = \omega_0 æ_0 \underline{a}L(2A_{10}^2 + A_{20}^2)/c$ is the maximum frequency shift.

If the signal is chirped in accordance with the square law $A_{30}(t) = A_{30} exp[-(1+im)t^2 / 2\tau_0^2]$, the width of the spectrum $\Delta\omega_{ph}$ is defined by $\tau_0 \Delta\omega_{ph} = 2[ln\,2(1+m^2)]^{1/2}$. The phase-conjugate pulse is obtained if the spectral width of the FWM-filter does not limit effective FWM of all spectral components of the chirped signal. It follows from the above estimates that the main constraint comes from the finite response time, i.e. it is necessary to satisfy the condition $\Delta\omega_{ph} < \Delta\omega_{4m}$. Full phase conjugation of a chirped pulse is possible if the duration of initial signal is satisfied the following condition:

$$\tau_0 > [ln\,2(1+m^2)]^{1/2} \tau_m . \tag{6}$$

The phase conjugation of PMS in a time is obtained without visual distortions, if from one side the spectral width of the FWM filter does not limit effective FWM of all spectral components of the chirped signal, and from another the spectral width of the initial signal is visibly gone beyond the broadening dependent by the cross-modulation:

$$\Delta\omega_{cm} << \Delta\omega_{ph} < \Delta\omega_{4c}, \Delta\omega_{4m} . \tag{7}$$

3. TRANSFORMATION of NOISY SIGNALS by FWM

The signal was described with the use of a statistical approach that makes it possible to represent a random pulse as optical noise bursts

$$E_{30(m)}(t,0) = s\xi_{(m)}(t)\Psi_0(t) , \tag{8}$$

where $\xi_{(m)}(t)$ is a complex Gaussian random process with a zero mean, a unit dispersion, and a Gaussian correlation function; $\Psi_0(t)$ is the deterministic component of the field; s is the parameter characterizing the level of noise. As a model of the initial signal we also considered the superposition "signal + noise"

$$E_{30(m)}(t) = \Psi_0(t) + s\xi_{(m)}(t) , \tag{9}$$

where the first term has a meaning of a regular, wholly predictable characteristic of the signal, and the second term is a fluctuation component. The most full information about the FWM process can be obtained in numerical experiments that make it possible to analyze both the behaviour of single realizations and the statistical characteristics obtained by averaging over the set of solutions of the system of the equations (1) – (2) with initial conditions (8) or (9).

3.1. FWM with the participation of a randomly amplitude-modulated signal. Numerical experiments performed for FWM of bandwidth-limited pumps and randomly amplitude-modulated signal (it was assumed that the phase of the signal has a constant value) allowed us to establish the following regularities. In a specific realization of the process we observed the smoothing of the amplitude fluctuations in the fourth pulse formed in the FWM. Such behaviour modeled for the initial random pulse by the formula (8) at $s = 0.2$ and $\Psi_0(t) = A_{30} \exp(-(t/\tau_0)^2)$ (doted line) is illustrated in Fig. 1. These results are corresponded to the following conditions of FWM: the duration of interactive pulses is $\tau_0 = 10 p_{21}^{-1}$; the intensities of pump pulses in maximum are $I_{1,2}^m = 0.5 I_{sat}$, where $I_{sat} = \alpha^{-1}$ is the saturation intensity of a resonant medium; and the interaction length is $\hat{L} = (2\omega æ_0 / c) = 1$. It is seen that the fluctuations of the amplitude of the fourth pulse (solid line) are practically absent at the wings of the profile and have a markedly smaller value, as compared with the initial signal, at the centre. Besides, the signal pulses are subjected to a regular phase modulation caused by the nonlinear cross-modulation in the presence of strong pump waves. The main future of the behaviour of the phase cross-modulation is similar to the manifestation of this effect in the FWM of deterministic bandwidth-limited signals.[6] The future is illustrated in Fig. 2.

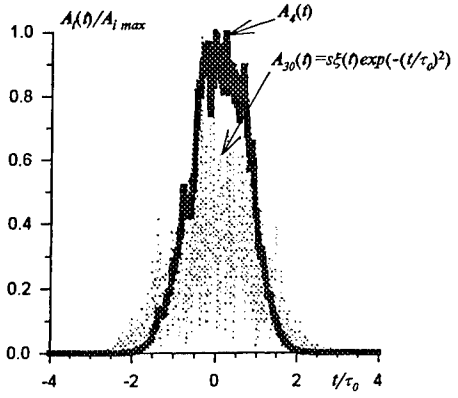


Fig. 1. Time behaviour of the amplitude of the fourth pulse (solid line) calculated for a randomly amplitude-modulated signal (doted line) at $\tau_0 = 10p_{21}^{-1}$, $I_{1,2}^m = 0.5I_{sat}$, $\hat{L} = 1$, s=0.2.

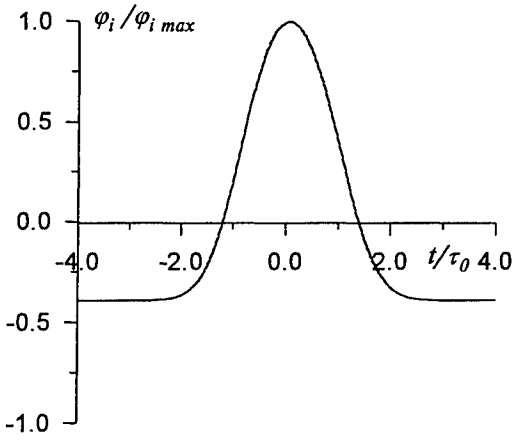


Fig. 2. Time behaviour of the induced phase of the fourth pulse calculated for a randomly amplitude-modulated signal at $\tau_0 = 10p_{21}^{-1}$, $I_{1,2}^m = 0.5I_{sat}$, $\hat{L} = 1$, s=0.2.

Correlation analysis of the FWM with the participation of a randomly AMS has shown that the statistic of signal pulses is markedly modified. Figure 3 shows the modules of the correlation coefficient

$$R_i(\tau) = B_i(\tau)/\sigma^2,\ \sigma^2 = B_{i\max}(\tau) = B(0), \tag{10}$$

where $B_i(\tau) = \langle A_i(t)A_i(t+\tau)\exp[i\varphi_i(t) - \varphi_i(t+\tau)]\rangle$ is the correlation function for the signal, i=3, (dashed line) and the fourth wave i=4 (solid line) formed at the exit from the nonlinear medium. As is seen, the behaviour of the correlation coefficient of the signal waves differs significantly from that of the initial signal, and the correlation time

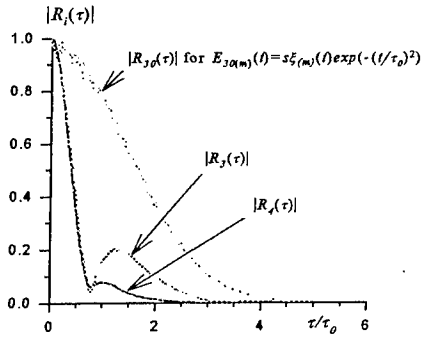


Fig. 3. Modulus of the correlation coefficient of the signal (dashed line) and the fourth pulse (solid line) at $\tau_0 = 10p_{21}^{-1}$, $I_{1,2}^m = 0.5I_{sat}$, $\hat{L} = 1$, s=0.2.

$$\tau_{ci} = 4\int_0^\infty |R_i(\tau)|d\tau \tag{11}$$

is markedly decreased. This, in turn, manifests itself as a transformation of the spectral distribution of signal waves, as a result of which the width of the spectra $\Delta\omega_i = \left|\int_0^\infty G_i(\omega)d\omega / G_{i\max}\right| = \sigma^2/2|G_{i\max}|$ increases with increasing the level of cross-modulation ($\Delta\omega_i\tau_{ci} = 2\pi$).

3.2. FWM with the participation of a randomly phase-modulated signal. FWM with the participation of a randomly phase-modulated signal (the amplitude of the signal was set by the deterministic function with a Gaussian profile) and

bandwidth-limited pumps causes a marked amplitude modulation of signal waves. This situation is illustrated in Fig. 4, where a specific realization of the amplitude of the fourth wave is shown. The specific feature of the influence of cross-modulation at FWM with the participation of noisy signal is consisted in that it is possible to smooth noticeably a random phase component of pulse in the case of high level of the phase cross-modulation.

The autocorrelation coefficients of the signal and fourth waves are shown in Fig. 5. Their behaviour points to the fact that the correlation time of both the signal and the fourth pulse decreases in the process of FWM. In this case the correlation time of the signal waves decreases more markedly as compared with the FWM for a randomly AMS.

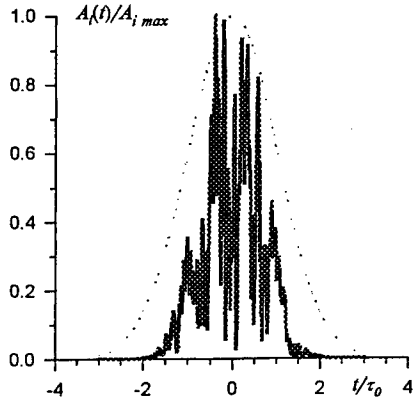


Fig. 4. Time behaviour of the amplitude of the fourth pulse (solid line) calculated for the randomly phase-modulated signal (doted line) at $\tau_0 = 10p_{21}^{-1}$, $I_{1,2}^m = 0.5I_{sat}$, $\hat{L} = 1$, s=0.2.

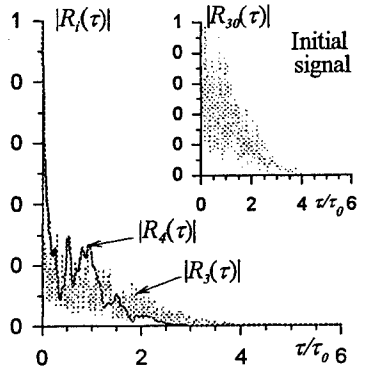


Fig. 5. Modulus of the correlation coefficient of the randomly phase-modulated signal (dashed line) and the fourth pulse (solid line) at $\tau_0 = 10p_{21}^{-1}$, $I_{1,2}^m = 0.5I_{sat}$, $\hat{L} = 1$, s=0.2.

4. CONCLUSION

In summary it should be said that in a specific realization of the process of four-wave mixing with the participation of the randomly AMS there can occur a marked smoothing of the amplitude fluctuations in the fourth pulse formed at FWM. In this regime of interaction the statistics of signal pulses at the exit from a nonlinear medium is markedly modified: the behaviour of the correlation coefficient points to the appreciable decrease in the correlation time and the corresponding broadening of the spectra as compared with the statistic characteristics of the initial signals. In the case of FWM with the participation of a randomly PCM there takes place a marked amplitude modulation of signal waves and an even more effective (as compared with a randomly AMS) decrease in the correlation time of the signal pulses at the exit from a nonlinear cell.

5. REFERENCES

1. S.A. Achmanov, Y.E. D'yakov, A.S. Chirkin. *Introdaction in statistic radio physics and optics*, Nauka, Moscow, 1981.
2. *Optical phase conjugation*, ed. By R. Fisher, Acad.Press, N.Y., 1983.
3. B.Ya. Zel'dovich, N.F. Pilipetsky, V.V. Shkunov. *Principal of Phase Conjugation*, Springer, Berlin, 1985.
4. V.V. Kabanov, A.S. Rubanov, "Dynamic gratings and four-wave phase conjugation in dye solutions", *IEEE J. Quantum Electron.*, **QE-26**, pp. 1990-1998, 1990.
5. V.V. Kabanov, "Four-wave mixing of chirped signal with bandwidth-limited pump waves in a resonant medium", *Kvantovaya Elektron. (Moscow)*, **25**, pp. 661-664, 1998; [*Quantum Eleerron.*, **28**, pp. 643-646, 1998].
6. V.V. Kabanov, "Influence of self-modulation on degenerate four-wave mixing in a resonant medium", *Kvantovaya Elektron. (Moscow)*, **22**, pp. 284-286, 1995; [*Quantum Eleerron.*, **25**, pp. 267-269, 1995].

Noise-immune interference fringe analysis by modification of local intensity histogram and 2D Fourier transform method

S. De Nicola†, P. Ferraro‡, I. Gurov§, R. Koviazin§ and M. Volkov§

†Istituto di Cibernetica del CNR, via Toiano 6, Arco Felice, I-80072, Italy
‡Istituto Nazionale di Ottica Applicata, Sez. di Napoli c/o Istituto di Cibernetica del CNR
§Institute of Fine Mechanics and Optics (Technical University),
14 Sablinskaya st., Saint-Petersburg, 197101, Russia

ABSTRACT

A noise-immune method of phase retrieval of single moiré interferometric fringe pattern is presented and discussed. The method is shown to provide accurate recovering of the phase information by combined method based on modification of local histogram of the fringe intensity and two dimensional Fourier transform of enhanced moiré fringe pattern. The principle of the method is described and the experimental results of moiré interferometric measurements with submicron sensitivity of the in-plane displacement fields of thick carbon fibre/PEEK composite laminates are presented as example of application of the technique.

Keywords: interference fringe analysis, local intensity histogram, Fourier transform, phase recovering

1. INTRODUCTION

Analysis of noisy interferometric signals and fringe patterns plays an important role in remote sensing, measurement of geometrical quantities of real objects and material evaluation. In many cases interference fringe pattern is distorted by noise influence and local fringe defects that make it difficult to process the intreferogram data quantitatively. The well-known fringe processing methods based on Fourier Transform (FTM)[1,2] or fringe approximation by non-linear polinomials[3] do not provide a noise-immunity of phase recovering and they demand taking much computing time.

The recently developed image enhancement method[4] relies on the modification of the gray-level image intensity histogram, that is the estimate of the intensity probability density function (PDF). The enhancement of the intensity distribution is performed by modifying the experimental histogram to the desired one and by the restoration of the signal from the modified histogram. It has been shown[4] that estimated PDF (histogram) can be transformed to the desired one by a simple transformation of the pixel values of digitized image. A drawback of a direct application of this method[4] is caused from the global character of interferogram data processing, which often makes it impossible to suppress local fringe defects.

The problem can be overcome by using the proposed method of modification of a local fringe pattern intensity histogram. Local histogram modification may be interpreted as a non-linear filtering with signal dependent filter impulse response. Such an operation allows to suppress the noise and local fringe defects without decreasing the fringe visibility compared to the conventional low-pass filtering techniques in frequency domain. The enhanced fringe pattern is processed by the standard 2-D fast Fourier transform algorithm applied to the single interferogram[5,6]. Since we apply the 2-D FTM to a fringe pattern with enhanced quality, the phase unwrapping procedure is stable and the full phase distribution can be retrieved completely without influences from false signals that distorts the phase data to be measured. We show that this technique can be efficiently used for automated moiré fringe pattern analysis.

2. HISTOGRAM MODIFICATION METHOD

In order to describe the principle of the method, let us denote with s and ξ the ideal and the observed signal values with PDFs $p(s)$ and $\hat{p}(\xi)$, respectively. In the discrete case the histograms $p(s_m)$ and $\hat{p}(\xi_m)$ are considered, where m indicates the quantization level, $m = 0,\ldots, M-1$. We must find the monotone transform function T, such that $T(\xi_m) = s_m$.

It had been shown[4] that the transform

$$z_m = T_1(\xi_m) = \sum_{i=0}^{m} \hat{p}(\xi_i) \qquad (1)$$

Laser Optics 2000: Control of Laser Beam Characteristics and Nonlinear Methods for Wavefront Control,
Leonid N. Soms, Vladimir E. Sherstobitov, Editors, Proceedings of SPIE Vol. 4353 (2001)
© 2001 SPIE · 0277-786X/01/$15.00

produces a histogram of the uniformly distributed values z_m. The same uniform histogram can also be calculated by transforming the ideal known histogram $p(s_i)$, namely

$$z_m = T_2(s_m) = \sum_{i=0}^{m} p(s_i). \tag{2}$$

From Eqs. (1), (2) one can find ideal values s_m are related to the observed values ξ_m by the following transformation

$$s_m = T(\xi_m) = T_2^{-1}[T_1(\xi_m)]. \tag{3}$$

The ideal PDF of harmonic stochastic process that describes the useful component of interference fringe,

$$s = b\cos\phi, \tag{4}$$

with the constant amplitude b and phase ϕ uniformly distributed inside the interval $(-\pi, \pi)$ is presented by the well-known formula:

$$p_s(s) = \begin{cases} \left(\pi\sqrt{2\sigma_s^2 - s^2}\right)^{-1}, & |s| < b, \\ 0, & |s| > b, \end{cases} \tag{5}$$

where $\sigma_s^2 = b^2/2$ is the dispersion of the harmonic process. The curve Eq. (5) is presented in Fig. 1 as the curve 1. If the signal value Eq. (4) is distorted by the noise n statistically independent on the signal s with PDF $p_n(n)$ the resulting PDF $p(s+n)$ is defined by the convolution of $p_s(s)$ and $p_n(n)$ and the peaks of the curve 1 in Fig. 1 are blurred as shown by the curve 2 for the case of Gaussian noise influence.

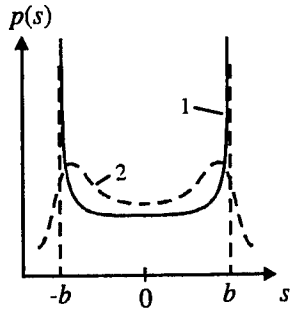


Figure 1. Ideal fringe PDF (curve 1) and PDF blurred by the influence of Gaussian noise (curve 2)

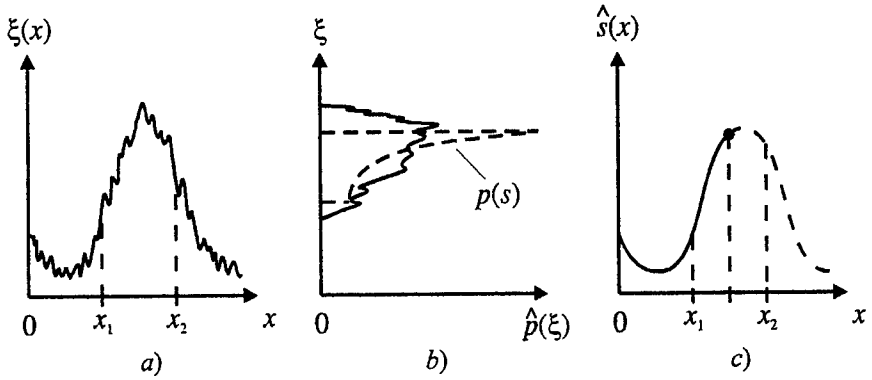


Figure 2. Restoration of the fringe profile from noisy fringe by modification of local intensity histogram to ideal PDF: the noisy fringe (*a*), the modified histogram $p(s)$ at the short interval (x_1, x_2) being found from the observed histogram $\hat{p}(\xi)$ (*b*), and restored fringe from the modified histogram (*c*)

The application of the restoration procedure by the histogram modification Eq. (3) is illustrated in Fig. 2. This procedure assumes that one has to preliminary know the background component and the local fringe amplitude b. However, these quantities are usually unknown and it is desirable to extend the histogram modification method in order to avoid the determination of the fringe parameters. Our approach relays to the consideration that in the ideal PDF (see curve 1 in Fig. 1) the probability to find the extreme values of the fringe pattern intensity distribution is higher than any other intermediate intensity values. Hence, it is possible to find the approximation for the enhanced fringe histogram by the simple transformation

$$p(s) \approx k[\hat{p}(\xi)]^{\alpha}, \tag{6}$$

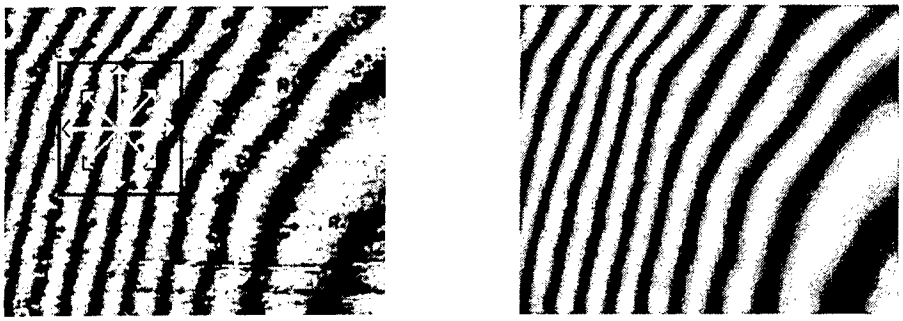
where k is the normalizing coefficient, $\alpha > 1$ is the histogram modification degree.

It can be easily shown that the averaged fringe intensity value to be calculated inside the interval (x_1, x_2) from the non-modified "sliding" local histogram, can be equivalently obtained by a convolution with the normalized rectangular impulse response $h(x_n)$ of linear filter with the length of N points, namely

$$\hat{s}(x_k) = \sum_{m=0}^{M-1} \xi_m \, p(\xi_m) \Big/ \sum_{m=0}^{M-1} p(\xi_m) = \sum_{n=0}^{N-1} h(x_n)\,\xi(x_k - x_n) = (1/N) \sum_{n=0}^{N-1} \xi(x_n) . \qquad (7)$$

It is clear that the convolution Eq. (7) will result in the decreasing of fringe amplitude by the factor $\mathrm{sinc}(L\Delta x / B)$, where Δx is the step of discretization, $\mathrm{sinc}(y) = \sin(\pi y) / (\pi y)$ and B is the fringe period. Transformation of the histogram by the Eq. (6) allows to compensate for the amplitude losses and to increase the fringe visibility. Thus, the transformation Eq. (6) may be interpreted as a non-linear filtering operation with the signal dependent filter impulse response.

An example of application the histogram modification method to noisy interferogram is shown in Fig. 3. Histograms were calculated in four directions inside the local area of the interferogram Fig. 3, *a*. Parameter α in Eq. (6) was chosen equal to 2. It can be clearly seen in the Fig. 3*b* the effective suppression of a local fringe defects without decreasing the fringe visibility.



a) *b)*

Figure 3. Initial interferogram distorted by noise and local fringe defects (*a*) and enhanced interferogram (*b*)

It is worth to emphasize that in difference to conventional low-pass filtering Eq. (7) the transformation Eq. (6) may be applied to fringe pattern enhancement iteratively without decreasing the fringe visibility. The application to the interferogram Fig. 3*a* of the iterative restoration procedure is shown in Fig. 4. It was found that the iterative process converges to the true intensity distribution without essential systematic error. Approximately after 4-th iteration, the fringe defects have been suppressed enough to allow for a stable calculation of the fringe phase.

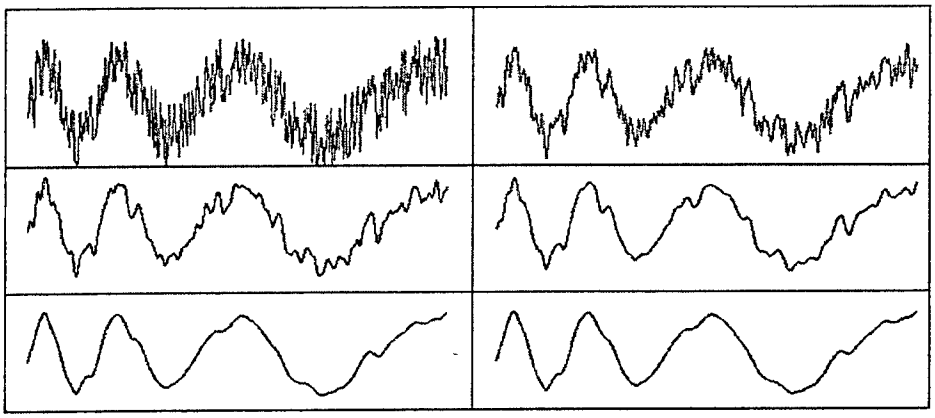


Figure 4. Iterative steps of fringe enhancement

3. PHASE RECOVERING OF INTERFERENCE FRINGE PATTERN

The signal value $s(x, y) = \mu\, I(x, y)$ proportional to the fringe pattern intensity distribution $I(x, y)$ may be written in the following form:

$$s(x, y) = a(x, y) + b(x, y) \cos \phi(x, y) , \qquad (8)$$

where $a(x, y)$ and $b(x, y)$ are the background and the envelope of the fringe pattern intensity distribution and $\phi(x, y)$ is the phase of the fringe pattern.

By Fourier transforming Eq. (8) and by using the well-known convolution theorem we obtain the 2-D fringe spatial frequency spectrum in the following form

$$\mathrm{F}\{s(x,y)\} = S(f_x,f_y) = A(f_x,f_y) + B(f_x,f_y) * C(f_x,f_y), \tag{9}$$

where $\mathrm{F}\{\cdot\}$ denotes the Fourier transform operation and we have defined $A(f_x,f_y) = \mathrm{F}\{a(x,y)\}$, $B(f_x,f_y) = \mathrm{F}\{b(x,y)\}$, and

$$C(f_x,f_y) = \mathrm{F}\{\cos\phi(x,y)\} = (1/2)\,\mathrm{F}\{\exp[-j\phi(x,y)]\} + (1/2)\,\mathrm{F}\{\exp[j\phi(x,y)]\}. \tag{10}$$

In Eq. (2) $*$ denotes the 2-D convolution symbol. Putting together Eqs. (9) and (10) it can be easily seen that the spectrum $S(f_x,f_y)$ contains essentially three components. The useful information about the fringe phase is contained in either of the two spectral terms in $C(f_x,f_y)$. In order to retrieve the phase one needs to filter out one of these terms.

As discussed in Refs.[5,6] one can calculate the phase estimate $\hat{\phi}(x,y)$ by processing of a single interferogram using the inverse Fourier transform of $C(f_x,f_y)$ on positive frequencies only, namely

$$\hat{\phi}(x,y) = \arg\mathrm{F}^{-1}\{C(f_x>0,f_y)\}. \tag{11}$$

The low frequency component $A(f_x,f_y)$ can be easily removed. The last term in Eq.(9) can be used for phase calculation in Eq.(11) if we neglect the influence of $B(f_x,f_y)$, taking into account that $\arg\mathrm{F}^{-1}\{B(f_x,f_y)\} = \arg b(x,y) = 0$ because $b(x,y)$ in Eq.(8) is real value.

According to Eq. (11) and to the relation $f_x(x,y) = \partial\phi(x,y)/\partial x > 0$ the phase estimate in Eq. (11) is recovered as a monotonically increasing function along x axis and the sign of the local phase deviations is lost. Recovering of the true phase $\phi(x,y)$ from phase estimate Eq. (11) of the single interferogram is generally based on *a priori* knowledge about the allowed form of phase function.

The enhanced fringe pattern is processed by the standard 2-D fast Fourier transform algorithm to determine the 2-D spectrum $S(f_p,f_q)$ at discrete spatial frequencies f_p, f_q, namely

$$S(f_p,f_q) = \sum_{k=0}^{K-1}\sum_{l=0}^{L-1} s(x_k,y_l)\exp[-j2\pi(f_p x_k + f_q y_l)], \tag{12}$$

where $s(x_k,y_l)$ denotes the $K\times L$ matrix of discrete samples of digitized pixel pattern at the points $x_k = k\Delta x$, $y_l = l\Delta y$ and where Δx, Δy are 2-D discretization steps, *i.e.* the pixel's steps of the CCD array. Once the 2-D Fourier transform has been applied, Eq. (11) is used to calculate the wrapped phase $\hat{\phi}(x_k,y_l)$ from the filtered spectrum.

Because we have computed the wrapped phase starting from an enhanced fringe pattern intensity distribution it is easy to apply the simple method of phase unwrapping based on location of phase jumps and 2π correction in order to recover the full phase $\phi(x_k,y_l)$ as samples of a smooth monotonically increasing function.

4. EXPERIMENTAL RESULTS AND DISCUSSION

We have applied the above discussed combined fringe processing method to retrieve the phase from the moiré fringe patterns shown in Fig. 5, *a* and Fig. 6,*a*. These interferograms were recorded by using a four-beam optical interferometric system configuration previously developed for characterizing optical transparent materials and presented in detail in the paper[7].

An expanded and collimated *He-Ne* laser beam (wavelength λ= 632.8 nm) is reflected downward onto the measuring arrangement which consists of a crossed-line highly-reflective diffraction grating of frequency $f_g = 1200$ lines/mm, firmly bonded onto the surface of the thick laminated composite specimen under investigation. When loads are applied to the specimen, the grating moves, deforms together with the specimen surface and the +1 and -1 diffraction orders suffer a

spatially dependent angular separation which produces interferometric moiré fringe pattern shown in Fig. 5*a*, i.e., the contour map of the horizontal in-plane u displacement fields recorded for a value of the bending moment corresponding to the load of 32Nm. The moiré interferogram of the vertical in-plane v displacement field is shown in Fig. 6,*a*. The moiré interferograms clearly show that increasing tensile/compressive forces produces increasing local changes in the fringe waviness at the interfaces of the laminate indicative of interlaminar shear stresses due to the different orientations of the embedded carbon fibers in the layers.

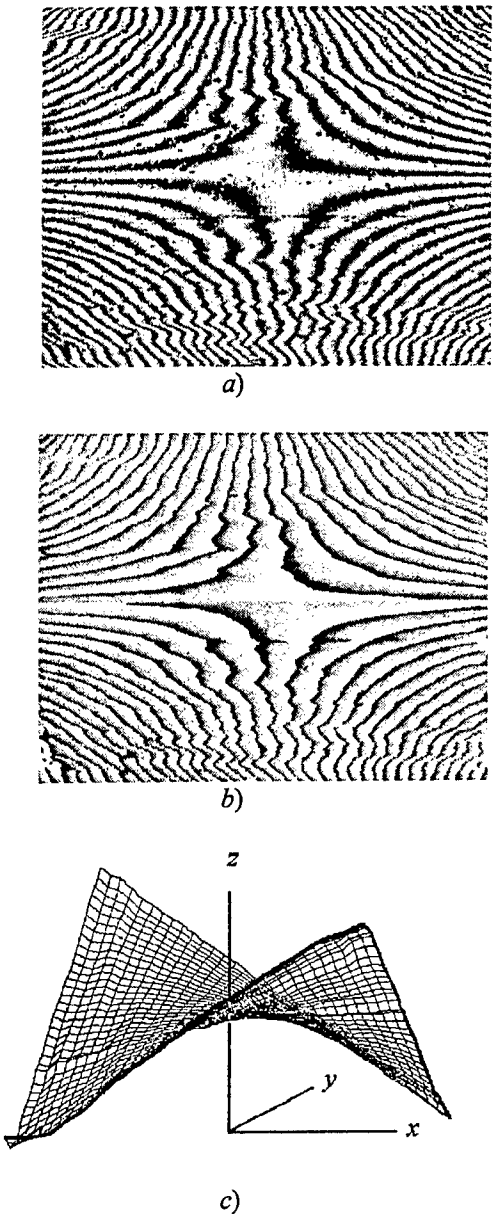


Figure 5. Initial fringe pattern (a), recovered wrapped phase (*b*) and full phase after sign correction (*c*)

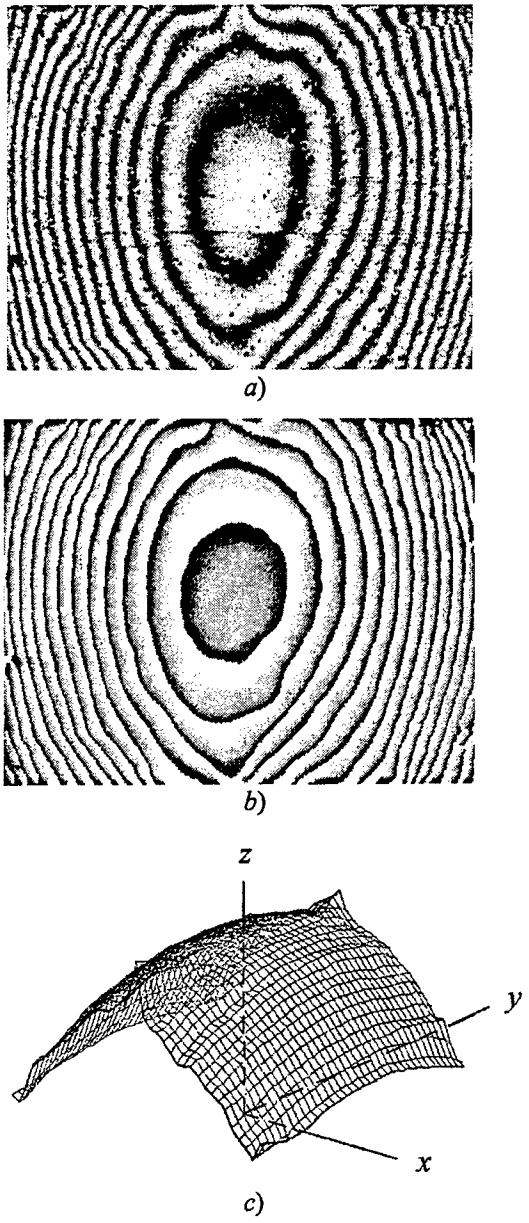


Figure 6. Initial fringe pattern (a), recovered wrapped phase after sign correction (*b*) and full phase (*c*)

The interferometric fringe patterns are viewed at normal incidence by a CCD camera array with an 8-bit gray scale, corresponding to 256 levels (array size 756×581, pixel size $11\mu m \times 11\mu m$) focused on the surface of the composite. The video analogue signals from the camera are digitized by a frame grabber plugged in a computer into 512×400 data points in the x and y directions respectively, corresponding in our experimental conditions to an area of about 12.2 mm × 9.5 mm .

The processing procedure applied to the initial moiré fringe pattern of Fig. 5*a* is shown in Fig. 5*b* and Fig. 5*c*. The wrapped phase computed from the fringe pattern of Fig. 5*a* without the correction of the phase sign is shown in Fig. 5*b*. The recovered full phase distribution $\phi(x, y)$ with the correction of the sign is shown in the 3-D plot of Fig. 5*c*.

The application of the fringe enhancement method to the moiré pattern of Fig. 6*a* is shown in Fig. 6*b* and Fig. 6*c*. The computed wrapped phase is shown in Fig. 6*b* after correction of the phase sign. Note that, when the topology of the fringe pattern is approximately symmetrical as in Fig. 5*b*, the correction of the phase sign can be performed before phase unwrapping. Preliminary fringe enhancement allows for a stable reconstruction of the full phase distribution shown in Fig. 6*c* from the values of wrapped phase shown in Fig. 6*b*.

A clear advantage of this method, when it is applied to a single moiré fringe pattern, relies on the possibility of processing interference pattern of essentially lower spatial frequencies compared to those analyzed by the well-known fringe carrier FTM. This is important when one wants to analyze fringe pattern in which the spatial frequencies of the fringe become comparable to that of the applied carrier. In fact, in these case, filtering in frequency space results in loss of useful information and care must be taken in order to properly select the size of the filter. Consequently, in the case of a single interferogram analysis the optical set-up is simplified and one can make use of a lower resolution CCD camera for fringe pattern recording. The amount of data is reduced, resulting in a faster fringe pattern processing, which enable one to use this method as a useful analysis tool for industrial applications.

5. CONCLUSION

We have described an automated combined fringe analysis method for phase retrieval of moiré interferometric fringe patterns based on preliminary enhancement of fringes by the modification of local intensity histogram followed by 2-D FTM. Application of 2-D FTM to the fringes of a good quality gave the possibility to recover the full phase of fringe by sign correction of phase calculated from a single moiré interferogram. Moiré interferometric measurements with submicron sensitivity of the in-plane displacement fields of thick carbon fibre/PEEK composite laminates are analyzed as example of application of this technique. For a grating of 1200 lines/mm, the sensitivity of the technique is $1 / 2f_g$ = 0,417 μm per fringe order. The ultimate resolution of the technique is limited by the spatial pixel resolution of the CCD camera.

6. REFERENCES

1. M. Takeda, H. Ina and S. Kobayashi, "Fourier-transform method of fringe-pattern analysis for computer-based topography and interferometry", J. Opt. Soc. Am **72** pp.156-160, 1982
2. C. Roddier and F. Roddier, "Interferogram analysis using Fourier transform techniques", Appl. Opt. **26**, pp. 1668-1673, 1987
3. J.B. Schemm and C.M. Vest, "Fringe pattern recognition and interpretation using nonlinear regression analysis" Appl. Opt. **22**, pp. 2850-2853, 1983
4. R.E. Woods and R. G. Gonzalez, "Real-time digital image enhancement", Proc. IEEE **69**, pp. 643-654, 1981
5. T. Kreis, "Digital holographic interference-phase measurement using the Fourier-transform method" J.Opt.Soc.Am. A **3**, pp. 847-855, 1986
6. Y. Tarbeyev and I. Gurov, "A noise-immune interferometric method for measuring the dimensions of regular-shaped bodies", Proc. 3rd Int. IMEKO-Symp. on Dimensional Metrology in Production and Quality Control (20-22 Sept. 1989, Aachen, FRG), pp. 15-20, 1989
7. S. De Nicola, P. Ferraro, A. Finizio, G. Pesce and G. Pierattini, "Reflective grating interferometer for measuring the refractive index of transparent material", Opt. Commun. **118**, pp. 491-494 , 1995

Analysis of associative properties of thin holograms with superposed registration

A.S.Rubanov, L.M.Serebryakova

Institute of Physics, National Academy of Sciences of Belarus
Scaryna Ave., 70, Minsk 220072, Belarus
serebr@ifanbel.bas-net.by

ABSTRACT

The approach is suggested, which permits more full description of correlation responses of thin holograms with superposed registration on the basis of account of contributions from all the nonlinear with respect to the recorded object fields inter- and cross-modulation diffraction structures. Based on this approach, from the common point of view the associative reconstruction of information by the thin quadratic off-axis hologram and the linear off-axis hologram - phase-conjugate mirror system was considered.

Keywords: associative memory, nonlinear holograms, thin superposed holograms, phase conjugation

1. INTRODUCTION

A number of ways[1-6] of holographic realization of associative memory (AM), being understood as reconstruction of complete information (image) by its incomplete or distorted version, demonstrate the fundamental role of nonlinearity of either the hologram itself[1-4] or the reading algorithm[5,6].

It was shown in our works[7-10], that the diffraction structures of higher than the 2nd power on field also contribute into associative reconstruction by quadratic hologram, and the role of nonlinearity is constructive not only at registration stage. So, for the case of one registered image the account of contributions from all the nonlinear diffraction structures (up to the 4th power on field) resulted in more full description of correlation response of a thin quadratic off-axis hologram[7], and generalization of nonlinearity upon the structures of fields, used for hologram writing and reading, gave the possibility to suggest associative retrieval by the hologram, recorded with mutually conjugate object waves[8], and by the "nonlinear matched reading" in the linear off-axis hologram - phase-conjugate (PC) mirror system[9-10]. The above two aspects should be especially important for the case of superposed recording[11,12], when the situations are possible of correlation of reading field with several registered fields, correlating with each other at the same time[12].

In this work for the case of superposed registration at arbitrary (in particular, large) extents of spatial correlation of recorded and reading fields the theoretical analysis of information contents of responses of the quadratically registered thin off-axis hologram[12] and the system, composed of the linear thin hologram and the PC mirror, is carried out under the supposition of essential role of nonlinear inter- and cross-modulation diffraction structures. The problem is solved for the case of lensless Fourier holograms by means of the method[7-10,12], based on the description of scattering object by a finite ensemble of coherent quasi-point secondary sources and decomposition of hologram transmission into the power series on exposition[13,2-4]. It consists in the derivation of information components of diffracted field from noise by means of separating the constant in the hologram plane components from the variable ones in non-averaged correlation functions (CFs), modulating the original non-distorted waves within the responses.

2. QUADRATICALLY REGISTERED OFF-AXIS HOLOGRAM

Let with the help of fields $p^{(\delta)}(\vec{r})$ of m off-axis reference point sources sequentially in time and in the general case at different wavelengths $\lambda^{(\delta)}$ fields $G^{(\delta)}(\vec{r})$ of m coherently illuminated diffusely scattering objects are quadratically registered (Fig. 1):

$$p^{(\delta)}(\vec{r}) = \left|p_0^{(\delta)}\right| \exp\left[i\left(\varphi_0^{(\delta)} - \vec{k}^{(\delta)}(\vec{r})\vec{\rho}_0^{(\delta)}(\vec{r})\right)\right], \quad G^{(\delta)}(\vec{r}) = \sum_{i=1}^{N_\delta} a_i^{(\delta)}(\vec{r}) = \sum_{i}^{\{\delta\}} \left|a_i^{(\delta)}\right| \exp\left[i\left(\varphi_i^{(\delta)} - \vec{k}^{(\delta)}(\vec{r})\vec{\rho}_i^{(\delta)}(\vec{r})\right)\right],$$

Laser Optics 2000: Control of Laser Beam Characteristics and Nonlinear Methods for Wavefront Control,
Leonid N. Soms, Vladimir E. Sherstobitov, Editors, Proceedings of SPIE Vol. 4353 (2001)
© 2001 SPIE · 0277-786X/01/$15.00

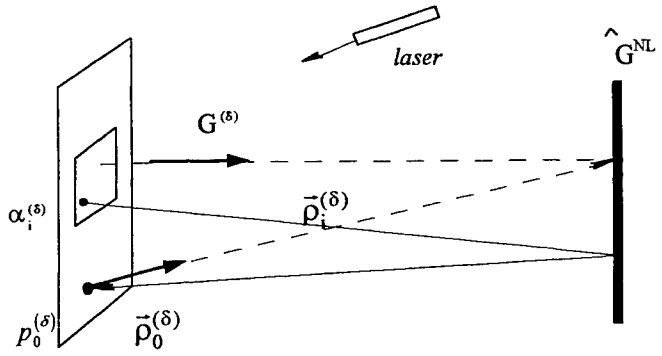


Fig. 1 The principal scheme of registration of a quadratic (or a linear) hologram

where δ - exposition number ($\delta = 1,\ldots,m$) and $\{\delta\} = \{\vec{\rho}_i^{(\delta)}(\vec{r})\}$ - discrete set of coherent sources (repeaters) of the object δ-field, with all object δ-repeaters lie in the same plane with the reference δ-source. In the registration plane each repeater (including the reference source) is characterized by the complex amplitude $\alpha_i^{(\delta)}$ ($p_0^{(\delta)}$), which is determined by the constant real amplitude $|\alpha_i^{(\delta)}|$ ($|p_0^{(\delta)}|$) and initial phase $\varphi_{i,o}^{(\delta)}$, as well as the variable phase $-\vec{k}^{(\delta)}(\vec{r})\vec{\rho}_{i,0}^{(\delta)}(\vec{r})$, in which $|\vec{k}^{(\delta)}(\vec{r})| = 2\pi/\lambda^{(\delta)}$ is wave vector and $\vec{\rho}_{i,0}^{(\delta)}(\vec{r})$ is the radius vector of the repeater relative to a running point at the registration plane.

The transmission operator of the quadratically registered superposed hologram is described by the expression:

$$\hat{G}^{NL} = T_0 + \sum_{\delta=1}^{m} T_1^{(\delta)} I^{(\delta)} + \sum_{\delta=1}^{m}\sum_{\nu=1}^{m} T_2^{(\delta\nu)} I^{(\delta)} I^{(\nu)} = \sum_{\delta=1}^{m}\left(\frac{1}{m} T_0 + T_1^{(\delta)} I^{(\delta)} + T_2^{(\delta\delta)}\left(I^{(\delta)}\right)^2\right) + \sum_{\delta=1}^{m}\sum_{\nu=1,\nu\neq\delta}^{m} T_2^{(\delta\nu)} I^{(\delta)} I^{(\nu)} =$$
$$= \sum_{\delta=1}^{m} \hat{G}^{(\delta\delta)} + 2\sum_{\delta=1}^{m}\sum_{\nu=1,\nu>\delta}^{m} \hat{G}^{(\delta\nu)} = \sum_{d=-2}^{+2}\left\{\sum_{\delta=1}^{m} \hat{g}_d^{(\delta\delta)} + 2\sum_{\delta=1}^{m}\sum_{\nu=1,\nu>\delta}^{m} \hat{g}_d^{(\delta\nu)}\right\}, \quad (1)$$

where $I^{(\delta)} = \left|p^{(\delta)}\right|^2 + \left|G^{(\delta)}\right|^2 + p^{(\delta)} G^{(\delta)*} + p^{(\delta)*} G^{(\delta)}$ is intensity distribution of total δ-field, $\hat{G}^{(\delta\nu)}$ are $m(m-1)$ combination operators, $\hat{G}^{(\delta\delta)}$ are m square operators (each of them is equivalent to the transmission operator of the quadratic hologram with one recorded δ-image). Diffraction into each of five (from -2nd to +2nd) orders of the hologram is described by square $\hat{g}_d^{(\delta\delta)}$ (d is the diffraction order number) and combination $\hat{g}_d^{(\delta\nu)}$ partial operators, with coefficients $T_2^{(\delta\nu)} \sim T_1^{(\delta)} T_1^{(\nu)}$ and operators $\hat{G}^{(\delta\nu)} = T_2^{(\delta\nu)} I^{(\delta)} I^{(\nu)}$ and $\hat{g}_d^{(\delta\nu)}$ are symmetric relative to interchange of indices.

Let the hologram is read by any field (reading, or x-field), defined over a discrete set $\{x\} = \left\{\tilde{\vec{\rho}}_i(\vec{r})\right\}$ of $\tilde{N}$ repeaters

$$\tilde{G}(\vec{r}) = \sum_{i=1}^{\tilde{N}} \tilde{\alpha}_i(\vec{r}) = \sum_{i}^{\{x\}} |\tilde{a}_i| \exp\left[i\left(\tilde{\varphi}_i - \tilde{\vec{k}}(\vec{r})\tilde{\vec{\rho}}_i(\vec{r})\right)\right].$$

If the common fragments of x- and δ-fields exist:

$$\tilde{A}^{(\delta)} = \sum_{i}^{\{\delta,x\}} \tilde{\alpha}_i^{(\delta)}, \quad A^{(\delta)} = \sum_{i}^{\{\delta,x\}} \alpha_i^{(\delta)}, \quad \{\delta,x\} = \{\delta\} \cap \{x\} \neq \varnothing,$$

than at $|\tilde{\vec{k}}| = |\vec{k}^{(\delta)}|$ the constant in hologram plane component $\tilde{\gamma}^{(\delta)}$ of CF of x- and δ-fields is defined over them, which is equal to the sum of products of complex amplitudes of fields of coinciding repeaters (as a consequence of compensation of their spatially-dependent phases), and the residuary part $\underbrace{G^{(\delta)*}\tilde{G}}$ of CF, which is calculated over $\{x\} \cup \{\delta\}$ as the sum of products of amplitudes of non-coinciding repeaters, is the variable one:

$$G^{(\delta)*}\tilde{G}=\sum_{i}^{\{\delta\}}\sum_{j}^{\{x\}}\alpha_i^{(\delta)*}\tilde{\alpha}_j\equiv\sum_{i}^{\{\delta,x\}}\alpha_i^{(\delta)*}\tilde{\alpha}_j+\sum_{i}^{\{\delta\}}\sum_{j,j\neq i}^{\{x\}}\alpha_i^{(\delta)*}\tilde{\alpha}_j\equiv\underbrace{\underbrace{G^{(\delta)*}}\tilde{G}}+\underbrace{G^{(\delta)*}}\tilde{G}\equiv\underbrace{\underbrace{A^{(\delta)*}}\tilde{A}}+\underbrace{G^{(\delta)*}}\tilde{G}=\tilde{\gamma}^{(\delta)}+\underbrace{G^{(\delta)*}}\tilde{G}=$$
$$=\sum_{i}^{\{\delta,x\}}\left|a_i^{(\delta)}\right|\left|\tilde{a}_j\right|\exp\left[i\left(\tilde{\varphi}_i-\varphi_i^{(\delta)}\right)\right]+\sum_{i}^{\{\delta\}}\sum_{j,j\neq i}^{\{x\}}\left|a_i^{(\delta)}\right|\left|\tilde{a}_j\right|\exp\left[i\left(\tilde{\varphi}_j-\varphi_i^{(\delta)}\right)-i\left(\vec{\tilde{k}}\vec{\tilde{\rho}}_j-\vec{k}^{(\delta)}\vec{\rho}_i^{(\delta)}\right)\right] \quad (2)$$

(as well as in[7-10,12], to symbolize summation over coinciding or non-coinciding repeaters denotations in the form of double or ordinary brackets respectively are used, which are convenient for compact formalization). When $|\vec{\tilde{k}}|\neq|\vec{k}^{(\delta)}|$, the quantities $\tilde{\gamma}^{(\delta)}\neq const$ and $\underbrace{G^{(\delta)*}}\tilde{G}$ (2) play the roles of low- and high-frequency variable components of CF respectively. Similarly, at $|\vec{k}^{(\delta)}|=|\vec{k}^{(\nu)}|$ the constant over hologram plane component of CF of original object δ- and ν-fields is defined over their common fragments $\{\delta,\nu\}=\{\delta\}\bigcap\{\nu\}\neq\varnothing$:

$$\gamma^{(\delta\nu)}=\underbrace{\underbrace{G^{(\delta)*}}G^{(\nu)}}=\sum_{i}^{\{\delta,x\}}\alpha_i^{(\delta)*}\alpha_i^{(\nu)}\equiv\gamma^{(\nu\delta)*}. \quad (3)$$

It's necessary to note, that at $\{\delta,x\}\neq\varnothing$ and $\{\delta,\nu\}\neq\varnothing$ the constant components of CFs of the type $\tilde{\gamma}^{(\delta)}$ and $\gamma^{(\delta\nu)}$ respectively may be equal to zero (as zero sums of non-zero complex terms), but at $\{\delta,x\}=\varnothing$ and $\{\delta,\nu\}=\varnothing$ they are equal to zero identically because of the absence of their definition domains.

The complete response of the -2nd diffraction order of the hologram is of the type:

$$\left\{\hat{G}^{NL}\tilde{G}\right\}_{-2}\cong\sum_{\delta=1}^{m}\left\{T_2^{(\delta\delta)}\left(p^{(\delta)}\right)^2\left(2\tilde{\gamma}^{(\delta)}G^{(\delta)*}-A^{(\delta\delta)*}+\underbrace{\underbrace{G^{(\delta)*}}\tilde{G}}\underbrace{G^{(\delta)*}}\right)+2\sum_{\nu=1,\nu>\delta}^{m}T_2^{(\delta\nu)}\left(p^{(\delta)}p^{(\nu)}\right)\left(\tilde{\gamma}^{(\delta)}G^{(\nu)*}+\tilde{\gamma}^{(\nu)}G^{(\delta)*}-A^{(\delta\nu)*}+\underbrace{\underbrace{G^{(\delta)*}}\tilde{G}}\underbrace{G^{(\nu)*}}\right)\right\}, \quad (4)$$

where $\underbrace{\underbrace{G^{(\delta)*}}\tilde{G}}\underbrace{G^{(\nu)*}}$ and $\underbrace{\underbrace{G^{(\delta)*}}\tilde{G}}\underbrace{G^{(\delta)*}}$ are noises (compensation of spatially-dependent phases is obviously excluded in them) of the third power on amplitude, $-A^{(\delta\nu)*}$, $-A^{(\delta\delta)*}$ are "distorting" fragmentary fields, which take into account deviation of actually reconstructed object fields from the original ones over their common with x-field fragments $\{x,\delta,\nu\}$ and $\{x,\delta\}$ respectively:

$$A^{(\delta\nu)*}=\underbrace{\underbrace{G^{(\delta)*}}\tilde{G}}\underbrace{G^{(\nu)*}}=\sum_{i=1}^{\{x,\delta,\nu\}}\alpha_i^{(\delta)*}\left(\tilde{\alpha}_i\alpha_i^{(\nu)*}\right)\equiv\sum_{i=1}^{\{x,\delta,\nu\}}\left(\alpha_i^{(\delta)*}\tilde{\alpha}_i\right)\alpha_i^{(\nu)*}. \quad (5)$$

A square -2nd δ-order performs autoassociative memory (at $|\vec{\tilde{k}}|=|\vec{k}^{(\delta)}|$, $\{x,\delta\}\neq\varnothing$, $\tilde{\gamma}^{(\delta)}\neq0$), and a combination -2nd (δν)-order performs either heteroassociative (if only one of the pair of quantities $\tilde{\gamma}^{(\delta)}$, $\tilde{\gamma}^{(\nu)}$ is constant and non-equal to zero) or "cross"-heteroassociative memory (at $|\vec{\tilde{k}}|=|\vec{k}^{(\nu)}|=|\vec{k}^{(\delta)}|$, $\{x,\delta\}\neq\varnothing$, $\{x,\nu\}\neq\varnothing$, $\tilde{\gamma}^{(\delta)}\neq0$, $\tilde{\gamma}^{(\nu)}\neq0$), which consists in simultaneous reconstruction of two complete object fields $\tilde{\gamma}^{(\delta)}G^{(\nu)*}+\tilde{\gamma}^{(\nu)}G^{(\delta)*}$ by fragments of each other and which is formally a consequence of the symmetry of operators relative to the interchange of indices.

There are several peculiar properties of the response (4) of the -2nd diffraction order At fist, the absence of transmitted without scattering x-field, which distorts diffractively reconstructed original object fields, is an essential advantage of the -2nd order relative to the 0th one from the viewpoint of AM realization, and may be also considered as tolerance of this response for non-correlated disturbances. At second, it is in principle possible to by-pair increase/decrease (by choosing the x-field) in parallel the common fragments of original object fields. And, at third, there is the possibility of reconstruction of complete object images by orthogonal to them at the same wavelength or possessing another wavelengths reading fields.

Indeed, as it is seen from (4), necessary and sufficient condition for reconstruction of any complete object δ-wave and the whole set of registered waves along with it, independently of levels of their correlation with x-field and with each other, is $\tilde{\gamma}^{(\nu)} = const \neq 0$ for any one ν (at $|\vec{\tilde{k}}|=|\vec{k}^{(\nu)}|$, $\{\nu,x\} \neq \varnothing$), therefore reconstruction of any complete δ-field is possible by an orthogonal to it at the same wavelength ($\tilde{\gamma}^{(\delta)} = 0$ at $\{x,\delta\} \neq \varnothing$ or $\tilde{\gamma}^{(\delta)} \equiv 0$ at $\{x,\delta\} = \varnothing$) or possessing another wavelength ($\tilde{\gamma}^{(\delta)} \neq const$) x-field.

It is possible to show[12], that in the general case the -1st and the 0th diffraction orders of the hologram are formed as sums of all kinds of inter- and cross-modulation contributions. Both in the total response of the -1st order (without noise):

$$\left\{G^{NL}\tilde{G}\right\}_{-1} \cong \sum_{\delta=1}^{m} p^{(\delta)}\left\{\left(T_1^{(\delta)}\tilde{\gamma}^{(\delta)} + 2T_2^{(\delta\delta)}\left(\tilde{\gamma}^{(\delta)}\left(\left|p_0^{(\delta)}\right|^2 + \gamma^{(\delta\delta)}\right) + \underbrace{\gamma^{(\delta\delta)}\tilde{\gamma}^{(\delta)}}\right)\right) + 2\sum_{\nu=1,\nu>\delta}^{m} T_2^{(\delta\nu)}\left(\tilde{\gamma}^{(\delta)}\left(\left|p_0^{(\nu)}\right|^2 + \gamma^{(\nu\nu)}\right) + \underbrace{\gamma^{(\delta\nu)}\tilde{\gamma}^{(\nu)}}\right)\right\}, \quad (6)$$

which incorporated contributions from cubic diffraction structures of the type $p^{(\delta)}\underbrace{G^{(\nu)*}G^{(\nu)}}G^{(\delta)*}$ and $p^{(\delta)}\underbrace{G^{(\delta)*}G^{(\delta)}}G^{(\delta)*}$ to the reconstruction of the reference δ-wave

$$\begin{aligned}\left(p^{(\delta)}\underbrace{G^{(\nu)*}G^{(\nu)}}G^{(\delta)*}\right)\tilde{G} \equiv p^{(\delta)}\Big(&\underbrace{\gamma^{(\delta\nu)}\tilde{\gamma}^{(\nu)}} + \underbrace{\tilde{\gamma}^{(\nu)}G^{(\delta)*}}G^{(\nu)} + \underbrace{\tilde{\gamma}^{(\delta)}G^{(\nu)*}}G^{(\nu)} + \underbrace{\gamma^{(\delta\nu)}G^{(\nu)*}}\tilde{G} + \\ &+ \underbrace{G^{(\nu)*}G^{(\nu)}G^{(\delta)*}}\tilde{G} - \underbrace{G^{(\nu)*}}A^{(\nu\delta x)} - \underbrace{A^{(\delta x\nu)*}}G^{(\nu)} - \underbrace{G^{(\delta)*}}A^{(x\nu\nu)} - \underbrace{A^{(\nu\nu\delta)*}}\tilde{G}\Big),\end{aligned} \quad (7)$$

and in the total response of the 0th order (without noise and "distorting" common fragments):

$$\begin{aligned}\left\{\hat{G}^{NL}\tilde{G}\right\}_0 \cong \tilde{G}\Bigg\{&T_0 + \sum_{\delta=1}^{m}\left[T_1^{(\delta)}\left(\left|p_0^{(\delta)}\right|^2 + \gamma^{(\delta\delta)}\right) + T_2^{(\delta\delta)}\left(\left(\left|p_0^{(\delta)}\right|^2 + \gamma^{(\delta\delta)}\right)^2 + \underbrace{\gamma^{(\delta\delta)}\gamma^{(\delta\delta)*}} + 2\left|p_0^{(\delta)}\right|^2\gamma^{(\delta\delta)}\right)\right] + \\ &+ 2\sum_{\delta=1}^{m}\sum_{\nu=1,\nu>\delta}^{m} T_2^{(\delta\nu)}\left[\left(\left|p_0^{(\delta)}\right|^2 + \gamma^{(\delta\delta)}\right)\left(\left|p_0^{(\nu)}\right|^2 + \gamma^{(\nu\nu)}\right) + \underbrace{\gamma^{(\delta\nu)}\gamma^{(\delta\nu)*}}\right]\Bigg\} + \\ &+ \sum_{\delta=1}^{m} G^{(\delta)}\Bigg\{\left[T_1^{(\delta)}\tilde{\gamma}^{(\delta)} + 2T_2^{(\delta\delta)}\left(\tilde{\gamma}^{(\delta)}\left(2\left|p_0^{(\delta)}\right|^2 + \gamma^{(\delta\delta)}\right) + \underbrace{\gamma^{(\delta\delta)}\tilde{\gamma}^{(\delta)}}\right)\right] + 2\sum_{\nu=1,\nu>\delta}^{m} T_2^{(\delta\nu)}\left[\tilde{\gamma}^{(\delta)}\left(\left|p_0^{(\nu)}\right|^2 + \gamma^{(\nu\nu)}\right) + \underbrace{\gamma^{(\delta\nu)}\tilde{\gamma}^{(\nu)}}\right]\Bigg\} \\ &+ 2\sum_{\delta=1}^{m}\sum_{\nu=1,\nu>\delta}^{m} T_2^{(\delta\nu)}\left\{\left(p^{(\delta)}p^{(\nu)*}\right)\left[\gamma^{(\delta\nu)}\tilde{G} + \tilde{\gamma}^{(\delta)}G^{(\nu)}\right] + \left(p^{(\delta)*}p^{(\nu)}\right)\left[\gamma^{(\nu\delta)}\tilde{G} + \tilde{\gamma}^{(\nu)}G^{(\delta)}\right]\right\},\end{aligned} \quad (8)$$

which took into account contributions from all components of $\hat{g}_0^{(\delta\nu)}$ operators (including those ones proportional to the second and the forth powers on amplitudes), the nonlinear on constant components of CFs inter- $\underbrace{\gamma^{(\delta\delta)}\tilde{\gamma}^{(\delta)}}$ and cross-modulation $\underbrace{\gamma^{(\delta\nu)}\tilde{\gamma}^{(\nu)}}$ terms (in addition to terms proportional to $\tilde{\gamma}^{(\delta)}$) as well as terms $\underbrace{\gamma^{(\delta\nu)}\gamma^{(\delta\nu)*}}$, $\underbrace{\gamma^{(\delta\delta)}\gamma^{(\delta\delta)*}}$ in (8) are present, which are defined by the identities:

$$\underbrace{\gamma^{(\delta\delta)}\tilde{\gamma}^{(\delta)}} = \sum_{i}^{\{\delta\}}\left(\alpha_i^{(\delta)*}\alpha_i^{(\delta)}\right)\sum_{j,j\neq i}^{\{x,\delta\}}\left(\alpha_j^{(\delta)*}\tilde{\alpha}_j\right) \equiv \gamma^{(\delta\delta)}\tilde{\gamma}^{(\delta)} - \underbrace{\underbrace{\gamma^{(\delta\delta)}\tilde{\gamma}^{(\delta)}}}, \quad (9a)$$

$$\underbrace{\gamma^{(\delta\nu)}\tilde{\gamma}^{(\nu)}} = \sum_{i}^{\{\delta,\nu\}}\left(\alpha_i^{(\delta)*}\alpha_i^{(\nu)}\right)\sum_{j,j\neq i}^{\{x,\nu\}}\left(\alpha_j^{(\nu)*}\tilde{\alpha}_j\right) \equiv \gamma^{(\delta\nu)}\tilde{\gamma}^{(\nu)} - \underbrace{\underbrace{\gamma^{(\delta\nu)}\tilde{\gamma}^{(\nu)}}}, \quad (9b)$$

$$\underbrace{\gamma^{(\delta\nu)}\gamma^{(\delta\nu)*}} = \sum_{i}^{\{\delta,\nu\}}\left(\alpha_i^{(\delta)*}\alpha_i^{(\nu)}\right)\sum_{j,j\neq i}^{\{\delta,\nu\}}\left(\alpha_i^{(\delta)}\alpha_j^{(\nu)*}\right) \equiv \gamma^{(\delta\nu)}\gamma^{(\delta\nu)*} - \underbrace{\underbrace{\gamma^{(\delta\nu)}\gamma^{(\delta\nu)*}}}. \quad (9c)$$

This identities are based on the fact, that constant components of CFs (2), (3) of fields, as well as fields themselves, are defined on discrete sets, so for their products identical splitting is also applicable into two groups of terms, in one of which summation is performed over coinciding, and in another one - over non-coinciding elements. At the same time, in contrast to (2), (3), there is no the aim to distinguish constant and variable components in (9), and all participating in (9) components of CFs are supposed to be already constant, with $\underbrace{\gamma^{(\delta\delta)}\tilde{\gamma}^{(\delta)}}$, $\gamma^{(\delta\delta)}\tilde{\gamma}^{(\delta)}$ ($|\vec{\tilde{k}}|=|\vec{k}^{(\delta)}|$) and $\underbrace{\gamma^{(\delta\nu)}\tilde{\gamma}^{(\nu)}}$, $\gamma^{(\delta\nu)}\tilde{\gamma}^{(\nu)}$ ($|\vec{\tilde{k}}|=|\vec{k}^{(\nu)}|=|\vec{k}^{(\delta)}|$) are defined upon the unions $\{\delta\}\cup\{x\}$ and $\{\delta,\nu\}\cup\{x,\nu\}$ respectively, and $\underbrace{\underbrace{\gamma^{(\delta\delta)}\tilde{\gamma}^{(\delta)}}}$ and $\underbrace{\underbrace{\gamma^{(\delta\nu)}\tilde{\gamma}^{(\nu)}}}$ - upon the intersections $\{\delta,x\}$ and $\{x,\delta,\nu\}$. All the constant components of CFs in (9c) at $\nu\neq\delta$ or $\nu=\delta$ are defined over $\{\delta,\nu\}$ or $\{\delta\}$ respectively.

The fact, that the nonlinear inter- and cross-modulation terms $\underbrace{\gamma^{(\delta\delta)}\tilde{\gamma}^{(\delta)}}$ and $\underbrace{\gamma^{(\delta\nu)}\tilde{\gamma}^{(\nu)}}$ (9) in the general case differ from simple products of corresponding cofactors (constant components of CFs), leads to the possibility of situations, when they are not equal to zero even if one or both of their cofactors are equal (but not identically) to zero (details see in[12]). (Indeed, let $\{x,\delta\}\neq\varnothing$ and consequently $\tilde{\gamma}^{(\delta)}\neq 0$, $\underbrace{\underbrace{\gamma^{(\delta\delta)}\tilde{\gamma}^{(\delta)}}}\neq 0$, so if $\tilde{\gamma}^{(\delta)}=0$, than may be $\underbrace{\gamma^{(\delta\delta)}\tilde{\gamma}^{(\delta)}}=-\underbrace{\underbrace{\gamma^{(\delta\delta)}\tilde{\gamma}^{(\delta)}}}\neq 0$. Further, let $\{x,\nu\}\neq\varnothing$, $\{\delta,\nu\}\neq\varnothing$ and consequently $\tilde{\gamma}^{(\nu)}\neq 0$, $\gamma^{(\delta\nu)}\neq 0$, $\underbrace{\gamma^{(\delta\nu)}\tilde{\gamma}^{(\nu)}}\neq 0$. If at the same time $\{x,\delta\}\neq\varnothing$ and besides $\{x,\delta,\nu\}\neq\varnothing$, than $\underbrace{\underbrace{\gamma^{(\delta\nu)}\tilde{\gamma}^{(\nu)}}}\neq 0$, and possibly $\underbrace{\gamma^{(\delta\nu)}\tilde{\gamma}^{(\nu)}}\neq 0$ even if $\tilde{\gamma}^{(\nu)}=0$ or $\gamma^{(\delta\nu)}=0$ or $\gamma^{(\delta\nu)}=\tilde{\gamma}^{(\nu)}=0$. At the same time, if $\{x,\delta\}=\varnothing$, than $\{x,\delta,\nu\}=\varnothing$ and $\underbrace{\underbrace{\gamma^{(\delta\nu)}\tilde{\gamma}^{(\nu)}}}\equiv 0$, so $\underbrace{\gamma^{(\delta\nu)}\tilde{\gamma}^{(\nu)}}\equiv\gamma^{(\delta\nu)}\tilde{\gamma}^{(\nu)}$ and we have $\underbrace{\gamma^{(\delta\nu)}\tilde{\gamma}^{(\nu)}}=0$ as soon as $\tilde{\gamma}^{(\nu)}=0$ or $\gamma^{(\delta\nu)}=0$ or $\gamma^{(\delta\nu)}=\tilde{\gamma}^{(\nu)}=0$.)

As a consequence of structure of the responses (6), (8), owing to nonlinear inter- or cross-modulations any reference or object δ-wave can be reconstructed under the prohibited for the linear hologram conditions of orthogonality of x- and δ-fields both at the existence of their common fragment ($\tilde{\gamma}^{(\delta)}=0$, $\{x,\delta\}\neq\varnothing$) and at the absence of it ($\{x,\delta\}=\varnothing$, $\tilde{\gamma}^{(\delta)}\equiv 0$). In the first case, in addition to intermodulation reconstruction of δ-waves, cross-modulation reconstruction may take place at $\{x,\delta,\nu\}\neq\varnothing$, even if $\tilde{\gamma}^{(\nu)}=0$ or $\gamma^{(\delta\nu)}=0$ or $\gamma^{(\delta\nu)}=\tilde{\gamma}^{(\nu)}=0$. In the second case, when $\{x,\delta,\nu\}=\varnothing$, only cross-modulation reconstructions are possible, but only if $\tilde{\gamma}^{(\nu)}\neq 0$, $\gamma^{(\delta\nu)}\neq 0$.

Similarly, for any pair of object δ- and ν -waves orthogonality of them in the sense $\{\delta,\nu\}\neq\varnothing$, $\gamma^{(\delta\nu)}=0$, allows for the possibility of mutual cross-modulation reconstruction of corresponding reference and object waves, and on the contrary, orthogonality in the sense $\{\delta,\nu\}=\varnothing$, $\gamma^{(\delta\nu)}\equiv 0$ excludes it.

It is seen from the comparison of the responses of quadratic (8), (6) and linear ((8), (6) at $T_2^{(\delta\nu)}=T_2^{(\delta\delta)}=0$) holograms, that due to nonlinear mixing of spatial frequencies of object fields, quadraticity of registration essentially extends the reconstruction conditions of original waves within the responses of the 0th and the -1st diffraction orders, with relations between spatial spectra of fields are in the foreground. So, at $|\vec{k}^{(\delta)}|=|\vec{\tilde{k}}|$ "linear" reconstruction conditions $\{x,\delta\}\neq\varnothing$, $\tilde{\gamma}^{(\delta)}\neq 0$ of original δ-waves owing to nonlinear intermodulations extend up to the conditions $\{x,\delta\}\neq\varnothing$, which allow $\tilde{\gamma}^{(\delta)}=0$, but exclude $\tilde{\gamma}^{(\delta)}\equiv 0$, and owing to nonlinear cross-modulations - up to the conditions $\{x,\nu\}\neq\varnothing$ (in which ν is any one of the recorded object waves with $\{\nu,\delta\}\neq\varnothing$ and $|\vec{k}^{(\nu)}|=|\vec{k}^{(\delta)}|=|\vec{\tilde{k}}|$), which allow both $\tilde{\gamma}^{(\delta)}=0$ and $\tilde{\gamma}^{(\delta)}\equiv 0$ ($\{x,\delta\}=\varnothing$).

So, for object fields of the same wavelength in the 0th and the -1st diffraction orders of quadratic superposed thin hologram we have some kind of "integration" of their spatial spectra (if $\{x,\nu\}\neq\varnothing$ for several ν-waves, than

simultaneously with this ν-waves those δ-waves may be also reconstructed, for which $\{\nu,\delta\}\neq\varnothing$ independently of $\{x,\delta\}\neq\varnothing$ or $\{x,\delta\}=\varnothing$) and "orthogonality breaking" (non-zero inter- and cross-modulation contributions from orthogonal fields with common fragments).

3. LINEAR OFF-AXIS HOLOGRAM - PHASE-CONJUGATE MIRROR SYSTEM

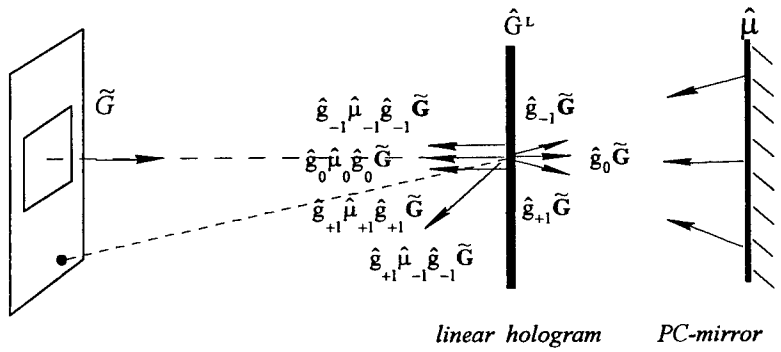


Fig. 2 The principal scheme of associative reconstruction in thin linear off-axis hologram - PC-mirror system

Owing to the unique ability of PC mirror to invert and therefore to retain, within a sign, the phase of incident radiation, in the case of thin holograms single scattering of field upon a quadratic hologram is in a certain sense equivalent to double scattering upon a linear hologram near a PC mirror. On the grounds of this analogy, it is possible to suppose, that one more way of nonlinear mixing and associative reconstruction of fields is "nonlinear matched reading"[9,10] in the linear hologram - PC mirror system, which consists in the diffraction by linear hologram of nonlinear (with respect to original fields) reversed components of previously scattered by it field, during which noise field components may be transformed to information components.

The three orders of field, diffracted by the transmission operator of linear off-axis hologram (described by (1) at $T_2^{(\delta\nu)}=T_2^{(\delta\delta)}=0$):

$$\hat{G}^L\tilde{G}=\left(T_0+\sum_{\delta=1}^{m}T_1^{(\delta)}I^{(\delta)}\right)\tilde{G}=\sum_{\delta=1}^{m}\left\{\left(\frac{1}{m}T_0+T_1^{(\delta)}\left(\left|p_0^{(\delta)}\right|^2+\left|G^{(\delta)}\right|^2\right)\right)+T_1^{(\delta)}p^{(\delta)}G^{(\delta)*}+T_1^{(\delta)}p^{(\delta)*}G^{(\delta)}\right\}\tilde{G}=$$

$$=\sum_{\delta=1}^{m}\left\{\hat{g}_0^{(\delta)}+\hat{g}_{-1}^{(\delta)}+\hat{g}_{+1}^{(\delta)}\right\}\tilde{G}=\sum_{\delta=1}^{m}\left\{\left(\frac{1}{m}T_0+T_1^{(\delta)}\left(\left|p_0^{(\delta)}\right|^2+\gamma^{(\delta\delta)}\right)\right)\tilde{G}+T_1^{(\delta)}\left(\left(\tilde{\gamma}^{(\delta)}G^{(\delta)}-A^{(\delta\tilde{\delta})}\right)+\underbrace{G^{(\delta)}G^{(\delta)*}\tilde{G}}\right)\right\}+ \quad (10)$$

$$+\sum_{\delta=1}^{m}T_1^{(\delta)}\left(\tilde{\gamma}^{(\delta)}p^{(\delta)}+p^{(\delta)}\underbrace{G^{(\delta)*}\tilde{G}}\right)+\sum_{\delta=1}^{m}T_1^{(\delta)}p^{(\delta)*}G^{(\delta)}\tilde{G},$$

after phase conjugation retain correspondence to the hologram scattering operator. At the repeated diffraction they may lead to reconstruction of whole object fields in the 0th and the +2nd orders of the system, being formed as the result of superposition of the following scattering channels[10] (Fig. 2):

$$\left\{\hat{G}^L\hat{\mu}\hat{G}^L\tilde{G}\right\}_0=\left(\hat{g}_0\hat{\mu}_0\hat{g}_0+\hat{g}_{+1}\hat{\mu}_{+1}\hat{g}_{+1}+\hat{g}_{-1}\hat{\mu}_{-1}\hat{g}_{-1}\right)\tilde{G}=\sum_{\nu=1}^{m}\sum_{\delta=1}^{m}\left(\hat{g}_0^{(\nu)}\hat{\mu}_0\hat{g}_0^{(\delta)}+\hat{g}_{+1}^{(\nu)}\hat{\mu}_{+1}\hat{g}_{+1}^{(\delta)}+\hat{g}_{-1}^{(\nu)}\hat{\mu}_{-1}\hat{g}_{-1}^{(\delta)}\right)\tilde{G}, \quad (11a)$$

$$\left\{\hat{G}^L\hat{\mu}\hat{G}^L\tilde{G}\right\}_{+2}=\hat{g}_{+1}\hat{\mu}_{-1}\hat{g}_{-1}\tilde{G}=\sum_{\nu=1}^{m}\sum_{\delta=1}^{m}\hat{g}_{+1}^{(\nu)}\hat{\mu}_{-1}\hat{g}_{-1}^{(\delta)}\tilde{G}. \quad (11b)$$

The action of mirror is described here with three-component operator $\hat{\mu}=\{\hat{\mu}_0,\hat{\mu}_{+1},\hat{\mu}_{-1}\}$, elements of which with complex efficiencies μ_0,μ_{+1},μ_{-1} perform inversion and complex conjugation of amplitudes of waves in the corresponding

diffraction orders. At $|\vec{\tilde{k}}|=|\vec{k}^{(\delta)}|$ the response $g_{-1}^{(\delta)}\tilde{G}$ is in the general case the original reference wave with square noise (halo) (10):

$$\hat{g}_{-1}^{(\delta)}\tilde{G} = T_1^{(\delta)}p^{(\delta)}\left(G^{(\delta)^*}\tilde{G}\right) = T_1^{(\delta)}p^{(\delta)}\left(\tilde{\gamma}^{(\delta)} + \underbrace{G^{(\delta)^*}\tilde{G}}\right). \tag{12}$$

Supposing spatial and angle nonuniformity of PC reflectance for the field, diffracted into the -1st order, let's later on represent the operator $\hat{\mu}_{-1}$ by a 2m-component vector $\hat{\mu}_{-1} = (\ldots, \mu_{-1}^{(\delta)p}, \mu_{-1}^{(\delta)h}, \ldots, \mu_{-1}^{(\nu)p}, \mu_{-1}^{(\nu)h}, \ldots)$, letters p or h in which denote peak or halo respectively, with $\mu_{-1}^{(\delta)p,h} \neq \mu_{-1}^{(\nu)p,h}$, $\mu_{-1}^{(\delta)p} \neq \mu_{-1}^{(\delta)h}$ in the general case.

The scattering channel, which is traditional for AM realization in such a system[5,6], is formed as superposition of every possible partial responses of the type $\hat{g}_{-1}^{(\nu)}\hat{\mu}_{-1}^{(\delta)}g_{-1}^{(\delta)}\tilde{G}$ in the 0th diffraction order. After the reflection on PC-mirror and diffraction on the lattices of operator $\hat{g}_{-1}^{(\nu)}$ into the 0th order of the system, the reconstructed reference δ-wave reads out the complete conjugate ν-field:

$$\hat{g}_{-1}^{(\nu)}\hat{\mu}_{-1}^{(\delta)}\left(T_1^{(\delta)}\tilde{\gamma}^{(\delta)}p^{(\delta)}\right) = \left(\mu_{-1}^{(\delta)p}T_1^{(\nu)}T_1^{(\delta)}\right)\left(p^{(\nu)}p^{(\delta)^*}\right)\left(\tilde{\gamma}^{(\delta)^*}G^{(\nu)^*}\right), \tag{13}$$

and the halo (which as the result of phase conjugation contains now a non-conjugate amplitude of δ -field) may be partially compensated by $G^{(\nu)^*}$ -cofactor of the operator to the conjugate x-field:

$$\begin{aligned}\hat{g}_{-1}^{(\nu)}\hat{\mu}_{-1}^{(\delta)}\left(T_1^{(\delta)}p^{(\delta)}\underbrace{G^{(\delta)^*}\tilde{G}}\right) &\equiv \left(\mu_{-1}^{(\delta)h}T_1^{(\nu)}T_1^{(\delta)}p^{(\nu)}p^{(\delta)^*}\right)\left(\underbrace{\underbrace{G^{(\nu)^*}G^{(\delta)}}\tilde{G}^*} + \underbrace{G^{(\nu)^*}G^{(\delta)}}\tilde{G}^*\right) \equiv \left(\mu_{-1}^{(\delta)h}T_1^{(\nu)}T_1^{(\delta)}p^{(\nu)}p^{(\delta)^*}\right)\left(\left(\underbrace{\underbrace{G^{(\nu)^*}G^{(\delta)}}\tilde{G}^*} - \right.\right.\\ &\left.\left. - \underbrace{\underbrace{G^{(\nu)^*}G^{(\delta)}}\tilde{G}^*}\right) + \underbrace{G^{(\nu)^*}G^{(\delta)}}\tilde{G}^*\right) \equiv \left(\mu_{-1}^{(\delta)h}T_1^{(\nu)}T_1^{(\delta)}p^{(\nu)}p^{(\delta)^*}\right)\left(\left(\gamma^{(\nu\delta)}\tilde{G}^* - A^{(\nu\delta x)^*}\right) + \underbrace{G^{(\nu)^*}G^{(\delta)}}\tilde{G}^*\right).\end{aligned} \tag{14}$$

So, the full field of the partial channel $\hat{g}_{-1}^{(\nu)}\hat{\mu}_{-1}g_{-1}^{(\delta)}$ and the information structure (i. e. without noises and distorting common fragments) of the total reconstructed by the channel $\hat{g}_{-1}\hat{\mu}\hat{g}_{-1}$ response are described by the expressions:

$$\hat{g}_{-1}^{(\nu)}\hat{\mu}_{-1}^{(\delta)}g_{-1}^{(\delta)}\tilde{G} = \left(T_1^{(\nu)}T_1^{(\delta)}p^{(\nu)}p^{(\delta)^*}\right)\left(\mu_{-1}^{(\delta)p}\tilde{\gamma}^{(\delta)^*}G^{(\nu)^*} + \mu_{-1}^{(\delta)h}(\gamma^{(\nu\delta)}\tilde{G}^* - A^{(\nu\delta x)^*} + \underbrace{G^{(\nu)^*}G^{(\delta)}}\tilde{G}^*)\right), \tag{15}$$

$$\hat{g}_{-1}\hat{\mu}_{-1}\hat{g}_{-1}\tilde{G} = \sum_{\delta=1}^{m}\left(T_1^{(\delta)}\right)^2\left|p^{(\delta)}\right|^2\left(\mu_{-1}^{(\delta)p}\tilde{\gamma}^{(\delta)^*}G^{(\delta)^*} + \mu_{-1}^{(\delta)h}\gamma^{(\delta\delta)}\tilde{G}^*\right) + \sum_{\delta=1}^{m}\sum_{\nu=1,\nu\neq\delta}^{m}\left(T_1^{(\delta)}T_1^{(\nu)}\right)\left(p^{(\delta)^*}p^{(\nu)}\right)\left(\mu_{-1}^{(\delta)p}\tilde{\gamma}^{(\delta)^*}G^{(\nu)^*} + \mu_{-1}^{(\delta)h}\gamma^{(\nu\delta)}\tilde{G}^*\right). \tag{16}$$

(It is necessary to remember, that all the information components of reconstructed fields exist only if the correspponding constant components of CFs exist, i. e. if there are common subsets of object sets of repeaters with equal wavelength.) It is taken into account in (15), (16), that under the supposition of independence of PC-reflectance for the peak and the halo, the object and the reading fields may in principle be reconstructed independently. It follows from (16), that 1) because of reconstruction of reading field (together with cubic noises) the role of the mechanism of rescattering of square noise in this channel is negative in the general case; 2) from the other side, owing to spatial superposition of object and reading fields the structure of the response is favorable for parallel increase/decrease of their common fragments; 3) if $\gamma^{(\nu\delta)} = 0$ for any pair of object fields (or for each pair, if the system of mutually orthogonal functions is recorded), than there is no reconstruction of x-fields at the corresponding spatial frequencies; 4) if the field, which was initially diffracted into the -1st order of hologram, is nothing but noise in the sense that no one of original reference waves is reconstructed ($\tilde{\gamma}^{(\delta)} = 0$ or $\tilde{\gamma}^{(\delta)} \equiv 0$ at $|\vec{\tilde{k}}|=|\vec{k}^{(\delta)}|$, or $\tilde{\gamma}^{(\delta)} \neq const$ at $|\vec{\tilde{k}}|\neq|\vec{k}^{(\delta)}|$), than at the repeated scattering the original object fields are not reconstructed.

In contrast to the 0th order, at the diffraction into the +2nd order of the system the halo reconstructs not the reading field, but the complete object field (here, x-cofactor of the halo is phase matched to object cofactor of the partial operator of ν-hologram):

$$\hat{g}_{+1}^{(\nu)}\hat{\mu}_{-1}^{(\delta)}\left(T_1^{(\delta)}p^{(\delta)}G^{(\delta)*}\widetilde{G}\right)\equiv\left(\mu_{-1}^{(\delta)h}T_1^{(\nu)}T_1^{(\delta)}p^{(\nu)*}p^{(\delta)*}\right)\left(\underline{\underline{G^{(\nu)}}}\,\underline{\widetilde{G}^{*}}\,\underline{G^{(\delta)}}+\underline{G^{(\nu)}}\,\underline{\widetilde{G}^{*}}\,\underline{G^{(\delta)}}\right)\equiv\left(\mu_{-1}^{(\delta)h}T_1^{(\nu)}T_1^{(\delta)}p^{(\nu)*}p^{(\delta)*}\right)\left((\underline{\underline{G^{(\nu)}}}\,\underline{\widetilde{G}^{*}}\,\underline{G^{(\delta)}}-\right.$$
$$\left.-\underline{\underline{G^{(\nu)}}}\,\underline{\underline{\widetilde{G}^{*}}}\,\underline{\underline{G^{(\delta)}}})+\underline{G^{(\nu)}}\,\underline{\widetilde{G}^{*}}\,\underline{G^{(\delta)}}\right)\equiv\left(\mu_{-1}^{(\delta)h}T_1^{(\nu)}T_1^{(\delta)}p^{(\nu)*}p^{(\delta)*}\right)\left(\widetilde{\gamma}^{(\nu)*}G^{(\delta)}-A^{(\nu\delta)}+\underline{G^{(\nu)}}\,\underline{\widetilde{G}^{*}}\,\underline{G^{(\delta)}}\right), \tag{17}$$

and this fact essentially differs the channel $\hat{g}_{+1}\hat{\mu}_{-1}\hat{g}_{-1}$ (17) from the channel $\hat{g}_{-1}\hat{\mu}_{-1}\hat{g}_{-1}$ (15), (16). Taking into account, that into the +2nd order, as well as into the 0th one, the reconstructed conjugate reference δ-wave reads out the complete object ν-field, we get the expressions for the whole response of this partial channel:

$$\hat{g}_{+1}^{(\nu)}\hat{\mu}_{-1}^{(\delta)}\hat{g}_{-1}^{(\delta)}\widetilde{G}=\left(T_1^{(\nu)}T_1^{(\delta)}p^{(\nu)*}p^{(\delta)*}\right)\left(\mu_{-1}^{(\delta)p}\ \widetilde{\gamma}^{(\delta)*}G^{(\nu)}+\mu_{-1}^{(\delta)h}\ (\widetilde{\gamma}^{(\nu)*}G^{(\delta)}-A^{(\nu\delta)}+\underline{G^{(\nu)}}\,\underline{\widetilde{G}^{*}}\,\underline{G^{(\delta)}})\right), \tag{18}$$

and the information structure of the total response of the system in the +2nd diffraction order:

$$\left\{\hat{G}^{NL}\widetilde{G}\right\}_{+2}\approx\sum_{\delta=1}^{m}\left(T_1^{(\delta)}\right)^2\left(p^{(\delta)*}\right)^2(\mu_{-1}^{(\delta)p}+\mu_{-1}^{(\delta)h})\widetilde{\gamma}^{(\delta)*}G^{(\delta)}+2\sum_{\delta=1}^{m}\sum_{\nu=1,\nu\neq\delta}^{m}\left(T_1^{(\nu)}T_1^{(\delta)}\right)\left(p^{(\nu)*}p^{(\delta)*}\right)(\mu_{-1}^{(\delta)p}\widetilde{\gamma}^{(\delta)*}G^{(\nu)}+\mu_{-1}^{(\delta)h}\widetilde{\gamma}^{(\nu)*}G^{(\delta)}). \tag{19}$$

It is seen, that the response (19) is similar to the response (4) of the -2nd order of the quadratic hologram, which results in their common informative properties (absence of superposition with x-fields; auto-, hetero- or "cross" heteroassociative memory; spatial superposition of object fields and therefore possibility of parallel highlighting of their common fragments; possibility of reconstruction at an orthogonal or at another wavelength x-field).

To consider the channel $\hat{g}_{+1}\hat{\mu}_{+1}\hat{g}_{+1}$, let's note, that the field $T_1^{(\delta)}p^{(\delta)*}G^{(\delta)}\widetilde{G}$, which was initially diffracted by the hologram into the +1st δ-order, may be interpreted as noise. At $\{\delta,\nu\}\neq\varnothing$, $\{x,\nu\}\neq\varnothing$ and $\gamma^{(\delta\nu)}\neq 0$, $\widetilde{\gamma}^{(\nu)}\neq 0$ amplitude and phase distribution of such a square noise field may be partially compensated after phase conjugation and diffraction upon $\hat{g}_{+1}^{(\nu)}$-lattices up to conjugate x- and δ-fields simultaneously:

$$\hat{g}_{+1}^{(\nu)}\hat{\mu}_{+1}\hat{g}_{+1}^{(\delta)}\widetilde{G}=\left(\mu_{+1}T_1^{(\nu)}T_1^{(\delta)}p^{(\nu)*}p^{(\delta)}\right)\left(G^{(\delta)*}G^{(\nu)}\widetilde{G}^{*}\right)\equiv\left(\mu_{+1}T_1^{(\nu)}T_1^{(\delta)}p^{(\nu)*}p^{(\delta)}\right)\left(G^{(\delta)*}\underline{\underline{G^{(\nu)}}}\,\widetilde{G}^{*}+\right.$$
$$\left.+(\underline{\underline{G^{(\delta)*}}}\,G^{(\nu)}\widetilde{G}^{*}-\underline{\underline{G^{(\delta)*}}}\,\underline{\underline{G^{(\nu)}}}\,\widetilde{G}^{*}+\underline{G^{(\delta)*}}\,\underline{G^{(\nu)}}\,\widetilde{G}^{*})\right)\equiv\left(\mu_{+1}T_1^{(\nu)}T_1^{(\delta)}p^{(\nu)*}p^{(\delta)}\right)\left(\widetilde{\gamma}^{(\nu)*}G^{(\delta)*}+\gamma^{(\delta\nu)}\widetilde{G}^{*}-A^{(\delta\nu)*}+\underline{G^{(\delta)*}}\,\underline{G^{(\nu)}}\,\widetilde{G}^{*}\right). \tag{20}$$

It is accounted here, that in contrary to (15), independent reconstruction of object and x-field is impossible here. It is seen, that the structures of the responses $\hat{g}_{+1}^{(\nu)}\hat{\mu}_{+1}\hat{g}_{+1}^{(\delta)}\widetilde{G}$ (20) and $\hat{g}_{-1}^{(\nu)}\hat{\mu}_{-1}^{(\delta)}\hat{g}_{-1}^{(\delta)}\widetilde{G}$ (15) qualitatively coincide within the exchange of indices. The resulting field possesses the following structure:

$$\hat{g}_{+1}\hat{\mu}_{+1}\hat{g}_{+1}\widetilde{G}\approx\mu_{+1}\left\{\sum_{\delta=1}^{m}\left(T_1^{(\delta)}\right)^2|p_0^{(\delta)}|^2\left(\widetilde{\gamma}^{(\delta)*}G^{(\delta)*}+\gamma^{(\delta\delta)}\widetilde{G}^{*}\right)+\sum_{\delta=1}^{m}\sum_{\nu=1,\nu\neq\delta}^{m}\left(T_1^{(\delta)}T_1^{(\nu)}\right)\left(p^{(\delta)}p^{(\nu)*}\right)\left(\widetilde{\gamma}^{(\nu)*}G^{(\delta)*}+\gamma^{(\delta\nu)}\widetilde{G}^{*}\right)\right\}. \tag{21}$$

An important feature of the channel $\hat{g}_0\hat{\mu}_0\hat{g}_0$ is the dependence of amplitudes of reconstructed object and reading waves on the nonlinear inter- and cross-modulation terms (9). This fact substantially differs this channel from the "linear" ones $\hat{g}_{-1}\hat{\mu}_{-1}\hat{g}_{-1}$ (16) and $\hat{g}_{+1}\hat{\mu}_{+1}\hat{g}_{+1}$ (21) and is based on the account of constructive contributions from all the nonlinear components of the response. So, separating in the operator $\hat{g}_0^{(\delta)}$ average transmission from the diffraction intermodulation structure:

$$\hat{g}_0^{(\delta)} = \frac{1}{m}T_0 + T_1^{(\delta)}\left(\left|p_0^{(\delta)}\right|^2 + \left|G^{(\delta)}\right|^2\right) \equiv \left(\frac{1}{m}T_0 + T_1^{(\delta)}\left(\left|p_0^{(\delta)}\right|^2 + \gamma^{(\delta\delta)}\right)\right) + T_1^{(\delta)}\underbrace{G^{(\delta)}G^{(\delta)*}} \equiv T_0^{(\delta)'} + T_1^{(\delta)}\underbrace{G^{(\delta)}G^{(\delta)*}}, \tag{22}$$

and the transmitted x-wave from the diffrated wave in the field, scattered by this operator:

$$\hat{g}_0^{(\delta)}\widetilde{G} = T_0^{(\delta)'}\widetilde{G} + T_1^{(\delta)}\underbrace{G^{(\delta)}G^{(\delta)*}}\widetilde{G} \equiv T_0^{(\delta)'}\widetilde{G} + T_1^{(\delta)}\left(\widetilde{\gamma}^{(\delta)}G^{(\delta)} - A^{(\delta\delta x)} + \underbrace{G^{(\delta)}G^{(\delta)*}}\widetilde{G}\right), \tag{23}$$

it is possible to show, that after phase conjugation of scattered field with one and the same for all its spatial components efficiency μ_0 and diffraction on $\hat{g}_0^{(\nu)}$ -lattices, the following field will be reconstructed in the partial 0th order of the system:

$$\begin{aligned}\hat{g}_0^{(\nu)}\mu_0\hat{g}_0^{(\delta)}\widetilde{G} \approx \mu_0\Big\{&\left(T_0^{(\nu)'}T_0^{(\delta)'} + T_1^{(\nu)}T_1^{(\delta)}\underbrace{\gamma^{(\delta\nu)}\gamma^{(\delta\nu)*}}\right)\widetilde{G}^* + T_1^{(\delta)}\left(T_0^{(\nu)'}\widetilde{\gamma}^{(\delta)*} + T_1^{(\nu)}\underbrace{\gamma^{(\nu\delta)}\widetilde{\gamma}^{(\nu)*}}\right)G^{(\delta)^*} + \\ &+ T_1^{(\nu)}\left(T_0^{(\delta)'}\widetilde{\gamma}^{(\nu)*} + T_1^{(\delta)}\underbrace{\gamma^{(\delta\nu)}\widetilde{\gamma}^{(\delta)*}}\right)G^{(\nu)^*}\Big\}.\end{aligned} \tag{24}$$

The results of diffraction on the intermodulation structure of ν -hologram of all the components of the response $\hat{g}_0^{(\delta)}\widetilde{G}$ are accounted in (24), particularly, of the conjugate transmitted x- and reconstructed δ -fields:

$$\left(T_1^{(\nu)}\underbrace{G^{(\nu)^*}G^{(\nu)}}\right)T_0^{(\delta)'}\widetilde{G}^* \equiv T_1^{(\nu)}T_0^{(\delta)'}\left(\widetilde{\gamma}^{(\nu)*}G^{(\nu)^*} - A^{(\nu\nu x)^*} + \underbrace{G^{(\nu)^*}G^{(\nu)}}\widetilde{G}^*\right), \tag{25}$$

$$\left(T_1^{(\nu)}\underbrace{G^{(\nu)^*}G^{(\nu)}}\right)T_1^{(\delta)}G^{(\delta)^*} \equiv T_1^{(\nu)}T_1^{(\delta)}\left(\gamma^{(\delta\nu)}G^{(\nu)^*} - A^{(\nu\nu\delta)^*} + \underbrace{G^{(\nu)^*}G^{(\nu)}}G^{(\delta)^*}\right), \tag{26}$$

as well as of the conjugate "distorting" fragment $-A^{(\delta\delta x)}$ and cubic noise $\underbrace{G^{(\delta)}G^{(\delta)*}}\widetilde{G}$:

$$\left(T_1^{(\nu)}\underbrace{G^{(\nu)^*}G^{(\nu)}}\right)T_1^{(\delta)}A^{(\delta\delta x)^*} \equiv T_1^{(\nu)}T_1^{(\delta)}\left(\underbrace{\gamma^{(\delta\nu)}\widetilde{\gamma}^{(\delta)*}}G^{(\nu)^*} - A^{(\nu\delta\delta x)^*} + \underbrace{G^{(\nu)^*}G^{(\nu)}}A^{(\delta\delta x)^*}\right), \tag{27}$$

$$\begin{aligned}&\left(T_1^{(\nu)}\underbrace{G^{(\nu)^*}G^{(\nu)}}\right)T_1^{(\delta)}\underbrace{G^{(\delta)^*}G^{(\delta)}}\widetilde{G}^* \equiv T_1^{(\nu)}T_1^{(\delta)}\Big\{\underbrace{\gamma^{(\delta\nu)}\gamma^{(\delta\nu)*}}\widetilde{G}^* + \underbrace{\widetilde{\gamma}^{(\nu)*}\gamma^{(\nu\delta)}}G^{(\delta)^*} - \gamma^{(\delta\nu)}A^{(x\delta\nu)^*} - \widetilde{\gamma}^{(\nu)*}A^{(\delta\delta\nu)^*} + A^{(\delta\delta x\nu\nu)^*} + \\ &+\Big[\underbrace{G^{(\nu)^*}G^{(\nu)}G^{(\delta)^*}G^{(\delta)}}\widetilde{G}^* + \gamma^{(\delta\nu)}\widetilde{G}^*\underbrace{G^{(\delta)}G^{(\nu)^*}} + \gamma^{(\delta\nu)*}\underbrace{G^{(x)^*}G^{(\nu)}}G^{(\delta)^*} + \widetilde{\gamma}^{(\nu)*}\underbrace{G^{(\delta)^*}G^{(\delta)}}G^{(\nu)^*} - \underbrace{A^{(\delta\nu x)^*}G^{(\delta)}}G^{(\nu)^*} - \\ &-\widetilde{G}^*\underbrace{G^{(\nu)}A^{(\delta\delta\nu)^*}} - \underbrace{G^{(\delta)^*}G^{(\delta)}}A^{(\nu\nu x)^*} - \underbrace{G^{(\delta)^*}A^{(\delta x\nu)}}G^{(\nu)^*} - \underbrace{\widetilde{G}^*G^{(\delta)}}A^{(\delta\nu\nu)^*} - \underbrace{\widetilde{G}^*A^{(\nu\delta\delta)}}G^{(\nu)^*} - \underbrace{G^{(\delta)^*}G^{(\nu)}}A^{(\delta\nu x)^*} - \underbrace{G^{(\delta)^*}A^{(\nu\nu\delta)}}\widetilde{G}^*\Big]\Big\},\end{aligned} \tag{28}$$

where $A^{(\delta\delta x\nu\nu)^*}$ is a common distorting fragment with modulation of fourth power on amplitude, and all the terms in square parenthesis are noises of third and fifth powers.

So, the information structure of field, formed by this channel, is of the type:

$$\begin{aligned}\hat{g}_0\hat{\mu}_0\hat{g}_0\widetilde{G} \approx \mu_0\Bigg\{&\sum_{\delta=1}^{m}\Bigg[\left(\left(T_0^{(\delta)'}\right)^2 + \left(T_1^{(\delta)}\right)^2\underbrace{\gamma^{(\delta\delta)}\gamma^{(\delta\delta)*}}\right)\widetilde{G}^* + 2T_1^{(\delta)}\left(T_0^{(\delta)'}\widetilde{\gamma}^{(\delta)*} + T_1^{(\delta)}\underbrace{\gamma^{(\delta\delta)}\widetilde{\gamma}^{(\delta)*}}\right)G^{(\delta)^*}\Bigg] + \\ &+2\sum_{\delta=1}^{m}\sum_{\nu=1,\nu>\delta}^{m}\Bigg[\left(T_0^{(\nu)'}T_0^{(\delta)'} + T_1^{(\nu)}T_1^{(\delta)}\underbrace{\gamma^{(\delta\nu)}\gamma^{(\delta\nu)*}}\right)\widetilde{G}^* + T_1^{(\delta)}\left(T_0^{(\nu)'}\widetilde{\gamma}^{(\delta)*} + T_1^{(\nu)}\underbrace{\gamma^{(\nu\delta)}\widetilde{\gamma}^{(\nu)*}}\right)G^{(\delta)^*} + T_1^{(\nu)}\left(T_0^{(\delta)'}\widetilde{\gamma}^{(\nu)*} + T_1^{(\delta)}\underbrace{\gamma^{(\delta\nu)}\widetilde{\gamma}^{(\delta)*}}\right)G^{(\nu)^*}\Bigg]\Bigg\}.\end{aligned} \tag{29}$$

It brings into the 0th diffraction order of the system the nonlinearity, characteristic of the 0th order of the quadratic hologram (8). Thus, such a realization of PC reflection, in which the channel $\hat{g}_0\hat{\mu}_0\hat{g}_0$ is excluded ($\mu_0 = 0$), may

essentially simplify the structure of the total response of the 0th order of the system and decrease noises in it, keeping at the same time important features of the quadratic hologram (particularly, the existence of the second order with inherent to it information properties). In contrary, the regime of phase conjugation, during which this channel is increased relative to the other channels, permits to increase the nonlinear and inherent information properties of the 0th order, such as integration of spatial spectra of registered object fields and breaking of their orthogonality with each other and with the reading field.

It's necessary to note, that the presence of additional, apart from the traditionally used, channels of information reconstruction in such a system, particularly, the channels $\hat{g}_{+1}\hat{\mu}_{-1}\hat{g}_{-1}$ in the +2nd diffraction order and $\hat{g}_{+1}\hat{\mu}_{+1}\hat{g}_{+1}$ in the 0th one, may give in principle several new possibilities of controlling the structure of yielding field.

4. CONCLUSIONS

So, the nonlinear (qudratic) registration of thin superposed holograms is an effective way of reconstruction of complete original fields as well as of detection of elements of their spatial spectra within the reading field. Due to the nonlinear mixing the dependencies of efficiencies of reconstruction of recorded fields upon the levels of their correlation with each other and with the reading field in the general case differ from a proportional dependence. Owing to this, the essential extention of possibilities of associative information reconstruction by the quadratic hologram relative to the linear one takes place.

"Nonlinear reading" in thin linear off-axis hologram - PC mirror system is one more effective way of realization of nonlinear mixing and associative reconstruction of fields. In essence, such a system may be considered as a quadratic hologram, the spatial structure of the response of which, given the possibilities of PC mirror reflectance control, can be modified by means of phase conjugation.

5. REFERENCES

1. R.J. Collier, C.B. Burckhardt, and L.H.Lin, Optical Holography, Academic Press, New York and London, 1971.
2. I.I. Mokhun', S.N. Roslyakov, "Investigation of qualitative characteristics of image, reconstructed from referenceless hologram", *Jurnal Prikladnoi Spektroskopii 42(1),* pp. 113-117, 1985.
3. P.V.Polyanskii, "On conjugate image formation at generalized matched filter scheme," *Optika i Spektroskopiya 65(2),* pp. 435-438, 1988.
4. P.V.Polyanskii, "On matched filtering using reflection hologram," *Avtometriya* 20(3), pp. 46-50, 1990.
5. B.H.Soffer, G.J.Dunning, Y.Owechko, E.Marom, "Associative holographic memory with feedback using phase-conjugate mirrors," *Optics Letters* 11(2), pp. 118-120, 1986.
6. Y. Owechko, "Nonlinear holographic associative memory," *IEEE J. Quant. El.* 25(3), pp. 619-634, 1989.
7. L.M.Serebryakova, "Phenomenological analysis of matched filtering by thin holograms," *Optika i Spektroskopiya* 78(6), pp. 984-988, 1995.
8. A.S.Rubanov, L.M.Serebryakova, "Informative properties of hologram of mutually conjugated waves," *Optika i Spektroskopiya* 79(6), pp. 1009-1013, 1995.
9. A.S.Rubanov, L.M.Serebryakova, "New mechanism of associative reconstruction of information in thin hologram - phase-conjugate mirror system," *Optical Memory and Neural Networks, Proc. SPIE*, Vol. 3402, pp. 72-83 (1998).
10. L.M.Serebryakova, "Analysis of the transformation of noise field components to information components in the thin hologram - PC mirror system," *Optika i Spektroskopiya* 85 (4), pp. 574-578, 1998.
11. P.V.Polyanskii, "Informative properties of second-order holograms", Holography, Correlation Optics, and Recording Materials, Proc. SPIE, Vol. 2108, pp. 435-442, 1993.
12. L.M.Serebryakova, "Phenomenological analysis of associative reconstruction of information by thin holograms with superposed registration", *Optika i Spektroskopiya* 89 (3), pp. 481-490, 2000 (be published).
13. J.W.Goodman, G.R.Knight, "Effects of film nonlinearities on wavefront-reconstruction images of diffuse objects", *J.Opt.Soc.Am.*, 58(10), pp. 1325-1334, 1968.

Phase sensitive parametric image amplification : Application to noiseless image amplification

F. Devaux and E. Lantz

Laboratoire d'Optique P.M. Duffieux
Centre National de la Recherche Scientifique, Unité Mixte de Recherche 6603
Université de Franche-Comté, F-25030 Besançon cedex, France

ABSTRACT

We report semi-classical numeric simulations of the quantum spatial fluctuations in parametric amplification of images limited by the shot noise. Noiseless amplification of images is demonstrated by the use of a degenerate type 2 phase sensitive amplifier.

Keywords: parametric amplification, noiseless amplification, image amplification, quantum fluctuations, phase sensitive amplifier

1. INTRODUCTION

Phase sensitive parametric amplification has been experimentally investigated[1] in the temporal domain in order to perform noiseless amplification or noise reduction of signals.[2,3] In the spatial domain, parametric amplification of images has been experimentally performed with phase insensitive[4,5] or phase sensitive[6] amplifiers. In a recent work,[7] images have been amplified with a type 2 phase sensitive parametric amplifier and noiseless amplification has been performed, but the considered noise fluctuations were the temporal fluctuations on pixels of the image. To the best of our knowledge, specific purely spatial properties of phase sensitive parametric image amplification, i.e. with the considered noise being purely spatial fluctuation in the transverse image plane,[8] have not yet been experimentally evidenced. These properties, that include noiseless image amplification and image entanglement have recently been theoretically described.[9,10] In previous papers we have theoretically[6] and experimentally[11] shown that phase sensitive parametric amplification of images leads, in the spatial domain, to amplification and deamplification depending on both the relative phase of the input image with respect to the pump plane wave and on its spatial frequency distribution. Here, we report numeric simulations showing the noiseless amplification, in a degenerate type 2 phase sensitive parametric interaction, of images where the spatial fluctuations are limited by the shot noise.

2. THEORETICAL BACKGROUND

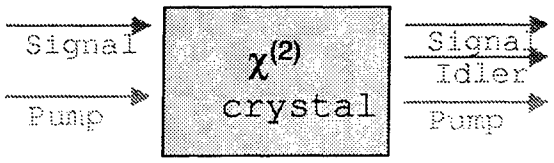


Figure 1. Parametric amplification : a weak signal pulse is amplified in a quadratic material by a strong pump pulse.

Parametric amplification is a three-wave-mixing interaction where a weak signal pulse is amplified by a strong pump pulse in a quadratic material when the phase matching condition is verified.[12] Usually, only the signal and

Further author information: (Send correspondence to Devaux F.)
Devaux F.: E-mail: fabrice.devaux@univ-fcomte.fr
Lantz E.: E-mail: elantz@univ-fcomte.fr

Laser Optics 2000: Control of Laser Beam Characteristics and Nonlinear Methods for Wavefront Control,
Leonid N. Soms, Vladimir E. Sherstobitov, Editors, Proceedings of SPIE Vol. 4353 (2001)
© 2001 SPIE · 0277-786X/01/$15.00

the pump beams are present at the input of the crystal. Hence, according to the laws of energy conservation, a third wave (the "idler") is generated along the amplification process (figure 1).

In the undepleted pump approximation, the variation of the complex amplitude of the signal and idler fields are given by :

$$dA_s/dz = -i\kappa A_p A_i^*(z)\exp^{-i\Delta kz},$$
$$dA_i/dz = -i\kappa A_p A_s^*(z)\exp^{-i\Delta kz}, \quad (1)$$

where κ is the coupling parameter, $\Delta k = |\vec{k_p} - \vec{k_s} - \vec{k_i}|$ is the phase mismatch vector and A_p the amplitude of the pump beam. In previous works we have shown that, at the degeneracy, the collinear phase matched type 1 and type 2 interactions are non critical with respect to the signal and the idler directions of propagation.[4,5] Hence, these waves can be amplified over a wide angular range by a pump plane wave around the perfect phase matching direction. If we consider now an image as the superposition of plane waves where each wave is associated to a spatial frequency, such property allows the amplification of images with the best resolution. For example we obtained the amplification of an image in a $7 \times 7\,mm^2$ square section and $2\,cm$ long type 2 KTP crystal (figure 2). The signal wavelength was $\lambda_s = 1064\,nm$. The gain was about $40\,dB$ over an angular range of $20\,mrad$, that gives a resolution of $90\,\mu m$ in the crystal. By taking in account the section of the crystal it corresponds to an amplified image with 80×80 resolution cells. We have shown that this number of resolution cells corresponds to the number of spatial modes that can be amplified at the signal wavelength.[8]

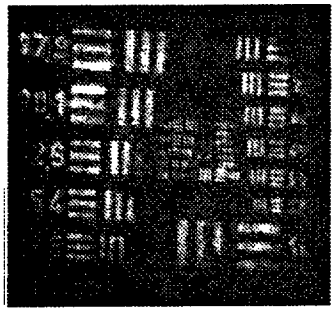


Figure 2. Amplified image in a $7 \times 7 \times 20\,mm^3$ KTP crystal. The amplification gain is $40\,dB$, the $90\,\mu m$ resolution in the crystal gives 80×80 resolved points in the amplified image.

In type 1 and type 2 degenerate interactions, when the signal and the idler channels are both excited, the amplification process strongly depends on the input relative phase of the interacting waves.[11] Such phase sensitive amplifier (PSA) can be use to amplify images limited by the shot noise without adding any noise while classical amplifiers (phase insensitive amplifiers - PIA) add $3\,dB$ of noise. Hence, with a PSA the signal-to-noise ratio (SNR) of the input signal can be conserved . When an image is limited by the shot noise, the spatial fluctuations of the intensity in the transverse plane can be described by a poissonian noise. Then, if there is a mean number of N photons per resolution cell in the input image, the variance of the fluctuations is $\langle \Delta N^2 \rangle = N$ and the signal-to-noise ratio is $SNR = N$. The amplifier is characterized by its noise figure (NF) wich is equal to :

$$NF = \frac{SNR_{in}}{SNR_{out}}, \quad (2)$$

where SNR_{in} and SNR_{out} are respectively the SNR of the input and of the ouput images. In order to describe theoretically these quantum spatial fluctuations in the parametric amplification process it is necessary to introduce the modal operator of the interacting fields. For one mode which is perfectly phase matched, the solutions of the equations 1 are :

$$\hat{a}_{out} = C\hat{a}_{in} - iS\hat{b}^{+}_{in},$$
$$\hat{b}_{out} = C\hat{b}_{in} - iS\hat{a}^{+}_{in}, \tag{3}$$

where $\hat{a}$ and $\hat{b}$ are respectively the input/ouput annihilation operator for the signal and idler field modes. $C = \cosh(\kappa A_p L)$ and $S = \sinh(\kappa A_p L)$, L is the crystal length. With a PIA, when there is no input in the idler channel ($N_b^{in} = \langle \hat{b}^{+}_{in}\hat{b}_{in}\rangle = 0$, $N_a^{in} = \langle \hat{a}^{+}_{in}\hat{a}_{in}\rangle = N_{in}$), the mean number of photons, the variance and the SNR at the output in the signal channel are :

$$\langle N_{out}\rangle_{PIA} = \langle \hat{a}^{+}_{out}\hat{a}_{out}\rangle = C^2 N_{in} + S^2,$$
$$\langle \Delta N^2_{out}\rangle_{PIA} = (C^4 + C^2S^2)N_{in} + S^4 + C^2S^2,$$
$$SNR^{PIA}_{out} = \frac{(C^2N_{in} + S^2)^2}{(C^4 + C^2S^2)N_{in} + S^4 + C^2S^2}. \tag{4}$$

When the number of photons at the input is greater than one ($N_{in} \gg 1$), parametric fluorescence can be neglected and SNR^{PIA}_{out} becomes :

$$SNR^{PIA}_{out} = N_{in}\frac{C^2}{C^2 + S^2}. \tag{5}$$

If the input signal is limited by the shot noise ($SNR_{in} = N_{in}$), then NF_{PIA} is :

$$NF_{PIA} = 1 + \frac{S^2}{C^2}. \tag{6}$$

For high gain, NF_{PIA} tends to 2 and PIA adds $3\,dB$ of noise. With a PSA, the output parameters are :

$$\langle N_{out}\rangle_{PSA} = (C^2 + S^2 - 2CS\sin 2\varphi)N_{in} + S^2,$$
$$\langle \Delta N^2_{out}\rangle_{PSA} = (C^4 + S^4 + 6C^2S^2 - 4CS(C^2 + S^2)\sin 2\varphi)N_{in} + 2C^2S^2,$$
$$SNR^{PSA}_{out} = \frac{((C^2 + S^2 - 2CS\sin 2\varphi)N_{in} + S^2)^2}{(C^4 + S^4 + 6C^2S^2 - 4CS(C^2 + S^2)\sin 2\varphi)N_{in} + 2C^2S^2}, \tag{7}$$

where φ is the input relative phase between the signal and the pump waves. When the number of photons at the input is greater than one, SNR^{PSA}_{out} becomes :

$$SNR^{PSA}_{out} = N_{in}\frac{(C^2 + S^2 - 2CS\sin 2\varphi)^2}{(C^4 + S^4 + 6C^2S^2 - 4CS(C^2 + S^2)\sin 2\varphi)}. \tag{8}$$

With an input signal limited by the shot noise, when $\varphi = -\pi/4$, $NF_{PSA} = 1$ whatever the amplification gain. Then the amplifier does not add any noise. When $\varphi = +\pi/4$, the input signal is strongly deamplified and parametric fluorescence can be no more neglected. Then, the SNR^{PSA}_{out} is strongly degraded and NF_{PSA} becomes greater than one.

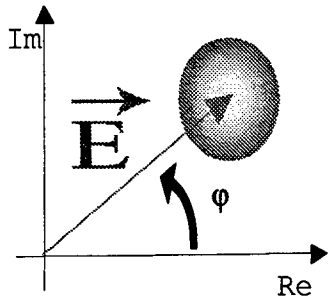


Figure 3. Poissonian signal : Classical field + random field corresponding to a mean amplitude of 1/2 photon.

3. NUMERIC SIMULATION

In order to simulate the quantum spatial fluctuations in the parametric amplification of images, we have performed semi-classical numeric calculations. In our simulations the input image is a plane wave with a mean intensity constant in the tranverse plane. A type 2 degenerate amplification occurs in a $2\,cm$ long KTP crystal with a $7 \times 7\,mm^2$ section. The shot noise is simulated by adding to a classical field, a random field (with a poissonian distribution) corresponding to a mean amplitude of 1/2 photon per pixel in the input image[13] (figure 3).

With a PIA, the signal and the idler channels are excited respectively by a poissonian signal and 1/2 photon of noise per pixel (figure 4). With a PSA, the classical field is projected onto the two input channels and 1/2 photon of noise per pixel in both channels is added.

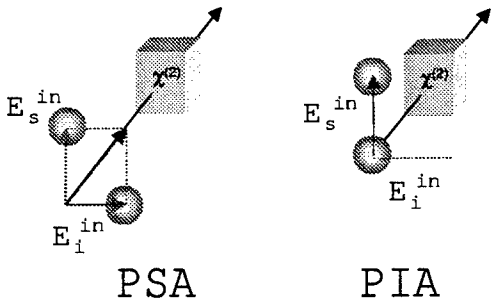


Figure 4. In PIA : poissonian signal in the signal channel and 1/2 photon of noise/pixel in the idler channel. In PSA : projection of the classical field onto the two channels + 1/2 photon of noise/pixel in both channels.

Figure 5 shows the results of the numeric simulation. The input image has 256 × 256 pixels, a mean number of 50 photons/pixel and the parametric gain is $\kappa A_p = 0.1\,mm^{-1}$. With a PSA, when $\varphi = -\pi/4$, the gain is maximum ($G_{PSA} \sim 17\,dB$) but the noise figure is smaller than one ($NF_{PSA} = 0.14$) and it does not agree with the theory. The explanation is that the collinear phase matching acts as a low pass-filter that rejects the high frequency noise.[4] This is clearly shown in the amplified image where spatial inhomogeneities are bigger than ones in the input image. As the SNR must be defined in the bandwidth of the amplifier, the number of independant pixels in the input image must be smaller than the number of resolution cells in the amplifier[9] (about 80 × 80 resolution cells).We have joined together 8 × 8 pixels of the images (binning 8 × 8) and then NF_{PSA} tends to 1 as it was predicted by the theory. With a PIA, NF_{PIA} tends to 2.

Figures 6 give different curves showing the variation of the noise figure for PIA and PSA versus different parameters. Figure 6a presents the NF versus the binning of the pixels. It clearly shows that when the number of independant pixels in the images is smaller than the number of resolution cells, NF tends to 1 for PSA and to 2 for PIA. Figure 6b shows the variation of the NF with respect to the input relative phase. The NF_{PIA} is equal to

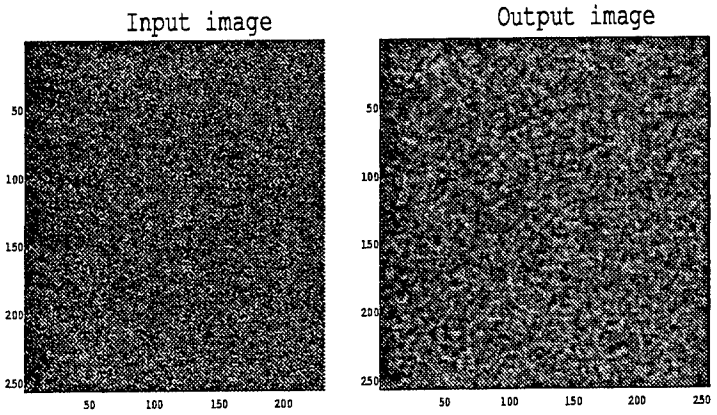


Figure 5. Result of the numeric simulation for PSA : in the ouput image spatial inhomogeneities are bigger than ones in the input image because the collinear phase matching acts as a low-pass filter that rejects the high frequency noise.

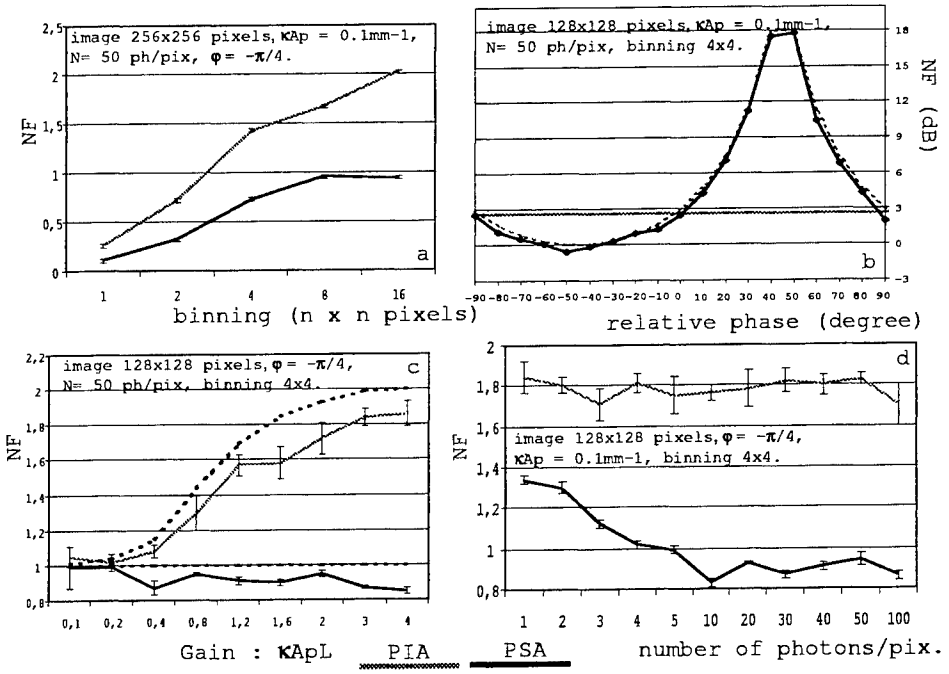


Figure 6. Variation of the noise figure versus the binning (a), the input relative phase (b), the gain (c) and the number of photons per pixel at the input for a PSA (black curves) and PIA (gray curves). In b, numeric simulation is fitted with the theoretical curve given by equation 7.

$3\,dB$ and does not depend on the relative phase. The NF_{PSA} is about $0\,dB$ when $\varphi = -\pi/4$ and strongly increases when $\varphi = +\pi/4$. The numerical simulation is fitted with the curve of the theoretical NF_{PSA} given by the equation 7. Figure 6c shows the variation of the NF with respect to the amplification gain. When $\varphi = -\pi/4$, NF_{PSA} is constant and equal to one and NF_{PIA} tends to 2 when the amplification gain increases. Figure 6d shows the NF versus the number of photons per pixel at the input. It shows that when N decreases, NF_{PSA} is greater than 1

because the parametric fluorescence becomes significant and degrades the output SNR_{PSA}.

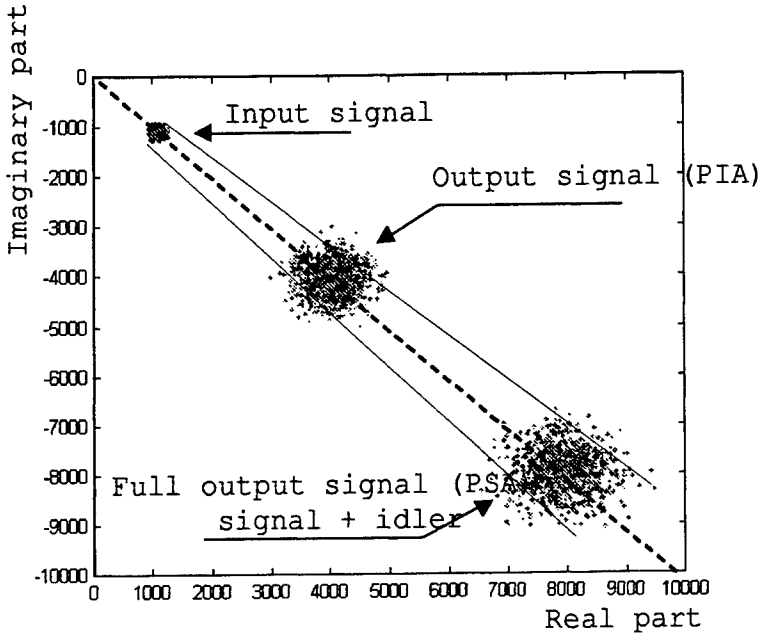


Figure 7. Input and output fields in the complex plane.

We have plotted in the complex plane the input and the output signal fields for PIA and PSA (figure 7). With the PIA, output signal exhibits excess of noise due to the amplifier while the input SNR is conserved with the PSA when $\varphi = -\pi/4$.

4. CONCLUSION

In conclusion, we have performed semi-classical numeric simulations of the quantum spatial fluctuations in parametric amplification of images. Noiseless amplification of images limited by the shot noise was demonstrated when a phase sensitive amplifier is used while a classical amplifier adds $3\,dB$ of noise.

REFERENCES

1. Sang-Kyung Choi, Ruo-Ding Li, Chonghoon Kim and P. Kumar, "Travelling-wave optical parametric amplifier : investigation of its phase-sensitive and phase-insensitive gain response", J. Opt. oc. Am. B **14** (1997) 1564-1575.
2. J.A. Levenson, I. Abram, T. Rivera and P. Grangier, "Reduction of quantum noise in optical parametric amplification", J. Opt. Soc. Am. B **10** (1993) 2233-2238.
3. Z.Y. Ou, S.F. Pereira and H.J. Kimble, "Quantum noise reduction in optical amplification", Phys. Rev. Lett. **70** (1993) 3239-3242.
4. F. Devaux and E. Lantz, "Transfer function of spatial frequencies in parametric image amplification : experimental analysis and application to picosecond filtering", Optics Commun. **114** (1995) 295-300.
5. E. Lantz and F. Devaux, "Parmetric amplification of images", Quantum Semiclass. Opt. **9** (1997) 279-286.
6. F. Devaux and E. Lantz, "Parametric amplification of a polychromatic image", J. Opt. Soc. Am. B **12** (1995) 2245-2252.
7. Sang-Kyung Choi, M. Vasilyev and P. Kumar, "Noiseless optical amplification of images", Phys. Rev. Lett. **83** (1999) 1938-1941.
8. F. Devaux and E. Lantz,"Spatial and temporal properties of parametric fluorescence around degeneracy in a type I LBO crystal" , Eur. Phys. J. D **8** (2000) 117-124.
9. I. Sokolov, M. Kolobov and L.A. Lugiato, "Quantum fluctuations in traveling-wave amplification of faint optical images ", Phys. Rev. A **60** (1999) 2420-2430.

10. A. Gatti, E. Brambilla, L.A. Lugiato and M. Kolobov, "Quantum entangled images", Phys. Rev. Lett. **83** (1999) 1763-1766.
11. F. Devaux and E. Lantz, "Gain in phase sensitive parametric image amplification",to be published in PRL.
12. A. Yariv, *Quantum Electronics 3rd Edition* (John Wiley and Sons, New York 1989) 430-435.
13. C.M. Caves, "Quantum limits on noise in linear amplifiers", Phys. Rev. D **26** (1982) 1817-1839.

On the cnoidal waves propagation in the medium with delayed response

Victor Aleshkevich[a], Victor Vysloukh[b] and Yaroslav Kartashov[a*]

[a]Chair of General Physics, Physics Department, M. V. Lomonosov Moscow State University, 119899 Moscow, Russia

[b]CIICAp. UAEM, Av. Universidad 1001, C.P. 62210, Cuernavaca, Mor., Mexico

ABSTRACT

We consider the influence of the inertial component of the optical fibre response on the cnoidal waves propagation dynamic and analyse the dependence of the self-bending parameter on the degree of the temporal localisation of the wave energy. We have shown that for the case of the cn-wave the role of self-bending effects increases (and for the case of the dn-wave decreases) with growth of degree of localisation.

Keywords: solitons, optical fibres, Raman self-frequency shift, cnoidal waves.

1. INTRODUCTION

The cnoidal waves concept is very attractive from the theoretical point of view because it enables one to analyse propagation dynamics of both single- and multicomponent periodical solutions of the nonlinear cubic Shrodinger equation (NLSE) for the cases of different temporal localisation of the wave field energy[1]. Earlier mathematically analogous problem was treated for the case of cnoidal waves in photorefractive crystals. As a rule, the cnoidal waves show structural stability with respect to the small input profile perturbations and collisions[2]. These properties make the cnoidal waves especially perspective for such practical purposes as the optical interconnects design and construction of the nonlinear optical devices for light by light control. One of the most important features of the cnoidal waves is that in the limit of the strong localisation they transform into the well-known dark and bright solitons[3].

From the practical point of view the main perspectives of the cnoidal waves operating devices construction connected with optical fibres. The several experimental works dealing with cnoidal waves propagation in the photorefractive crystals has already been successfully performed[4,5]. As was shown in one of the earliest works connected with photorefractive solitons[6], the use of the additional incoherent background illumination of the photorefractive crystals (PRC) enables one to realise nonlinearity close to that in Kerr materials. The influence of the spatially nonlocal diffusion component of the nonlinear response gives an additional refractive index contribution, which is proportional to the derivative of the light intensity on the transverse coordinate[7]. The physical manifestation of the latter effect is the well known beam self-bending[8,9]. Specific features of the self-bending of photorefractive solitons were also studied in the reference[10].

Note that in the optical fibre transmission systems one in fact dealing not only with localised soliton-like pulses but also with the objects of the cnoidal wave type. In this temporal case, the presence of the inertial Raman component of the nonlinear response (which is described by the term with temporal derivative of light intensity) results in the Raman self-frequency downshift[11]. This phenomenon is by mathematical description analogous to the spatial beam self-bending.

Thus, the cnoidal wave theory extension to the case of more complicated then the cubic one mechanism of nonlinearity is of great importance. In the present work, we investigate the influence of the inertial component of the fibre response on the cnoidal waves propagation dynamic with using of the approximate analytical consideration and numerical simulation. We analyse dependence of the self-bending parameter on the degree of the localisation of the wave energy.

* Correspondence: e-mail: azesh@gateway.phys.msu.su; phone: (095) 939-34-38; fax: (095) 939-14-89

Laser Optics 2000: Control of Laser Beam Characteristics and Nonlinear Methods for Wavefront Control, Leonid N. Soms, Vladimir E. Sherstobitov, Editors, Proceedings of SPIE Vol. 4353 (2001)
© 2001 SPIE · 0277-786X/01/$15.00

2. THEORETICAL MODEL

The propagation of the ultrashort laser pulse in the optical fibre can be described with the standard shortened wave equation regarding normalised complex amplitude $q(\eta,\xi)$ expressed in the "soliton" units[12-15]

$$i\frac{\partial q}{\partial \xi} = -\frac{1}{2}\frac{\partial^2 q}{\partial \eta^2} - |q|^2 q + \mu q \frac{\partial}{\partial \eta}|q|^2 . \tag{1}$$

Here η corresponds to the normalised running time $(t\text{-}z/c)/\tau_0$; ξ corresponds to the longitudinal coordinate z/L_d normalised by the dispersion length $L_d=\tau_0^2/|k''|$; parameter μ is proportional to the ratio τ_R/τ_0, where τ_R is the Raman response characteristic time. The nonlinear Shrodinger equation of the type (1) was also considered in refererences[16,17]. The last term in the right side of Equation (1) describes the self-frequency shift effect resulting from the energy transfer from the high- to the low-frequency spectral components. The first term in the right part of Equation (1) describes the dispersion spreading and the second one the self-compression due to the Kerr component of nonlinear response of optical fibre.

In the case of the comparatively long optical pulses (when parameter μ is very small) Equation (1) is transformed into the well-known nonlinear Shrodinger equation, which has two periodical solutions in the form of the cnoidal waves:

$$\begin{aligned} q_{cn}(\eta,\xi) &= m\,\mathrm{cn}(\eta,m)\exp[i\xi(m^2-1/2)], \\ q_{dn}(\eta,\xi) &= \mathrm{dn}(\eta,m)\exp[i\xi(1-m^2/2)], \end{aligned} \tag{2}$$

which can propagate undistorted through the optical fibre. In the formula (2) $\mathrm{cn}(\eta,m)$ and $\mathrm{dn}(\eta,m)$ are the periodical elliptical functions of the coordinate η. The $\mathrm{cn}(\eta,m)$ function has the unity amplitude and can take both positive and negative signs; $\mathrm{dn}(\eta,m)$ function is always positive and reaches close to zero values only for the case of the strong localisation (see Fig. 1). Parameter m varies from 0 to 1 and describes the degree of localisation of the cnoidal waves.

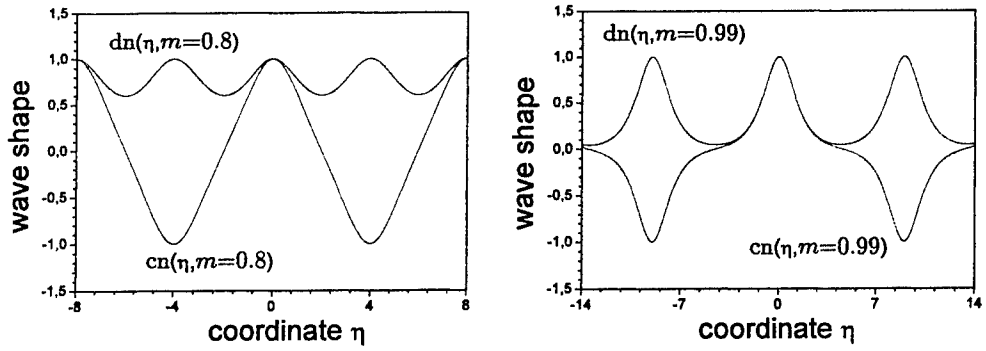


Figure 1. Shapes of the cn- and dn-waves for the different degree of localisation of the wave field energy.

The role of localisation parameter m can be easily interpreted for the second solution $q_{cn}(\eta,\xi)$. When the localisation parameter m is close to zero, the amplitude of this solution also goes to zero providing that the nonlinear terms in the NLSE can be neglected. In this linear limiting case $\mathrm{cn}(\eta,m)$ function is well approximated by $\cos(\eta)$ with 2π period, that corresponds to the weak localisation. With increasing of the localisation parameter m the contribution from the nonlinear terms increases. The wave period increases with increase of m and for m=1 goes to infinity. The profile of the cnoidal wave $\mathrm{cn}(\eta,m)$ is then well described by the well-known hyperbolic secant type solution of the NLSE. Thus one can write the following asymptotic expansions:

$$q_{cn}(\eta,\xi)\big|_{m\to 0} = m\cos(\eta)\exp(-i\xi/2), \qquad q_{cn}(\eta,\xi)\big|_{m\to 1} = \mathrm{sech}(\eta)\exp(i\xi/2). \tag{3}$$

The second solution $q_{dn}(\eta,\xi)$ presented by the formula (2), for the case of small m transforms into the planar wave of the unity amplitude and for $m=1$ is described by the hyperbolic secant type solution of NLSE just as $q_{cn}(\eta,\xi)$:

$$q_{dn}(\eta,\xi)\big|_{m\to 0} = \exp(i\xi), \qquad q_{dn}(\eta,\xi)\big|_{m\to 1} = \operatorname{sech}(\eta)\exp(i\xi/2). \tag{4}$$

Hereafter we consider self-bending of the presented above cnoidal waves due to the inertial component of the nonlinear response of the optical fibres. Parameter μ describing the strength of this effect is chosen to be of the order of 0.1 (this is a quite character value for the real experiments). In this case the shape of the cnoidal wave (2) launched into the nonlinear medium only slightly changes during the propagation process owing to the inertial component of the nonlinear response. Our main task was to analyse the dependence of the trajectory of motion of the cnoidal wave on the localisation parameter m. Further we separately consider the cases of cn-wave $q_{cn}(\eta,\xi)$ and dn-wave $q_{dn}(\eta,\xi)$. Notice that non-periodic multi-hump stationary solutions of equation (1) are also known[15].

3. SELF-BENDIING OF THE CN-WAVE

To describe self-bending of the cn-wave we use the fact, that for the values of the localisation parameter m lying within the rather wide range the spectrum of such wave consists of only two harmonics. One can clearly see it for example from the well-known expansion

$$\operatorname{cn}(\eta,m) = \frac{2\pi}{mK}\sum_{n=0}^{\infty}\frac{g^{n+1/2}}{1+g^{2n+1}}\cos\frac{(2n+1)\pi\eta}{2K}, \tag{5}$$

where $g(m)=\exp[-\pi K'(m)/K(m)]$ is the Jacobi parameter; $K(m)=\int_0^{\pi/2}[1-m^2\sin^2\varphi]^{-1/2}d\varphi$ and $K'(m)=\int_0^{\pi/2}[1-(1-m^2)\sin^2\varphi]^{-1/2}d\varphi$ are the elliptical integrals, which describe the period of the cnoidal wave and depend on the value of the localisation parameter m. This expansion is valid for m ranges from 0 to approximately 0.8. For this values of localisation parameter the first two harmonics in spectrum (5) with frequencies $\pm\pi/2K$ contains more than 95 % of the energy of cnoidal wave.

In accordance with the two harmonics approximation we write the field in the following way:

$$q(\eta,\xi) = a_l(\xi)\exp(-i\omega\eta) + a_h(\xi)\exp(i\omega\eta). \tag{6}$$

Here $a_l(\xi)$ and $a_h(\xi)$ are the complex amplitudes of the harmonics and $\omega=\pi/2K$ is the frequency. We assume that at the entrance of the nonlinear medium both harmonics have equal positive and real amplitudes. In the propagation process the energy transfers directly from the higher a_h to the lower a_l harmonic leading to the self-bending of the cn-wave. Of course, the energy from both a_l and a_h transfers into the harmonics with higher frequencies $|\omega|=n\pi/2K$ (where $n\geq 2$). However, the rate of this process strongly depends on the amplitudes of harmonics with higher frequencies and on the initial stage of propagation (up to ten dispersion lengths for the given value of the parameter μ) is rather small that enables one to consider only two harmonics approximation.

Substituting the expression (6) into the shortened wave equation (1) and equating terms with the same frequencies we obtain the following system of two coupled differential equations for the amplitudes of the harmonics:

$$\begin{aligned} i\frac{da_l}{d\xi} &= \frac{1}{2}\omega^2 a_l - a_l\left(|a_l|^2+2|a_h|^2\right)+2i\mu\omega a_l|a_h|^2,\\ i\frac{da_h}{d\xi} &= \frac{1}{2}\omega^2 a_h - a_h\left(|a_h|^2+2|a_l|^2\right)-2i\mu\omega a_h|a_l|^2. \end{aligned} \tag{7}$$

Using the set of Equations (7) one can be convinced of the wave energy conservation $|a_l|^2 + |a_h|^2 = w_0$ (where w_0 is the energy flux). The complex amplitudes of the harmonics can then be presented in the following form: $a_l = |a_l|\exp(i\varphi_l)$ and $a_h = |a_h|\exp(i\varphi_h)$. If we substitute these expressions into Equations (7) and derive real and imaginary parts, we obtain the system of four coupled equations for the real amplitudes and phases of two harmonics. This system can be easily solved and its solution has the following form:

$$|a_l| = \left(\frac{w_0}{1+\exp(-4\mu\omega w_0\xi)}\right)^{1/2}, \qquad |a_h| = \left(\frac{w_0}{1+\exp(4\mu\omega w_0\xi)}\right)^{1/2},$$
$$\varphi = \frac{1}{2\mu\omega}\ln[\cosh(2\mu\omega w_0\xi)]. \tag{8}$$

Here we present formula only for the phase difference $\varphi = \varphi_h - \varphi_l$ between the two harmonics because one can clearly see from the expression for the pulse power

$$qq^* = |a_l|^2 + |a_h|^2 + 2|a_l||a_h|\cos(\varphi + 2\omega\eta), \tag{9}$$

that the trajectory of the local maximum of the cnoidal wave is given by the equation $\varphi + 2\omega\eta = 0$. One should take into account that in the propagation process the shape of the initially symmetric cn-wave is slightly changed due to the inertial component of the optical fibre nonlinear response. It means that the trajectory of the stationary (asymmetric due to the inertial response component) wave slightly differs from the trajectory of the initially unperturbed symmetric wave that we consider. Nevertheless, this difference is of the order of μ (~10 %) and does not affect really on the applicability of the obtained results in practice. We have already mentioned that the two harmonics approximation is valid at the initial stage of wave propagation when $\mu\omega w_0\xi << 1$. This fact enables one to expand the right part of the last expression in the set (8) in the power series on the small parameter μ and obtain that the cn-wave propagates along the parabolic trajectory

$$\eta = \frac{1}{2}a_{par}\xi^2 = \frac{1}{2}\mu w_0{}^2\xi^2, \tag{10}$$

where the parabolic self-bending coefficient a_{par} is proportional to the parameter μ (one can clearly see this trajectory on the Figure 2a, which presents the result of the numerical simulation of the cn-wave propagation by the split-step Fourier method).

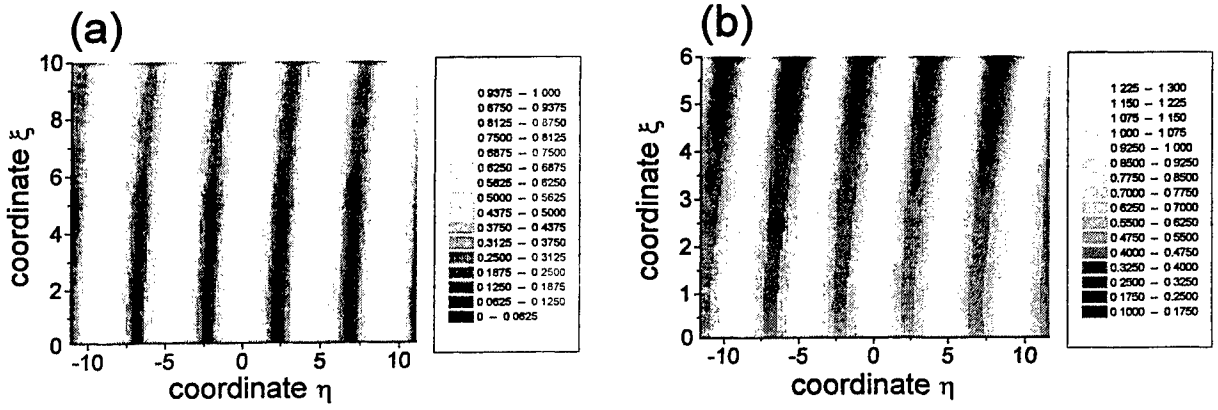


Figure 2. Propagation dynamic of the cn-wave (a) and dn-wave (b) in the optical fibre with inertial component of nonlinear response for the case of localisation parameter m=0.9 (parameter μ=0.1).

Using the expansion (5), one can obtain the parabolic coefficient as a function of the localisation parameter m:

$$a_{par} = 4\mu \frac{\pi^4 g^2(m)}{K^4(m)[1+g(m)]^4}, \tag{11}$$

where $g(m)$ is the Jacobi parameter and $K(m)$ is the elliptical integral. This dependence is presented on Figure 3 by curve

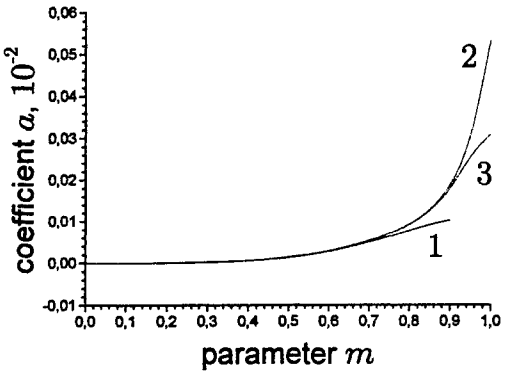


Figure 3. Self-bending coefficient versus localisation parameter m for the case of cn-wave: results obtained with the aid of two harmonics approximation (1); results of the numerical integration by split-step Fourier method (2); results obtained with the aid of four harmonic approximation (3). Parameter μ=0.1.

1. Note that the last formula is valid only for the values of the localisation parameter m from 0 to approximately 0.8. Curve 2 on Figure 3 shows the results obtained with the numerical simulation of wave propagation by the split-step Fourier method. One can see that within the range of validity of the last formula the curve 1 demonstrates good correspondence with numerical results presented by curve 2. Curve 3 shows the dependence of the self-bending coefficient on the parameter m obtained with the aid of numerical integration of the set of energy transfer equations (analogous to 7) written already for the four harmonics. Note the rather well coincidence of this result with the results obtained by the split-step Fourier method. One can see from the figure 3 that in fact the cn-wave practically does not experience considerable self-bending up to $m = 0.5$ because of small influence of nonlinear terms on the propagation dynamics. For the larger values of the localisation parameter self-bending coefficient quickly increases and at $m = 1$ reaches its maximal value of (8/15)μ (for analytical results for the strong localisation limit see Section 5). In the spectral domain this means that the speed of the energy transfer from the higher to the lower harmonic (which determine the strength of the self-bending effect) strictly depends on the harmonic amplitude and greatly increases as harmonic amplitude grows up when $m \to 1$.

4. SELF-BENDING OF THE DN-WAVE

To investigate the self-bending of the dn-wave we use the finite number harmonic approximation analogously to the previous section. The case of dn-wave, however, is more complicated for the analytical treatment. The spectrum of the dn-wave consists at least of three harmonics: one is the most powerful with zero frequency represents the wave of the constant amplitude, and two sideband harmonics have the smaller amplitudes and frequencies $\omega = \pm\pi / K$. This is clearly seen from the expansion analogous to that used for the cn-wave:

$$\mathrm{dn}(\eta, m) = \frac{\pi}{2K} + \frac{2\pi}{K}\sum_{n=1}^{\infty} \frac{g^n}{1+g^{2n}} \cos\frac{n\pi\eta}{K}. \tag{12}$$

This expansion is once again valid for the values of the localisation parameter from 0 to approximately 0.8 (with the 95 % energy criterion).

The other circumstance making the problem more complicated is that the finite number harmonic approximation is valid for the dn-wave at distances which is smaller than that for the cn-wave. This is due to that the dn-wave becomes unstable in the optical fibre with inertial component of the nonlinear response (the zero frequency harmonic quickly transfers their energy into the lower frequency sidebands resulting in the breaking of the cnoidal wave to the set of comparatively localised pulses. One can clearly see this process on the Figure 2b, which presents the result of the numerical simulation of the dn-wave propagation by the split-step Fourier method. Nevertheless the finite number harmonic approximation remains valid up to the 4-6 dispersion lengths. So, we write the field in the following manner:

$$q(\eta,\xi) = a_l(\xi)\exp(-i\omega\eta) + a_0(\xi) + a_h(\xi)\exp(i\omega\eta). \tag{13}$$

Here $a_l(\xi)$, $a_0(\xi)$ and $a_h(\xi)$ are the complex amplitudes of the lower, zero and higher harmonics, correspondingly, and $\omega = \pi / K$ is the frequency. At the input plane of the nonlinear medium both lower and higher harmonics have equal positive and purely real amplitudes. Substituting expansion (13) into the shortened wave equation (1) and equating terms with the same frequencies we obtain the following system of three coupled complex equations:

$$\begin{aligned}
i\frac{da_l}{d\xi} &= \frac{1}{2}\omega^2 a_l - a_l\left(2w_0 - |a_l|^2\right) - {a_0}^2 a_h^* + i\mu\omega\left(a_l|a_0|^2 + {a_0}^2 a_h^* + 2a_l|a_h|^2\right),\\
i\frac{da_0}{d\xi} &= -a_0\left(2w_0 - |a_0|^2\right) - 2a_l a_h a_0^* - i\mu\omega\left(a_0|a_l|^2 - a_0|a_h|^2\right),\\
i\frac{da_h}{d\xi} &= \frac{1}{2}\omega^2 a_h - a_h\left(2w_0 - |a_h|^2\right) - {a_0}^2 a_l^* - i\mu\omega\left(a_h|a_0|^2 + {a_0}^2 a_l^* + 2a_h|a_l|^2\right).
\end{aligned} \tag{14}$$

Here we introduce the wave energy $w_0 = |a_l|^2 + |a_0|^2 + |a_h|^2$. Now the energy exchange between harmonics is more complicated then that for the case of the cn-wave. The lower harmonic receives the energy from both higher and zero harmonics (in fact the energy exchange between lower and zero harmonic is much intensive then that between higher and lower harmonic because of large amplitude of the zero harmonic). The zero-frequency harmonic transfers energy to the lower harmonic and receives the energy from the higher harmonic. Nevertheless, this picture can be significantly simplified if one use the results of the numerical integration of the system (14) that shows that at the initial stage of propagation (up to the dispersion length) the amplitude of the zero harmonic practically does not change in comparison with the amplitudes of the lower and higher harmonics. In this case the zero harmonic in fact determines the speed of the energy exchange between sideband harmonics. Thus, using the approximation of the constant pump we can in fact transform the three harmonics problem to the previous case of the two harmonics. Introducing the real amplitudes and phases of harmonics we obtain that they changes at the initial stage of propagation accordingly to the following laws:

$$\begin{aligned}
&|a_l(\xi)| \approx |a_l(0)|\left(1 + 2\mu\omega|a_0|^2\xi\right), \quad a_0 \approx \text{const}, \quad |a_h(\xi)| \approx |a_h(0)|\left(1 - 2\mu\omega|a_0|^2\xi\right),\\
&\varphi_0 - \varphi_l \approx \varphi_h - \varphi_0 \approx 2\mu\omega|a_0|^4\xi^2.
\end{aligned} \tag{15}$$

Here we once again present results only for the phase differences because the trajectory of motion of the local maximum of the dn-wave is described by the equation $\omega\eta + \varphi_0 - \varphi_l = 0$. Finally we obtain that at the initial stage of propagation the dn-wave propagates along the parabolic trajectory with the parabolic coefficient

$$a_{\text{par}} = 4\mu|a_0|^4. \tag{16}$$

One can use the expansion (12) to obtain the dependence of the parabolic coefficient on the localisation parameter m ranges from 0 to 0.8 (see curve 1 on Figure 4):

$$a_{par} = \mu \frac{\pi^4}{4K^4(m)}, \tag{17}$$

where $K(m)$ is the elliptical integral. Curve 2 on Figure 4 presents the results obtained with the help of the numerical simulation of dn-wave propagation dynamic by the split-step Fourier method. Curve 3 presents the results obtained by the direct numerical integration of the energy transfer equations for the extended case of five harmonics of the dn-wave. One can see that in the case of dn-wave the finite number harmonic approximation works better then for the cn-wave. The surprising feature of the self-bending of the dn-wave is that parabolic coefficient reaches it maximum value for the close to zero localisation parameter m. This is a consequence of the fact that the self-bending effect strength (i.e. the intense of the energy exchange between two sideband harmonics) in the case of dn-wave is determined only by the zero harmonic amplitude which growth as m goes to zero. With increase of the degree of localisation of the cnoidal wave the self-bending coefficient decreases (see curve 2 on Figure4) and reaches the value (8/15)μ at m=1.

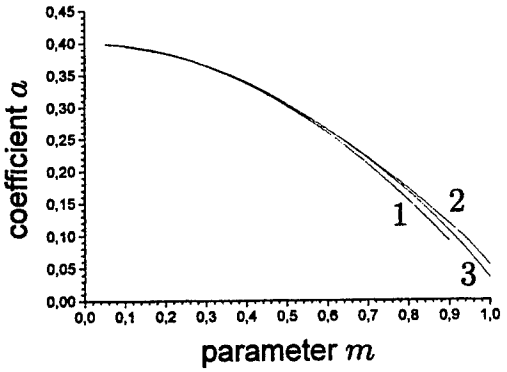


Figure 4. Self-bending coefficient versus localisation parameter m for the case of dn-wave: results obtained with the aid of three harmonic approximation (1); results of the numerical integration by split-step Fourier method (2); results obtained with the aid of five harmonic approximation (3). Parameter μ=0.1.

5. THE METHOD OF THE EFFECTIVE PARTICLES

In the two previous sections we have discussed the self-bending of the cnoidal waves on the basis of the finite number harmonic approximation. As have been mentioned above this method enables one to obtain parabolic coefficient a_{par} only for the localisation parameter m ranges from 0 to 0.8. Nevertheless, for the case of the strong localisation, when $m = 1$ and both cn- and dn-waves transform into the hyperbolic secant type solution, one can obtain the trajectory using so-called method of the effective particles. This method is very frequently used in quantum mechanics and enables one to obtain trajectories of particle motion in different potentials if the evolution of the localised particle wave function is governed by the Equation of the type (1) (perturbed NLSE). With this method one can obtain that the pulse trajectory (conditions $q(\eta \to \pm\infty, \xi) = 0$ and $\partial q(\eta \to \pm\infty, \xi)/\partial\eta = 0$ are necessary) in the medium with inertial component of nonlinear response is described by:

$$w_0 \frac{d^2}{d\xi^2} \eta_c(\xi) = \mu \int_{-\infty}^{\infty} \left(\frac{\partial |q|^2}{\partial \eta} \right)^2 d\eta. \tag{18}$$

Here we introduce the pulse power $w_0 = \int_{-\infty}^{\infty} qq^* d\eta$ and the pulse centre coordinate

$$\eta_c(\xi) = \int_{-\infty}^{\infty} q^* \eta q d\eta \Big/ \int_{-\infty}^{\infty} q^* q d\eta. \tag{19}$$

One can see from the Equation (18) that optical pulse propagates along the parabolic trajectory provided that the pulse profile remains unperturbed. The parabolic coefficient depends on the pulse shape, and for the hyperbolic secant type solution is given by $a_{par} = 8\mu/15$. As one can see from the curves 2 on the Figures 3 and 4 this result is confirmed by results of numerical simulation by split-step Fourier method. Unfortunately, the generalisation of the method of the effective particles to the case of periodical cnoidal waves (low localisation) is complicated by the certain difficulties arising due to the boundary conditions.

6. CONCLUSION

Summarising, we considered the influence of the inertial component of the optical fibre response on the cnoidal waves propagation dynamic using the approximate analytical treatment and computer simulation. We analysed the dependence of the self-bending parameter on the degree of the localisation of the wave energy. Both analytically and numerically calculated dependencies of the self-bending parabolic coefficient on the localisation parameter m have been presented. It was shown that the self-bending coefficient for the cn-wave increases with growth of localisation parameter m. In the frames of the finite number harmonic approximation we obtained that in the case of the dn-wave the self-bending coefficient monotonically decreases as parameter m goes to unity.

REFERENCES

1. V. Zakharov, S. Manakov, S. Novikov and A. Pitayevskii, *Soliton Theory – Inverse Scattering Method* (Nauka, Moscow, 1980 [in Russian]).
2. V.M. Petnikova, V.V. Shuvalov, and V.A. Vysloukh, *Phys. Rev. E* 60, p. 1009, 1999.
3. V. Kutuzov, V. M. Petnikova, V. V. Shuvalov and V. A. Vysloukh, *Phys. Rev. E* 57, p. 6056, 1998.
4. D. Iturbe Castillo, M. Torres Cisneros, J. Sanchez Mondragon, S. Chavez Cerda, S. Stepanov and V. Vysloukh, *Optics Lett.* 20, p. 1853, 1995.
5. M. Mendez Otero, S. Chaves Serda, M. Iturbe Castillo and V. Vysloukh, *CLEO/QELS'99*, Baltimore, USA; Advance program, p. 113, Paper QWD13, 1999.
6. M. Iturbe Castillo, P. Marquez Aguilar, J. Sanchez Mondragon, S. Stepanov and V. Vysloukh, *Appl. Phys. Lett.* 64, p. 408 1994.
7. D. Christodoulidies and M. Carvalho, *J. Opt. Soc. Am. B* 12, p. 1628, 1995.
8. J. Feinberg, *J. Opt. Soc. Am.* 72, p. 46 (1982).
9. D. Christodoulidies and M. Carvalho, *Optics Lett.* 19, p. 1714, 1994.
10. W. Krolikowski, N.N. Akhmediev, B. Luther-Davies, and M. Cronin-Golomb, *Phys. Rev. E* 54 (1996) 5761.
11. F. Mitschke and L. Mollenauer, *Optics Lett.* 11, p. 659, 1986.
12. J. Gordon, *Optics Lett.* 11, p. 66, 1986.
13. Y. Kodama and K. Nozaki, *Optics Lett.* 12, p. 1038, 1987.
14. Y. Kodama and A. Hasegawa, *IEEE J. Quantum Electron.* QE-23, p. 510, 1987.
15. N.N. Akhmediev, W. Krolikowski, and A.J. Lowery, *Opt. Commun.* 131, p. 260, 1996.
16. D. Pathria, and J.LI. Morris, *Physika Scripta*, 39, p. 673, 1989.
17. Gedalin, T.C. Scott M, and Y.B. Band, *Phys. Rev. Lett.* 78, p. 448, 1997.

Formation and propagation of the localized surface waves at the interface between the linear dielectric and photorefractive medium

Victor Aleshkevich[a], Victor Vysloukh[b] and Yaroslav Kartashov[a*]

[a]Chair of General Physics, Physics Department, M. V. Lomonosov Moscow State University, 119899 Moscow, Russia
[b]CIICAp, UAEM, Cuernavaca, Mor., Mexico

ABSTRACT

We consider the propagation of the laser beam near the interface between the linear dielectric and photorefractive medium with drift and diffusion nonlinearity. We demonstrated the possibility of the surface waves formation, found the profiles of such surface modes and investigated waveguiding properties of the dielectric – photorefractive medium boundary. The effective particle theory was used to derive an ordinary differential equation that describes the beam center trajectory during the reflection from the interface.

Keywords: spatial solitons, photorefractive medium, nonlocal nonlinear response, surface waves

1. INTRODUCTION

The laser beam propagation at the interface between two media that exhibit different optical properties has been always an attractive problem from both physical and practical point of view. Among the variety of such several optical materials combined structures, the special cases of nonlinear optical interfaces (when at least one of the media exhibits some kind of optical nonlinearity) give rise to a number of interesting phenomena such as laser beam filamentation, near-boundary fanning, surface wave formation, etc. The characteristic features of laser beam interaction with boundary and, for instance, the surface wave formation are defined by the specific properties of the nonlinear media forming the interface, i.e. by the exact nonlinearity laws. The cases of Kerr-type materials (including the linear-nonlinear[1,2] and the nonlinear-nonlinear[3] interfaces), quadratic nonlinerity[4], and Kerr-type – saturable absorber boundary[5] have already been considered. Investigation of the surface waves at the interface between materials with more complicated nonlinearities seems to be of great importance for the practical purposes. The considerable achievements[6,7] in the spatial soliton excitation in the photorefractive crystals (PRC) performing very strong nonlinearity, give rise to the further activity in the area of the investigation of surface waves formation conditions.

Recently the possibility of propagation of the nonlinear surface waves near the boundary of PRC with diffusion nonlinearity and linear medium (dielectric or metal) was considered[8], and it was shown, that this type of optical nonlinearity ensures light propagation in the narrow layer near the surface of the sample. These nonlinear waves are formed because of the interference between the two waves reflecting into each other from the boundary of the sample and from the Bragg-type grating formed in the sample volume. Later[9,10] a similar near-surface propagation of the laser beam was interpreted as a result of the interplay between the boundary reflection and self-bending effects[11] arising due to the nonlocal diffusion component of the PRC nonlinear response. Perhaps, the most attractive feature of the near-boundary laser beam propagation is that the concentration of beam energy in the narrow surface layer significantly increases the operation speed of the photorefractive devices without the need for specially prefabricated waveguiding structures[12,13]. The use of the interplay between the boundary reflection and self-bending effects enables one to construct waveguiding structures that are able to play a role of logical gates and light-by-light operating devices.

In spite of the big number of publications devoted to the photorefractive surface waves this problem calls for the further consideration. In fact, the authors of the earlier works[8-10] investigated surface waves for the specific logarithm-type nonlinearity which for the case of rather small dark conductivity of the PRC sample enables one to obtain the linearised equations for the wave envelope. In the present work, we consider the laser beam – boundary interaction and surface waves formation at the interface between the linear dielectric and typical PRC with comparatively high dark conductivity. Both drift and diffusion component of the PRC nonlinear response are taken into account (this means we take into account an additional contribution to the refractive index which is proportional to the derivative of the light intensity and accounts for the self-bending effects[14]). We apply both analytical approach based on

Laser Optics 2000: Control of Laser Beam Characteristics and Nonlinear Methods for Wavefront Control, Leonid N. Soms, Vladimir E. Sherstobitov, Editors, Proceedings of SPIE Vol. 4353 (2001)
© 2001 SPIE · 0277-786X/01/$15.00

the well known in the classical mechanics method of the effective particles (for details of the method see for example reference[3]) and numerical simulation based on the shooting and beam propagation methods.

2. THEORETICAL MODEL

We consider the propagation of the linearly polarized slit beam (transverse extent of the beam in the y-direction greatly exceeds that in the x-direction) near the interface of the linear dielectric and nonlinear photorefractive medium. To describe optical response of a photorefractive medium in such two-dimensional case we use the standard set of scalar material equations in the form suggested by Kuhtarev and Vinetskii[15] without taking into account the photovoltaic effect:

$$\begin{aligned}
\frac{\partial n_e}{\partial t} &= \frac{\partial n_d^+}{\partial t} - \frac{1}{e}\frac{\partial j}{\partial x}, \\
\frac{\partial n_d^+}{\partial t} &= s(I + I_{dark})(n_d - n_d^+) - \gamma_r n_e n_d^+, \\
j &= e\mu n_e(E_0 + E_{sc}) - \mu\theta\frac{\partial n_e}{\partial x}, \\
\frac{\partial E_{sc}}{\partial x} &= \frac{4\pi e}{\varepsilon}(n_e + n_a - n_d^+).
\end{aligned} \tag{1}$$

Here $E_{sc}(x,z,t)$ is the internal space-charge electric field; n_e, n_d, n_d^+ and n_a are the concentrations of free carriers, donors, ionized donors and acceptors correspondingly; s is the cross-section of the photoionization; $I(z,t)$ is the radiation intensity; I_{dark} describes the dark conductivity of PRC; γ_r is the recombination rate coefficient; e and μ are the charge and mobility of free carriers (negative for the electrons and positive for the holes); ε is the static dielectric constant of PRC; θ is the temperature in energy units; E_0 is the static electric field applied to PRC in transverse x-direction (which means both drift and diffusion components of the current density j are taken into account). It is supposed that the optical radiation propagates along z-axis.

The set of material equations (1) is completed with the standard scalar shortened wave equation for the complex amplitude of the light field $A(x,z,t)$

$$i\frac{\partial A}{\partial z} = -\frac{1}{2k_0}\frac{\partial^2 A}{\partial x^2} - \frac{k_0}{n}\delta n A \tag{2}$$

written in the paraxial approximation. Here $k_0=\omega n/c$ is the wave number; $\delta n=(1/2)r_{eff}n^3E_{sc}(x,z,t)$ is the perturbation of the refractive index n; r_{eff} is the effective electrooptic coefficient. In (2) the spatially uniform component of n resulting from the static electric field E_0 is dropped out.

We solve the set of material equations (1) in a steady state approximation, that is for $\partial/\partial t\to 0$, $j=j(x)$. For the typical photorefractive crystals with rather large dark conductivity and a weak diffusion current, $n_a>>n_e$, $I<<I_{dark}$, $(\varepsilon/4\pi e n_a)(\partial E/\partial x)<<1$, one can reduce the set of material equations (1) to a single linear equation of the second order regarding E_{sc}

$$\frac{\partial^2 E_{sc}}{\partial x^2} - \frac{eE_0}{\theta}\frac{\partial E_{sc}}{\partial x} - \frac{eE_{sc}}{\theta a(\chi+1)} = \frac{1}{a(\chi+1)I_d}\left(\frac{eE_0}{\theta}I - \frac{\partial I}{\partial x}\right) \tag{3}$$

Here parameters $a=\varepsilon/4\pi e n_a$ and $\chi=n_a/(n_d-n_a)$. Solution of the equation (3) can be written[14,16] as the expansion on derivatives of the radiation intensity

$$E_{sc} = \frac{1}{aI_d(\chi+1)(\lambda_1-\lambda_2)}\sum_{m=0}^{\infty}\left(\frac{\lambda_1}{\lambda_2^{m+1}}-\frac{\lambda_2}{\lambda_1^{m+1}}\right)\frac{\partial^m I(x)}{\partial x^m} \tag{4}$$

where

$$\lambda_{1,2} = \frac{eE_0}{2\theta} \pm \left(\left(\frac{eE_0}{2\theta}\right)^2 + \frac{e}{a\theta(\chi+1)}\right)^{1/2}. \tag{5}$$

It should be noticed that in any real experiment with $E_0 \leq 10$ kV/cm and $\theta \sim 300$ K all terms in expression (4) with $m \geq 2$ will be important only when the spatial scale of the changing light field is less than the wavelength. So, in the expression (4) we can retain only two first terms that are proportional to $I(x)$ and $\partial I(x)/\partial x$. Further, these terms will be called the local and nonlocal components of the nonlinear response. Substitution of the internal space-charge field of the form (4) into the shortened wave equation (2) leads to the following nonlinear wave equation regarding normalized complex field amplitude q describing the propagation of the linearly polarized slit beam in the volume of PRC

$$i\frac{\partial q}{\partial \xi} = -\frac{1}{2}\frac{\partial^2 q}{\partial \eta^2} - |q|^2 q + \mu q \frac{\partial}{\partial \eta}|q|^2 \tag{6}$$

Here $\eta = x/x_0$ is the normalized transverse coordinate; x_0 is an arbitrary spatial scale; $\xi = z/L_{dif}$ is the normalized propagation distance; $L_{dif} = k_0 x_0^2$ is the diffraction length corresponding to x_0; $k_0 = n\omega/c$ is the wave number; n is the unperturbed refractive index; ω is the light frequency; $q(\eta,\xi) = A(\eta,\xi)(R_{dr}/I_{dark})^{1/2}$; nonlinear parameter $R_{dr} = L_{dif}/L_{ref}$; $L_{ref} = 2/(k_0 r_{eff} n^2 E_0)$ is the nonlinear refraction length. Parameter

$$\mu = \frac{k_0^2 n^2 r_{eff} E_0 x_0}{2R_{dr}}\left(\frac{\theta}{eE_0} + \frac{\varepsilon E_0 n_d}{4\pi e n_a (n_d - n_a)}\right) \tag{7}$$

describes the magnitude of the nonlocal component of PRC response. The sign of μ depends on the direction of the externally applied electric field E_0. The last term in the right side of equation (6) describes the self-bending effects resulting from the energy transfer from the low- to the high-frequency spatial component. The first term in the right part of equation (6) describes the diffraction spreading of the beam, the second one - its self-focusing due to the drift component of nonlinear response which is quasi-local in the two-dimensional case. Further throughout the paper we will use the typical for real experiments values of $\mu \sim 0.1$. Equations similar to equation (6) have been previously studied extensively within the context of self-bending effects[11,16,17] and nonlinear fiber optics, in which the term $\mu q(\partial I/\partial x)$ stood for the effects arising from intrapulse Raman scattering.

To describe the beam propagation near the interface between the linear dielectric and nonlinear photorefractive medium (PRC) with drift and diffusion nonlinearity we use composed (somewhat phenomenological) equation

$$i\frac{\partial q}{\partial \xi} = -\frac{1}{2}\frac{\partial^2 q}{\partial \eta^2} - S(\eta)q\left(p + |q|^2 - \mu\frac{\partial}{\partial \eta}|q|^2\right). \tag{8}$$

which is analogous to (6) and enables one to describe the beam propagation in both linear dielectric (situated at $\eta \in (0,+\infty)$) and nonlinear photorefractive medium (situated at $\eta \in (-\infty,0]$) with one shortened wave equation. This is due to the introduction of the artificial step-like function

$$S(\eta) = 1 \text{ for } \eta \in (-\infty,0],$$
$$S(\eta) = 0 \text{ for } \eta \in (0,+\infty). \tag{9}$$

In equation (8) propagation distance z normalized now to the diffraction length in the linear dielectric medium $L_{dif} = k_0 x_0^2$, where $k_0 = n_0\omega/c$ is the wave number; n_0 is the refraction index of the dielectric medium; nonlinear parameter changes to $R_{dr} = kL_{dif}/k_0 L_{ref}$; nonlinear refraction length changes to $L_{ref} = 2/(kr_{eff}n^2E_0)$; $k = n\omega/c$; n ($\geq n_0$) is the unperturbed refraction index of the PRC; parameter $p = x_0^2(k^2 - k_0^2)/2$ characterizes the boundary waveguiding

properties and is proportional to the difference between refractive indexes of the dielectric and photorefractive medium; parameter μ as earlier defined by expression (7). Now the first term in the round brackets in (8) characterizes the beam interaction with dielectric-PRC boundary. In the area of dielectric medium (where $S(\eta)=0$) equation (8) transforms into usual linear equation describing the free beam diffraction.

Equation (8) is written in the scalar approximation for the linearly polarized light beam. It was also derived on the basis of Kuhtarev-Vinetskii model by D. Christodoulides in low intensity limit (see equation (24) in reference[17]). Note that inclusion of the second principal orthogonal component of the optical field leads to the more complicated coupled set of evolution equations for the field components[18-20]. In such geometry new effects besides predicted by our model will certainly take place. For example additional polarization modulation appears due to the birefringence induced by the space-charge field or due to the optical activity of the PRC sample[21,22]. One should also note that the applicability of the equation (8) is restricted by the gradual development of modulation instability of the slit beam in the photorefractive medium with nonlocal component of nonlinear response[14].

For the positive values of μ and p and chosen disposition of the dielectric and PRC the light beam propagating in PRC far from the boundary self-bends toward the boundary due to the diffusion component of the nonlinear response (to describe the typical regimes of the beam propagation near the boundary we use direct integration of equation (8) by the beam propagation method with initial condition $q(\eta,\xi=0)=\mathrm{sech}(\eta-\eta_c)$ and set $p=1.0$ and $\mu=0.1$). As the beam approaches the dielectric-PRC boundary it will experience boundary influence which finally can result (if the incidence angle exceeds the total internal reflection angle) in the total internal beam reflection from the less optical dense dielectric medium (see Fig. 1a).

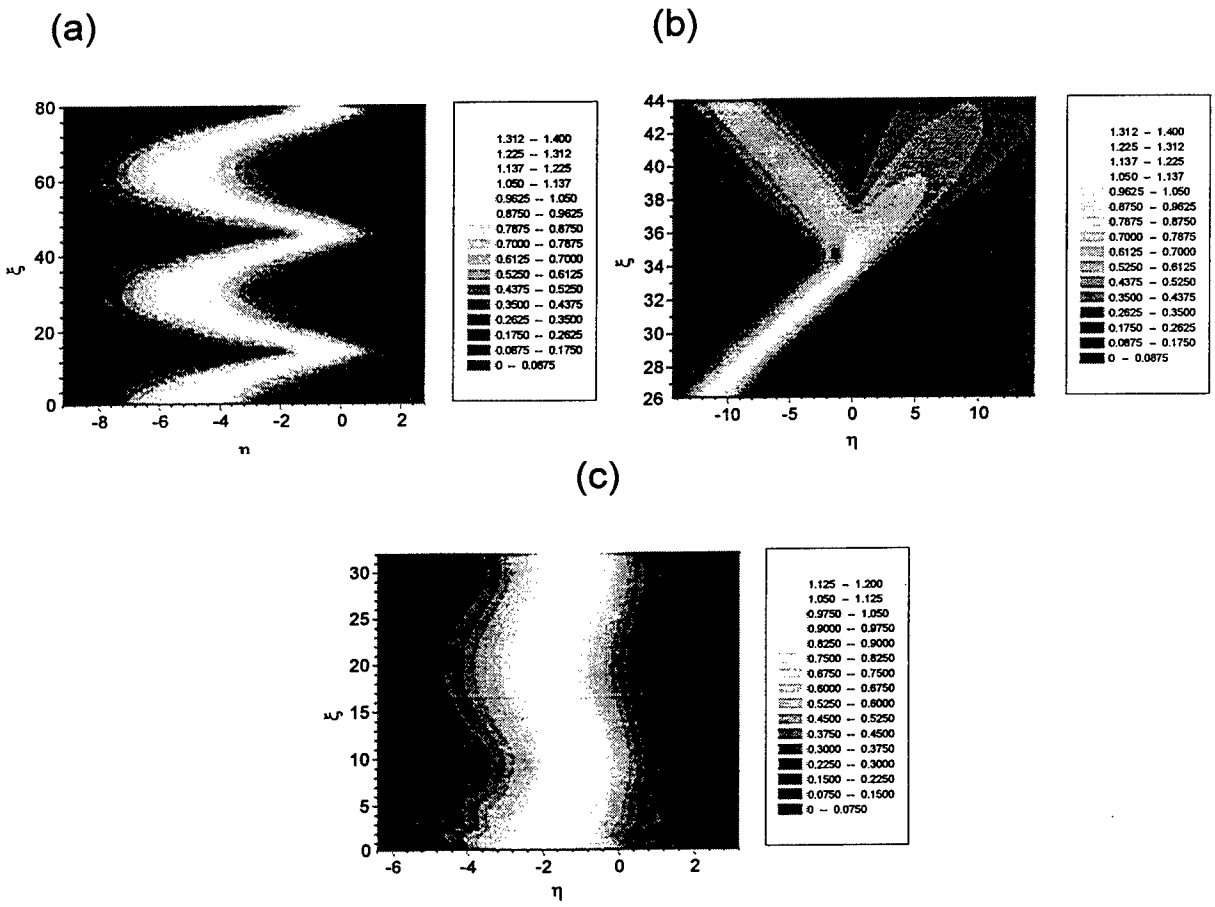


Figure 1. Interaction of the hyperbolic secant type profile beam with the dielectric-PRC boundary for the case of $\mu=0.1$, guiding parameter $p=1.0$, zero incidence angle and refractive index profile width $\eta_0=0.05$. Launching distance is $\eta_{in}=-5.0$ (a); -28.0 (b); -1.81 (c). The boundary between dielectric and PRC situated at $\eta=0$. The numerical gray scale values present the beam intensity in different points.

After reflection the light beam returns to the boundary because of influence of the diffusion component in the PRC nonlinear response thus resulting in the periodical near-boundary oscillations. If the incidence angle is less then the total internal reflection angle the beam can be refracted into the dielectric medium and after this experience diffraction spreading (Fig. 1b). The other propagation regime occurs when the laser beam launched too close to the boundary, and reflection overcomes the self-bending effects. In this case the beam initially goes away from the boundary to the certain distance determined by the initial launching point and after this returns to the boundary. Nevertheless, if the light beam launched close enough to the dielectric medium the self-bending effect and repulsion from the boundary can be exactly balanced resulting in the stationary surface wave formation (Fig. 1c). Further we perform the simple analysis of the beam reflection from the dielectric-PRC boundary and surface waves properties based on the analogies between the optical solitons (in Kerr materials) and mechanical particles[3].

3. BEAM REFLECTIION FROM THE BOUNDARY AND SURFACE WAVES FORMATION

The point of the stationary beam launching that corresponds to the surface wave formation can be easily found with the aid of methods of usual mechanics because of the direct analogy between soliton-like objects propagating in nonlinear materials and particles situated in the field with definite potential (thus, the stationary beam launching point corresponds to the point of the local minimum of the potential energy). In this section we consider the dynamic of the near-boundary beam propagation and surface wave formation processes with using of the so-called method of the effective particles. This method is very frequently used in quantum mechanics and enables one to obtain trajectories of particle motion in different potentials if the evolution of the localized particle wave function is governed by the equation of the type (8) (perturbed nonlinear Shrödinger equation). The used mathematical procedure is in fact analogous to the very powerful perturbation theory based on the inverse scattering transform technique that enables to obtain the changes of the parameters of the sech type soliton solution of the unperturbed Shrödinger equation due to the influence of the higher order terms. The method is applicable for the localized laser beams with $q(\eta\to\pm\infty,\xi)=0$ and $\partial q(\eta\to\pm\infty,\xi)/\partial\eta=0$). To obtain the equation for the beam center trajectory we multiply equation (8) by ηq^* (here sign * denotes complex conjugation). Integrating over η from $-\infty$ to ∞ and subtracting from the obtained expression its complex conjugate we obtain (taking into account that the beam is localized) that

$$iw_0 \frac{d}{d\xi}\eta_c(\xi) = \frac{1}{2}\int_{-\infty}^{\infty}\left(q^*\frac{\partial q}{\partial \eta} - q\frac{\partial q^*}{\partial \eta}\right)d\eta. \tag{10}$$

Here we introduce the beam power $w_0 = \int_{-\infty}^{\infty} qq^*\,d\eta$ and the beam center coordinate

$$\eta_c(\xi) = \int_{-\infty}^{\infty} q^*\eta q\,d\eta \Big/ \int_{-\infty}^{\infty} q^* q\,d\eta. \tag{11}$$

Differentiating (10) over ξ and performing integration over η we obtain

$$iw_0 \frac{d^2}{d\xi^2}\eta_c(\xi) = \int_{-\infty}^{\infty}\left(\frac{\partial q^*}{\partial \xi}\frac{\partial q}{\partial \eta} - \frac{\partial q}{\partial \xi}\frac{\partial q^*}{\partial \eta}\right)d\eta. \tag{12}$$

Finally, substituting in (12) expressions for $\partial q/\partial\xi$ and $\partial q^*/\partial\xi$ from the shortened wave equation (8) after easy calculations we obtain that the beam trajectory near the dielectric-PRC boundary is described by:

$$w_0 \frac{d^2}{d\xi^2}\eta_c(\xi) = \int_{-\infty}^{\infty}\left(p\frac{\partial S}{\partial \eta}|q|^2 + \frac{1}{2}\frac{\partial S}{\partial \eta}|q|^4 + \mu S\left(\frac{\partial |q|^2}{\partial \eta}\right)^2\right)d\eta. \tag{13}$$

The first term under the integral sign in Equation (13) describes the influence of the repulsion from the dielectric-PRC boundary on the beam trajectory. Second term describes specific beam self-action in the presence of the guiding surface and the third one characterizes self-bending effects. As beam goes away from the boundary into the volume of the PRC sample (i.e. when $\eta \to -\infty$), the influence of the boundary on the beam trajectory disappears and Equation (13) transforms into that describing self-bending of the localized beam in the PRC with nonlocal diffusion component in nonlinear response. Further, within the frames of the method of the effective particles, we assume that the self-bending and repulsion from the boundary do not strongly affect the stationary beam shape (this assumption is valid even when the laser beam reflects from the boundary at the angle close to the total internal reflection angle). This means to obtain the approximate beam center trajectory one can substitute into the integral in the right part of Equation (13) an approximate expression for $q(\eta,\xi)$ in the form of hyperbolic secant type solution $|q(\eta,\xi)| = \chi \operatorname{sech}[\chi(\eta-\eta_c(\xi))]$ (where χ is the form-factor), which is the solution of the standard unperturbed Shrödinger equation. We also approximate step-like function describing the properties of the dielectric-PRC boundary by function

$$S(\eta) = [1 - \tanh(\eta/\eta_0)]/2, \tag{14}$$

where the small parameter η_0 (hereafter we use the value η_0=0.05) describes the width of the transition area between dielectric and PRC (this approximation is convenient for the numerical simulation and accounts for the fact that the real boundaries are always smooth). This approximation enables one to use the following expression for the derivative of the step-like function:

$$(\partial S/\partial \eta)\big|_{\eta_0 \to 0} = -\delta(\eta), \tag{15}$$

where $\delta(\eta)$ is the Dirac delta-function.

Substituting the hyperbolic secant type approximation for the beam shape into the integral in Equation (13) and taking into account the expressions for S and $\partial S/\partial \eta$, one can readily obtain that the trajectory of the localized beam with hyperbolic secant shape near dielectric-PRC boundary is described by:

$$\frac{\partial^2 \eta_c}{\partial \xi^2} = -\frac{1}{2} p\chi \operatorname{sech}^2(\chi\eta_c) - \frac{1}{4}\chi^3 \operatorname{sech}^4(\chi\eta_c) + \frac{4}{15}\mu\chi^4 + \frac{2}{5}\mu\chi^4(\operatorname{sech}^4(\chi\eta_c) - 1)\tanh(\chi\eta_c) + \frac{2}{15}\mu\chi^4 \tanh^3(\chi\eta_c). \tag{16}$$

As it was already mentioned, when $\eta_c \to -\infty$ (that means the beam goes away from the dielectric-PRC boundary into the volume of PRC) the last equation transforms into that describing the beam self-bending along the parabolic trajectory in the volume of PRC:

$$\frac{d^2 \eta_c}{d\xi^2} = \frac{8}{15}\mu\chi^4. \tag{17}$$

Equation (16) is analogous to that describing the motion of the particle subjected to the influence of the certain force $f(\eta_c)$. Because of absence of the energy dissipation (mentioned above force does not include derivatives $d^m\eta_c/d\xi^m$ of any order m), for the qualitative analysis of the properties of the solutions of Equation (16) it is convenient to use the potential $U(\eta_c) = -\int f(\eta_c)d\eta_c$, which can be written in the following form:

$$U = -\frac{4}{15}\mu\chi^4\eta_c - \frac{1}{12}\chi^2 \tanh^3(\chi\eta_c) + \left(\frac{p}{2} + \frac{\chi^2}{4}\right)\tanh(\chi\eta_c) + \mu\chi^3\left(\frac{\tanh^2(\chi\eta_c) - 1}{15} + \frac{\operatorname{sech}^4(\chi\eta_c)}{10} + \frac{4\ln(2\cosh(\chi\eta_c))}{15}\right) - \frac{p}{2} - \frac{\chi^2}{6}. \tag{18}$$

The constant terms in the right side of expression (18) appears due to the convenient normalization of the potential U to

the zero value as $\eta_c \to \infty$. Figure 2 shows the form of potential U for the different values of the guiding parameter p and values of parameter μ=0, 0.05 and 0.1 (hereafter form-factor χ chosen to be 1.0). One can see, that $U(\eta_c)$ has the form of the potential hole (so the finite type motions are possible) with the infinite height at $\eta_c \to -\infty$ and zero height at $\eta_c \to \infty$. The inclination angle of the right wing of the potential hole linearly increases with increase of the parameter μ (Fig. 2b). For the zero value of μ potential has the form of the step, so there are no finite types of motions available. The value of the guiding parameter p defines in fact the potential hole depth that increases with increase of p (Fig. 2a). According to the classical mechanics, the minimum of the potential corresponds to the steady equilibrium point, which is characterized by the exact balance between self-bending effects and repulsion from the dielectric-PRC boundary. For example for the values μ=0.1, p=1.0, χ=1.0 the equilibrium point situated at η_{in}=–1.81. Figure 1c shows the propagation dynamic of the beam with hyperbolic secant profile launched into the system at this point (we use here the shortened wave Equation (8) solved numerically by the beam propagation method). One can see that the beam only slightly oscillates in the transverse direction during the propagation process. These oscillations are mainly due to the transformation of the initial hyperbolic secant shape into the asymmetric surface wave profile. The trajectories of the beam propagation calculated for the different incident distances η_{in} with the differential equation (16) also show the good agreement with results obtained by the beam propagation method.

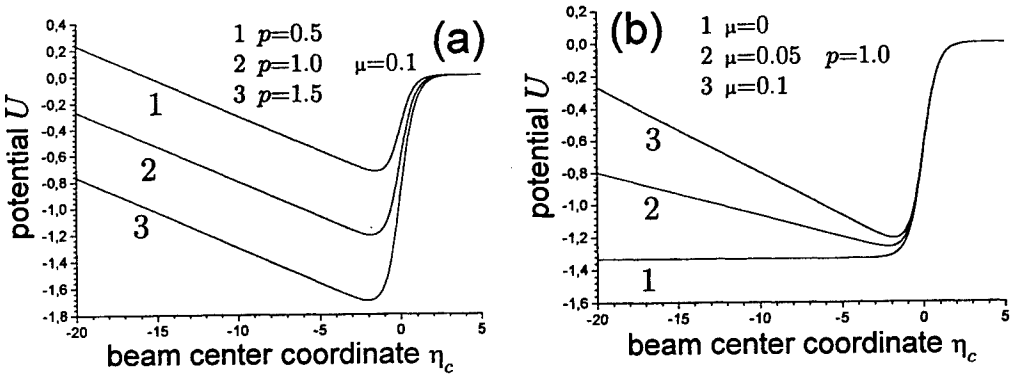


Figure 2. The form of the potential $U(\eta_c)$ for the different values of the guiding parameter p and parameter μ describing the strength of the self-bending effect. Refractive index profile width η_0=0.05. The boundary between dielectric and PRC situated at η=0.

Potential (18) enables one to obtain the critical launching distance η_{cr}. The optical beam being launched into the nonlinear PRC far enough from the boundary ($\eta_{in}<\eta_{cr}$) can refract into the linear dielectric. The critical launching distance can be found from the relation $U(\eta_{cr})$=0 that defines the boundary between the areas of the finite ($U(\eta_c)<0$) and infinite ($U(\eta_c)>0$) types of motions. Taking into account the fact that for the large negative values of η_c functions $\tanh(\chi\eta_c) \to -1$ and $\mathrm{sech}(\chi\eta_c) \to 0$ one can obtain that the critical distance is given by

$$\eta_{cr} = -\frac{15p + 5\chi^2}{8\mu\chi^4}. \tag{19}$$

The turning points corresponding to the finite motion (i.e. the penetration depth of the laser beam into the dielectric area or the minimal rapprochement distance with boundary) can be found graphically from the form of the potential U as is clearly seen from the first integral of Equation (16):

$$\left(\frac{d\eta_c}{d\xi}\right)^2 = 2U(\eta_{in}) - 2U(\eta_c), \tag{20}$$

where η_{in} is the launching point. The turning points correspond to the condition $d\eta_c/d\xi$=0, so, if one know η_{in}, the second turning point can be found from the relation $U(\eta_c)=U(\eta_{in})$. One can see from the Figure 2 that the right wing of the potential hole near the point η_c=0 can also be approximated by the linear function. This enables one to obtain the following relation between the positions of the left and right turning points lying at the linear sections of the potential U:

$$\left(\frac{1}{2}p\chi+\frac{1}{4}\chi^3-\frac{4}{15}\mu\chi^4\right)\eta_{\text{right}}=\left(\frac{3}{2}p+\frac{1}{2}\chi^2-\frac{1}{3}\mu\chi^3-\frac{4}{15}\chi^3\ln 2+\frac{8}{15}\mu\chi^4\eta_{\text{left}}\right). \tag{21}$$

The effective particles method works well for the localized beams with shape close to the first guided mode shape but can not give any information about profiles of the higher order modes, so, further it is necessary to apply methods based on the numerical integration of the shortened wave Equation (8).

4. STATIONARY SURFACE WAVES PROFILES

In this section, we consider the stationary surface wave profiles and wave-guiding properties of the dielectric-PRC boundary with the aid of the numerical integration. We search for the stationary solutions of the shortened wave Equation (8) in the standard steady-state form $q(\eta,\xi)=\varrho(\eta)\exp(ib\xi)$. After the substitution we have

$$\frac{d^2\varrho}{d\eta^2}=2b\varrho-2S(\eta)\varrho\left(p+\varrho^2-2\mu\varrho\frac{d\varrho}{d\eta}\right). \tag{22}$$

Equation (22) can be solved numerically by the shooting method taking into account the fact that in the area of the linear dielectric (where the step-like function $S(\eta)=0$) the initial values of function ϱ and its derivative $d\varrho/d\eta$ can be written in the following way:

$$\begin{aligned}\varrho(\eta>0)&=\exp[-(2b)^{1/2}\eta],\\ \frac{d\varrho(\eta>0)}{d\eta}&=-(2b)^{1/2}\exp[-(2b)^{1/2}\eta].\end{aligned} \tag{23}$$

During the numerical calculations, we vary the value of the propagation constant b with the aim to obtain the different field distributions. Note that the left asymptotic of the surface wave (where amplitude ρ is so small that the nonlinear terms can be neglected) is described by the formula $\varrho(\eta\to-\infty)\sim\exp[(2(b-p))^{1/2}\eta]$.

Figure 3 shows the profiles of the first three modes available at the dielectric-PRC boundary for the case of comparatively strong diffusion nonlinearity $\mu=0.2$ and a weak guiding $p=0.5$. The width of refractive index profile (η_0 in Equation (14)) practically does not affect on the shapes of the localized surface waves and as earlier, we set $\eta_0=0.05$. One can see from the Figure 3 that the wave profiles is sloped toward the dielectric-PRC boundary due to the influence of diffusion component in PRC nonlinear response. The wave amplitude decreases but the total wave power $P=\int\varrho^2(\eta)d\eta$ increases with increase of the surface mode number m.

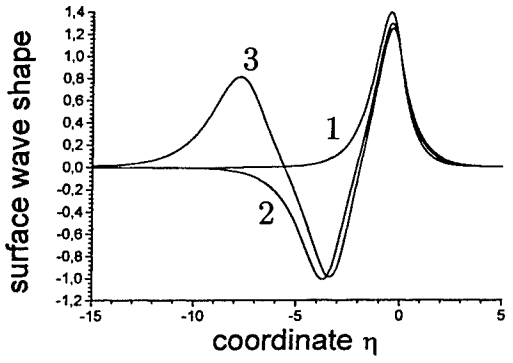


Figure 3. First three eigenmodes of the dielectric-PRC guiding surface for the case of $\mu=0.2$, guiding parameter $p=0.5$ and refractive index profile width $\eta_0=0.05$. Propagation constants used for the numerical integration is $b_1=1.202$, $b_2=0.904$, $b_3=0.775$. The boundary between dielectric and PRC situated at $\eta=0$.

As the strength of the diffusion effects increases (i.e. as μ growth) the amplitude and degree of the spatial localization of the surface waves increases. At the limit of the purely cubic nonlinearity (μ=0) there are no localized solutions exist and surface waves transform into the periodical half-infinite nonlinear waves. Note that the duration of the half-period of the surface wave increases in fact linearly from right to the left. Guiding parameter p practically does not affect the shape of the surface wave (it will be shown further that p strongly affects only the left wing of the wave) and in general determines the value of the propagation constant b. Equation (22) does not enable one to obtain an exact analytical expression for the wave shape. Nevertheless, with using of the variation approach one can write an approximate expression for the wave shape if find an appropriate trial function.

We considered the stability of the obtained surface modes using the technique of the dispersion diagrams[23]. It was proved that the total wave power $P(b)$ is a monotonically decreasing function of the propagation constant b provided that the surface waves in such a geometry are stable with respect to the small perturbations of the input profiles according to the stability criterion[24]. We also verify this assumption numerically with the aid of the beam propagation method and obtain that the surface waves are stable even with respect to the significant (up to 10% in intensity) harmonic and noise perturbations.

Now let us discuss briefly the waveguiding properties of the dielectric-PRC boundary. Figure 4 shows the dependence of the difference b-p between the propagation constant and guiding parameter on the value of guiding parameter p for the case of μ=0.2. One can see that there is no cut-off frequency for the higher-order modes. In fact, propagation constant b is practically linear function of the guiding parameter p. Increase of the guiding parameter results mainly in increasing difference of propagation constants for the modes of different orders and steeping of the left surface wave wing which is described by $\varrho(\eta\to-\infty)\sim\exp[(2(b-p))^{1/2}\eta]$. Figure 4 shows that the higher order modes group under the first order mode with increasing density. The difference between propagation constant b and guiding parameter p goes to zero as the mode order m goes to infinity.

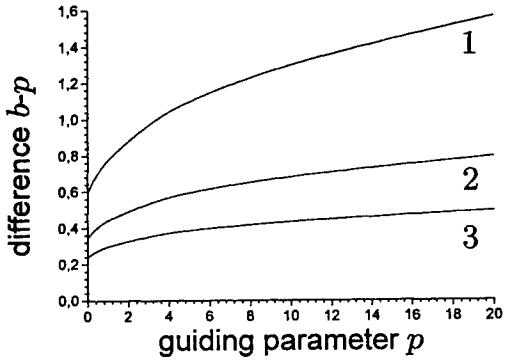


Figure 4. Difference b-p between the propagation constant and guiding parameter versus the value of guiding parameter p for the first three eigenmodes of the dielectric-PRC guiding surface. Parameter μ=0.2, refractive index profile width η_0=0.05.

Figure 5 shows the dependence of propagation constant b on the parameter μ describing the strength of diffusion component of PRC response for the case of guiding parameter p=0.5. One can see that for the available in the real experiment values of μ propagation constant ranges within rather wide frames. Note the infinite increase of b as parameter μ goes to zero. As was already mentioned, b defines the right wave asymptotic, so the increase of propagation constant corresponds to the decreasing of left wing value of ϱ. That means the surface waves goes away into the volume of PRC sample and in the limiting case μ=0 transforms into the periodical wave.

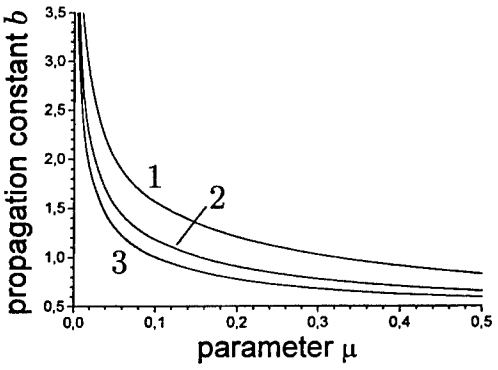


Figure 5. Propagation constant as a function of the parameter μ describing the strength of the self-bending effect for the first three eigenmodes of the dielectric-PRC guiding surface. Guiding parameter p=0.5, refractive index profile width η_0=0.05.

5. CONCLUSION

Summarizing, we have considered the interaction of the laser beam with the dielectric-PRC boundary and surface wave formation taking into account both drift and diffusion components of the PRC nonlinear response. Taking into account the particle-like properties of the optical solitons and using the method of the effective particles, we derive an ordinary differential equation (16) and potential (18) that describes the near-boundary beam trajectories and enables one to classify the possible types of motion. The waveguiding properties of the dielectric-PRC boundary were characterized and the eigenmode profiles were found with the aid of the numerical integration.

REFERENCES

1. W. Tomlinson, J. Gordon, P. Smith and A. Kaplan, *Appl. Optics* **21**, p. 2041, 1982.
2. P. Smith and W. Tomlinson, *IEEE J. Quantum Electron.* **QE-20**, p. 30, 1984.
3. A. Newell and J. Moloney, *Nonlinear Optics* (Addison-Wesley, Redwood City, 1992).
4. H. Tran, *Journal of Nonlinear Optical Physics & Materials* **5**, p. 133, 1996.
5. J. Powell, E. Wright and J. Moloney, J. Appl. Math. **54**, p. 774, 1994.
6. G. Duree, J. Shultz, G. Salamo, M. Segev, A. Yariv, B. Crosignani, P. Di Porto, E. Sharp and R. Neurgaonkar, *Phys. Rev. Lett.* **71**, p. 533, 1993.
7. M. Iturbe-Castillo, P. Marquez-Aguilar, J. Sanchez-Mondragon, S. Stepanov and V. Vysloukh, *Appl. Phys. Lett.* **64**, p. 408, 1994.
8. G. Garcia-Quirino, J. Sanchez-Mondragon and S. Stepanov, *Phys. Rev. A* **51**, p. 1571, 1995.
9. M. Cronin-Golomb, *Optics Lett.* **20**, p. 2075, 1995.
10. G. Garcia-Quirino, J. Sanchez-Mondragon, S. Stepanov and V. Vysloukh, *J. Opt. Soc. Am. B* **13**, p. 2530, 1996.
11. D. Christodoulides and T. Coskun, *Optics Lett.* **21**, p. 1220, 1996.
12. E. Raita, A. Kamshilin and T. Jaaskelainen, *J. Opt. Soc. Am. B* **15**, p. 2023, 1998.
13. A. Kamshilin, E. Raita and A. Khomenko, *J. Opt. Soc. Am. B* **13**, p. 2536, 1996.
14. V. Kutuzov, V. Petnikova, V, Shuvalov and V. Vysloukh, *Journal of Nonlinear Optical Physics & Materials* **6**, p. 421, 1997.
15. N. Kuhtarev, V. Markov and S. Odulov, *Ferroelectrics* **22**, p. 949, 1979.
16. V.Aleshkevich, V.Vysloukh and Y.Kartashov, *Optics Commun.* **173**, p. 277, 2000.
17. D.Christodoulides and M.Carvalho, *J. Opt. Soc. Am. B* **12**, p. 1628, 1995.
18. U. Hempelmann, *J. Opt. Soc. Am. B* **12**, p. 77, 1995.
19. M. Segev, G. Valley, S. Singh, M. Carvalho and D. Christodoulides, *Optics Lett.* **20**, p. 1764, 1995.
20. S. Singh and D. Christodoulides, *J. Opt. Soc. Am. B* **13**, p. 719, 1996.
21. C. Fuentes-Hernandez and A. Khomenko, *Phys. Rev. Lett.*, **83**, p. 1143, 1999.
22. A. Kamshilin, K. Paivasaari, A. Khomenko and C. Fuentes-Hernandez, *Optics Lett.* **24**, p. 832, 1999.
23. A. Snyder, D. Mitchell and Y. Kivshar, *Modern Physics Letters B* **9**, p. 1479, 1995.
24. D. Mitchell and A. Snyder, *J. Opt. Soc. Am. B* 10, p. 1572, 1993.

* Correspondence: e-mail: azesh@gateway.phys.msu.su; phone: (095) 939-34-38; fax: (095) 939-14-89

Nonfeedback nonresonant control of laser systems

A. N. Pisarchik
Centro de Investigaciones en Optica,
Loma del Bosque No. 115, Fracc. Lomas del Campestre,
37150 Leon, Guanajuato, Mexico

ABSTRACT

The control implies a slow small harmonic modulation with properly chosen frequency and amplitude to the available laser parameter, for example, to the loss, pumping, or cavity detuning. This type of the control results in exiting phenomena such as nonlinear parametric resonances, a shift of bifurcation points (period-doubling and saddle-node), deformation of boundaries of attractors and even their destruction.

Keywords: Nonlinear dynamics, Chaos, Parameter modulation

1. INTRODUCTION

Since the appearance of the work of Roy and his colleagues[1] in 1992 who demonstrated for the first time dynamical control based on the Ott-Grebogi-Yorke method[2] with Hunt's algorithm[3] in an autonomous chaotic multimode Nd:YAG laser, an active search for other methods of the control is being conducted. Most of the methods are based on the stabilization of unstable periodic orbits embedded within a chaotic attractor. Successful experiments on controlling dynamics in solid-state lasers,[1,4,5] CO_2 lasers,[6-10] and semiconductor lasers[11,12] have been realized by applying either *feedback* control algorithms[2,3,13] or by a periodic modulation to one of the system parameters at the appropriate frequency, what is known as *nonfeedback* control.[14-16] The methods of nonfeedback control do not require a prior knowledge of the system behavior and therefore, they are particularly appealing for systems whose state is impossible or difficult to measure in real time and where feedback control is very hard to realize. The simple classification diagram of the existing types of controlling methods is shown in Fig. 1.

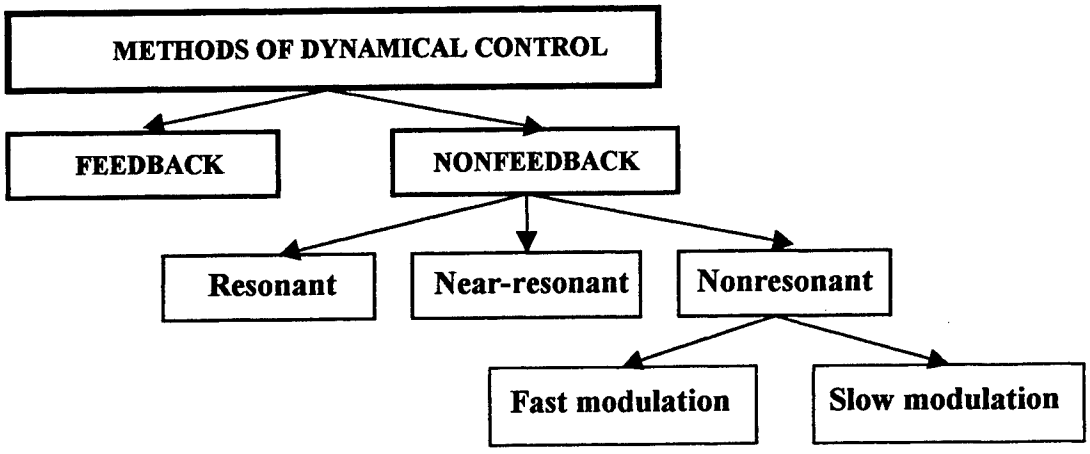


Figure 1. Schematic classification of control methods.

The nonfeedback control can be performed by applying resonant, near-resonant, or nonresonant perturbation to a parameter. The efficiency of the nonfeedback control depends strongly on the frequency of the control modulation. Generally, the *resonant* control means that the ratio between the control frequency f_c and a characteristic frequency of the system, f_r, is a rational number, i.e., $f_c = (1/n)f_r$ (where $n = 1,2,...$). At the resonant frequency small parametric perturbations enable to bring the system to a regular regime,[5,7,10,14,15] while the *near-resonant* control,[9,16] close to a subharmonic of the relaxation oscillations, $f_c \approx (1/n)f_r$, and the *nonresonant* control, $f_c \neq (1/n)f_r$,[17-22] require a relatively large perturbation amplitude. In actual practice the nonresonant control is more convenient for laser systems because the exact measuring of

Other author information: On leave from Stepanov Institute of Physics of National Academy of Sciences of Belarus; Email: apisarch@foton.cio.mx; Telephone: 52-47-175823; Fax: 52-47-175000; Supported by CONACYT (Mexico).

Laser Optics 2000: Control of Laser Beam Characteristics and Nonlinear Methods for Wavefront Control,
Leonid N. Soms, Vladimir E. Sherstobitov, Editors, Proceedings of SPIE Vol. 4353 (2001)
© 2001 SPIE · 0277-786X/01/$15.00

the characteristic frequency is not needed. Moreover, as we showed recently,[10] the resonant (subharmonic) parametric perturbation makes the system to be bistable by splitting the original attractor into two new ones. As a rule, the system is attracted to the attractor with lower complexity, while the unstable periodic orbit of the original attractor is not stabilized.

The nonfeedback control may be realized either in the form of fast[17] or slow parameter modulation.[18-24] In this paper I will demonstrate by the example of a loss-modulated CO_2 laser that a slow nonresonant control can efficiently applied to laser systems. The term "slow" means that the frequency of the control modulation is much smaller than a characteristic frequency of the system, e.g., the natural frequency in case of a nonlinear oscillator or the driving frequency in a nonautonomous system ($f_c << f_f$). The slow modulation can induce parametric resonances and cause shifting and removing the bifurcation points in the parameter space. The last effect provides a unique method for controlling monostability in lasers. In this paper I will review each of these phenomena with numerical simulations and experiments without going into details.

2. PARAMETRIC RESONANCES

The problem of finding nonlinear resonances is closely related to the problem of optimal control of nonlinear dynamical systems. First, we consider the model of the laser equations and then we provide the experimental evidence of the parametric resonance in a CO_2 laser. The parametric resonances appear as a consequence of an interaction between stable and unstable periodic orbits that leads to growing the largest (negative) Lyapunov exponent in the system operated in a period-doubling range.

In the numerical simulations here and after, we use the model equations of a driven class-B laser:[10]

$$du/dt = \tau^{-1}(y - k_0 - k)u, \tag{1}$$

$$dy/dt = (y_0 - y)\gamma - uy. \tag{2}$$

Here u is proportional to the radiation density, y and y_0 are the gain and the unsaturated gain in the active medium respectively, τ is half round-trip time of light in the cavity, γ is the decay rate of the gain, k_0 is the constant part of the losses, k_d and f_d are the driving amplitude and frequency, respectively. The variable cavity losses k are modulated with two incommensurable frequencies so that

$$k = k_d \cos(2\pi f_d t) + k_c \cos(2\pi f_c t), \tag{3}$$

where f_d, k_d, and f_c, k_c are the frequencies and amplitudes of the driving and control signals, respectively. The term $k_c \cos(2\pi f_c t)$ provides a slow ($f_c << f_d$), small ($k_c << k_d$) modulation of the laser intensity. The following fixed parameters are used in the calculations: $\tau = 3.5 \times 10^{-9}$ s, $\gamma = 2.5 \times 10^5$ s^{-1}, $y_0 = 0.175$, $k_0 = 0.173$, $f_d = 10^5$ s^{-1}, $f_c = 10^4$ s^{-1}, while the other parameters k_d and k_c are varied in the numerical simulations.

The laser described by the system of Eqs. (1-2) exhibits a period-doubling route to chaos with increasing the bifurcation parameter k_d. The bifurcation diagram of stroboscopically measured u at each period $T = 1/f_d$ without the control modulation ($k_c = 0$) is shown in Fig. 2(a). The laser response on the slow parametric modulation Eq. (3) was studied by measuring the amplitude S of the f_c component from the Fourier spectrum of the laser intensity at each fixed bifurcation parameter k_d. In Fig. 2(b) we plot the normalized amplitude $A = S/S_0$ (where S_0 is the amplitude of the f_c-spectral component at $k_d = 0$) versus the driving amplitude k_d for two different control amplitudes, $k_c = 10^{-4}$ (dots) and $k_c = 10^{-5}$ (crosses). As seen from the figure, the positions of the resonances do not depend on k_c. The value of A can be considered as an *amplification* of the additive slow signal by the laser as a nonlinear dynamical system. One can see from Fig. 2(b), the laser begins to amplify the signal just after the first period-doubling threshold, and that A has a wide resonance at $k_d = 3.7$. With a further increase in k_d, the amplification decreases and the control signal is suppressed by the system, i.e., $A < 1$. Figure 2(c) shows the Lyapunov exponents λ in the presence (closed dots) and in the absence (open dots) of the control modulation. One can see that the control leads to destabilization of the period 2 because λ approaches to 0. It is clearly seen that the resonance in λ strongly correlates with the resonance in A.

The experimental setup has been described in our previous works.[19,20] The electric signal $V = V_d \cos(2\pi f_d t) + V_c \cos(2\pi f_c t)$ was applied to an acousto-optic modulator providing time-dependent cavity losses. Here V_d and V_c are the driving and control amplitudes, respectively, f_d= 110 kHz and f_c= 12 kHz.

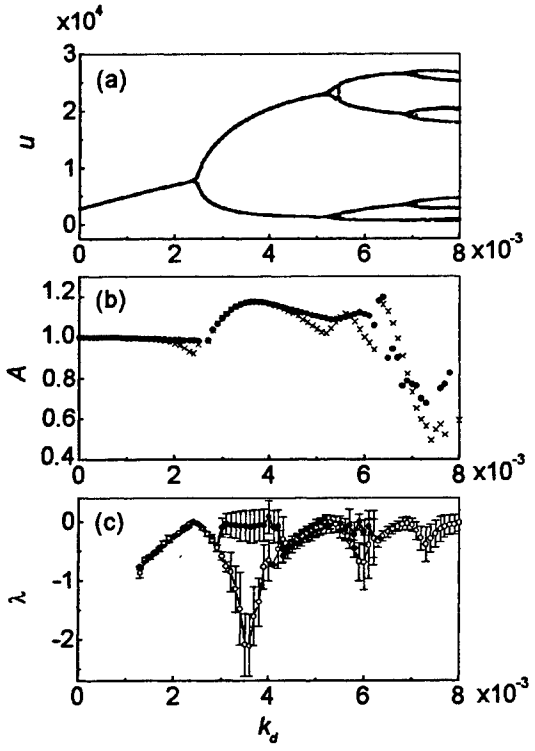


Figure 2. (a) Bifurcation diagram of the CO_2 laser Eqs. (1,2), (b) amplification of the control signal $k_c = 10^{-4}$ (dots) and $k_c = 10^{-5}$ (crosses), and (c) leading Lyapunov exponents at the absence (open dots) and at the presence (closed dots) of the control.

In Fig. 3 we plot the signal-to-noise ratio (SNR) at the control frequency f_c versus the driving voltage. The boundaries of the period-doubling and chaotic regimes (in the absence of the control modulation) are schematically shown in the figure by the dotted lines. One can see that SNR has a resonance situated approximately at the middle part of the period-doubling range. It should be noted that the control signal added to the system is relatively small as compared with the driving signal.

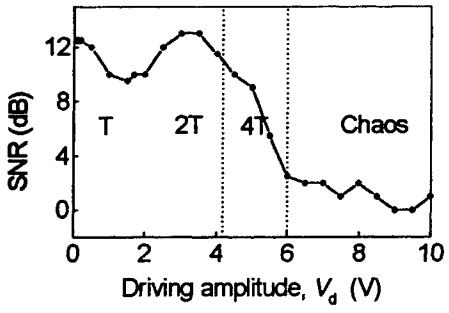


Figure 3. Experimental signal-to-noise ration at the control frequency.

Thus, the slow nonresonant control can produce parametric resonances in a period-doubled laser. The origin of this phenomenon lies in the interaction between stable and unstable periodic orbits. The existence of the resonance amplification can be crucial for communications implying that a period-doubled system can be used as a signal amplifier. We believe that the resonance observed in the laser system is a general phenomenon because it has been also observed in a modulated quadratic map.[23]

3. SHIFT OF BIFURCATION POINTS

Dynamical systems are normally regulated by their parameters. When the parameters change, so do the properties of the system. In particular, the stability of a system may be investigated by considering the results of small disturbance. If the disturbances die with time the system is stable, and if the disturbances grow the system is unstable. At some points in the space of parameters some of these properties may change discontinuously as a function of one or more parameters. This happens in *bifurcation points*. The problem of bifurcation control in lasers can be posed as shifting or removing the bifurcation point in the parameter space.

In this paper we consider two types of bifurcations: *period-doubling bifurcation* (PDB) and *saddle-node bifurcation* (SNB). One of the methods for studying dynamical properties of a system near a bifurcation point is a slow variation of a system parameter. By such a way, Kapral and Mandel[25] found out a characteristic hysteresis in the bifurcation diagram for forward and backward linear sweeps of the control parameter in a one-dimensional iterative map. The hysteresis appears because of the shift of the PDB point. The postponement of bifurcations has been also obtained with the Lorenz equations.[18,26] Later, the shift of PDB points has been observed in lasers with a slow harmonic modulation.[19-21,27] First, consider the influence of the nonresonant control on the PDB.

3.1. PERIOD-DOUBLING BIFURCATION

Recently, we have shown[10] that a resonant modulation can split the original attractor into two attractors, each is shifted to opposite directions and the values of these shifts depend on the modulation phase. A near-resonant modulation can be considered as a superposition of a resonant modulation and a low-frequency modulation or frequency detuning; the resonant modulation induces the attractor splitting and the low-frequency modulation plays a role of the phase varied in time. The shift of PDB points depends on the detuning and the direction of the shift can be either positive or negative, as shown by Vohra and his colleagues,[16] that may be a consequence of the attractor splitting. At the contrary, a slow modulation does not induce new attractors but tracks a periodic orbit from its stable range to the range where the orbit is originally unstable and by such a way the dynamical stabilization can be realized. Tracking an unstable periodic orbit (UPO) constrains a system's trajectory within a periodic orbit as the system is moved, via large parameter shifts, through various bifurcations into a regime where the orbit is inherently unstable. The first successful experiment on tracking of the UPOs in a laser has been carried out by Gill and his colleagues[4] in a solid-state laser. Later, *dynamical* tracking by shifting the PDB points has been realized in a CO_2 laser[19,21] and in an optically pumped far-infrared laser.[27]

The first experimental realization of *dynamical* stabilization of the UPO's in lasers has been performed by us[20,21] in a loss-driven CO_2 laser with a slow modulation of cavity detuning. The driving electric signal, $A_0 \cos(2\pi f_0 t)$, at frequency $f_0 = 1/T$ and amplitude A_0 is applied to the modulator providing time-dependent cavity losses. Varying the driving amplitude A_0 from 0 to 10 V, it is possible to obtain different dynamic regimes from a period 1 to chaos. The cavity detuning was chosen as a control parameter. The changes in the cavity length within a longitudinal mode of the laser cavity lead to the appropriate changes in the gain factor.

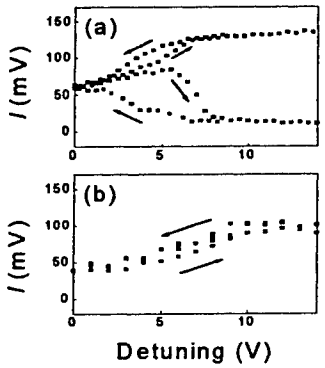


Figure 4. Bifurcation diagrams at the control frequencies (a) 850 Hz and (b) 5 kHz.

Figure 4 demonstrates the results in dynamic tracking unstable period-1 orbit at two different control frequencies. At the relatively slow modulation of detuning, f_1 = 850 Hz, the period-1 and period-2 regimes successively alternate at each period of the control modulation [Fig. 4(a)], while with increasing the control frequency up to f_1 = 5 kHz the period 2 does not appear in the laser response [Figs. 4(b)].

Thus, a large slow periodic modulation of a control parameter allows dynamical tracking of unstable periodic orbits by in a laser.

3.2. SADDLE-NODE BIFURCATION

In contrast with a PDB where a new stable period $2n$ (n = 1,2,3,...) orbit is created from a stable period n orbit belonging to a period N (N = 1,2,3,...) branch, in a SNB a new period $N + i$ (i = 1,2,3,...) branch is born and a new attractor is created. Therefore, the modulation of the control parameter near a SNB point can change radically the organization of coexisting basins of attraction by shifting SNB points or even eliminating them [24]. It appeared that the shift of the SNB point increases with the velocity at which the control parameter changes.

In this section we will show how far and in what direction the boundaries which separate two coexisting basins of attraction can be shifted when a control parameter is periodically modulated. Quantitatively it is expressed in location of the SNB points. Thus, we investigate the influence of the slow modulation of cavity losses on the positions of coexisting attractors in a loss-driven CO_2 laser.

In order to move the SNB points, we use the following simple algorithm. In the model Eqs. (1-2) the amplitude k_d of the variable cavity losses $k = k_d \sin(2\pi f_d t)$ is modulated by the following way

$$k_d = k_d^0 \{1 - 0.5m [1 - \cos(2\pi f_c t)]\}, \quad (4)$$

where m is the control amplitude and k_d^0 is the initial driving amplitude (at m = 0 or f_c = 0) without the control modulation. We assume that the control frequency f_c is small, i.e., $f_c << f_d$. Thus, the driving amplitude k_d is modulated between its maximal value k_d^0 and its minimal value $k_d^0 (1 - m)$. We find that period-1 and period-2 attractors coexist at the following set of the fixed parameters: : $\tau = 3.5 \times 10^{-9}$ s, $\gamma = 10^5$ s^{-1}, $y_0 = 0.18$, $k_0 = 0.173$, $f_d = 1.12 \times 10^5$ s^{-1}. The parameters k_d, k_c, and m are varied in the numerical simulations.

In Fig. 5 we show the bifurcation diagram of stroboscopically measured u (sampled with the driving $T = 1/f_d$) in the absence of the control modulation [m = 0 in Eq. (4)].

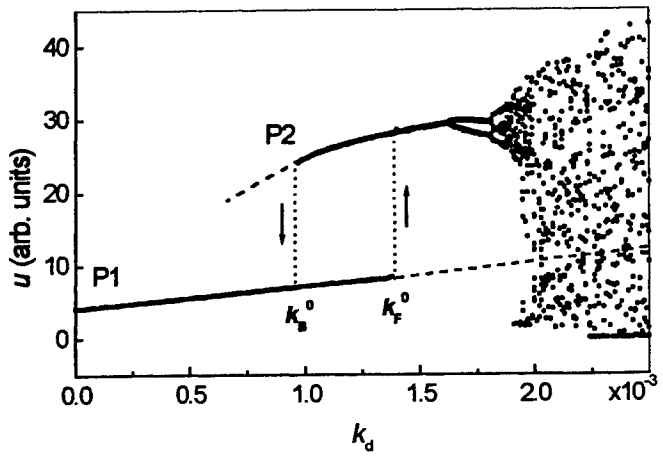


Figure 5. Bifurcation diagram with coexisting branches of period 1 (P1) and period 2 (P2). The arrows indicate the positions of the forward and backward SNB points without the control. The dashed lines show the new positions of the branches in the laser with the additional slow modulation Eq. (4).

As seen from Fig. 5, there exist two SNB points where the system changes the attractor. One of them occurs at $k_F^0 \approx 1.4 \times 10^{-3}$, when we increase the control parameter, while the system stays on the period-1 branch. We call this bifurcation a *forward saddle-node bifurcation* (FSNB). This point indicates the upper boundary of the period-1 branch. When k_d decreases the SNB appears at $k_B^0 \approx 10^{-3}$. This point indicates the lower boundary of the period-2 branch. We call this bifurcation a *backward saddle-node bifurcation* (BSNB). Thus, without an additional modulation the attractors coexist at $10^{-3} < k_d < 1.4 \times 10^{-3}$.

The parameter modulation Eq. (4) deforms basins of coexisting attractors. This reveals itself as a shift of the SNB points, so that the branches in the diagram can be extended along the dashed lines. One can see here a principal difference between dynamical properties of the FSNB and BSNB points. The FSNB point always moves along the branch, which is unstable without the control modulation. This behavior is similar to the dynamical tracking due to the shift of the PDB point.[21] However, the extension of the branch due to the movement of the BSNB is not a stabilization of an unstable orbit, because this is a new prolongation of the branch. The additional modulation makes the system different and the locations of the branches are also changed.

The basins of attraction as a function of f_c for two different modulation amplitudes are shown in Fig. 6. The dashed ranges correspond to the initial conditions of u at which the phase trajectory is attracted to the period-2 orbit and the blank ranges display the basin of attraction for the period-1 orbit. As seen from the figures, the slow modulation can significantly deform the basins and at certain frequency and amplitude the SNB occurs (shown by the arrows).

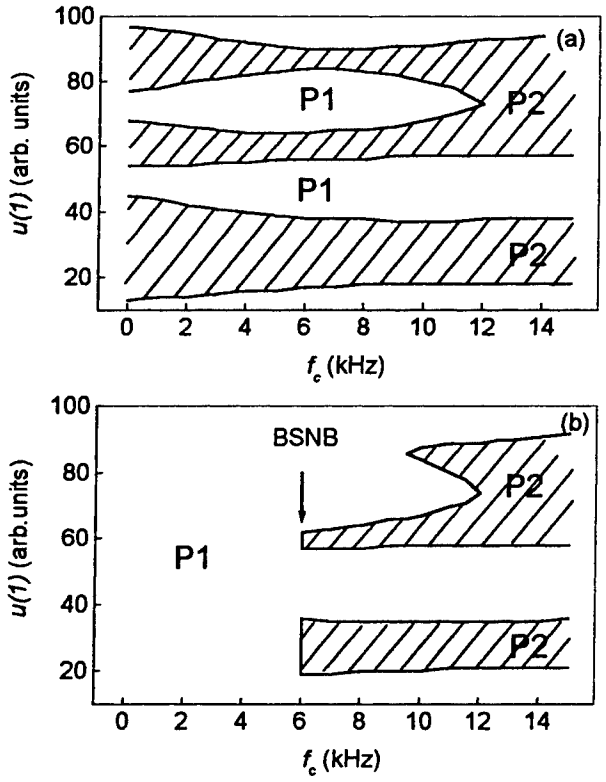


Figure 6. Basins of attraction of the period-1 and period-2 attractors at (a) $m = 0.3$ and (b) 0.4.

In the experiments with a single-mode CO_2 laser,[19,20] we explore the sets of parameters where period-1 and period-2 attractors coexist. The additional slow modulation was applied to the driving amplitude in the same form as in the numerical simulations [see Eq. (4)]:

$$A_d = A_0 \{1 - 0.5m [1 - \cos(2\pi f_c t)]\}, \quad (5)$$

where A_0 is the initial driving amplitude without the control (at $m=0$ or $f_c = 0$).

Coexisting period-1 and period-2 attractors can be found experimentally in the CO_2 laser with relatively high gain and driving frequency. In Fig. 7(a) we show schematically the bifurcation diagram in the absence of the control modulation ($m = 0$), where the driving amplitude A_d is used as a control parameter. The values of A_d at the boundaries between different dynamical regimes without the control modulation are indicated in the figure. With slowly increasing A_d, the laser follows the period-1 branch and reaches the higher boundary of this branch at A_F = 5.2 V. Then it is involved in the period-2 attractor. While with decreasing A_d, the laser stays in the period-2 branch up to A_B = 5 V, the lower boundary of the period-2 branch. Thus, there exists a small hysteresis range where these two attractors coexist without an additional control modulation. The control modulation can extend significantly the range of coexistence of the attractors by shifting the SNB points along the hollow boxes. In Fig. 7(b) we show how the new position of the FSNB point depends on the amplitude and frequency of the control modulation.

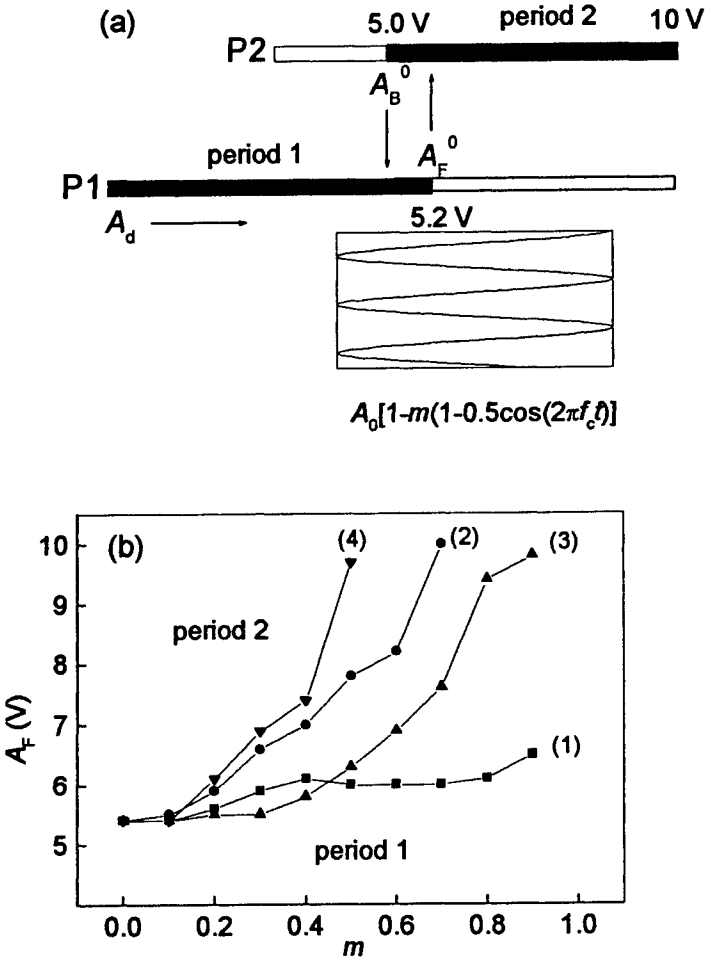


Figure 7. (a) Experimental bifurcation diagram. The arrows show the directions for the change of the attractor. The application of the control modulation Eq. (5) shifts the SNB points along the hollow boxes. (b) Position of the FSNB point versus the control amplitude for different control frequencies (1) f_c=50, (2) 100, (3) 500, and (4) 1000 Hz. f_d = 254 kHz.

Thus, we have shown that the additional slow periodic modulation applied to the loss changes the range of coexistence of attractors by shifting SNB points. We have demonstrated that this shift depends strongly on the amplitude and frequency of the control modulation.

4. ATTRACTOR ANNIHILATION

Some kinds of instabilities in optical devices result from the coexistence of multiple attractors and occasional involuntary jump of the system from one attractor to another. Thus, the stabilisation of dynamical system is often related to the problem of controlling monostability. A slow parameter modulation makes the system a little different from the unperturbed system so that one of the attractors can be destroyed and the new system becomes monostable. Notice that no qualitative change of the behaviour would have occurred if the value of the system parameter were increased by the same magnitude as that of the control amplitude but without the additional slow modulation.

In the model Eqs. (1-2) of a CO_2 laser with modulated losses $k = k_d \cos(2\pi f_d t)$ the location of the subcritical SNB and supercritical PDB in parameter space of k_d and y_0 is shown in Fig. 8. These bifurcations are the boundaries between different dynamical regimes: the period 1, period 2, and bistability. The bifurcations are merged when the driving frequency coincides with the double relaxation oscillation frequency, $f_d = 2f_r$. In this work we are interested in the bistability range.

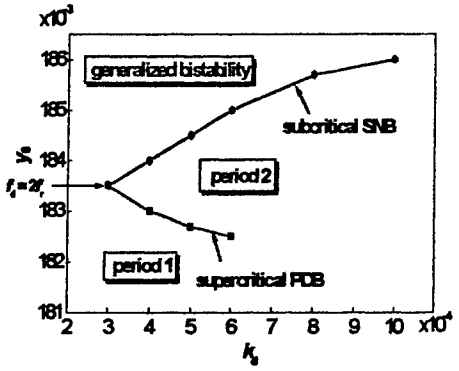


Figure 8. Parameter diagram of the laser with coexisting attractors.

The control is applied to the gain $y_0 = y_0` + y_c \sin(2\pi f_c t)$, where $y_0`$ is the gain of the uncontrolled laser, and y_c and f_c are the amplitude and frequency of the control. We assume this additional modulation to be slow ($f_c << f_d$) and weak ($y_c << y_0`$) and $y_0`$ is fixed at 0.1855 to keep the operating condition in the bistable region. The effect of the control is demonstrated in Fig. 9. A periodically forced CO_2 laser, prior to the control, is in a period-2 state. Under the control modulation, we observe the annihilation of the period-2 attractor followed by a jump to the period-1 orbit. When the control is switched on, the period 2 disappears and the system jumps, after transients, to the remaining period 1.

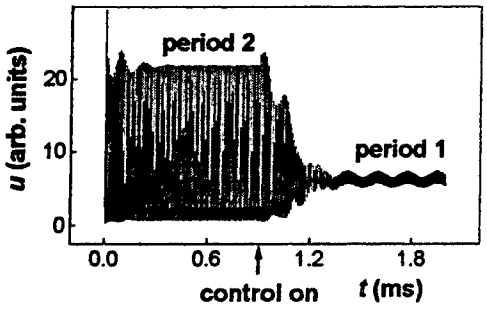


Figure 9. Annihilation of the period-2 attractor.

This phenomenon occurs over a certain range of the control frequency and amplitude. The bifurcation diagrams with f_c as a control parameter at different y_c are shown in Fig. 10. These diagrams are obtained by sampling the laser intensity at the interval $1/f_c$. One can see a bubble cascade (i.e., P1 → P2 → P4 ... chaos ... P4 → P2 → P1) in Fig. 10(a), where the periodicity is referred to in the sense of the control signal. The chaotic orbit, in the interior of the cascade, gets annihilated in the range of the control frequency $0.030 < f_c/f_d < 0.036$.

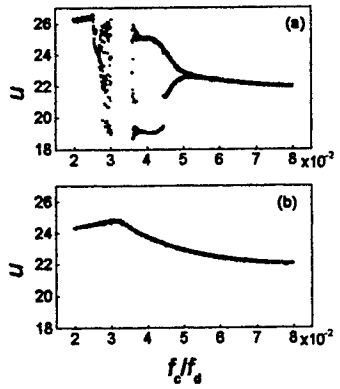


Figure 10. Bifurcation diagrams with respect to f_c in the vicinity of annihilation curve for (a) $y_c = 5 \times 10^{-4}$ and (b) 4×10^{-4}.

This annihilation is expected to be due to the collision with the regular period-2 (in the sense of f_d) saddle. After such boundary crisis, the system jumps to the remaining period-1 attractor (not shown). The validity of the method is confirmed experimentally in a loss-driven CO_2 laser with a control in the form of a slow modulation of cavity detuning. Numerical simulations and experiments suggest that the annihilation of the attractor results from its destabilization by the control modulation and the system switches to the remaining stable state. At certain frequencies, complex dynamical behavior (a period-doubling route to chaos and crisis) can appear in the system response at the control frequency, while the original periodicity (driving frequency) acts as a carrier. The temporal behavior of the laser before crisis is shown in Fig. 11.

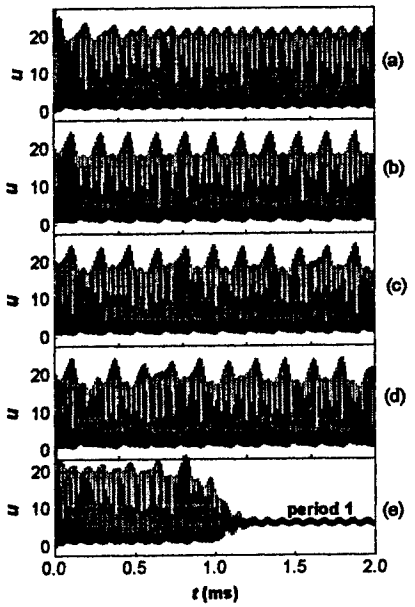


Figure 11. Time series of laser intensity before attractor is annihilated at fixed $f_c = 6 \times 10^{-2} f_d$. (a) Period 1 in the slow envelope of the control frequency f_c at $y_c = 5 \times 10^{-4}$, (b) period 2 at $y_c = 6.6 \times 10^{-4}$, (c) period 10 at $y_c = 7.2 \times 10^{-4}$, and (d) chaos at $y_c = 7.5 \times 10^{-4}$. (e) Crisis and destruction of the period-2 attractor in f_d at $y_c = 8.1 \times 10^{-4}$.

The subharmonics in the control result from the resonance with the driving frequency. Both the driving frequency and the fundamental (relaxation oscillation) frequency are much larger then the control frequency. However, the difference between the subharmonic frequency in driving and the fundamental frequency gets in resonance with the control frequency that results in boundary crisis of the attractor. The method may have important applications in stabilization of optical devices whose instabilities are caused by system switches from one coexisting attractor to another, for example, in lasers with nonlinear crystals or in multimode lasers.

CONCLUSIONS

We have demonstrated numerically and experimentally that nonfeedback nonresonant control of laser dynamics can be efficiently achieved by applying a slow harmonic modulation to an available system parameter. Such a control can induce parametric resonances, shift bifurcation points, deform basins of attraction, and even annihilate one of the coexisting attractors. In spite of the fact that the nonresonant control looks like a shift of the system parameters, no qualitative change of the behavior would have occurred if the value of the parameter were increased by the same magnitude as that of the control amplitude but without the additional slow modulation. This method does not require any real-time measurement or prior knowledge on the system. We expect that the approaches we have used are general to be applied to many other nonlinear systems.

ACKNOWLEDGMENTS

I have gained much from discussions with many, including Ramon Corbalán, Ramon Vilaseca, Viacheslav N. Chizhevsky, Binoy K. Goswami, and F. T. Arecchi. This work has been supported by CONACYT (Mexico).

REFERENCES

1. R. Roy, T. W. Murphy, Jr., T. D. Maier, Z. Gills, and E. R. Hunt, "Dynamical control of a chaotic laser: Experimental stabilization of a globally coupled system", *Phys. Rev. Lett.*, **68**, pp. 1259-1262, 1992.
2. E. Ott, C. Grebogi, and J. Yorke, "Controlling chaos", *Phys. Rev. Lett.*, **64**, pp. 1196-1199, 1990.
3. E. R. Hunt, "Stabilizing high-period orbits in a chaotic system – the diode resonator," *Phys. Rev. Lett.*, **67**, pp. 1953-1955, 1991.
4. Z. Gills, C. Iwata, R. Roy, I. Schwartz, and I. Triandaf, "Tracking unstable phenomena in chaotic laser experiments: Extending the stability regime of a multimode laser," *Phys. Rev. Lett.*, **69**, pp. 3169-3172, 1992.
5. K. Otsuka, J.-L. Chern, and J.-S. Lih, "Experimental suppression of chaos in a modulated multimode laser," *Optics Letters*, **22**, pp. 292-294, 1997.
6. S. Bielawski, D. Derozier, and P. Glorieux, "Controlling unstable periodic orbits by a delayed continuous feedback," *Phys. Rev. E*, **49**, pp. R971-R974, 1994.
7. R. Meucci, W. Gadomski, M. Ciofini, and F. T. Arecchi, "Experimental control of chaos by means of weak parameter perturbations," *Phys. Rev. E*, **49**, pp. R2528-R2531, 1994.
8. M. Ciofini, R. Meucci, and F. T. Arecchi, "Experimental control of chaos in a laser," *Phys. Rev. E*, **52**, pp. 94-97, 1995.
9. V. N. Chizhevsky and R. Corbalán, "Experimental observation of parametric effects near period doubling in a loss-modulated CO_2 laser," *Phys. Rev. E*, **53**, pp. 1830-1833, 1996.
10. V. N. Chizhevsky, R. Corbalán, and A. N. Pisarchik. "Attractor splitting induced by resonant perturbations," *Phys. Rev. E*, **56**, pp. 1580-1584, 1997.
11. A. Gavrielides, V. Kovanis, and P. M. Alsing, "Controlling chaos in semiconductor laser devices," *Proc. of the SPIE – The Int'l Society for Optical Engr.*, **2039**, pp. 250-262, 1993.
12. Y. Liu, N. Kikuchi, and J. Ohtsubo, "Controlling dynamical behavior of a semiconductor laser with external optical feedback," *Phys. Rev. E*, **51**, pp. 2697-2700, 1995.
13. K. Pyragas, "Control of chaos via extended delay feedback," *Phys. Lett. A*, **206**, pp. 323-330, 1995.
14. R. Lima and M. Pettini, "Suppression of chaos by resonant perturbations," *Phys. Rev. A*, **41**, pp. 726-733, 1990.
15. Y. Brain and I. Goldhrisch, " Taming chaotic dynamics with weak periodic perturbations," *Phys. Rev. Lett.*, **66**, pp. 2445-2548, 1991.
16. S. T. Vohra, F. Fabini, and F. Bucholtz, "Suppressed and induced chaos by near resonant perturbations," *Phys. Rev. Lett.*, **75**, pp. 65-68, 1995.
17. Y. S. Kivshar, F. Rödelspeger, and H. Benner, "Suppression of chaos by nonresonant parametric perturbations," *Phys. Rev. E*, **49**, pp. 319-324, 1994.

18. R. Vilaseca, A. Kul'minskii, and R. Corbalán, "Tracking unstable steady states by large periodic modulation of a control parameter in a nonlinear system," *Phys. Rev. E*, **54**, pp. 82-85, 1996.
19. A. N. Pisarchik, V. N. Chizhevsky, R. Corbalán, and R. Vilaseca, "Experimental control of nonlinear dynamics by slow parametric modulation," *Phys. Rev. E*, **55**, pp. 2455-2461, 1997.
20. A. N. Pisarchik, R. Corbalán, V. N. Chizhevsky, R. Vilaseca, and B.F. Kuntsevich, "Dynamic stabilization of unstable periodic orbits in a CO_2 laser by slow modulation of cavity detuning," *Int. J. Bifurcation and Chaos*, **8**, pp. 1783-1789, 1998.
21. A. N. Pisarchik, "Dynamical tracking unstable periodic orbits," *Phys. Lett. A*, **242**, pp. 152-162, 1998.
22. A. N. Pisarchik, B. F. Kuntsevich, and R. Corbalán, "Stabilizing unstable orbits by slow modulation of a control parameter in a dissipative dynamic system," *Phys. Rev. E*, **57**, pp. 4046-4053, 1998.
23. A. N. Pisarchik and R. Corbalán, "Parametric nonfeedback resonance in period doubling systems," *Phys. Rev. E*, **59**, pp. 1669-1674, 1999.
24. A. N. Pisarchik and B. K. Goswami, "Annihilation of one of the coexisting attractors in a bistable system," *Phys. Rev. Lett.*, **84**, pp. 1423-1426, 2000.
25. R. Kapral and P. Mandel, "Bifurcation structure of the nonautonomous quadratic map," *Phys. Rev. A*, **32**, pp. 1076-1081, 1985.
26. P. Mandel and T. Erneux, "Laser Lorenz equations with a time-dependent parameter," *Phys. Rev. Lett.*, **53**, pp. 1818-1820, 1984.
27. R. Dykstra, A. Rayner, D. Y. Tang, and N. R. Heckenberg, "Experimental tracking unstable steady states by large periodic modulation," *Phys. Rev. E*, **57**, pp. 397-401, 1998.

Delayed feedback control of the chaotic dynamics of the optoelectronic system with a laser diode.

V.V. Jakutkin[a], S.P. Kotova[a], H.D. Lamaghapov[b]

[a]Lebedev Physical Institute of Russian Academy of Sciences,
Novo-Sadovaya Street 221, Samara 443011, Russia. E-mail: kotova@fian.samara.ru.
[b] Samara Railway Engineering Institute

ABSTRACT

The delayed feedback control of the chaotic dynamics of the optoelectronic system with a laser diode is analyzed and experimental results are presented. The degree of the chaos suppression and suppression time were measured for three cases differing in the functional dependence of the control signal on the change of the laser output power: proportional, exponential or combined. It was found that the degree of the chaos suppression did not depend much on the control technique. The suppression time was different in all cases and in the third one it was minimal.

Keywords: chaos, control of chaos, laser diode, optoelectronic delayed feedback.

1. INTRODUCTION

In many laser systems the areas of chaotic dynamics occur as the result of the system parameters change [1]. The research of the mechanisms of chaos emergence and ways of its control is important for many practical applications [2,3]. We made both theoretic and experimental investigation of a delayed feedback control for a simple optoelectronic model system. The system is similar to one described in [4] and consists of a single mode laser diode, collimator, Fabry-Perot interferometer, delayed optoelectronic feedback loop for chaos initiating and two optoelectronic feedback loops for chaos suppressing. The nonlinear delayed feedback on the laser current leads to the chaotic dynamics of the laser wavelength and the output power. This chaotic condition is controlled by perturbations of system parameters by the delayed feedback. The idea of this method was originated with K.Pyragas [5]. In this work the study is made for the case of the chaos suppressing that is of major importance for practical applications. Three cases of suppression were examined. In the first case the control signal was proportional to the changes of the output power within the delay of the system and was summarized with the laser current. In the second case the control signal was exponential to the changes of the output power within the delay of the system and multiplied by the chaotic loop amplification ratio. In the third case the control signal was combined, i.e. both techniques were used simultaneously.

2. THEORY

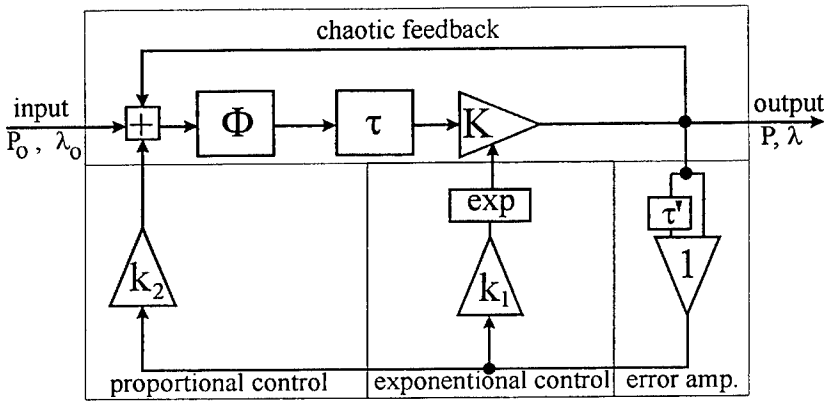


Fig. 1. The equivalent scheme of delayed nonlinear system.

Laser Optics 2000: Control of Laser Beam Characteristics and Nonlinear Methods for Wavefront Control,
Leonid N. Soms, Vladimir E. Sherstobitov, Editors, Proceedings of SPIE Vol. 4353 (2001)
© 2001 SPIE · 0277-786X/01/$15.00

The system under investigation belongs to the nonlinear time-delayed systems. The equivalent scheme is shown in Fig. 1. The chaotic part of the system composed of nonlinear element Φ, delay line τ, amplifier K was enveloped with the feedback loop. The controlling part of the system consists of differential amplifier generating the signal equal to the alteration of the output power within the delay time τ' proportional and exponential controlling loop. The delay time in this case is much more than the time of the system response, and provided that the transition process are neglected, the system dynamics could be described by the difference equations for optical power and wavelength of laser diode:

$$\begin{aligned} P(t) &= P_0 - \alpha \cdot K \cdot \exp\left(k_1 \cdot \left(P(t) - P(t-\tau')\right)\right) \cdot \Phi\left(P(t-\tau), \lambda(t-\tau)\right) + \alpha \cdot k_2 \cdot \left(P(t) - P(t-\tau')\right) \\ \lambda(t) &= \lambda_0 - \beta \cdot K \cdot \exp\left(k_1 \cdot \left(P(t) - P(t-\tau')\right)\right) \cdot \Phi\left(P(t-\tau), \lambda(t-\tau)\right) + \beta \cdot k_2 \cdot \left(P(t) - P(t-\tau')\right) \end{aligned} \quad (1)$$

where the initial conditions - P_0, λ_0 are the optical power and wavelength corresponding to the injection current I_0 of the laser diode ; α, β - proportionality factors; Φ - power of light, transmitted through the Fabry-Perot interferometer; k1, k2 - the coefficients of the terms responsible for the chaos control; τ - time delay of the feedback loop generating the chaotic oscillations; τ' - time delay of the control feedback loop and K - amplification coefficient. A specific type of the non-linearity depends on the optical scheme configuration. In our investigations the spectral width of the emitted line is much less than interferometer resonance, hence the following approximation can be used:

$$\Phi(P,\lambda) = \frac{P}{1 + F \cdot \sin^2\left(\frac{2\pi L}{\lambda}\right)} \quad (2)$$

where F, L are the finesse and the thickness of the interferometer.

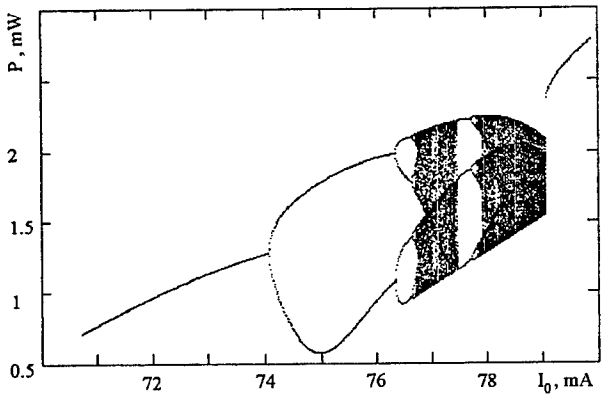


Fig. 2. The bifurcation diagram without control (k1, k2 =0) for K=0,8 (numerical simulation).

When there's no control (k1, k2=0) the change of the initial conditions leads to the system transition to a chaotic dynamics through the period doubling bifurcation. The behavior of the system is investigated by means of a numerical simulation. In Fig. 2 the typical bifurcation diagram for K = 0.8 is presented and optical power dependence on time is shown in Fig. 3 corresponding to its different regions. The result of the numerical simulations show that for the initial conditions P_0, λ_0 less than a certain value the unique dependence of the optical power on the injection current is valid. At first a part of the diagram conforms to the light-current characteristics of the laser and corresponds to the case when the wavelength is far enough from the interferometer resonance, i.e. transmittance $\Phi(P, \lambda)$ is close to zero and the disturbance caused by the nonlinear feedback is quenching quickly. For the case of increasing the injection current I_0, the wavelength λ_0 approaches the interferometer resonance, the transmittance grows and the system passes through the first bifurcation point - the stable periodic oscillations of the 2τ-period are generated (Fig. 3a). The further increase of the injection current leads to the rise of the oscillation amplitude and it is apparent in the diagram with the forked opposite branches. Near the transmission peak the oscillation amplitude reaches its maximum. While passing through the resonance, the oscillation amplitude decreases and the opposite branches in the diagram become closer. Then the system is getting over the second, third ..., and so on,

bifurcation point and the period of optical power oscillation redoubles (Fig. 3b). It should be mentioned that the opposite branches in the diagram behave similarly two the first ones. The highest oscillation amplitude is achieved when the system comes to the area of the interferometer maximal transmission. In the chaotic succession (Fig. 3c) some quasi states of a higher probability can be distinguished. They correspond to the diffused branches in the bifurcation diagram. A number of such branches, while merging with each other, give rise to the windows of stability (Fig. 3d), which are later on destroyed (Fig. 3e). The biggest window of stability corresponds to the power oscillation of the 3τ-period (Fig.3f). Stable oscillations of lower dimensions could also be destroyed according to the scenario of the period doubling (Fig. 3g) resulting in appearance of new chaotic areas (Fig. 3h). A breakdown of the chaotic generation occurs when the initial wavelength value, λ_0 substantially differs from the interferometer resonance. Then the optical power dependence on the injection current becomes unique again till the next interferometer resonance.

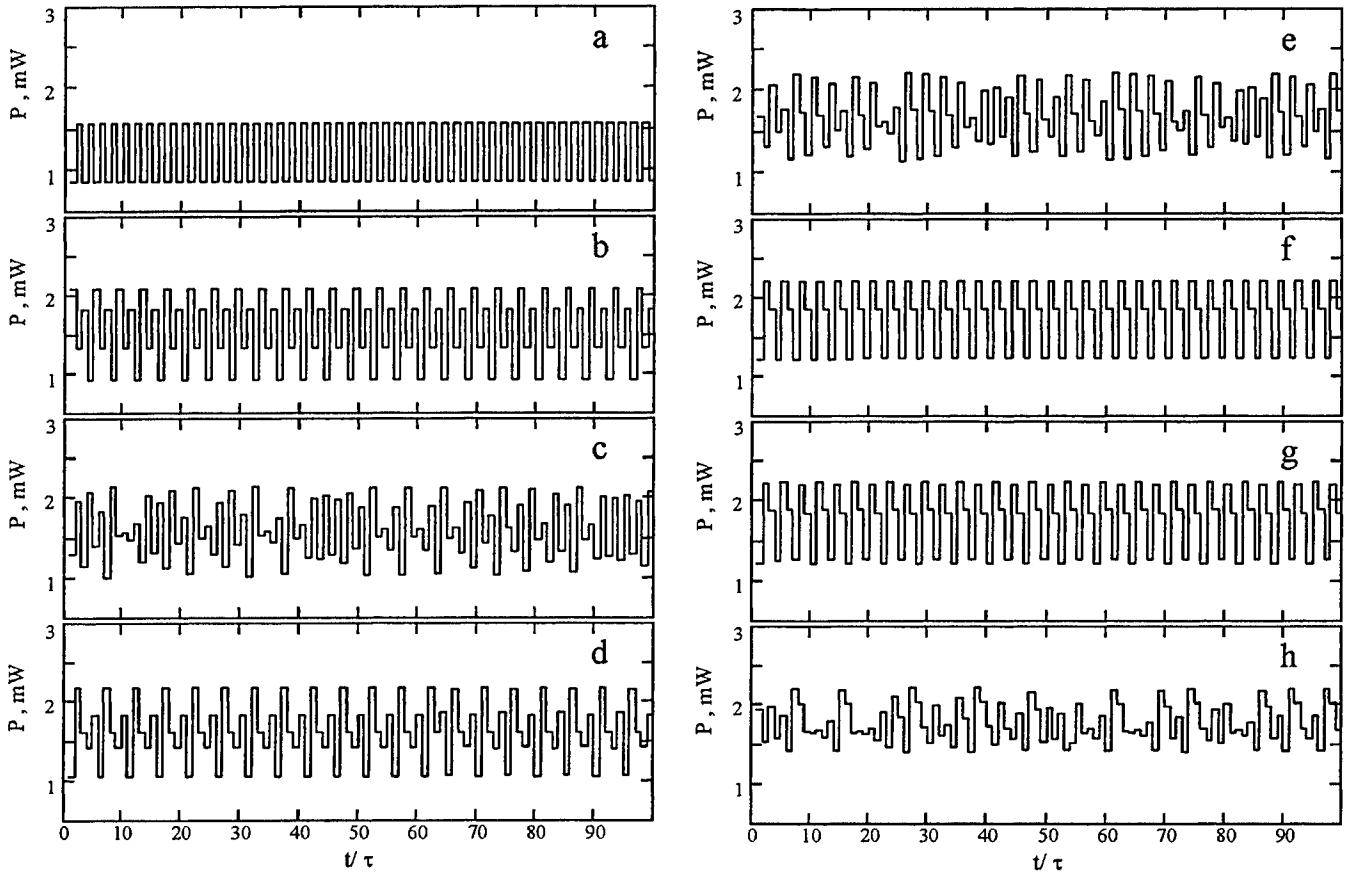


Fig. 3. The time series (numerical simulation): a - two cycle period, b - four cycle period, c - chaotic series from the first chaotic region, d - stable five cycle period from the first chaotic region, e - chaotic series before the region of three cycle period, f - three cycle period, g - six cycle period, h - chaotic series before the generation breakdown.

Presented numerical results correspond to a rather big K value. As a rule, at higher values the scaling of this diagram takes place, while at lower values qualitative changes of the dynamics nature occur. At first the stability windows and chaotic areas are reduced, then the diagram pattern is changed qualitatively: instead of a sharp boundary a backward bifurcation cascade appears at the dynamics breakdown. At low K-values the chaotic area disappears and only the states with low dimensions are realized. For K-values less than 0.1, the unique dependence is only realized.

As it was shown in [5] the controlling feedback $(P(t) - P(t - \tau'))$ can stabilize periodic oscillations of the *n*-dimension out of the chaos at $\tau' = n\tau$. The controlling signal shape should be selected so that the requirement of the unperturbed laser dynamics under the controlling signal influence was fulfilled. This means that on achieving the state of controllability, the component designating the linear feedback is close to zero, and the factor designating the exponential feedback is approaching the value of unit.

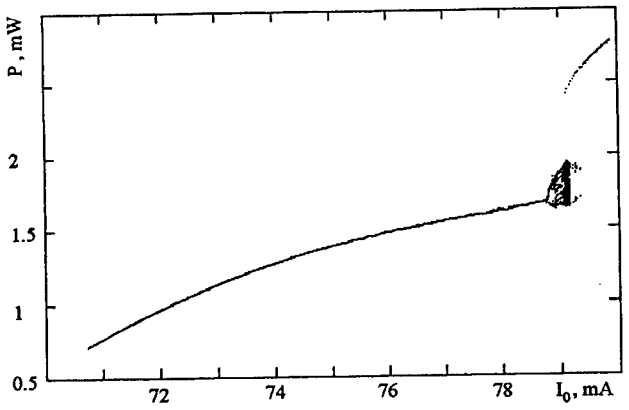


Fig. 4. The bifurcation diagram with proportional control for K=0,8 (numerical simulation).

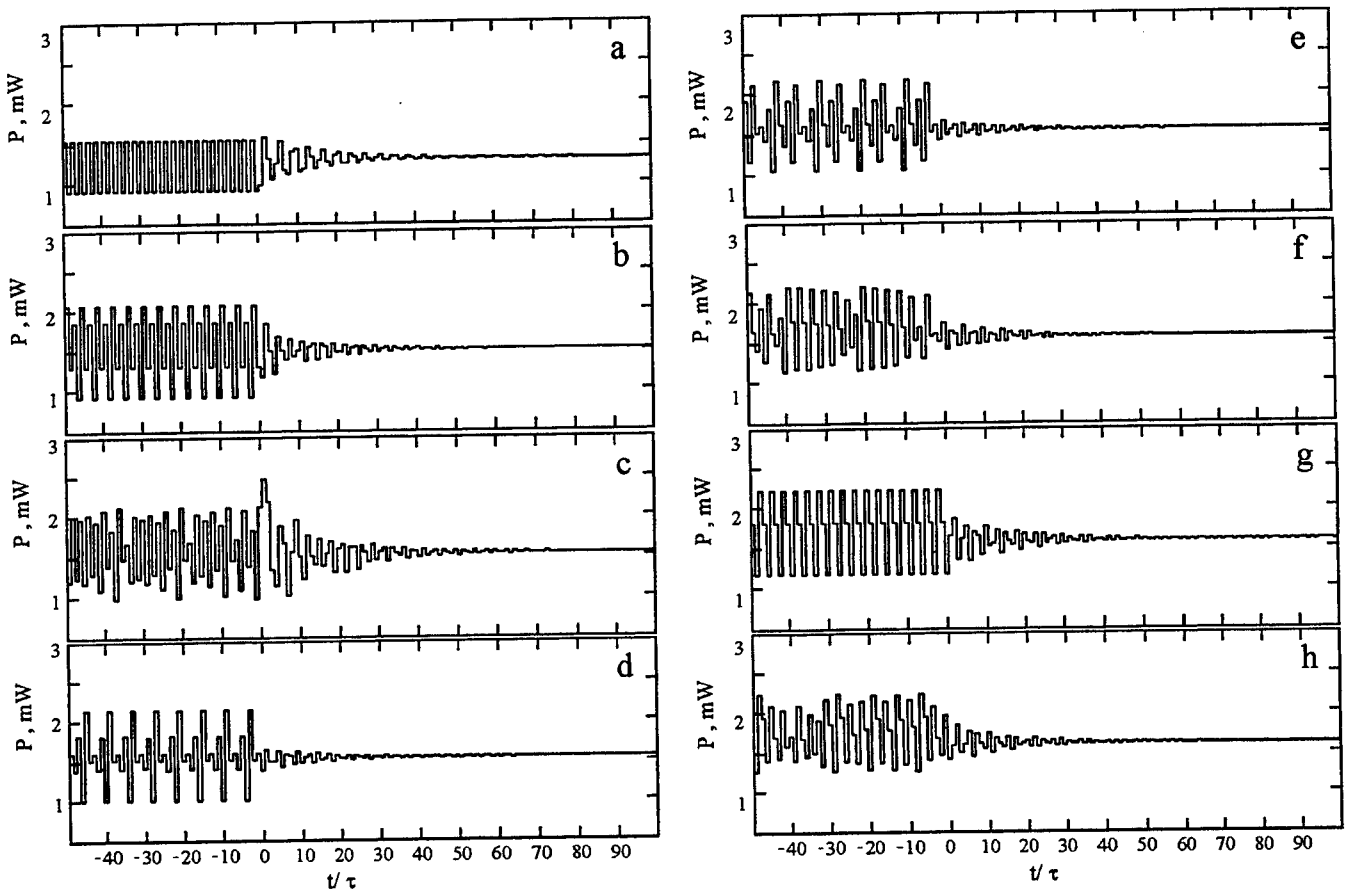


Fig. 5. The time series of chaos suppression (numerical simulation) from: a – two cycle period, b - four cycle period, c - chaotic series, d - stable six cycle period, e - stable eleven cycle period, f - chaotic series before the region of three cycle period, g - three cycle period, h - chaotic series before the generation breakdown.

The bifurcation diagram shown in Fig 4 differs from the diagram in Fig. 2 by switching on the proportional control (k1 = 0, $k2 \neq 0$, $\tau' = \tau$). The suppression of the system dynamics occurs totally except for a small fragment in the area of chaotic generation breakdown. In Fig. 5 the time series for different parts of the diagram are presented that illustrate the process of the suppression at the switched control. The switching moment corresponds to the zero point and the necessary time for establishing one stable state is approximately the same for different parts of the diagram. In case the transmittance coefficient K increases, the time interval needed for the suppression increases too because the dynamics of the system

becomes more complicated. When the depth of the controlling feedback is fixed and the K-value is increasing a moment sets in when it is impossible to stabilize the single state and in the diagram the region of low dimension oscillations and then chaotic region will emerge. These regions could be eliminated by means of a more accurate adjustment of the control depth.

3. EXPERIMENT

The experimental setup is presented in Fig. 6. The 763 nm single mode laser diode was used. The built-in photodiode was registering the optical power. The spectral width of the emitted line was estimated as 200 MHz. The wavelength was fluently adjusted with the injection current increasing within a large range. The laser radiation was passing through the Fabry-Perot interferometer. The interferometer finesse was equal to 10, the air gap thickness was equal to 1 mm. In order to decrease the power reverted to the laser after the reflection from the interferometer the radiation was transformed into a low-diverging beam with the help of collimation lens (f = 20 mm, NA = 0,4). The same aim was pursued when the interferometer was settled under the small angle to the optical axis. The laser radiation passing through the interferometer formed the interference pattern in the shape of a ring at the diaphragm plane. The signal registered with a photo-detector was amplified and then, after a delay was subtracted out of the injection current. The feedback loop delay of 1 ms-duration was selected. Both the feedback loop delay and the delay in the error amplifier arm were achieved with a couple of 12 - bit computer-aid ADC-DAC. The delayed feedback loop along with the non-linearity caused by the interferometer provided the generation of chaotic oscillations. The differential amplifier formed the error signal proportional to the optical power change for the time divisible by the delay time. This controlling signal was added up to the injection current and through the exponential amplifier was multiplied by the amplification factor of the control loop.

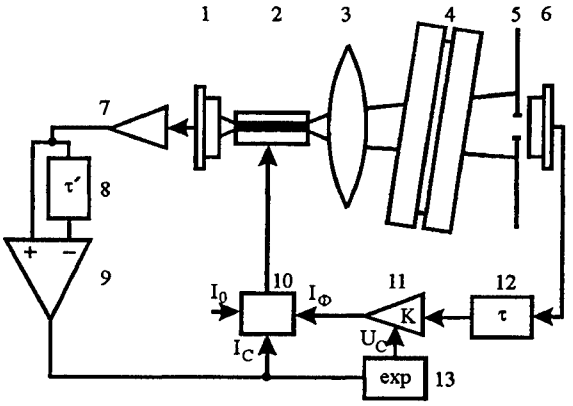


Fig. 6. The experimental setup: 1, 6 - photo diode, 2 - laser diode, 3 - collimator lens, 4 - Fabry-Perot interferometer, 5 - diaphragm, 7,11 - amplifier, 8,12 - time delay, 9 - differential amplifier, 10 - laser current driver, 13 - exponential converter.

In the experiments the optical power dependence on time for different values of injection current, amplifier factor of the feedback loop and various types of controlling feedback was registered. The obtained data allowed to plot bifurcation diagrams characterizing the system. In Fig. 7 the experimental results are presented for the scheme of chaotic dynamics suppressing with the help of the proportional controlling signal. The full oscillation suppression is achieved (Fig. 7b) with a small amplifier factor of the feedback loop when only the low-dimension chaos is observed in the optical power (Fig. 7a). The amplification factor increase leads to the complication of dynamics, and a full suppression becomes only possible at amplification values lower than a certain critical level. The diagram of the system bifurcation for this critical value is shown in Fig. 7c and the corresponding diagram with the 2τ-period oscillations is presented in Fig. 7d. When the amplification factor exceeds the critical value the area of an incomplete suppression of optical power is growing. In Fig. 7e the experimental bifurcation diagram similar to the numerical simulation (Fig.2) is shown. When the suppression is switched on, the oscillations of the 4τ- and 6τ-period, as well as chaotic ones in the fist area are suppressed completely. In the areas of the 2τ, 3τ, 4τ...- period oscillations and in the following chaotic areas the bistable oscillations are synchronized. In the areas where chaotic oscillations are disturbed for lack of suppression the chaotic splashes occur, caused by the system response to the suppression.

The similar bifurcation diagrams were obtained in the experiments for the exponential and combined types of suppression.

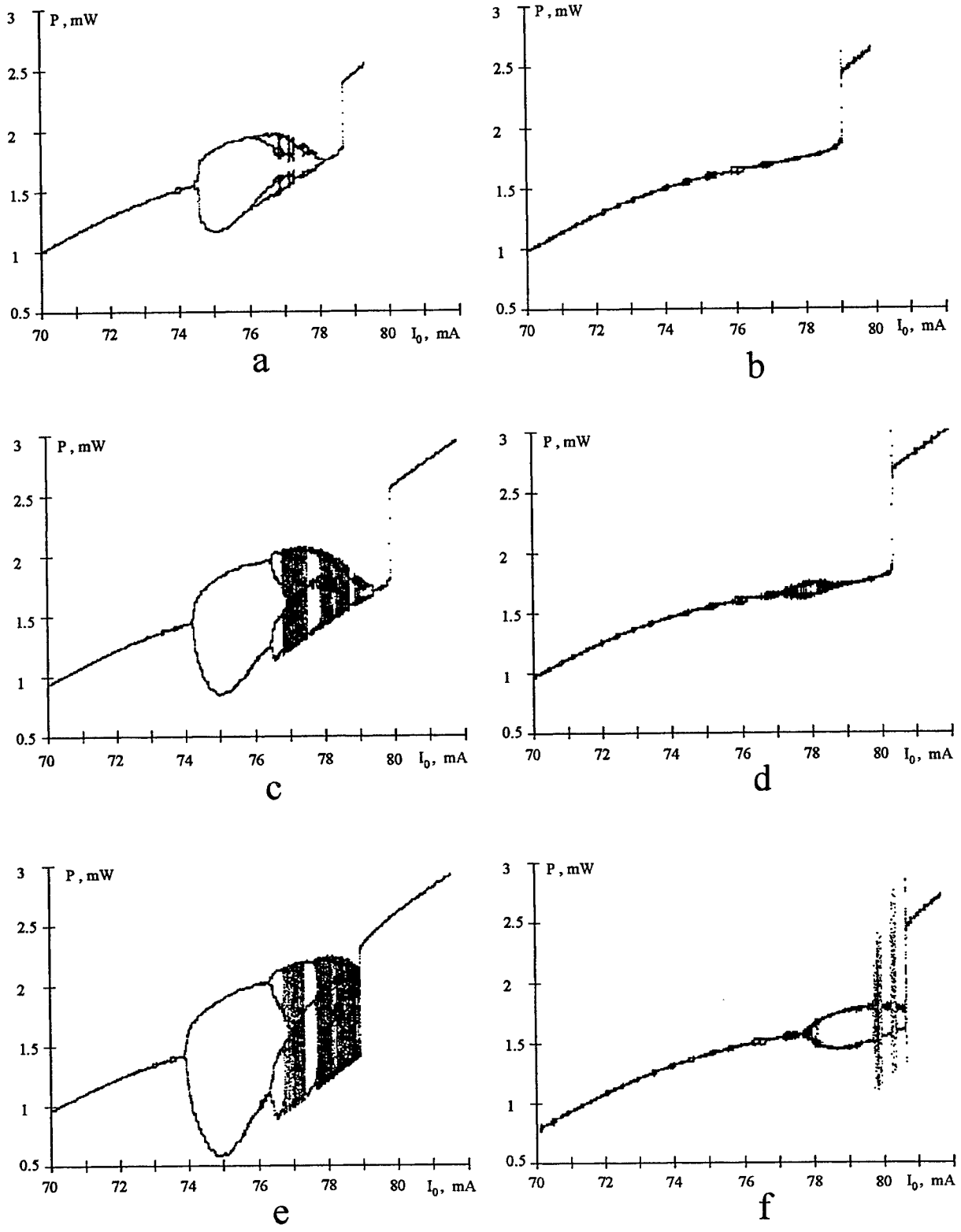


Fig. 7. The bifurcation diagram without and with proportional control (experimental results) for: a, b - K=0,4; c, d - K=0,6; e, f - K=0,8.

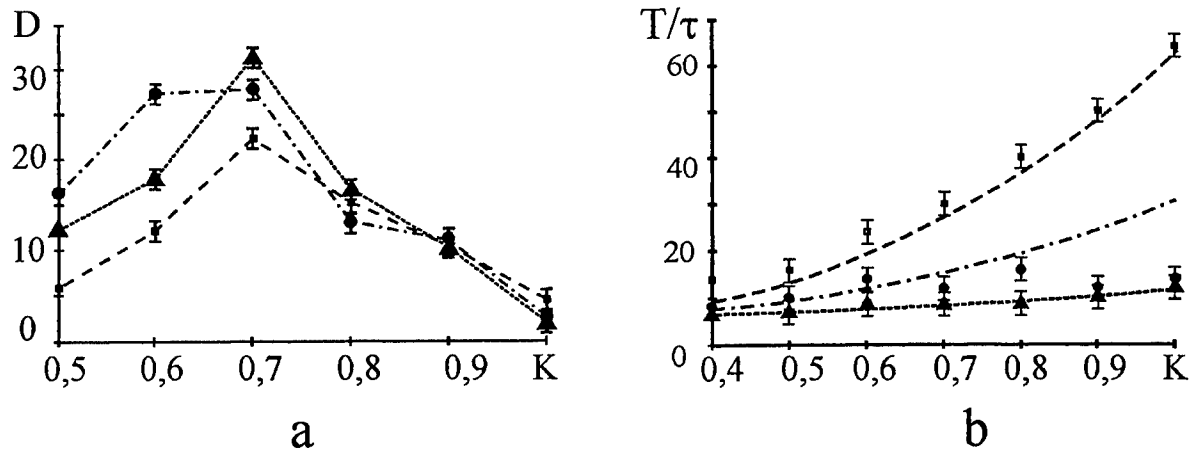


Fig. 8. Suppression degree (a), suppression time (b) versus dynamic complexity (experimental results).

The suppression degree D was determined as the ratio of the volumes occupied in the phase space ($\dot{P}$, P, I_0) without suppression and with it. This estimation of the suppression degree permits to take into consideration both a dynamics complexity and influence of the optical power amplitude. The suppression degree was calculated from the experimental data for every factor of amplification all over the injection current range.

The results are presented in Fig. 8a, the dash line and rectangle points correspond to the proportional control, the d& dot line and circle points correspond to the exponential control and the dot line and triangle points – to the combined control. With small amplification factors the suppression degree increases as the result of the system dynamics complexity. This behavior is in a good agreement with the exponential growing of the suppression degree proved by the numerical simulations. Here the suppression degree for the system with the combined control twice as much exceeds the suppression degree for the system with the proportional control, and the suppression degree for the system with the exponential control twice as much exceeds the suppression degree for the system with the combined control. However, when the amplification factor exceeds the critical value the similar decrease of the suppression degree is observed with increasing of the system dynamics complexity for all the three schemes of suppression.

The application of the combined suppression allowed to obtain only one gain, it was in the speed of the system transition from the chaotic to stable state. In order to estimate the speed, the transition time T was measured since the moment when the suppression scheme was switched on till the moment of establishing a stable mode. In Fig. 8b the relative transition time T/τ versus the amplification factor value for the injection current within the first chaotic region is illustrated. The dash line corresponds to the numerical simulations, rectangle points – to the experimental results for the proportional control, the d&dot line –to the numerical simulations, and circle points – to the experimental results for exponential control, and the dot line – to the numerical simulations, triangle points – to the experimental results for the combined control. In the scheme of the proportional control the transition time increases significantly with the chaotic oscillation amplitude increase. For the scheme with the exponential control the transition time is less noticeable. And for the scheme with the combined control the minimal transition time is achieved.

4. CONCLUSION

Thus the experiments show that the optical power dynamics of the semiconductor laser with a nonlinear delayed feedback could be suppressed by means of a small controlling signal exerting its influence on one of the controlling parameters of the system. The continuous disturbances make it feasible to synchronize one stable state not only from the chaotic oscillations but also from the low-dimension oscillations. As a result the full suppression is achieved for low complexity of the system dynamics. But as the dynamics complexity is growing, the suppression intensity becomes lower irrespective of the selected method of suppression. Probably it is caused by the fact that although the amplification factor is the system parameter, still the controlling signal finally effects the injection current, too. The suppression intensity practically does not depend on the controlling method and is decreasing with the increase of the system complexity. The suppression time for different methods was also measured. The type of the functional dependence of the controlling signal on the output power determined the value of the suppression time. It increased significantly with the rise of the system complexity in case of the proportional control, a low increase was observed in case of the exponential control and practically no increase and minimal level of the suppression time was in the combined control.

The use of the combined suppression method, simultaneously with two parameters, has only one advantage, the higher suppression speed, while the time of the transition from a chaotic to stable state decreases and weekly depends on the complexity of the system dynamics.

5. REFERENCES

1. Loiko N.A., Samson A.M., Kvantovaja electronika, 21, 713, 1994.
2. Roy R., Murphy T.W., et al. Phis. Rev. Lett., 68, 1259, 1992.
3. Dmitriev A. S., Panas A. I., Starkov S. O., Kuzmin L. V. International Journal of Bifurcation and Chaos, 7, 2511, 1997.
4. Takizawa T., Liu Y., Ohtsubo J. IEEE J. Quantum Electron., 30, 334, 1994.
5. Pyragas K. Phys. Lett. A, 170, 421, (1992).

Author Index

Abramochkin, Eugeny G., 237
Agishev, I. N., 125
Aleshkevich, Victor A., 315, 323
Alouini, M., 145
Andreev, Nikolay F., 29
Antipov, Oleg L., 84, 221
Apollonov, Victor V., 121
Araki, Kenichi, 247
Babin, S. A., 130
Bagrov, Ig. V., 115
Baraulya, V. I., 183
Basiev, Tasoltan T., 214
Belousov, Vlidilen P., 75
Belousova, Inna M., 75, 106, 115
Belyi, V. N., 157
Bretenaker, Fabien, 145
Brun, Alain, 138
Brunel, Michel, 145
Buscher, David F., 273
Chausov, Dmitry V., 221
Chauvat, D., 145
Clark, Paul, 273
Danilov, Oleg B., 75, 106
De Nicola, Sergio, 292
Deveaux, Fabrice, 308
Dolgopolov, Yu. V., 202
Domrachev, George A., 84
Douglas, William E., 84
Dubreuil, Nicolas, 138
Dunlop, Colin N., 273
Emile, Olivier, 145
Fedin, Alexander V., 214
Ferraro, Pietro, 292
Fimin, Pavel N., 51
Gavrilov, Andrey V., 214
Gavronskaya, E. A., 75
Georges, Patrick M., 138
Gerasimenko, Natalia N., 202
Gerke, Rudolf R., 46
Glova, Alexander F., 151
Grigor'ev, Vladimir A., 75, 106
Guralnik, Igor R., 1, 9
Gurov, Igor P., 281, 292
Hall, Thomas, 230
Hinze, Ulf, 130
Hlubina, Petr, 281
Jakutkin, V. V., 344
Jidkov, N. V., 92
Jonathan, Jean-Michel, 138
Kabanov, Vladimir V., 287
Kablukov, S. I., 130
Kalintsev, Alexander G., 75, 106
Kamanina, Natalia V., 75, 101, 115
Kaporskii, Lev N., 101, 115
Karapetyan, Garegin O., 23
Karasev, Vyatcheslav B., 51
Kargin, V. A., 92
Kartashov, Yaroslav V., 315, 323
Katranji, Evgeni G., 157, 164, 172
Kazak, Nikolai S., 157, 172
Kelly, Thu-Lan, 273
Khasanov, O. K., 125
Khazanov, Efim A., 29
Khilo, Nikolay A., 157, 164, 172
Khonineva, E. V., 69
Khramov, Valery Yu., 51
Klapshina, Larisa G., 84
Klingenberg, Hans H., 230
Kobtsev, S. M., 183, 189
Kochemasov, Gennady G., 202
Kopalkin, A. V., 202
Korablev, A. V., 189
Kotiaev, Oleg, 266
Kotlikov, E. N., 69
Kotova, Svetlana P., 242, 344
Kovaldov, S. A., 202
Koviazin, R., 292
Kris'ko, A. V., 75, 106
Krotov, V. A., 92
Kukarin, S. V., 183, 189
Kulikov, Stanislav M., 202
Kuzhelev, Alexander S., 84
Kyalbieva, Svetlana A., 214
Ladagin, Vladimir K., 202
Lamaghapov, H. D., 344
Lantz, Eric, 308
Le Floch, Albert, 145
Lebedev, Energui A., 151
Letfullin, Renat R., 59
Lipovskii, Andrey A., 23
Loboda, V. V., 23
Loktev, Mikhail Yu., 9
Lopatina, T. I., 84
Love, Gordon D., 273
Lysikov, A. Yu., 151
Maksimov, L. V., 23
Mehl, Oliver, 29
Meilhac, Laurent, 138
Mironova, N. G., 75, 106
Mizin, Vitaly M., 92
Molchanov, Vladimir Ya., 17
Musyona, E. I., 151
Myers, Richard M., 273
Naumov, Alexander F., 9
Nazarov, Vyacheslav V., 51
Okamoto, Atsushi, 247
Palashov, Oleg V., 29
Parygin, Vladimir N., 17
Pauliat, Gilles, 138
Pisarchik, Alexander N., 333

Ponomarev, Alexander N., 75
Poteomkin, Anotoly K., 29
Prokashev, V. N., 69
Pustovskikh, A. A., 183
Putilin, Eduard S., 51
Pyatakhin, Mikhail V., 92
Rakhmatulin, M. A., 242
Reitze, David H., 29
Roosen, Gérald, 138
Ropars, Guy, 145
Rubanov, Alexander S., 298
Ruliov, Andrey V., 214
Ryzhevich, Anatol A., 157, 164, 172
Sall, E. G., 46
Sawada, Hiroshi, 266
Semenov, Vladimir V., 84
Senatsky, Yuri V., 92
Serebryakova, Lyudmila M., 298
Sergeev, Alexandr M., 29
Shakir, Yu. A., 121
Sharples, Ray M., 273
Shchetnikov, S. B., 151
Sizov, Valentin N., 101
Smetanin, Sergey N., 214
Smirnov, Alexandre J., 256
Smirnov, V. A., 75
Sobolev, Serge K., 92
Sorokin, V. B., 183, 189
Sosnov, Eugene N., 75
Sozinova, I. V., 1
Spindler, Gerhard, 230
Starikov, Fedor A., 202
Stasel'ko, Dmitry I., 101
Sukharev, Stanislav A., 202
Svistunov, Dmitry V., 23
Tagantsev, Dmitrii K., 23
Takayama, Yoshihisa, 247
Tatarintsev, B. V., 23
Tiemann, E., 130
Tolstik, Alexei L., 125
Tul'skii, Stanislav A., 115
Uchida, Shigeaki, 266
Udoev, Yuri P., 41
Utkin, Andrei B., 256
Vallet, M., 145
Vetrov, Andrey A., 23
Victori, Stéphane, 138
Vinogradsky, Leonid M., 92
Vinokurova, Vera D., 46
Volkov, Mikhail V., 292
Voloshinov, Vitaly B., 17
Volostnikov, Vladimir G., 237, 242
Vysloukh, Victor A., 315, 323
Wellegehausen, Bernd, 130
Yakimovich, V. N., 125
Yarovoy, Vladimir V., 221
Yashin, Vladimir E., 75
Yur'ev, Michail S., 75, 106
Yurasova, I. V., 84
Zadrozny, Andrew, 273
Zaporozhchenko, Valentin A., 194
Zaporozhchenko, Yury V., 198
Zayakin, Oleg A., 59
Zgonnik, V. N., 75
Zhevlakov, Aleksandr P., 75, 115
Zubarev, Iosif G., 92